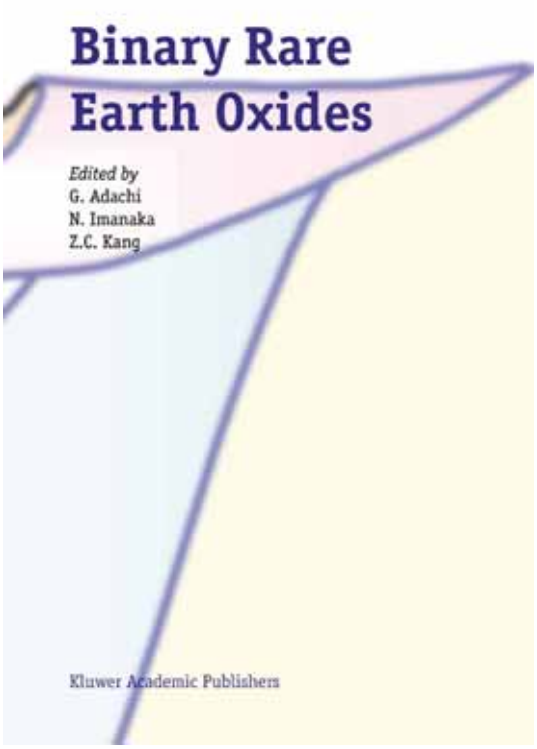
Binary Rare
Earth Oxides
Edited by
G. Adachi
N. Imanaka
Z.C. Kang
Kluwer Academic Publishers

Binary Rare Earth Oxides

Binary Rare Earth Oxides

Edited by

G. Adachi

Juri Institute for Environmental Science and Chemistry,
Osaka, Japan

N. Imanaka

Osaka University,
Osaka, Japan

and

Z.C. Kang

International Center for Quantum Structures
and State Key Laboratory for Surface Sciences,
Beijing, China

KLUWER ACADEMIC PUBLISHERS
NEW YORK, BOSTON, DORDRECHT, LONDON, MOSCOW

eBook ISBN: 1-4020-2569-6
Print ISBN: 1-4020-2568-8

Created in the United States of America

Visit Springer's eBookstore at: http://ebooks.springerlink.com
and the Springer Global Website Online at: http://www.springeronline.com

To Professor LeRoy Eyring

PREFACE

A number of functional materials based on rare earth oxides have been developed in various fields. Up to 1990, many review articles describing rare earth oxides have been reported and several intensive articles deal the properties e.g. preparation, structure and transformation and have been published early nineteen nineties. In these ten years, much progress has been made in the characterization of rare earth oxides from high-resolution electron microscopy (HREM), as well as in a unique preparation of ultra-fine particles and in the theoretical calculation.

The purpose to publish this book arose out of the realization that, although excellent surveys and reviews of rare earths are available, some of them have been already several decades passed since their publication and in these years, there is no single source covering the field of rare earth oxides. This book means to provide guidance through a comprehensive review of all these characteristics of rare earth oxides for scientists and engineers from universities, research organizations, and industries.

We have chosen a multi-author format in order to benefit from scientists who are active in their fields and who can give the best account for their subjects. As is true for nearly all fields of modern science and technology, it is impossible to treat all subjects related to rare earth oxides in a single volume. In the present case, therefore, we have focused on the binary rare earth oxides and their physical and chemical properties are mainly discussed in detail, because these provide both basic knowledge and fundamental aspects which make it possible to control a variety of properties in many materials.

We cordially hope that this reference book will be appreciated by material scientists and solid-state chemists with an interest in rare earth oxides, as well as researchers and graduate students who require an approach to familiarize them with this field.

The editors are much obliged to all those who cooperated in bringing this project to a successful close. In the first place, we thank the authors of the individual chapters. We are also grateful to Publishing Manager, Dr. Liesbeth Mol and the staffs of Mrs. Vaska Krabbe and Mrs. Marianne van den Hurk, Kluwer Academic Publishers. Finally, it is our great honor to dedicate this book to Professor Dr. LeRoy Eyring, who is a professor emeritus at Arizona State University and has done an enormous contribution not only to rare earth oxides but also to all aspects of rare earths.

Osaka, Japan
April 2004

Gin-ya Adachi
Nobuhito Imanaka
Zhenchuan Kang

TABLE OF CONTENTS

1. INTRODUCTION

G. ADACHI
Juri Institute for Environmental Science and Chemistry, College of Analytical Chemistry
2-1-8 Temma, Kita-ku, Osaka 530-0043, Japan

Z.C. KANG
International Center for Quantum Structures and State Key Laboratory for Surface Sciences,
Beijing 100080, People's Republics of China

1. Why are rare earth oxides so important?

From your personal items such as a portable compact disc player to a super computer or a huge atom-smashing accelerator, there are many rare earth materials having crucial roles in such systems. An automobile is a heap of rare earth materials. This is because rare earth ions exhibit some unique properties. Usefulness of rare earth materials for permanent magnets and luminescent materials for television and lighting systems goes without saying. Most of rare earth materials have been produced from rare earth oxides. Perovskite type rare earth mixed oxides are well known for high temperature super conductors, ferroelectric materials, or refining processes of rare earth metals needs their oxides as starting materials. Rare earth oxides are of importance for glass industry, for example, not only glass components but also surface polishing [1].

Most rare earth oxides are thermally stable, as well as chemically active. As is seen below, the C-type sesquioxides R_2O_3, are related to the fluorite structure CaF_2 or RO_2, from which the C-type sesquioxides are derived by removing one-quarter of the oxide anions. In other words, the C-type sesquioxides have a lot of defects which may act as effective diffusion paths for reactants at chemical reactions. Rare earth sesquioxides of other type structures too are in similar situation. Relatively, low reactivity of rare earth dioxide, CeO_2, are understandable form this point of view.

2. A variety of rare earth oxides

Oxidation states of rare earth ions in oxides can be understood in terms of reduction potentials. a) Generally the trivalent state is the most stable in aqueous solution and therefore, sesquioxides R_2O_3 exist for all rare earth ions [2]. However,

G. Adachi et al. (eds.), Binary Rare Earth Oxides, 1–7.

some conditions allow lower or higher oxides. As a matter of course, the composition of any rare earth oxide depends on the temperature, oxygen potential and whether or not it is in equilibrium although, the stability of the valence state of a given ion in aqueous solution is a good quick reference for the stability of the oxide.

The sesquioxides R_2O_3 crystallize in three forms, A-type(hexagonal), B-type(monoclinic) and C-type(cubic) structures, according to the ionic radius of the rare earth ion. Lighter rare earth ions, from La^{3+} to Nd^{3+} give A-form. These ions have happened to be seen to form the C-type structure, but this observation seems to be due to impurity stabilization or a metastable phase. An example of the B-type oxide is given by Sm_2O_3. Other rare earth sesquioxides yield the C-type oxides [3-6].

Stability of divalent ions is in order of $Eu^{2+} >> Yb^{2+} >> Sm^{2+}$ and a NaCl type monoxide EuO is the most stable one among these three monoxides but the existence of SmO seems to be doubtful. A unique orthorhombic 34 oxide Eu_3O_4 where Eu^{2+} and Eu^{3+} coexist is also stable [7].

The higher oxides where the oxygen to metal ratio x in the oxides is in the range of 1.5 to 2.0 are observed for cerium, praseodymium and terbium. These oxides exhibit fluorite-typed dioxides, which do not necessary mean x = 2.0 but usually the x value is slightly smaller than 2.0. Again, the composition of these oxides depends on the temperature, oxygen potential and physical state, besides their history of preparation and treatment [8-11].

This compositional obscurity is named as non-stoichiometry. However, the phase may mean an equilibrium state between stoichiometric oxides having slightly different composition. Details of this phase shall be discussed separately.

3. Simplicity and complexity of rare earth oxides

It is shunless to have some kinds of defects in solids, especially in transition metal oxides and rare earth oxides, because molecules of oxygen, which is a counter component of the metal oxide, are highly volatile even at low temperatures and are able to escape easily from the solid. More basically, the entropy term of the state requires the existence of defects. Most of the transport phenomena in solids, for example, diffusion of ions, are controlled by defects [12, 13].

In last century the knowledge of defects in a solid, especially an oxide, has been explored comprehensively. The contribution of Schottky and Wagner successfully put the problem on a quantitative basis and promote the discovery of semiconductor transistor. The idea of non-stoichiometry was developed by Berthollet more than a hundred years ago and the controversy between berthollides, which do not obey the Dalton's law, and daltonides, which follow Dalton's law of constant and multiple proportions based originally upon the study of simple ionic and molecular species, encouraged the scientific debates on how existence of point defect in a compound is: is it random statistic distribution or the structure related? The experimental data are the best way to explore the truth. Indirect and direct observations of atom

arrangement of a solid are powerful experimental method. X-ray, neutron, and electron diffraction theory and techniques were developed for indirect observation of atom structure of a compound [14] and high-resolution electron microscopy was developed for direct observation of atom arrangement of a compound at atomic level.

Now it seems to be clear that there are two categories of non-stoichiometry: (a) the non-stoichiometry of a compound is structurally accommodated, which means it does not caused by traditional "point defects", but by disordered arrays of blocks of ordered structure forming by corner- or edge-sharing of MO_6 octahedra and/or MO_4 tetrahedra. In other words, it contains the "chemical twinning", "crystallographic shear planes". Therefore, the result of a local rearrangement of coordination polyhedra eliminates the point defect. The compounds with a strong ligand field, for example transition metal oxides, always have this type of non-stoichiometry, and (b) the non-stoichiometry is due to assimilation of vacancies or interstitial atoms as structure elements of the crystal [15]. The non-stoichiometry of rare earth higher oxides is the best example. The composition domains in rare earth higher oxides have different content of oxygen vacancy, but the fluorite structure is still held with modulated displacement of metal and oxygen atom. Ordered oxygen vacancies of oxygen deficient fluorite-related rare earth higher oxides form the superstructures in parent fluorite lattice as homologous series phases, R_nO_{2n-2m}.

The so called "line phases" are compounds of ordered structure and definite composition. Thermodynamic sense means that in equilibrium a single phase has univariant: $\mu_i = \mu(T)$. However wide non-stoichiometry of rare earth higher oxides definitely has bivariant: $\mu_i = \mu(T, X)$ (X is oxygen content), even the homologous series phases also have bivariant because their oxygen content varies in narrow range as temperature changes. At constant oxygen partial pressure, the oxygen content of cerium, praseodymium, and terbium oxides varies as temperature increases or decreases and at constant temperature. The composition of cerium, praseodymium, and terbium oxides varies as oxygen partial pressure increased or decreased. The response time of composition change of the rare earth higher oxides for varying temperature or oxygen partial pressure is very short (for example at 300 ^oC it is about a second for PrO_x). It is worth to notice that the published phase diagrams of CeO_2-O_2, PrO_2-O_2, and TbO_2-O_2 only given the existed phases, but it does not mean that the composition of a phase existed at corresponding temperature shown on the diagram, because these diagrams were built at different oxygen partial pressures. Usually a phase diagram is built at a constant pressure, for example one atmospheric pressure.

In general, the point defect in a crystal is a function of temperature, especially at higher temperature, but not sensitive to the environment oxygen pressure or temperature. However, the oxygen vacancy in cerium, praseodymium, and terbium oxides communicates with the environment oxygen.

$$4M^{4+} + O^{2-}/\square_{ox} \rightarrow 4M^{4+} + 2e^{-}/\square_{ox} + 1/2O_2 \leftrightarrow 2M^{4+} + 2M^{3+} + \square_{ox} + 1/2O_2$$

The reaction between gas oxygen and oxygen vacancy in the oxides is easy and fast even at above 300 ^{o}C as mentioned before. This is a unique feature of rare earth higher oxides.

For transition metal oxides, for example TiO_2, the non-stoichiometry does not create the "point defect" and is induced by the "crystallographic shear planes" and intergrowth of "chemical twinning" block structures. The oxygen content variation is due to changing the corner-or edge-sharing of the MO_6 octahedra. This change may be related to the valence variation of the metal and form mixed valence compound. The electron transfer between different metal cation usually has to be helped by the ligand oxygen, i.e. M-O-M. However the electron hopping between the rare earth cation is facilitated by oxygen vacancy having positive charge. Therefore correlation between oxygen vacancy and mixed valency is a significant property for rare earth higher oxides.

Based on thermodynamics, the "point defects" in a solid lattice are natural tendency due to increasing the configuration entropy to minimizing the free energy of the system. However, the oxygen vacancy and non-stoichiometry of rare earth higher oxides are closely related to a peculiar electron configuration of cerium, praseodymium and terbium atom and inscrutable relationship between the valence instability and the electron transfer of 4f electron of the Ce, Pr, and Tb cations. Decipherment of these formidable relationships will make the rare earth higher oxides to be most important materials for catalyst, solid oxide fuel cell, sensor, and hydrogen production devices [16].

Surface, interface between two grains or phases, dislocation, and stacking faults are the imperfections of a solid. In rare earth sesquioxides, the twining and twin boundary are common phenomenon. Especially in B-type of rare earth sesquioxide the twinning is basic feature due to its low symmetry of the structure. The phase transformation between A- and B-type or C- and B-type structure of rare eath sesquioxides can form the twinning and twin boundary. Mechanical stress may also cause the twinning [17]. In rare earth higher oxides the twinning is not dominate imperfection, but the composition domain boundary, which is coherent interface, dislocation and stacking fault usually have been observed. The surface of rare earth oxide has steps and the facet of the steps usually is closed packing plane, especially in the rare earth oxides with C-type and fluorite-related structure.

Professor L. Eyring spent 50 years to search and to decipher the formidable structural principle of the rare earth higher oxides and the clue unraveling the mysterious phenomena in non-stoichiometry of the rare earth higher oxides. There are several reasons to be resisted solution for these problems, one of which is that the synthesis of complete ordered crystal of these rare earth higher oxides is inhibited by the extraordinary ease of transfer of oxygen between the RO_x lattice and gaseous oxygen.

Since the mid 1970s, the principle and technique of transmission electron microscopy have made significant progress, in which the electron beam probe can

be minimized to less than 1 μm and imaging technique is able to demonstrate the atom arrangement of a small thin crystal on an image with atomic scale. Eyring immediately used these techniques to solve the formidable task. The micro-beam electron diffractions have revealed the unit cell dimensions, space groups, and transformation matrices defining the unit cells in terms of the fluorite subcell. In comparison of the electron diffraction data with thermodynamic data of the rare earth higher oxides there are some contradictions, especially the composition derived from the formulae of the homologous series, R_nO_{2n-2}, and the tensimetric thermodynamic data.

Based on the understanding the structure of the R_7O_{12} phase, Eyring suggested that linear infinite RO_6 "strings", surrounded by a contiguous "sheaths" of RO_7, were the structural entities that generated the series R_nO_{2n-2} from the parent RO_2 [18]. If 1/n of the cations were located in the "strings", the compositions of the ordered phases become $RO_{2\ [1-1/n]}$ or R_nO_{2n-2}. The "string" might then be regarded as the "extended defect" in the f transition metal oxides analogous to the Wadsley "shear defect" in the d transition metal oxides.

The formula, $R_nO_{2n-2,}$ was used as the generic homologous series formula of the rare earth higher oxides for more than 30 years until Kang and Eyring established an all-inclusive formula, R_nO_{2n-2m}, based on the fluorite-type module theory.

Using high-resolution neutron diffraction data, Eyring published the refined structures of Tb_7O_{12}, Pr_9O_{16}, $Pr_{40}O_{72}$, $Tb_{11}O_{20}$, and $Pr_{24}O_{44}$. These refined structures have useful information for structural principle of rare earth higher oxides [19].

In 1996, Kang and Eyring published the fluorite-type module theory [20], which rationalizes all of the known experimental intermediate phases in the rare earth higher oxides into the single generic formula $R_nO_{2n-2m.}$ The fluorite-type module theory is not only providing a method to modeling the structure, but also giving the basis for elucidating the hysteresis, transition between homologous series phases, and interaction between the oxide and gas oxygen. For example, the thermodynamic data show that when the temperature is decreased from 800 ^oC to 650 ^oC the Pr_7O_{12} is transformed to the Pr_9O_{16} at 150 Torr oxygen partial pressure according to the following reaction.

$$9Pr_7O_{12} + 2\,O_2 = 7Pr_9O_{16}$$

The Pr_7O_{12} phase is the most reduced phase in the homologous series of the praseodymium oxides. The seven fluorite-type modules that compose the structure of the Pr_7O_{12} phase contain one W and six U and V unit modules. The meaning of these symbols will be given in 3.2.4. As this is oxidized to the Pr_9O_{16} phase the module W disappears, and an F module has replaced it. Using the modular formula to write the above reaction, it will be:

$$9\,(W3U3V) + 8\,O_2 = 7\,(F4U4V)$$

or $9W\ 27U27V + 8O_2 = 7F28U28V$

or $9W + 8\,O_2 = 7FUV$

These equations may be stated as follows: there are two W modules each of which absorbs one oxygen atom to become a U or V module. Each of remaining W modules takes two oxygen atoms to become F modules. The reaction process is the absorption of oxygen from the gaseous phase at the surface followed by oxygen migration into the bulk. The oxygen atoms migrating from the surface fill the oxygen vacancies in the W modules. This changes the W modules to F, U or V modules with the concomitant change of the coordination numbers of the cations producing the oxidized phase Pr_9O_{16}.

It seems that as the module theory developed the knowledge of rare earth higher oxides may be matured and multi-component rare earth higher oxides may be developed. Rare earth higher oxides, for which Professor L. Eyring spent his lifetime to understand, will be the most important materials for catalyst, solid oxide fuel cell, hydrogen production, and sensors.

References

1. K.A. Gschneidner, Jr. ed., *Industrial Applications of Rare Earth Element*s, ACS Symposium Series 164, American Chemical Society, Washington, D.C., 1981.
2. G.R. Choppin, Chemical properties of the rare earth elements, in J.-C.G. Bunzli and G.R. Choppin (eds.), *Lanthanide Probes in Life, Chemical and Earth Sciences*, Elsevier, Amsterdam, p.1, 1989.
3. L. Eyring, The binary rare earth oxides, in *Handbook of Physics and Chemistry of Rare Earths*, Vol. 3, eds. K.A. Gschneidner, Jr., and L. Eyring, North Holand, Amsterdam, p.337, 1979.
4. H. Bergmann (ed.), Gmelin Handbuch der Anorganischen Chemie, Seltenerdelemente, Teil C1, No. 39, Springer-Verlag, Berlin, p.85, 1974.
5. A.F. Wells, *Structural Inorganic Chemistry*, Oxford Science Publications, Oxford, p.543, 1984.
6. G. Adachi and N. Imanaka, *Chem. Rev.*, **98**, 1479 (1998).
7. M.W. Shafer, J.B. Torrance, and T.J. Perry, *J. Phys. Chem. Solids*, **33**, 2251 (1972).
8. U.E. Kuntz and L. Eyring, Diffusion of Oxygen in Rare-earth Oxides, in W.D. Kingery (ed.), *Kinetics of High-Temperature Processes*, John Wiley & Sons, Inc., New York, p.50, 1959.
9. L. Eyring, The Binary Rare Earth Oxides: Synthesis and Identification, in G. Meyer and L.R. Morss (eds.), *Synthesis of Lanthanide and Actinide Compounds*, Kluwer Academic Publishers, Dordrecht, p.187, 1990.
10. L. Eyring, The Higher Oxides of the Rare Earths; A Paradigm for Solid State Chemistry, in R. Saez Puche and P.A. Caro (eds.), *Rare Earths*, Editorial Complutense, Madrid, p.119, 1998.
11. A. Trovarelli, Structural Properties and Nonstoichiometric Behavior of CeO_2, in A. Trovarelli (ed.), *Catalysis by Ceria and Related Materials*, Imperial College Press, London, p.15, 2002.
12. Z.M. Jarzebski, translated by B. Grzybowska-Swierkosz, *Oxide Semiconductors*, Pergamon Press, Oxford, 1973.
13. F.A. Kroeger, *The Chemistry of Imperfect Crystals*, North-Holland Publishing, Amsterdam, 1964.
14. A. Guinier, *X-ray Diffraction*, W.H. Freeman and Company, San Francisco and London, 1963; B.K. Vainshtein, *Structure Analysis by Electron Diffraction*, Pergamon Press, 1964.
15. J.S. Anderson, The Thermodynamics and Theory of Nonstoichiometric Compounds, in A. Rabenau (ed.), *Problems of Nonstoichiometry*, North-Holland Publishing Company, p.1, 1970.

16. J.P. Connerade and P.R.C. Karnatak, Electronic Excitation in Atomic Species, in K.A. Gschneidner, Jr. and L. Eyring (eds.), *Handbook of Physics and Chemistry of Rare Earths*, Vol.28, Elsevier, Amsterdam, p.1, 1979.

17. C. Boulesteix, Defects and Phase Transformation Near Room Temperature in Rare Earth Sesquioxides, in K.A. Gschneidner, Jr. and L. Eyring (eds.), *Handbook of Physics and Chemistry of Rare Earths*, Vol.5, Elsevier, Amsterdam, p.321, 1982.

18. B.G. Hyde, D.J.M. Bevan, and L. Eyring, *Internat. Conf. Electron Diffraction and Crystal Defects*, Austral. Acad. Sci., C-4, p.11, 1965.

19. J. Zhang, R.B. Von Dreele, and L. Eyring, *J. Solid State Chem.*, **104**, 21 (1993); J. Zhang, R.B. Von Dreele, and L. Eyring, *J. Solid State Chem.*, **118**, 133 (1995); J. Zhang, R.B. Von Dreele, and L. Eyring, *J. Solid State Chem.*, **118**, 141 (1995); J. Zhang, R.B. Von Dreele, and L. Eyring, *J. Solid State Chem.*, **122**, 53 (1996).

20. Z.C. Kang, J. Zhang, and L. Eyring, *Z. Anorg. Allg. Chem.*, **622**, 465 (1966); Z. C. Kang and L. Eyring, *J. Alloys. Comp.*, **249**, 206 (1997); Z.C. Kang and L. Eyring, *Aust. J. Chem.*, **49**, 981 (1997).

2. CHEMICAL REACTIVITY OF BINARY RARE EARTH OXIDES

S. BERNAL, G. BLANCO, J.M. GATICA, J.A. PÉREZ-OMIL, J.M. PINTADO, H. VIDAL
Departamento de Ciencia de los Materiales, Ingeniería Metalúrgica y Química Inorgánica, Facultad de Ciencias. Universidad de Cádiz, Apartado 40. E-11510, Puerto Real (Cádiz), Spain

2.1. INTRODUCTION

Despite the term traditionally applied to this group of elements, rare earths, their crustal abundance is not particularly low. Cerium ranks around 25th in the listing of all the naturally occurring elements, its abundance being similar to that of Ni or Cu [1]. Even the least abundant lanthanoid elements, Tb, Tm, and Lu, are more abundant than Ag [2]. Because of their geo-chemical characteristics, however, the rare earth-containing minerals consist of mixtures of the elements with relatively low concentration of them [3]. Accordingly, the number of their exploitable deposits, mainly consisting of phosphates and fluoro-carbonates, is rather small [1,3].

The development of appropriate separation technologies has therefore represented a classic, very challenging, chemical and technological problem [3]. Wet methods are presently used for this purpose [3,4]. Though laborious, these methods have allowed the preparation of high purity rare earths at, in some cases, reasonable costs. As a result, a continuous increase of the research effort on lanthanoid-containing materials, and particularly on their oxides, has occurred during the last twenty five years. Very recently, an alternative dry procedure, very much enhancing the separation efficiency of the in-use technology, has been developed [5]. As stressed in [3], the application of this new methodology would substantially reduce the number of separation steps, and therefore, the overall production costs. A scenario of accelerated increase of both fundamental and applied research on rare earth oxides may reasonably be devised for the years to come.

As deduced from a recent review work [6], a great deal of data on the structural, physical and chemical properties of the binary rare earth oxides are presently available. This wealth of information has substantially modified our view about them. Formerly considered as a rather exotic group of oxides, with mainly academic interest, it is presently acknowledged that they may find very relevant applications as catalysts [7-11], optical materials [1,2,4,12,13], or ionic conductors [14-17]. Some of these applications have reached the technological maturity, large scale industrial consumption of the rare earth oxides being associated with them [4]. Such is the case of the three-way catalysts [9,10,18,19], or the lighting applications of lanthanoid-containing photo-luminescent materials [1,4,13].

This chapter is aimed at reviewing the chemical reactivity of rare earth oxides. Special attention will be paid to those aspects closely related to the thermal

G. Adachi et al. (eds.), Binary Rare Earth Oxides, 9–55.

and chemical environments associated with their current applications either as pure phases, as components of multi-phasic systems, or as reactants in the preparation of several other lanthanoid-containing materials.

From the chemical point of view, the lanthanoid elements are characterized by a regular variation of their 4f electron configuration throughout the series, Table 2-1. Due to the nature of the orbital group, (n-2)f, involved in the variation of their electron configuration, these elements are often referred to as the first inner transition series. Inherent to this peculiar electron configuration, the lanthanoid elements show a number of atomic properties that are considered to determine the chemical and structural properties of their compounds, and, particularly, those of their oxides.

TABLE 2-1. Some relevant properties of the lanthanoid elements

Element	Electron Conf.	ΔH^{o}_{atom} (KJ.mol^{-1})	ΣIP (1-3) (KJ.mol^{-1})	4th. IP (KJ.mol^{-1})	$r_{ion}(M^{3+})$ (pm)*
La	$5d^1 6s^2$	431.0	3455	4819	117
Ce	$4f^1 5d^1 6s^2$	420.1	3523	3547	115
Pr	$4f^3 6s^2$	356.9	3627	3761	113
Nd	$4f^4 6s^2$	326.9	3697	3899	112
Pm	$4f^5 6s^2$	-----	3740	3966	111
Sm	$4f^6 6s^2$	206.9	3869	3994	110
Eu	$4f^7 6s^2$	177.4	4036	4110	109
Gd	$4f^7 5d^1 6s^2$	397.5	3749	4245	108
Tb	$4f^9 6s^2$	388.7	3791	3839	106
Dy	$4f^{10} 6s^2$	290.4	3911	4001	105
Ho	$4f^{11} 6s^2$	300.6	3924	4101	104
Er	$4f^{12} 6s^2$	316.4	3934	4115	103
Tm	$4f^{13} 6s^2$	232.4	4045	4119	102
Yb	$4f^{14} 6s^2$	155.6	4194	4220	101
Lu	$4f^{14} 5d^1 6s^2$	427.6	3887	4360	100

Ionic Radius for Y^{3+} (C.N. = 6): 104 pm
(*) Shannon ionic radii (C.N. = 6) taken from ADVANCED INORGANIC CHEMISTRY (6th. Ed.), F.A. Cotton, G. Wilkinson, C.A. Murillo, and M. Bochman; John Wiley & Sons (1999)

As deduced from Table 2-1, the lanthanoid elements show relatively low standard atomization enthalpies and ionization potentials. These properties make them highly active reducing metals, with Allred-Rochow electronegativities ranging from 1.01 (Eu) to 1.14 (Lu), similar to that reported for Ca (1.04) [20].

In accordance with the variation observed in their successive ionization potentials, Table 2-1, the (3+) oxidation state is a common characteristic chemical feature of the lanthanoid series. With a few exceptions, typically associated with elements having a relatively low fourth ionization potential (Ce, Pr, Tb), Table 2-1, the (3+) oxidation state exhibits a high stability. In the case of the three elements mentioned above, the (4+) oxidation state is very relevant as well. In particular, higher oxides, i.e. dioxides and mixed-valent (+3/+4) compounds are well known for

them. In the latter case, an extensive and complex homologous series, whose generic formula is Ln_nO_{2n-2m}, has been prepared and characterized [6,21]. As will be shown throughout this chapter, these oxides, particularly ceria and ceria-based mixed oxides, are finding very interesting applications [9,11]. Thermochemical data corresponding to both sesquioxides and dioxides of the lanthanoid elements are reported in refs. [22,23].

Lower rare earth oxides, those corresponding to the occurrence of the (2+) oxidation state, are also known. The information currently available about them has been recently reviewed [6]. In accordance with the standard redox potentials reported in [24], for Ln^{3+}/Ln^{2+} pairs (Ln: Sm, Eu, Tm and Yb), in solution, the Ln (2+) ions typically behave as reducing species, Eu^{2+} being by far the less reductant of them (ε^o Eu^{3+}/Eu^{2+}: -0.35 V; to be compared with those for Sm^{3+}/Sm^{2+}: - 1.5 V; Tm^{3+}/Tm^{2+}: - 2.3 V; Yb^{3+}/Yb^{2+}: - 1.1 V). This observation may qualitatively be extended to the oxides, LnO, that of Eu showing the highest stability [6].

In general, strong reducing conditions are required for the preparation of LnO phases [6]. Thus, EuO can be obtained by heating a mixture of the metal and the corresponding sesquioxide at 2053-2098 K [25]. Though some other monoxides have been proposed to occur, all of them with NaCl-type structure [6], EuO and YbO are probably the best characterized ones [6,26]. In the case of Eu, a mixed-valent Eu^{2+}/Eu^{3+} oxide, Eu_3O_4, has also been prepared by reducing the sesquioxide in a flow of hydrogen, at 1573 K [27].

In accordance with the special thermal/chemical conditions required for the preparation of LnO oxides, and their inherent strong reducing behavior, the rare earth mono-oxides cannot be easily stabilized and manipulated. This probably explains why they have not been extensively investigated nor found relevant applications as yet.

The Ln^{3+} ions exhibit large ionic radii ranging from 117 pm for La^{3+} to 100 pm for Lu^{3+}, Table 2-1. Also well known, the Ln^{3+} radii steadily decrease throughout the series as a result of the so-called lanthanoid contraction effect. These are very characteristic chemical features of the lanthanoid elements.

Because of the inner nature of the 4f orbitals, the differences of electron configuration between the lanthanoid elements are associated to electrons relatively well screened from the chemical surroundings by the outer ($5s^2p^6$) shell. This implies weak crystal fields splitting effects [28], and a relatively small covalent contribution to the bonding, particularly in the sesquioxides. Accordingly, the ionic model plays an important role in determining their chemistry [21]. Also related to these chemical characteristics, the lanthanoid compounds exhibit a rich variety of structures, often reflected in the occurrence of polymorphism phenomena.

In accordance with the well known phase diagram for the rare earth sesquioxides [6], as much as five different structural varieties have been identified for them. They are referred to as: A, B, C, H, and X types. A theoretical analysis of the equilibrium crystal lattice dimensions for A, B, and C structures in Ln_2O_3 has also been recently reported [29]. Three of the polymorphs above, the hexagonal, A-type, monoclinic, B-type, and cubic, C-type, are known to occur at room temperature, and atmospheric pressure, whereas H and X forms have only been observed at temperatures above 2273 K [6]. For the lighter members of the series, La through Nd, though not exclusively [6,30], the hexagonal, A-type, form is the most usually found, Fig. 2-1. By contrast, the heaviest lanthanoid sesquioxides, from

Gd_2O_3 onwards, normally occur as cubic, C-type, phase. For Sm and Eu, though the stable form under the usual temperature and pressure conditions is the cubic one, the rate of B $\rightarrow$ C phase transition is slow enough as to allow the observation of the monoclinic phase at room temperature and atmospheric pressure.

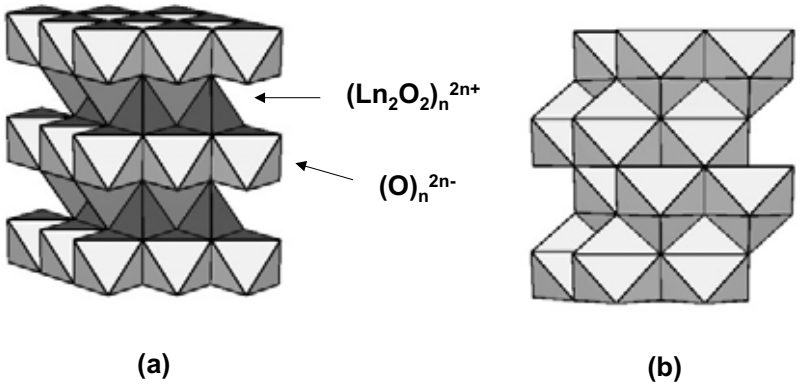

Figure 2-1. A-Ln_2O_3 structure. It consists of a hcp Ln^{3+} sublattice with one half of both octahedral and tetrahedral holes occupied by O^{2-} (a). The $(Ln_2O_2)_n^{2n+}$ layers have C_3 symmetry. An alternative description consists of linked sevenfold LnO_7 polyhedra (b).

The considerations above suggest that the rare earth oxides, particularly the sesquioxides, might well be described as an ensemble of mainly ionic, basic oxides made up by cations with a rather large size smoothly decreasing throughout the series. This regular variation, as a result of which the basic behavior of the sesquioxides would be expected to steadily decrease throughout the series, makes them an appealing family of oxides for checking the likely existence of correlations between chemical properties, particularly acid-base behavior, and their catalytic activity and selectivity [7]. A number of attempts pointing at this direction have been reported in the literature [31].

These general principles have allowed Johnson [32] to propose the existence of two major categories of chemical processes involving the lanthanoid elements. The first one, that implying changes in their oxidation state, would be essentially controlled by the differences in their successive ionization potential. For this group of processes, irregular variations of behavior throughout the lanthanoid series should be expected to occur. The second category would consist of reactions implying no changes in the oxidation state of the rare earth elements. In accordance with [32], in this second case, the chemical behavior would show a rather smooth regular variation throughout the series. When applied to the oxides, the first category of reactions would obviously be related to their redox chemistry. In the second category, the acid-base processes might well be included. Some relevant examples of these two types of chemical processes involving the rare earth oxides will be discussed in the following sections. Accordingly, this chapter has been organized in two major sections. The first one, will be devoted to the rare earth sesquioxides, the reactivity of which is mainly determined by their acid-base properties. The second

one will deal with the reactivity of the higher oxides, being therefore focused on their redox chemistry.

2.2. CHEMICAL REACTIVITY OF THE RARE EARTH SESQUIOXIDES

2.2.1. *Preliminary Considerations about the Ln_2O_3-H_2O-CO_2 System*

Because of their acknowledged basic character [7], the rare earth sesquioxides are expected to be highly active against H_2O and CO_2. In fact a good deal of information is at present available about the ternary system Ln_2O_3-CO_2-H_2O. In the next pages we shall review this information. The attention will be focused on two major aspects: the processes occurring when the oxides are exposed to atmospheric CO_2 and H_2O under the usual storage and handling conditions, and those inherent to their soaking in water, at room temperature, under variable CO_2 pressure. These latter conditions are, for instance, those occurring during the preparation of rare earth oxide-supported metal catalysts [33-36].

To rationalize these behaviors, we shall review first the information available on the phases belonging to the binary systems: Ln_2O_3-H_2O and Ln_2O_3-CO_2, then we shall analyze the structural nature of the ternary phases: Ln_2O_3-H_2O-CO_2. Finally, we shall discuss the chemical aspects of these interactions.

This section is aimed at establishing how the textural, structural and chemical properties of the rare earth oxides are modified by their interaction with the atmospheric H_2O and CO_2. Both, thermodynamic and kinetic information about the aging-in-air phenomena is relevant. Likewise, the nature of the phases resulting from these processes, and the way of recovering the oxides from them will be analyzed. This information can be critically important to fully understand their behavior, and to properly use them when applied as pure oxides, as one of the phases constituting a multi-component system, or as starting reactant in the preparation of a variety of materials.

2.2.1.1. Phases Belonging to the Ln_2O_3-H_2O System

Though a number of phases resulting from the hydration of the rare earth sesquioxides have been suggested to occur, only two are well characterized: the hydroxide, $Ln(OH)_3$, Fig. 2-2, and the corresponding oxy-hydroxide: LnO(OH), Fig. 3-3. The first one is known for all the lanthanoid elements. Except the hydroxide of lutetium for which a cubic structure (Space group: Im3) has been reported [37], all the rare earth hydroxides show a hexagonal UCl_3-type structure (Space Group: $P6_3/m$) [38]. According to [39], the reaction of the lanthanoid sesquioxides with water leads to the corresponding hydroxides phases, the process becoming slower and less intense throughout the series. Though this point will be discussed below in some detail, it has been stated that from Dy_2O_3 onwards bulk hydration is impossible, even by soaking the oxides in boiling water [39].

If lanthana is previously treated with CO_2, however, the hydration reaction becomes slower [40]. Also worth of noting, with a few exceptions, like the one reported in ref. [41], where the hydration of the monoclinic B-Nd_2O_3 is proposed to occur through an intermediate NdO(OH) phase, there is a general agreement in the sense that the hydration of the rare earth oxides leads directly to the formation of the corresponding hydroxide [39].

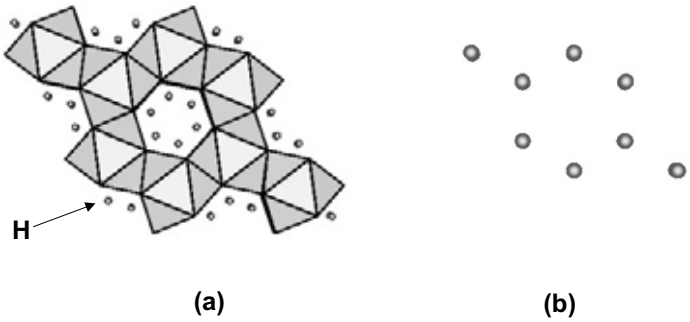

Figure 2-2. The structure of $Ln(OH)_3$ contains a ninefold coordinated polyhedra showing empty columns (a). The projected cation sublattice along the c-axe shows a close relationship with the hcp sub-structure present in A-La_2O_3 (b) but expanded.

The oxyhydroxide phase, LnO(OH), has been identified in experimental studies aimed at establishing the phase diagram for the binary Ln_2O_3-H_2O system under hydrothermal conditions [42,43]. It has also been observed as intermediate phase in the decomposition of the hydroxides[7,30,43-49]. Though not proved, it has been suggested that the two step decomposition of $Ln(OH)_3$ to Ln_2O_3 throughout LnO(OH) requires the presence of traces of carbonate species [50].

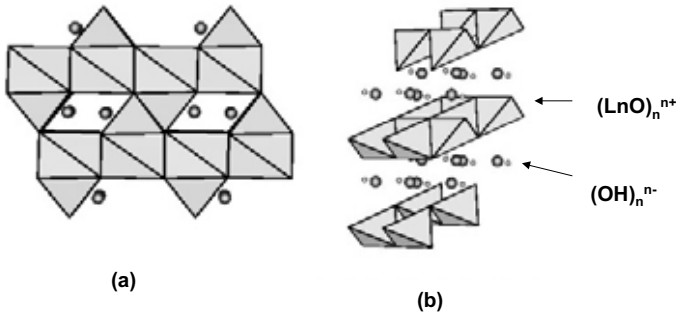

Figure 2-3. LnOOH structure. The cations (a) are sevenfold coordinated and the oxygen anions fourfold coordinated (b). The $(LnO)_n^{n+}$ layers have a symmetry (C_4) different from the one observed in Ln_2O_3.

The lanthanoid oxyhydroxides, LnO(OH), show a monoclinic structure which can be described in terms of $(LnO)_n^{n+}$ layers consisting of sharing edges tetrahedral OLn_4 units, the interlayer space being occupied by the OH^- groups. As will be commented on further below, the structure of a number of phases belonging to the Ln_2O_3-H_2O-CO_2 system can be described with the help of layer models like the one mentioned above [51].

The lanthanoid hydroxide and oxyhydroxide phases have also been characterized by means of infrared spectroscopy [30,37,45,46,52-58]. The

hexagonal $Ln(OH)_3$ phases exhibit two characteristic features: a strong narrow band at 3600 cm^{-1}, the position of which not being very much sensitive to the nature of the lanthanoid cation [54], that has been assigned to the stretching mode of the hydroxide ions [53,54]; and an intense and broader band, the wavenumber of which shifting from 640 cm^{-1} for $La(OH)_3$ [57], to 650 cm^{-1} for $Nd(OH)_3$ [56], and to 680 cm^{-1} for $Sm(OH)_3$ [58]. In accordance with the structural analysis of the vibration modes of the hexagonal $Ln(OH)_3$ phase reported in [54], this latter band has been assigned to a deformation mode Ln-O-H [55]. In the case of a $La(OH)_3$ sample prepared by "in situ" hydration of the oxide, two O-H stretching bands at 3590 and 3610 cm^{-1} are observed. They are interpreted as due to the two structurally distinct hydroxyl species present in the hydroxide [52]. In [52], the dehydration of the hydroxide phase was also investigated by heating the sample disk in an infrared cell, under vacuum, at increasing temperatures. The authors observe two decomposition steps. During the first one, at 473 K, the high frequency OH species would be preferentially eliminated, thus leading to the corresponding oxyhydroxide phase, LaOOH, which would be further dehydrated to sesquioxide at 573 K, under vacuum. In accordance with this interpretation, the OH stretching region of the LaO(OH) infrared spectrum would be characterized by a major band at 3590 cm^{-1}. Also characteristic, this latter band shows a broad tail towards the low frequency region interpreted as due to extensive hydrogen bonding. This interpretation was further confirmed by parallel hydration/dehydration experiments with D_2O [52].

The structural evolution undergone by a $La(OH)_3$ gel throughout its decomposition to sesquioxide has also been investigated by EXAFS [59] and ^{17}O-NMR spectroscopy [44]. Though EXAFS data suggest the formation of highly disordered phases which do not allow their unambiguous characterization [59], the changes occurred in the ^{17}O-NMR spectra support that, as already noted, the decomposition process takes place throughout a LaO(OH) intermediate phase.

2.2.1.2. Phases Belonging to the Ln_2O_3-CO_2 System

The most interesting Ln_2O_3-CO_2 binary phases are the three well characterized structural varieties of lanthanoid dioxymonocarbonate: $Ln_2O_2CO_3$. Amorphous or very poorly crystallized anhidrous phases, $Ln_2(CO_3)_3$, resulting from the dehydration of the corresponding hydrated carbonates are also known.

The dioxymonocarbonate phases are known for the whole series of lanthanoid elements [60]. They are stable intermediate phases in the thermal decomposition to oxides of a number of salts including: formates [61,62], acetates [63-67], benzoates [66], oxalates [67,68], carbonates [69-71], and hydroxycarbonates [69,72-76]. In [60], the structural nature of the three lanthanoid dioxymonocarbonate phases is discussed. They are referred to as I (Tetragonal; Fig. 2-4a), IA (Monoclinic) and II (Hexagonal; Fig. 2-4b). All of them can be described as layered structures built up of slabs of $(Ln_2O_2^{2+})_n$, the carbonate ions occupying the interlaminar space. Type I, isostructural of the $Bi_2O_2CO_3$, would consist of layers like the ones exhibited by the lanthanoid oxyhydroxides or oxychlorides, LnOCl. As deduced from the results reported in [60], type I polymorph is known for all the lanthanoid elements. Type IA, which has been prepared for lanthanum and praseodymium, can be described as a monoclinic distortion of the tetragonal unit cell of type I [60]. Finally, type II would consist of hexagonal $(Ln_2O_2^{2+})_n$ layers like

those found in A-Ln_2O_3 sesquioxides. Type II polymorph has been identified for the lighter lanthanoid elements: La, Pr, Nd, Sm, and possibly Gd [60].

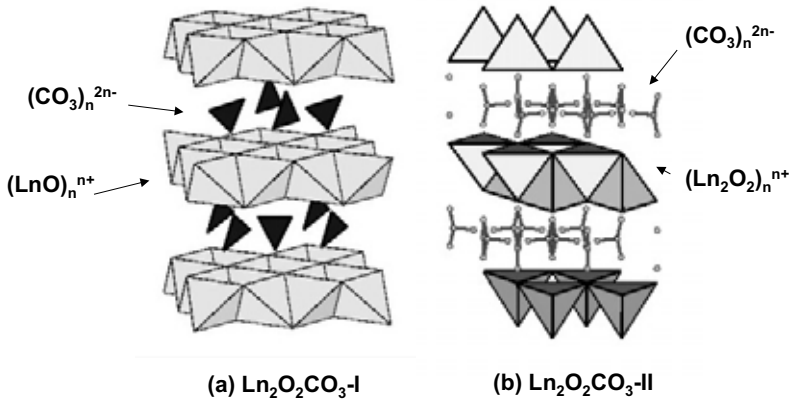

Figure 2-4. $Ln_2O_2CO_3$ structures I (a) and II (b). $(LnO)_n^{n+}$ layers in type I are similar to those observed in LnOOH. $(Ln_2O_2)_n^{2n+}$ structure in type II resembles that found in A-La_2O_3. The carbonate groups in type II are statistically distributed in 3 positions.

As a function of the specific nature of the precursor salt and the experimental reaction conditions, different polymorphs often coexist. This is particularly true for the lighter elements of the series. Though a considerable scatter may be found in the available thermodynamic data for the decomposition of lanthanoid dioxymonocarbonate phases [77], it is generally assumed that, as expected, their thermal stability progressively decreases throughout the series. Thus, decomposition temperatures, as determined by thermogravimetric analysis, ranging from 1188 K for $La_2O_2CO_3$ (II) to 873 K for the heavier, type I, dioxymonocarbonates have been reported in [60].

The IR spectra of the different dioxymonocarbonate polymorphs have also been discussed in detail [60]. For type II, Turcotte et al propose a C_{2v} site symmetry for the carbonate ions with a week splitting of modes ν_3 (E' Asymmmetric stretching modes in D_{3h} free ion), and a nondetectable splitting in modes ν_4 (E' Bending modes in D_{3h} free ion). For types I and IA the spectra are more complex, being interpreted as due to the presence of two and three non-equivalent carbonate positions, respectively. The number of bands, two for type I and three for type IA, associated to the non-degenerate ν_2 mode (A''$_2$ out of plane bending mode in D_{3h} free ion) is particularly relevant in this respect. Multiple splitting of ν_3 is also observed. In [60], C_{2v} symmetry is proposed for the two nonequivalent carbonates in phase I, whereas for carbonate species in phase IA, C_{2v} symmetry is suggested for one of them, the symmetry of the remaining two crystallographic positions being C_s. Table 2-2 summarizes the wavenumbers associated to some characteristic carbonate bands in dioxymonocarbonate phases. They were estimated from the spectra reported in [60] for the different $La_2O_2CO_3$ polymorphs.

TABLE 2-2. Infrared spectra corresponding to phases I, IA and II of $La_2O_2CO_3$. Wavenumbers (cm^{-1}) estimated from the spectra reported in [60].

Polymorph	ν_3	ν_1	ν_2	ν_4
Type I	1375	1070	870	730
	1500		850	680
Type IA	1500	1080	880	730
	1470	1060	870	680
	1380	1050	860	660
Type II	1510	1090	860	750
	1480			

2.2.1.3. Phases Belonging to the Ln_2O_3-CO_2-H_2O System

Among the phases belonging to the Ln_2O_3-CO_2-H_2O two major groups can be distinguished: the hydrated carbonates and the hydroxycarbonates.

For the first of these groups, two crystalline phases: $Ln_2(CO_3)_3.nH_2O$ (n = 3; n = 8), both orthorombic, have been reported [68,74,78]. Some other hydrated carbonates reported in the literature are: $La_2O(CO_3)_2.1.4H_2O$, which has been prepared by ultrasound activation of an aqueous solution containing urea and $La(NO_3)_3$ [71], and a neodymium peroxycarbonate, $Nd_2O_2(CO_3)_2.2H_2O$ [79].

Regarding the hydroxycarbonate phases, there are two well characterized structural varieties which are known for most of the lanthanoid elements [80]: the ancylite-like, orthorombic, A-$Ln(OH)CO_3$, Fig. 2-5, the structure of which is described in detail in [81,82]; and the hexagonal one, B-$Ln(OH)CO_3$, Fig. 2-6, isostructural of the bastnaesite mineral ($LnFCO_3$), the characterization of which is reported in [83,84].

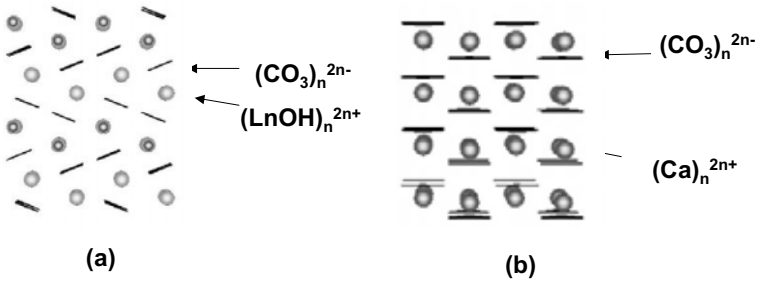

Figure 2-5. Structure of the A-variety of $LnOHCO_3$ (a). View stressing its relationship with the structures of the ancylite and aragonite-form of $CaCO_3$ (b).

Bastnaesite-like hydroxycarbonates are more easily prepared under hydrothermal conditions [84,86,87], while the ancylite-type phases can be obtained at ordinary pressure and temperature conditions by hydrolysis of carbonates [88] and trichloroacetates [74], or homogenous precipitation of the corresponding lanthanoid cations from hot aqueous solutions of urea [89-91].

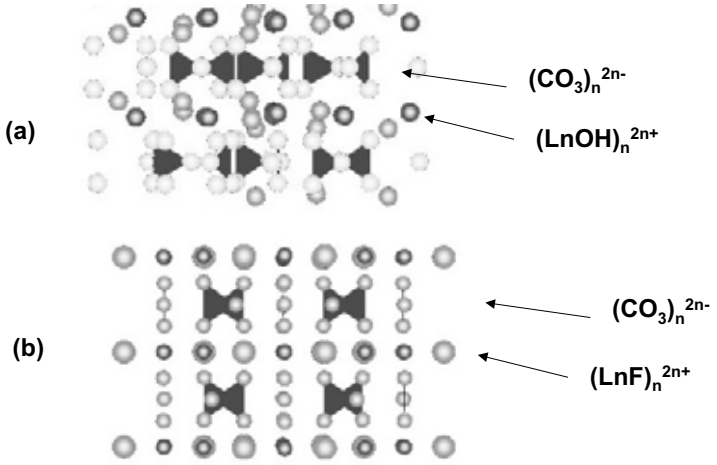

Figure 2-6. Structure of the B-variety of $LnOHCO_3$ (a). View stressing its close relationship with the one of the bastnaesite mineral, $CeFCO_3$ (b).

Some additional hydroxycarbonate phases are known. Thus, a monoclinic phase, $Ln_2(OH)_4CO_3$, has been reported for holmium [80]. Likewise, in a review work on the ternary Ln_2O_3-H_2O-CO_2 hydrothermal systems [85], a number of phases: $Ln_6(OH)_4(CO_3)_7$, $Ln_2O(OH)_2(CO_3)$, $Ln_{12}O_7(OH)_{10}(CO_3)_6$, $Ln_6O_2(OH)_8(CO_3)_3$, and $Ln_4(OH)_6(CO_3)_3$, have been identified for the heavier lanthanoid elements: Tm, Yb, and Lu. X-ray powder diffraction data for the five phases mentioned above are reported in [85].

Infrared spectroscopic data for both hydrated carbonates [69,92] and the hydroxycarbonate phases [53,84,92,93] are available from the literature. According to [53], the IR spectra of the ancylite-like hydroxycarbonates in the range 3000-4000 cm^{-1} are characterized by a doublet, hardly resolved for the elements belonging to the first half of the lanthanoid series. The average wavenumber of this doublet ranges from 3425 cm^{-1} to 3515 cm^{-1} as the atomic weight of the rare earth element increases. In the case of the bastnaesite-type phases, two well resolved OH stretching bands can easily be observed even in the case of $La(OH)CO_3$ [84,93], for which they are found at 3630 cm^{-1} and 3490 cm^{-1} [93].

2.2.2. *The Chemistry of the Ln_2O_3-CO_2-H_2O Systems*

Upon reviewing the available literature on Ln_2O_3-CO_2-H_2O, Ln_2O_3-H_2O, and Ln_2O_3-CO_2 chemical systems, we may note three different types of studies. The first one deals with experiments carried out under hydrothermal conditions [42,81,83,85,87,93-99]. In the second one, the interest was focused on the evolution undergone by different starting phases belonging to the Ln_2O_3-CO_2-H_2O system when dispersed in water, at room temperature, under different CO_2 pressures ranging from 1 atm to $1x10^{-6}$ atm. A major part of this work has been carried out by Caro et al [50,69,88,92,100-103]. The third type of studies was aimed at investigating the processes occurring upon exposure of the rare earth sesquioxides to the atmospheric

air, at room temperature [30,46,48,55-58,104-106]. As already noted, in this chapter special attention will be paid to the latter two groups of studies.

Table 2-3 summarizes some thermodynamic data reported in [107,108] for the hydration of the rare earth sesquioxides to hydroxydes. ΔH^o_r data were estimated from the corresponding ΔH^o_f for $Ln(OH)_3$, Ln_2O_3, and $H_2O(g)$. $\Delta H^o_f(Ln_2O_3)$ data were taken from the literature, whereas those for $\Delta H^o_f(Ln(OH)_3)$ were estimated by means of a Born-Haber cycle as described in [107]. More recently, the standard thermodynamic data for the rare earth hydroxides have been critically reviewed, a new set of revised values being proposed [109]. For the calculation of ΔG^o_r (298 K), an average value $T\Delta S^o_r = 158 \pm 15$ KJ/mol Ln_2O_3 was used for all the oxides [107].

Table 2-3 suggests that, as expected, the hydration of the sesquioxides is progressively less favored throughout the lanthanoid series. The anomalous behavior of lutetia has been interpreted [107] as due to the different structure exhibited by $Lu(OH)_3$, cubic instead of the hexagonal one shown by the remaining lanthanoid hydroxides [37].

TABLE 2-3. Some thermodynamic data about the reaction: Ln_2O_3 (s) + $3H_2O$ (g) → $2Ln(OH)_3$ (s)

Element	Electronic Configuration (Ln^{3+})	ΔH^0_r* (kJ.mol^{-1})	ΔG^0_r* (kJ.mol^{-1})	$P_{H2O}$$^{\#}$ (Torr)
La	$4f^0$	-360	-202	$1.1x10^{-9}$
Nd	$4f^3$	-335	-177	$3.3x10^{-8}$
Sm	$4f^5$	-303	-145	$2.5x10^{-6}$
Eu	$4f^6$	-278	-120	$7.2x10^{-5}$
Gd	$4f^7$	-268	-110	$2.8x10^{-4}$
Tb	$4f^8$	-240	-82	$1.2x10^{-2}$
Dy	$4f^9$	-224	-66	$1.0x10^{-1}$
Ho	$4f^{10}$	-218	-60	$2.3x10^{-1}$
Er	$4f^{11}$	-199	-41	$3.0x10^{0}$
Tm	$4f^{12}$	-169	-11	$1.7x10^{2}$
Yb	$4f^{13}$	-178	-20	$5.1x10^{1}$
Lu	$4f^{14}$	-251	-93	$2.7x10^{-3}$

(*) ΔH^0_r and ΔG^0_r in KJ/mol Ln_2O_3, data taken from refs. [107,108]
($^{\#}$) Equilibrium P_{H2O} in Torr at 298 K
$T\Delta S^0_r \approx 158$ KJ/mol Ln_2O_3 for all the Ln elements [107]

As deduced from the equilibrium data (P_{H2O}) reported in Table 2-3, the hydration process would be favorable, at room temperature, for most of the rare earth oxides. Moreover, experimental hydration studies carried out on sesquioxides belonging to the second half of the lanthanoid series: Sm_2O_3 [107,110,111], Ho_2O_3 [111], Yb_2O_3 [107,111,112], and Lu_2O_3 [107,113,114] have confirmed that the process is actually favorable for the whole series of oxides. Thus, in the case of ytterbia, at 298 K, bulk hydration does occur for water pressures higher than 8 Torr [112], a limit value well below the equilibrium vapor pressure for water, at 298 K. These observations contrast with earlier studies suggesting that hydration in bulk of dysprosia and heavier sesquioxides is impossible [39]. Nevertheless, it would be

noted that kinetic studies indicates that for lanthana, the reaction occurs in hours by contacting the oxide with water vapor at 298 K [39,52], the process being instantaneous at 368 K [39]. By contrast, for the last terms of the lanthanoid series, particularly for ytterbia, the reaction, though exceeding the monolayer (8 H_2O molec.nm^{-2}), becomes very slow [111]. As a result, for the heaviest rare earth sesquioxides, an apparent stabilization is reached far from completion.

The rate of hydration is also sensitive to the preparation procedure and/or the pre-treatment applied to the oxides [111]. This suggests that the differences noted between results reported in [39] and [107,111,112] probably have a kinetic origin, and therefore, that there are no thermodynamic limitations to the bulk hydration of the whole series of rare earth sesquioxides.

2.2.2.1. Behavior of the Ln_2O_3-CO_2-H_2O Systems. Solid Phases Dispersed in Water

The study of the evolution undergone by a number of lanthanoid phases: Ln_2O_3, $Ln(OH)_3$, $Ln_2O_2CO_3$, and $Ln_2(CO_3)_3.nH_2O$, when dispersed in liquid water, at 298 K, under variable pressures of CO_2 ranging from 1 atm to $1x10^{-6}$ atm, has been the major goal of the Caro's work [50,69,88,92,100,101,103,115]. Though significant kinetic differences were observed throughout the series of lanthanoid oxides, some rather general conclusions may be drawn from these studies. Thus, the suspension in water, at 298 K, under P_{CO2} = 1 atm, of sesquioxides, hydroxides or dioxymonocarbonate phases lead to the formation of the corresponding hydrated carbonates: $Ln_2(CO_3)_3.nH_2O$, where n = 8 (La-Nd), n = 3 (Sm-Tm) and n = 6 (Yb-Lu) [50,100,101]. In the case of the latter phases (n = 6), the carbonates were found to be amorphous. The stability of the hydrated carbonate phases under 1 atm CO_2, was confirmed by hydrolysis experiments performed under variable P_{CO2} [115]. In effect, it was shown in [115] that the $Ln_2(CO_3)_3.nH_2O$ phases only undergo hydrolysis for $P_{CO2} < 0.1$ atm. Likewise, the XRD and IR spectroscopy have revealed that, under the atmospheric CO_2 pressure ($P_{CO2} = 3.4 \times 10^{-4}$ atm = 0.25 Torr), the carbonates transform into hydroxycarbonate phases [115]. Rather similar hydroxycarbonate phases could also be detected when $La(OH)_3$ was dispersed in water, in contact with air, i.e. under P_{CO2} = 0.25 Torr. Though the H_2O/CO_2 ratios determined for these phases significantly varied throughout the lanthanoid series, it has been suggested that they all are closely related to the ancylite type hydroxycarbonate, being described by a general formula: $Ln_2(CO_3)_x(OH)_{2(3-x)}.nH_2O$ [88].

The simplified scheme below summarizes some of the most interesting results from the studies reported in the previous paragraphs. These observations are helpful to interpret the evolution undergone by the rare earth oxides, or phases resulting from their hydration and/or carbonation, in processes implying their handling in water suspension.

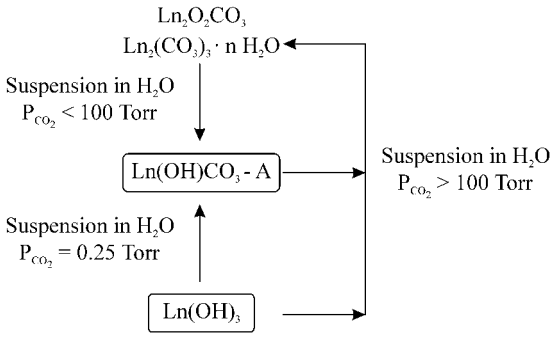

2.2.2.2. Aging in Air of Rare Earth Sesquioxides

Other processes relevant for fully understanding the acid-base chemistry of rare earth oxides are those involved in their aging-in-air. In accordance with the results commented on above, under the conditions occurring in the air ($T \approx 298$ K, $P_{CO2} \approx 0.25$ Torr; $P_{H2O} \approx 20$ Torr), the rare earth sesquioxides are thermodynamically unstable against hydration and carbonation. As shown in Table 2-3 [107], bulk hydration of the oxides would be favored for all the members of the series. Likewise, the results reported in [88,115] suggest that the thermodynamically stable phase should actually consist of a hydroxycarbonate phase. In spite of these guesses, the experimental studies reported in refs. [30,46,48,55-58,104-106] show a far more complex behavior.

This series of studies were performed on 14 different sesquioxide samples belonging to seven elements distributed throughout the whole lanthanoid series. The aged samples were systematically characterized by X-ray diffraction (XRD), infrared (IR) spectroscopy, and thermal analysis techniques: thermogravimetric analysis (TG), and temperature programmed decomposition (TPD). The analysis of evolved gases in TPD experiments was performed by either mass spectrometry, gas chromatography, or both. In some cases [30,46], the structural characterization also included the XRD and IR spectroscopy study of the phases resulting from quenching the decomposition of the aged oxides at intermediate steps of the process.

Table 2-4 summarizes the quantitative results obtained from the series of TG and TPD studies. The rare earth sesquioxides were stabilized in air, at room temperature, for long periods of time, several months or even years [30,46,48,55-58,104-106].

From the analysis of Table 2-4, a number of observations should be outlined. Firstly, as expected from the results commented on above, the intensity of the aging-in-air process decreases throughout the series. However, this should be taken as a rough indication, because, as shown below, the apparent stabilization of the samples, particularly that of the heavier oxides, depends on the preparation procedure and pre-treatments. Secondly, the hydration is in general heavier than the corresponding carbonation process. Thirdly, when referred to 1 nm^{-2} of BET surface area, the amounts of H_2O and CO_2 evolved from the aged-in-air oxides are larger than the reported limiting values for a surface monolayer of CO_2 and H_2O chemisorbed on the rare earth oxides: ≤ 8 molec.nm^{-2} [52,104].

TABLE 2-4. Aging-in-air of the rare earth sesquioxides. Quantitative data as determined from thermogravimetric analysis (TG) or temperature programmed descomposition (TPD).

Oxide Sample	S_{BET}	Weight Loss (%)		Molecules.nm^{-2}		Molar ratio	
	$m^2.g^{-1}$	H_2O	CO_2	H_2O	CO_2	H_2O/Ln_2O_3	CO_2/Ln_2O_3
A-La_2O_3*	3.4	16.4	1.1	1372	38	3.00	0.07
A-La_2O_3*	5.2	15.7	1.5	859	34	2.77	0.11
A-La_2O_3*	16.3	14.2	2.8	250	20	2.57	0.21
A-Nd_2O_3*	5.9	13.3	2.3	717	51	2.49	0.18
A-Nd_2O_3 [#]	6.4	15.0	2.5	289	20	2.86	0.17
A-Nd_2O_3 [#]	2.2	15.3	2.2	389	23	2.86	0.17
C-Nd_2O_3 [#]	5.0	12.4	2.2	696	50	2.32	0.17
C-Nd_2O_3 [#]	17.4	12.3	2.8	226	21	2.30	0.21
B-Sm_2O_3*	6.4	15.6	1.6	696	29	3.00	0.12
C-Sm_2O_3*	8.2	4.9	1.7	187	28	0.93	0.14
C-Sm_2O_3*	14.9	6.3	3.2	130	27	1.23	0.25
C-Eu_2O_3*	25.6	10.6	2.0	111	9	2.08	0.16
C-Dy_2O_3*	22.3	5.4	2.5	74	14	1.12	0.21
C-Ho_2O_3*	32.5	3.2	2.6	30	10	0.67	0.22
C-Yb_2O_3*	40.0	6.4	4.6	48	14	1.40	0.40

(*) Data taken from [55]
([#]) Data taken from [30]
A, B, and C account respectively for the hexagonal, monoclinic or cubic structure of the starting sesquioxide sample [6]

Accordingly, we may conclude that, though much heavier for the earlier members of the series, the aging-in-air processes do in general affect the bulk of the oxides to some extent. Moreover, while hydration data range from 1372 to 30 molec.nm^{-2}; those for the carbonation vary within a much narrower range: 38-10 molec.nm^{-2}. This suggests that carbonation is in general a surface related process, whereas the hydration of the lighter oxides may be independent of the BET surface area.

In addition to the quantitative differences noted above, the analysis of the whole ensemble of results has allowed to propose at least three different types of behavior for the rare earth sesquioxides exposed to atmospheric H_2O and CO_2, at 298 K [55]. This proposal was confirmed by further studies performed on samaria [48] and neodymia [30,56].

After [55], Group I of oxides would include the lanthana samples, all of them with hexagonal, type A, structure [46,57], the hexagonal neodymium oxides [30,56], and the monoclinic, B-type, samaria [48,58]. The behavior of these samples is characterized by the following features:

a) Though the rate of aging becomes slower from lanthana through samaria, the stabilization of the samples being reached after 24 h in the case of La_2O_3 [57], several weeks in the case of neodymia [56], and months in the latter oxide [48], the intensity of the aging processes is always very high, implying the disappearance of the starting oxide.

b) The aged samples consist of partly carbonated hydroxide, the hydration being much heavier than the corresponding carbonation process.
c) As deduced from the XRD and IR characterization studies, hexagonal hydroxide, $Ln(OH)_3$, is a major component of the aged oxide.
d) Very remarkable, no crystalline carbonated phases could be detected by XRD. This contrasts with some observations commented on above [115], and with those reported in [36]. As in the case of the Caro's studies, the XRD pattern for a lanthana sample submitted to a number of soaking in liquid water/drying at 383 K cycles shows the presence of an ancylite-like hydroxycarbonate phase [36]. Moreover, the amount of this phase significantly increased upon exposure to air of the cycled sample [36]. Since no crystalline hydroxycarbonate could be observed on lanthanum oxides simply aged in air, even for years, we may conclude that the carbonate phase resulting from the aging process would be other than that formed during the experiments implying the dispersion of the oxide in liquid water, in contact with air.

The observations above suggest that the carbonate-containing phase resulting from the aging-in-air of Group I oxides consists of a few surface layers of a heavily disordered hydroxycarbonate-like phase surrounding a nucleus of crystalline hydroxide. This suggestion, which is consistent with the quantitative data reported in Table 2-4, is also supported by the High Resolution Electron Microscopy (HREM) images shown in Fig. 2-7.

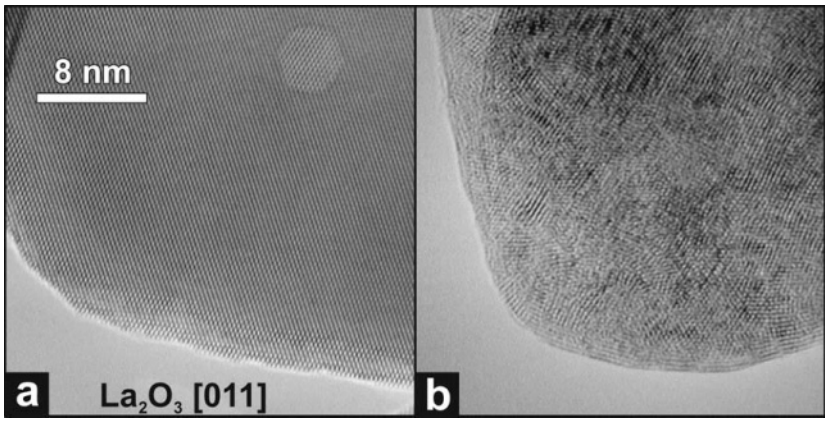

Figure 2-7. HREM images of clean lanthana (a), and the corresponding aged-in-air oxide (b). Micrograph (b) is consistent with the existence of a nucleus of hydroxide surrounded by a thin layer of heavily disordered hydroxycarbonate-like phase.

Figure 2-8 summarizes the characteristic XRD, TG, and TPD-MS diagrams for the aged oxides belonging to Group I.

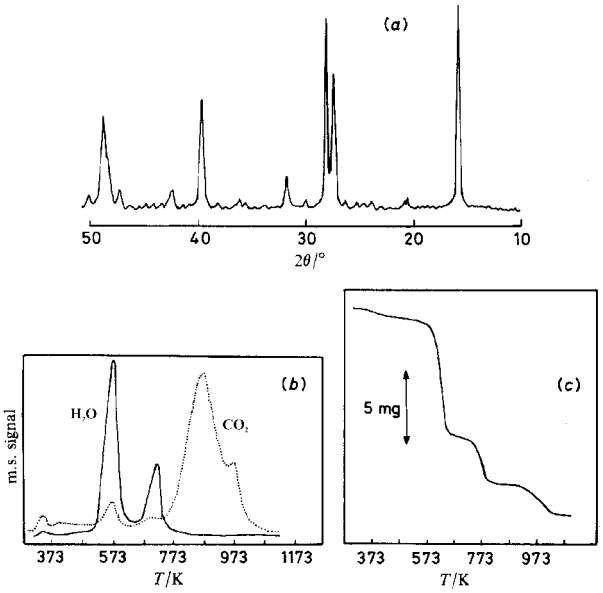

Figure 2-8. XRD (a), TPD-MS (b), and TG (c) diagrams corresponding to an aged-in-air lanthana sample. (Reproduced with permission from ref. 105. Copyright 1987 The Royal Society of Chemistry)

The TG and TPD-MS traces in Fig. 2-8 clearly show the existence of three well defined steps in the thermal decomposition of the aged-in-air lanthana. The first two of them mainly consist of dehydration processes, whereas CO_2 is the only gaseous product evolved throughout the third one. These steps approximately occur at temperatures ranging from: 500 K - 600 K, 673 K - 773 K, and 773 - 1073 K, respectively. For aged A-Nd_2O_3 and B-Sm_2O_3 these three ranges are slightly and progressively shifted towards lower temperatures.

By combining the thermal analysis data with the XRD and IR spectroscopy characterization studies performed on both the aged oxides and the intermediate phases resulting from their decomposition, the reaction scheme below has been proposed [46]:

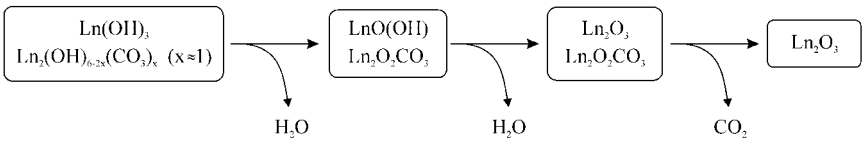

Group II of lanthanoid sesquioxides would include the lighter cubic, C-type, oxides: neodymia [30], samaria [55,58,106] and europia [55]. As deduced from XRD [30] and IR spectroscopy data [30,55], the main structural feature characterizing these aged-in-air oxides is the presence of a crystalline hydroxycarbonate, which has been described as $Ln_2(OH)_4CO_3.nH_2O$. Though not well characterized, this hydroxycarbonate phase does not seem to agree with any of the three types described in [30]. A difference of behavior can be noted between C-Nd_2O_3 samples and the other

Group II oxides, C-Sm_2O_3 and C-Eu_2O_3. In the first case, additional hydration does occur, so that, as shown in [30], the hydroxycarbonate phase coexists with $Nd(OH)_3$. For the remaining two oxides, no hydroxide could be detected [55,106].

Group III would include the heaviest sesquioxides: Dy_2O_3, Ho_2O_3 and Yb_2O_3, all of them cubic [55]. On this Group, the aging-in-air effects are much less intense. However, the amounts of CO_2 and H_2O evolved from the aged oxides usually exceed the monolayer, thus suggesting that even for the heaviest lanthanoid sesquioxides aging cannot be considered as a purely surface process. The IR spectra, and the absence of XRD diffraction lines other than those due to the starting cubic oxides suggest that the aged phases probably consist of a few layers thick amorphous hydrated carbonate coexisting with a nucleus of the unreacted oxides [55].

As revealed by the TG and TPD-MS diagrams reported in [55], the thermal stability of the aged phases also shows significant differences. It generally decreases throughout the lanthanoid series. As a rough indication, heating, in a flow of inert gas, at temperatures as high as 973K-1073 K would be recommended for cleaning the light aged-in-air oxides, like lanthana or neodymia, whereas 873 K would be high enough for the heaviest ones. In the case of non-reducible light rare earth oxides, like lanthana, heating in a flow of H_2 may allow the elimination of the carbonate-containing phase at significantly lower temperatures. Carbonate species become fully reduced at about 873 K, CO and CH_4 being the major gaseous reduction products [105].

Regarding the regeneration of the oxides from the corresponding aged phases, it is also noteworthy, that, depending on the preparation procedure, traces of undecomposed carbonate can be trapped in the bulk of the oxides. They can only be eliminated at fairly high temperature: 1073 K or above, even for the last terms of the lanthanoid series [116,117]. The likely presence of such a type of carbonate species should always be considered when analyzing TG and/or TPD data. Though they may not strongly modify the surface properties of the oxides, they would certainly disturb the interpretation of the thermal analysis diagrams.

The textural effects induced by the aging-in-air processes may also be relevant. It is well known the increase of BET surface area induced on lanthana by the hydration process [52]. In fact, this observation allowed the authors [52] to devise a clean procedure for developing the surface area of lanthana samples to be used as catalysts. The procedure consists of applying to a previously cleaned oxide successive hydration with water vapor/dehydration at moderate temperatures (673 K - 773 K) cycles [7]. A rather similar effect has been observed upon aging-in-air hexagonal neodymia samples [56]. This can be understood in terms of the strong lattice expansion induced by the hydration of the A-type oxides [118-120]. Therefore, it seems to be a characteristic feature of the hydration of Group I oxides. The Rosynek's procedure has been used by others as a routine method for increasing the surface area of the lanthanoid oxides [121]. In accordance with the results commented on above, however, the procedure developed for lanthana should not be generalized. Even for C-Nd_2O_3 samples, the aging in air does not seem to have any significant effect on their BET surface area [30].

To summarize, the experimental studies commented on above show that aging-in-air is very relevant in the chemistry of the lanthanoid sesquioxides. We may also conclude that both, the intensity of the process and the actual nature of the aged phases are kinetically controlled. Consequently to this, the rare earth oxides exhibit a rich variety of behaviors, far more complex than presumed on the basis of purely thermodynamic considerations. In this respect, it is worth recalling that, after [32], for

processes implying no change of oxidation state in the lanthanoid elements, a regular smooth variation of behavior throughout the series should be expected. This does not seem to be the case for the process considered here. Moreover, significant differences of behavior have been observed between different samples of the same oxide. In particular, the structural nature of the oxide seems to play a key role in determining the mechanism of aging, and consequently, the actual nature of the aged phases. In this respect, hexagonal and monoclinic oxides would behave similarly, which might well be understood in terms of their structural analogy. According to [122,123], the monoclinic, B-type, structure of Ln_2O_3 can be described in a similar way to the hexagonal one, the main difference consisting of a slight distortion of the tetrahedral units forming the $(LnO)_n^{n+}$ layers characteristic of the A-Ln_2O_3 phase. For the cubic oxides at least two distinct behaviors could be observed as a function of the position of the lanthanoid element in the series. Likewise, differences in the rate and intensity of aging may be noted as a function of the preparation procedure and/or pre-treatments applied to the cubic oxides, even the heaviest ones, like ytterbia [111].

Since the rare earth oxides are usually stored and handled in air, the likely occurrence of aging processes should always be considered. They may profoundly modify the actual nature of the lanthanoid containing phase, and therefore their surface behavior and general properties. Moreover, the actual nature of the phase to be investigated or used would be critically dependent on the specific pre-treatments applied to the oxide prior running any further assay. Accordingly, a good knowledge of the nature and thermal evolution of the aged phases, under different chemical atmospheres, is critically important in the design of preparation/pre-treatment procedures allowing a much better control of the textural, micro-structural, and chemical properties of the final rare-earth-oxide-based materials.

2.2.3. *Other Studies on the Chemical Reactivity of the Rare Earth Sesquioxides*

There are several other aspects of the chemical reactivity of rare earth sesquioxides deserving some comments.

2.2.3.1. Surface Chemical Properties of Rare Earth Sesquioxides

The surface acid-base properties of rare earth sesquioxides have also received some attention. A number of oxides including lanthana [124,125]and neodymia [124] have been characterized by means of a microcalorimetric study of NH_3 and CO_2 chemisorption. These two molecules are typically used to probe acidic and basic sites respectively. Both, differential and integral heats of adsorption are reported in ref. [124]. From these results, the strength and energy distribution of both acidic and basic surface centers could be determined. As deduced from the CO_2 chemisorption data, La_2O_3 and Nd_2O_3 exhibit the highest concentration and heats of adsorption amongst the investigated oxides [124]. By contrast, the comparative analysis of the NH_3 chemisorption results shows the occurrence on the rare earth oxides above of moderate concentrations of very weak acidic sites, the weakest ones among the investigated oxides [124]. Though these observations are fairly consistent with the acknowledged basic character of the rare earth oxides, it is worth outlining that prior the calorimetric studies, the oxides were heated at 673 K overnight, under oxygen, and then evacuated (1.33 mPa) at 673 K (2 h). In [125], rather similar pre-treatment conditions were applied. In accordance with the results reported in previous sections of this chapter, these cleaning conditions may hardly guarantee the

complete removal of carbonate species present in lanthana or even neodymia, which in turn introduces some doubts about the actual nature of the investigated surfaces.

Attempts have been made of correlating the oxide acid-base properties, as determined by calorimetric techniques, and the corresponding catalytic activity and selectivity for the decomposition of propan-2-ol [126] and 4-methylpentan-2-ol [125]. As discussed in ref. [127], however, this sort of correlations, in addition to the limitations inherent to the cleaning procedure applied in the calorimetric measurements, has a second difficulty; under reaction conditions, the interaction of alcohols with the surface of rare earth sesquioxides leads to the formation of carboxilate and carbonate species which certainly will modify the acid-base properties of the actual catalytic surface.

The H/D exchange reaction of CH_4 with D_2 has also been used to characterize the oxide surface properties. Some of these studies have dealt with rare earth oxides [128,129]. The catalyst basicity plays an important role in this exchange process, which is interpreted as due to the capability of surface basic sites for activating the heterolytic dissociation of methane: $CH_4 \rightarrow CH_3^- + H^+$. In good agreement with this proposal, rare earth sesquioxides show some of the highest activities among the tested oxides [128]. Moreover, for the series: Yb_2O_3, Gd_2O_3, Sm_2O_3, Nd_2O_3, and La_2O_3, a rough correlation is observed between the ionic radius of the Ln^{3+}, and the exchange rate at 773 K; the larger the ionic radius the higher activity [128]. In spite of these observations, the authors consider that any attempt to rank the oxides in terms of their acid-base properties may be misleading. Among other reasons, they mention the likely occurrence on some of the oxides of inactive surface phases not removed by the pre-treatment routine applied by them.

Lanthana is known to be an effective catalyst for selective NO reduction to N_2, with CH_4 [130]. Accordingly, its interaction with NO has been investigated with some detail [117,131-133]. Diffuse reflectance FTIR (DRIFT), temperature programmed desorption (TPD), and thermogravimetric analysis (TGA) were used as experimental techniques. In [131], DRIFT spectra were recorded after treating the lanthanum oxide with flowing NO at temperatures ranging from 298 K to 773 K. The interpretation of the spectra, with a notable complexity, required the application of peak deconvolution routines, and the use of isotopically labeled ^{15}NO. Upon adsorption at 298 K, vibration modes assigned to NO^-, $N_2O_2^{2-}$, chelating NO_2^-, nitrito, and unidentate and bidentate nitrates, were observed. Details of the peak positions and assignments to the species above are tabulated in refs. [131,132]. At higher adsorption temperatures, the recorded spectra mainly consisted of chemisorbed nitrate species accompanied by small amounts of nitrites. NO^- and $N_2O_2^{2-}$ species are proposed to be formed by adsorption on anion vacancies. The hyponitrate species ($N_2O_2^{2-}$) is considered to be an active intermediate in the NO decomposition to yield N_2 and O_2 [132]. By contrast NO_2^- and particularly NO_3^-, with a much higher thermal stability, would be formed by NO adsorption onto basic oxygen anions [132].

The effect of CO_2, H_2O and SO_2, three typical flue gas components, on the kinetics of NO + CH_4 reaction over lanthana has also been studied [130]. Between 773 K and 973 K, lanthana activity for the reaction above is reversibly inhibited by CO_2 and H_2O. A difference may be noted between the nature of the effects induced by CO_2 and H_2O. In accordance with the already discussed chemistry of La_2O_3-CO_2 system, within the temperature range mentioned above, CO_2 reacts with lanthana

leading to the formation of type II $La_2O_2CO_3$, which has been confirmed by X-ray diffraction (XRD). In the case of water, because of the lower thermal stability of $La(OH)_3$ and LaO(OH) phases, no evidence for the bulk hydration of lanthana could be obtained from the XRD study. The inhibiting effect of H_2O is therefore interpreted as due to its competition with the reactants for the adsorption sites at the lanthana surface [130]. Contrary to that observed in the case of CO_2 and H_2O, the poisoning effect of SO_2 is irreversible [130]. Under the experimental conditions of these assays, the XRD study reported in [130] shows the formation of an oxysulfate phase, $La_2O_2SO_4$. Compared to $La_2O_2CO_3$, the thermal stability of the oxysulfate is much higher, thus explaining the irreversible nature of the effect. In fact, partial regeneration could only be achieved upon heating the SO_2-exposed lanthana at 1023 K, a temperature well above those investigated in the catalytic experiments, 773 K–973 K.

2.2.3.2. Chemical Properties of Supported Rare Earth Sesquioxides

Lanthana, and to a lesser extent other rare earth sesquioxides [134-155], have long been recognized as very interesting catalytic promoters. As usually defined, the promoters are additives incorporated to the catalyst formulations in order to improve their performance (activity and/or selectivity) or their resistance against deactivation. The promoted catalytic systems typically consist of an active phase, and one or more promoter phases highly dispersed on an oxide support. Though other lanthanoid-sesquioxide-promoted active phases like sulfides [156,157] and oxides [158-160] have been studied, in most of cases they consist of transition metals. High surface area transition aluminas and silicas are by far the most investigated supports.

The rare earth oxides are usually deposited onto the support by conventional impregnation techniques from aqueous solutions of the corresponding lanthanoid nitrate [136,137,161]. The impregnated samples are further dried at 373 K, and finally calcined at temperatures ranging from 773 K to 973 K. Though widely variable [162], 5% - 15% are typical weight percent loadings for the rare earth oxide promoters.

The structural characterization of supported lanthanoid phases, and the evaluation of their dispersion state on the oxide supports, represent two major aspects of the investigation carried out on these systems. A variety of experimental techniques including XRD [137,142,161,163-175], XAFS [136,138,152,153], Raman Spectroscopy [138,176], XPS [152,159,160,167,169,171-173,177,178] and TEM/HREM [142,165, 168,170,179,180] have been applied.

As discussed in ref. [181], upon increasing the lanthana loading on alumina there is a critical surface concentration for lanthana, 5,12 $La^{3+}.nm^{-2}$, above which tridimensional lanthana particles are observed. This threshold value, which is roughly equivalent to 20 wt% lanthana loading onto an alumina support with a BET surface area of 150 $m^2.g^{-1}$, is in fairly good agreement with the surface concentration of La^{3+} in the $LaAlO_3$ perovskite [170]. These observations suggest that supported lanthana strongly interacts with the alumina surface, thus leading to the formation of a bidimensional layer of the lanthanum-containing phase. This would explain why for oxide loadings below the theoretical monolayer no lanthanoid-contaning phase is usually detected by XRD [138,156,164,165], or even HREM [179]. The results of a EXAFS study on Yb_2O_3/Al_2O_3 [138] are fairly consistent with those reported above

for lanthana. For ytterbia loadings below 1 mmol.(g of Al_2O_3)$^{-1}$, no evidence of Yb-O-Yb bonds could be obtained, Yb-O-Al being the only ones observed. By contrast, for higher loadings, the EXAFS spectra support the existence Yb-O-Yb bonds, thus indicating the growth of ytterbia particles. If the alumina-supported rare earth oxide samples are heated at approximately 1100 K or above, a solid state reaction with inherent tri-dimensional growth of Ln-Al mixed oxide phases occurs. Consistently, the perovskite, $LnAlO_3$, and several other Ln_2O_3-Al_2O_3 phases [138], have been observed by means of XRD [165,171,175,182,183] or HREM [179].

The strong chemical interaction alumina-rare earth sesquioxide is considered to play a key role in the textural stabilization of the transition aluminas [142,145,170,171,184-187]. In the presence of the supported rare earth oxide, the γ-$Al_2O_3 \rightarrow \alpha$-$Al_2O_3$ phase transition, and inherently the sintering mechanism, is inhibited.

There seem to be some differences between the structural properties of alumina- and silica-supported rare earth sesquioxides. Thus, on lanthana/silica systems no clear XRD indication of free La_2O_3, or any phase resulting from its exposure to air, could be observed in samples with loadings as high as 75% [168]. In [168], on the basis of XRD and HREM data, a model for the La_2O_3-SiO_2 interaction is proposed. In accordance with this model, for all the lanthana loadings, tri-dimensional patches of a very poorly crystallized lanthanum silicate would coexist with free-from-lanthanum silica regions, the size and density of the silicate patches increasing with the amount of supported lanthana. These observations are consistent with the EXAFS study carried out on Yb_2O_3/SiO_2 samples with different ytterbia loading [136].

As expected, supported Ln_2O_3 materials exhibit acid-base properties significantly different from those of the unsupported oxides [138,164,168]. Thus, in [168], the interaction of H_2O and CO_2 with a number of La_2O_3/SiO_2 samples has been investigated by means of temperature programmed desorption (TPD), and volumetric chemisorption of CO_2. The traces recorded for the H_2O and CO_2 desorption from the supported samples look like very different from those characterizing bulk La_2O_3. Much lower desorption temperatures are observed in the former case, thus indicating that the dispersion on silica profoundly modifies the chemical properties of lanthana. This observation is fully consistent with the formation of a lanthanum silicate [168]. In [164], the changes occurred in the acid-base properties of both supported lanthana and the silica and alumina oxide supports were investigated by means of FTIR spectroscopy of chemisorbed pyridine, a probe molecule for surface acid centers, and catalytic assays towards propan-2-ol decomposition. In the case of the silica-supported systems, stronger Lewis acid and weaker basic sites than those respectively observed on pure silica and lanthana are reported. Likewise, the catalytic activity and selectivity substantially change as compared to those shown by pure silica or the unsupported lanthana. Regarding the alumina-supported systems, both acid and basic sites stronger than those observed in the pure oxides are reported [164].

In [138] a number of silica- and alumina-supported Ln_2O_3 samples are investigated by means of TPD of chemisorbed CO_2 and pyridine, FTIR of adsorbed pyridine, as well as catalytic assays of α-pinene isomerization and 2-butanol decomposition. Particular attention is paid to the supported ytterbia systems. In good agreement with the results commented on above, supported rare earth oxide systems

show significantly distinct chemical behavior as compared to those of the pure oxides.

Regarding the chemical promoting effects induced by the rare earth sesquioxides, there are also numerous observations indicating that chemical interaction occurs not only with the support but also with the active phases. Though the precise nature of such interactions are often not well established, the incorporation of Ln_2O_3, and particularly lanthana, to the catalyst formulations is acknowledged to improve the resistance against sintering of the active phase [156]. Likewise, it has been shown that the addition of both lanthana and praseodymia to a Pd/Al_2O_3 catalyst for CH_4 combustion, very much improves its resistance against deactivation [134]. This effect is interpreted as due to the stabilization of the supported PdO phase, which is considered to be the true active phase in the above mentioned process.

2.3. CHEMICAL REACTIVITY OF THE HIGHER RARE EARTH OXIDES

As already noted, the most relevant aspects of the chemical reactivity of the higher binary rare earth oxides, i.e, ceria, praseodymia and terbia, deal with their redox properties. Typical acid-base processes, like hydration and carbonation phenomena, very important for the sesquioxides, have much less significance in the case of the higher oxides. Except for praseodymia [188,189], the information available about the interaction of the higher binary oxides, particularly ceria, with CO_2 and H_2O, under the usual experimental conditions, suggests the occurrence of purely surface processes [190]. Accordingly, this section of the chapter will be mainly devoted to the redox chemistry of the higher rare earth oxides.

2.3.1. *Redox Chemistry of the Higher Rare Earth Oxides*

Two different periods may clearly be distinguished in the evolution of the research activities on the redox behavior of the higher rare earth oxides. During the first one, the effort was focused on very fundamental aspects of the chemistry of ceria, praseodymia and terbia, and to a much lesser extent on mixed oxide systems formed by two of them [191-195]. Significant progress was made in the elucidation of the structural nature of the extensive homologous series of oxygen-deficient, fluorite-related phases, nowadays described by the generic formula: Ln_nO_{2n-2m} [21,27,196-221]. Likewise, considerable efforts were devoted to establishing the complex phase diagrams exhibited by these oxides [21,26,197,217,219,220,222-228], and to the thermodynamic [26,229-231] and kinetic [232-240] characterization of the redox processes involving the different terms of these homologous series. Structural techniques like HRTEM [196,202,205,206,209,215,241,242], electron- [21,196,202,209], neutron- [199,201,203,243], and X-ray- [203,218-221] diffraction, calorimetric measurements [230,231], and thermogravimetric analysis [193,194,202,222,224,233-236,239,244], constituted the major source of experimental information. These earlier studies, which are essential to fully understand the extraordinary development occurred during the last decade, have been recently reviewed [6,245]. Moreover, some of the most outstanding contributions occurred during this period will also be discussed at length in Chapter 3 of this volume. Accordingly, we shall mainly devote this section to the second of the periods mentioned above.

The second period is closely related to the development of the so-called three-way catalysts (TWC). As is known, TWCs constitute the current technology of election for the abatement of exhaust emissions (Unburned hydrocarbons, CO, and NO_x) from gasoline-fuelled vehicles [10,18,19,246,247]. More than 95% of the gasoline vehicles nowadays produced in the world are equipped with a TWC converter [247]. The economic importance is also extraordinary, the TWC sales representing about one fourth of global catalyst market [246].

Ceria first, and since the mid 1990s ceria-zirconia mixed oxides, are key components in the formulation of TWCs [18,19]. A variety of functions are attributed to them, those related to their redox properties being particularly relevant [247]. Under the usual TWC operation conditions, the chemical composition of the exhaust gases rapidly oscillates between net reducing and net oxidizing conditions [8]. This implies deviations from the optimum stoichiometric air to fuel (A/F) ratio (A/F = 14.63), and therefore, loss of efficiency in the auto-exhaust catalyst. To attenuate these oscillations, oxygen buffer materials are required, ceria-based oxides constituting the best option at present available [19].

During this second period the research activity on ceria and closely related mixed oxides has very steeply grown. As reported in [248], in 1981, 100 papers dealing with the catalytic applications of ceria had been published, the number being increased by a factor of six, up to 600, in 1997. A rather similar evolution has been observed for the number of patents [248]. In recent years, this extraordinary effort has continued and even augmented. As a clear indication of it, during the last few years, numerous review works have been published on the subject [8-11,33,246,249,250].

As noted above, the oxygen buffer materials for TWC applications must fit very demanding kinetic and thermodynamic requirements. They should be able to rapidly release/uptake large amounts of oxygen, within a range of operation temperatures as wide as possible. Accordingly, alternative redox characterization parameters like oxygen storage capacity (OSC) [8,249,251-254], or oxygen buffering capacity (OBC) [255-257], have been developed. These new parameters are aimed at evaluating, under certain pre-determined experimental conditions (temperature, redox nature of the chemical environment, and time of treatment), the properties of redox materials which are particularly relevant in TWC applications, i.e. the amount and kinetics of their oxygen exchange with the surrounding atmosphere.

In the case of oxygen storage capacity studies, ultimate [251,258-261] and dynamic [249,251,260-262,262-266] OSC concepts are usually distinguished. The objective of the first type of OSC measurements is the evaluation of the highest amount of oxygen that may be extracted from the oxide, at a pre-established temperature and reductant, usually H_2 or CO, partial pressure [252]. On the contrary, dynamic OSC measurements consist of injecting H_2 (CO) and O_2 pulses alternately. In this way, the amount of the most reactive oxygen species in the redox material is evaluated [252]. OBC technique has also a dynamic character. As described in ref. [255], it allows to quantitatively determine the capacity of the evaluated material for attenuating the oscillations occurring in the oxygen partial pressure over the sample. These oscillations are generated by fast (0.1 Hz) injection of O_2(5%)/He pulses in a helium stream flowing through the investigated material. Therefore, this technique mimics the actual role of the redox buffer component in three-way catalysts.

During the second period, a rich variety of experimental techniques have been applied to the characterization of the redox behavior of the higher rare earth oxides, in general, and more specifically of ceria, and ceria-based mixed oxides. Some of the key data allowing us to arrive at our current understanding of this complex behavior were obtained by applying: thermal analysis techniques, like thermogravimetric analysis (TGA) [267,268], temperature-programmed-desorption (TPD-O_2) [257,268-270], -reduction (TPR) [249,271-283], -oxidation (TPO) [260,284-286], oxygen (hydrogen, CO) pulse techniques, usually applied in the OSC and OBC studies commented on above, Faraday magnetic balance [258,259,272,275,283,287-292], X-ray absorption near edge spectroscopy (XANES) [293-303], electron energy loss spectroscopy (EELS) [304-307], X-ray photo-electron spectroscopy (XPS) [256,268,270,294,295,298,303, 308-316], electron paramagnetic resonance (EPR) [294,317-321], FTIR of appropriate chemisorbed probe molecules [260,322-326], and electronic conductivity measurements [327,328].

Table 2-5 summarizes standard enthalpy and Gibbs free energy formation data for some higher rare earth oxide phases.

TABLE 2-5. Standard enthalpy and Gibbs free energy of formation for some higher oxides of Ce, Pr and Tb. Data in (KJ/mol of Ln) [26].

Ln	ΔH^o_f / ΔG^o_f	LnO_x x: 1.500	LnO_x x: 1.717	LnO_x x: 1.804	LnO_x x: 1.817	LnO_x x: 1.833	LnO_x x: 2.000	ΔH^o_r $LnO_2 \rightarrow LnO_{1.5} + ¼\ O_2$
Ce	ΔH^o_f	- 897					- 1088	+191
Ce	ΔG^o_f	- 853					- 1025	
Pr	ΔH^o_f	- 904	- 936	- 947		- 943	- 958 *	+ 54
Pr	ΔG^o_f	- 866						
Tb	ΔH^o_f	- 932		- 946	- 961		- 971	+ 39
Tb	ΔG^o_f	- 888						

(*) Data taken from ref. [22]

In accordance with the ΔH^o_r data reported in the last column of Table 2-5, ceria is by far the less reducible of the rare earth dioxides. In fact, the usual procedure for obtaining these oxides, heating in air different precursor phases, does not allow the preparation of the fully oxidized forms (LnO_2) of praseodymia and terbia, whereas the cerium dioxide can be easily obtained. Consequently, the actual stoichiometry of the praseodymia and terbia phases may vary depending on the specific preparation conditions, particularly, the temperature and time of treatment, the oxygen partial pressure and the cooling conditions. Likewise, the pre-treatment conditions applied to praseodymia [329] and terbia [330] samples in order to clean them prior to any further experiment may significantly modify their actual redox state.

2.3.2. Temperature Programmed Oxygen Evolution Studies

If the oxidized forms of the higher rare earth oxides are heated in a flow of inert gas, they desorb oxygen, becoming reduced. Figure 2-9 shows the Temperature

Programmed Desorption-Mass Spectrometry (TPD-MS) traces for O_2 evolution from ceria, praseodymia and terbia samples pretreated as indicated.

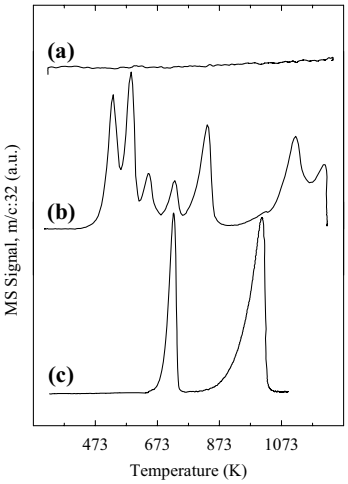

Figure 2-9. TPD-MS study of ceria (a), praseodymia (b), and terbia (c). Traces for O_2 (m/c: 32). Prior to the experiments, the oxides were heated in flowing O_2(5%)/He (P_{O2}: 38 Torr) at 973 K for 1 h, further cooled to 373 K also in a flow of oxygen, and finally flushed with inert gas up to 298 K. Weight of sample: 100 mg; He flow rate: 60 $cm^3 \cdot min^{-1}$; heating rate: 10 $K \cdot min^{-1}$.

The different reducibility of the three oxides is clearly revealed by these experiments. In the case of ceria, the oxygen evolution is almost negligible [331]. A rather similar observation has been recently reported for TPD studies on ceria single crystals [332]; though on thin films prepared by vapor deposition on α-Al_2O_3 (0001) the authors observe some ceria reduction from 900 K. The difference is interpreted as due to the crystal size and defect content of the latter sample. In any case, heating under flowing inert gas or high vacuum induces slight reduction on the cerium dioxide.

By contrast, praseodymia and terbia may be fully reduced to sesquioxide in a flow of inert gas. Moreover, in the case of terbia, though shifted to higher temperatures, the two reduction peaks observed in the TPD diagrams do also occur upon heating the oxide up to 1223 K in a flow of O_2(5%)/He (P_{O2}: 38 Torr) [333].

In accordance with Fig. 2-9, terbia reduction starts at approximately 623 K, being completed at approximately 973 K. The process takes place through two well resolved steps characterized by oxygen peaks at 673 K and 950 K. The first peak has been interpreted as due to the decomposition of the so-called δ phase ($TbO_{1.818}$) to the ι phase ($TbO_{1.714}$); the second one being assigned to the decomposition of $TbO_{1.714}$ to sesquioxide [330,334]. Accordingly, the theoretical weight loss ratio: $\Delta W_2(\iota \rightarrow Tb_2O_3)/\Delta W_1(\delta \rightarrow \iota)$ would be 2.06. In the case of the TPD experiment reported in Fig. 2-9, however, the ratio of the areas under the TPD peaks is significantly larger, 2.52, thus indicating that, under the cleaning/pre-treatment conditions applied in this particular case, complete re-oxidation of the ι to δ phase does not occur. As already noted [330], the intensity of the first peak in the TPD diagram for terbia is sensitive to the specific pre-treatment conditions.

In the case of praseodymia, the reduction under flowing He is far more complex implying seven resolved steps, Fig. 2-9. The first reduction peak, which may be interpreted as due to the decomposition of a β to δ phase, is observed at 530

K; whereas the last one, that assigned to the decomposition of the ι phase (Pr_7O_{12}) to Pr_2O_3, takes place at approximately 1210 K, a temperature significantly higher than that observed on terbia for the same process. As expected from Fig. 2-9, the intensity and even the number of peaks observed in the TPD trace for praseodymia may be strongly modified by the specific pre-treatment applied to the oxide sample [329].

2.3.3. Temperature Programmed Reduction Studies

The study of the evolution undergone by the higher rare earth oxides on heating under flowing pure or diluted hydrogen is a very common way of characterizing their redox properties. Figure 2-10 shows the temperature programmed reduction (TPR-MS) diagrams recorded for ceria, praseodymia and terbia. The oxides were pretreated in a flow of oxygen in the same way as described in Fig. 2-9.

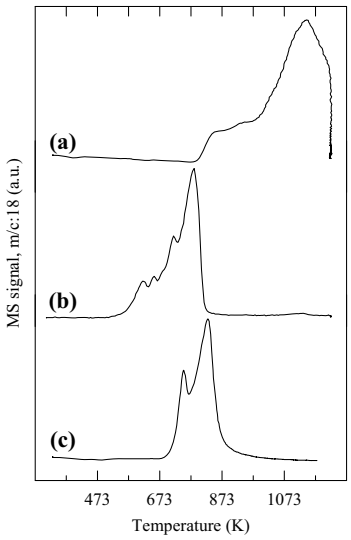

Figure 2-10. TPR-MS study of ceria (a), praseodymia (b), and terbia (c). Traces for H_2O (m/c: 18). Prior to the experiment, the oxides were heated in flowing O_2(5%)/He (P_{O2}: 38 Torr) at 973 K for 1 h and further cooled to 373 K also in a flow of oxygen, and finally flushed with inert gas up to 298 K. Weight of sample: 100 mg; H_2(5%)/Ar flow rate: 60 $cm^3.min^{-1}$; heating rate: 10 $K.min^{-1}$.

As in the case of the TPD-MS diagrams commented on above, the TPR-MS traces also show notable differences of reducibility among ceria, praseodymia and terbia. Upon comparison of Figs. 2-9 and 2-10, we may also conclude that under flowing H_2(5%)/Ar the reduction to Ln_2O_3 of both praseodymia and terbia is completed at much lower temperature, below 873 K. Likewise, the successive steps of the reduction process become much poorly resolved. Rather similar conclusions can be obtained from earlier TPR studies on praseodymia [335] and terbia [336,337]. In the latter case, under flowing pure H_2 [336], the oxide becomes fully reduced at a temperature as low as 600 K.

If run under flowing H_2(5%)/Ar, the TPR-MS experiments for praseodymia and terbia show that, in addition to water formation and hydrogen consumption, some oxygen evolution occurs at the lowest temperature region of the diagrams, Figure 2-11. This suggests that the reduction of these oxides starts at temperatures

lower than those at which hydrogen becomes effective. Under these circumstances, the redox state of the starting oxide samples cannot simply be determined on the basis of either the hydrogen consumption or the amount of released water. Moreover, if a TPR-TCD device is used, misleading interpretation of the recorded traces may occur because of the disturbing effect of the evolved O_2.

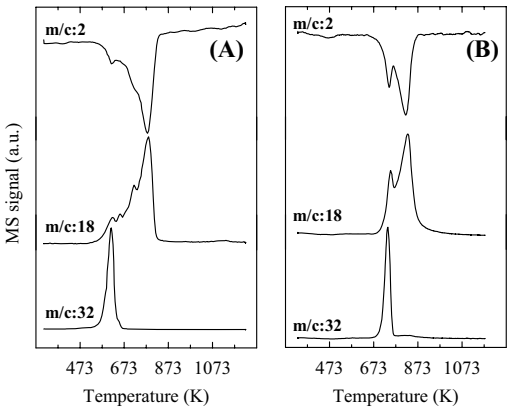

Figure 2-11. TPR-MS study of praseodymia (A), and terbia (B). Traces for H_2 (m/c: 2), H_2O (m/c: 18), O_2 (m/c: 32). Experimental conditions: 100 mg of the oxides were pretreated as indicated in Figs. 2-7 and 2-8, and further heated in flowing H_2(5%)/Ar (60 $cm^3.min^{-1}$) at 10 $K.min^{-1}$.

The thermal evolution of ceria under reducing conditions has received special attention. Several authors have reported TPR diagrams for this oxide [47,190,281-283,338]. The experiments were performed under hydrogen pressures ranging from 760 Torr [47,190] to 7.6 Torr [281-283]. Mass spectrometry (MS) and thermal conductivity detectors (TCD) have been used as analytical devices.

In the case of the TPR studies on ceria, however, the classic TCD-based experimental setups may have some serious drawbacks, which prevent the straightforward interpretation of the corresponding diagrams [249,272,282,339]. In effect, the TPR-TCD trace is assumed to be generated by the hydrogen consumption associated to the reduction of ceria with inherent evolution of H_2O. However, there may be some additional contributions. Two major disturbing factors have been considered in [282]. Firstly, for high surface area ceria samples, superimposed to the reduction process mentioned above, reversible hydrogen adsorption/desorption do occur [47,272,291,339,340]. This side effect may obviously distort the TCD signal, and consequently, the meaning of the recorded diagram. Secondly, residual bulk carbonate species are often present in the ceria samples [282,283,324], the reduction of which, in addition to imply some hydrogen consumption, may lead to the formation of CO not retained by the trap at the reactor exit. The evolved CO would therefore reach the detector thus contributing, in some cases very significantly [283], to the overall recorded signal.

For TPR experiments ranging as usual from 298 K to 1173 K-1223 K, the traces for ceria typically show more than one reduction peak [249], the position of which shifting towards lower temperatures as the H_2 pressure is increased [47,341]. As deduced from Fig. 2-10, under flowing H_2(5%)/Ar, the first peak is observed at approximately 650 K, whereas the last one, much stronger, appears at approximately

1100 K, 900 K when the experiment is run under flowing pure H_2 [47]. The results above are in good qualitative agreement with those reported in [283], where two ceria samples, with 115 $m^2.g^{-1}$ (A) and 5 $m^2.g^{-1}$ (B) respectively, were heated step by step from 473 K to 900 K under flowing pure H_2. By monitoring the ceria redox state with the help of a Faraday magnetic balance, the authors [283] observe the very first indication of reduction at approximately 473 K, the temperature at which hydrogen chemisorption on ceria has been reported to start [340]. After 2 h treatment at 673 K, the reduction degree was found to be 23% (percentage of Ce^{4+} reduced to Ce^{3+}) for the so-called sample A, not exceeding 3% for sample B. As suggested in [338], this might be interpreted as due to the surface nature of the low temperature feature in the TPR diagram. From a study on seven different ceria samples, a rather similar conclusion was drawn [281]. It would be noted, however, that parallel experiments on sample A, in which the reduction time per step was 20 h instead of 2 h, lead to a very significant increase of the ceria reduction degree [283]. Thus after 20 h reduction at 673 K, 32 % of the cations were present in the oxide sample as Ce^{3+}. This reduction degree is considered to exceed the expected value for a purely surface reduction, 20% for sample A [283]. The effect of the time of reduction would therefore indicate that the low temperature reduction of ceria is a kinetically controlled process. As suggested in ref. [301], at moderate reduction temperature, i.e. 673 K, the ceria reduction would consist of a relatively fast surface process followed by a much slower diffusion into the bulk of the oxygen vacancies created at the surface. Very recently, however, this interpretation has been critically revised [273]. On the basis of oxygen diffusion data, Trovarelli et al [273] propose that the reduction of ceria is not controlled by the diffusional step, differences in the thermodynamic properties of ceria microcrystals, as a function of their size, and the sintering undergone by ceria during the experiment, being in their opinion the key alternative factors in determining the shape of the TPR diagram. As deduced from some other very recent TPR studies on ceria [274] and ceria-zirconia mixed oxides [274,342], this issue still remains as an important matter of debate.

In the case of the low surface area ceria sample (B), the concentration of paramagnetic Ce^{3+} species is rather small up to 750 K (reduction percentage: 5%), then it increases sharply with the temperature, reaching a plateau at 850 K - 900 K for 36% reduction degree [283]. This latter value is consistent with the formation of the δ phase ($CeO_{1.818}$), thus suggesting that the high temperature peak in the TPR trace corresponds to the bulk reduction of ceria with inherent formation of $CeO_{1.818}$. This high temperature feature can be observed in TPR studies performed on ceria samples with surface areas varying in wide range of values [47,190]

Even for experiments run in pure hydrogen, the complete reduction of ceria to Ce_2O_3 can hardly be achieved in conventional TPR studies. Thus, after reduction for 1 h at 1173 K, the percentage of reduced cerium ions is 63% [47], being necessary a prolonged treatment (5 h) at 1223 K to arrive at 85% reduction [284]. In the latter case, the XRD pattern of the reduced sample clearly showed the presence of A-Ce_2O_3. The formation of the hexagonal (A) cerium sesquioxide upon high temperature reduction has also been reported in [281].

2.3.4. Reduction by CO of the Higher Rare Earth Oxides

The behavior of the higher rare earth oxides against reducing agents other than H_2, in particular CO, is also interesting. The quantitative information available

is however much less detailed than in the case of hydrogen. In [292], the two ceria samples investigated in [283] (A and B), were heated step by step under 50 Torr of CO, and their evolution followed with the help of magnetic, gravimetric and FTIR spectroscopy measurements. For the high surface area sample (A), reduction starts at room temperature; it becomes important at 473 K (15%), reaching the 34% at 673 K. This contrasts with the behavior of low surface area sample (B), for which at temperatures as high as 973 K the reduction degree is moderate: 21%. The authors conclude that surface reduction starts at temperatures lower than those observed for hydrogen, but diffusion into the bulk of the oxygen vacancies may be disturbed by the presence of adsorbed carbonate species. The formation of surface carbonates by CO interaction with ceria has been shown by a number of FTIR spectroscopic studies [292,343,344].

Though rather limited, some data about the reduction of $TbO_{1.818}$ by CO are also available [330]. The redox state of terbia was checked by running a TPD-O_2 experiment on the oxide resulting from the treatment of the starting sample with 10 Torr CO, at 573 K, for periods of time ranging from 1 h to 6 h. As the time of treatment was increased, the intensity of the first peak in the TPD diagram for terbia ($\delta \rightarrow \iota$) progressively diminished, becoming almost negligible after 6 h. By contrast, the second TPD-O_2 peak, that associated to the decomposition of the ι phase, remained unmodified. Because of the low surface area of the investigated terbia sample, 3.2 $m^2.g^{-1}$, these observations have been interpreted as a proof of the occurrence of bulk reduction of terbia at such a moderate temperature [330].

Over partially reduced ceria, CO can undergo disproportionation [345]. The process, which has been reported to occur even at room temperature [345], leads to the formation of surface carbon deposits and CO_2. This side reaction should always be considered when studying the thermal evolution of ceria under CO pressure. In this respect, it would be recalled that CO has been used as reducing agent in numerous studies aimed at evaluating the Oxygen Storage Capacity (OSC) of both bare ceria and ceria-containing materials.

2.3.5. Re-oxidation of Pre-reduced Higher Rare Earth Oxides

The re-oxidation behavior of reduced higher rare earth oxides also deserves some comments. In good agreement with the earlier studies reviewed in [26], some more recent magnetic balance [281,283] and temperature programmed oxidation (TPO) [282] results, have shown that ceria re-oxidation occurs rapidly and to a large extent at room temperature. The same conclusion may be drawn from [47,284,285], where the re-oxidation of a ceria sample, which had been reduced at temperatures ranging from 623 K to 1223 K, was investigated by combining oxygen pulses at 298 K with TPO. Figure 2-12 summarizes these results.

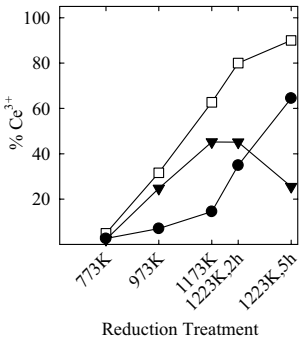

Figure 2-12. Ceria re-oxidation: Oxygen consumption associated to both pulse experiments at 298 K (●), and TPO (▼) as a function of the reduction treatment with flowing pure hydrogen. Total oxygen consumption, pulse + TPO experiments, (□). Surface area of the starting oxide sample: 4 $m^2.g^{-1}$. (Reproduced with permission from ref. 285. Copyright 1998 Kluwer Academic Publishers)

In accordance with Fig. 2-12, by pulsing oxygen at room temperature ceria becomes re-oxidized to a large extent. This is so in spite of injecting small pulses (0.25 cm^3) of diluted oxygen (P_{O2}: 4 Torr), and of the low surface area (4 $m^2.g^{-1}$) of the oxide sample investigated in [284,285]. For 773 K or higher reduction temperatures, complete re-oxidation does not occur on pulsing, some oxygen consumption being always associated with TPO experiment. For the highest reduction temperature, 1223 K, the relative contribution of pulses drastically diminishes. After 5 h reduction at 1223 K, the major oxygen consumption takes place during the TPO run. In parallel with this observation, for heavily reduced ceria, the TPO traces show two peaks, the second one dominating the diagram after 5 h reduction at 1223 K, Figure 2-13.

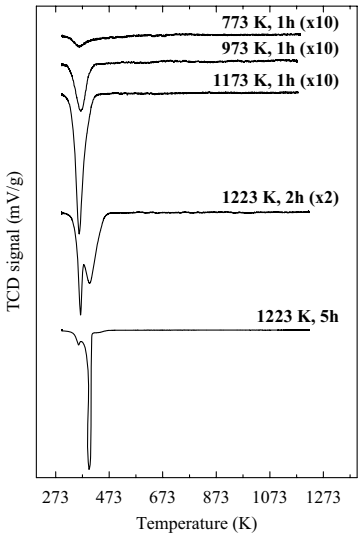

Figure 2-13. TPO study of the ceria re-oxidation. Influence of the reduction temperature. Prior to running the TPO experiments the sample was pulsed with diluted oxygen (P_{O2}: 4 Torr) at 298 K. (Reproduced with permission from ref. 285. Copyright 1998 Kluwer Academic Publishers)

The change of re-oxidation behavior observed in heavily reduced ceria has been interpreted as due to the formation of hexagonal Ce_2O_3 [281,284,285].

Moreover, as reported in ref. [284], the XRD study of the heavily reduced ceria further exposed to air for days, at room temperature, shows that the A-Ce_2O_3 phase is still present. Though no similar studies are to our knowledge available on praseodymia, the activation energy data for the re-oxidation of both hexagonal (210 KJ/mol) and cubic (105 KJ/mol) Pr_2O_3 reported in [26] would be in agreement with the results commented on above for ceria.

The re-oxidation of Tb_2O_3 has also been studied in the same manner as that of ceria, i.e. by combining oxygen pulses at 298 K and TPO [333]. Re-oxidation mainly occurs during the TPO run (890 µmole $O_2.g^{-1}$), the oxygen uptake associated with the pulse experiment at 298 K being much smaller (5 µmole $O_2.g^{-1}$). As already noted, under the TPO conditions (P_{O2}: 38 Torr) re-oxidation to dioxide is far from completion (theoretical uptake for full re-oxidation to dioxide: 1340 µmole $O_2.g^{-1}$).

When submitted to heating/cooling cycles, under oxygen pressure, the higher rare earth oxides exhibit a very characteristic hysteresis phenomenon, by the virtue of which, during the cooling part of the cycle, the reduction degree of the oxide is higher than that determined, for the same temperature, during the heating part of it. Both isobaric and isothermal reduction/reoxidation experiments performed on these oxides have clearly shown the occurrence of a hysteresis loops [26,202]. Though not reflected in the phase diagrams because of the metastable nature of the involved phases, hysteresis seems to be an intrinsic property of the higher rare earth oxides, the precise origin of which remains unclear [26]. Detailed kinetic and thermochemical studies of redox processes involving different two phase regions exhibiting hysteresis phenomena have been reported for praseodymia [230,233,234,236] and terbia [231,235].

In the case of ceria, the reduced phases, Ce_nO_{2n-2m}, may also be re-oxidized by molecules much less active than dioxygen. Studies on ceria re-oxidation, both in the presence and in absence of a supported metal phase, by H_2O [26,346,347], CO_2 [348,349], NO [350,351], and even CO [352-356], are presently available.

2.3.6. Modification of the Redox Behavior of the Higher Rare Earth Oxides

The redox properties of bare ceria, praseodymia and terbia may be significantly modified by a number factors. In this section, some of the most relevant ones will be briefly overviewed.

Modifiers, typically deposited onto the surface of higher rare earth oxides by conventional impregnation techniques, may notably change their redox chemistry. The shift occurred in the low-temperature peak of the TPR-H_2 diagrams for higher oxide-supported noble metal systems is particularly noticeable [249,267,272,291,357-361]. This enhancement of the oxide reducibilities is interpreted as due to the low-temperature activation of H_2 occurred on the surface of the metal crystallites, and the subsequent transfer of H atoms onto the oxide supports (spillover) [249,272].

Some not very much conclusive studies are also available about the promoting role of alkaline modifiers on the reducibility of ceria [282,362]. Examples of additives inducing both positive and negative kinetic effects on the terbia redox behavior have also been reported [334].

The redox properties of the higher rare earth oxides may also be strongly modified by alio-cations forming mixed oxides with them. For the last few years a considerable research effort has been devoted to this family of fluorite-related oxide

systems; most of this work being related to the development of new, more efficient, materials for TWC [10,19,247,363] and ionic conduction [14,15] applications. Though ceria-zirconia has been by far the most extensively investigated system [9-11,279,280,364-369], studies dealing with (Ce-Hf)O_2 [366,370], (Ce-Ln)O_{2-x} (Ln: La, Pr, Nd, Sm, Gd, Tb, Yb, Y) [15-17,255,267,270,285,295,296,304,331,371-380], (Pr-Zr)O_{2-x} [381], (Ln-Pr)O_{2-x} [382,383] and even ceria-zirconia-doped systems [333,341,374,384-394] are also available.

The incorporation of ceria-zirconia in TWC formulations has represented a major breakthrough in the development of this technology [10,19]. With reference to the cerium dioxide, CeO_2-ZrO_2 mixed oxides show better textural stability [395,396], enhaced redox activity, which has been interpreted as due to the higher oxygen mobility in the mixed oxide lattice [396], and better resistance to the chemical (redox) deactivation upon thermal ageing [396]. In effect, it is well known that, upon sintering, either under oxidizing or reducing conditions, the TPR diagram exhibited by ceria is very significantly modified, the low-temperature feature usually observed in high-surface area samples completely disappearing [273,283,396]. This strong redox deactivation effect contrasts very markedly with the evolution undergone by the TPR traces recorded for high surface area ceria-zirconia samples submitted to successive cycles of high temperature reduction followed by re-oxidation [259]. As reported in [259], in spite of the very notable sintering undergone by these oxides on cycling, their TPR traces do not show any significant deactivation effect. On the contrary, a moderate enhancement of their reducibility could be observed in some cases. Finer details of the peculiar effects of thermal ageing on the redox properties of ceria-zirconia samples are presently known. Thus, it has been reported that the temperature of re-oxidation following the high-temperature reduction part of cycle plays a key role in determining the redox behavior of the resulting mixed-oxide [275,277], the sample re-oxidized at 823 K, mild oxidation conditions (MO), showing much enhanced reducibility, as compared to that of the one re-oxidized at 1223 K, high temperature oxidation conditions (HTO). As shown in [275], this strong modification of the ceria-zirconia reducibility is reversible, so that by alternating MO and HTO treatments after the corresponding TPR experiment, successive enhancement and deterioration of the reducibility of the oxide is observed. Though a number of factors, including textural properties [246,397], bulk structural constitution [253,277,278,398,399], surface modifications [342], or hydrogen activation [274,342], have been considered to play a role in determining the redox behavior of the ceria-zirconia mixed oxides, the precise origin of this very peculiar chemical phenomenon is still a matter of discussion.

The effect of some anionic modifiers has also been investigated. It is well known the structural and chemical changes induced on ceria by the incorporation of chloride ions into its lattice. This incorporation has been observed during the reduction step of the preparation of some ceria-supported noble metal catalysts, specifically, when chloride-containing noble metal precursors were used [272,289,339,400-403]. As a result, the chemisorptive [272,403] and redox [272,289,339] properties of ceria are drastically modified. Likewise, as revealed by XRD and HREM characterization studies [272,400,404], the incorporation of Cl^- ions into the ceria lattice leads to the formation of the corresponding oxychloride phase, CeOCl, with inherent stabilization of the Ce^{3+} oxidation state. According to the TPO study reported in [289], the elimination of the trapped chloride species,

with inherent recovery of the conventional chemical and structural properties of ceria, requires heating the sample in a flow of pure oxygen at temperatures well above 773 K.

A considerable research effort has also been devoted to the investigation of higher rare earth oxides supported on SiO_2 [271,405], and particularly, on γ-Al_2O_3 [138,165,167,381,406-412]. Though some studies on alumina-supported praseodymia [381] or terbia [138] are available, most of them have dealt with ceria and ceria-containing mixed oxides. Compared to the Ln_2O_3/Al_2O_3 systems discussed in a previous section of this chapter, the chemistry of supported ceria shows some differences worth of commenting on. For oxide loadings well below the theoretical monolayer [406], under oxidizing conditions, ceria tends to form tri-dimensional crystallites on alumina supports. HRTEM studies on a $Ce_{0.8}Tb_{0.2}O_{2-x}/Al_2O_3$ sample do also confirm the presence of well faceted micro-crystals of the supported mixed oxide phase [165,410]. A rather similar behavior has been reported for CeO_2/SiO_2 [405]. On the contrary, heating the supported ceria samples under reducing conditions favors the solid state reaction with the support. As a result, a perovskite, $CeAlO_3$ [406,411], or cerium silicates [405] are formed. The occurrence of these phases, an effect which resembles the behavior already noted for the supported sesquioxides, implies the stabilization of the Ce^{3+} oxidation state, and, therefore, the deactivation of the supported ceria as an oxygen buffer [411]. The process is at least partly reversible, so that, upon heating under oxidizing conditions the deactivated alumina- [411] or silica-supported [271] samples the perovskite or silicate phases are destroyed, with inherent recovery of cerium dioxide. In the case of alumina-supported praseodymia, the formation of the corresponding perovskite, $PrAlO_3$, though sensitive to the preparation procedure, has been observed on heating under oxidizing conditions [381]. This noticeable difference between the supported ceria and praseodymia systems is interpreted as due to the mixed-valent nature of the latter, even under oxygen pressure [381].

2.3.7. Other Studies on the Reactivity of the Higher Rare Earth Oxides

2.3.7.1. Strong Metal/Support Interaction Effects in NM/CeO_2 Systems

The strong metal/support interaction (SMSI) effect is presently a well known chemical and nano-structural phenomenon exhibited by $NM/CeO_2(Ce_xM_{1-x}O_{2-y}$; M: Zr, Tb) catalysts [272]. First reported for M/TiO_2 catalysts [413], this effect, which is typically associated to reducible oxide supports [353], consists of a strong and reversible modification of the chemisorptive and catalytic properties of the supported noble metal phase by the virtue of its chemical interaction with the reduced oxide support. As discussed in a recent review work [353], upon increasing the reduction temperature, typically under flowing hydrogen, perturbations in the electronic structure of the metal nano-crystals are observed first; then, at higher reduction temperatures, typically 973 K for NM/CeO_2 catalysts, an additional effect consisting of the partial covering of the metal particles by moieties of the reduced support occurs. This second phenomenon, which is referred to as decoration effect, has been well characterized by means of HRTEM [353,414], Figure 2-14.

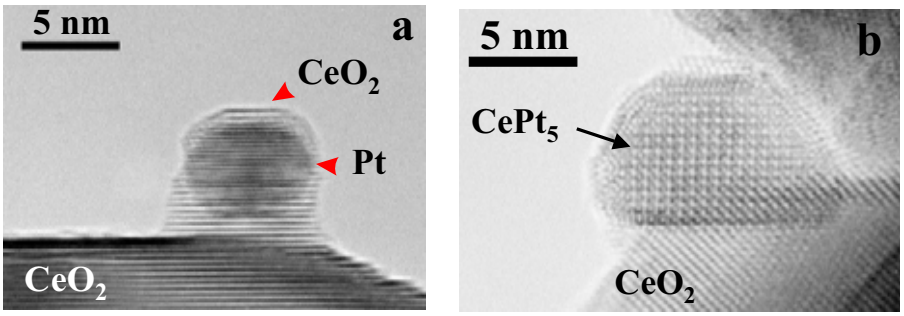

Figure 2-14. HRTEM micrographs showing the occurrence of metal decoration (a) and alloying phenomena (b) in a Pt/CeO_2 catalyst reduced at 973 K and 1173 K, respectively. Images taken from ref. [414].

Moreover, in the specific case of ceria-supported platinum catalyst reduced at 1173 K or above, the HRTEM images have unequivocally shown the occurrence of an additional chemical/nano-structural effect consisting of the formation of an inter-metallic $CePt_5$ phase. This implies the incorporation of heavily reduced cerium into the Pt lattice. No similar effect could be detected on Rh/CeO_2 [353]. By contrast, in Pd/CeO_2 catalysts, though no inter-metallic phases have been observed, shifts in the XRD diffraction peaks assigned to Pd has been interpreted as due to some dissolution of Ce into the palladium lattice [401,415].

Initially investigated on NM/CeO_2 systems, there are presently available data indicating that NM/$Ce_{0.8}Tb_{0.2}O_{2-x}$, and NM/$Ce_{0.68}Z_{0.32}O_2$ catalysts do also show some of the manifestations of the strong metal/support interaction effect. Thus, the HREM studies carried out on $Ce_{0.8}Tb_{0.2}O_{2-x}$-supported Rh and Pt clearly indicate the occurrence of metal decoration, and even, in the case of the Pt catalyst, the formation of the inter-metallic $LnPt_5$ phase, mentioned above [272]. The effect of the reduction temperature on the chemisorptive properties of $Ce_{0.68}Z_{0.32}O_2$-supported Rh, Pd and Pt has also been investigated [416,417]. In [416,417], by jointly analyzing hydrogen adsorption, and metal dispersion data as determined by HRTEM, it is concluded that, upon increasing the reduction temperature, a progressive loss of the metal chemisorption capabilities occurs. The effect is stronger in Pt and Pd, as compared to Rh, thus suggesting that the chemistry involved in this phenomenon depends on the nature of the noble metal [417]. These studies have also shown that deactivation in NM/Ceria-Zirconia catalysts reduced up to 1173 K, under flowing diluted H_2 (P_{H2} = 38 Torr), mainly consists of an electronic perturbation of metal nano-crystals, decoration effects playing a minor role. Likewise, no indication of alloying phenomena could be deduced from the analysis of the HRTEM images reported in refs. [416,417].

The reversible nature of the above-mentioned phenomena has also been investigated. In the case of purely electronic effects, i.e. on catalysts reduced at 773 K or below, very mild re-oxidation treatments allow to partly recover the catalyst from the deactivated state [348,353]. By contrast, reversion from the decorated or alloyed states requires re-oxidation treatments at temperatures well above 773 K [272,353,418]. This behavior contrasts with that exhibited by the NM/TiO_2 catalysts,

the classic SMSI systems, for which re-oxidation at 773 K is high enough as to ensure the regeneration of the catalysts from the deactivated state [353].

2.3.7.2. Disproportionation Processes induced on the Higher Rare Earth Oxides by Acidic Solutions or Aging-in-Air

It is well known that intermediate praseodymia [419] and terbia [420] phases undergo solvolytic disproportionation in diluted acidic solutions. As a result the Ln^{3+} ions present in the starting oxide sample are leached out, and dioxide, LnO_2, crystals are formed. In accordance with the HREM studies reported in [420-422], the reaction mechanism would imply the transfer of the Ln^{3+} from the surface reaction sites into the solution. The surface concentration of reduced lanthanoid ions (Ln^{3+}) would be regenerated by the virtue of a process consisting of the electron transfer from the interior to the surface of the crystal coupled with oxygen ion migration in the opposite sense [202]. The reaction, which proceeds to completion, also induces very important textural changes in the solid phase [202,423].

In a 5% aqueous solution of acetic acid, at room temperature, the disproportionation reaction is relatively slow, particularly in the case of terbia, for which one month treatment is approximately required for completion [423]; nevertheless, as shown in [423-425], the rate of reaction can be increased very significantly (less than 1 day treatment) by ultrasound irradiation.

The occurrence of leaching phenomena may be very relevant in catalyst preparation. In particular, supported noble metal catalysts are often prepared by impregnation techniques from acidic aqueous solutions of the corresponding metal precursor salts. When applied this procedure, some support dissolution may occur during the impregnation step, the rare earth containing dissolved phase being later on co-deposited with noble metal salt during the subsequent drying treatment. In this way, the final reduction step of the procedure may lead to a partial covering (decoration) and even encapsulation of the dispersed noble metal. This preparation-induced nano-structural effect, in addition to modify the general chemical properties of the final active phases, and particularly their catalytic behavior, is also important when discussing the likely occurrence of a true strong metal/support interaction effect [413] in reducible rare earth oxide supported metal catalysts [33]. Though no experimental proofs are to our knowledge available, support dissolution/co-deposition processes should not be disregarded when conventional impregnation procedures are applied to the preparation of catalysts consisting of noble metals highly dispersed on praseodymia, terbia, or their mixed oxides. In fact, this kind of effect have been reported to occur during the impregnation of rhodium onto rare earth sesquioxides soluble in acidic aqueous solutions like lanthana [426,427] or samaria [428].

Disproportionation of the praseodymium and terbium oxides may also be induced by prolonged exposure to air, at room temperature [26,189]. As a result, $Ln(OH)_3$ and LnO_2 phases are formed. It would be therefore important to verify the likely occurrence of this phase segregation effect, because of its influence on the actual structural constitution and chemical behavior of the resulting material. Likewise, the formation of $Ln(OH)_3$ (Ln: Pr, Tb) may strongly favor the occurrence of dissolution/coprecipitation phenomena during the preparation of praseodymia (terbia) supported metal catalysts. These phenomena may induce nanostructural effects similar to those commented on above.

2.3.7.3. Surface Chemical Properties of the Higher Rare Earth Oxides

To a very large extent the surface characterization studies on higher rare earth oxides have dealt with ceria. Special attention has been paid to its interaction with H_2 and CO, both in the presence and in the absence of a highly dispersed metal phase. The specific interest on these studies is mainly due to the very wide use of H_2 and CO as probe molecules in the characterization of supported metal phases. Two recent review works have dealt with this particular topic [272,323].

The interaction hydrogen with ceria and ceria-related mixed oxides is acknowledged to be rather complex. As deduced from [272], significant progress has been made in the understanding of the chemical phenomena involved in it. There are however, some particular aspects which still remain open to discussion. In particular, it is uncertain, whether heating ceria under hydrogen pressure may lead to the formation of purely surface chemisorbed hydrogen atoms, as suggested by the results reported in [47], or implies the incorporation of some hydrogen atoms into the bulk of the oxide, also proposed in the literature [429]. Some very recent results suggest the latter as the most likely option [293,430].

Though some microcalorimetric studies of CO_2 and NH_3 chemisorption on praseodymia [124], and ceria and related mixed oxides [125] are available, the FTIR spectroscopy is the most commonly used technique for the surface chemical characterization of these materials [323]. The application of FTIR as a tool for investigating the surface properties of ceria has been recently reviewed [323]. Numerous probe molecules are considered, and their usefulness in both acid-base and redox characterization of ceria discussed [323]. In addition to the studies on H_2 and CO adsorption, the results on chemisorbed methanol have proved to be particularly interesting. When adsorbed at room temperature on ceria [323] or ceria-zirconia mixed oxides [342,431], methanol dissociates into methoxy groups (CH_3O^-) as a result of its O-H bond breaking [323]. This chemisorbed species exhibits a characteristic ν(O-C) IR absorption band, the position of which being sensitive to the coordination, linear or bridged, to the surface cations, but also to the oxidation state of the surface cationic species [323]. Likewise, in the case of ceria-zirconia mixed oxides the methoxy species coordinated to cerium and zirconium cations are distinguishable [342,431]. Accordingly, the FTIR investigation of the methanol adsorption on these oxides may be used for evaluating both the Ce^{3+}/Ce^{4+} ratio, i.e. their surface redox state [323], and the Ce/Zr ratio, i.e. their surface composition [342,431]. These two parameters are very relevant in the surface characterization of ceria, and ceria-zirconia mixed oxide materials.

Acknowledgements: Financial support from the MCYT (Project MAT2002-02782) and the Junta de Andalucía (Group FQM-110) is gratefully acknowledged.

References

1. B.T. Kilbourn, *Cerium: A Guide to Its Role in Chemical Technology*, Molycorp Inc., New York, 1992.
2. B.T. Kilbourn, *A Lanthanide Lanthology. Part I, A-L*, Molycorp Inc., New York, 1993.
3. D.J. Fray, *Science,* **289,** 2295 (2000).
4. K. Schermanz, Production, Application and Safety Issues of Cerium-Based Materials, in A. Trovarelli (ed.), *Catalysis by Ceria and Related Materials,* Imperial College Press, London, p.1, 2002.
5. T. Uda, K.T. Jacob, and M. Hirasawa, *Science,* **289,** 2326 (2000).
6. G. Adachi and N. Imanaka, *Chem. Rev.,* **98**, 1479 (1998).
7. M.P. Rosynek, *Catal. Rev. Sci. Eng.,* **16**, 111 (1977).
8. A. Trovarelli, *Catal. Rev. Sci. Eng.,* **38,** 439 (1996).
9. S. Bernal, J. Kaspar, and A. Trovarelli, *Catal. Today,* **50**, 173 (1999).
10. J. Kaspar, M. Graziani, and P. Fornasiero, Ceria-Containing Three-Way Catalysts, in K.A. Gschneidner, Jr. and L. Eyring, (eds.), *Handbook on the Physics and Chemistry of Rare Earths (Vol. 29),* Elsevier Science B.V., p.159, 2000.
11. A. Trovarelli (ed.), *Catalysis by Ceria and Related Materials*, Imperial College Press, London, 2002.
12. B. T. Kilbourn, *A Lanthanide Lanthology. Part II, M-Z*, Molycorp Inc., New York, 1994.
13. G. Blasse and B.C. Grabmaier, *Luminescent Materials*, Springer, Berlin, 1994.
14. G. Adachi, N. Imanaka, and S. Tamura, *Chem. Rev.*, **102,** 2405 (2002).
15. M. Mogensen, Ceria-Based Electrodes, in A. Trovarelli (ed.), *Catalysis by Ceria and Related Materials,* Imperial College Press, London, p.453, 2002.
16. T. Mori, J. Drennan, J.H. Lee, J.G. Li, and T. Ikegami, *Solid State Ionics,* **154-155**, 461 (2002).
17. C. Peng, Y. Wang, K. Jiang, B.Q. Bin, H.W. Liang, J. Feng, and J. Meng, *J. Alloys Compds.,* **349,** 273 (2003).
18. M. Shelef and R.W. McCabe, *Catal. Today,* **62,** 35 (2000).
19. M. Shelef, G.W. Graham, and R.W. McCabe, Twenty-Five Years After Introduction of Automotive Catalysts: What Next?, in A. Trovarelli (ed.), *Catalysis by Ceria and Related Materials,* Imperial College Press, London, p.343, 2002.
20. J.E. Huheey, E.A. Keiter, and R.L. Keiter, *Inorganic Chemistry. Principles of Structure and Reactivity, 4th. Ed.*, HaperCollins College Publishers, New York, 1993.
21. Z.C. Kang and L. Eyring, *Aust. J. Chem.,* **49,** 981 (1997).
22. L.R. Morss, *J. Less Common Met.,* **93,** 301 (1983).
23. E.H.P. Cordfunke and R.J.M. Konings, *Thermochim. Acta*, **375**, 65 (2001).
24. D.A. Johnson, *Some Thermodynamic Aspects of Inorganic Chemistry*, Cambridge University Press, Cambridge, 1982.
25. M.W. Shafer, J.B. Torrance, and T. Penney, *J. Phys. Chem. Solids*, **33**, 2251 (1972).
26. L. Eyring, The Binary Rare Earth Oxides, in K.A. Gschneidner, Jr. and L. Eyring, (eds.), *Handbook of the Physics and Chemistry of Rare Earths,* North-Holland Publishing Company, p.337, 1979.
27. R.L. Martin, *J. Chem. Soc., Dalton Trans.*, 1335 (1974).
28. E. Antic-Fidancev, J. Holsa, and M. Lastusaari, *J. Alloys Compds.,* **341,** 82 (2002).
29. N. Hirosaki, S. Ogata, and C. Kocer, *J. Alloys Compds.,* **351,** 31 (2003).
30. S. Bernal, F.J. Botana, R. García, and J.M. Rodríguez-Izquierdo, *J. Chem. Soc. , Dalton Trans.,* 1765 (1988).
31. P. Pomonis, *React. Kinet. Catal. Lett.,* **18,** 247 (1981).
32. D.A. Johnson, *J. Chem. Ed.,* **57,** 475 (1980).
33. S. Bernal, J.J. Calvino, M.A. Cauqui, J.M. Gatica, C. Lopez Cartes, J.A. Perez Omil, and J.M. Pintado, *Catal. Today,* **77,** 385 (2003).
34. S. Bernal, J.J. Calvino, C. López-Cartes, J.M. Pintado, J.A. Pérez-Omil, J.M. Rodríguez-Izquierdo, K. Hayek, and G. Rupprechter, *Catal. Today,* **52,** 29 (1999).
35. S. Bernal, F.J. Botana, R. García, F. Ramírez, and J.M. Rodríguez-Izquierdo, *Appl. Catal.,* **31,** 267 (1987).
36. S. Bernal, F.J. Botana, R. García, F. Ramírez, and J.M. Rodríguez-Izquierdo, *J. Mater. Sci.,* **22,** 3793(1987).
37. D.F. Mullica and W.O. Milligan, *J. Inorg. Nucl. Chem.,* **42,** 223 (1980).
38. G.W. Beall, W.O. Milligan, and H.A. Wolcott, *J. Inorg. Nucl. Chem.,* **39,** 65 (1977).
39. D. Touret and F. Queyroux, *Rev. Chim. Min.,* **9,** 883 (1972).

40. M.P. Rosynek and D.T. Magnuson, *J. Catal.,* **48,** 417 (1977).
41. R.S. Roth and S.J. Schneider, *J. Res. Nat. Bur. Stand. A- Phys. Chem.,* **64A,** 309 (1960).
42. J.A.K. Tareen and T.R.N. Kutty, *Proc. Indian Acad. Sci. -Chem. Sci.,* **89,** 277 (1980).
43. M.W. Shafer and R. Roy, *J. Am. Ceram. Soc.,* **42,** 563 (1959).
44. F. Ali, M.E. Smith, S. Steuernagel, and H.J. Whitfield, *J. Mater. Chem.,* **6,** 261 (1996).
45. B. Klingenberg and M.A. Vannice, *Chem. Mater.,* **8,** 2755 (1996).
46. S. Bernal, F.J. Botana, R. García, and J.M. Rodríguez-Izquierdo, *Thermochim. Acta,* **66,** 139 (1983).
47. S. Bernal, J.J. Calvino, G.A. Cifredo, J.M. Gatica, J.A. Pérez-Omil, and J.M. Pintado, *J. Chem. Soc. , Faraday Trans.,* **89,** 3499 (1993).
48. S. Bernal, F.J. Botana, R. García, and J.M. Rodríguez-Izquierdo, *Mater. Lett.,* **6,** 71 (1987).
49. S. Bernal, F.J. Botana, R. García, M.L. López, and J.M. Rodríguez-Izquierdo, *Inorg. Chim. Acta,* **140,** 49 (1987).
50. H. Dexpert, M. Lemaitre-Blaise, and P. Caro, London, *Proc. 7th. Int. Symp. Reactiv. Solids*, Chapman&Hall, p.758, 1972.
51. P. Caro, *C. R. Acad. Sci. Paris,* **273,** 1169 (1971).
52. M.P. Rosynek and D.T. Magnuson, *J. Catal.,* **46,** 402 (1977).
53. H. Dexpert, E. Antic-Fidancev, J.P. Coutures, and P. Caro, *J. Crystallog. Spectrosc. Res.,* **12,** 129 (1982).
54. B.I. Swanson, C. Machell, G.W. Beall, and W.D. Milligan, *J. Inorg. Nucl. Chem.,* **40,** 694 (1978).
55. S. Bernal, F.J. Botana, R. García, and J.M. Rodríguez-Izquierdo, *Reactiv. Solids,* **4,** 23 (1987).
56. S. Bernal, F.J. Botana, R. García, and J.M. Rodríguez-Izquierdo, *J. Mater. Sci.,* **23,** 1474 (1988).
57. S. Bernal, J.A. Díaz, R. García, and J.M. Rodríguez-Izquierdo, *J. Mater. Sci.,* **20,** 537 (1985).
58. S. Bernal, F.J. Botana, J. Pintado, R. García, and J.M. Rodríguez-Izquierdo, *J. Less Common Met.,* **110,** 433 (1985).
59. F. Ali, A.V. Chadwick, and M.E. Smith, *J. Mater. Chem.,* **7,** 285 (1997).
60. R.P. Turcotte, J.O. Sawyer, and L. Eyring, *Inorg. Chem.,* **8,** 238 (1969).
61. R.P. Turcotte, J.M. Haschke, M.S. Jenkins, and L. Eyring, *J. Solid State Chem.,* **2,** 593 (1970).
62. S. Bernal and J.M. Criado, *Rev. Inst. Mex. Petrol.,* **8,** 80 (1976).
63. S.M.R. da Rocha, C.A. da Silva Queiroz, and A. Abrao, *J. Alloys Compds.,* **344,** 389 (2002).
64. I. Mayer and F. Kassierer, *J. Inorg. Nucl. Chem.,* **28,** 2430 (1966).
65. K.C. Patil, G.V. Chandras, M.V. George, and C.N.R. Rao, *Can. J. Chem.,* **46,** 257 (1968).
66. J.S. Shaplygin, V.P. Komarov, and V.B. Lazarev, *J. Thermal Anal.,* **15,** 215 (1979).
67. A. Glasner, E. Levy, and M. Steimberg, *J. Inorg. Nucl. Chem.,* **25,** 1415 (1963).
68. K.G. Nair, W.W. Sreerayan, and V.S.V. Nayar, *Thermochim. Acta,* **39,** 253 (1980).
69. P. Caro, J.C. Achard, and O. de Pous, Propriétés Physiques et Stabilité Thermique des Carbonates, Hydroxycarbonates et Oxycarbonates de la Série des Terres Rares, Paris, Ed. CNRS. Colloques Internationaux du CNRS. **Vol. I**, p.285, 1970.
70. Y. Watanabe, S. Miyazaki, T. Maruyama, and Y. Saito, *J. Mater. Sci. Lett.,* **5,** 135 (1986).
71. P. Jeevanandam, Y. Koltypin, and A. Gedanken, *J. Mater. Chem.,* **11,** 869 (2001).
72. J.J. Bentzen, P.L. Husum, and O.T. Sorensen, *High Tech. Ceramics,* 385 (1987).
73. H. Dexpert, G. Schiffmacher, and P. Caro, *J. Solid State Chem.,* **15,** 301 (1975).
74. H. Hinode, R. Sharma, and L. Eyring, *J. Solid State Chem.,* **84,** 102 (1990).
75. Z.C. Kang and L. Eyring, *J. Solid State Chem.,* **88,** 303 (1990).
76. M. Akinc, D.J. Sordelet, and M. Munson, *Adv. Ceram. Mater.,* **3,** 211 (1988).
77. A. Olafsen and H. Fjellvag, *J. Mater. Chem.,* **9,** 2697 (1999).
78. R.G. Charles, *J. Inorg. Nucl. Chem.,* **27,** 1489 (1965).
79. C. da S.Queiroz, J.R. Matos, M.E. Vasconcellos, and A. Abrao, *J. Alloys Compds.,* **344,** 32 (2002).
80. A.N. Christensen and R.G. Hazell, *Acta Chem. Scand. Ser. A-Phys. Inorg. Chem.,* **38A,** 157 (1984).
81. J.A.K. Tareen, M.N. Viswanathiah, and N. Krishnankutty, *Rev. Chim. Min.,* **17,** 50 (1980).
82. G.W. Beall, W.O. Milligan, and S. Mroczkowski, *Acta Crystallogr. B,* **32,** 3143 (1976).
83. J.M. Haschke and L. Eyring, *Inorg. Chem.,* **10,** 2267 (1971).
84. A.N. Christensen, *Acta Chem. Scand.,* **27,** 2973 (1973).
85. T.R.N. Kutty, J.A.K. Tareen, and I. Mohammed, *J. Less Common Met.,* **105,** 197 (1985).
86. J.M. Haschke and L. Eyring, *Inorg. Chem.,* **10,** 2267 (1971).
87. P. Caro, M. Lamaitre-Blaise, H. Dexpert, and J.O. Sawyer, *C. R. Acad. Sci. Paris (Ser. C),* **272,** 57 (1971).
88. P. Caro and M. Lemaitre-Blaise, *C. R. Acad. Sci. Paris (Ser. C),* **269,** 687 (1969).

89. M. Akinc and D. Sordelet, *Adv. Ceram. Mater.,* **2,** 232 (1987).
90. Q. Li, Z. Han, M. Shao, X. Liu, and Y. Qian, *J. Phys. Chem. Solids,* **64,** 295 (2003).
91. C.H. Lu and H.C. Wang, *Mater. Sci. Eng. B,* **90,** 138 (2002).
92. P. Caro, J.O. Sawyer, and L. Eyring, *Spectrochim. Acta A-Molec. Spectrosc.,* **28,** 1167 (1972).
93. R. Aumont, F. Genet, M. Passaret, and Y. Toudic, *C. R. Acad. Sci. Paris (Ser. C),* **272,** 314 (1971).
94. A.N. Christensen, *Acta Chem. Scand.,* **24,** 2440 (1970).
95. A.N. Christensen, *Acta Chem. Scand.,* **24,** 3074 (1970).
96. S. Mroczkow and J. Eckert, *J. Cryst. Growth,* **13,** 549 (1971).
97. A.N. Christensen, *Acta Chem. Scand.,* **27,** 1835 (1973).
98. M.N. Viswanathiah, J.A.K. Tareen, and T.R.N. Kutty, *Mater. Res. Bull.,* **15,** 855 (1980).
99. J.A.K. Tareen and T.R.N. Kutty, *J. Cryst. Growth,* **50,** 527 (1980).
100. P. Caro, M. Lemaitre-Blaise, and F. Trombe, *C. R. Acad. Sci. Paris (Ser. C),* **267,** 1594 (1968).
101. P. Caro and M. Lemaitre-Blaise, *Proc. 7th. Rare Earth Res. Conf.,* **1,** 187 (1968).
102. J.O. Sawyer, P. Caro, and L. Eyring, *Rev. Chim. Min.,* **10,** 93 (1973).
103. H. Dexpert and P. Caro, *Mater. Res. Bull.,* **9,** 1577 (1974).
104. S. Bernal, R. García, J.M. López, and J.M. Rodríguez-Izquierdo, *Collect. Czech. Chem. Comm.,* **48,** 2205 (1983).
105. S. Bernal, F.J. Botana, R. García, F. Ramírez, and J.M. Rodríguez-Izquierdo, *J. Chem. Soc. , Faraday Trans. I,* **83,** 2279 (1987).
106. S. Bernal, F.J. Botana, R. García, J.M. Pintado, and J.M. Rodríguez-Izquierdo, *Mater. Res. Bull.,* **22,** 131 (1987).
107. R. Alvero, A. Bernal, I. Carrizosa, J.A. Odriozola, and J.M. Trillo, *J. Mater. Sci.,* **22,** 1517(1987).
108. A. Bernal, *Estudio Del Sistema Lu_2O_3-H_2O: Influencia Del Método De Preparación Del Sesquióxido*, PhD Thesis, University of Seville, 1985.
109. I.I. Diakonov, K.V. Ragnarsdottir, and B.R. Tagirov, B.R., *Chem. Geology,* **151,** 327 (1998).
110. R. Alvero, I. Carrizosa, J.A. Odriozola, and J.M. Trillo, *J. Less Common Met.,* **109,** 197 (1985).
111. R. Alvero, A. Bernal, I. Carrizosa, J.A. Odriozola, and J.M. Trillo, *J. Thermal Anal.,* **32,** 637 (1987).
112. R. Alvero, J.A. Odriozola, and J.M. Trillo, *J. Mater. Sci.,* **20,** 1828 (1985).
113. R. Alvero, A. Bernal, I. Carrizosa, J.A. Odriozola, and J.M. Trillo, *J. Less Common Met.,* **110,** 425 (1985).
114. R. Alvero, A. Bernal, I. Carrizosa, A. Justo, J.A. Odriozola, and J.M. Trillo, *J. Less Common Met.,* **112,** 347 (1985).
115. J.O. Sawyer, P.Caro, and L. Eyring, *Rev. Chim. Min.,* **10,** 93 (1973).
116. R. Alvero, I. Carrizosa, J.A. Odriozola, J.M. Trillo, and S. Bernal, *J. Less Common Met.,* **94,** 139 (1983).
117. B. Klingenberg and M.A. Vannice, *Chem. Mater.,* **8,** 2755 (1996).
118. R. Tueta and A.M. Lejus, *Rev. Chim. Min.,* **10,** 105 (1973).
119. G. Bacquet, C. Bouysset, and C. Escribe, *J. Solid State Chem.,* **18,** 247 (1976).
120. H.T. Fullam and F.P. Roberts, Reactions of the Sesquioxides of Pm, Nd and Sm With Water, Richland, Washington 99352, Batelle Memorial Institute, Pacific Northwest Laboratories, **BNWL-1421**, 1 (1970).
121. C. Sudhakar and M.A. Vannice, *Appl. Catal.,* **14,** 47 (1985).
122. D.T. Cromer, *J. Phys. Chem.,* **61,** 753 (1957).
123. H.L. Yakel, *Acta Crystallogr.,* **B35,** 564 (1979).
124. A. Auroux and A. Gervasini, *J. Phys. Chem.,* **94,** 6371 (1990).
125. M.G. Cutrufello, I. Ferino, R. Monaci, E. Rombi, and V. Solinas, *Topics in Catalysis,* **19,** 225 (2002).
126. A. Gervasini and A. Auroux, *J. Catal.,* **131,** 190 (1991).
127. S. Bernal, C. Blanco, R. García, A.M. Oliván, and J.M. Trillo, *J. Catal.,* **71,** 21 (1981).
128. J.S.J. Hargreaves, G.J. Hutchings, R.W. Joyner, and S.H. Taylor, *Appl. Catal. A,* **227,** 191 (2002).
129. M. Utiyama, H. Hattori, and K. Tanabe, *J. Catal.,* **53,** 237 (1978).
130. T.J. Toops, A.B. Walters, and M.A. Vannice, *Appl. Catal. B,* **38,** 183 (2002).
131. B. Klingenberg and M.A. Vannice, *Appl. Catal. B,* **21,** 19 (1999).
132. S.J. Huang, A.B. Walters, and M.A. Vannice, *J. Catal.,* **192,** 29 (2000).
133. V.G. Milt, M.L. Pissarello, E.E. Miro, and C.A. Querini, *Appl. Catal. B,* **41,** 397 (2003).
134. Y. Ozawa, Y. Tochihara, M. Nagai, and S. Omi, *Catal. Commun.,* **4,** 87 (2003)
135. S. Suhonen, M. Valden, M. Pessa, A. Savimaki, M. Harkonen, M. Hietikko, J. Pursiainen, and R. Laitinen, *Appl. Catal. A,* **207,** 113 (2001).

136. T. Yamamoto, T. Tanaka, T. Matsuyama, T. Funabiki, and S. Yoshida, *Solid State Commun.,* **111,** 137 (1999).
137. T. Yamamoto, T. Matsuyama, T. Tanaka, T. Funabiki, and S. Yoshida, *Phys. Chem. Chem. Phys.,* **1,** 2841 (1999).
138. T. Yamamoto, T. Tanaka, T. Matsuyama, T. Funabiki, and S. Yoshida, *J. Phys. Chem. B,* **105,** 1908 (2001).
139. Y. Takita, T. Yoko-o, N. Egashira, and F. Hori, *Bull. Chem. Soc. Jpn.,* **55,** 2653 (1982).
140. J.S. Rieck and A.T. Bell, *J. Catal.,* **99,** 278 (1986).
141. D. Yu-Hua, C. De-An, and T. Khi-Rui, *Appl. Catal.,* **35,** 77 (1987).
142. F. Oudet, P. Courtine, and A. Vejux, *J. Catal.,* **114,** 112 (1988).
143. B.A. Milligan and J.A. Dumesic, *J. Catal.,* **115,** 180 (1989).
144. J.A. Odriozola, I. Carrizosa, and R. Alvero, *Stud. Surf. Sci. Catal.,* **48,** 713 (1989).
145. M. Ozawa, M. Kimura, and A. Isogai, *J. Less Common Met.,* **162,** 297 (1990).
146. J.J. Benítez, R. Alvero, M.J. Capitán, I. Carrizosa, and J.A. Odriozola, *Appl. Catal.,* **71,** 219 (1991).
147. D. Wang, X. Cheng, Z. Huang, X. Wang, and S. Peng, *Appl. Catal.,* **77,** 109 (1991).
148. T. Shido and Y. Iwasawa, *J. Catal.,* **137,** 267 (1992).
149. J.J. Benítez, I. Carrizosa, and J.A. Odriozola, *Appl. Surf. Sci.,* **68,** 565 (1993).
150. M.J. Capitán, P. Malet, M.A. Centeno, A. Muñoz-Páez, I. Carrizosa, and J.A. Odriozola, *J. Phys. Chem.,* **97,** 9233 (1993).
151. J.J. Benítez, I. Carrizosa, and J.A. Odriozola, *Appl. Surf. Sci.,* **84,** 391 (1995).
152. M.J. Capitán, M.A. Centeno, P. Malet, I. Carrizosa, I. Odriozola, A. Márquez, and J. Fernández Sanz, *J. Phys. Chem.,* **99,** 4655 (1995).
153. P. Malet, J.J. Benítez, M.J. Capitán, M.A. Centeno, I. Carrizosa, and J.A. Odriozola, *Catal. Lett.,* **18,** 81 (1993).
154. Y.N. Nogin, N.V. Chesnokov, and V.I. Kovalchuk, *Stud. Surf. Sci. Catal.,* **75,** 2031 (1993).
155. Y. Kadowaki and K. Aika, *J. Catal.,* **161,** 178 (1996).
156. Y. Ogawa, M. Toba, and Y. Yoshimura, *Appl. Catal. A,* **246,** 213 (2003).
157. Y.Q. Yang, S.J. Dai, Y.Z. Yuan, R.C. Lin, D.L. Tang, and H.B. Zhang, *Appl. Catal. A,* **192,** 175 (2000).
158. R. Zhou, Y. Cao, S.R. Yan, and K.N. Fan, *Appl. Catal. A,* **236,** 103 (2002).
159. B.M. Reddy, B. Chowdhury, and P.G. Smirniotis, *Appl. Catal. A,* **219,** 53 (2001).
160. R. Craciun and N. Dulamita, *Catal. Lett.,* **46,** 229 (1997).
161. Y.Z. Chen, B.J. Liaw, and W.H. Lai, *Appl. Catal. A,* **230,** 73 (2002).
162. R.M. Ferrizz, G.S. Wong, T. Egami, and J.M. Vohs, *Langmuir,* **17,** 2464 (2001).
163. T.J. Toops, A.B. Walters, and M.A. Vannice, *Appl. Catal. A,* **233,** 125 (2002).
164. G.A.H. Mekhemer, *Phys. Chem. Chem. Phys.,* **4,** 5400 (2002).
165. S. Bernal, G. Blanco, G.A. Cifredo, J.J. Delgado, D. Finol, J.M. Gatica, J.M. Rodríguez-Izquierdo, H. Vidal, and A. Hoser, *Chem. Mater.,* **14,** 844 (2002).
166. S.T. King, *J. Catal.,* **131,** 215 (1991).
167. A. Galtayries, G. Blanco, G.A. Cifredo, D. Finol, J.M. Gatica, J.M. Pintado, H. Vidal, R. Sporken, and S. Bernal, *Surf. Interf. Anal.,* **27,** 941 (1999).
168. H. Vidal, S. Bernal, R.T. Baker, D. Finol, J.A. Pérez-Omil, J.M. Pintado, and J.M. Rodríguez-Izquierdo, *J. Catal.,* **183,** 53 (1999).
169. J.S. Ledford, M. Houalla, A. Proctor, D.M. Hercules, and L. Petrakis, *J. Phys. Chem.,* **93,** 6770 (1989).
170. B. Béguin, E. Garbowski, and M. Primet, *Appl. Catal.* **75,** 119 (1991).
171. L.P. Haack, C.R. Peters, J.E. de Vries, and K. Otto, *Appl. Catal. A,* **87,** 103 (1992).
172. J.S. Church, N.W. Cant, and D.L. Trimm, *Appl. Catal. A,* **101,** 105 (1993).
173. N.S. Fígoli, P.C. L'Argentiere, A. Arcoya, and X.L. Seoane, *J. Catal.,* **155,** 95 (1995).
174. G.T. Haddad, B. Chen, and G.T. Goodwin, *J. Catal.,* **160,** 43 (1996).
175. R.A. Shkrabina, N.A. Koryabkina, V.A. Ushakov, M. Lausberg, E.M. Moroz, and Z.R. Ismagilov, *Kinet. Katal.,* **37,** 109 (1996).
176. M. Scheithauer, H. Knözinger, and M.A. Vannice, *J. Catal.,* **178,** 701 (1998).
177. Y. Jun-Ying and W.E. Swartz Jr., *Spectros. Lett.,* **17,** 331 (1984).
178. L.P. Haack, J.E. de Vries, K. Otto, and M.S. Chattha, *Appl. Catal. A,* **82,** 199 (1992).
179. C. López-Cartes, G. Blanco, J.J. Calvino, J.M. Gatica, H. Vidal, C.J. Kiely, J.G. Zheng, and J.A. Pérez-Omil, *Inst. Phys. Conf. Ser.,* **168,** 413 (2001).
180. F. Oudet, A. Vejux, and P. Courtine, *Appl. Catal.,* **50,** 78 (1989).
181. M. Bettman, R.E. Chase, K. Otto, and W.H. Weber, *J. Catal.,* **117,** 447 (1989).

182. L. Zhang, J. Lin, and Y. Chen, *J. Chem. Soc. , Faraday Trans.,* **88,** 497 (1992).
183. H. Arai and M. Machida, *Appl. Catal. A,* **138,** 161 (1996).
184. H. Schaper, E.B.M. Doesburg, and L.L. Van Reijen, *Appl. Catal.,* **7,** 211 (1983).
185. H. Schaper, D.J. Amesz, E.B.M. Doesburg, and L.L. Van Reijen, *Appl. Catal.,* **9,** 129 (1984).
186. P. Burtin, J.P. Brunelle, M. Pijolat, and M. Soustelle, *Appl. Catal.,* **34,** 225 (1987).
187. P. Burtin, J.P. Brunelle, M. Pijolat, and M. Soustelle, *Appl. Catal.,* **34,** 239 (1987).
188. S. Bernal, F.J. Botana, A. Laachir, P. Moral, G.A. Martin, and V. Perrichon, *Eur. J. Solid State Chem.,* **28,** 421 (1991).
189. S. Bernal, F.J. Botana, G.A. Cifredo, J.J. Calvino, A. Jobacho, and J.M. Rodríguez-Izquierdo, *J. Alloys Compds.,* **180,** 271 (1992).
190. S. Bernal, F.J. Botana, R. García, F. Ramírez, and J.M. Rodríguez-Izquierdo, *Mater. Chem. Phys.,* **18,** 119 (1987).
191. J. Tong, J. Liu, Z.C. Kang, and L. Eyring, *J. Alloys Compds.,* **207-208,** 416 (1994).
192. Z.C. Kang, J. Tong, and L. Eyring, *J. Alloys Compds.,* **207-208,** 420 (1994).
193. L. Eyring, *J. Solid State Chem.,* **1,** 376 (1970).
194. J. Kordis and L. Eyring, *J. Phys. Chem.,* **72,** 2044 (1968).
195. J. Kordis and L. Eyring, *J. Phys. Chem.,* **72,** 2030 (1968).
196. C. López-Cartes, J.A. Pérez-Omil, J.M. Pintado, J.J. Calvino, Z.C. Kang, and L. Eyring, *Ultramicroscopy,* **80,** 19 (1999).
197. Z.C. Kang and L. Eyring, *J. Alloys Compds.,* **249,** 206 (1997).
198. B.F. Hoskins and R.L. Martin, *Aust. J. Chem.,* **48,** 709 (1995).
199. J. Zhang, R.B. Von Dreele, and L. Eyring, *J. Solid State Chem.,* **122,** 53 (1996).
200. Z.C. Kang, J. Zhang, and L. Eyring, *Z. Anorg. Allg. Chem.,* **622,** 465 (1996).
201. J. Zhang, R.B. Von Dreele, and L. Eyring, *J. Solid State Chem.,* **118**, 133 (1995).
202. L. Eyring, *J. Alloys Compds.,* **207-208**, 1 (1994).
203. J. Zhang, R.B. Von Dreele, and L. Eyring, *J. Solid State Chem.,* **104**, 21 (1993).
204. Z.C. Kang and L. Eyring, *J. Alloys Compds.,* **181**, 48 (1992).
205. E. Schweda, D.J.M. Bevan, and L. Eyring, *J. Solid State Chem.,* **90**, 109 (1991).
206. E. Schweda and L. Eyring, *J. Solid State Chem.,* **78**, 1 (1989).
207. C. Boulesteix and L. Eyring, *J. Solid State Chem.,* **75**, 291 (1988).
208. E. Schweda, L. Eyring, and D.J. Smith, *Ultramicroscopy,* **23**, 443 (1987).
209. M. Gasgnier, G. Schiffmacher, L. Eyring, and P. Caro, *J. Less Common Met.,* **127**, 167 (1987).
210. C. Boulesteix and L. Eyring, *J. Solid State Chem.,* **66**, 125 (1987).
211. P. Knappe and L. Eyring, *J. Solid State Chem.,* **58**, 312 (1985).
212. L. Eyring, *Mater. Res. Soc. Symp. Proc.,* **24**, 187 (1984).
213. R.T. Tuenge and L. Eyring, *J. Solid State Chem.,* **41**, 75 (1982).
214. R.T. Tuenge and L. Eyring, *J. Solid State Chem.,* **29**, 165 (1979).
215. E. Summerville, R.T. Tuenge, and L. Eyring, *J. Solid State Chem.,* **24**, 21 (1978).
216. P. Kunzmann and L. Eyring, *J. Solid State Chem.,* **14**, 229 (1975).
217. R.P. Turcotte, M.S. Jenkins, and L. Eyring, *J. Solid State Chem.,* **7**, 454 (1973).
218. M.Z. Lowenstein, L. Kihlborg, K.H. Lau, J.M. Haschke, and L. Eyring, *National Bureau of Standards Special Publication,* **364**, 343 (1972).
219. D.A. Burnham and L. Eyring, *J. Phys. Chem.,* **72**, 4415 (1968).
220. D.A. Burnham, L. Eyring, and J. Kordis, *J. Phys. Chem.,* **72**, 4424 (1968).
221. N.C. Baeziger, H.A. Eick, H.S. Schuldt, and L. Eyring, *J. Am. Chem. Soc.,* **83**, 2219 (1961).
222. R.P. Turcotte, J.M. Warmkessel, R.J.D. Tilley, and L. Eyring, *J. Solid State Chem.,* **3**, 265 (1971).
223. L. Eyring, *Adv. Chem. Ser.,* **71**, 67 (1967).
224. B.G. Hyde, D.J.M. Bevan, and L. Eyring, *Phil. Trans. Roy. Soc.,* **259**, 583 (1966).
225. B.G. Hyde and L. Eyring, On Phase Equilibria and Phase Reactions in TbO_x-O_2 and Related Systems, in L. Eyring, (ed.), *Rare Earth Research III,* Gordon and Breach, New York, London, Paris, p.623, 1965.
226. B.G. Hyde, D.J.M. Bevan, and L. Eyring, *Rare Earth Research II,* Gordon & Breach, New York, p.277, 1964.
227. L. Eyring and B. Holmberg, *Adv. Chem. Ser.,* **39**, 46 (1963).
228. R.E. Ferguson, E.D. Guth, and L. Eyring, *J. Am. Chem. Soc.,* **76**, 3890 (1954).
229. L.R. Morss, Comparative Thermochemical and Oxidation-Reduction Properties of Lanthanides and Actinides, in K.A. Gschneidner, Jr., L. Eyring, G.R. Choppin, and G.H. Lander (eds.), *Handbook on the Physiscs and Chemistry of Rare Earths, Vol. 18,* Elsevier Science, New York, p.239, 1994.

230. H. Inaba, A. Navrotsky, and L. Eyring, *J. Solid State Chem.,* **37**, 67 (1981).
231. H. Inaba, A. Navrotsky, and L. Eyring, *J. Solid State Chem.,* **37**, 77 (1981).
232. A. Maren, S.H. Lin, R.H. Langley, and L. Eyring, *J. Solid State Chem.,* **53**, 329 (1984).
233. H. Inaba, S.H. Lin, and L. Eyring, *J. Solid State Chem.,* **37**, 58 (1981).
234. T. Sugihara, S.H. Lin, and L. Eyring, *J. Solid State Chem.,* **40**, 226 (1981).
235. T. Sugihara, S.H. Lin, and L. Eyring, *J. Solid State Chem.,* **40**, 189 (1981).
236. H. Inaba, S.P. Pack, S.H. Lin, and L. Eyring, *J. Solid State Chem.,* **33**, 295 (1980).
237. C. Boulesteix and L. Eyring, *J. Solid State Chem.,* **71**, 458 (1987).
238. L. Eyring, D.J. Smith, and G.J. Wood, *Inst. Phys. Conf. Ser.,* **78**, 333 (1985).
239. A.T. Lowe and L. Eyring, *J. Solid State Chem.,* **14**, 383 (1975).
240. B.G. Hyde, E.E. Garver, U.E. Kuntz, and L. Eyring, *J. Phys. Chem.,* **69**, 1667 (1965).
241. H.A. Eick, L. Eyring, E. Summerville, and R.T. Tuenge, *J. Solid State Chem.,* **42**, 47 (1982).
242. A.J. Skarnulis, E. Summerville, and L. Eyring, *J. Solid State Chem.,* **23**, 59 (1978).
243. J. Zhang, R.B. Von Dreele, and L. Eyring, *J. Solid State Chem.,* **118**, 141 (1995).
244. A.T. Lowe, K.H. Lau, and L. Eyring, *J. Solid State Chem.,* **15**, 9 (1975).
245. A. Trovarelli, Structural Properties and Nonstoichiometric Behavior of CeO_2, in A. Trovarelli (ed.), *Catalysis by Ceria and Related Materials,* Imperial College Press, London, p.15, 2002.
246. J. Kaspar and P. Fornasiero, *J. Solid State Chem.,* **171**, 19 (2003).
247. J. Kaspar, P. Fornasiero, and N. Hickey, *Catal. Today,* **77**, 419 (2003).
248. A. Trovarelli, C. Leitenburg, M. Boaro, and G. Dolcetti, *Catal. Today,* **50**, 353 (1999).
249. M. Boaro, M. Vicario, C. de Leitenburg, G. Dolcetti, and A. Trovarelli, *Catal. Today,* **77**, 407 (2003).
250. S. Bernal, F.J. Botana, J.J. Calvino, G.A. Cifredo, J.A. Pérez-Omil, and J.M. Pintado, *Catal. Today,* **28**, 219 (1995).
251. S. Bedrane, C. Descorme, and D. Duprez, *Catal. Today,* **73**, 233 (2002).
252. D. Duprez and C. Descorme, Oxygen Storage Capacity and Related Phenomena on Ceria-Based Catalysts, in A. Trovarelli (ed.), *Catalysis by Ceria and Related Materials,* Imperial College Press, London, p.243, 2002.
253. A. Trovarelli, M. Boaro, E. Rocchini, C. de Leitenburg, and G. Dolcetti, *J. Alloys Compds.,* **323-324**, 584 (2001).
254. D. Terribile, J. Llorca, M. Boaro, C. de Leitenburg, G. Dolcetti, and A. Trovarelli, *Chem. Commun.,* 1897 (1998).
255. S. Bernal, G. Blanco, M.A. Cauqui, P. Corchado, J.M. Pintado, and J.M. Rodriguez-Izquierdo, *Chem. Commun.,* 1545 (1997).
256. S. Bernal, G. Blanco, M.A. Cauqui, A.I. Martin, J.M. Pintado, A. Galtayries, and R. Sporken, *Surf. Interf. Anal.,* **30**, 85 (2000).
257. S. Bernal, G. Blanco, J.J. Delgado, J.M. Pintado, and J.M. Rodriguez-Izquierdo, *J. Alloys Compds.,* **344**, 347 (2002).
258. H. Vidal, J. Kaspar, M. Pijolat, G. Colón, S. Bernal, A.M. Cordón, V. Perrichon, and F. Fally, *Appl. Catal. B:Environmental,* **30**, 75 (2001).
259. H. Vidal, J. Kaspar, M. Pijolat, G. Colón, S. Bernal, A.M. Cordón, V. Perrichon, and F. Fally, *Appl. Catal. B,* **27**, 49 (2000).
260. F. Fally, V. Perrichon, H. Vidal, J. Kaspar, M. Daturi, J.C. Lavalley, G. Blanco, J.M. Pintado, and S. Bernal, *Catal. Today,* **59**, 387 (2000).
261. N. Hickey, P. Fornasiero, R. Di Monte, J. Kaspar, M. Graziani, and G. Dolcetti, *Catal. Lett.,* **72**, 45 (2001).
262. N. Hickey, P. Fornasiero, J. Kaspar, J.M. Gatica, and S. Bernal, *J. Catal.,* **200**, 181 (2001).
263. M. Boaro, C. Leitenburg, G. Dolcetti, and A. Trovarelli, *J. Catal.,* **193**, 338 (2000).
264. N. Hickey, P. Fornasiero, J. Kaspar, M. Graziani, G. Blanco, and S. Bernal, *Chem. Commun.*, 357 (2000).
265. Y. Sakamoto, K. Kizaki, T. Motohiro, Y. Yokota, H. Sobukawa, M. Uenishi, H. Tanaka, and M. Sugiura, *J. Catal.,* **211**, 157 (2002).
266. S. Bedrane, C. Descorme, and D. Duprez, *Catal. Today,* **75**, 401 (2002).
267. A.D. Logan and M. Shelef, *J. Mater. Res.,* **9**, 468 (1994).
268. M.Y. Sinev, G.W. Graham, L.P. Haack, and M. Shelef, *J. Mater. Res.,* **11**, 1960 (1996).
269. E.S. Putna, J.M. Vohs, R.J. Gorte, and G.W. Graham, *Catal. Lett.,* **54**, 17 (1998).
270. G. Blanco, J.M. Pintado, S. Bernal, M.A. Cauqui, M.P. Corchado, A. Galtayries, J. Ghijsen, R. Sporken, T. Eickhoff, and W. Drube, *Surf. Interf. Anal.,* **34**, 120 (2002).
271. E. Rocchini, M. Vicario, J. Llorca, C. de Leitenburg, G. Dolcetti, and A. Trovarelli, *J. Catal.,* **211**, 407 (2002).

272. S. Bernal, J.J. Calvino, J.M. Gatica, C. López-Cartes, and J.M. Pintado, Chemical and Nano-Structural Aspects of the Preparation and Characterisation of Ceria and Ceria-Based Mixed Oxide Supported Metal Catalysts, in A. Trovarelli (ed.), *Catalysis by Ceria and Related Materials,* Imperial College Press, London, p.85, 2002.
273. F. Giordano, A. Trovarelli, C. de Leitenburg, and M. Giona, *J. Catal.,* **193**, 273 (2000).
274. P. Fornasiero, J. Kaspar, and M. Graziani, *Appl. Catal. B,* **22**, L11 (1999).
275. R.T. Baker, S. Bernal, G. Blanco, A.M. Cordon, J.M. Pintado, J.M. Rodriguez-Izquierdo, F. Fally, and V. Perrichon, *Chem. Commun.*, 149 (1999).
276. N. Izu, H. Kishimoto, T. Omata, K. Ono, and S. Otsuka-Yao-Matsuo, *Sci. Tech. Adv. Mater.,* **2**, 397 (2001).
277. S. Otsuka-Yao-Matsuo, T. Omata, N. Izu, and H. Kishimoto, *J. Solid State Chem.,* **138**, 47 (1998).
278. N. Izu, T. Omata, and S. Otsuka-Yao-Matsuo, *J. Alloys Compds.,* **270**, 107 (1998).
279. P. Fornasiero, G. Balducci, R. di Monte, J. Kaspar, V. Sergo, G. Gubitosa, A. Ferrero, and M. Graziani, *J. Catal.,* **164**, 173 (1996).
280. G. Balducci, P. Fornasiero, R. di Monte, J. Kaspar, S. Meriani, and M. Graziani, *Catal. Lett.,* **33**, 193 (1995).
281. V. Perrichon, A. Laachir, G. Bergeret, R. Frety, L. Tournayan, and O. Touret, *J. Chem. Soc., Faraday Trans.,* **90**, 773 (1994).
282. F.M.Z. Zotin, L. Tournayan, J. Varloud, V. Perrichon, and R. Frety, *Appl. Catal.,* **98**, 99 (1993).
283. A. Laachir, V. Perrichon, A. Badri, J. Lamotte, E. Catherine, J.C. Lavalley, J. El Fallah, L. Hilaire, F. Le Normand, E. Quéméré, G.N. Sauvion, and O. Touret, *J. Chem. Soc., Faraday Trans.,* **87**, 1601 (1991).
284. S. Bernal, G. Blanco, J.M. Gatica, J.A. Pérez Omil, and J. Pintado, *Bol. Soc. Esp. Cerám. Vidrio,* **36**, 353 (1997).
285. S. Bernal, G. Blanco, M.A. Cauqui, G.A. Cifredo, J.M. Pintado, and J.M. Rodríguez-Izquierdo, *Catal. Lett.,* **53**, 51 (1998).
286. S. Bernal, G. Blanco, J.J. Calvino, G.A. Cifredo, J.A. Pérez-Omil, J.M. Pintado, and A. Varo, *Stud. Surf. Sci. Catal.,* **82**, 507 (1994).
287. M. Daturi, E. Finocchio, C. Binet, J.C. Lavalley, F. Fally, and V. Perrichon, *J. Phys. Chem. B,* **103**, 4884 (1999).
288. S. Salasc, V. Perrichon, M. Primet, M. Chevrier, F. Mathis, and N. Moral, *Catal. Today,* **50**, 227 (1999).
289. S. Bernal, J.J. Calvino, G.A. Cifredo, J.M. Gatica, J.A. Pérez-Omil, A. Laachir, and V. Perrichon, *Stud. Surf. Sci. Catal.,* **96**, 419 (1995).
290. A. Laachir, V. Perrichon, S. Bernal, J.J. Calvino, and G.A. Cifredo, *J. Molec. Catal.,* **89**, 391 (1994).
291. S. Bernal, J.J. Calvino, G.A. Cifredo, J.M. Rodríguez-Izquierdo, V. Perrichon, and A. Laachir, *J. Chem. Soc. , Chem. Commun.*, 460 (1992).
292. A. Badri, J. Lamotte, J.C. Lavalley, A. Laachir, V. Perrichon, O. Touret, G.N. Sauvion, and E. Quéméré, *Eur. J. Solid State Inorg. Chem.,* **28**, 445 (1991).
293. J.A. Rodríguez, J.C. Hanson, J.Y. Kim, G. Liu, A. Iglesias Juez, and M. Fernández García, *J. Phys. Chem. B,* **107**, 3535 (2003).
294. J.C. Conesa, M. Fernández-García, and A. Martínez-Arias, *Catalysis by Ceria and Related Materials,* Imperial College Press, London, p 169 (2002).
295. E. López-Navarrete, A. Caballero, A.R. Gonzalez-Elipe, and M. Ocaña, *J. Mater. Res.,* **17**, 797 (2002).
296. S. Yamazaki, T. Matsui, T. Ohashi, and Y. Arita, *Solid State Ionics,* **136-137**, 913 (2000).
297. A. Norman, V. Perrichon, A. Bensaddik, S. Lemaux, J.H. Bitter, and D.C. Koningsberger, *Topics in Catalysis,* **16**, 363 (2001).
298. S.H. Overbury, D.R. Mullins, D.R. Huntley, and Lj. Kundakovic, *J. Catal.,* **186**, 296 (1999).
299. H. Arashi, H. Naitoh, and M. Ishigame, *Solid State Ionics,* **40-41**, 539 (1990).
300. P. Li and I.W. Chen, *J. Am. Ceram. Soc.,* **77**, 118 (1994).
301. J. El Fallah, S. Boujana, H. Dexpert, A. Kiennemann, J. Majerus, O. Touret, F. Villain, and F. Le Normand, *J. Phys. Chem.,* **98**, 5522 (1994).
302. P. Li, I.W. Chen, J.E. Penner-Hahn, and T.Y. Tien, *J. Am. Ceram. Soc.,* **74**, 958 (1991).
303. F. Le Normand, L. Hilaire, K. Kili, G. Krill, and G. Maire, *J. Phys. Chem.,* **92**, 2561 (1988).
304. C. López-Cartes, S. Bernal, J.J. Calvino, M.A. Cauqui, G. Blanco, J.A. Pérez-Omil, J.M. Pintado, S. Helveg, and P.L. Hansen, *Chem. Commun.*, 644 (2003).
305. R. Sharma, *Microsc. Microanal.,* **7**, 494 (2001).

306. G. Blanco, J.J. Calvino, M.A. Cauqui, M.P. Corchado, C. López-Cartes, C. Colliex, J.A. Pérez-Omil, and O. Stephan, *Chem. Mater.,* **11**, 3610 (1999).
307. L.A.J. Garvie and P.R. Buseck, *J. Phys. Chem. Solids,* **60**, 1943 (1999).
308. J.P. Holgado, R. Alvarez, and G. Munuera, *Appl. Surf. Sci.,* **161**, 301 (2000).
309. J.P. Holgado, G. Munuera, J.P. Espinos, and A.R. Gonzalez-Elipe, *Appl. Surf. Sci.,* **158**, 164 (2000).
310. M. Daturi, C. Binet, J.C. Lavalley, A. Galtayries, and R. Sporken, *Phys. Chem. Chem. Phys.,* **1**, 5717 (1999).
311. D.I. Kondarides and X.E. Verykios, *J. Catal.,* **174**, 52 (1998).
312. A. Galtayries, R. Sporken, G. Blanchard, and R. Caudano, *J. Electron Spectr. Related Phenom.,* **88-91**, 951 (1998).
313. A. Pfau, J. Sanz, K.D. Schierbaum, W. Göpel, J.P. Belzunegui, and J.M. Rojo, *Stud. Surf. Sci. Catal. (11th. Int. Congr. Catal.),* **101**, 931 (1996).
314. A. Pfau, K.D. Schierbaum, and W. Göpel, *Surf. Sci.,* **331-333**, 1479 (1995).
315. Y. Zhou, M. Nakashima, and J.M. White, *J. Phys. Chem.,* **92**, 812 (1988).
316. T. Jin, Y. Zhou, G.J. Mains, and J.M. White, *J. Phys. Chem.,* **91**, 5931 (1987).
317. M. Fernandez-Garcia, A. Martinez-Arias, A. Iglesias-Juez, A.B. Hungria, J.A. Anderson, J.C. Conesa, and J. Soria, *Appl. Catal. B,* **31**, 39 (2001).
318. A. Martinez-Arias, M. Fernandez-Garcia, A. Iglesias-Juez, A.B. Hungria, J.A. Anderson, J.C. Conesa, and J. Soria, *Appl. Catal. B,* **31**, 51 (2001).
319. M. Fernández-García, A. Martinez-Arias, A. Iglesias-Juez, C. Belver, A.B. Hungria, J.C. Conesa, and J. Soria, *J. Catal.,* **194**, 385 (2000).
320. A. Martinez-Arias, M. Fernández-García, J. Soria, and J.C. Conesa, *J. Catal.,* **182**, 367 (1999).
321. A. Martínez-Arias, J. Soria, and J.C. Conesa, *J. Catal.,* **168**, 364 (1997)
322. M. Daturi, E. Finocchio, C. Binet, J.C. Lavalley, F. Fally, V. Perrichon, H. Vidal, J.N. Hickey, and J. Kaspar, *J. Phys. Chem. B,* **104**, 9186 (2000).
323. C. Binet, M. Daturi, and J.C. Lavalley, *Catal. Today,* **50**, 207 (1999).
324. C. Binet, A. Badri, and J.C. Lavalley, *J. Phys. Chem.,* **98**, 6392 (1994).
325. C. Binet, A. Badri, M. Boutonnet-Kizling, and J.C. Lavalley, *J. Chem. Soc., Faraday Trans.,* **90**, 1023 (1994).
326. C. Binet, A. Jadi, and J.C. Lavalley, *J. Chem. Phys.,* **88**, 499 (1991).
327. S. Bernal, J.J. Calvino, G.A. Cifredo, A. Laachir, V. Perrichon, and J.M. Herrmann, *Langmuir,* **10**, 717 (1994).
328. J.M. Herrmann, E. Ramaroson, J.F. Tempere, and M.F. Guilleux, *Appl. Catal.,* **53**, 117 (1989).
329. Y. Takasu, M. Matsui, H. Tamura, S. Kawamura, Y. Matsuda, and I. Toyoshima, *J. Catal.,* **69**, 51 (1981).
330. Y. Takasu, T. Yoko-o, M. Matsui, Y. Matsuda, and I. Toyoshima, *J. Catal.,* **77**, 485 (1982).
331. S. Bernal, G. Blanco, G.A. Cifredo, J.A. Pérez-Omil, J.M. Pintado, and J.M. Rodríguez-Izquierdo, *J. Alloys Compds.,* **250**, 449 (1997).
332. E.S. Putna, J.M. Vohs, and R.J. Gorte, *J. Phys. Chem.,* **100**, 17862 (1996).
333. S. Bernal, G. Blanco, F.J. Botana, J.M. Gatica, J.A. Pérez Omil, J. Pintado, and J.M. Rodríguez-Izquierdo, *J. Alloys Compds.,* **207/208**, 196 (1994).
334. K. Otsuka and T. Nakajima, *J. Catal.*, **103**, 216 (1987).
335. X. Liu, Y. Yang, and J. Zhang, *Appl. Catal.,* **71**, 167 (1991).
336. S. Bernal, J.J. Calvino, G.A. Cifredo, J.M. Gatica, C. Larese, and J. Pintado, *J. Alloys Compds.,* **225**, 633 (1995).
337. G. Blanco, *Alternativas Al CeO_2 Como Componente De Catalizadores De Tres Vias: Óxidos Mixtos De La/Ce, Y/Ce y Tb/Ce*, PhD Thesis, University of Cadiz, 1997.
338. M.F.L. Johnson and J. Mooi, *J. Catal.,* **103**, 502 (1987).
339. S. Bernal, J.J. Calvino, G.A. Cifredo, and J.M. Rodríguez-Izquierdo, *J. Phys. Chem.,* **99**, 11794 (1995).
340. S. Bernal, J.J. Calvino, G.A. Cifredo, J.M. Rodríguez-Izquierdo, V. Perrichon, and A. Laachir, *J. Catal.,* **137**, 1 (1992).
341. Z.C. Kang and L. Eyring, *J. Solid State Chem.,* **155**, 129 (2000).
342. P. Fornasiero, T. Montini, M. Graziani, J. Kaspar, A.B. Hungría, A. Martínez-Arias, and J.C. Conesa, *Phys. Chem. Chem. Phys.,* **4**, 149 (2002).
343. C. Binet, A. Jadi, and J.C. Lavalley, *J. Chem. Phys.,* **89**, 1779 (1992).
344. C. Li, Y. Sakata, T. Arai, K. Domen, K. Maruya, and T. Onishi, *J. Chem. Soc., Faraday Trans.,* **85**, 929 (1989).

345. C. Li, Y. Sakata, T. Arai, K. Domen, K. Maruya, and T. Onishi, *J. Chem. Soc., Chem. Commun.,* 410 (1991).
346. F. Sadi, D. Duprez, F. Gerard, and A. Miloudi, *J. Catal.,* **213**, 226 (2003).
347. K. Otsuka, M. Hatano, and A. Morikawa, *J. Catal.,* **79**, 493 (1983).
348. S. Bernal, G. Blanco, J.M. Gatica, C. Larese, and H. Vidal, *J. Catal.,* **200**, 411 (2001).
349. T. Jin, T. Okuhara, G.J. Mains, and J.M. White, *J. Phys. Chem.,* **91**, 3310 (1987).
350. M. Haneda, Y. Kintaichi, and H. Hamada, *Phys. Chem. Chem. Phys.,* **4**, 3146 (2002).
351. M. Daturi, N. Bion, J. Saussey, J.-C. Lavalley, C. Hedouin, T. Seguelong, and G. Blanchard, *Phys. Chem. Chem. Phys.,* **3**, 252 (2001).
352. A. Holmgren, B. Andersson, and D. Duprez, *Appl. Catal. B,* **22**, 215 (1999).
353. S. Bernal, J.J. Calvino, M.A. Cauqui, J.M. Gatica, C. Larese, J.A. Pérez-Omil, and J.M. Pintado, *Catal. Today,* **50**, 175 (1999).
354. D.R. Mullins and S.H. Overbury, *J. Catal.,* **188**, 340 (1999).
355. E.S. Putna, R.J. Gorte, J.M. Vohs, and G.W. Graham, *J. Catal.,* **178**, 598 (1998).
356. J. Stubenrauch and J.M. Vohs, *Catal. Lett.,* **47**, 21 (1997).
357. H.C. Yao and Y.F.Y. Yao, *J. Catal.*, **86**, 254 (1984).
358. B. Harrison, A.F. Diwell, and C. Hallett, *Platinum Metals Rev.,* **32**, 73 (1988).
359. J.P. Holgado and G. Munuera, *Stud. Surf. Sci. Catal.,* **96**, 109 (1995).
360. A. Trovarelli, G. Dolcetti, C. Leitenburg, and J. Kaspar, *Stud. Surf. Sci. Catal.,* **75C**, 2781 (1993).
361. J. Barrault and A. Alouche, *Appl. Catal.,* **58**, 255 (1990).
362. J. Barbier Jr., F. Marsollier, and D. Duprez, *Appl. Catal., A,* **90**, 11 (1992).
363. J. Kaspar and P. Fornasiero, Structural Properties and Thermal Stability of Ceria-Zirconia and Related Materials, in A. Trovarelli (ed.), *Catalysis by Ceria and Related Materials,* Imperial College Press, London, p.217, 2002.
364. G.R. Rao, J. Kaspar, S. Meriani, R. di Monte, and M. Graziani, *Catal. Lett.,* **24**, 107 (1994).
365. P. Fornasiero, R. di Monte, G.R. Rao, J. Kaspar, S. Meriani, A. Trovarelli, and M. Graziani, *J. Catal.,* **151**, 168 (1995).
366. F. Zamar, A. Trovarelli, C. Leitenburg, and G. Dolcetti, *J. Chem. Soc., Chem. Commun.*, 965 (1995).
367. A. Trovarelli, F. Zamar, J. Llorca, C. Leitenburg, G. Dolcetti, and J.T. Kiss, *J. Catal.,* **169**, 490. (1997)
368. G.R. Rao, P. Fornasiero, R. di Monte, J. Kaspar, G. Vlaic, G. Balducci, S. Meriani, G. Gubitosa, A. Cremona, and M. Graziani, *J. Catal.,* **162**, 1 (1996).
369. P.Fornasiero, G. Balducci, J. Kaspar, S. Meriani, R. di Monte, and M. Graziani, *Catal. Today,* **29**, 47 (1996).
370. F. Zamar, A. Trovarelli, C. Leitenburg, and G. Dolcetti, *Stud. Surf. Sci. Catal.,* **101**, 1283 (1996).
371. S. Yamazaki, T. Matsui, T. Sato, Y. Arita, and T. Nagasaki, *Solid State Ionics,* **154-155**, 113 (2002).
372. M. Katsuki, S. Wang, K. Yasumoto, and M. Dokiya, *Solid State Ionics,* **154-155**, 589 (2002).
373. A. Mineshige, T. Yasui, N. Ohmura, M. Kobune, S. Fujii, M. Inaba, and Z. Ogumi, *Solid State Ionics,* **152-153**, 493 (2002).
374. H. Yoshida, H. Deguchi, K. Miura, M. Horiuchi, and T. Inagaki, *Solid State Ionics,* **140**, 191 (2001).
375. S. Dikmen, P. Shuk, and M. Greenblatt, *Solid State Ionics,* **126**, 89 (1999).
376. J.G. Li, T. Ikegami, Y. Wang, and T. Mori, *J. Solid State Chem.,* **168**, 52 (2002).
377. W.M. O'Neill and M.A. Morris, *Chem. Phys. Lett.,* **305**, 389 (1999).
378. M. Ocaña, *Colloid. Polym. Sci.,* **280**, 274 (2002).
379. P. Knauth and H.L. Tuller, *J. Eur. Ceram. Soc.,* **19**, 831 (1999).
380. M.Y. Sinev, G.W. Graham, L.P. Haack, and M. Shelef, *11th International Congress on Catalysis,* Baltimore, USA, Po-128, 1996.
381. C.K. Narula, L.F. Allard, and G.W. Graham, *J. Mater. Chem.,* **9**, 1155 (1999).
382. M. Rajendran, K.K. Mallick, and A.K. Bhattacharya, *Mater. Sci. Eng. B,* **52**, 162 (1998).
383. M. Rajendran, M. Ghanashyam Krishna, K.K. Mallick, and A.K. Bhattacharya, *Mater. Sci. Eng. B,* **58**, 215 (1999).
384. T. Takeguchi, S.N. Furukawa, M. Inoue, and K. Eguchi, *Appl. Catal. A,* **240**, 223 (2003).
385. J. Kimpton, T.H. Randle, and J. Drennan, *Solid State Ionics,* **154-155**, 473 (2002).
386. J. Kimpton, T.H. Randle, and J. Drennan, *Solid State Ionics,* **149**, 89 (2002).
387. T. Otake, H. Yugami, H. Naito, K. Kawamura, T. Kawada, and J. Mizusaki, *Solid State Ionics,* **135**, 663 (2000).
388. H. Naito, N. Sakai, T. Otake, H. Yugami, and H. Yokokawa, *Solid State Ionics,* **135**, 669 (2000).

389. Y.L. Zhang, X.J. Jin, and X.Z. Hsu, *J. Eur. Ceram. Soc.,* **23**, 685 (2003).
390. M. Fernández-García, A. Martínez-Arias, A. Guerrero-Ruiz, J.C. Conesa, and J. Soria, *J. Catal.,* **211**, 326 (2002).
391. S. Rossignol, C. Descorme, C. Kappenstein, and D. Duprez, *J. Mater. Chem.,* **11**, 2587 (2001).
392. H. Yasuda, L.N. He, and T. Sakakura, *J. Catal.,* **209**, 547 (2002).
393. M. O'Connell and M.A. Morris, *Catal. Today,* **59**, 387 (2000).
394. P. Vidmar, P. Fornasiero, J. Kaspar, and M. Graziani, *J. Catal.,* **171**, 160 (1997).
395. G. Colón, F. Valdivieso, M. Pijolat, R.T. Baker, J.J. Calvino, and S. Bernal, *Catal. Today,* **50**, 271 (1999).
396. J. Kaspar, P. Fornasiero, and M. Graziani, *Catal. Today,* **50**, 285 (1999).
397. C. Cannas, M. Casu, A. Lai, A. Musinu, and G. Piccaluga, *Phys. Chem. Chem. Phys.,* **4**, 2286 (2002).
398. S. Lemaux, A. Bensaddik, A.M.J. van der Eerden, J.H. Bitter, and D.C. Koningsberger, *J. Phys. Chem. B,* **105**, 4810 (2001).
399. P. Fornasiero, E. Fonda, R. Di Monte, G. Vlaic, J. Kaspar, and M. Graziani, *J. Catal.,* **187**, 177 (1999).
400. L. Kepinski and J. Okal, *J. Catal.,* **192**, 48 (2000).
401. L. Kepinski, M. Wolcyrz, and J. Okal, *J. Chem. Soc. , Faraday Trans.,* **91,** 507 (1995).
402. F. Fajardie, J.F. Tempere, J.M. Manoli, G. Djega-Mariadassou, and G. Blanchard, *J. Chem. Soc. , Faraday Trans.,* **94,** 3727 (1998).
403. S. Bernal, F.J. Botana, J.J. Calvino, M.A. Cauqui, G.A. Cifredo, A. Jobacho, J.M. Pintado, and J.M. Rodríguez-Izquierdo, *J. Phys. Chem.,* **97,** 4118 (1993).
404. S. Bernal, F.J. Botana, J.J. Calvino, G.A. Cifredo, and J.A. Pérez-Omil, *Inst. Phys. Conf. Ser.,* **138,** 485 (1993).
405. L. Kepinski, M. Wolcyrz, and M. Marchewka, *J. Solid State Chem.,* **168,** 110 (2002).
406. A. Martínez-Arias, M. Fernández-García, L.N. Salamanca, R.X. Valenzuela, J.C. Conesa, and J. Soria, *J. Phys. Chem. B,* **104,** 4038 (2000).
407. W.P. Dow, Y.P. Wang, and T.J. Huang, *Appl. Catal. A,* **190,** 25 (2000).
408. M. Ozawa, K. Matuda, and S. Suzuki, *J. Alloys Compds.,* **303-304,** 56 (2000).
409. J.H. Holles, M.A. Switzer, and R.J. Davis, *J. Catal.,* **190,** 247 (2000).
410. S. Bernal, J.J. Calvino, G.A. Cifredo, D. Finol, J.M. Gatica, C.J. Kiely, C. López-Cartes, J.G. Zheng, and H. Vidal, *Chem. Mater.,* **14,** 1405 (2002).
411. T. Miki, T. Ogawa, M. Haneda, N. Kakuta, A. Ueno, S. Tateishi, S. Matsuura, and M. Sato, *J. Phys. Chem.,* **94,** 6464 (1990).
412. J.Z. Shyu, W.H. Weber, and H.S. Gandhi, *J. Phys. Chem.,* **92,** 4964 (1988).
413. G.L. Haller and D.E. Resasco, *Adv. Catal.,* **36,** 173 (1989).
414. S. Bernal, J.J. Calvino, J.M. Gatica, C. Larese, C. López-Cartes, and J.A. Pérez-Omil, *J. Catal.,* **169,** 510 (1997).
415. L. Kepinski and M. Wolcyrz, *Appl. Catal. A:General,* **150,** 197 (1997).
416. J.M. Gatica, R.T. Baker, P. Fornasiero, S. Bernal, G. Blanco, and J. Kaspar, *J. Phys. Chem. B,* **104,** 4667 (2000).
417. J.M. Gatica, R.T. Baker, P. Fornasiero, S. Bernal, and J. Kaspar, *J. Phys. Chem. B,* **105,** 1191 (2001).
418. S. Bernal, G. Blanco, J.J. Calvino, C. López-Cartes, J.A. Pérez-Omil, J.M. Gatica, O. Stephan, and C. Colliex, *Catal. Lett.,* **76,** 131 (2001).
419. Z.C. Kang and L. Eyring, *J. Solid State Chem.,* **75,** 52 (1988).
420. Z.C. Kang and L. Eyring, *J. Solid State Chem.,* **75,** 60 (1988).
421. Z.C. Kang, L. Eyring, and D.J. Smith, *Ultramicroscopy,* **22,** 71 (1987).
422. Z.C. Kang and L. Eyring, *Metall. Trans. A,* **22,** 1323 (1991).
423. M. Gasgnier, L. Albert, J. Derouet, L. Beaury, P. Maestro, T. Chopin, and P. Caro, *J. Solid State Chem.,* **112,** 367 (1994).
424. M. Gasgnier, J. Derouet, L. Albert, L. Beaury, P. Caro, and M. Deschamps, *J. Solid State Chem.,* **107,** 179 (1993).
425. M. Gasgnier, L. Albert, J. Derouet, L. Beaury, and P. Caro, *C. R. Acad. Sci. Paris,* **318, Série II** 915 (1994).
426. R. Kieffer, A. Kiennemann, M. Rodríguez, S. Bernal, and J.M. Rodríguez-Izquierdo, *Appl. Catal.,* **42,** 77 (1988).
427. S. Bernal, F.J. Botana, R. García, and J.M. Rodríguez-Izquierdo, *Stud. Surf. Sci. Catal.,* **48,** 123 (1989).

428. S. Bernal, F.J. Botana, J.J. Calvino, G.A. Cifredo, R. García, and J.M. Rodríguez-Izquierdo, *Ultramicroscopy,* **34,** 60 (1990).
429. J.L.G. Fierro, J. Soria, J. Sanz, and J.M. Rojo, *J. Solid State Chem.,* **66,** 154 (1987).
430. K. Sohlberg, S.T. Pantelides, and S.J. Pennycook, *J. Am. Chem. Soc.,* **123,** 6609 (2001).
431. M. Daturi, C. Binet, J.C. Lavalley, A. Galtayries, and R. Sporken, *Phys. Chem. Chem. Phys.,* **1,** 5717 (1999).

3. STRUCTURAL FEATURES OF RARE EARTH OXIDES

EBERHARD SCHWEDA[1] AND ZHENCHUAN KANG[2]
[1] *Universität Tübingen, Institut für Anorganische Chemie, Auf der Morgenstelle 18, 72076 Tübingen, Germany*
[2] *International Center for Quantum Structures and State Key Laboratory for Surface Sciences, Beijing 100080, Peoples Republic of China*

3.1. INTRODUCTION

Non-stoichiometry is a phenomenon in solid compounds related to defects and mixed valence. Fifty years ago a wide-range of non-stoichiometric phases were interpreted in terms of homologous series of ordered intermediate oxides. Small oxygen content variations in the dioxides of the binary rare earths lead to oxygen-deficient, fluorite-related phases [1–4]. The assimilation of oxygen vacancies establishes ordered superstructures to the fluorite type crystal and is characteristic for the non-stoichiometric higher oxides of the binary rare earths [5]. These oxides occur in several oxidation states of which the trivalent is the most common. Based on the structure solution of numerous intermediate binary rare earth higher oxides during the last decade (see section 3.2.2) several review articles were published, summarizing [6] and interpreting the results using different approaches to formulate a theory in order to predict the yet unknown defect distributions of fluorite related anion deficient compounds in the system [7–10].

For several reasons it is difficult to determine the structures of the homologous series phases by X-ray diffraction due to the weak scattering of X-rays by oxygen atoms. Neutron diffraction turned out to be the best method to determine the structures of these ordered oxygen deficient phases but it is almost impossible to prepare a sample consisting of a single phase because the oxygen content of the sample will easily vary with temperature and oxygen partial pressure. However the refinement of the neutron diffraction data from a powder sample needs proposed models. Those models might come from the knowledge about a structural principle for the homologous series phases. The crux of solving these structures is to obtain the diffraction data from a monophase sample. To overcome this

G. Adachi et al. (eds.), Binary Rare Earth Oxides, 57–93.

problem the use of high-resolution electron microscopy (HREM) is suitable in order to unravel the real structures in the different materials.

The following article will present the efforts undertaken during the last decades, utilizing all three different diffraction methods and HREM, in order to elucidate the structures of the binary rare earth oxides.

3.2. THE DIOXIDES

3.2.1. *The Fluorite Structure*

Ceria, praseodymia and terbia are crystallizing with the fluorite C1 structure. This structure type is the aristotype for all the intermediate rare earth oxides. It consists of a c.c.p. (cubic close packed) array of rare earth metals and a cubic primitive arrangement of oxygen atoms. The metal atoms are coordinated by eight anions and the oxygen atoms are coordinated tetrahedrally by metal atoms. Within a $\langle 211 \rangle_F$ projection (the subscript F refers to fluorite) perpendicular to $\langle 111 \rangle_F$ one might distinguish two sets of tetrahedral voids in this f.c.c. (face centred cubic) arrangement occupied by oxygen atoms. They are drawn in Fig. 3-1 and 3-2 in green and red color.

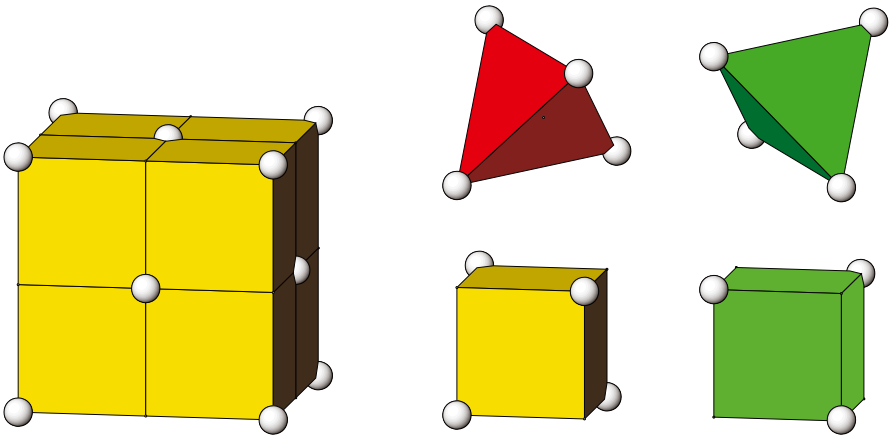

Figure 3-1. Fluorite unit cell and one octant of the cell ($M_{4/8}O$-module). Different orientations of the tetrahedral voids in the f.c.c. unit cell in different colors.

3.2.2. *The Structures of intermediate Ce-, Pr- and Tb-Oxides*

Binary oxides of Ce, Pr and Tb exhibit between the oxidation states +III and +IV a number of phases with compositions all belonging to a homologous series M_nO_{2n-2m}. The phase composition depends strictly on temperature and oxygen partial pressure. It is well established that these

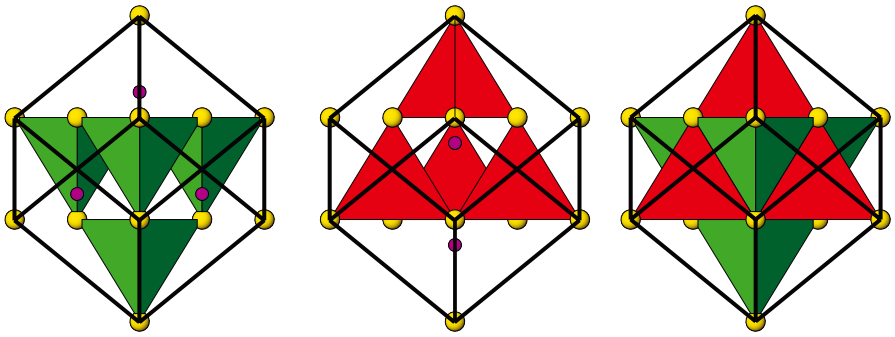

Figure 3-2. The two different sets of tetrahedral anion coordination in a f.c.c. unit cell.

phases are oxygen deficient and the structures are fluorite related. Defects within the fluorite structure type always occur in the cubic primitive anion sublattice while the f.c.c. cation array will remain rather unchanged.

TABLE 3-1. All phases in the binary rare earth intermediate oxides R_nO_{2n-2m} as identified by **electron diffraction**.

Symbol	Composition	Unit cell content	n	m
α	$MO_{1.72}$-MO_2	disordered nonstoichiometric	-	-
ι	$MO_{1.714}$	$Ce_{11}O_{20}$, $Pr_{11}O_{20}$, $Tb_{11}O_{20}$	7	1
ζ	$MO_{1.788}$	Ce_9O_{16} (?), Pr_9O_{16}	9	1
M19	$MO_{1.789}$	$Ce_{19}O_{34}$	19	2
M29	$MO_{1.793}$	$Ce_{29}O_{52}$	29	3
M39	$MO_{1.795}$	$Ce_{39}O_{70}$	39	4
ϵ	$MO_{1.800}$	$Ce_{40}O_{72}$ (?), $Pr_{40}O_{72}$	40	4
δ‘	$MO_{1.806}$	$Ce_{62}O_{112}$, $Pr_{62}O_{112}$, $Tb_{62}O_{112}$	62	6
$\delta(1)$	$MO_{1.818}$	$Ce_{11}O_{20}$, $Tb_{11}O_{20}$	11	1
$\delta(2)$	$MO_{1.818}$	$Pr_{88}O_{160}$	88	8
$\beta(0)$	$MO_{1.833}$	$Pr_{12}O_{22}$	12	1
$\beta(1)$	$MO_{1.833}$	$Pr_{24}O_{44}$	24	2
$\beta(2)$	$MO_{1.833}$	$Tb_{24}O_{44}$	24	2
$\beta(3)$	$MO_{1.833}$	$Tb_{48}O_{88}$	48	4
σ	$MO_{1.7}$-$MO_{1.6}$	disordered nonstoichiometric	-	-

Introducing a vacancy in the oxygen sublattice will have a certain impact on the positions of the surrounding atoms. All of the void surrounding atoms will relax in one or the other way. In almost all the structure deter-

minations it was found that the four metal atoms will move away by 20 pm and the six nearest oxygen neighbours will move towards the vacancy by 20-30 pm. This leaves the vacancy with a slight positiv charge.

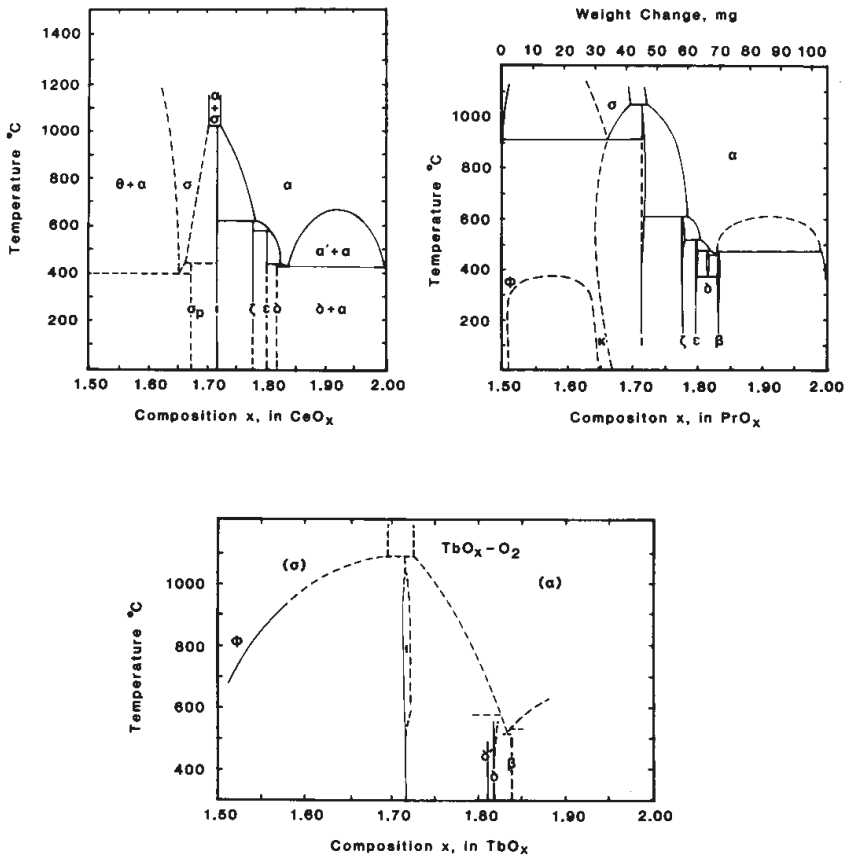

Figure 3-3. Phase diagrams for the cerium, praseodymium and terbium oxygen system (see [11]).

Fig. 3-3 shows the phase diagrams for the cerium, praseodymium and terbium oxides. It reveals several phases in each of the systems with their compositions depending on temperature and oxygen partial pressure. The different phases have been named as $\iota = MO_{1.714}$, $\zeta = MO_{1.788}$, $\epsilon = MO_{1.800}$, $\delta = MO_{1.818}$ and $\beta = MO_{1.833}$. Electron diffraction patterns (see Fig. 3-21) revealed the unit cells of those phases and their relationship to the

TABLE 3-2. Crystallographic data of intermediate rare earth oxides. All structures have been solved using **neutron powder diffraction**.

Compound	Space group	lattice constants[pm]		
		a	b	c
		α	β	γ
Ce_7O_{12} (ι) [15]	$R\bar{3}$	680		
	rhomb.	99.4		
	hex.	1037.83		967
Pr_7O_{12} (ι) [16]	$R\bar{3}$	674.31(6)		
	rhomb.	99.306(6)		
	hex.	1027.83		960.69
Tb_7O_{12} (ι) [17]	$R\bar{3}$	650.82(3)		
	rhomb.	99.342(1)		
	hex.	992.29		926.37
Pr_9O_{16} (ζ) [18]	$P\bar{1}$	673.96(8)	871.1(1)	667.26(8)
		97.424(1)	99.973(1)	75.301(1)
$Pr_{40}O_{72}$ (ϵ) [19]	$P2_1/c$	673.40(5)	1939.0(1)	1279.4(1)
			100.213(1)	
$Tb_{11}O_{20}$ (δ) [17]	$P\bar{1}$	650.992(4)	982.98(6)	648.78(4)
		90.019(2)	99.966(1)	95.88(1)
$Pr_{12}O_{22}$ ($\beta(1)$) [20]	$P2_1/c$	668.50(2)	1160.04(4)	1282.71(4)
			99.974(1)	

fluorite type subcell. $\iota = Pr_7O_{12}$, $\zeta = Pr_9O_{16}$, $\epsilon = Pr_{40}O_{72}$, $\delta(1) = Tb_{11}O_{20}$ and $\beta(1) = Pr_{24}O_{44}$. All these phases correspond to a general formula Pr_nO_{2n-2m} with m = 1 for ι, ζ, δ and m = 2 for β and m = 4 for ϵ. For more details see Table 3-1. The lattice constants of the different phases are given according to [12] in Table 3-2. The relationships of the different unit cells are presented in Table 3-3.

It should be noted that recently in nano-scale powders of CeO_2 Frenkel type defects have been found. From a neutron diffraction study interstitial oxygen defects have been proofed to exist depending on the fomation conditions of the ceria material [13]. The interstitial oxygen was revealed on the octahedral sites of the structure which is the center of the anion cube. These interstitials are charge compensated by oxygen vacancies in the structure.

TABLE 3-3. Relationship of the unit cells of the intermediate rare earth oxides to the fluorite subcell. The matrix contains the transformation vectors as column vectors. Data from electron diffraction. See also [12]. Matrix determinats give the relative volume compared to fluorite ($Fm\bar{3}m$). Question marks indicate speculative space groups from electron diffraction.

Ce_7O_{12} (ι) Pr_7O_{12} (ι) Tb_7O_{12} (ι)	$Fm\bar{3}m \rightarrow R\bar{3}_{\mathbf{(rhomb)}}$	$\mathbf{(a,b,c)}_7 = \mathbf{(a,b,c)}_F \quad \frac{1}{2}\begin{pmatrix} 2\bar{1}1 \\ 12\bar{1} \\ \bar{1}12 \end{pmatrix}$
	$Fm\bar{3}m \rightarrow R\bar{3}_{\mathbf{(hex)}}$	$\mathbf{(a,b,c)}_7 = \mathbf{(a,b,c)}_F \quad \frac{1}{2}\begin{pmatrix} 3\bar{2}2 \\ \bar{1}32 \\ \bar{2}\bar{1}2 \end{pmatrix}$
Pr_9O_{16} (ζ)	$Fm\bar{3}m \rightarrow P\bar{1}$	$\mathbf{(a,b,c)}_9 = \mathbf{(a,b,c)}_F \quad \frac{1}{2}\begin{pmatrix} 201 \\ 13\bar{1} \\ \bar{1}12 \end{pmatrix}$
$Ce_{19}O_{34}$	$Fm\bar{3}m \rightarrow P\bar{1}$ (?)	$\mathbf{(a,b,c)}_{19} = \mathbf{(a,b,c)}_F \quad \frac{1}{2}\begin{pmatrix} 2\bar{1}2 \\ 14\bar{1} \\ \bar{1}13 \end{pmatrix}$
$Pr_{40}O_{72}$ (ϵ)	$Fm\bar{3}m \rightarrow P2_1/c$	$\mathbf{(a,b,c)}_{40} = \mathbf{(a,b,c)}_F \quad \frac{1}{2}\begin{pmatrix} 202 \\ 15\bar{3} \\ \bar{1}53 \end{pmatrix}$
$Pr_{62}O_{112}$ (δ')	$Fm\bar{3}m \rightarrow P\bar{1}$ (?)	$\mathbf{(a,b,c)}_{62} = \mathbf{(a,b,c)}_F \quad \frac{1}{2}\begin{pmatrix} \bar{1}\bar{1}4 \\ 0\bar{4}\bar{2} \\ 5\bar{2}0 \end{pmatrix}$
$Ce_{11}O_{20}$ ($\delta(1)$) $Tb_{11}O_{20}$ ($\delta(1)$)	$Fm\bar{3}m \rightarrow P\bar{1}$	$\mathbf{(a,b,c)}_{11} = \mathbf{(a,b,c)}_F \quad \frac{1}{2}\begin{pmatrix} 2\bar{1}1 \\ 13\bar{1} \\ \bar{1}22 \end{pmatrix}$
$Pr_{24}O_{44}$ ($\beta(1)$)	$Fm\bar{3}m \rightarrow P2_1/c$	$\mathbf{(a,b,c)}_{24} = \mathbf{(a,b,c)}_F \quad \frac{1}{2}\begin{pmatrix} 202 \\ 13\bar{3} \\ \bar{1}33 \end{pmatrix}$
$Tb_{48}O_{88}$ ($\beta(3)$)	$Fm\bar{3}m \rightarrow P2_1/c$ (?)	$\mathbf{(a,b,c)}_{48} = \mathbf{(a,b,c)}_F \quad \frac{1}{2}\begin{pmatrix} 202 \\ 16\bar{3} \\ \bar{1}\bar{6}3 \end{pmatrix}$

Such Frenkel type defects are known to exist in many anion excess fluorite related compounds forming clusters, at higher defect concentration, like in U_4O_{9-x} [14]. This interstitial oxygen was made responsible for the excellent behaviour of ceria as an oxygen storage medium.

3.2.3. *The structures of the intermediate rare earth oxides*

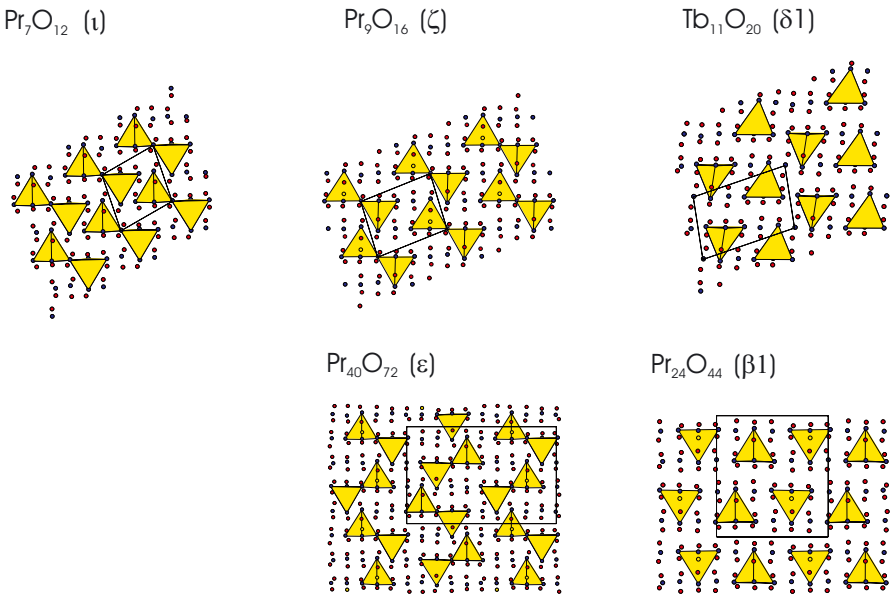

Figure 3-4. Determined structures of the intermediate rare earth oxides, M_nO_{2n-2m} (all $\langle 211\rangle_F$-projection). The defects are marked as vacancy centred metal tetrahedra (yellow).

The structures of the yet determined phases come all from neutron powder diffraction experiments and exhibit the best fits in the Rietveld refinements [21]. The refined models were extracted from ideas outlined in the next section. Fig. 3-4 presents the structures so far determined in a $\langle 211\rangle_F$-projection which in all cases corresponds to the common [100]-direction for almost all the phases. The locations for defects are marked by vacancy centred tetrahedra (yellow).

Pr_7O_{12} exhibits the highest and $Pr_{24}O_{44}$ the lowest defect concentration in the Pr_nO_{2n-2m} homologous series. However Fig. 3-21 shows an electron diffraction pattern of a phase with a superstructure multiplicity of 16 corresponding possibly to a member $M_{16}O_{30}$ (M = Ce, Pr, Tb: $MX_{1.875}$) [22]. Indeed there are, though in other systems, anion deficient fluorite related ordered superstructures with lower defect concentration than $MX_{1.833}$. In the

Zr/Sc-oxide system recently the single crystal structure of a $Zr_{50}Sc_{12}O_{118}$, $MX_{1.9032}$, was solved using X-rays [23].

The structures of the anion deficient rare earth phases with higher defect concentration i.e. ι, ζ and ϵ form paired defects, paired along the body diagonal of the primitive anion cube. The structures between $MO_{1.818}$ and $MO_{1.833}$ form isolated defects with larger defect separations than $1/2\langle 211\rangle_F$.

A common feature of almost all of the known phases in the cerium, praseodymium and terbium oxide systems is the common a-axis which corresponds to the $1/2[21\bar{1}]_F$ vector (see Table 3-3). The odd members of the series, M_nO_{2n-2m}, even exhibit a common c-axis which is a vector $1/2[1\bar{1}2]_F$. However the phase $M_{62}O_{112}$ has a different orientation for the a-axis of the supercell with respect to fluorite and modelling studies argue that these phase has divacancies like Pr_7O_{12} [9]. The phase can be observed in thermoanalytical runs during oxidation of Pr_7O_{12} but not in reduction on the higher temperature branch of the hysteresis loop.

3.2.4. *Interpretation and simulation of defect separations in the rare earth oxides*

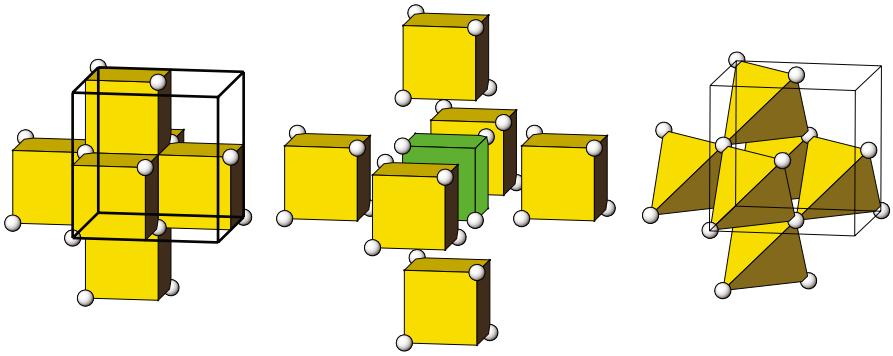

Figure 3-5. Coordination defect (c.d.) $M_{28/8}\square O_6$ i.e. $M_{3.5}\square O_6$ or $MO_{1.714}$. Anion centred octants of the fluorite cell. Exploded drawing at the center and at the right the coordination defect (CD), the vacancy centred octahedron of tetrahedra. Circles = metal atoms.

The coordination defect approach for modelling

A vacancy in the anion lattice of the rare earth oxides and the relaxation of its nearest neighbours generates a cluster which can be considered as a coordinated defect **(c.d.)** [7]. The size of this cluster is essential for modelling studies since it determines possible connectivities and therefore the defect distribution within the different structures. The topology of these c.d.s is structure determining and the total composition of the c.d. was

formulated as $M_{3.5}\square O_6$. The presentation of this c.d. can be given either by the arrangement of octants of the fluorite cell (see. Fig. 3-5) or by plotting an octahedron of OM_4 tetrahedra sharing corners to enclose an empty tetrahedron, $\square M_4$ (Fig. 3-6). This latter type of coordination defect is designated **CD** and will be used in the further course of this article [10].

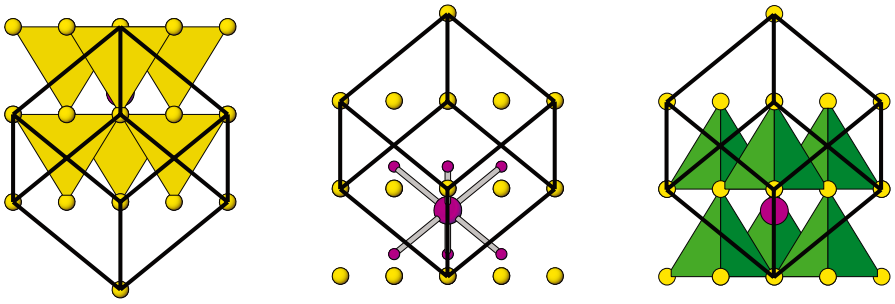

Figure 3-6. Two sets of different CDs. showing the octahedron of tetrahedra and in the center the six nearest oxygen neighbours of the vacancy (large circles).

Since the fluorite structure exhibits a f.c.c. array of metal atoms two different sets of tetrahedral voids are possible. Depending on this the central vacancy in the CD can belong to one of the two different sets. Such CDs can be linked in any way other than face-sharing in order to be consistent with the f.c.c. array of cations. In Fig. 3-6 two different sets of the CDs ($M_{16}\square O_6$ clusters) are shown according to the different orientation of the tetrahedral voids between adjacent f.c.c. metal layers. Linkages between clusters can be distinguished as beeing in-phase (same subset) or anti-phase (different subset). The shortest and most important in-phase linkage is of the type $1/2\langle 211\rangle_F$ and illustrated in Fig. 3-7. Other short in-phase linkages are $1/2\langle 220\rangle_F$ and $1/2\langle 310\rangle_F$. Thereafter there is no direct connection, but it should be mentioned that any vector linking anions of one subset must be of the form $h^2 + k^2 + l^2 =$ even.
The shortest anti-phase linkage is the $1/2\langle 111\rangle_F$ CD linkage. It may occur in two different ways corresponding to vacancies across the body diagonal of either a filled or empty cube of fluorite. In the former case the two tetrahedra are corner-shared (the so called divacancy). For the latter the $\square M_4$ tetrahedra (centers of the CD) are not connected. The next shortest linkage occurs along $1/2\langle 210\rangle_F$ when two edges of each of two tetrahedra from each CD are shared. Other linkages are $1/2\langle 300\rangle_F$ and $1/2\langle 311\rangle_F$. All vectors linking anions or vacancies of one subset to the other are of the form $h^2 + k^2 + l^2 =$ odd. For further details see [10].

Usually for all of the rare earth oxides the separation of defects can now be expressed in form of these vectors. Fig. 3-8 shows these vector

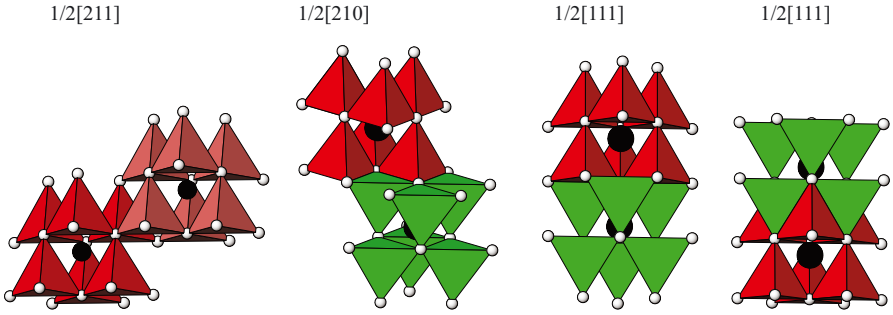

Figure 3-7. Different linkages between CDs. From the left to right the $1/2\langle 211\rangle_F$ in-phase linkage and and the anti-phase linkages $1/2\langle 210\rangle_F$ as well as the two $1/2\langle 111\rangle_F$ separations of which the left one corresponds to the divacancy around a metal.

presentation for Ce_7O_{12} and one observes the separations of type anti-phase $1/2\langle 210\rangle_F$ which will generate the so called motif plane and then the $1/2\langle 111\rangle_F$ across the empty O_8 cube. The patterns generated by these $1/2\langle 210\rangle_F$ vectors on a certain plane e.g. $\langle 211\rangle_F$ i.e. $\langle 100\rangle$ for all the phases in the rare earth oxide system are called a motif plane. These nets generated of anti-phase $1/2\langle 210\rangle_F$ linkages are usually puckered of type 6^3.

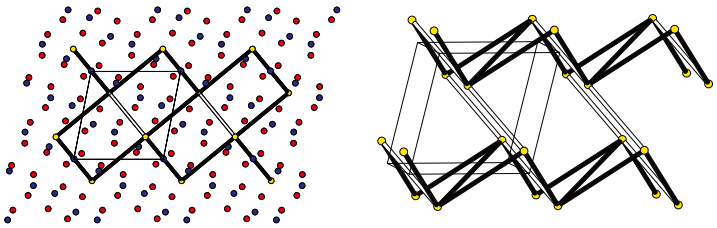

Figure 3-8. $1/2\langle 210\rangle_F$ (black) separations forming a heavily puckered 3^6 net as well as the $1/2\langle 111\rangle_F$ (white) separation in Pr_7O_{12}.

In order to use these motifs for further structure prediction several points are beeing assumed.

- All structures considered have at least $P\bar{1}$ symmetry and $1/2\ \langle 211\rangle_F$ as a-axis, which means that only motifs in projection along this axis need to be considered.
- All motif linkages are between antiphase linkages
- The motif, always comprising a sub-motif and its inverse will be a polygone (in projection) bounded only by $1/2\ \langle 211\rangle_F$ linkages, always remembering that linkages of the type $1/2[10\bar{2}]$ inevitable generate $1/2[111]_F$ linkages too.

– The resulting polygon with 1/2 $\langle 211 \rangle_F$ edges will have at least six sides but this number can increase as the number of cations increases.

Besides this CD approach introduced by Bevan and Martin [10] other points of view are discussed in the literature. In the c.d. theory an octant of the fluorite cell, M_4O_8, is employed as the basic building block or primary module. Other modules depicted for explaining those phases are the fluorite quadrant or the fluorite hemicube which are explained in detail by Martin [24].

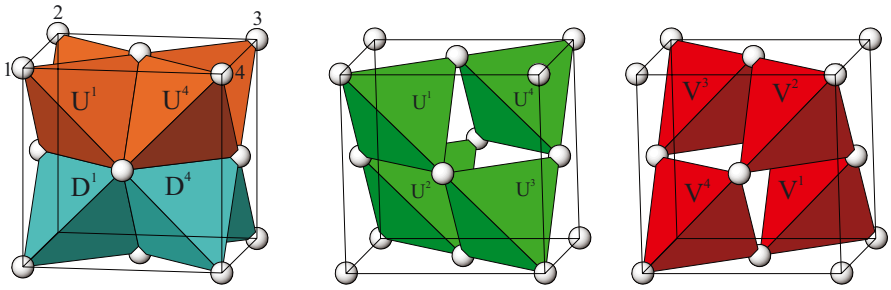

Figure 3-9. Left: The fluorite cell and the two sets of tetrahedra designated as U (up, red) and D (down, green). Right: The fluorite cell and the two sets of tetrahedra (related by a center of inversion in the center of the cell) designated as U and V.

The fluorite module approach for modelling

The rules established by Kang and Eyring [8] to predict the ideal structures of the intermediate rare earth oxides are using the fluorite unit cell als the primary building block. Further building blocks are fluorite unit cells containing one or two vacant oxygen sites. These building blocks are designated U if the vacancy is placed in one of the 4 tetrahedra in the upper part of the fluorite cell and D if the vacancy is placed in the lower part of the fluorite unit cell (see Fig. 3-9 left). The numbers show in which corner of the fluorite unit cell the vacancy is placed in a $\langle 211 \rangle_F$-projection (see Fig. 3-10). In case of the W modules two tetrahedra one of the upper (type U) and one of the lower (type D) part of the unit cell are making up the anion deficient fluorite cell. The F module is the filled fluorite unit cell.

Recently a new designation introduced by Kang is taking into account the two different sets of tetrahedra in between two hexagonal layers of a f.c.c. arrangement [25]. The relationship of this nomenclature to the old one is given in Fig. 3-10 and in Table 3-4. In the new designation W_1^1 is the same as the superimposed modules U^1 and V^1. They are oriented along the body diagonal and related by a center of inversion.

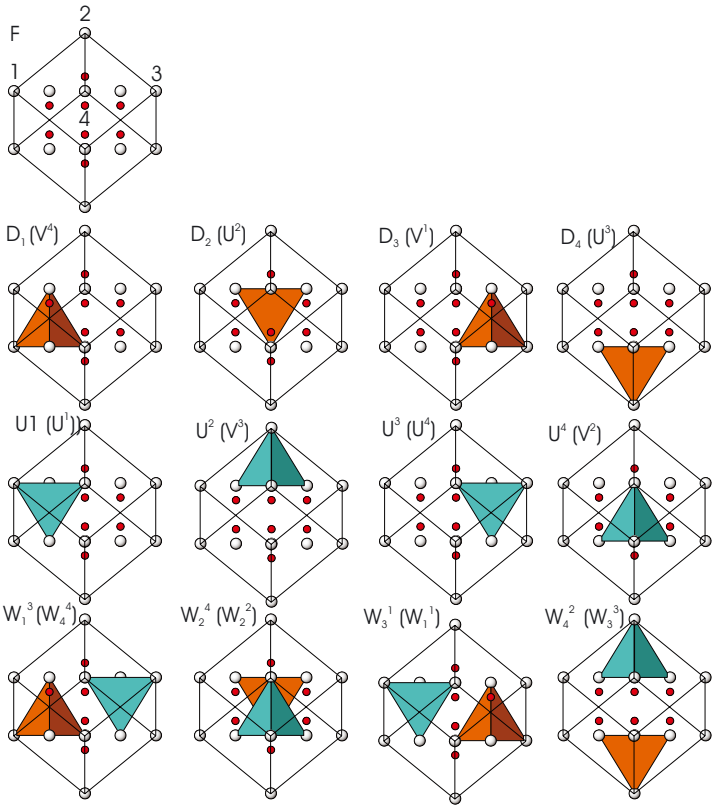

Figure 3-10. The 13 different fluorite modules oriented along $\langle 211 \rangle_F$ containing 0, 1 and 2 vacant anion sites. In parentheses the new designation (see [25] and Table 3-4).

TABLE 3-4. Look up table for modular designations [25].

old		new	old		new	old		new
U^1	=	U^1	V^1	=	D_3	W_1^1	=	W_3^1
U^2	=	D_2	V^2	=	U^4	W_2^2	=	W_2^4
U^3	=	D_4	V^3	=	U^2	W_3^3	=	W_4^2
U^4	=	U^3	V^4	=	D_1	W_4^4	=	W_1^3

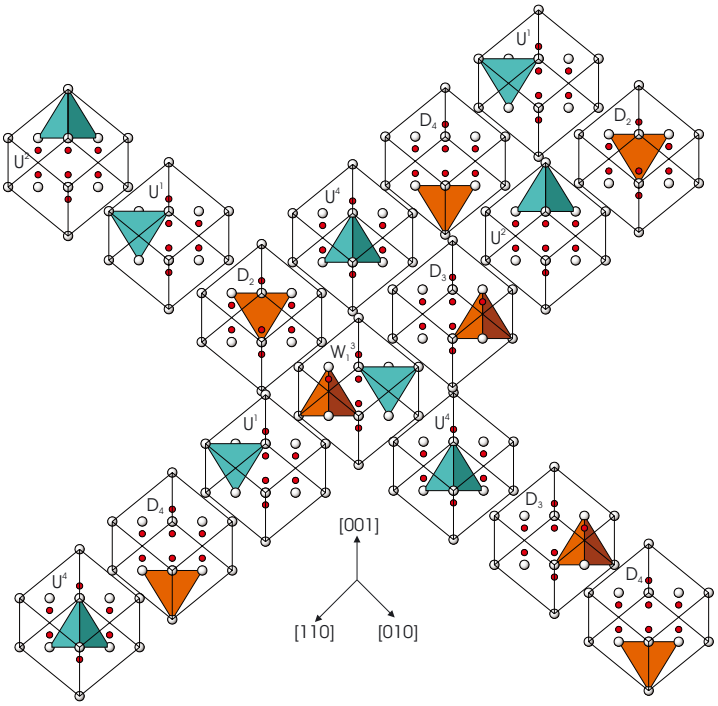

Figure 3-11. Modular sequences of Ce_7O_{12} along [010] and [100]. Exploded drawing of the face sharing fluorite modules

In order to deal with this theory a few experimental informations are required.

1. a) A low index electron diffraction pattern of the known unit cell in which n is apparent.
   b) The composition, from which m can be calculated
   c) The set of required modules oriented along the zone axis of the diffraction pattern in use.
2. Each modul has six face sharing neighbours. Only those that provide vacant anion sites separated by at least $\frac{1}{2}\langle 111\rangle_F$ are allowed juxtaposition.
3. The required n modules, oriented according to the zone axis of the electron diffraction pattern are aligned following the crystallographic requirements of the unit cell. This will be a trial and error process guided by experience, a perception of thermodynamic considerations and the emerging order in the growing sequence.
4. Since the modul is a rational fraction of the unit cell, packing in a two dimensional slab will be periodic in the two dimensions, just as the modular unit cell will be. The slabs can then be stacked in the third dimension to yield the full structure.

The rules and their applications are given in detail by Kang and Eyring [8, 9] and [26].

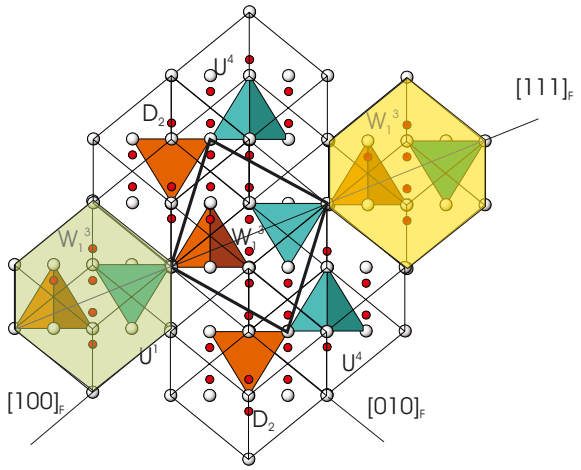

Figure 3-12. Projection of the unit cell of Pr_7O_{12} down $[100]_{rhomb.}$. White cubes in plane yellow up by one and green down by one.

If one can find a way in which adjoining fluorite modules can be placed in juxtaposition it will be possible to determine the constitution of all the

TABLE 3-5. Modular sequences for the known and some proposed modular sequences for yet unknown structures.

Symbol	Composition	Unit cell content	n	m	Modular content
ι	$MO_{1.714}$	$Ce_{11}O_{20}$, $Pr_{11}O_{20}$, $Tb_{11}O_{20}$	7	1	W3U3D
ζ	$MO_{1.788}$	Ce_9O_{16} (?), Pr_9O_{16}	9	1	F4U4D
M19	$MO_{1.789}$	$Ce_{19}O_{34}$	19	2	3F8U8D
M29	$MO_{1.793}$	$Ce_{29}O_{52}$	29	3	5F12U12D
M39	$MO_{1.795}$	$Ce_{39}O_{70}$	39	4	7F16U16D
ϵ	$MO_{1.800}$	$Ce_{40}O_{72}$ (?), $Pr_{40}O_{72}$	40	4	8F16U16D
δ‘	$MO_{1.806}$	$Ce_{62}O_{112}$, $Pr_{62}O_{112}$, $Tb_{62}O_{112}$	62	6	14F24U24D
$\delta(1)$	$MO_{1.818}$	$Ce_{11}O_{20}$, $Tb_{11}O_{20}$	11	1	3F4U4D
$\delta(2)$	$MO_{1.818}$	$Pr_{88}O_{160}$	88	8	24F32U32D
$\beta(0)$	$MO_{1.833}$	$Pr_{12}O_{22}$	12	1	4F4U4D
$\beta(1)$	$MO_{1.833}$	$Pr_{24}O_{44}$	24	2	8F8U8D
$\beta(2)$	$MO_{1.833}$	$Tb_{24}O_{44}$	24	2	8F8U8D
$\beta(3)$	$MO_{1.833}$	$Tb_{48}O_{88}$	48	4	16F16U16D

members of the homologues series M_nO_{2n-2m}. The constitution can then be expressed in terms of a specific sequencing for n modules required to characterize each phase. For Pr_7O_{12} n equals seven, which is the number of modules required. In Fig. 3-11 the modular sequences for Pr_7O_{12} is given along [100] as $D_2U^2D_3W_1^3U^1D_4U^4$. This determines the sequence in the a-direction of the unit cell. If the sequence starts anywhere with a D_3 -modul then it will be continued in a-direction with always the same sequence namely then $D_3W_1^3U^1D_4U^4D_2U^2$. If the sequencies are given along the three axis of the unit cell the structure will be completely described. A closer look at these sequencies reveals that always the same amount of U and D moduls appear in such a sequence and that vacancies are always paired along certain body diagonals like U^2D_4, U^1D_3 and U^4D_2. For the case of Pr_7O_{12} (see Fig. 3-12) the modules U^3 and D_1 are missing because of the W_1^3 module beeing present in the sequence.

These two approaches, the Bevan/Martin and the Kang/Eyring approach, in order to generate models for the structural description of the rare earth oxides led the different authors to predict yet unknown structures. The defects have been introduced in the ideal fluorite cells according to the electron diffraction data for the different unit cells. There are models published for the phases $Ce_{19}O_{34}$ and $M_{16}O_{28}$ [10], $\beta(2)$, $\beta(3)$ [27], $Ce_{19}O_{34}$, $M_{16}O_{30}$ and $Pr_{62}O_{112}$ [9] as well as $Pr_{88}O_{160}$ [25], which might be very useful for future Rietveld refinements of powder data.

The Kang-Eyring system interpreting fluorite related anion deficient structures has recently been extended to a wide range of fluorite related structures with vacancies in both anion and cation sites [28, 29].

3.2.5. *Phase transformation*

Phase transformations in the system of the rare earth oxides can be observed between polymorphs like $\beta(2)\rightarrow\beta(3)$ (see section 3.5.5). Very often in an electron microscope simple rearrangements of the structure can be observed, i.e. a different orientation of the superstructures a-axis in the fluorite cation arrangement. There are at least 12 different possible orientations like $[211]_F$ or $[\bar{1}21]_F$ as choices for the a-axis for most of the superstructures. Fig. 3-13 shows an intermediate stage of such a reorientation in $Pr_{24}O_{44}$ from a $[21\bar{1}]_F = [100]_{24}$ to a $[1\bar{1}2]_F = [100]_{24}$ former $[313]_{24}$-orientation. The structural features of $Pr_{24}O_{44}$ at the thin edge of the crystal are blurred out along $[010]_{24}$. The reorientation front can be observed moving towards the edge of the crystal [30].

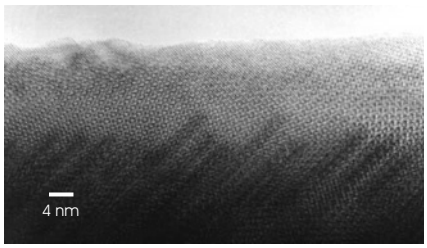

Figure 3-13. Rearrangement of the superstructure in $Pr_{24}O_{44}$ from $a_{24} = [21\bar{1}]_F$ to $a_{24} = [1\bar{1}2]_F$. Displayed is an intermediate stage during the beam heating of the crystal.

But in most of the cases phase transformations are chemical reactions either oxidizing or reducing the rare earth metal atom. Examples for these "phase transformations" are given in section 3.5.

However these "phase transformations" are driven by processes involving ion diffusion and electron hopping generating vacancies and reducing the metal atoms. The formation of a single vacancy is an elementary step in the reduction of Ce^{4+} to Ce^{3+} in these oxides. To study in detail the energetics of the oxygen-vacancy formation in the CeO_2 crystal simulations using DFT (density functional theory) revealed that the density of states of CeO_2 shows the presence of a narrow, empty f-band in the gap between valence and conduction band [31]. In CeO_2 all four valence electrons of Ce ($6s^2 5d^1 4f^1$) nominally leave the host atoms and transfer into the p-bands of two oxygen atoms while in Ce_2O_3 the Ce f-electron is fully localized. According to this calculations the condensation of the f-electron into the

core state of a Ce atom (i.e. its localisation) leads to a 10% volume increase as compared to calculations with the f-electron in the valence band.

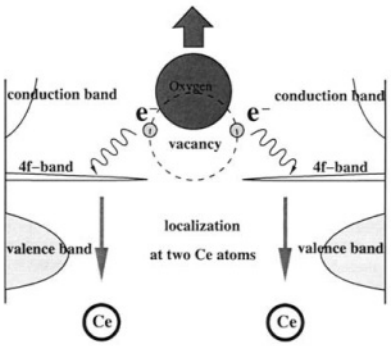

Figure 3-14. The process of oxygen-vacncy formation in ceria. An oxygen atom moves away from its lattice position leaving behind two electrons, which localize on two cerium atoms, turning Ce^{4+} into Ce^{3+} (from [31]).

Under reduction conditions, oxygen leaves the surface forming a vacant site. The oxygen vacancy formation process is essentially facilitated by a simultaneous condensation of two electrons into localized f-level traps on two cerium atoms. Thus, when an oxygen moves diffusively towards the surface, e.g. oxygen vacancy moves into the crystal these electrons localize on cerium atoms in the immediate surrounding of the vacancy and correspondingly they delocalize and transfer to oxygen from cerium sites when the vacancy leaves. In other words the formation of reduced oxides can be viewed upon as a formation, migration, and ordering of virtual Ce^{3+}- vacancy complexes (see Fig. 3-14). Clearly, on the microscopic level, the removal of an oxygen atom is made possible due to the ability of the cerium atom to easily and drastically adjust its electronic configuration to best fit its immediate environment. Thus, the process of oxygen vacancy formation is closely coupled with the quantum effect of localization and delocalisation of the 4f electron of cerium. It was pointed out that the most favorable position of these two Ce^{3+} atoms in the CeO_2 (fluorite structure) matrix is next to the oxygen vacancy.

3.3. THE SESQUIOXIDES

3.3.1. *Structure of Sesquioxides*

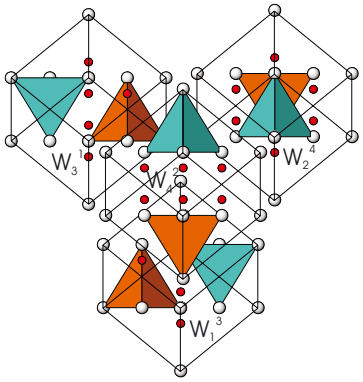

Figure 3-15. The four fluorite W modules describing the C-type structure of the rare earth sesquioxides. Modular sequencing along [100] $W_4^2W_2^4$ along [010] $W_4^2W_3^1$ and along [001] $W_4^2W_1^3$.

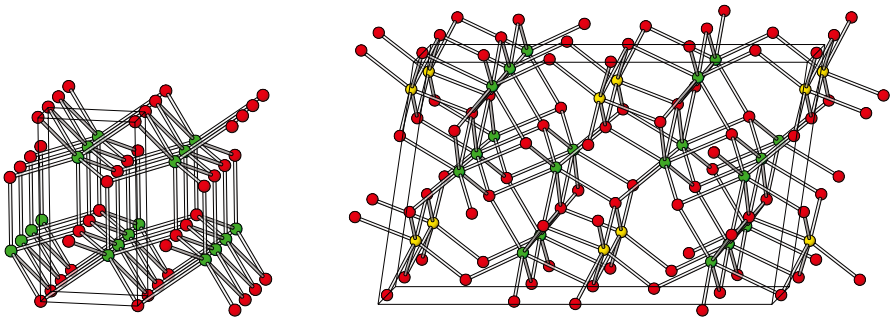

Figure 3-16. Structures of A-type (left) and B-type (right) sesquioxides of the lanthanoids projected almost along the common axis. Metals green (sevencoordinated) and yellow (sixcoordinated), oxygens red.

The C-type sesquioxides (space group (SG): $Ia\bar{3}$) crystallize isostructural to the mineral bixbyite and are best described by a simple fluorite cell with two vacancies paired along the body diagonal of the anion cube. The unit cell of bixbyite contains eight fluorite cells obtained by a doubling of the fluorite lattice constant. The vacancy pairs in the eight fluorite subcells are oriented along the four possible directions for body diagonals in the cube. The structure might be interpreted by modular sequencing shown in Fig.

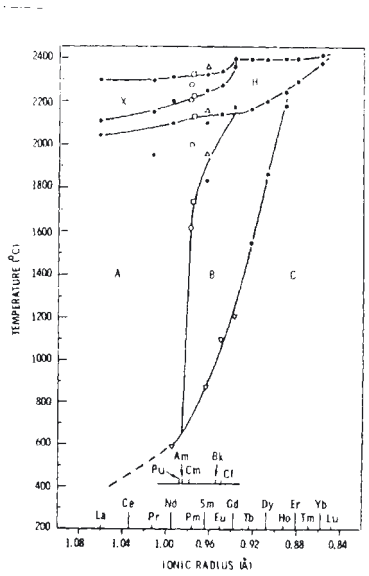

Figure 3-17. Polymorphic transformations of the lanthanoid sesquioxides. (Reproduced with permission from ref. Copyright 1966 Revue International des Hautes Temperatures et des Refractaires.

3-15. The sequences along the different views are along [100] $W_4^2W_2^4$ along [010] $W_4^2W_3^1$ and along [001] $W_4^2W_1^3$. For the nomenclature of the single modules see subsection 3.2.4.2. It must be said, although the structure is most easily described in terms of a fluorite substructure, it is topologically not related to fluorite. All metal atoms are coordinated by heavily distorted octahedra of oxygen atoms i.e. the coordination number of the cation is six. The coordination number of the anion remains 4 like in fluorite.

Increasing the temperature results in the formation of B-type structures at least for some rare earth metal atoms. In this structure (SG: C2/m) some of the metal atoms are seven coordinated by oxygen atoms others are still in distorted octahedral environment. The metal atoms are seen to be approximately hcp (hexagonal closed packed). The coordination polyhedra for the anions are octahedra and half octahedra, tetrahedra and trigonal bipyramids. The relation to the A-typ structure formed at even higher temperatures is very close. Only small shifts in the oxygen sublattice are necessary to transform the B-type structure into the A-type structure (SG: $P\bar{3}2/m$). The cation array is now perfect hcp and alternal layers of tetrahedral and octahedral sites are then filled with anions (see Fig. 3-16). All metal atoms are seven coordinated. Lattice constants and bond distances

Figure 3-18. A star pattern found as a consequence of a A- to B-type phase transition in Sm_2O_3. Additional domains can be interpreted by epitaxial growth on different interfaces. (Image by courtesy of C. Boulesteix).

are given in several articles [6, 32–35]. The existence of two high temperature polymorphs named H-type and X-type has been reported [36, 37]. The H-type structure is closely related to that of A-type with hexagonal symmetry and a neutron diffraction study [38] revealed H-type to crystallize hexagonal in $P6_3/mmc$ and X-type to have a cubic space group Im3m. Transformations are observed for A- to H-type (Pr_2O_3, Nd_2O_3) and for the H- to X-type (La_2O_3 through Gd_2O_3)

3.3.2. *Polymorphism*

The phase diagram for all the lanthanoid sesquioxides is given in Fig. 3-17 and shows the different transformation temperatures. From the diagram it is obvious that promethium, Pm, was the first metal for which the existence of all three polymorphs and the transition temperatures could be established [39]. For praseodymium, Pr, under atmospheric pressure the C-type structure is formed above 500 ^oC and transforms to A-type above 700 ^oC . Depending on the ionic radii only for the rare earth metals from Pm to Gd all five polymorphs will be formed. With increasing temperature the order of transition is C→B→A.

The transformation B→A is according to the Landau theory a second order

transition. The atomic positions of the oxygen atoms will move by small quantities causing a change in the coordination of certain metal atoms of which some will then be six coordinated instead of seven in the high temperature A-type structure. The situation of this ferroelastic phase transition is given by the group subgroup relationsship P$\bar{3}$m –t3→ C2/m –i3→ C2/m. The change in lattice constants for the first step is a = 2a + b, b = b and c = c. For the second step a = a - 2c, b = b and c = a + c. The complete transformation matrix is then

$$(a,b,c)_B = (a,b,c)_A \begin{pmatrix} 201 \\ 110 \\ \bar{4}01 \end{pmatrix}$$

This corresponds to a volume increase of the unit cell so that the B-type cell has approximately six times the volume of the A-type cell. The A-type sesquioxides are the high temperature or paraelastic phases with the high symmetry structure while the B-type sesquioxides are the low temperature or ferroelastic phases with the low symmetry structure. From group theoretical considerations the number of expected twins and orientational domains might be predicted. A phase transition from A-type to B-type sesquioxide might produce during a cooling cycle triple twins according to the index of the transition t3 and at least 3 orientational domains according to i3 [33]. Additional orientational domains are found due to epitaxial growth [40–43]. Fig. 3-18 shows multiple twin domains in B-Sm_2O_3 formed from A-Sm_2O_3. The star pattern reveals the triple twins and additional domains formed by epitaxial growth [44]. All phase transitions between C-type and B-type are of first order or reconstructive phase transitions.

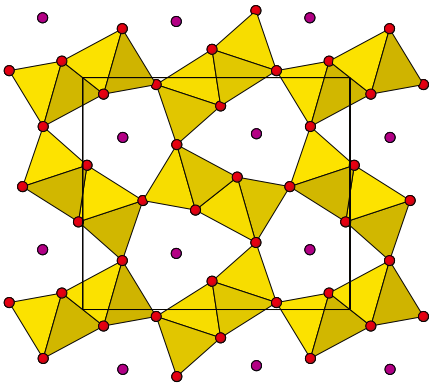

Figure 3-19. The structure of Eu_3O_4 along [010] (setting Pnma). Yellow oxygen octahedra are outlined around Eu^{2+}.

3.4. THE LOWER OXIDES (MONOXIDES LnO AND Eu_3O_4).

The monoxides are known for all of the rare earth metals. They are all crystallizing at low temperatures isostructural to the NaCl-type. Eu_3O_4 crystallizes orthorhombic [45, 46] with space group Pnam. This mixed valent compound contains Eu^{2+} and Eu^{3+} in the cation sublattice with a distorted octahedral coordination around Eu^{2+} and a coordination number of eight around Eu^{3+}. Fig. 3-19 shows the projection of the structure down [010]. The octahedral framework around Eu^{2+} can be related by a twinning operation (glide reflection) to the structure of ramsdellite (hcp).

3.5. HIGH RESOLUTION ELECTRON MICROSCOPY (HREM)

High-resolution electron microscopy (HREM) is a powerful tool for unraveling the structural features in non-stoichiometric rare earth oxides. HREM is able to give an insight in the **real** structure of the rare earth oxides and therefore overcomes the problem of multidomains, even with different composition. HREM opens up the possibility to simultaneously obtain diffraction data in the back focal plane and images showing the projection of the atoms arrangement of a structure at atomic scale in the image plane of the objective lens. The beam size, which can be changed from 100 μm to 1 nm restricts the area on a sample where the diffraction data and the structure image come from. It is possible to record an electron diffraction pattern and a structure image at time intervals of 1/16 of a second [47]. If the sample is located in an environmental cell of the electron microscope it is possible to record even the valence variation using EELS and a CCD camera. This means that the transition of different homologous series phases either at reduction or oxidation processes can be observed. Therefore HREM is a key method to study the higher oxides of the binary rare earths. Fig. 3-20 generally outlines some of the informations obtained by HREM.

3.5.1. *Electron diffraction data of the oxygen deficient, fluorite-related homologous series of the binary, rare earth oxides.*

Tensimetric studies of cerium, praseodymium, and terbium binary oxides [48–50] show that

1. In the equilibrium condition between the oxygen partial pressure and the solid oxide, **as the oxygen partial pressure increases or decreases**, the oxygen content of the solid oxide will be increased or decreased at any constant temperature higher than 300 ^{o}C. There is a hysteresis loop of the oxygen content of the solid oxide between increasing and decreasing the oxygen partial pressure.

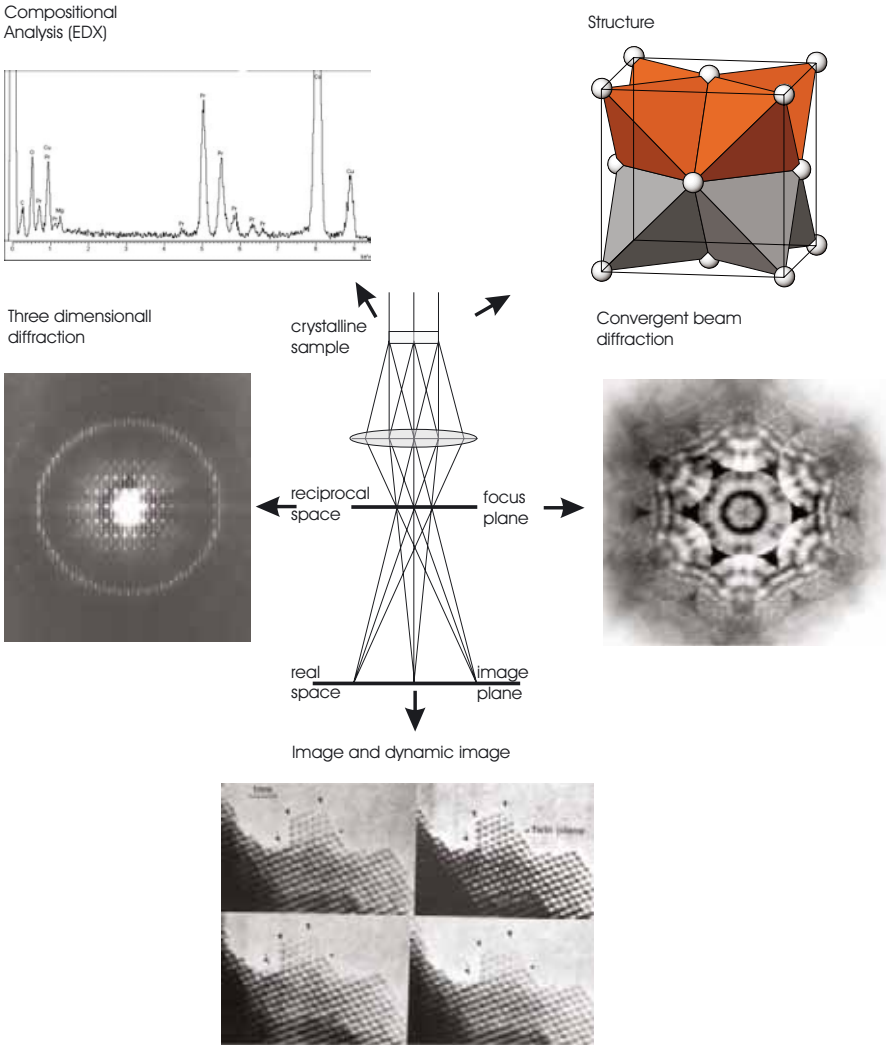

Figure 3-20. Some important informations that can be obtained from investigations in an electron microscope.

2. At constant oxygen partial pressure, **as temperature varies up and down**, the oxygen content of the solid oxides will decrease and rise simultaneously. Here again hysteresis loops are observed for the oxygen contents of the solid oxides with varying temperatures.
3. At an oxygen content of the solid oxide MO_x with x being 1.714, 1.778,

1.789, 1.800, 1.808, 1.818, 1.833 and 1.850 stable intermediate phases with very narrow variation of the composition are observed.

4. Additionally wide range non-stoichiometric phases (called α-phase) are observed in this systems.

In order to relate the thermodynamic properties [2] to the structures of the binary rare earth oxides the structures needed to be solved.

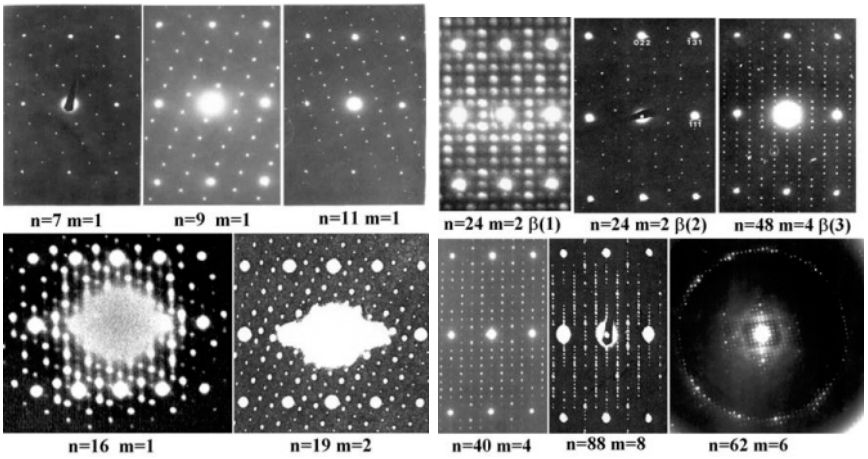

Figure 3-21. Electron diffraction patterns of the homologous series phases, RO_x (x=2(1-$\frac{m}{n}$)) or R_nO_{2n-2m}. x=1.714 (n=7, m=1), x=1.778 (n=9, m=1), x=1.789 (n=19, m=2), x=1.800 (n=40, m=4), x=1.808 (n=62, m=6), x=1.818 (n=11, m=1; n=88, m=8)), x=1.833 (n=24, m=2; n=48, m=4), x=1.875 (n=16, m=1).

Fig. 3-21 shows the electron diffraction patterns of some of the binary, oxygen deficient rare earth oxides. These electron diffraction patterns exhibit the following features. Any diffraction pattern in this figure has a common array of strong spots, which is the result of diffraction from the metal atoms f.c.c. lattice. The orientation of the strong diffraction spots corresponds to the $\langle 112 \rangle$ orientation of the f.c.c. lattice except in the last example (n=62, m=6). As mentioned before, the rare earth dioxide has the fluorite structure in which the cations occupy positions of the f.c.c. lattice. These diffraction patterns indicate that the homologous series phases have a common sub-lattice, based on the c.c.p. cation arrangement. The array of the ordered oxygen vacancies causes the superstructure in the electron diffraction patterns. Of course as mentioned before, the rare earth metals and the surrounding oxygens will have different distortions caused by an oxygen vacancy. That may lead to variations in intensity for the superstructure spots, but does not change the periodicity and the array of the

superstructure of the homologous series phases. For further information see also [51].

There are three different kinds of arrays for the superstructures. One superstructure is oriented along the $\langle 135 \rangle_F$ direction another is in the $\langle 220 \rangle_F$ direction. The last occuring in the phase with n=62 and m=6 has 62 spots in the $\langle 1\bar{2},6,26 \rangle_F$ and $\langle 22,20,4 \rangle_F$ of the fluorite structure. These diffraction patterns also indicate that the short axes ($a \approx 6.5$ Å) of the superstructures unit cell is along the beam orientation $\langle 112 \rangle_F$, except again for the phase with n=62 and m=6.

If one pays more attention to the intensities of the superstructure spots one might see that the intensities in the electron diffraction patterns of the phases with n=7, n=9, n=11, and n=62 are almost uniform. However the remaining electron diffraction patterns exhibit an intensity variation of the superstructure spots. This difference would imply that the arrangement of oxygen vacancies in this two groups of intermediate oxides has different symmetry. It might be possible to develop a structural model of these phases from the diffraction patterns if they were taken from very thin crystals.

Fig. 3-22 shows the electron diffraction pattern of the samples quenched from the α-phase region which has a wide range of non-stoichiometry.

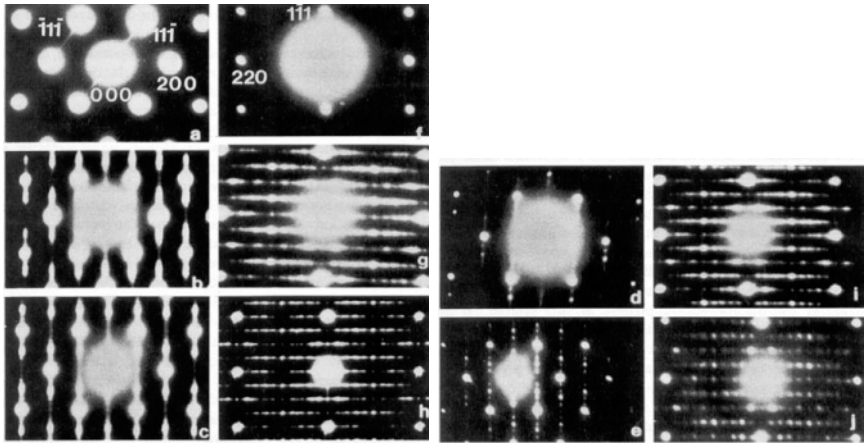

Figure 3-22. Electron diffraction patterns of the PrO_x samples quenched from the α-phase region (x=1.80, 580 ^{o}C, p_{o_2} = 58 torr for 24 hours).

It reveals the structural feature of the non-stoichiometric phase and the memory effect of the α-phase in the thermodynamic data [52, 53]. In these electron diffraction patterns the strong diffraction spots of the $\langle 110 \rangle_F$ and $\langle 112 \rangle_F$ orientations correspond to the fluorite structure. From a to e and f to j the diffraction patterns show that:

1. At fastest quenching the α-phase has fluorite structure with some streaks along the $\langle 111 \rangle_F$ direction. That seems to suggest that the oxygen vacancies are distributed irregularly within the oxygen sublattice.
2. At slower quenching the oxygen vacancies were ordering, but the periodicity of the ordered superstructure is not unique. Several phases exhibit patterns which are similar to the MO_x-phases with x = 1.8, 1.833 and 1.85. In other words there exists multi-ordered phases with different oxygen content.
3. At a certain quenching rate the ordered phase with x = 1.8 is formed.

Based on the experimental electron diffraction data and the results of thermodynamic studies the following ideas are developed.

1. The oxygen content of a phase in the homologous series is determined by the oxygen partial pressure and temperature.
2. The non-stoichiometric α-phases have fluorite structure with random distributed oxygen vacancies.
3. The configuration of the ordered oxygen vacancies is dominated by the oxygen content and the memorizing effect of the high temperature α-phase which conserves somehow the vacancy distribution of the low temperature phase.

3.5.2. *Composition domain and hysteresis loop*

The isotherm and isobar thermodynamic data [1–3, 48, 49] reveal a hysteresis in phase transition and show that and the homologous series phases always have narrow variation in their oxygen content. HREM observations [54–56] reveal that the composition domains, including ordered phases and modulations with different vacancy distribution, are responsible for the hysteresis in the transition. Fig. 3-23 shows that the sample with nominal composition $PrO_{1.80}$ contains domains with different oxygen content. The arrows indicate the contrast modulation due to the defects. This is a common feature of the rare earth higher oxides. Fig. 3-24 shows the HREM image of a sample with $TbO_{1.833}$. In this image the domain of α-phase exists on the left edge of the crystal. The lattice fringes are continuous in both phases and the boundary between the two phases is coherent.

The difference between the two phases is only the oxygen content, because the phase transition between the homologous series phases is caused by a change of the oxygen content without reconstruction of the metal sublattice. The energy for the phase boundary movement is the excitation energy for the oxygen atom diffusion. However, the energy for oxygen atom diffusion in the fluorite structure is very small [57], therefore, the energy for the boundary movement, dominated by the oxygen content, is controlled by absorbing and releasing oxygen atoms from the surface. Composition

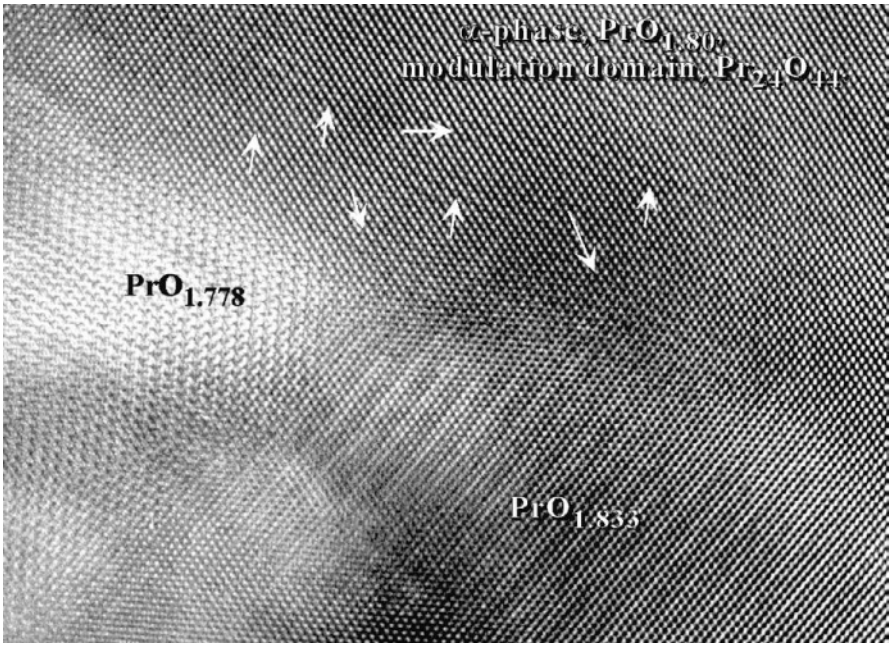

Figure 3-23. Composition domain in the sample quenched from α-phase PrO_x with x=1.80.

domains in these systems have been indicated as microdomains [58, 59]. X-ray studies and analyses of the oxygen content in PrO_x explored the pseudophase behavior, but did not give a clear picture of the wide non-stoichiometry of the rare earth higher oxides. HREM images exhibited the existence and characteristics of the composition domains in the binary rare earth higher oxides. This is a completely different type of non-stoichiometry compared to the situation in transition metal oxides. Here the elimination of point defects occurs as a result of a local rearrangement of coordination polyhedra and is interpreted in terms of crystallographic shear planes and intergrowths of different line phases [60].

3.5.3. *Surface structure of the rare earth higher oxides*

Rare earth higher oxides are catching more and more attention for redox catalytic reactions. Surface structure is very important for the catalytic process and chemical reactivity because the defect on a surface is an active reaction site. HREM profile images do not only show the surface structure, but also reveal the relationship between the surface and internal intermediate phases [61, 62].

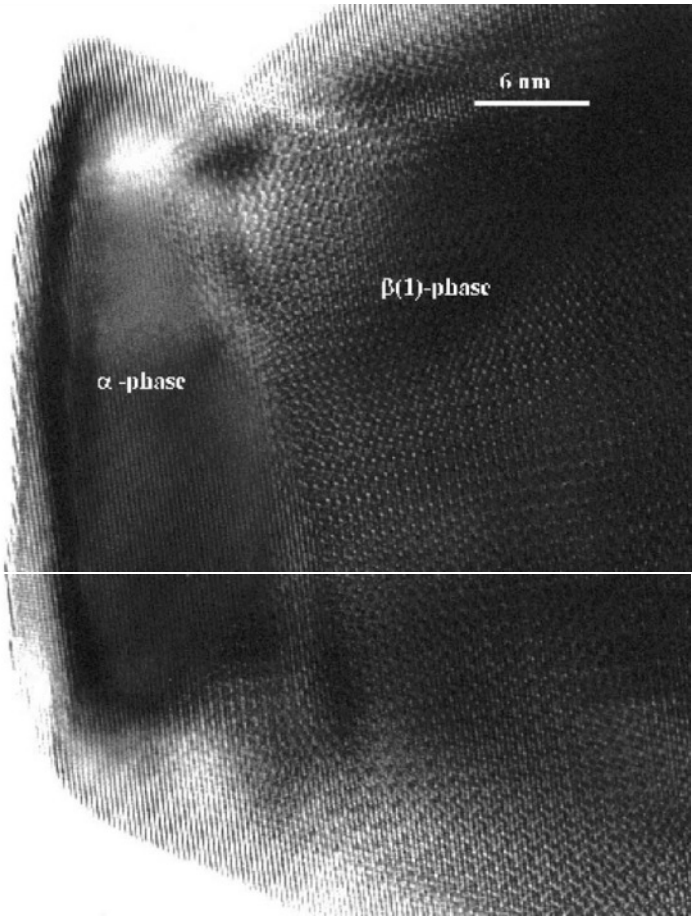

Figure 3-24. Domains of the α-phase and ordered $Tb_{24}O_{44}$ ($\beta(1)$) in $TbO_{1.833}$ sample.

Steps and flat surface

Fig. 3-25a shows the surface of CeO_2 colloid particles, 3-25b shows a CeO_2 particle annealed at 500 ^{o}C and finally 3-25c shows a TbO_2 particle. The surface of all of them is build from {111}-facets forming steps on a flat surface. This step surface exhibits a high surface area, which might be of interest for the reactivity of catalysts.

Atom activity on the surface of rare earth higher oxides

In general, the rare earth cations have a very weak ligand field effect and the bonding situation is almost ionic. Therefore the atoms on the surface of

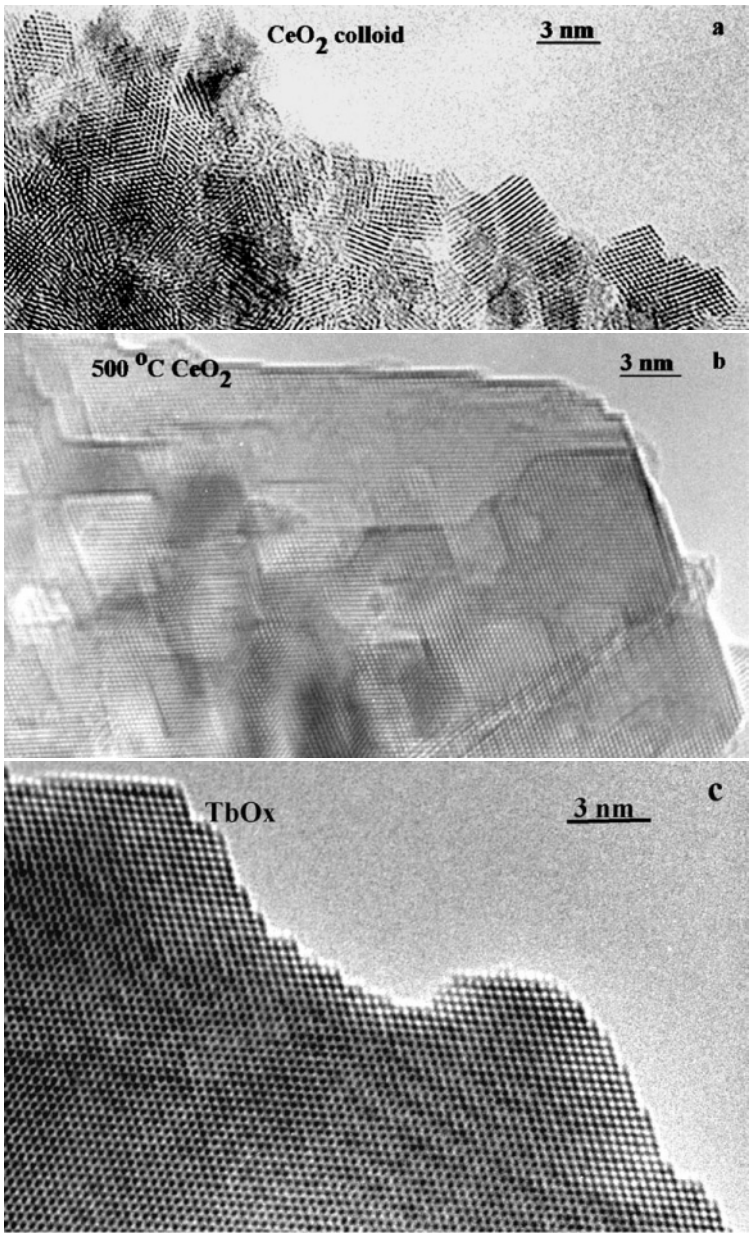

Figure 3-25. $\{111\}_F$ facets construct the steps and flat surface of CeO_2 colloids, annealed particles of CeO_2 and TbO_2.

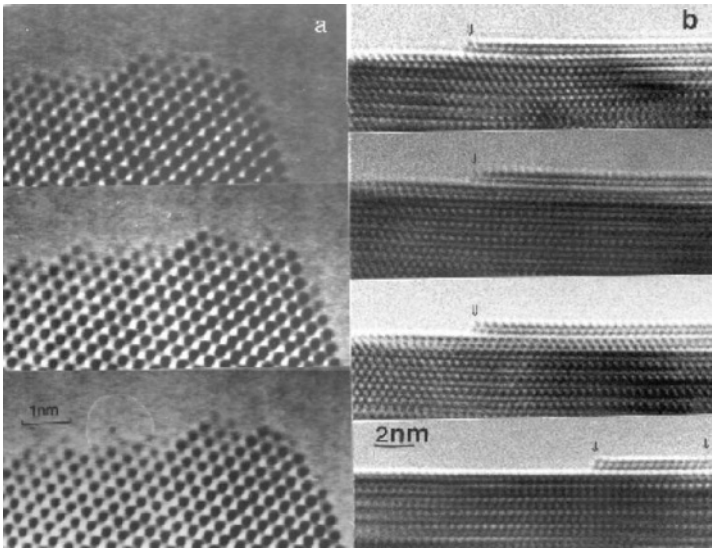

Figure 3-26. Surface atom activity difference between terbium dioxide (a) and lead dioxide (b).

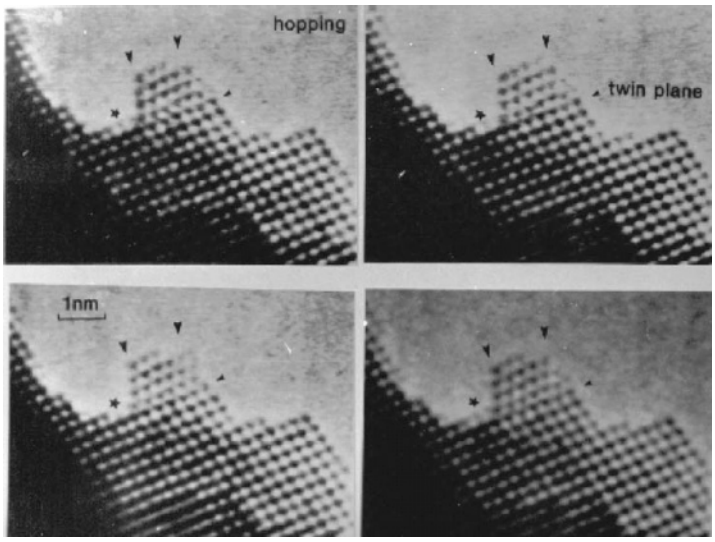

Figure 3-27. A small twinned TbO_2 crystal demonstrates its drastic surface atom movement under electron beam radiation.

the rare earth oxides behave different compared to transition metal oxides. Fig. 3-26 demonstrates this difference. In Fig. 3-26a columns of terbium atoms close to the surface contain variable atoms from a few to more than ten. They are moving as shown from top to bottom and their mobility can be interpreted as an individual jumping.

In lead oxide (see Fig. 3-26b) the surface atom migration is cooperative and atoms are grouped together. This is due to the strong ligand effect between the lead metal and the oxygen atoms. Therefore the two layers on the surface were getting smaller from top to bottom by groups of lead atoms moving away together.

As the crystal size decreases atom hopping at the surface becomes more intense as shown in Fig. 3-27. In this figure a small crystal of TbO_2 connected to a larger one at the surface drastically rearranged under electron beam radiation. This surface mobility may be the reason why the rare earth higher oxides can easily be sintered under the conditions in an electron microscope. They absorb the beam energy and additional they take up or release oxygen which keeps the surface clean of contamination.

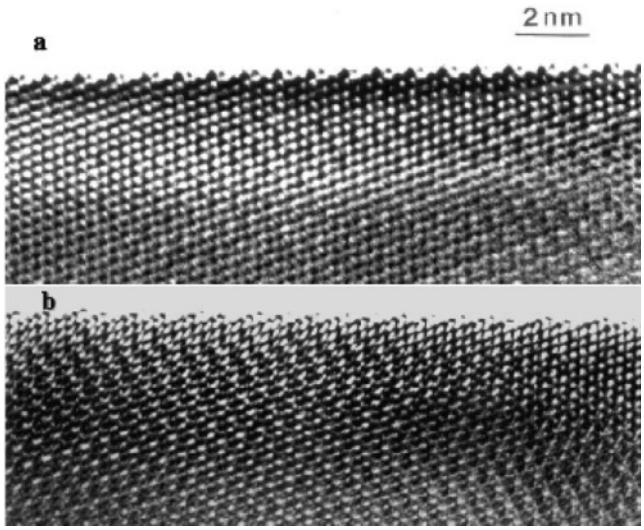

Figure 3-28. Relationship between the surface structure and internal superstructure.

Relationship between the surface structure and the intermediate phase
The existence of oxygen deficient fluorite-related intermediate phases of the rare earth higher oxides is due to vacancy ordering. Fig. 3-28 demonstrates the relationship between the surface structure and the bulk superstructure

phase, $Pr_{24}O_{44}$. Oxygen vacancies beneath the surface cause the relaxation of surface metal atoms and the regular periodicity on the surface related to the unit cell of the $Pr_{24}O_{44}$ ($\beta(1)$) phase becomes visible. That experimental evidence may be interpreted in terms of a loss or absorption of oxygen by the crystal through the {111} plane. In the case of a relaxation of the vacancy surrounding cations the calculated energy for the creation of an oxygen vacancy will be lower than from calculations for non relaxed cations [63].

3.5.4. *Defect and chemical reactivity of the rare earth higher oxides*

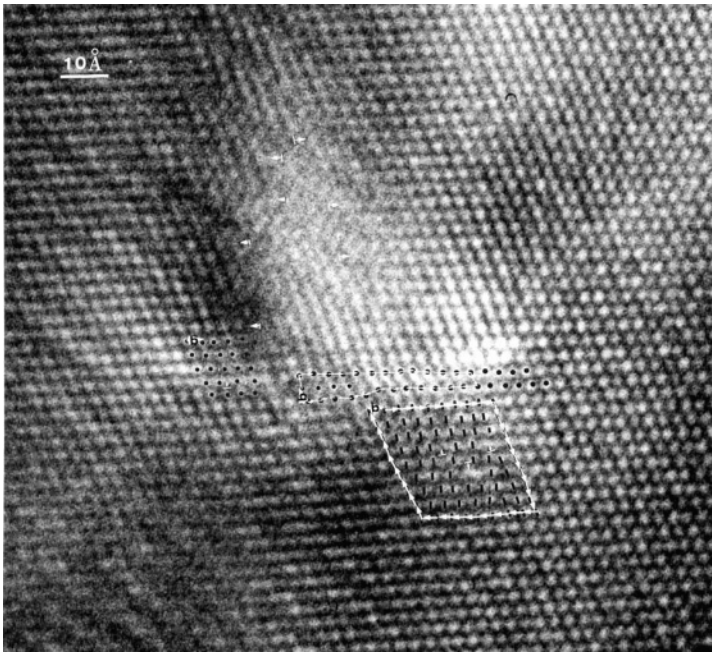

Figure 3-29. HREM image of the dislocation in the $Tb_{24}O_{44}$ crystal. The white arrows indicate the Burgers loops.

Defects in a solid could dramatically influence its chemical reactivity. Fig. 3-29 shows the HREM image of an edge dislocation in $TbO_{1.833}$ pointed out by Burgers loop. It seems that the edge dislocation does not change the character of the contrast modulations, which are related to a certain ordering of oxygen vacancies. Here the white dots indicate the metal atom columns. Actually it is not clear how the edge dislocation influences the ordering of oxygen vacancies.

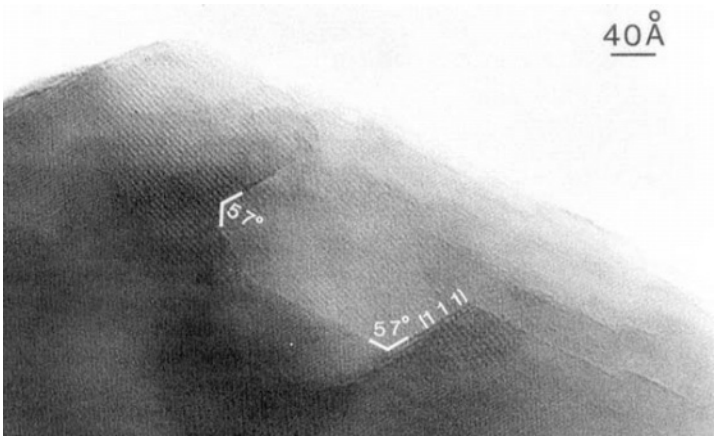

Figure 3-30. A leach pit developed at the dislocation site. The fast reaction generates {111}-surface steps as pit walls.

However a chemical leaching reaction, using acids, shows that the site of the dislocation could develop a leach pit (see Fig. 3-30). Due to higher reaction rates around a dislocation, surface steps are created and generate a "wall" around the pit. The rare earth higher oxides consist of the mixed valent cations M^{3+} and M^{4+} but the hydroxide formed is not $M(OH)_4$ but $M(OH)_3$ since M^{4+} is easily reduced to M^{3+}. The site of the dislocation and the relaxed surface atoms related to ordered oxygen vacancies may consist mainly of M^{3+} cations and are the energy favorable place for O^{2-} to react with H^+. The resulting OH^- group at the surface leads to an enlargement of the fluorite lattice and the formation of the amorphous pit on the surface as shown in Fig. 3-31.

3.5.5. *Phase transition from $Tb_{48}O_{88}$ ($\beta(3)$) to $Tb_{24}O_{44}$ ($\beta(2)$)*
Transformations (reductions or oxidations) between the homologous series phases mainly are the migration of the oxygen atoms from one configuration of oxygen vacancies into another without reconstruction of the metal sub-lattice. The different configurations of voids in the oxygen lattice will cause different kinds of relaxation in the metal sub-lattice.

In HREM images one might argue that contrast modulations with different modulation lengths correspond to different oxygen contents. The change in the contrast modulation as far as the modulation length is concerned, indirectly demonstrates the movement of oxygen atoms. The transformation of one phase into the next within the homologous series might be interpreted as a change in the modulation length. Fig. 3-32 shows this type of transition

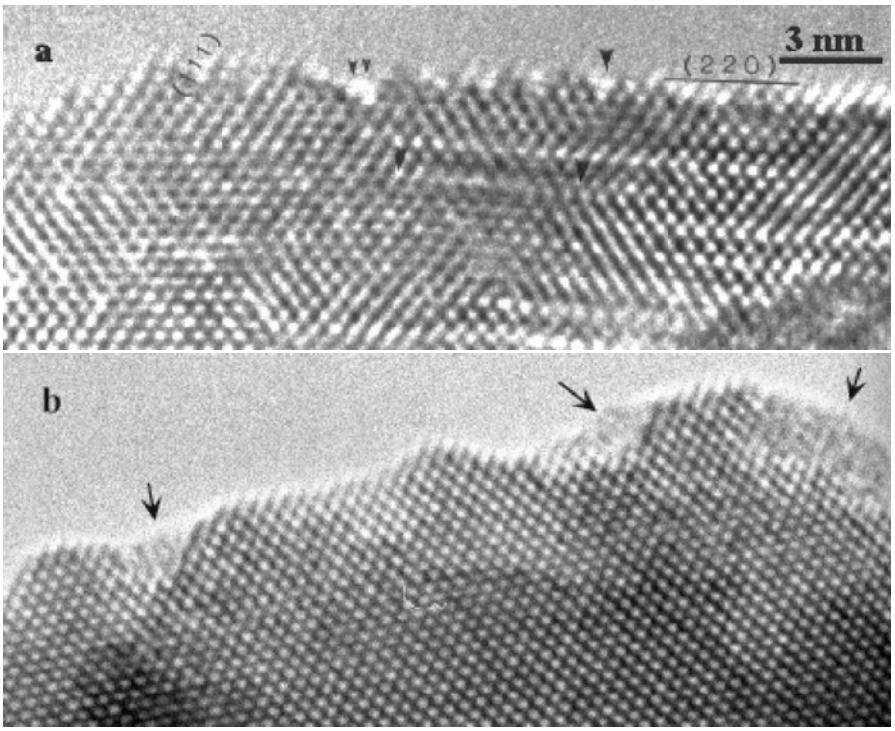

Figure 3-31. The surface defect (a) and the reacted sites (b) after treatment of $TbO_{1.833}$ in an acidic solution. The formation of $Tb(OH)_3$ after a leaching process generates an "amorphous" state in the lattice.

from $Tb_{48}O_{88}$ ($\beta(3)$) to $Tb_{24}O_{44}$ ($\beta(2)$). The oxygen content of these phases is the same but the configuration of the oxygen vacancies is different. In Fig. 3-32a the contrast modulation lengths are indicated by the inserted diffraction pattern (b) $\beta(3)$ and (c) $\beta(2)$. The boundary between the two phases is not defined and the modulation between the two phases is either continuous or has some dislocations. The pattern of metal atoms remains always the same during the formation of $Tb_{24}O_{44}$ ($\beta(2)$). This is typical for transitions between the phases in the homologous series.

In summary HREM is a powerful tool to study the rare earth oxides especially the higher oxides. The wide range of non-stoichiometry of the rare earth higher oxides is due to composition domains with different oxygen content. The composition domains may be reckognized by contrast modulations with different length corresponding to different oxygen vacancy content or by the formation of ordered phases belonging to the homologous

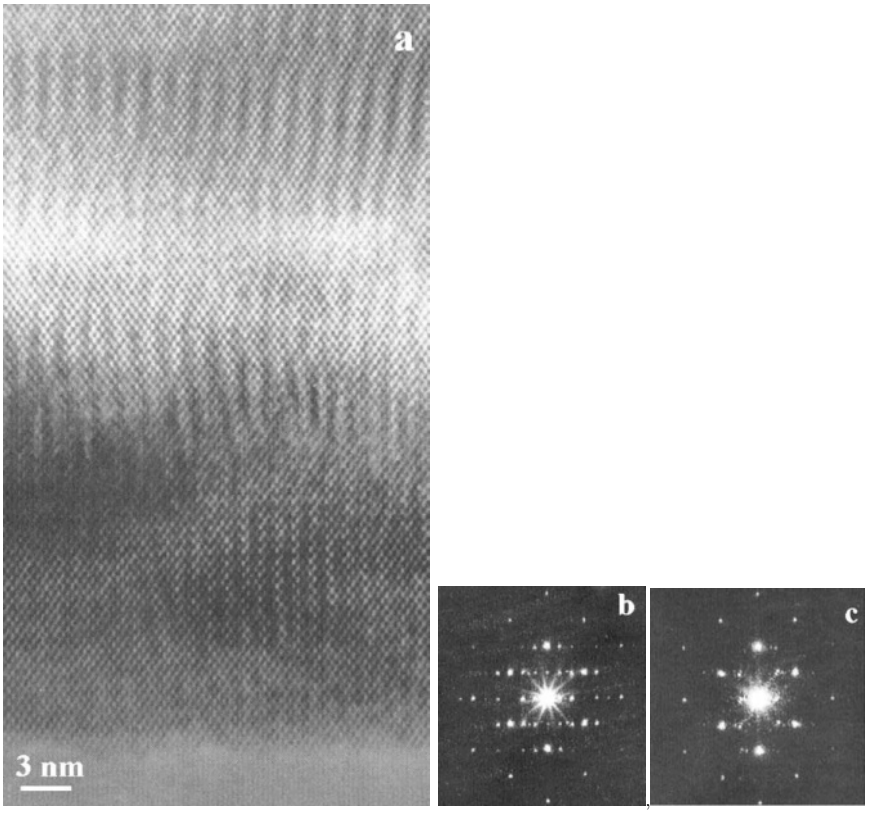

Figure 3-32. Intermediate stage of the transition between $Tb_{48}O_{88}$ ($\beta(3)$) and $Tb_{24}O_{44}$ ($\beta(2)$). (a) HREM image of the intermediated stage. (b) Diffraction pattern of the top part of the image. (c) Diffraction from bottom part of the image.

series of oxygen deficient fluorites. It is difficult to obtain a pure phase of only one intermediate composition and structure. The hysteresis in phase transformation is due to the energy needed for absorbing or releasing lattice oxygen and the boundary movement between different composition domains. The surface atoms are active and there is no strong ligand field effect between rare earth cation and oxide anion. The surface atoms of the rare earth oxides may reconstruct in order to correspond to the internal ordered superstructure of the bulk phase. Rare earth oxides are ideal materials for oxidation and reduction reactions and show a high surface mobility. Finally the information coming from those experimental electron diffraction patterns like the unit cells, symmetry and superstructure spots intensity can be used for modelling the structures of those phases within

the homologous series of the binary oxygen deficient fluorite-related rare earth higher oxides.

References

1. B. G. Hyde, D. J. M. Bevan and L. Eyring, *Philos. Trans. R. Soc. London,*, **259**, 583 (1966).
2. E. D. Guth, J. R. Holden, N. C. Baenziger and L. Eyring, *J. Am. Chem. Soc.*, **76**, 5239 (1954).
3. R. E. Ferguson, E. D. Guth and L. Eyring, *J. Am. Chem. Soc.*, **76**, 3890 (1954).
4. L. Eyring, *High Temp. Sci.*, **20**, 185 (1985).
5. J. S. Anderson, *Problems of nonstoichiometry*, edt. Rabenau A., North-Holland, Amsterdam pp1. (1970).
6. G. Adachi and N. Imanaka *Chem.Rev.*, **98**, 1479 (1998).
7. B. F. Hoskins and R. L. Martin, *Aus.J.Chem.*, **48**, 709 (1995).
8. Z. C.Kang and L. Eyring, *Aus.J.Chem.*, **49**, 981 (1996).
9. Z. C. Kang and L. Eyring, *Key Engineering Materials*, **155-56**, 301 (1998).
10. D. J. M. Bevan and R. L. Martin. *Z.anorg.allg.Chem.*, **625**, 57 (1999).
11. L. Eyring, *Synthesis of Lanthanide and Actinide Compounds*, *Kluwer Academic Publishers*, Netherlands 187, 1991.
12. J. Zhang, Z. C. Kang and L. Eyring. *J. Alloys and Compd.*, **192**, 57 (1993).
13. E. Mamontov and T. Egami, *J.Phys.Chem.Solids*, **61**, 1345 (2000).
14. D. J. M. Bevan, I. E. Grey and B. T. M. Willis, *J.Solid State Chem.*, **61**, 1 (1986).
15. S. P. Ray and D. E. Cox, *J. Solid State Chem.*, **15**, 333 (1975).
16. R. B. Von Dreele, L. Eyring, A. L. Bowman and J. L. Yarnell, *Acta Cryst.*, **B31**, 971 (1975).
17. J. Zhang, R. B. Von Dreele and L. Eyring, *J. Solid State Chem.*, **104**, 21 (1993).
18. J. Zhang, R. B. Von Dreele and L. Eyring, *J. Solid State Chem.*, **118**, 133 (1995).
19. J. Zhang, R. B. Von Dreele and L. Eyring, *J. Solid State Chem.*, **118**, 141 (1995).
20. J. Zhang, R. B. Von Dreele and L. Eyring, *J. Solid State Chem.*, **122**, 53 (1996).
21. J. Zhang, L. Eyring and R. B. Von Dreele, *Appl.Cryst.*, **15th**, 22 (1992).
22. Z. C. Kang and L. Eyring, *J. Alloys and Compd.*, **275-77**, 721 (1998).
23. K. Wurst, E. Schweda, D. J. M. Bevan, J. Mohyla, K. Wallwork and M. Hofmann, *Solid State Sciences*, **5**, 1491 (2003).
24. R. L. Martin, *Inorg.Chem.*, **20**, 3659 (1997).
25. Kang, private communication.
26. Z. C. Kang, J. Zhang and L. Eyring. *Z.anorg.allg.Chem.*, **622**, 465 (1996).
27. Z. C. Kang and L. Eyring. *J. Alloys and Compd.*, **275-77**: 30 (1998).
28. S. V. Krivovichev, *Solid State Sciences*, **1**, 211 (1999).
29. S. V. Krivovichev, *Solid State Sciences*, **1**, 221 (1999).
30. E. Schweda, L. Eyring, and D.J. Smith, *Ultramicroscopy*, **23**, 443 (1987).
31. N. V. Skorodumova, S. I. Simak, B- I. Lundquist, I. A. Abrikosov and B. Johansson, *Phys.Rev.Let.*, **89**, 166601-4 (2002).
32. D. A. Mac Donaill and P. W. M. Jacobs *J.Solid State Chem.*, **84**, 183 (1990).
33. E. Schweda, Rare earth oxides, *in Diffusionless Phase transition and related structures in oxides*, edt. Claude Boulesteix, Trans Tech Publication: Switzerland Vol. 68, 187, 1992.
34. T. Schleid and G. Meyer, *J. Less Common Met.*, **149**, 73 (1989).
35. H. Otobe and A. Nakamura, *Proc. Electrochemical Society*, **99-19**, 463 (1999).

36. G. Brauer, *Structural and solid state chemistry of pure rare earth oxides*, *in Progress in the science and technology of the rare earths* , *Pergamon Press*, Oxford Vol.2, 312, 1966
37. M. Foëx, *Z.Anorg.Allg.Chem.*, **337**, 313 (1965).
38. P. Aldebert and J. P. Traverse. *Mater.Res.Bull.*, **14**, 303 (1979).
39. V. F. Weigel and V. Scherer, *Radiochim. Acta*, **4**, 197 (1965).
40. C. Boulesteix, *Defects and phase transformation near room temperature in reare earth sesquioxides. in Handbook on the Physics and Chemistry of Rare Earths*, eds. K. A. Gschneidner and L. Eyring, North-Holland, Chapt.44, 321 (1982)
41. M. Ben Salem, B. Yangui, G. Schiffmacher and C. Boulesteix, *Phys. Status Solidi A*, **87**, 527 (1985).
42. M. Ben Salem, B. Yangui, and C. Boulesteix, *J. Phys.*, **48**, 1147 (1987).
43. M. Ben Salem and B. Yangui, *Key Eng. Mater.*, **101/102**, 61 (1995).
44. C. Boulesteix, *Phys.Stat.Sol. a)*, **86**, 11 (1984).
45. H. Bärnighausen and G. Brauer, *Acta Cryst.*, **15**, 1059 (1962).
46. R. Rau, *Acta Cryst.*, **20**, 716 (1966).
47. Z. C. Kang and L. Eyring, *Ultramicroscopy*, **52**, 377 (1993).
48. D. J. M. Bevan, *J. Inorg. Nucl. Chem.*, **1**, 49 (1955).
49. D. J. M. Bevan and J. Kordis, *J. Inorg. Nucl. Chem.*, **26**, 1509 (1964).
50. J. Kordis and L. Eyring, *J. Phys. Chem.*, **72**, 2044 (1968).
51. C. Lopez-Cartes, J. A. Perez-Omil, J. M. Pintado, J. J. Calvino, Z. C. Kang and L. Eyring *Ultramicroscopy*, **80**, 19 (1999).
52. M. S. Jenkins, R. P. Turcotte and L. Eyring, *On the thermodynamic and X-ray diffraction behavior of a widely non-stoichiometric region of the praseodymium oxide system. in The chemistry of extended defects in non-metallic solids*, eds. LeRoy Eyring and Michael O'Keeffe, North-Holland, Amsterdam, 36 (1970).
53. Z. C. Kang, J. Zhang, and L. Eyring, *Aust. J. Chem.*, **45**, 1499 (1992).
54. C. Boulesteix and L. Eyring, *J. Solid State Chem.*, **66**, 125 (1987).
55. Z. C. Kang, C. Boulesteix and L. Eyring, *J. Solid. State. Chem.*, **81**, 96 (1989).
56. C. Boulesteix, E. Schweda, Z. C. Kang and L. Eyring, *Ferroelectrics*, **111**, 247 (1990).
57. J. A. Kilner and B. C. H. Steele, *Mass transport in anion-deficient fluorite oxides. in Nonstoichiometric oxides* , edt. O. Toft Sorensen, Academic Press, 233, (1981).
58. K. Otsuka, M. Kunitomi and T. Saito, *Inorg. Chim. Acta.*, **15**, 115 L31 (1986).
59. R. P.Turcotte, M. S. Jenkins and L. Eyring, *J. Solid State Chem.*, **7**, 454 (1973).
60. A. D. Wadsley, *Inorganic non-stoichiometric compounds*. 98 (1964).
61. Z. C. Kang, L. Eyring and D. Smith, *Ultramicroscopy*, **22**, 71 (1987).
62. Kang and L. Eyring, *J. Alloys and Compd.*, **181**, 483 (1991).
63. T. X. T. Sayle, S. C. Parker and C. R. A. Catlow, *J. Chem. Soc. Chem. Commun.*, 977, 1992.

4. CHEMICAL BONDS AND CALCULATION APPROACH TO RARE EARTH OXIDES

Y. MAKINO
Joining and Welding Research Institute
Osaka University
Osaka 565-0871, Japan

S. UCHIDA
Institute of Multidisciplinary Research for Advanced Materials,
Tohoku University
Sendai 980-8577, Japan

4.1. INTRODUCTION

Until now, many experimental and theoretical investigations on atomic and metallic states of rare-earth elements have been systematically summarized. For example, the nature of 4f bonding in lanthanide elements and their compounds was described on the basis of the phenomenological approach [1]. These electronic states were experimentally determined on the basis of spectroscopic measurements and the energy levels have been theoretically assigned by quantum mechanical calculations. The electronic states of rare-earth metals and compounds were also investigated extensively from both theoretical and experimental approaches. Although the electronic structures of rare-earth metals[2,3,4] and some special compounds [5] have been investigated by various theoretical and spectroscopic approaches, systematic investigation on the those of rare-earth sesquioxides has been not so extensively performed.

In this section, systematic results on the electronic structures and chemical bonding of rare-earth sesquioxides and fluorite-type oxides are introduced briefly. In the subsection 4-1, systematic results on the electronic structures and chemical bonding of sesquioxides are described and the description on rare-earth fluorite-type oxides is mainly focused on cerium dioxide in the subsection 4-2.

Electronic structures of some sesquioxides were calculated from the special interests on these materials properties. For example, Skorodumova et al. [5] calculated the electronic structure of Ce_2O_3 by FP-LMTO method for the purpose of clarifying the role of oxygen-poor Ce_2O_3 in catalytic property and its band gap and magnetic property were discussed on the basis of valence-band and core-state

G. Adachi et al. (eds.), Binary Rare Earth Oxides, 95–110.

models. Mishra et al. [6] calculated the electronic structure of La_2O_3 by FP-LMTO and ASM methods in order to understand the optical property by the electronic structure of $LaPO_4$. The calculation of electronic structure of La_2O_3 was also performed by CNDO method for obtaining useful knowledge on lattice properties of imperfect La-based crystals [7].

On the other hand, a few systematic investigations on the electronic structures of rare-earth sesquioxides have been found until now. Ryzhkov et al. [8,9] calculated the electronic structures of twelve lanthanide sesquioxides except for La_2O_3, Ce_2O_3 and Pm_2O_3 using spin-restricted DV-Xα method and compared with the X-ray photoelectron spectra. Further, they calculated the overlap populations of the important bonds between Ln and oxygen, which take the important roles on the chemical bond of Ln-O. Chemical bonding of compounds including sesquioxides was reviewed by Gubanov and Ryzhkov [10]

Recently, Arai et al. [11] investigated the electronic structures of ten kinds of rare-earth sesquioxides single crystals (Ln_2O_3: Ln=La, Pr, Nd, Sm, Gd, Er, Tm, Yb and Lu) by 4d-4f resonant photoemission. Later, Kimura et al. also measured reflectivity spectra of nine rare-earth sesquioxides except Gd_2O_3 from the above ten sesquioxides in the photon energy range form 0.5eV to 50eV [12].

4.2. ELECTRONIC STRUCTURE OF SESQUIOXIDES

As indicated in the beginning of this chapter, the electronic structures on the lanthanide sesquioxides have been systematically considered by Ryzhkov et al.[8,9]. They calculated the electronic structures of twelve lanthanide sesquioxides (from Pr_2O_3 to Lu_2O_3 except Pm_2O_3) by using spin-polarized DV method. Figure 4-1 shows the schematic energy diagrams for thirteen lanthanide sesquioxides that are illustrated by simplifying the original energy level diagrams. The partial contributions of different electronic states to the chemical bonding were also analyzed on the basis of the overlap populations of various pairs of atomic orbitals between lanthanides and oxygen. These overlap populations were calculated under the assumptions that the sesquioxides of light lanthanides have C_{3v} symmetry and those of heavy lanthanides have D_{3d} or C_2 symmetry. Atomic arrangements of the four model clusters are shown in Figure 4-2. Interatomic distances for these clusters are given in Table 4-1. Interaction between atomic orbitals of oxygen and 5d, 6s or 6p orbitals of lanthanide atom is given in Table 4-2. As shown in the table, the interaction Ln 5d and O2p orbitals has the predominant contribution to the Ln-O chemical bonding. Change of coordination number, symmetry of the local environment and the distance between lanthanide metal and oxygen gives only weak influence on the overlap populations of these diffuse orbitals. The variation was within the range of 10% for light lanthanide sesquioxides and 30% for heavy lanthanide sesquioxides.

On the other hand, the interactions between 4f electrons and oxygen are more complex. The calculated values of overlap populations between 4f and O2p orbitals

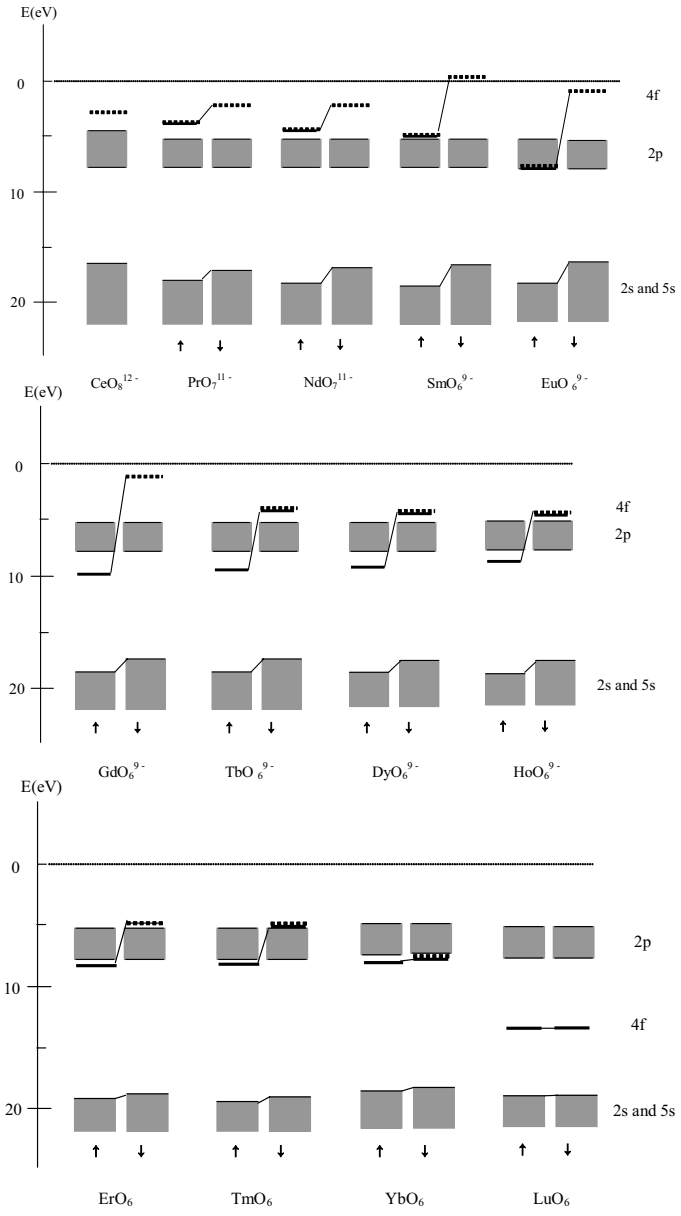

Figure 4-1. Schematic energy diagrams of lanthanide sesquioxides. (Energy diagrams of sesquioxides of light lanthanides) (Reproduced with permission from ref.8 and 9. Copy right 1985 Springer-Verlag)

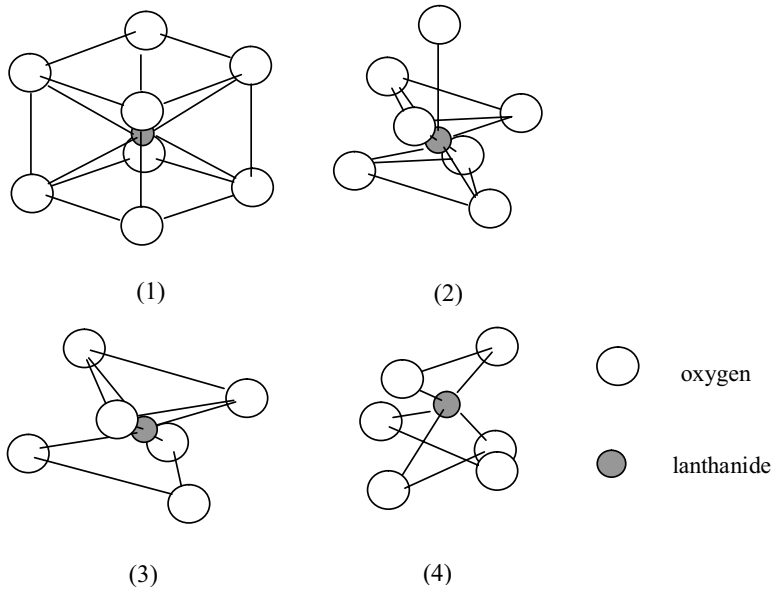

Figure 4-2. Atomic arrangements of four model clusters.(Reproduced with permission from ref.8 and 9. Copy right 1985 Springer-Verlag)

TABLE 4-1(a). Interatomic distances of Ln-O for the clusters in the light lanthanide oxides (unit: nm).

Point symmetry	CeO_2	Pr_2O_3	Nd_2O_3
O_h	0.234	–	–
C_{3v}	–	0.237 0.262	0.237 0.263

TABLE 4-1(b). Interatomic distances of Ln-O for the clusters in the heavy lanthanide oxides (unit: nm).

Point symmetry	Sm_2O_3	Eu_2O_3	Gd_2O_3	Tb_2O_3	Dy_2O_3
D_{3d}	0.233	0.233	0.232	0.230	0.229
C_2	0.227 0.230 0.241	0.225 0.229 0.240	0.224 0.228 0.238	0.223 0.226 0.236	0.221 0.224 0.235
Point symmetry	Ho_2O_3	Er_2O_3	Tm_2O_3	Yb_2O_3	Lu_2O_3
D_{3d}	0.228	0.227	0.226	0.233	0.223
C_2	0.220 0.223 0.234	0.219 0.222 0.233	0.219 0.222 0.232	0.216 0.219 0.230	0.216 0.219 0.229

TABLE 4-2. Overlap populations in some oxides of rare-earth methals. ($\times 10^3$, calculated per ligand; In the case of inequivalent ligands, the results are given in order of increasing values of the intratomic distance of Ln-O.) (Reproduced with permission from ref.8 and 9. Copy right 1985 Springer-Verlag)

Compound	Overlap populations		
	Ln5d-O2p	6s-O2p	6p-O2p
Pr_2O_3	102	4	21
	74	9	22
Nd_2O_3	99	6	21
	71	8	22
$Dy_2O_3(D_{3d})$	104	6	27
$Dy_2O_3(C_2)$	106	4	26
	109	6	28
	95	8	27
$Yb_2O_3(D_{3d})$	103	7	28
$Yb_2O_3(C_2)$	99	4	25
	106	7	28
	94	9	29

are listed in Table 4-3. The contribution of 4f orbitals fairly rapidly decreases in the first half of lanthanide series. Further decrease is still found in the latter half and the overlap population is very small in the heavy lanthanides. In the case of Ln sesquioxides with both C_{3v} and C_2 symmetry, the contributin of 4f orbitals to the chemical bonding is fairly sensitive to the variation of Ln-O interatomic distance. Conclusively, Ln-O interatomic distance is the main factor for the contribution of 4f orbitals to Ln-O chemical bonding, compared with the symmetry variation of the environment.

TABLE 4-3. Overlap populations between 4f and O2p AO's ($\times 10^3$, calculated per ligand) in oxides of light rare-earth elements (C_{3v} clusters with two types of ligands) and heavy rare-earth elements (D_{3d} clusters and C_2 clusters with three types of ligands.) (Reproduced with permission from ref.8 and 9. Copy right 1985 Springer-Verlag)

Oxide	Overlap populations with inequvalent ligands (C_{3v} and C_2 clusters)	Mean values (C_{3v} and C_2 clusters)	Overlap populations (D_{3h} clusters)
Pr_2O_3	25 14	19	−
Nd_2O_3	18 12	15	−
Sm_2O_3	16 8 11	12	13
Eu_2O_3	7 4 5	5	7
Gd_2O_3	15 11 9	12	12
Tb_2O_3	15 9 9	11	12
Dy_2O_3	13 8 7	9	10
Ho_2O_3	10 8 4	7	9
Er_2O_3	7 5 4	5	7
Tm_2O_3	3 2 2	2	4
Yb_2O_3	–2 –2 –2	–2	–1
Lu_2O_3	–1 –1 –1	–1	–1

Ryzhkov et al. [8,9] also reported on the relation between XPS spectra and the electronic structures calculated by DV method. According to their calculation results, the relative positions of molecular orbital levels change very slightly from one cluster to another except for Ln 4f levels. The groups of electronic levels just lower than the gap consist of oxygen 2s and Ln 5s and these levels are located between -22eV and –17eV for light lanthanides, and between –23eV and –16eV for heavy lanthanides. The groups of electronic levels just upper than the gap consist of oxygen 2p and Ln 4f. The levels of Ln 4f are vacant, of course, in the case of CeO_2. Energy splitting of Ln 4f levels due to spin polarization increases with the number of 4f electrons from $La_2O_3(LaO_6)$ to Gd_2O_3 (GdO_6) clusters, then decreases from $Tb_2O_3(TbO_6)$ to $Tm_2O_3(TmO_6)$, and finally becomes zero for $Yb_2O_3(YbO_6)$and $Lu_2O_3(LuO_6)$. Further, relative positions of Ln 4f with up-spin states to oxygen 2p levels come to overlap with the increase of the number of 4f electrons because the positions of Ln 4f with up-spin state are lowered. As shown in Table 3, the interaction between Ln4f and oxygen 2p for covalent hybridization is not so large, compared with the interaction between Ln5p and oxygen 2s. However, the interaction between Ln4f and oxygen 2p becomes important when Ln4f levels with up-spin state and oxygen 2p levels can overlap, that is, in the case of Sm_2O_3 and Eu_2O_3 because Ln4f electrons can hybridize oxygen 2p electrons, as shown in the energy diagrams. On the other hand, Ln4f levels with down-spin state hybridize oxygen 2p electrons in the case of Tb_2O_3, Dy_2O_3 and Ho_2O_3.

XPS spectra of sesquioxides of light lanthanides show good agreement with the calculation results except for Ln5s levels. It is suggested that the disagreement is attributed to the relativistic interaction. It is also indicated that the difference of point symmetry between D_{3d} and C_2 shows only slight influence on the shape of valence band when XPS are compared with theoretical spectra of these clusters. In the XPS and theoretical spectra of heavy lanthanide sesquioxides, some discrepancy is observed for $Ln5p^{3/2}$ and $Ln5p^{1/2}$ spectra and the discrepancy is attributed to the non-relativistic calculation. Further, it is explained that appearance of third peak or shoulder in the right side (higher energy side) of main $5p^{3/2}$ band in the XPS spectra of the heavy lanthanide sesquioxides is due to the contribution of molecular orbitals with oxygen 2s character that is mixed with Ln5p.

Recently, F.Arai et al. [11] investigated the electronic structures of eleven rare-earth sesquioxides by 4d-4f resonant photoemission measurement. They observed that some peaks in the energy distribution curves (EDCs) become resonantly large at the energy of the peak of constant final spectra. For example, the peaks at 16eV and 33eV in La_2O_3, which originate from the La5p and La5s, are enhanced by the excitation at 117eV, as shown in Figure 4-3, which corresponds to the 4d-4f absorption. Further, the 4f character in the valence band and the mixing effect was analyzed by examining the difference between on- and off-resonance EDC spectra of Ln_2O_3. The difference spectra was obtained by subtracting the off-resonance EDC spectrum (for example, spectrum of La_2O_3 obtained in the case of 117eV photon

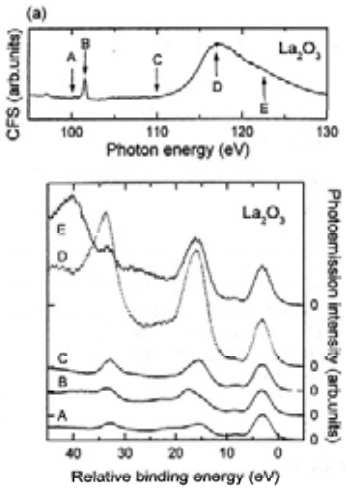

Figure 4-3. 4d-4f resonant photoemission and constant final state(CFS) spectra of La_2O_3. (Reproduced with permission from ref.11. Copy right 2000 J. Phys. Soc. Japan)

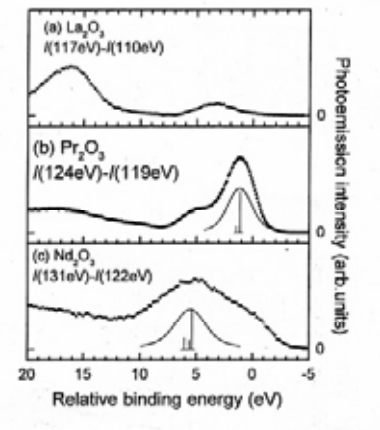

Figure 4-4. Difference spectra between on- and off-resonance photoemission spectra of La_2O_3, Pr_2O_3 and Nd_2O_3. (The vertical bars are the multiplet structure of 4fn-1 final state. The solid lines are convolutions of the multiplet structures with Lorentz and Gauss functions. (Reproduced with permission from ref.11. Copy right 2000 J. Phys. Soc. Japan)

energy) from the on-resonance EDC spectrum (for example, spectrum of La_2O_3 obtained in the case of 110eV photon energy). The difference spectra of light rare-earth oxides are shown in Figure 4-4. In this figure, the calculated multiplet structures, which originate from the excitation of $4f^n+h\nu \rightarrow 4f^{n-1}+$ electron, in the trivalent rare-earth ion are shown by vertical bars and the convoluted spectra are given by the solid lines.

As shown in Figure 4-4, the difference spectra seem to be explained well by 4f multiplet structures of trivalent rare-earth ions except Pr_2O_3 and Nd_2O_3. In Pr_2O_3 and Nd_2O_3, there are additional shoulder structures that are considered to be originated from the final state related to hole state of O2p band. According to the analysis based on cluster model, the hybridization intensities between Ln4f and O2p states for Pr_2O_3 and Nd_2O_3 are estimated to be 1.52eV and 0.74eV, respectively. The additional shoulder structures are also observed at the low binding energy side of $4f^{n-1}$ main peaks in Sm_2O_3 and Eu_2O_3, but these intensities are low on account of the hybridization intensities in these oxides (see ref. [10]]). Conclusively, the 4f photoemission spectra of rare-earth sesquioxides are almost explained by the multiplet structure of $Ln^{3+}4f^{n-1}$ state and it is observed that the binding energy of occupied 4f state is close to that of O2p valence band. Detailed discussion is given in the reference [11].

As described in the beginning of the section, we can find several investigations focusing the electronic structure of a lanthanide sesquioxide such as La_2O_3 and

Ce_2O_3. Because Ce_2O_3 is a metastable sesquioxide in the standard state, the electronic structure was not discussed in the above-described systematic investigations. The electronic structure of Ce_2O_3 was calculated by Skorodumova et al.[5] on the basis of first principles. They calculated the electronic structure in the framework of local-density approximation (LDA) and the generalized gradient approximation (GGA) for the exchange-correlation energy density and potential in the Predew-Wang parametarization. The calculation was performed for the experimental value of the c/a, i.e., 1.55. Further, the valence band model (VBM) and core state model(CSM) were considered for the Ce 4f states. Their results on the calculated lattice parameter and bulk modulus of Ce_2O_3 are shown in Table 4-4. Best agreement with the experimental lattice parameter was obtained in the calculation based on LDA and CSM and the calculation in the framework of GGA and CSM overestimates the lattice parameter by the value of 2%. On the other hand, VBM

TABLE 4-4. Theoretical and calculated lattice parameter [a(nm)] and bulk modulus [B(GPa)] of Ce_2O_3. (# from R.G. Wyckoff and E.O. Wollen; Acta Crystallogr., 6 (1953) 741.) (Reproduced with permission from ref.5. Copy right 2000, The American Physical Society)

	Core-state model		Valence-band model		Experiment[#]
Property	LDA	GGA	LDA	GGA	
a (nm)	0.3888	0.3967	0.3720	0.3805	0.3888
B(GPa)	165.79	145.27	208.63	131.83	–

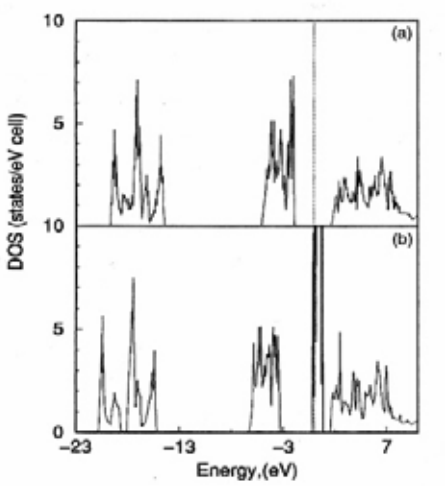

Figure 4-5. Density of states (DOS) for Ce_2O_3 calculated within the core-state model (a) and valence-band model (b). (Reproduced with permission from ref.5. Copy right 2000, The American Physical Society)

calculation shows a clear underestimate, especially for the LDA. Thus it is indicated that the description of the 4f electron as a localized core electron is appropriate for Ce_2O_3. Further, they showed more support from the electronic structures of Ce_2O_3 calculated within the CSM and VBM, respectively (see Figure 4-5). As shown in the figure, a partly filled f band appears in the right side at the Fermi level in the DOS calculated within VBM, while the DOS calculated within CSM reveals a band gap between the valence and conduction bands that shows good agreement with experimental result.

Subsequently, they discussed the absolute magnetic moment of Ce_2O_3 that means a sum of the absolute values of moments on all atoms in the unit cell, based on the spin-polarized calculation in the framework of CSM and VBM for both ferromagnetic (FM) and antiferromagnetic (AFM) configurations. According to their results, the AFM state is energetically more stable than the FM one and the calculated absolute magnetic moment is $2.13\mu_B$ for both the AFM and the FM configurations, that is very close to the experimental value $2.17\mu_B$. On the other hand, the calculated absolute magnetic moment at the equilibrium volume is substantially smaller than the experimental value ($1.35\mu_B$ for the FM case and $0.72\mu_B$ for the AFM case). Conclusively, it is indicated that the magnetic property of Ce_2O_3 is well explainable by the CSM framework of 4f electron.

More recently, a report on the electronic structures of rare-earth sesquioxides have been presented by Suzuki et al. for the purpose of explaining 3d x-ray photoemission spectra (XPS) of these sesquioxides [13]. In the measurement of 3d XPS of rare-earth sesquioxides, it has been reported that clear double-peaks structure, the shoulder (or broad foot) and single-peak structure are observed for La_2O_3, for Pr_2O_3, Nd_2O_3 and Sm_2O_3, and for Eu_2O_3, Gd_2O_3 and Dy_2O_3, respectively. They explained these behaviors of 3d XPS by the electronic structures of ground state and 3d-1 core-hole state that were calculated by the spin-unrestricted DV-Xα MO method for model clusters chosen as $[LnO_6]^{9-}$ for Ln_2O_3. According to their results, the clear double-peak structures of 3d XPS for La_2O_3 and Ce_2O_3 are attributed to the increase of unpaired 4f electrons by less than one due to weak charge-transfer effect. On the other hand, the shoulder or broad foot of 3d XPS for Pr_2O_3, Nd_2O_3 and Sm_2O_3 can be explained by the increase of unpaired 4f electrons by more than one due to strong charge-transfer effect. The clear single peak structures for heavy lanthanide sesquioxides (Gd_2O_3,Dy_2O_3, Ho_2O_3, Er_2O_3 andTm_2O_3) except $Yb_2O_3$and Lu_2O_3 is interpreted by the decrease of 4f electrons by more than one. Lastly, the 3d XPS for Eu_2O_3 and Yb_2O_3 is explained by the increase or decrease of 4f electrons by less than one due to the restricted charge-transfer effect by filling $4f^{\uparrow}$ and 4f orbitals with electrons. Though the electronic structures for Ce_2O_3 Sm_2O_3, Eu_2O_3 and Tm_2O_3 were reported in their papers, only the electronic structures of ground state and the $3d^{-1}$ core-hole state for Ce_2O_3 are shown in Figure 4-6. Before the report by Suzuki et al., Kotani and Ogasawara have reviewed the core-level spectroscopic data of lanthanide sesquioxides [14]. Here, we

only point out that the core-level spectroscopic data of lanthanide sesquioxides can be well analyzed with the impurity Anderson model in their review.

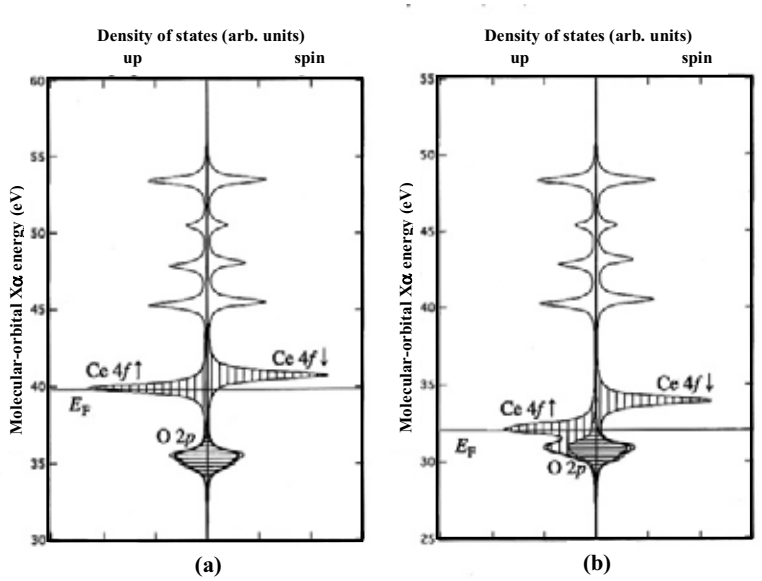

Figure 4-6. Calculated Ce 4f, 5d, 6s and 6p and O2p DOS of $[CeO_6]^{9-}$ is cluster in the (a) ground state, (b) the 3d $^{-1}$core-hole state. Horizontally hatched range:O 2p, vertically hatched range: Ce 4f, full range: Ce 4f, 5d, 6s, and 6p and O 2p. (Reproduced with permission from ref.13. Copy right 2000, Elsevier B.V.)

4-3. ELECTRONIC STRUCTURE OF FLUORITE OXIDES

In this section, fluorite-type oxides, for example, the cerium dioxide (CeO_2, ceria) is discussed. It has been very widely investigated because of the high chemical stability with high melting point 2730 °C. It belongs to the cubic system

TABLE 4-5. Crystal structure parameters of CeO_2.

Composition		CeO_2		
System		Cubic		
A, b, c (Å)		5.4112(10)	5.4112(10)	5.4112(10)
α, β, γ (deg)		90	90	90
Unit cell volume (Å^3)		158.4		
Z		4		
Space group		*Fm*3*m* (No.225)		
atom	site	x/a	y/b	z/c
Ce	4*a*	0	0	0
O	8*c*	1/4	1/4	1/4

and the lattice mismatch is quite low, less than 0.35%, with silicon semiconductor as shown in Table 4-5 [15]. The perspective view of crystal structure and the first Brillouin zone are also shown in Figure 4-7.

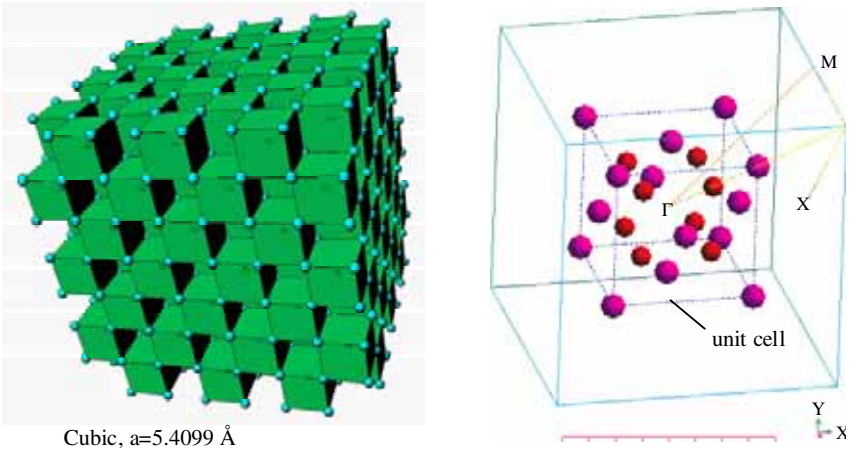

Figure 4-7. The perspective view of crystal structure and the first Brillouin zone of CeO_2.

Here conventional *ab*-initio studies have been performed using CASTEP code. Pseudo potential used for band structure calculation is shown in Table 4-6.

TABLE 4-6. Pseudo potential used for ab-initio band structure calculation.

Element	Type	Configuration
Ce	Troullier-Martins psp	
O	Ming Hsien Lee psp	$2s^2\ 2p^4$

Before the calculation, followed by above potential sets, optimization of structure by using Local Density Approximation, LDA method was examined. The result of lattice constant of CeO_2 is shown in Table 4-7. It almost agrees with that value already reported in ICDD Card (#43-1002) within the error of ±0.4%.

TABLE 4-7. Lattice constant of cerium oxide. Experimental data are given in brackets.

Material (structure)	Calculation details (Task, # of atom, Ecut, grid, k-points, grid)	a(Å)
CeO_2	GGA, 16 atoms, 330 eV, 43, 30×30×30	5.3914(5.41134)

In spite of well agreement of the lattice constant, the calculated band gap was rather low 1.89 eV than that of observed value 3.78 eV [16]. This can not be avoided in any kind of *ab*-initio calculation so called gap-problem.

Figure 4-8 shows the results of band structure and density of state (DOS) profiles of CeO_2. The results show that CeO_2 is semiconductor with indirect transition type such as Si. This indicates that the excited electron requires not only energy change but also momentum change along with the transition from the top of valence band M to the bottom of conduction band S. The electron transfer does not occur just by interaction between the electron and the photon because the momentum of the light is zero. It is only allowed by receiving the momentum such as atomic vibration (phonon) of the crystal. Therefore, band edge spectra would be a little broadened due to the effect of phonon absorption and desorption.

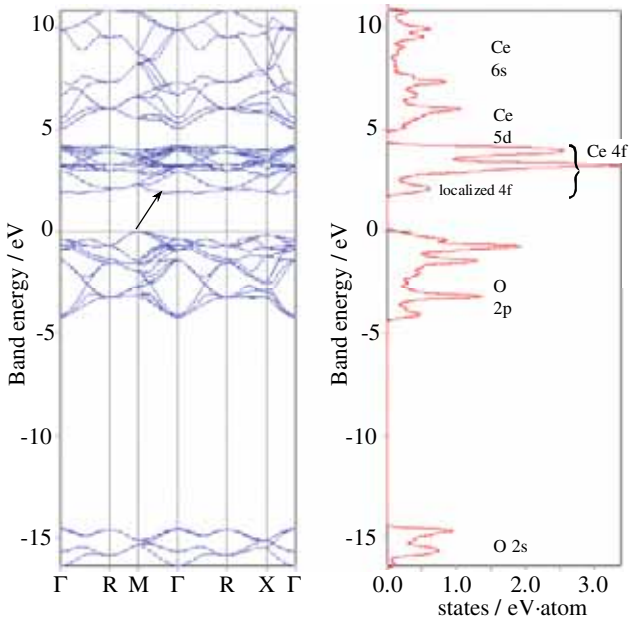

Figure 4-8. Band structure and DOS profiles of CeO_2 along high-symmetry directions of the irreducible Brillouin zone. The valence-band maximum is taken as the energy zero.

Pure stoichiometric CeO_2 has the calcium fluoride (fluorite) type of structure with space group *F*m3m. It has been also well known as a Non-stoichiometri compound and there are variety of studies concerning about the defect and redox chemistry [17-19]. Among them, Stefano has already reported the electron localization in pure and defective ceria by a unified LDA+U approach as shown in Figure 4-9 [20]. Here we can see the decrease of band gap of both cerium sub oxide

(Ce_2O_3) and defective ceria ($CeO_{1.875}$). These phenomena quite agree with conventional experimental results of yellow coloration.

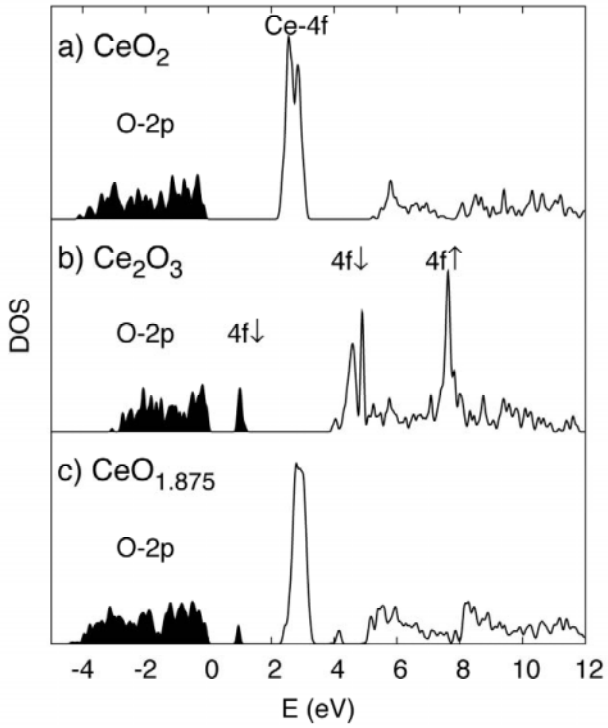

Figure 4-9. Density of electronic states for pure CeO_2 (a) and Ce_2O_3 (b) bulk phases, and for defective (c) ceria structures CeO_{2-X}. Occupied states are indicated as shaded areas, and the zero energy is set to the top of the valence band.

The lattice defect of CeO_2 is always an issue in the field of cosmetic application for UV shield materials. In order to reduce the photo catalytic activity, a small amount of metal ions are doped to keep the stoichiometry. Similarly this doping method is taken in the sintering process of CeO_2 to control the grain growth [21, 22]. In such cases, qualitatively, computational analysis gives an interpretation for the mechanism of functional properties. Table 4-8 shows pseudo potential used for *ab*-initio band structure calculation and Figure 4-10 shows the results of band structure

TABLE 4-8. Pseudo potential used for *ab*-initio band structure calculation.

Element	Type	Configuration
Ca	Qc-tuned Optimized Highly Ionic Ca[+10] psp	$3s^2\ 3p^6$ (This adds up to Ca[+2])
Ce	Troullier-Martins psp	
O	Ming Hsien Lee psp	$2s^1\ 2p^{1.75}\ 3d^{0.25}$

and density of state (DOS) profiles of Ca 10 atomic % doped CeO_2.

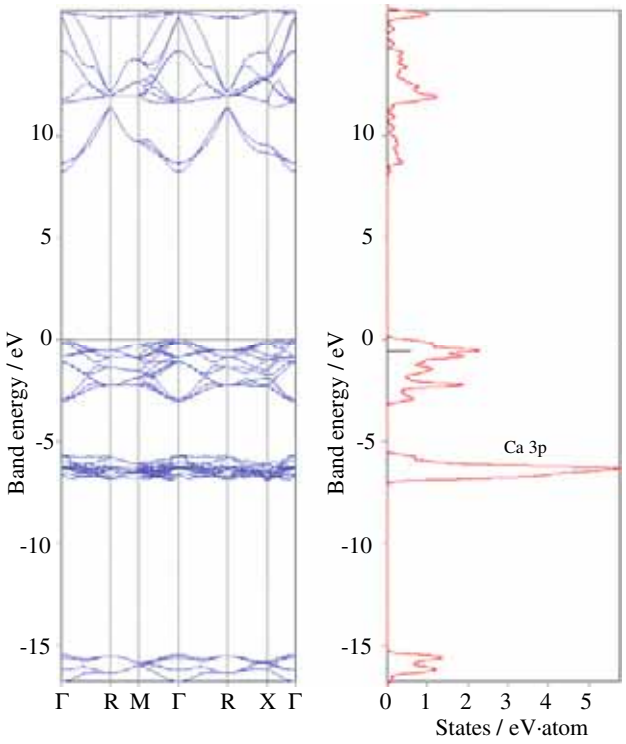

Figure 4-10. Band structure and DOS profiles of $Ca_{0.1}Ce_{0.9}O_{1.9}$ along high-symmetry directions of the irreducible Brillouin zone. The valence-band maximum is taken as the energy zero.

The conduction band where unoccupied MO of CeO_8 polyhedra form is almost diminished (as expected) because Ca atom is located on the same position of Ce site statistically in this calculation. Interestingly, the structure of valence band was little changed and the top of valence band returned to the Γ point. This results direct transition of photo-assist excitation. The band edge spectra will be expected as a sharpened one by doping Ca. It can be considered that the band gap was extended by tightly bonded to make new hybridization of orbital both Ca 2s and Ce 4f. Because of this, it can be explained electronically that CeO_2 loses the semiconductor property to be more stable compound.

Ionic and covalent bonds in CeO_2 crystal has also been studied by Nakamatsu et al by using the relativistic discrete-variational Xα method [23]. The electron charge distribution of CeO_2 is compared with those of ZrO_2 and CaF_2. The charge density in the metal atomic region indicates stronger covalency for CeO_2 than that in Zr for ZrO_2. The repulsion between the metal and oxygen ionic cores is, however, strong

and superior to the covalent interaction, and thus the ionic character determines the static bonding nature in the CeO_2 crystal.

To clarify covalent bonds in the interatomic region, the charge density of an ideally isolated ion is subtracted from that of the compound. The differential charge density is shown in Figure 4-11.

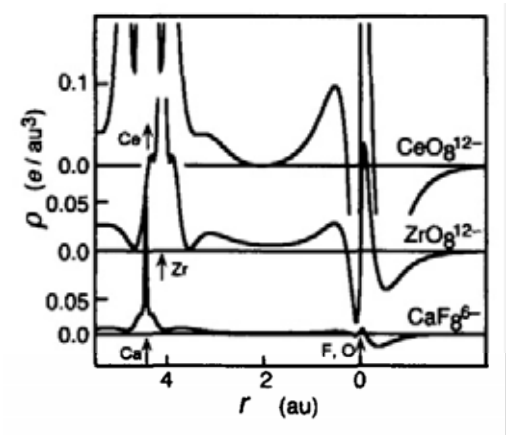

Figure 4-11. Cross sectional view of the difference in charge density for the valence band (O 2p, F 2p). The charge density of each compound is reduced by that of a corresponding ideal ion (O^{2-}, F^-). (Reproduced with permission from ref. 23. Copy right 1995, Elsevier B.V.)

The ideally isolated ion used here means a charge sphere which consists of the fully filled O 2p (or F 2p) atomic orbitals used in the molecular orbital calculations. The charge density for CaF_2 is subtracted almost completely in the fluorine region and only a little difference from the ideal ion remains. On the other hand, the charge density for ZrO_2 appreciably increases in the interatomic region. This increase is the origin of the covalent bonding. The covalent interaction causes the redistribution of the charge density with the movement from the O ion to the Zr ion. The charge density distribution of the CeO_2 compound has a different nature from those of ZrO_2 and CaF_2. To generate covalent bonding, a net increase in the charge density in the interatomic region where electron charges bind two nuclei is necessary. In the case of CeO_2, the participation of the Ce atomic orbitals in the valence state is appreciable. However, this does not mean an effective contribution to the chemical bonding because the charge density in the inter- atomic region exhibits almost no increase on formation of the Ce-O bond. This fact suggests that another kind of bonding interaction dominates the bonding nature in CeO_2.

A population analysis shows that the mixed interaction due to the independent ionic and covalent contributions arises from the ionic Ce 5s, 5p and covalent Ce 4f, 5d orhitals which are proximate to each other in the bond region.

References

1. K.A. Gschneidner, Jr., *J. Less-Common Metals,* **25,** 405-422 (1971).
2. J.O. Dimmock, *Solid State Physics,* ed. by Ehrenreich, Seitz and Turnbull, Acadenic, **26,** 223-244 (1971).
3. H.L. Skriver, *Systematics and the Properties of the Lanthanides*, ed. by S.P. Sinha, D.Reidel, Publishing Co., p 213-254 (1983).
4. S.H. Liu, *Handbook of Physics and Chemistry of Rare Earths*, ed. K.A. Gschneidner Jr., and L.R. Eyring, North-Holland, Amsterdam, **l.1**, 233-258 (1978).
5. N.V. Skorodumova, A.Ahuja, S.I. Simak, I.A. Abrikosov, B.Johansson, and B.I. Lundquvist; *Phys. Rev. B64,* 115108/1 (2001).
6. K.C. Mishra, I.Osterloh, H.Anton, B.Hannebauer, P.C. Schmidt, and K.H. Johnaon, *J.Mater. Res.,* **12**, 2183-2190 (1997).
7. R.A. Evarestov, A.V. Leko, I.V. Murin, A.V. Petrov, and V.A. Veryazov, *Phys. Stat. Sol.* **170,** 145-153 (1992).
8. M.V. Ryzhkov, V.A. Gubanov, Yu.A. Teterin, and A.S. Baev, *Z.Phys.B- Condensed Matter,* **59**, 1-6 (1985).
9. M.V. Ryzhkov, V.A. Gubanov, Yu.A. Teterin, and A.S. Baev, *Z.Phys.B- Condensed Matter* **59**, 7-14 (1985).
10. V.A. Gubanov, and M.V. Ryzhkov, *Zh. Strukt. Khim.,* **27**, 123-136 (1986). (Eng. Trans., *J. Structural Chemistry*, **27**, 781-794 (1986).)
11. F.Arai, S.Kimura, and M.Ikezawa, *J. Phys. Soc. Japan*, **67**, 225-229 (1998).
12. S.Kimura, F.Arai, and M.Ikezawa, *J. Phys. Soc. Japan,* **67**, 3451-3457 (1998).
13. C.Suzuki, J.Kawai, M.Takahashi, A.M. Vlaicu, H.Adachi, and T.Mukoyama, *Chem.Phys.*, **253,** 27-40 (2000).
14. A.Kotani, and H.Ogasawara, *J. Electron Spectrosc. Relat. Phenom.*, **60**, 257-299 (1992).
15. E. A. Kummerle, and G. Heger, *Solid State Chem.*, **147**, 485-500 (1999).
16. T. R. Griffiths, M. J. Davies, and H. V. Hubbard, *J. Chem. Soc. Farad II,* **4**, 765 (1976).
17. M. Mogensen, N. M. Sammes, and G. A. Tompsett, *Solid State Ionics,* **129**, 63-94 (2000).
18. A. Hartridge, M. Ghanashyam Krishna, and A. K. Bhattacharya, *International Journal of Modern Physics B*, **12(15)**, 1573-1583 (1998).
19. I. Kosacki, T. Suzuki, H. U. Anderson, and P. Colomban, *Solid State Ionics,* **149**, 99-105 (2002).
20. S. Fabris, S. Gironcoli, and S. Baroniinvited, *INTERNATIONAL WORKSHOP ON COMPUTATIONAL PHYSICS AND MATERIALS SCIENCE*: Progress in Ab Initio Computational Methods for Condensed Matter *8-10 January 2004, Château de Gif sur Yvette (France).*
21. T. Zhang, P. Hing, H. Huang, and J. Kilner, *Journal of the European Ceramic Society,* **22**, 27-34 (2002).
22. C. Agrafiotis, A. Tsetsekoua, C. J. Stournaras, A. Julbe, L. Dalmazio, and C. Guizard, *Journal of the European Ceramic Society,* **22**, 15-25 (2002).
23. H. Nakamatsu, T. Mukoyama, and H. Adachi, *Chem. Phys. Lett.*, **247**, 168-172 (1995).

6. PARTICLES AND SINGLE CRYSTALS OF RARE EARTH OXIDES

N. IMANAKA and T. MASUI
Department of Applied Chemistry, Faculty of Engineering,
Osaka University
2-1 Yamadaoka, Suita, Osaka 565-0871, Japan

6.1. PARTICLES

6.1.1. *Breakdown and buildup method*

Since 1980's ultrafine particles ranging from nanometer to sub-micrometer scale have attracted us because of their remarkably different physical and chemical properties from those of bulk materials. The origin of the property change has been explained by the quantum size effect and the surface effect.

There are two main ways to synthesis and prepare the fine particles. One is the breakdown method and the other is the buildup method. The breakdown method is simply recognized as crushing. Although the limit size obtained in this process was thought to be 1μm, recent improvement of the facilities has enabled us to prepare fine particles in sub-micrometer scale. On the other hand, the buildup method is growing particles from an atom, a molecule, and an ion, and it is possible to synthesize smaller particles than those given by the breakdown method. In addition, this method is suitable to get particles of high quality because we can use high purity starting materials. Generally, ultrafine nanoparticles are prepared by the buildup method. In this section, synthesis and preparation of fine particles of binary rare earth oxides have been reviewed especially focused on nanoparticles.

6.1.2. *Gas Condensation*

The advantage of the inert gas condensation is that the particles of high purities can be prepared in a very clean condition. The illustration of a typical apparatus is presented in Fig. 6-1. The chamber is first pumped to ultrahigh vacuum under 10^{-5} Pa, and the chamber is then filled with a few hundred Pa of a high-purity inert gas. The source material usually in the form of a solid powder (mostly a metal) is vaporized by resistive heating in a boat or crucible made from a refractory metal (e.g. Mo, W or Ta). Analogous evaporation energy can be employed such as high-power lasers, ion bombardment (sputtering), or electron beam.

The metal vapor produced by the evaporation collides with the inert gas atoms, and nanoparticles are formed by the condensation of vapor atoms. A convective flow of the inert gas between the warm region near the vapor source and the cold

G. Adachi et al. (eds.), Binary Rare Earth Oxides, 135–161.

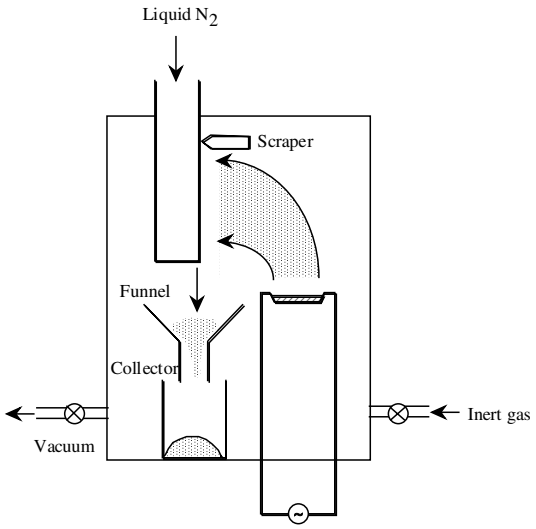

Figure 6-1. Schematic apparatus of the typical gas condensation method.

surface carries the nanoparticles to the cooled finger where they deposit on. The characteristics of the particles depend on the inert gas pressure, the evaporation rate, and the gas composition. For example, decreasing either the gas pressure in the chamber or the rate of evaporation of the metal decreases the particle size. The particles formed are then scraped from the cold finger and collected. Metal oxide nanoparticles can be produced by mixing or replacing the inert gas with oxygen or by the subsequent oxidation of metal nanoparticles synthesized by the evaporation of metal.

For example, yttrium oxide nanoparticles were prepared by gas condensation and subsequent oxidation of Y metal particles, where the yttrium metal was evaporated from a tungsten crucible by direct current heating in a pressure of 659 Pa pure He gas [1]. Once a suitable deposition of Y metal is established, the helium gas is evacuated and pure oxygen gas is slowly introduced into the chamber. The oxide particles obtained are scraped from the collection device and heated to 473 K in 650 Pa of pure O_2 gas in order to oxidize completely. It is notable that the crystalline structure is not cubic but hexagonal. The average particles size and BET specific surface area of the Y_2O_3 nanoparticles were 7 nm and 78 $m^2 \cdot g^{-1}$, respectively. Yttrium oxide nanoparticles were also prepared by the direct evaporation of oxide granules in a He-atmosphere of 100 Pa [2]. The evaporation energy used was high voltage electron beam (45 kV). In this case, yttrium oxide nanoparticles had cubic structure and were in the size of 4 – 6 nm. Europium oxide nanoparticles were also prepared by gas condensation with a laser ablation equipment [3-6]. Average

particles size was controlled from 4 to 18 nm by the N_2 gas pressure in the synthesis chamber.

It has been reported that Y_2O_3 nanoparticles as-prepared by gas phase synthesis have the monoclinic structure of high pressure phase, which transforms into cubic Y_2O_3 above 873 K [7,8]. It has been elucidated from the dependence of the phase transition temperature on the state of compaction that the stability of the high pressure phase is due to the nanostructured particle size.

Non-stoichiometric cerium oxide, CeO_{2-x}, has also been prepared by the spattering method [9-11]. The average particle size is about 8 nm and the CeO_{2-x} nanoparticles exhibited greater catalytic activities; the light off temperatures of the CeO_{2-x} nanoparticles for SO_2 reduction by CO, CO oxidation, and CH_4 oxidation were lower by 100 K than for the precipitated samples [9]. Cerium oxide nanoparticles have also been synthesized by direct thermal evaporation of cerium oxide from a tungsten crucible in a He-atmosphere of 1000 Pa [12]. The particle size distributes in a range from 3 to 3.5 nm.

In addition, the hydrogen plasma-metal reaction (HPMR) method was applied to synthesize rare earth oxide nanoparticles [13], which has been used to prepare better metallic ultrafine particles industrially at low cost. Pure Sm and Nd oxide nanoparticles were prepared through the HPMR method followed by oxidation treatment. The first step is to fabricate hydride nanoparticles; the second is to oxidize them at room or elevated temperatures. Cubic neodymium and samarium oxides were synthesized with their average sizes of 20 and 40 nm, respectively.

6.1.3. *Chemical vapor deposition*

Chemical vapor deposition (CVD) is a process that reactive vapor precursors react to produce solid materials in the gas phase at appropriate temperatures. Metal hydrides, metal chlorides, and metal organic compounds are the typical precursors used in the CVD method. In the case that the precursor species are metal organic compounds, the process is called metal-organic chemical vapor deposition (MOCVD). When the precursor molecules are introduced into a reactor with a carrier gas, they are decomposed by means of heat, irradiation of UV light, or electrical plasma formed in the gas. Among them, thermal CVD is the most commonly used method. This technique has an advantage that refractory materials can be vapor-deposited at relatively low temperatures.

Although the CVD method is usually used to produce a thin film material which is formed on a heated substrate, nanoparticles of cerium oxide have been synthesized by some arrangements of the apparatus. Figure 6-2 shows the schematic CVD reactors for synthesizing CeO_2 nanoparticles [14]. There are two types of rectors. The CeO_2 particles are collected either on a cooled quartz suscepter in a furnace (A), or in a cold wall container outside the furnace (B). The cerium chloride precursor on the container is evaporated and introduced into the reactor with argon carrier gas, and oxygen gas is fed separately into the reactor. The Ar gas velocity of

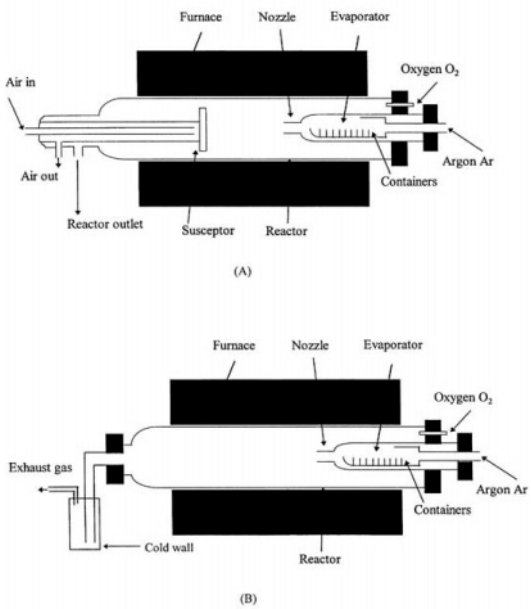

Figure 6-2. Schematic illustration of the chemical vapor deposition apparatus. (Reproduced with permission from ref. 14. Copyright 1999 Elsevier B.V.)

the nozzle is adjusted such that oxygen will not diffuse back into the precursor's area. The average size of the powders collected using apparatus B is about 20 – 30 nm, while that obtained from apparatus A is around 30 – 80 nm.

6.1.4. *Precipitation method*

Chemical precipitation is a popular method for synthesizing solid materials from solution in which a liquid-phase reaction is utilized to prepare insoluble compounds. The precipitates are composed of crystalline or amorphous fine particles. Usually, rare earth oxides are prepared by calcinations of the hydroxide or oxalate gel precipitated from a reaction of an aqueous or alcohol solution of inorganic salt (nitrate, chloride, sulfate, and ammonium nitrate, etc.) with an alkali solution (NaOH, NH_4OH, and $(NH_2)_2{\cdot}H_2O$) or an oxalic acid solution [15-21]. However, it is very difficult to obtain ultrafine particles because of growth and sintering of the particles during the calcinations.

The discontinuous nature of precipitates formation during the reaction sometimes makes it difficult to control particle size and morphology. To improve this disadvantage, a homogenous precipitation method has been developed. In this process, a precipitant is generated simultaneously and uniformly throughout the solution by controlling the production of the precipitant from another chemical source in the solution. For example, urea and hexamethylenetetramine slowly decomposed to yield ammonia by heating at 343 – 353 K. Monodispersed particles

of rare earth oxides such as scandium [25], yttrium [26-29], lanthanum [30], cerium [31, 32], samarium [33, 34], europium [33, 35], gadolinium [33], and terbium oxides [33] were prepared by this method.

In addition, controlled chemical precipitation of yttrium hydroxynitrate has been used to synthesize nanocrystalline yttrium oxide powders with high thermal stability [36]. The type of base employed as the precipitating agent has a significant effect on the properties of the yttrium oxide product. Precipitation with tetraalkylammonium hydroxides was shown to produce a much finer-grained product (9 nm) than a conventional ammonium hydroxide synthesis route (11 nm). This is attributed to the higher pH that can be achieved with tetraalkylammonium hydroxides, as well as the ability of tetraalkylammonium cations to inhibit precipitate particle growth by lowering the rate of diffusion of soluble precursors to the particle surface.

In order to obtain rare earth oxide fine particles directly as precipitants, the synthesis should be carried out only in a non-aqueous solvent such as alcohol. Dehydrating properties of alcohol result in direct formation of the oxide. For example, europium oxide [22] and terbium oxide [23] nanoparticles have been synthesized by this precipitation method. Tri-octylphosphine oxide (TOPO) is used as a surface capping agent to prevent particle agglomeration. Figure 6-3 shows high-electron micrographs of a number of Eu_2O_3 and Tb_2O_3 nanocrystals obtained. The particles appear as a regular array of dots on the amorphous contrast from the carbon support. The average size of the Eu_2O_3 and the Tb_2O_3 particles were 4.0 and 4.2 nm, respectively. It is notable that cubic C-type sesquioxide was formed in both cases.

Direct precipitation from high-boiling polyalcohol solutions is also available to synthesize ultrafine and monodisperse rare earth oxide particles with an average diameter in the range 2-5 nm [24]. Colloidal Eu_2O_3, Tb_2O_3, and Nd_2O_3 sesquioxide particles with spherical shape have been synthesized and the average size can be controlled by adjusting the concentrations of the starting materials.

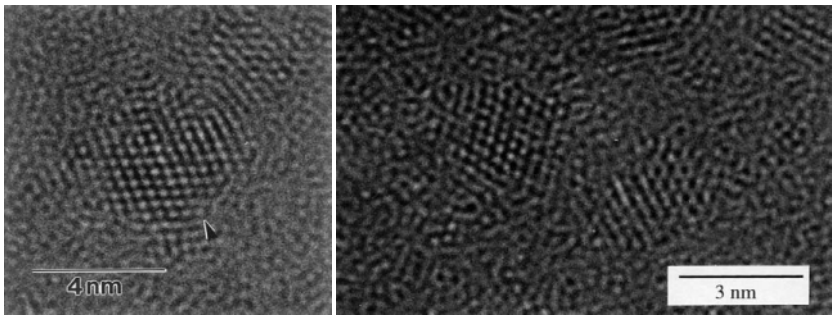

Figure 6-3. High resolution TEM micrographs of europium oxide (left) and terbium oxide (right) nanoparticles. (Reproduced with permission from refs. 22 (left) and 23 (right). Copyright 1999 Academic Press and Copyright 1999 Elsevier LTD., respectively)

6.1.5. *Hydrothermal and solvothermal methods*

Hydrothermal synthesis is a well-known method to synthesis, prepare, and grow some useful materials in several scales from nanoparticles to single crystals. In this method, high temperature and high pressure water is used as a transfer medium of heat, pressure, and mechanical energy. Water also works as a solvent which dissolves and recrystallize the solid materials as well as a reagent which acts as a mineralizer. These properties have been used in processing of inorganic materials in the preparation of single crystals and particularly of fine powders with nanosized to submicron particles [37]. Not only water (hydrothermal synthesis), but also ammonia water or some organic solvents are utilized as reaction medias, which is generally called a solvothermal method.

The hydrothermal method composes of three types of processes: hydrothermal synthesis, hydrothermal oxidation, and hydrothermal crystallization. Hydrothermal synthesis is usually used to synthesize oxides from their component salts, oxides or hydroxides. Pressures, temperatures, and mineralizer concentrations control the size and morphology of the particles. Forced hydrolysis of solutions of a rare earth salt is effective to obtain uniform and fine particles. For example, cerium oxide fine particles were prepared from tetravalent cerium salt solution ($CeSO_4 \cdot 4H_2O$, $(NH_4)_4Ce(SO_4)_4 \cdot 2H_2O$, and $(NH_4)_2Ce(NO_3)_6$) in low concentrations by low temperature aging in a sealed vessel (see Fig. 6-4) [38-41]. The metal ions are solvated by water molecules which can be deprotonated to give hydroxide or oxide particles. This method is very sensitive to the concentration, temperature, and pH value of the solution.

In the hydrothermal oxidation method, fine oxide particles can be prepared from metals, alloys, and intermetallic compounds by oxidation with high temperature and pressure solvent and as a result, the starting metals are directly changed into fine

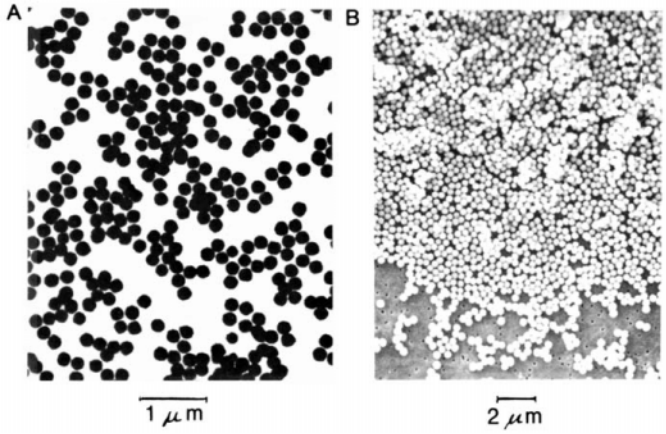

Figure 6-4. Transmission (A) and scanning (B) electron micrograph of CeO_2 particles obtained by aging a $Ce(SO_4)_2$-H_2SO_4 solution at 363 K for 48 h. (Reproduced with permission from ref. 38. Copyright 1988 American Chemical Society)

oxide powders. For example, the solvothermal oxidation of cerium metal in 2-methoxyethanol at 473-523 K yields ultrafine ceria particles (*ca.* 2 nm) [42].

The hydrothermal crystallization is the most popular technique in preparing rare earth oxide nanoparticles. Precipitation and crystallization from aqueous solutions under elevated temperature and high pressure are carried out in the following process. An excess amount of precipitates is added to a rare earths salt solution. The precipitated gels are sealed in a Teflon-lined autoclave and heated at 423-573 K for several hours. The autoclave is quenched and the crystalline powder products obtained are washed and dried. Using the hydrothermal crystallization method, a number of yttria [43, 44] and ceria [45-50] nanoparticles have been prepared. The obtained particles are small crystallites from 3 nm to 0.8 μm in size, which depends on the reaction temperature, crystallization time, and starting materials. It is shown a tendency that low temperature heating and using tetravalent rare earth salt solutions are effective to obtain smaller particles.

6.1.6. *Sol-gel method*

A sol-gel process is an important method to synthesize many materials in a variety of shapes and forms such as particles, films, and bulks. This method is especially suited for the synthesis and preparation of ultrafine rare earths oxide particles at relatively low temperatures. A sol is a stable colloidal dispersion of small particles suspended in a liquid. The particles are amorphous or crystalline and particle aggregation is prevented by electrostatic repulsion. The particles in some sols interact to form a continuous network of connected particles called a gel, instead of aggregating to form larger particles (precipitates).

Drying the gel simply by evaporating the interstitial liquid gives rise to capillary forces that the gel shrinks, and cracks form as a result of the differential stresses generated in the drying gel. The resulting dried gel is known as a *xeroge*l. When the wet gel is dried in a condition that no capillary forces in the supercritical fluid regime like supercritical conditions, the pore and network structure of the gel should be maintained even after drying. The resulting gel is called *aerogel* in this case. These sol-gel materials are often applied to catalysts and catalyst supports because of high surface area.

The sol is produced by the hydrolysis of reactive metal compounds. A typical example is a metal alkoxide, $M(OR)_n$, where M is a metal (e.g. Rare earths, Al, Ti, Zr, etc.) and R is an alkyl group such as methyl ($-CH_3$), ethyl ($-C_2H_5$), and propyl ($-C_3H_7$) groups. In the sol-gel method, metal alkoxides are generally dissolved in an alcohol solvent (methanol, ethanol, or iso-propanol are frequently used) and addition of water causes hydrolysis of them.

$$M(OR)_n + n\ H_2O \rightarrow M(OH)_n + n\ ROH$$

This reaction is followed by a series of condensation reactions between hydroxide groups and the overall reaction is represented by the next chemical

equation. It goes without saying that mixed oxide gels can be produced by mixing of plural alkoxides.

$$M(OH)_n \rightarrow MO_{n/2} + n/2\ H_2O$$

The sol-gel synthesis of some rare earths oxides has been reported for the first time in 1971 [51]. For the preparation of their oxides, rare earth isopropoxide, acetylacetonate, and nitrate are used as the precursors. The water necessary for the hydrolysis is brought by adding directly or by the hydrated water. Using this method, Sc_2O_3 [52], La_2O_3 [53], CeO_2 [53], Gd_2O_3 [53], Dy_2O_3 [51], Er_2O_3 [51], and Yb_2O_3 [51] nanoparticles have been synthesized. This process is a good method to obtain fine powders, but has a demerit of high cost of metal alkoxides.

Preparation of fine particles by pyrolysis of a precursor gel is often included in the category of the sol-gel method involving chelating agent. In some cases, this method is called the combustion synthesis. A variety of organic acids are used as the chelating agents such as citric acid, tartaric acid, malonic acid, oxalic acid, and acetic acid [54]. For example, nanosize Y_2O_3 [54, 55] and CeO_2 nanoparticles [56] have been prepared at low temperatures by pyrolysis of the complex gels, which is prepared by the evaporation of the water solvent from the aqueous solution of the rare earth salt and organic acid. The crystallite size of yttria increased moderately during calcination of the oxide powder from about 25 nm at 1023 K to 60 nm at 1373 K (Fig. 6-5) [54, 55], while in the case of ceria, the particle size increased from 8 nm at 523 K to 85 nm at 1273 K [56].

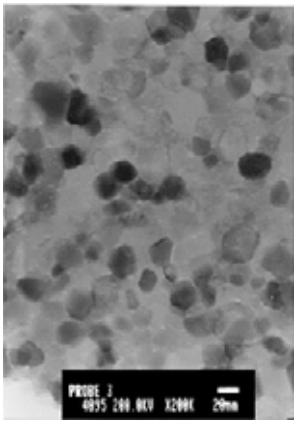

Figure 6-5. Transmission electron micrograph of Y_2O_3 particles obtained by combustion of a yttrium citrate gel at 1023 K for 2 h. (Reproduced with permission from ref. 54. Copyright 1999 Materials Research Society)

6.1.7. *Emulsion and microemulsion method*

An emulsion liquid membrane (ELM, water-in-oil-in-water (W/O/W) emulsion) system has been studied for the separation of metals, in which the metal ions are

extracted, from the external water phase, into the organic membrane phase, where they are then stripped and concentrated into the internal water phase (Fig. 6). Recently, it has been found that the internal water phase is capable of being used for the preparation of size-controlled and morphology-controlled fine particles [57], since the micrometer-sized internal water droplet has a restricted reaction area.

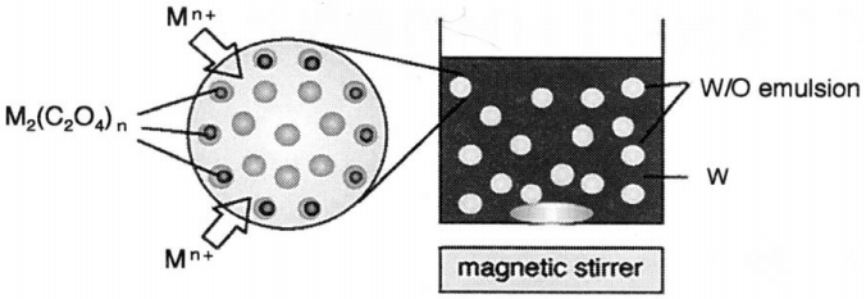

Figure 6-6. Schematic diagram of particle formation in emulsion liquid membrane (W/O/W emulsion) system. (Reproduced with permission from ref. 58. Copyright 2001 The Society of Chemical Engineers, Japan)

Rare earth oxalate and oxide particles have been prepared using this system, and the particle size is controllable by changing the extractant (cation carrier). For example, some rare earth oxalate particles of submicrometer size were prepared in the ELM system containing 2-methyl-2-ethylheptanoic acid (VA-10) and bis(1,1,3,3-tetramethylbutyl)phosphinic acid (DTMBPA) as the extractant [58-61]. In the VA-10 system, ultrafine particles of 20-60 nm in diameter were obtained, while spherical oxalate particles of 0.2-0.6 μm in diameter were obtained in the DTMBPA system. Preparation of oxide particles are attained by calcination of the oxalate particles at 873-1073 K (Fig. 6-7), though it brings about some construction

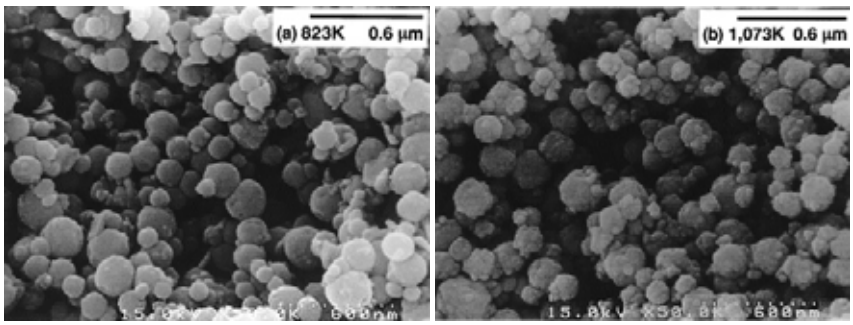

Figure 6-7. Scanning electron micrographs for yttrium oxide particles obtained by calcination of yttrium oxalate particles for 6h at 823 K (a) and 1073 K (b). (Reproduced with permission from ref. 60. Copyright 1998 American Chemical Society)

of the particles probably caused by carbon dioxide elimination.

In addition to the formation of several single-component fine particles [57-61], the preparation of complex oxide particles, such as rare earth phosphate [61], Y_2O_3:Eu^{3+} [63], Y_2O_3:Yb^{3+},Er^{3+} [64], Gd_2O_3:Eu^{3+} [65], and Gd_2O_2S:Eu^{3+} [65] fine particles has also been reported, using the ELM system.

No doubt, the ELM method is convenient to synthesize fine particles in μm scale but not suitable for the preparation of nanoparticles. Particle synthesis in single nanometer scale is nowadays one of the most important and attractive subjects and chemical reaction in microemulsions is an effective method to prepare nanoparticles.

The microemulsion method is based on the use of reversed micelles as small reactors restricted spatially. The microemulsion composes of two immiscible liquids and a surfactant. In water-in-oil microemulsions, nanodroplets of aqueous phase within the reversed micelles disperse in oil phase and the system is thermodynamically stable. Figure 6-8 shows a schematic illustration of the reaction process to produce nanoparticles [66]. After mixing two microemulsions containing

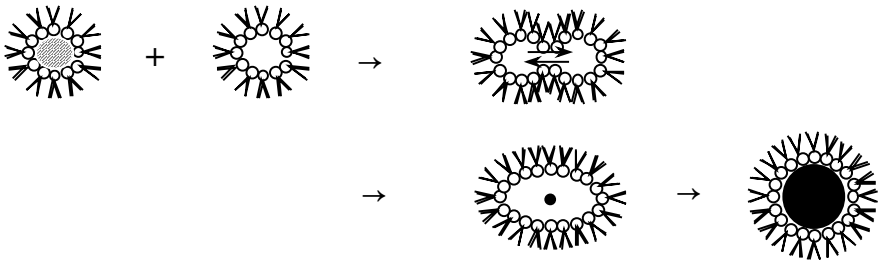

Figure 6-8. Schematic mechanism for the formation of particles in the microemulsion method. (Reproduced with permission from ref. 66. Copyright 1993 Elsevier Inc.)

the reactants, the interchange of reactants is carried out during the collisions of the nanodroplets in the microemulsions. The interchanging process is very quick and the final size of the particles is controlled by the droplet size. Once the particles attain the final size, the surfactant molecules layer around the particle inhibit further growth of the particle.

The size of the nanodroplets can be controlled in the range of 5 – 80 nm by changing the concentration ratio of water/surfactant in the microemulsion system. By this method, yttrium oxide [67], cerium oxide [68-70], neodymium oxide [71], and erbium oxide [72, 73] nanoparticles have been synthesized. The average particle size of the particles adopts values in the range from 2 to 70 nm, which depends on the synthesis conditions.

6.1.8. *Ultrasound and microwave irradiation method*

In recent years, ultrasound and microwave irradiation have been extensively used to synthesize some materials with unusual properties. Ultrasound irradiation can

induce the formation of particles with a much smaller size and higher surface area than those reported by other methods [74]. The effect arises from acoustic cavitation which occurs due to the stresses induced by the passing of a sound wave through the liquid which consists of compression and decompression cycles. As a result, the formation, growth and implosive collapse of bubbles in a liquid are induced. The implosive collapse of the bubbles generates a localized hotspot though adiabatic compression or shock wave formation within the gas phase of the collapsing bubbles. Each one of these imploding bubbles can therefore be seen as a microreactor, with temperatures reaching an estimated ~ 5000 K and pressures of >1800 atm [75].

Microwave irradiation has been developed as a heating method and is widely used in various fields in chemistry [76], and is generally quite fast, simple and efficient in energy. It is known that the interaction of dielectric materials, liquids or solids, with microwaves leads to what is generally known as dielectric heating. Electric dipoles present in such materials respond to the applied electric field. In liquids, this constant reorientation leads to friction between molecules and consequently generates heat.

Ultrasound and microwave irradiation processes are known as excellent methods for the preparation of nanoparticles. Recently, nanoparticles of rare earth (Y, La, Ce, Sm, Eu, and Er) oxides have been synthesized [77-81]. In these cases, rare earth nitrates were used as starting materials. When sodium dodecyl sulfate (SDS) was added as a templating agent, layered and hexagonal mesostructures of high specific surface area (225-250 $m^2 \cdot g^{-1}$) can be obtained [77]. Monodispersed CeO_2 nanoparticles with a mean particle of ca. 3 nm are obtained when tetrametylammonium hydroxide [78] or polyethylene glycol [79, 80] are used as the additives. In addtion, europium oxide nanorods are obtained by the sonication of an aqueous solution of europium nitrate in the presence of ammonia [81]. The particle sizes were about 50 × 500 nm ($W \times L$) as described in Fig. 6-9.

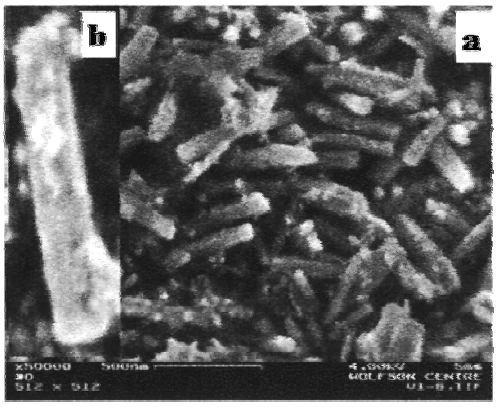

Figure 6-9. High resolution scanning electron micrograph of (a) europium oxide nanorods and (b) a single nanorod of europium oxide (50 × 500 nm) at higher resolution. (Reproduced with permission from ref. 81. Copyright 2002 American Chemical Society)

6.1.9. *Spray Pyrolysis*

Spray pyrolysis is one of the effective methods to prepare homogenous and non-agglomerated spherical particles [82]. A representative spray pyrolysis system is illustrated in Figure 6-10. A starting solution is prepared by dissolving the metal salt of the product in a solvent. The particles are generated by spraying the droplets atomized from the starting solution into an electronic furnace. The atomization process is carried out using variety of atomizers (pressure, ultrasonic, vibration, disk rotation, electrostatic force, etc.). Heating the droplets in air converts them to oxide after evaporation of the solvent. Instead of the electronic furnace, r.f. inductively coupled plasma (ICP) is also used to generate high temperatures. This method is named a spray-ICP technique and has been applied for a wide variety of oxides [83]. The average size and size distribution of the final particles depend on the size of the atomized droplet and the initial concentration of the starting solution as well as the concentration and velocity of the droplet generated by the atomizers. Spray drying is similar to spray pyrolysis, and the colloidal particles or sols are typically used as precursors. Supercritical carbon dioxide is sometimes used as an alternative liquid antisolvent [84, 85]. These processes typically produce uniform and spherical particles such as Y_2O_3 [85, 86], CeO_2 [87], and Sm_2O_3 [84] from submicron to micron sizes because it is difficult to efficiently generate very fine droplets for nanoparticles.

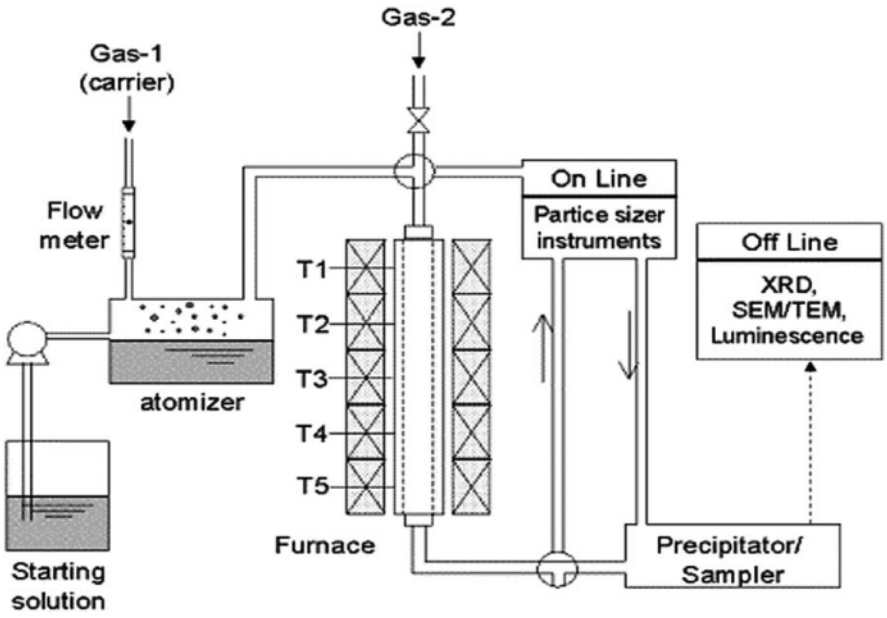

Figure 6-10. Representative spray pyrolysis system used for particle preparation. (Reproduced with permission from ref. 82. Copyright 2003 Elsevier LTD.)

Although the spray pyrolysis method is has been successfully used to prepare a variety of powdered materials, it is difficult to efficiently produce considerably fine separable particles in nanometer scale due to the formation of a three-dimensional network. The salt-assisted spray pyrolysis method has been proposed for separating these nanoparticles by introducing some compounds that can distribute on the surface of the particles to prevent agglomeration [88, 89].

In this process, the conventional method was modified simply by adding inert inorganic salts to the precursor solution before the aerosol decomposition, followed by washing the product to remove the salts. A eutectic mixture or single salt of chlorides or nitrates of Li, Na, K, is added in an aqueous precursor solution of rare earth salt. When the aerosol particles pass through the reactor, the additional salts melt and act as high-temperature solvents. As a result, the dissolution, precipitation, and reaction of the rare earth component are carried out within an aerosol particle, which leads to the formation of some nanoparticles in the aerosol particle. After the cooling, the particles containing the final nanoparticles within a salt matrix are collected. The nanoparticles can be obtained after washing the product with water to remove the salts.

Figure 6-11 shows CeO_2 nanoparticles synthesized by this technique at 1073 K with the addition of the eutectic salts of sodium and potassium nitrate to the precursor solution prior to the aerosol decomposition [89]. The particles are composed of isolated nanoparticles whose mean size was 51 nm.

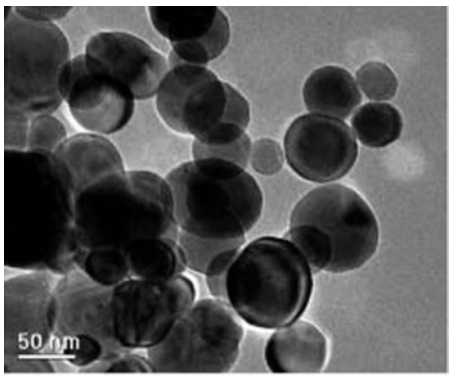

Figure 6-11. CeO_2 nanoparticles synthesized by the salt-assisted spray pyrolysis method at 1073 K (Reproduced with permission from ref. 89. Copyright 2003 The Royal Society of Chemistry.)

6.1.10. *Electrochemical method*

Electrochemical synthesis is an attractive method to prepare oxide ceramic films and powders, because it offers the several advantages such as low processing temperature, low cost, high purity, normal handling pressure, and controlled microstructure. In the electrochemical synthesis of oxide fine particles, both anodic

(redox change) and cathodic methods (base generation) can be employed. In the anodic method, a metal ion or complex is oxidized at the electrode surface. The pH value of the solution is adjusted so that the initial oxidation state becomes stable, and the higher oxidation state generated electrochemically is subjected to hydrolysis to a metal hydroxide or oxide. In the cathodic method, on the other hand, cathodic currents are used to generate a base at an electrode surface, and the base hydrolyses metal ions or complexes because the pH value at the electrode surface becomes considerably higher than that of the electrolyte solution.

It has been demonstrated that cerium (IV) oxide thin films and nanocrystalline powders have been prepared by the anodic [90, 91] and cathodic method [92, 93], respectively. Particularly, the latter cathodic method is effective to obtain the CeO_2 nanoparticles. The cathode is a platinum wire and the anode is a platinum mesh electrode. The cathode compartment in the divided cell contacts 0.5 $mol \cdot l^{-1}$ cerium (III) nitrate and 0.5 $mol \cdot l^{-1}$ ammonium nitrate, and the anode compartment contained 0.5 $mol \cdot l^{-1}$ ammonium nitrate. The two compartments are separated with a medium porosity glass frit. The electrochemical synthesis is run in the galvanostatic mode at a current density of 1 $A \cdot cm^{-2}$ and the average particle size is controlled by adjusting the solution temperature. Nanocrystalline CeO_2 particles with an average particle size of 10 – 14 nm can be electrochemically prepared by the cathodic electrogeneration of base [93].

6.1.11. *Mechanochemical method*

Mechanochemical processing has been recently applied to the synthesis of a wide range of nanocrystalline rare earth oxides. Milling of precursor powders leads to the formation of a composite of the starting materials which react during milling or subsequent heat treatment to form a mixture of separated fine particles of the desired phase within a soluble salt matrix.

For example, fine Gd_2O_3 powder was synthesized via the milling and subsequent heat treatment of a mixture of $GdCl_3$ and CaO powder according to the following reaction: $2GdCl_3 + 3CaO \rightarrow Gd_2O_3 + 3CaCl_2$ [94]. However, only large particles (100 nm in size) were obtained, because of the formation of oxychloride species during the milling, and the reaction of $6GdOCl + 2Ca_4OCl_6 + CaO \rightarrow 3Gd_2O_3 + 9CaCl_2$ occurred only at high temperatures. In addition, this reaction between a rare-earth chloride and an alkali-earth oxide cannot be applied to synthesize light-rare-earth oxides such as La_2O_3, CeO_2, Nd_2O_3, and Sm_2O_3, because the free energy change in the reaction of $2LnOCl + CaO \rightarrow Ln_2O_3 + CaCl_2$ (where Ln is lanthanoid) becomes positive for lightweight lanthanoides.

For the synthesis of nanoparticles, sodium hydroxide has been applied in the mechanochemical processing. The solid-state displacement reaction of $GdCl_3 + 3NaOH \rightarrow Gd(OH)_3 + 3NaCl$ was induced during milling, and calcination of the as-milled powder at 500°C led to the formation of Gd_2O_3 particles [95]. The addition of a sufficient amount of NaCl diluent in the starting powder resulted in the formation

of ultrafine Gd_2O_3 particles (20 nm in size), as shown in Fig. 6-12. This reaction is applicable for the synthesis of the light-rare-earth oxides. Ultrafine CeO_2 particles of 10 nm in size have also been synthesized by the same procedure [96]. The particle size was controlled in the range of 10 - 500 nm by changing the calcination temperature.

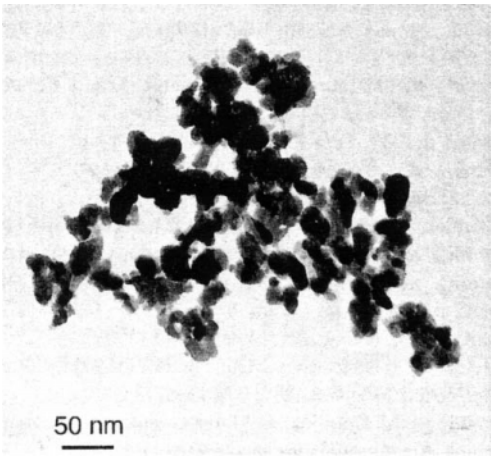

Figure 6-12. TEM image of the Gd_2O_3 nanoparticles synthesized by the mechanochemical method. (Reproduced with permission from ref. 95. Copyright 1999 Acta Metallurgica Inc.)

CeO_2 nanoparticles have also been synthesized at room temperature by a similar solid-state reaction of $(NH_4)_2Ce(NO_3)_6$ and $Ce(NO_3)_3 \cdot 6H_2O$ with NaOH [97, 98]. The particles have very fine sizes (3 nm) and the surface area of the particles was 96.2 $m^2 \cdot g^{-1}$. The color of the particles changed from light yellow to white with the increase in the size of these particles by the calcination. After the calcination at 873 and 1073 K, the size of the CeO_2 particles grew up to 5 and 50 nm, respectively.

6.1.12. *Flux method and alkalide reduction method*

The flux method is a well-known method used for single crystal growth as discussed below. It has not been applied to the synthesis of fine powders because usually high temperature heating is necessary to obtain molten salts. However, nanosized CeO_2 particles have been synthesized by the flux method at relatively low temperature (873 K), utilizing tetravalent cerium salt and three different eutectic mixtures of KOH/NaOH, $NaNO_3/KNO_3$, and LiCl/KCl as molten salts [99]. Well-crystallized CeO_2 powders with very fine size (14 – 20 nm), narrow size distribution, and a clearly spherical shape are obtained.

In addition, Y_2O_3 [100], Gd_2O_3 [101], and Dy_2O_3 [102] nanoparticles, with size of 10 – 20 nm, have been synthesized by homogeneous reduction using alkalide solutions and subsequent oxidation at 1273 K. Alkalides are crystalline ionic salts

consisting of crown ether or cryptand complexed alkali metal cations charge balanced by a stoichiometric number of alkali metal anions. Alkalides produce alkali metal anions when dissolved in nonreducible solvents. The alkali metal anion is nearly as thermodynamically powerful a reductant as a solvated electron, the most powerful reductant possible in any given solvent, and is capable of simultaneous two electron transfers. Mixing of alkalide and metal salt solutions results in the formation of a colloid of nanoscale (2-15 nm diameter) particles with a narrow size distribution. Colloid stability varies from minutes to hours, depending on the metal reduced and the reaction conditions. Following aggregation and removal of the solvent, the byproducts can be washed away, recovering the crown ether and leaving bare metal nanoparticles. The particles are exposed to air and are thus oxidized.

6.2. SINGLE CRYSTALS

6.2.1. *Conventional Crystal Growth from Melt*

There are some major methods producing single crystals from a melt. The most popular technique for single crystal growth of rare earth oxides is the Verneuil method. Figure 6-13 shows the illustration of the apparatus. Powder of the oxide to be made into a single crystal is dropped through a high-temperature flame. The flame originally used is oxy-hydrogen, $H_2 + O_2$, and nowadays it is sometimes substituted for argon plasma with an oxidizing or reducing condition controlled by

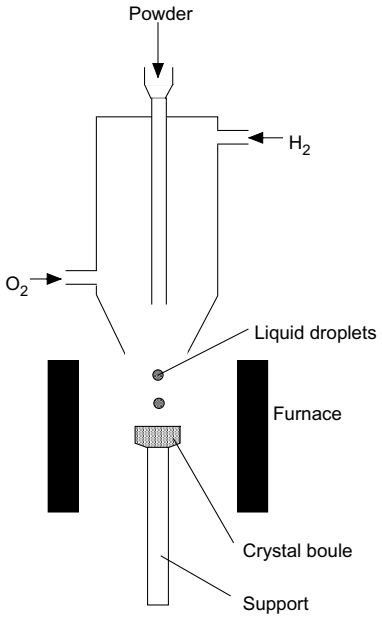

Figure 6-13. Schematic illustration of the Verneuil method.

adding either small amounts of oxygen or hydrogen. The dropped powder melts and forms liquid droplets. These molten droplets then fall onto a seed crystal which is held on a rotating pedestal support, and they solidify to form a single crystal boule. This flame fusion technique is inexpensive and commonly used to grow crystals of high melting point oxides.

Single crystal growth of A-type (hexagonal) and B-type (monoclinic) Ln_2O_3 (M = La, Pr, Nd, Sm, Eu, and Gd) by the Verneuil method using a single burner has been reported [103]. A photograph of the typical boules grown is depicted in Figure 6-14 [103]. Preparation of cubic C-type Ln_2O_3 (M = Sc, Y, Dy, Ho, Er, Tm, and Lu) has also been reported by the same authors [104]. There is a similar reference on the Verneuil flame fusion method. The monoclinic form (B-type) of Sm_2O_3 and Eu_2O_3 and the cubic oxides Gd_2O_3, Dy_2O_3, Ho_2O_3, Er_2O_3, Tm_2O_3, Yb_2O_3, and Lu_2O_3 [105] were grown. The H_2:O_2 ratio in the flame to obtain the single crystals is summarized in Table 6-1.

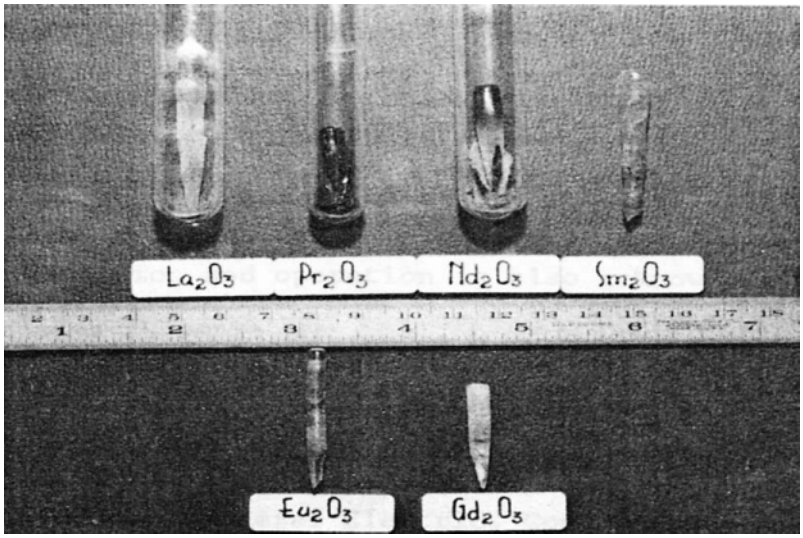

Figure 6-14. Boules of rare earth oxides grown by the conventional Verneuil method. (Reproduced with permission from ref. 103. Copyright 1966 Elsevier LTD.)

TABLE 6-1. Growth condition and formed structure of rare earth oxide single crystal by the Verneuil method. (Reproduced with permission from ref. 105. Copyright 1966 Москва : Издво Академии наук СССР)

Sample	Sm_2O_3	Eu_2O_3	Gd_2O_3	Dy_2O_3	Ho_2O_3	Er_2O_3	Tm_2O_3	Yb_2O_3	Lu_2O_3
H_2:O_2	2.5:1	2.7:1	7.5:1	3.6:1	3.6:1	3.6:1	3.6:1	3.6:1	3.6:1
Type	B	B	B	C	C	C	C	C	C

Single crystals of La_2O_3, Nd_2O_3, Gd_2O_3, and Er_2O_3 were also grown by another researchers with an oxyhydrogen heater at 2573-2373 K. Good-quality crystals of diameters 5-20 mm and lengths 20-30 mm were obtained [106].

Scandium oxide single crystals can be synthesized in only H_2 atmosphere by the Verneuil method [107]. The linear growth rate was about 8 $mm \cdot h^{-1}$ and the size of the obtained crystal has 45 mm length and 4 mm diameter. Pycnometric density of the obtained Sc_2O_3 single crystal was 3.91 $g \cdot cm^{-3}$, Mohse hardness was 6.5, and refractive index was 1.91.

The plasma float-zone technique for growing Y_2O_3 single crystals has been reported [108]. It is a floating zone technique with the use of localized hollow cathode plasma as the heat source. The intense heat conveyed to the sample results from its bombardment by high energy electrons emitted from the hollow cathode walls. The single crystals could be successfully grown using a feed rod scanning to compensate for evaporation losses from the molten zone.

In order to prepare single crystals with perfect crystal structure without internal strains, the flux technique was applied to Y_2O_3 single crystal growth [109]. The method consists in dissolving oxides with high melting point in solvents such as B_2O_3, Bi_2O_3, PbO, PbF_2, and PbO-PbF_2. The use of these solvents allows the growing of crystals in a weak temperature gradient with cooling rates of 0.5 $K \cdot h^{-1}$.

The single crystal growth of CeO_2 was typically carried out by the flux technique to make these materials available for lasers and other optical components. The CeO_2 single crystal was grown from melts of the oxides in various solvents such as KF, PbO-PbF_2, Li_2O-WO_3, BaO-B_2O_3, and Bi_2O_3-PbF_2 mixture [110]. A typical photograph is shown in Figure 6-15 [111]. The best CeO_2 single crystals were grown from melts of PbO-PbF_2 (1:10) by cooling from 1573 K at CeO_2:flux = 1:15 and a rate of 3-4 $K \cdot h^{-1}$. The crystal size was 5 x 4 x 3 mm. CeO_2 has also been grown by

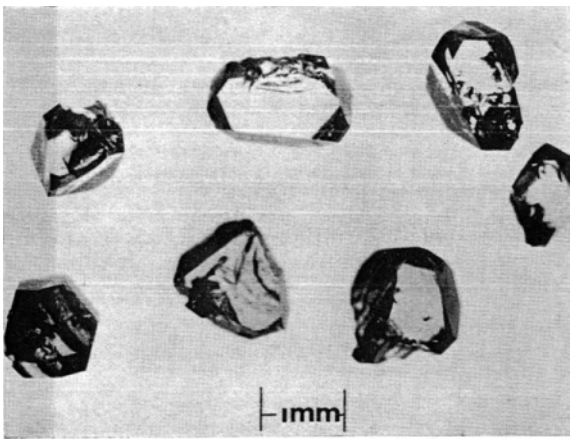

Figure 6-15. CeO_2 single crystals grown by the flux method. (Reproduced with permission from ref. 111. Copyright 1967 Elsevier LTD.)

the slow cooling and gradient flux techniques by using $2NaF{\cdot}B_2O_3$, $Li_2Mo_2O_7$, $NaBO_2$, $PbF_2{\cdot}PbO{\cdot}0.1B_2O_3$ and mixtures of these as solvents [9]. Two growth morphologies, cube and octahedron, were found to exist which depended on flux composition, and CeO_2 crystals up to 3 mm on an edge were grown from the PbF_2-PbO-B_2O_3 flux.

Single crystals of Pr_2O_3 with hexagonal A structure were prepared by using the Verneuil process [112]. Paramagnetic susceptibility measurements were performed for various orientations of the crystal with respect to the magnetic field at constant temperatures (5, 77, and 300 K) as well as at increasing temperatures. (5-1000 K), and it has been elucidated they show an exceptional magnetic anisotropy.

Large single crystals (2-3 cm long and 0.5 cm in diameter) of Nd_2O_3 was prepared by the Verneuil method adapted to a plasma furnace [113]. Physical properties including distribution of dislocations, and crystallographic parameters of the crystals were studied by electron microscopy and electron diffraction, and by x-ray diffraction. Nd_2O_3 is hexagonal type A of lattice constant a=0.3829 nm and c=0.6000 nm. The density was 7.23 $g{\cdot}cm^{-3}$.

Single crystals of Sm_2O_3 with monoclinic B structure were prepared by the Verneuil process adapted to a plasma torch [114]. Some properties of these crystals were studied including cleavage, Vickers hardness (480 $kg{\cdot}mm^{-2}$), and the magnetic properties. Paramagnetic susceptibilities measurements were performed for various orientations of the crystal with respect to the magnetic field at constant tempseratures (5, 77, and 300 K) as well as at increasing temps. (5-1000 K) and indicate an anisotropy.

EuO single crystal has been synthesized by reacting Eu metal and Eu_2O_3 in a solution containing an excess of europium metal at 2223-2373 K [115, 116]. Because of low boiling point of Eu metal (1713 K), the growth was carried out in a sealed W or Mo crucible. After reacting the Eu_2O_3-Eu mixtures for several hours to several days, they were cooled at the rate of about 23-360 $K{\cdot}h^{-1}$. As the concentration of europium in the initial melt is increased, the growth temperature is lowered, and the crystals become richer in europium. The single crystals in cm scale were grown and have a lattice constant of 0.51451 nm and a density of 8.180 $g{\cdot}cm^{-3}$ [115]. Single crystals of Eu_2O_3 with monoclinic B structure were also grown from a PbO flux [117] as well as by the Verneuil process [118, 119], and cell dimensions and some physical properties of the monoclinic crystals were determined.

Although most of the Gd_2O_3 single crystal has been grown by the Verneuil flame fusion method [105, 106], the fiber has been prepared by the laser heated pedestal growth (LHPG) method [120]. Polycrystalline Gd_2O_3 pellets sintered at 1473 K were cut into rods to serve as feed and seed sticks. The grown Gd_2O_3 single crystal fivers were 0.5 mm in diameter and had monoclinic $C_{2/m}$ structure.

Single crystals of the monoclinic B form of Tb_2O_3 were prepared from a melt of an equimolar mixture of MgO and Tb_4O_7. X-ray analysis indicated that the

compound belongs to the space group C^3_{2h}-$C_{2/m}$ and is isotypic with the B form of Sm_2O_3 [121].

Single crystals of Er_2O_3 were successfully synthesized using a xenon optical floating zone single crystal growth apparatus with a temperature capability of 3273 K [122]. The xenon optical floating zone unit is sited in Figure 6-16 [122]. The optical power of xenon lamp is focused at a spot by an ellipsoidal mirror cavity. Seed and feed rods are positioned vertically within a sealed quartz tube and these rods are counter-rotating. As the rod tips are located at the xenon lamp focal point, the lamp power is gradually increased until the rod tips become molten. After the molten zone becomes stable, the rods are translated vertically in tandem to move the molten zone along the rod. As a result, a single crystal produces. This method has a major advantage of being containerless which is effective to grow high melting point oxides. By this method, an Er_2O_3 single crystal of 5 mm diameter and 70 mm length was grown (Figure 6-17).

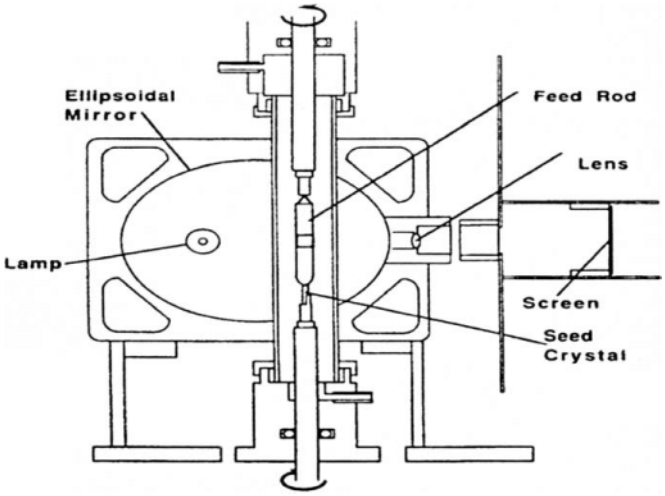

Figure 6-16. Schematic illustration of xenon optical floating zone single crystal growth apparatus. (Reproduced with permission from ref. 122. Copyright 1999 American Ceramic Society)

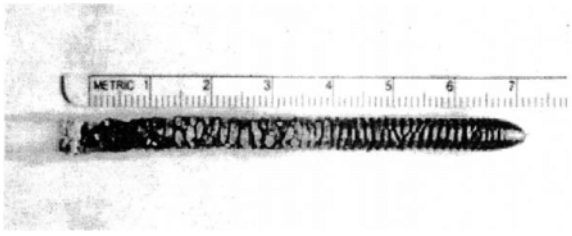

Figure 6-17. Er_2O_3 single crystal grown by the xenon optical floating zone method. (Reproduced with permission from ref. 122. Copyright 1999 American Ceramic Society)

Yb_2O_3 and Er_2O_3 single crystals with cubic C-type structure were grown from melt by the similar arc-image floating zone method [123]. These powders were pressed into rod shape and were calcined at 1473 K for 24 h. The sintered rods were then heated at 2773 K in the arc-image furnace at a rate of 42.5 $mm \cdot h^{-1}$. The prepared crystals had 3-4 mm diameter and 40-50 mm length and the color of the Yb_2O_3 and the Er_2O_3 single crystals were light pale yellow and red, respectively.

6.2.2. *Hydrothermal Crystallization Growth*

Supercritical water is an effective solvent for many inorganic materials, and at high pressure and temperature the solubility of many oxides becomes particularly very appreciable in the presence of a mineralizer [124]. This technique involving supercritical water is known as the hydrothermal-growth method. Crystal growth under hydrothermal conditions takes place in a metal pressure cell, normally called an autoclave, depicted in Fig. 6-18 [125]. In the autoclave, the material to be dissolved and subsequently crystallized is placed at the bottom, with seed crystals suspended at the top, and the autoclave is part-filled with water. The autoclave is placed in a temperature gradient so that the temperature, T_2, at the bottom is higher than at the top, T_1. The material at bottom of the autoclave is dissolved and the resulting solution is conveyed by convection to the top where the solution becomes supersaturated and crystallized onto the seeds.

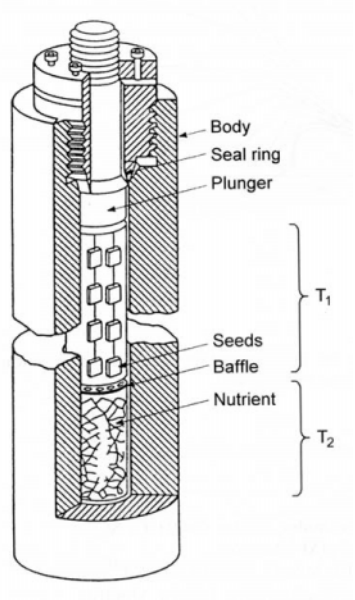

Figure 6-18. Schematic illustration of an autoclave for hydrothermal single crystal growth. (Reproduced with permission from ref. 125. Copyright 2000 John Wiley & Sons Inc)

Single crystals of praseodymium dioxide and intermediate terbium oxides were grown by the hydrothermal method [126]. The pressure in the sample autoclave was smoothly raised and lowered by control of heating and cooling of the autoclave. The rare earth oxide and nitric acid sealed in capsules of thin-walled gold tubing. The pressure of the capsules was raised to 165 MPa and isobarically heated to the run temperature (1003 – 1143 K). Holding at least for two hours to reach equilibrium, the samples were isothermally depressurized according to the procedure cycling procedure, where the procedure is composed of slow uniform pressure decrease and rapid pressure increase. After equilibration at the final pressure of 115 MPa, the autoclave was cooled isobarically to 673 K and then smoothly depressurized to 40 MPa while cooling to room temperature. Then the excess pressure was slowly released. The pressure cycling is very effective for obtaining large crystals. Nitric acid was used as a mineralizer to promote solubility and the optimum PrO_x:HNO_3 ratio for crystal growth was 1.0:1.0 by weight. A photograph of PrO_2 crystals are shown in Figure 6-19.

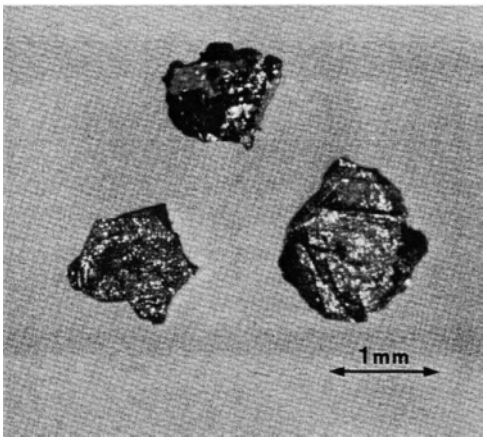

Figure 6-19. PrO_2 crystals obtained from hydrothermal crystal growth. (Reproduced with permission from ref. 126. Copyright 1983 Elsevier B.V.)

6.2.3. *Recent Advance in Single Crystal Growth of Rare Earth Oxides*

As mentioned above, single crystal growth of several materials of high melting points is usually very difficult and takes times in many cases. Therefore, it is significant to find new methods to grow such compounds as rare earth oxides in a single crystal form. Very recently, it has been reported that scandium oxide single crystal was successfully grown by a simple dc electrolysis method at the temperatures as low as 1223 K [127, 128]. The selective growth of Sc_2O_3 crystals has been achieved by electrolyzing the Sc^{3+} ion conducting solid electrolyte of $Sc_2(MoO_4)_3$ [129, 130]. The sintered $Sc_2(MoO_4)_3$ pellets were placed between two

ion-blocking Pt electrodes for the crystal growth electrolysis as shown in Figure 6-20. The electrolysis was carried out by dc voltage at 11 V at 1223 K for 2 weeks in air. In this process, successive dc electrolysis supplies Sc metal from inside the solid electrolyte by reducing Sc^{3+} ions migrated on the cathodic surface and finally the Sc_2O_3 single crystals are formed in air atmosphere as shown in Figure 6-21. The single crystal growth can be regulated by the electrolysis condition, and the crystal size can be intentionally controlled by adjusting the electrolysis period.

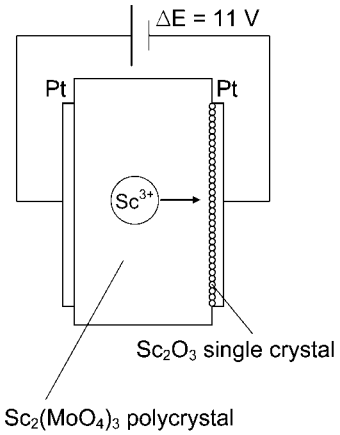

Figure 6-20. Schematic representation of the Sc_2O_3 single crystal growth method by dc electrolysis. (Reproduced with permission from ref. 127. Copyright 2003 American Chemical Society)

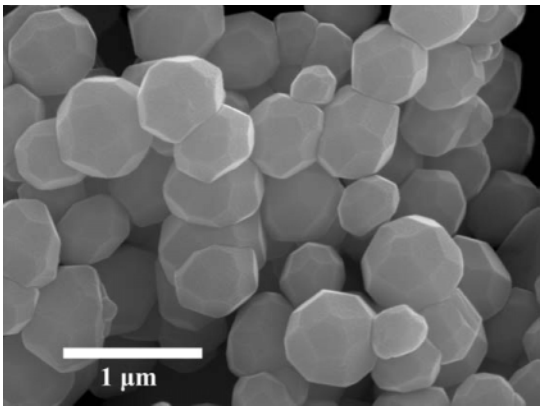

Figure 6-21. Sc_2O_3 single crystals grown by dc electrolysis method. (Reproduced with permission from ref. 127. Copyright 2003 American Chemical Society)

References

1. G. Skandan, H. Harn, and J.C. Parker, *Scr. Metall. Mater.*, **25**, 2389 (1991).
2. B. Gunter and A. Kumpmann, *Nanostruct. Mater.*, **1**, 27 (1992).
3. H. Eilers and B.M. Tissue, *Mater. Lett*., **24**, 261 (1995).
4. dK.S. Hong, R.S. Meltzer, B. Bihari, D.K. Williams, and B.M. Tissue, *J. Lumin.*, **76-77**, 234 (1998).
5. B.M. Tissue, *Chem. Mater.*, **10**, 2837 (1998).
6. W. Zhang, Y. Zhang, J. Tang, Y. Zhang, L. Wang, and Q. Ling, *Thin Solid Films*, **417**, 43 (2002).
7. G. Skandan, C.M. Foster, H. Frase, M.N. Ali, J.C. Parker, and H. Hahn, *Nanostruct. Mater.*, **1**, 313 (1992).
8. Z.K. Zhang and Z.L. Cui, *Nanostruct. Mater.*, **4**, 823 (1994).
9. A. Tschöpe and J.Y. Ying, *NATO ASI Ser. E*., **260**, 781 (1994).
10. A. Tschöpe and J.Y. Ying, *Nanostr. Mater*., **4**, 617 (1994).
11. A. Tschöpe, W. Liu, M. Flytzani-Stepahanopoulos, and J.Y. Ying, *J. Catal*., **157**, 42 (1995).
12. N. Guillou, L.C. Nistor, H. Fuess, and H. Hahn, *Nanostruct. Mater*., **8**, 545 (1997).
13. T. Liu, Y. Zhang, H. Shao, and X. Li, *Langmuir*, **19**, 7569 (2003).
14. W. Bai, K.L. Choy, N.H.J. Stelzer, and J. Schoonman, *Solid State Ionics*, **116**, 225 (1999).
15. L. Eyring L., *The Binary Lanthanide Oxides: Synthesis and Identification, in Synthesis of Lanthanide and Actinide Compounds*, eds. Morss L.R. and Meyer G. Kluwer, Dordrecht, 187 (1991).
16. N. Audebrand, J.P. Auffredic, and D. Louër, *Chem. Mater.*, **12**, 1791 (2000).
17. X.T. Dong, Z.R. Liu, K.S. Yang, and J.H. Liu, *Chin. Chem. Lett.*, **6**, 1017 (1995).
18. M. Lequitte and D. Autisser, *Nanostruct. Mater.*, **6**, 333 (1995).
19. S. Nakane, T. Tachi, M.Yoshinaka, K. Hirota, and O. Yamaguchi, *J. Am. Ceram. Soc.*, **80**, 3221 (1997).
20. M.D. Rasmussen, M. Akink, and O. Hunter, Jr., *Ceram. Int.*, **11**, 51 (1985).
21. B. Djuričić and S. Pickering, *J. Eur. Ceram. Soc.*, **19**, 1925 (1999).
22. G. Wakefield, H.A. Karon, P.J. Dobson, and J.L. Hutchison, *J. Phys. Chem. Solids*, **60**, 503 (1999).
23. G. Wakefield, H. A. Karon, P.J. Dobson, and J.L. Hutchison, *J. Colloid Interface Sci.*, **215**, 179 (1999).
24. R. Bazzi, M.A. Flores-Gonzalez, C. Louis, K. Lebbou, C. Dujardin, A. Brenier, W. Zhang, O. Tillement, E. Bernstein, and P. Perriat, *J. Lumin.*, **102-103**, 445 (2003).
25. J.G. Li, T. Ikegami, T. Mori, and Y. Yajima, *J. Mater. Res.*, **18**, 1149 (2003).
26. M. Ciftcioglu, M. Akinc, and L. Burkhart, *J. Am. Ceram. Soc.*, **70**, C329 (1987).
27. D. Sordeket and M. Akinc, *J. Colloid Interface Sci.*, **122**, 47 (1988).
28. M. Kobayashi, *J. Mater. Sci. Lett.*, **11**, 767 (1992).
29. P.L. Chen and I.W. Chen, *J. Am. Ceram. Soc.*, **79**, 3129 (1996).
30. C.Y. Xie, S.Z. Li, and J. Li, *Chin. Chem. Lett.*, **3**, 951 (1992).
31. P.L. Chen and I.W. Chen, *J. Am. Ceram. Soc*., **76**, 1577 (1993).
32. X. Chu, W. Chung, and L.D. Shumidt, *J. Am. Ceram. Soc*., **76**, 2115 (1993).
33. E. Matijević and W.P. Hsu, *J. Colloid Interface Sci.,* **118**, 506 (1987).
34. J. Gao, Y. Zhao, W. Yang, J. Tian, F. Guan, Y. Ma, J. Hou, J. Kang, and Y. Wang, *Mater. Chem. Phys.*, **77**, 65 (2002).
35. J. Ma and Q.J. Yan, *Chin. Chem. Lett.*, **6**, 915 (1995).

36. M.D. Fokema, E. Chiu, and J.Y. Ying, *Langmuir*, **16**, 3154 (2000.
37. M. Yoshimura and S. Somiya, *Mater. Chem. Phys*., **61**, 1 (1999).
38. W.P. Hsu, L. Rönnquist, and E. Matijević, *Langmuir*, **4**, 31 (1988).
39. M. Hirano, Y. Fukuda, H. Iwata, Y. Hotta, and M. Inagaki, *J. Am. Ceram. Soc.*, **83**, 1287 (2000).
40. M. Hirano and M. Inagaki, *J. Mater. Chem.*, **10**, 437 (2000).
41. M. Hirano, T. Miwa, and M. Inagaki, *J. Solid State Chem.*, **158**, 112 (2001).
42. M. Inoue, M. Kimura, and T. Inui, *Chem. Commun*., 957 (1999).
43. H. Tomaszewski, H. Weglaz, and R.D. Gryse, *J. Eur. Ceram. Soc*., **17**, 403 (1997).
44. P.K. Sharma, M.H. Jilavi, R. Naß, and H. Schmidt, *J. Mater. Sci. Lett*., **17**, 823 (1998).
45. Y.C. Zhou and M.N. Rahaman, *J. Mater. Res.*, **8**, 1680 (1993).
46. W. Chengyun, Q. Yitai, X. Yi, W. Changsui, Y. Li, and Z. Guiwen, *Mater. Sci. Eng.*, **B39**, 160 (1996).
47. M. Hirano and E. Kato, *J. Mater. Sci. Lett.*, **15**, 1249 (1996).
48. M. Hirano and E. Kato, *J. Am. Ceram. Soc.*, **79**, 777 (1996).
49. Y. Hakuta, S. Onai, H. Terayama, T. Adschiri, and K. Arai, *J. Mater. Sci. Lett.*, **17**, 1211 (1998).
50. M. Hirano and E. Kato, *J. Am. Ceram. Soc.*, **82**, 786 (1999).
51. K.S. Mazdiyasni and L.M. Brown, *J. Am Ceram. Soc.*, **54**, 479 (1971).
52. D. Grosso and P.A. Sermon, *J. Mater. Chem.*, **10**, 359 (2000).
53. F. Imoto, T. Nanataki, and S. Kaneko, *Ceram. Trans.*, **1**, 204 (1988).
54. S. Roy, W. Sigmund, and F. Aldinger, *J. Mater. Res.*, **14**, 1524 (1999).
55. A. Dupont, C. Parent, B. Le Garrec, and J.M. Heintz, *J. Solid State Chem.*, **171**, 152 (2003).
56. X. Dong, G. Hong, D. Yu, and D. Yu, *J. Mater. Sci. Technol.,* **13**, 113 (1997).
57. H. Majima, T. Hirato, Y. Awakura, and T. Hibi, *Metall. Trans. B*, **22B**, 397 (1991).
58. T. Hirai and I. Komasawa, *Kagaku Kogaku Ronbunshu*, **27**, 303 (2001).
59. T. Hirai, N. Okamoto, and I. Komasawa, *J. Chem. Eng. Jpn.,* **31**, 474 (1998).
60. T. Hirai, N. Okamoto, and I. Komasawa, *Langmuir,* **14**, 6648 (1998).
61. T. Hirai, N. Okamoto, and I. Komasawa, *AIChE J.*, **44**, 197 (1998).
62. S. Nishihama, T. Hirai, and I. Komasawa, *J. Mater. Chem.*, **12**, 1053 (2002).
63. T. Hirai, T. Hirano, and I. Komasawa, *J. Mater. Chem.*, **10**, 2306 (2000).
64. T. Hirai, T. Orikoshi, and I. Komasawa, *Chem. Mater.*, **14**, 3576 (2002).
65. T. Hirai, T. Hirano, and I. Komasawa, *J. Colloid Interface Sci.*, **253,** 62 (2002).
66. M.A. López-Quintela and H. Rivas, *J. Colloid Interface Sci*., **158**, 446 (1993).
67. M.H. Lee, S.G. Oh, and S.C. Yi, *J. Colloid Interface Sci.*, **226**, 65 (2000).
68. T. Masui, K. Fujiwara, K. Machida, G. Adachi, T. Sakata, and H. Mori, *Chem. Mater*., **9**, 2197 (1997).
69. Z. Wu, R.E. Benfield, L, Guo, H. Li, Q. Yang, D. Grandjean, Q. Li, and H. Zhu, *J. Phys. Condens. Matter*, **13**, 5269 (2001).
70. Y. He, B. Yang, and G. Cheng, *Mater. Lett.*, **57**, 1880 (2003).
71. W. Que, S. Buddhudu, Y. Zhou, Y.L. Lam, Y.C. Chan, C.H. Kam, L.H. Gan, and G.R. Deen, *Mater. Sci. Eng. C*, **16**, 153 (2001).
72. W. Que, Y. Zhou, C.H. Kam, Y.L. Lam, Y.C. Chan, L.H. Gan, and G.R. Deen, *Mater. Res. Bull.,* **36**, 889 (2001).

73. W. Que, S. Buddhudu, Y. Zhou, Y.L. Lam, J. Zhou, Y.C. Chan, C.H. Kam, L.H. Gan, and G.R. Deen, *Mater. Sci. Eng. C*, **16**, 51 (2001).
74. K.S. Suslick, *Ultrasound: Its Chemical, Physical and Biological Effects*, John Wiley & Sons Inc., Weinheim, Germany, 1988.
75. K.S. Suslick, S.-B. Choe, A.A. Cichowlas, and M.W. Grinstaff, *Nature*, **353**, 414 (1991).
76. S.A Galema, *Chem. Soc. Rev.*, **26**, 233 (1997).
77. Y. Wang, L. Yin, and A. Gedanken, *Ultrasonics Sonochem.*, **9**, 285 (2002).
78. L. Yin, Y. Wang, G. Pang, Y. Koltypin, and A. Gedanken, *J. Colloid Interface Sci.*, **246**, 78 (2002).
79. X.H. Liao, J.M. Zhu, J.J. Zhu, J.Z. Xu, and H.Y. Chen, *Chem. Commun.*, 937 (2001).
80. H. Wang, J.J. Zhu, X.H. Liao, S. Xu, T. Ding, and H.Y. Chen, Phys. *Chem. Chem. Phys.*, **4**, 3794 (2002).
81. V.G. Pol, O. Palchik, A. Gedanken, and I. Felner, *J. Phys. Chem. B*, **106**, 9737 (2002).
82. K. Okuyama and I.W. Lenggoro, *Chem. Eng. Sci.*, **58**, 537 (2003).
83. M. Suzuki, M. Kagawa, Y. Syono, and T. Hirai, *J. Mater. Sci*., **27**, 679 (1992).
84. E. Reverchon, G.D. Porta, D. Sannino, L. Lisi, and P. Ciambelli, *Stud. Surf. Sci. Catal.*, **118**, 349-358 (1998).
85. C. Xu, B.A. Watkins, and R.E. Sievers, *Appl. Phys. Lett*., **71**, 1643 (1997).
86. A.J. Rulison and R.C. Flagan, *J. Am. Ceram. Soc.*, **77**, 3244 (1994).
87. T.V. Mani, H.K Varma., A.D. Damodaran, and K.G.K. Warrier, *Ceram. Int.*, **19**, 125 (1993).
88. B. Xia, I.W. Lenggoro and K. Okuyama, *Adv. Mater.*, **13**, 1579 (2001).
89. B. Xia, I.W. Lenggoro, and K. Okuyama, *J. Mater. Chem.*, **13**, 2925 (2001).
90. A.Q. Wang and T.D. Golden, *J. Electrochem. Soc.*, **150**, C616 (2003).
91. T.D. Golden and A.Q. Wang, *J. Electrochem. Soc.*, **150**, C621 (2003).
92. J.A. Switzer, *Am. Ceram. Soc. Bull.*, **66**, 1521 (1987).
93. Y. Zhou, R.J. Phillips, and J.A. Switzer, *J. Am. Ceram. Soc*., **78**, 981 (1995).
94. T. Tsuzuki, W.T.A. Harrison, and P.G. McCormick, *J. Alloys. Comp.*, **281**, 146 (1998).
95. T. Tsuzuki, E. Pirault, and P.G. McCormick, *Nanostr. Mater.*, **11**, 125 (1999).
96. T. Tsuzuki and P.G. McCormick, *J. Am. Ceram. Soc.*, **84**, 1453 (2001).
97. F. Li, X. Yu, H. Pan, M. Wang, and X. Xin, *Solid State Sciences*, **2**, 767 (2000).
98. X. Yu, F. Li, X. Ye, X. Xin, and Z. Xue, *J. Am. Ceram. Soc.*, **83**, 964 (2000).
99. F. Bondioli, A.B.Corradi, C. Leonelli, and T. Manfredini, *Mater. Res. Bull.*, **34**, 2159 (1999).
100. J.A. Nelson and M.J. Wagner, *Chem. Mater.*, **14**, 915 (2002).
101. J.A. Nelson, L.H. Bannett, and M.J. Wagner, *J. Am. Chem. Soc.*, **124**, 2979 (2002).
102. J.A. Nelson, L.H. Bannett, and M.J. Wagner, *J. Mater. Chem.*, **13**, 857 (2003).
103. R.C. Pastor and A.C. Pastor, *Mater. Res. Bull.*, **1**, 275 (1966).
104. A.C. Pastor and R.C. Pastor, *Mater. Res. Bull.*, **2**, 555 (1967).
105. A.A. Popova and V.B. Zotkina, *Dokl. Akad. Nauk SSSR*, **169**, 92 (1966).
106. A.M. Lejus and J.P. Connan, *Rev. Intern. Hautes Temp. Refract.,* **11**, 215 (1974).
107. Č. Bárta, F. Petrů, and B. Hájek, *Naturwissenschaften*, **45**, 36 (1958).
108. W. Class, H.R. Nesor, and G.T. Murray, *J. Phys. Chem. Solids Suppl.*, **1**, 75 (1967).
109. H. Makram, A.M. Anthony, and Vu Tien Loc., *Rev. Intern. Hautes Temp. Refract.*, **3**, 395 (1966).
110. Z.N. Zonn and V.A. Ioffe, *Rost Kristallov*, **8**, 78 (1968).

111. R.C. Linares, *J. Phys. Chem. Solids*, **28**, 1285 (1967).
112. A.M. Lejus, J.C. Bernier, and R. Collongues, *J. Solid State Chem.*, **16**, 349 (1976).
113. R. Tueta and A.M. Lejus, *Rev. Chim. Miner.*, **11**, 27 (1974).
114. J.C. Bernier, A.M. Lejus, and R. Collongues, *Solid State Commun.*, **16**, 349 (1975).
115. C. F. Guerci and M.W. Shafer, *J. Appl. Phys.*, **37**, 1406 (1966).
116. M.W. Shafer, J.B. Torrance, and T. Penney, *J. Phys. Chem. Solids*, **33**, 2251 (1972).
117. M. Drofenik, L.Golic, and D. Kolar, *J. Cryst. Growth*, **21**, 170 (1974).
118. A.M. Lejus and J.C. Bernier, *Mater. Res. Bull*., **11**, 477 (1976).
119. A.M. Lejus, J.C. Bernier, and R. Collongues, *Rev. Intern. Hautes Temp. Refract.,* **13**, 25 (1976).
120. D. Jia, L. Lu, L., and W.M. Yen, *Opt. Commun.*, **212**, 97 (2002).
121. E. Hubbert-Paletta and H. Müller-Buschbaum, *Z. Anorg. Allgem. Chem.*, **363**, 145 (1968).
122. J.J. Petrovic, R.S. Romero, D. Mendoza, A.M. Kukla, R.C. Hoover, and K.J. McClellan, *Ceram. Eng. Sci. Proc.*, **20**, 3 (1999).
123. A. Saiki, N. Ishizawa, N. Mizutani, and M. Kato, *Yogyo Kyokaishi*, **93**, 649 (1985).
124. L. Eyring, *Solid State Chemistry*; Marcell Dekker, New York, p 565 (1974).
125. U. Shubert and Nicola Hüsing, *Synthesis of Inorganic Materials*, Wiley-VCH, Weinheim, p.187 (2000).
126. M. McKelvy and L.Eyring, *J. Crystal Growth*, **62**, 635 (1983).
127. N. Imanaka, Y.W. Kim, T. Masui, and G. Adachi, *Cryst. Growth Des.*, **3**, 289 (2003).
128. T. Masui, Y.W. Kim, N. Imanaka, and G. Adachi, *J. Alloys Comp*., in press.
129. N. Imanaka, T. Ueda, Y. Okazaki, S. Tamura, and G. Adachi, *Chem. Mater.*, **12**, 1910 (2000).
130. N. Imanaka, Y. Kobayashi, S. Tamura, and G.Adachi, *Solid State Ionics,* **136–137**, 319 (2000).

9. APPLICATIONS

J.-P. CUIF (9.1), E. ROHART (9.2.1),
P. MACAUDIERE (9.2.2), and C. BAUREGARD (9.3)
Rhodia Electronics & Catalysis
Z.I. 26 rue chef de baie, 17041 La Rochelle Cedex 1 - France

E. SUDA and B. PACAUD (9.4)
Anan Kasei Co., Ltd.
210-51 Ohgata-cho, Anan, Tokushima 774-0022, Japan

N. IMANAKA, T. MASUI, and S. TAMURA (9.5 – 9.8)
Department of Applied Chemistry, Faculty of Engineering,
Osaka University
2-1 Yamadaoka, Suita, Osaka 565-0871, Japan

9.1. PHOSPHORS

9.1.1. *A wide range of applications, thanks to a great variety of emissions*

Luminescent materials have been under development since the 1960's, in conjunction with the industrial availability of rare-earths of sufficient purity: television color, fluorescent lighting, and medical X-ray photography. The intense emissions and almost monochromatic tones obtained by diluting the rare-earths based activators in the appropriate host networks (very often simple rare-earth compounds at 0, 7, or 14 *f* electrons: yttrium, lanthanum, gadolinium and lutetium)

Figure 9-1. A great variety of emissions from rare earths phosphors.

G. Adachi et al. (eds.), Binary Rare Earth Oxides, 215–255.

are the primary reason for this development. They made it possible to meet the very specific criteria for use that traditional band emission phosphors could not satisfy. A great variety of emissions can be obtained, depending on the type of activator brought into play and on the respective positions of the excited or fundamental energy levels as shown in Figure 9-1.

9.1.1.1. Color television with cathode ray tube (CRT)

In color television, where the image is reproduced by selective cathode excitation of three phosphors (blue, green and red) deposited on the internal face of the screen, yttrium oxysulfides activated with trivalent europium ($Y_2O_2S:Eu^{3+}$) facilitate such a gain in the brilliance of red over ZnS:Ag (more than double it) that they have totally replaced it at a cost about five times less. The exceptional performance of the rare-earth phosphors has also been used gainfully in a vast number of cathode tubes for professional applications: color computer monitors, tubes for aviation use, projection television, etc.

9.1.1.2. Fluorescent lighting

In the fluorescent lighting domain, rare-earth phosphors have made it possible in theory that daylight can be reconstituted by adding three primary emissions in defined proportions at 450, 550 and 610 mm. In a low pressure fluorescent tube, conversion ultraviolet rays emitted by excited mercury into visible light is traditionally done using an off-white band emitter, the calcium halophosphate activated by antimony and manganese. The perfection of phosphors using blue emissions from divalent europium (specific case of a narrow band emission from transitions bringing the 5d levels into play) and green emissions from trivalent terbium co-activated by cerium, respectively, and red from trivalent europium has made it possible to make tri-chromatic fluorescent tubes recently miniaturized in the form of compact lights for use in the home. Giving off a color very close to

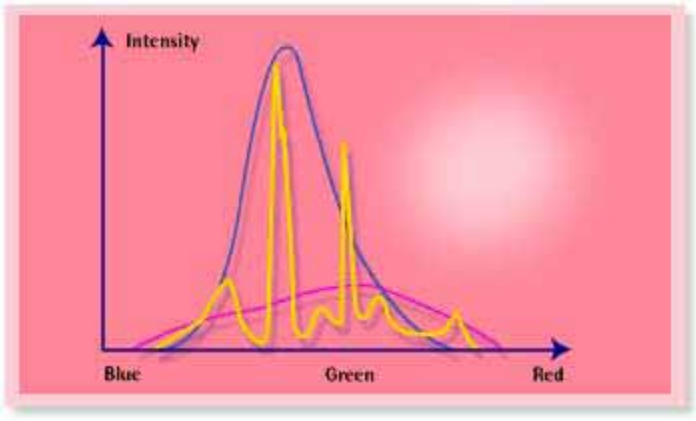

Figure 9-2. Production of daylight in the tri-chromatic lighting system.

incandescent lights, the tri-chromatic system of fluorescent light bulbs has a 5 to 8 times greater light output and a life span that is more than a thousand hours longer, resulting in significant savings to the user. In the tri-chromatic lighting system, daylight is reproduced by adding 3 fundamental emissions around 450, 550, and 610 nm as shown in Figure 9-2.

9.1.1.3. Flat screen technology

There is a strong demand for replacing the cumbersome cathode ray tubes on TVs and computers with large dimension flat screens. Different technologies using rare earths are emerging:

- Field emission screens operating at low tension (< 8000 V) use rare-earth based phosphors:
  Red (Y_2O_3:Eu^{3+}; $SrTiO_3$:Pr^{3+})
  Green ($Y_3(Al,Ga)_5O_{12}$:Tb^{3+}; Y_2SiO_5:Tb^{3+})
  Blue (Y_2SiO_5:Ce^{3+})
- Plasma technology screens
  In this case, the phosphors are excited by the discharge of the plasma placed between two electrodes. The screen is broken down into small cells or pixels, the size of which is small enough to obtain high definition screens. There is a clear improvement in the life span of these screens. Rare earths are present in the blue $BaMgAl_{10}O_{17}$:Eu^{2+} and red $(Y,Gd)BO_3$:Eu^{3+} phosphors. The latter is preferable to Y_2O_3:Eu^{3+} due to its stronger VUV absorption. Comparable technologies are now used in lamps.

9.1.1.4. Signs and Signals

There has also been a marked increase in the use of phosphors in signs and signals. Numerous safety signs (exit lights, reflective safety bands and highway markings, etc.) require the use of phosphorescent. Rare earths are part of the mineral phosphorescent product with the longest known phosphorescence duration, namely $SrAl_2O_4$:Eu^{2+}, Dy^{3+}.

9.1.1.5. Medical Radiography

A third domain using rare-earth luminescence is medical radiography. The radiological image is transformed into an optical image by a screen intensifier using the ability of a phosphor to transform the X-ray into visible blue or green light, to which photographic emulsions are far more sensitive than X-rays.

The use of rare-earth phosphors for this application was developed and thus replaced the calcium tungstate used in traditional systems.

This results in :

- the intrinsic absorption of X-rays on the range of energies brought into play
- the more effective conversion into visible light (10 to 20% output rather than 6% for $CaWO_4$)

- the spectral separation of the emission (from trivalent terbium or thulium) adapted to the maximum sensitivity of the emulsions used,

which are three essential criteria in defining the efficiency factor of screen intensifiers.

There are three major types of rare-earth phosphors used: $Gd_2O_2S:Tb^{3+}$ (green), $LaOBr:Tm^{3+}$ in $YTaO_4:Nb^{5+}$ or Tm^{3+} (blues), which make it possible to appreciably improve the quality of the images obtained and at the same time decrease patient exposure time by a factor of 2 to 4.

TABLE 9-1. Use of rare-earth phosphors in electronic applications

Excitation	Phosphor	Application	
γ-Rays	$CaSO_4:Dy^{3+}$	Detection of ionizing radiation	
	$Gd_2O_2S:Pr^{3+}$	Ceramic scintillators	
X-rays	$Gd_2O_2S:Tb^{3+}$		
	$LaOBr:Tm^{3+}$		
	$YTaO_4:Nb^{5+}$ or Tm^{3+}	X-ray screen intensifiers	
	$BaFBr:Eu^{2+}$		
Electrons	$ZnS:Tb^{3+}$	Electroluminescent Panels	
Cathode Rays	$Y_2O_2S:Eu^{3+}$	Red for television	
	$Gd_2O_2S:Tb^{3+}$	Green for professional tubes	
	$Y_3Al_5O_{12}:Ce^{3+}$		
UV (High pressure)	$YVO_4:Eu^{3+}$	Red corrector for high pressure mercury vapor lamps	
	$Y_3Al_5O_{12}:Ce^{3+}$		
UV (Low pressure)	$BaMgAl_{16}O_{17}:Eu^{2+}$	Blue Component	
	$Sr_5(PO_4)_3Cl:Eu^{2+}$		
	$LaPO_4:Ce^{3+},Tb^{3+}$	Green Component	Tri-chromatic fluorescent tubes
	$(Ce,Tb)MgAl_{11}O_{19}$		
	$(Gd,Ce,Tb)MgB_5O_{10}$		
	$Y_2O_3:Eu^{3+}$	Red Component	
Laser Pumping	$Y_3Al_5O_{12}:Nd^{3+}$	Lasers	

9.1.2. *New demands and recent developments in applications: a step forward for phosphors*

There are plenty of advanced products for phosphors used in tri-chromatic fluorescent lighting, phosphor converted light emission diodes (pcLED), X-ray imaging, specialty lamps, back lighting for liquid crystal displays (LCD), cathode ray tubes (CRT) for televisions and monitors, plasma display panels (PDP), projection televisions (PRT), and field emission displays (FED).

During the past several years, the lighting industry has witnessed a significant growth in high energy saving lamps such as tri-chromatic lamps and a need for higher quality standards. At the same time, the display industry has seen new technologies emerging such as flat CRT, high resolution CRT and flat panel displays. These changes have created the challenging demand for “New phosphors”:

- More efficient phosphors with improved brightness and performance
- Lower cost products allowing technology expansion

These new applications show some significant benefits:

- High rare-earth purity as well as very low luminescence killer content
- Controlled reactivity facilitating phosphor manufacture

Customized products combining controlled composition of a high number of elements included in various matrices.

9.1.2.1. Tri-chromatic lamps and colored phosphors

Tri-chromatic fluorescent lamps generate white light using three primary emissions at around 450 nm (blue), 550 nm (green) and 610 nm (red). Some advanced rare-earth based raw materials used for the three phosphors are being manufactured. For red, yttrium and europium based co-precipitates only are used by the industry. The new range of Y-Eu oxide co-precipitates include highly controlled products with improved purity. Only the highest purity and carefully controlled products deserve the new applications quality standard. A range of $LaPO_4:Ce^{3+},Tb^{3+}$ products [1, 2] is facilitating the manufacture of lanthanum phosphate (LAP) green phosphor. The LAP phosphor is now the standard for green phosphors in tri-chromatic lamps. Composition, purity as well as special morphology are carefully controlled in these proprietary products.

Recently, new proprietary advanced products for blue phosphors based on a $BaMgAl_{10}O_{19}:Eu^{2+}$ are also launched. A single thermal treatment is sufficient to make highly efficient blue BAM phosphor with controlled morphology and particle size distribution.

9.1.2.2. Tri-chromatic lamps and colored phosphors

Although CRT monitors are partially being replaced by LCD, there is still a significant demand for large screen CRT, high resolution CRT and flat CRT. The typical red phosphor used for CRT is $Y_2O_2S:Eu^{3+}$. This phosphor is manufactured from separate or mixed oxides based on yttrium and europium. Some additives such as terbium or samarium are used as doping agents in these phosphors, to enhance brightness for instance. The new range of products for red CRT phosphor includes high purity $Y_2O_3:Eu^{3+}$ with some doping agents. Products with various Eu^{3+} contents from 4.0 to 10% are manufactured for this application depending on the specific requirements of customers.

9.1.2.3. New phosphors for PDP

The new flat screen PDP uses ultra-violet as a source of excitation. This still new technology has required the development of new phosphors in the 90's. The most common phosphors are for red $(Y,Gd)BO_3:Eu^{3+}$, for green $(Y,Gd)BO_3:Tb^{3+}$ as well as $Zn_2SiO_4:Mn^{2+}$ and for blue $BaMgAl_{10}O_{17}:Eu^{2+}$ called BAM. For all three color PDP phosphors, three ranges of advanced, proprietary rare-earth based new products have been developed [3, 4]:

Red: $(Y, Gd)BO_3:Eu^{3+}$

Green: $(Y, Gd)BO_3:Tb^{3+}$

Blue: $BaMgAl_{10}O_{17}:Eu^{3+}$

Examples of morphology of precursors are shown in Figures 9-3 and 9-4. All products can be easily transformed into PDP phosphor by adding a flux and applying a thermal treatment. The composition of each product can be customized upon request.

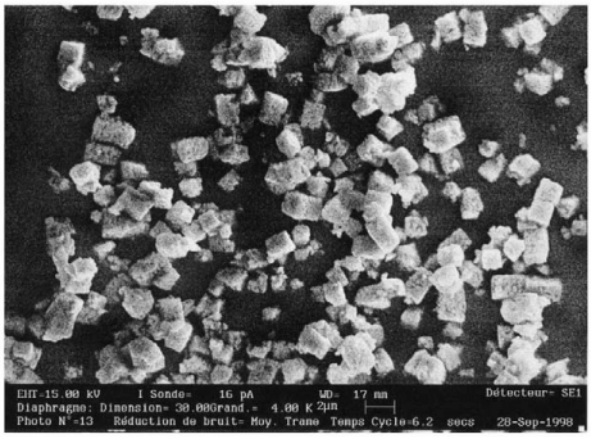

Figure 9-3. SEM image of cubic shape europium doped yttrium orthoborate particles.

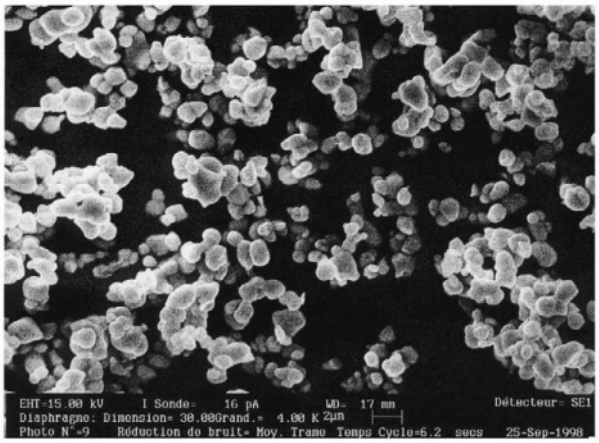

Figure 9-4. SEM image of spherical shape europium doped yttrium orthoborate particles.

9.1.2.4. Other applications

Some other applications of these brand-new products include field emission displays (FED), CRT projection TV (PTV), various lighting and medical imaging applications.

9.2. CATALYSTS

9.2.1. *Three Way Catalysis (TWC) and NO_x trap catalyst*

Among the different applications of rare earths, intensively investigated, catalysis is undoubtedly one of the most important.

Large amounts of catalysts, including lanthanides (i.e. cerium oxide; ceria [5]) are used for refinery operations to convert crude oil into lower molecular-weight fractions. However, today a major technological application of steadily growing importance for cerium and its '*derivatives*' (i.e. other rare earth oxides such as Nd_2O_3, Pr_6O_{11}, La_2O_3, and Y_2O_3) is the vehicle emission control to remove pollutants from vehicle (auto-exhaust) emissions. Since the early 70's, there has been a large number of scientific communications relating to this topic.

9.2.1.1. Use of rare earths in Three-Way Catalysis (TWC) for gasoline engines

There are three main types of pollutants at the outlet of the exhaust pipe :

- Carbon monoxide (CO)
- Unburned hydrocarbons (HC)
- Nitrogen oxides (NOx)

The quantity of pollutants varies with the operating conditions of the engine, but is influenced predominantly by the Air/Fuel ratio in the combustion cylinder. Generally speaking, when the engine is operated in *rich* of stoichiometric, CO and HC emissions are high, while NO_x emissions are low (in lean of stoichiometric, trends are reversed). Thus the very first and important challenge for catalysis was to convert CO and HC when engine operates under lean conditions according to the reactions from eq.1 to 3 and to convert NO_x when engine operates under rich conditions as summarized from eq.4 to 6.

$$C_xH_n + (1+n/4)\ O_2 = x\ CO_2 + (n/2)\ H_2O \quad (1)$$

$$CO + ½\ O_2 = CO_2 \quad (2)$$

$$CO + H_2O = CO_2 + H_2 \quad (3)$$

$$NO + CO = ½\ N_2 + CO_2 \quad (4)$$

$$NO + H_2 = ½\ N_2 + H_2O \quad (5)$$

$$(2 + n/2)\ NO + C_xH_n = x\ CO_2 + (n/2)\ H_2O + (1+n/4)\ N_2 \quad (6)$$

These reactions take place in a very short period of time (1 sec or less) and in many cases are performed in a honeycomb monolith made of cordierite or metal. The monolith is coated with some freely-available components such as:

- noble metals, mainly Rh, Pt and Pd
- alumina
- promoters and/or stabilizers such as La, Nd, Ba
- **oxygen storage promoters such as ceria**

Among all the components, the 'oxygen storage material' is certainly the one which has been the most studied [6] and is definitely considered as a key component

of the washcoat. The beneficial effects of ceria-based materials were already discussed about 30 years ago by Gandhi et al. [7]. Ceria promotes:

- the precious metal dispersion and boost their 'intrinsic' activity
- the thermal stability of alumina
- the water gas shift reaction (eq.3) and steam reforming reaction
- CO and HC oxidation under lean conditions
- NO_x reduction under rich conditions
- store and release oxygen when richness varies from lean to rich

Generally speaking, the most important role of ceria is the oxygen storage capacity (OSC). Among the rare earths, cerium oxide (and in a small proportion of Pr and Tb oxides) shows different valences (Ce^{4+}/Ce^{3+}) in respect of the temperature and the nature of the atmosphere. The OSC is the result of this very particular property.

In the 80's pure ceria was used as an OSC component in the catalytic converter. But as the legislation got more and more severe to reduce exhaust emissions, car manufacturers developed new sophisticated technologies. Among them, the Close-Coupled Catalyst (CCC), located closer to the manifold, showed improved performance and especially very good light-off activity. Nevertheless, this type of catalyst is submitted to harsh ageing conditions (>1000°C) and the OSC components had to be more thermally stable. The 1st generation CeO_2/ZrO_2 mixed oxides have thus gradually replaced pure ceria. These materials show not only higher surface area at 900°C than pure ceria [8, 9] but also improved OSC behavior. Reference [6] highlights the main reasons for this improvement.

To meet the future legislation requirements (such as SULEV in California), modern TWC technologies have recently taken the lead with different washcoat architectures to enhance the activity including inorganic carriers able to resist temperatures as high as 1100°C. Highly thermally-stable ternary (Ce/Zr/X) and even quaternary (Ce/Zr/X/Y) mixed oxides are emerging [10-12].

Recently, a new generation of CeZr based mixed oxide for severe demanding temperature applications and low loading precious metal (PM) catalysts have been developed [13, 14]. The sinterability of such new OSC materials (referred as 2nd generation CeZr materials) is less than 1st generation OSC materials (Figure 9-5). The open-pore texture of the oxide (Figure 9-6 and 9-7) as well as the fine tuning of the homogeneous solid solution at the wet part of the process leads to significantly improved materials with no phase segregation up to 1100°C (Figure 9-8).

To conclude, continued improvements in ceria and its derivatives will be needed within the next years to increase thermal durability in order to meet the more stringent legislation. In parallel new materials with very high and fast OSC (much more than the current one) and/or completely stable OSC materials within the range from 900 to 1200°C will be needed for the development of low-cost, reduced-load, noble metal catalysts [15].

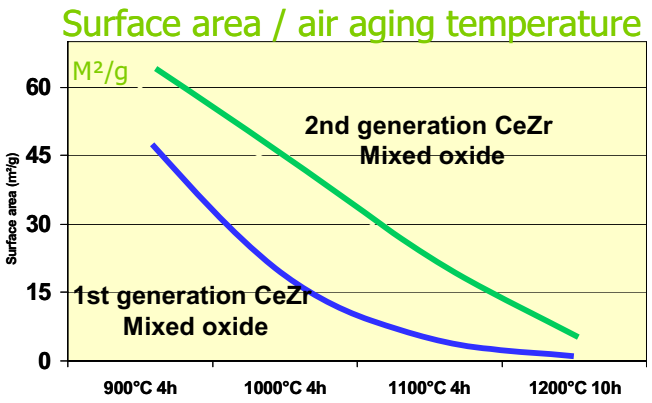

Figure 9-5. BET surface area (m^2/g) versus temperature of calcinations in air for two CeZr mixed oxides [13].

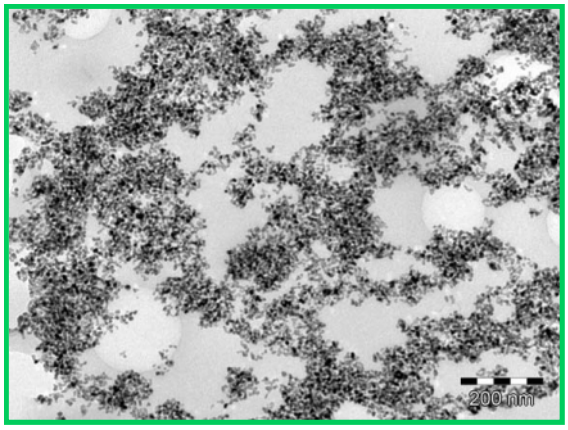

Figure 9-6. TEM analysis of the 2nd generation CeZr mixed oxide after air calcination at 900°C [13]

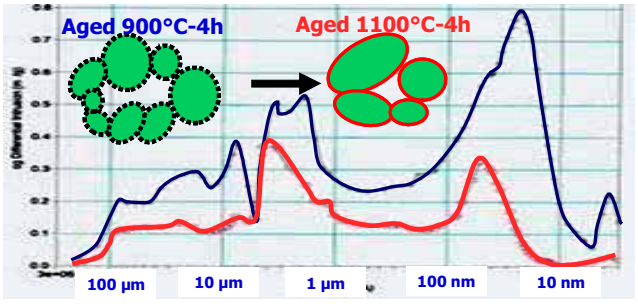

Figure 9-7. Mercury porosimetry profile of 2nd generation CeZr mixed oxide after air calcination respectively at 900°C and 1100°C [13].

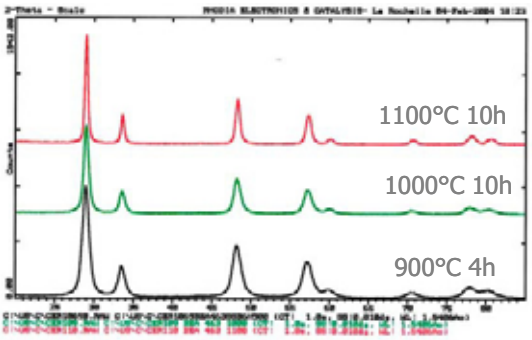

Figure 9-8. XRD analysis of 2nd generation CeZr mixed oxide (composition : $CeO_2/ZrO_2/La_2O_3/Pr_6O_{11}$ – 60/30/3/7 wt oxide %) after air calcination at 900°C / 1000°C / 1100°C [13] – Pure cubic solution up to 1100°C.

Finally, as suggested by M. Shelef and co-authors [6], ceria's dual role as an oxygen storage component in the TWC and as the basis for on-board catalyst monitoring, suggests that there may be future opportunities to 'tune' these characteristics separately (some OSC material designed for oxygen storage and PM carrier, some for on-board diagnoses).

9.2.1.2. Use of rare earths in NO_x-trap Catalysts for diesel and lean-burn engines

The demand for better fuel economy and lower CO_2 emissions from automotive engines leads to the development of lean-combustion technology. Under these conditions, conversion of NO_x is much more critical than for TWC. Recently, Toyota [16] proposed to store NO_x on a trap during extended periods of engine operation under lean conditions, and periodically to regenerate the trap by having engine operation shifted briefly to rich conditions.

Barium carbonate is the most commonly proposed material to trap NO_x. Nevertheless, due to its high sulfur sensitivity, catalyst makers are looking at alternative solutions including rare earth oxides such as La, Pr or Ce [17, 18].

On the other hand, incorporation of an oxygen storage component (such as ceria and/or ceria/zirconia mixed oxide) into the NO_x-trap leads to the generation of exothermic heat during NO_x trap regeneration, which helps for NO_x and SO_x desorption [6, 17, 19].

9.2.2. *A new catalytic solution for diesel engine exhausts cleaning*

The reduction of pollutant emission from passenger and utility vehicles is one of the major challenges of the new century due to the impact of such emissions on public health and environment (acid rains, destruction of ozone shelter…). One of the major challenges concerns diesel engines: compared to it gasoline counterparts, diesel engine displays improved long-term reliability and greater fuel efficiency (up

to 20% lower fuel consumption). This engine is the choice for the foreseeable future if its NO_x and particulate matter emission can be sufficiently reduced.

One elegant solution to get rid of particulate matter (PM) is to use a diesel particulate filter (DPF). The DPF system consists of a filter positioned in the exhaust stream designed to physically collect the particulate emissions, preventing thus their release to the atmosphere, while allowing the exhaust gases to pass through the system. DPF technology is the most effective means for reducing particulate emissions, with efficiencies exceeding 99.5% based on particulate number.

The most common design of DPF is the wall-flow monolith, which consists of many small parallel ceramic channels running axially through the part (Figure 9-9).

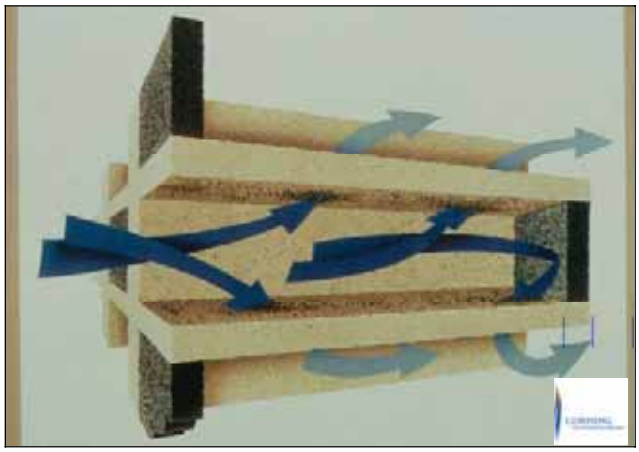

Figure 9-9. Ceramic wall-flow filtration design.

Adjacent channels are alternatively plugged at each end in order to force the diesel exhaust gases through the porous substrate walls which act as a mechanical filter. The filtration mechanism is a combination of surface and cake filtration. As the soot load increases, a particulate layer develops at the inlet channel walls and the cake filtration becomes the prevailing mechanism.

Since the volume of PM generated by a diesel engine is sufficient to fill up and plug a reasonably sized filter in a matter of few hundred kilometers, combustion of the accumulated soot in the DPF must occur frequently in order to regenerate the trap for the next accumulation step.

In fact, contrary to what one might expect, it is the regeneration of the DPF that poses the major technological challenge and not the filtration of the particulates.

One attractive method to meet the regeneration challenge is to dose diesel fuel with a Ceria-based fuel-borne catalyst at low concentration. Combustion of the resulting fuel leads to in-cylinder generation of ceria particles (a highly effective catalyst for soot combustion) intimately mixed with the diesel particulates which are

simultaneously formed from incomplete combustion of the diesel fuel. These mixed ceria-soot particles are trapped in the downstream DPF giving a soot bed containing a homogeneous dispersion of Ceria (Figure 9-10).

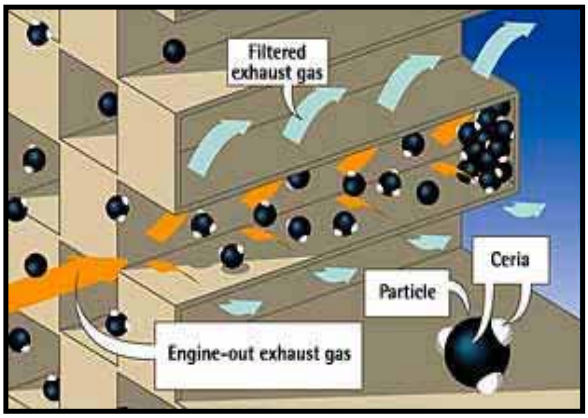

Figure 9-10. Principle of Operation of the Ceria-based fuel-borne catalyst.

The primary function of the ceria-based fuel-borne catalyst (FBC) [20] is to lower the combustion temperature of the soot accumulated in the DPF (currently around 450°C) compared to that of non-catalytically assisted combustion (usually around 600°C), thus allowing the DPF to regenerate more readily (Figure 9-11, combustion temperature of model soot decreases by the addition of a ceria-based catalyst).

As shown in Figure 9-12, the interest of the FBC technology is to ensure homogeneous and large number of contact points between the nano-crystals of ceria-based catalyst, the carbonaceous particulate forming the large soot aggregates and oxygen from the gas phase.

In addition, FBC [21] technology provides constant and continuously fresh ceria-based catalyst to the soot layer. This explains why, unlike many other catalyst-based DPF-regeneration technologies, the ceria-based fuel-borne catalyst is relatively insensitive to fuel-sulfur levels and is able to function with fuel containing over 2,500ppm of sulfur, as demonstrated in marine and stationary applications. However, in the presently described automotive application, the permissible level of sulfur is limited by the sulfur-sensitivity of other components of the complete DPF system.

The secondary function of the ceria-based fuel-borne catalyst [22] is to ensure, once the soot combustion is initiated, a complete and smooth regeneration avoiding exothermic peaks responsible for DPF aging, potentially leading to DPF breakage (Figure 9-13). This is achieved either by the good dispersion of the catalyst in the

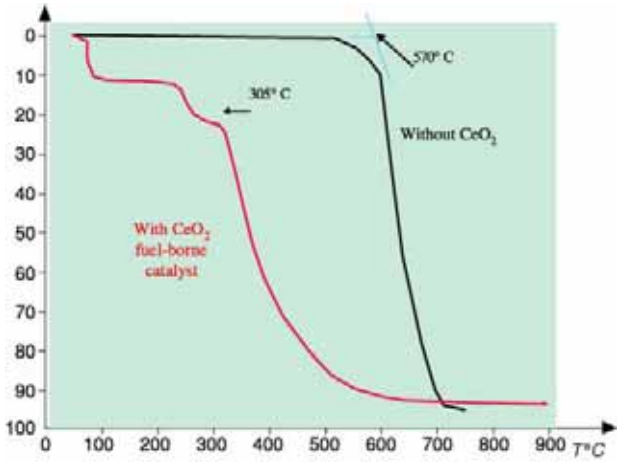

Figure 9-11. Comparison of combustion efficiency between a virgin (black) and cerium containing (red) carbon black. The ignition temperature of the cerium containing carbon black is more than 200ºC lower.

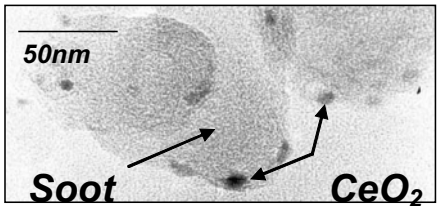

Figure 9-12. Ceria repartition within the soot particles

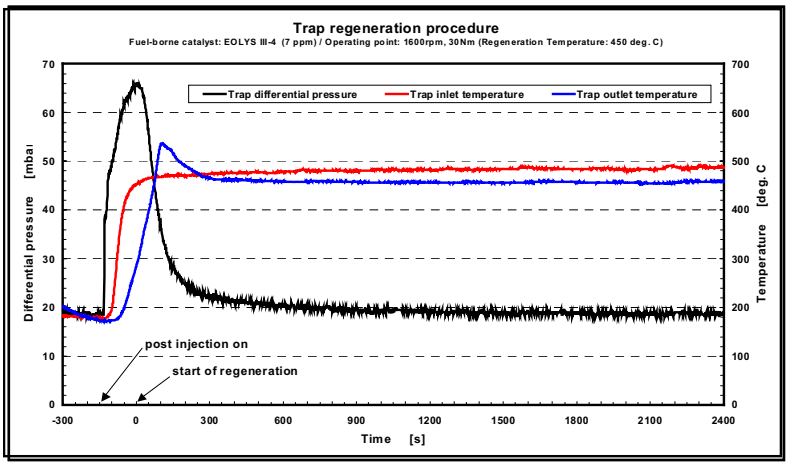

Figure 9-13. Exothermic peak observed during regeneration in specific conditions

soot bead or by the specific catalytic oxidation process of ceria, that could be the consequence of the well known oxygen-storage-capacity (OSC) properties of ceria nanocrystals that can provide locally native and reactive oxidizing species to burn soot and adsorbed hydrocarbons.

In order to introduce the catalyst inside the soot particles, it has been proposed that a fuel-borne catalyst made of cerium nanoparticles (Figure 9-14**)** perfectly dispersed in a solvent compatible with the Diesel fuel.

This first catalyst generation was used in 2000 by PSA-PEUGEOUT-CITROËN (hereafter PSA) on the Peugeot 607. One drawback of the solution was the necessity to clean the filter after 80,000 km due to ash accumulation in the DPF (Figure 9-15).

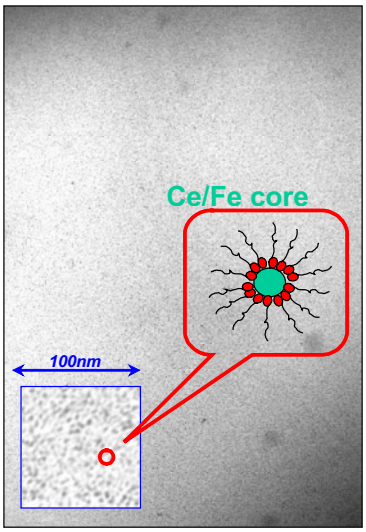

Figure 9-14. Fuel-borne catalyst made of cerium nanoparticles dispersed in an organic solvent.

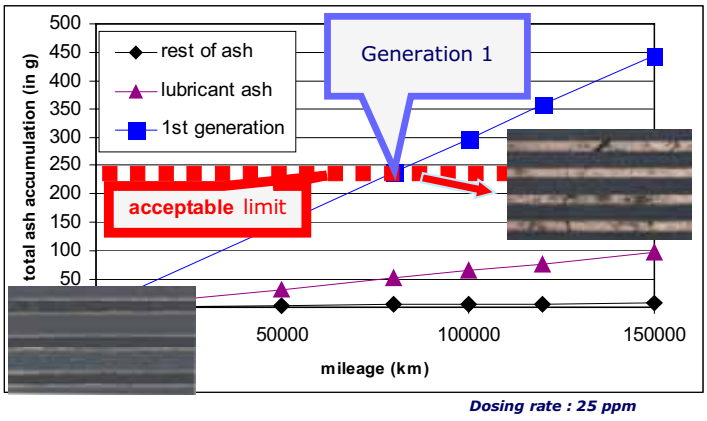

Figure 9-15. Ash accumulation observed for the first generation of ceria based catalyst

During the last two years, numerous research programs were launched in order to improve the catalytic activity of the cerium-based catalyst. The introduction of iron into ceria nanoparticles, multiplying by 2.5 the activity of the catalyst, allowed us to decrease the amount of catalyst from 25 ppm to 10 ppm while keeping constant the ignition temperature and the exothermic peak observed on the filter during regeneration. With the same filter size, the interval between servicing (ie. the cleaning of the filter) increase from 80000 to 120-150 000 km depending on vehicle engines (Figure 9-16).

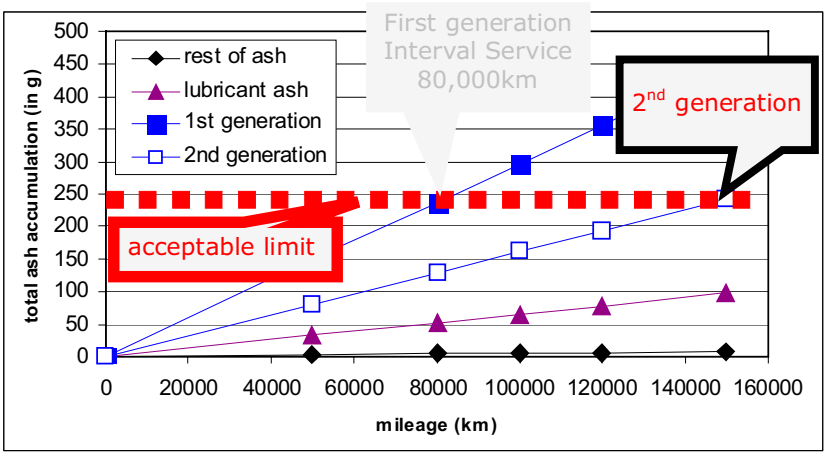

Figure 9-16. Ash accumulation observed for the second generation of ceria based catalyst.

The second generation catalyst was introduced by PSA on the European market End of 2002. Up to date, more than 600,000 passenger cars have been equipped without noticeable problem. Ford is also introducing the technology for its European diesel passenger cars.

However, achieving reliable and durable filter regeneration in automotive applications under all operating conditions is a major challenge, since driving cycle conditions are unpredictable and can range from prolonged periods of idling and low speed driving, to high speed cruising under laden conditions. Even using our Ceria-based fuel-borne catalyst, it is strongly recommended to use a completely active system approach for passenger car, light-duty, and heavy-duty vehicle applications, as it is done on all reliable commercial developments.

With a high level of activity whatever the quality of the fuel (sulfur content), the fuel-borne catalyst allows emission levels lower than the ones requested by the most severe regulations that will be effective in 2007 in the US and 2008 in Europe.

9.3. GLASS INDUSTRY

The glass industry is a traditional big user of Rare Earths, which are used both for the manufacturing of the glass material itself, and also for the surface treatment of glass pieces.

9.3.1. *Glass composition*

9.3.1.1. Glass coloration

The use of Rare Earths oxides in the glass composition allows the manufacturing of bright and stable colored glass pieces with good thermal and chemical resistance. Choice of Rare Earth element and concentration of addition, usually ranging from 2 to 6%, is driven by final desired shade [23].

Glass colored with neodymium shows pink to purple colors. The corresponding transmission curve (Figure 9-17) shows absorption peaks at 570-600nm (yellow) and 530nm (green).

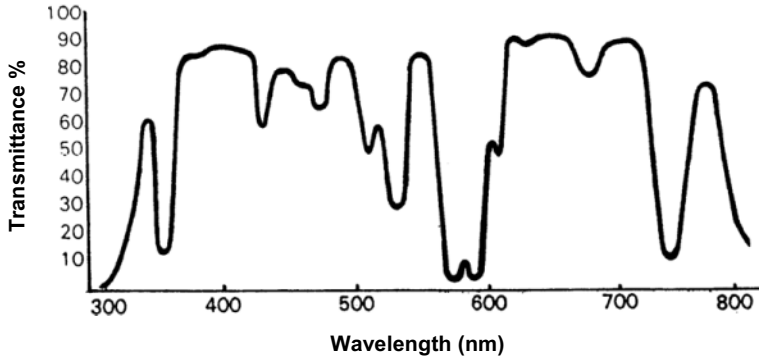

Figure 9-17. Transmission spectrum of a glass colored with 2.5% Nd_2O_3.

With an absorption zone at 450nm (Figure 9-18), praseodymium gives light and bright green tones.

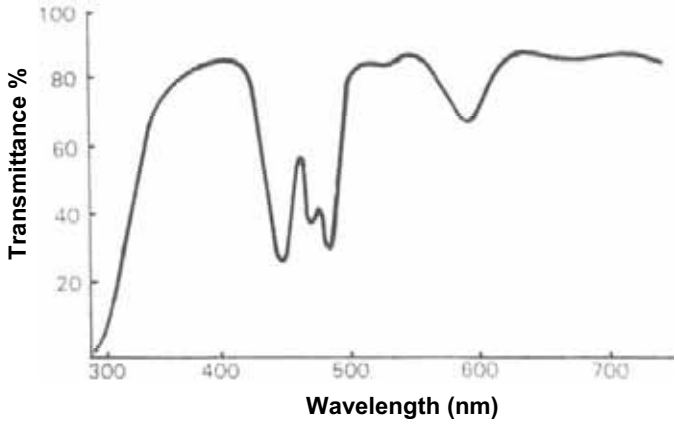

Figure 9-18. Transmission spectrum of a glass colored with Pr_6O_{11}.

Thanks to Erbium a specific light pink shade can be obtained, characterized by an absorption peak at 525nm (Figure 9-19).

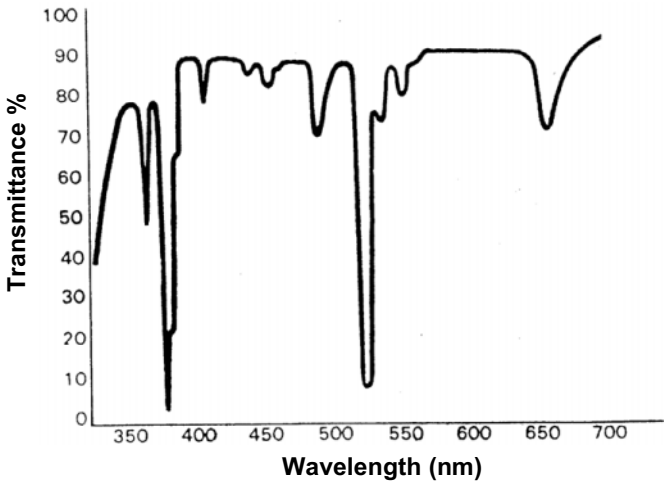

Figure 9-19. Transmission spectrum of a glass colored with Er_2O_3.

9.3.1.2. Glass discoloration

As some impurities may remain in the glass, namely iron oxides FeO or Fe_2O_3, an undesirable coloration can be observed, which can be eliminated in two steps:

- first chemical action followed by
- secondly physical discoloration

The tetravalent cerium ion in CeO_2 acts as an oxidizing agent relative to Fe^{2+}:

$$Fe^{2+} + Ce^{4+} \rightarrow Fe^{3+} + Ce^{3+}$$

The deep blue color of FeO disappears and turns into the light yellowish shade of Fe_2O_3. The resulting yellowish tone is eliminated with an element absorbing light in the yellow range of the visible light. Neodymium, possibly completed by Erbium in the case of greenish tone, provides the adequate spectrum and preserves the transparency of the glass.

9.3.1.3. Special Glasses

Rare Earths are also used to tune properties of glass for a series of applications like optical glass, irradiation stabilized glass, Laser glass, optical fibers [23].

Lanthanum oxide (La_2O_3) is thus widely added to increase refraction index and decrease light scattering in optical pieces like lenses and prisms. Cerium oxide (CeO_2) stabilises glass towards strong irradiation and avoids consequent darkening effect on CRT screens for example. Cerium is also recognized as an UV filter. Used at ca. 1%, neodymium enhances contrast and allows better image quality without changing colors. High purity neodymium also used, is certain types of laser glass.

9.3.2. *Glass polishing*

Cerium oxide is of major importance in the glass industry because of its ability to polish glass, thanks to its natural hardness and to the chemical reaction [24, 25] that takes place at the interface between the glass silica substrate and the cerium oxide particles. This reaction occurs in water and involves the creation of a silicate stratum which makes the glass surface more fragile and less resistant to mechanical erosion and physical modifications.

Cerium oxide powders can be incorporated into synthetic polishing pads or wheels or more frequently they are used in aqueous slurry fed onto the polishing tool. Cerium oxide polishing powders are thus traditionally used in numerous applications like spectacles, precision optics lenses for camera, CRT displays. Their role is to remove damaged layers of glass resulting from previous operations (moulding, grinding) and provide a smooth and glossy surface. Performance criteria are removal rate (ability to remove a certain amount of glass in a given time) and surface quality.

9.3.2.1. Removal rate

Removal rate is resulting from:

- first polishing powder characteristics
- second polishing conditions

Based on long experience of Rare Earths technology, it becomes possible to design ceria powders with proper physical properties for polishing applications, namely hardness, morphology and particle size distribution as shown in Figure 9-20.

Polishing conditions are driven by productivity and quality targets defined by the glass polisher and the equipment (machine, pad) used. They may also be adjusted depending on glass type. Speed, pressure, and slurry concentration are obvious key parameters, but water hardness and slurry temperature also influence polishing efficiency as shown in Figure 9-21.

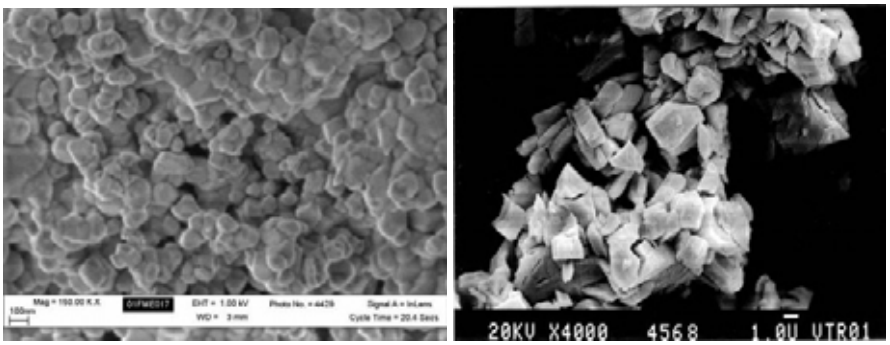

Figure 9-20. Morphology of cerium oxide powders tuned for polishing; cerium oxide powder composed of aggregates of fine and round particles (left) and cerium oxide powder composed of large and sharp edges particles (right).

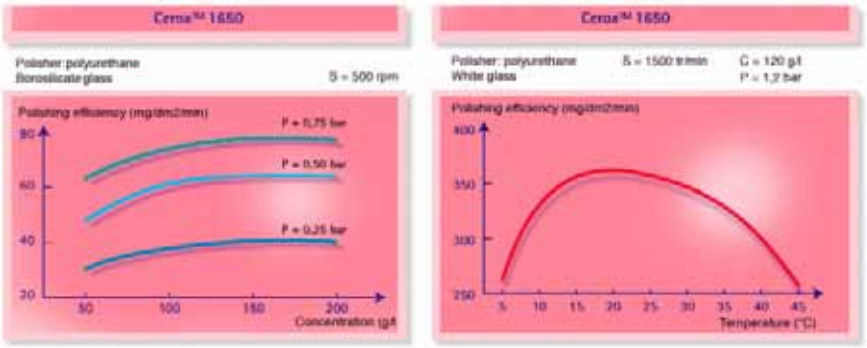

Figure 9-21. Influence of operating conditions on polishing efficiency.

9.3.2.2. Surface quality

A glossy and defectless surface is expected after polishing. Scratches, spots and any other marks coming either from previous operating steps or from polishing can cause rejection of glass piece. Glass should also be perfectly clean. Surface quality is often judged visually, usually under specific illumination conditions.

Surface quality is the consequence of:

a) processing steps prior to polishing
b) proper polishing and handling conditions
c) absence of contamination
d) quality of polishing powder.

Finer particles tend to give better surface quality. Hard particles and contamination should also be eliminated from the product are they can scratch the surface.

With evolution of technologies and markets, cerium oxide polishing powders, are now used for demanding applications like photomasks, LCD displays and glass hard disks. In these markets control of the surface quality, roughness and flatness is critical for the end application. LCD industry for example requires surface polishing prior to ITO (Indium Tin Oxide) sputtering. Not only the glass substrate must be free of any scratch and residue, but it must also comply with precise specifications of roughness. Surfaces are first examined visually, and evaluated more accurately with surface analysers, which can detect microscratches and measure roughness properties of the surface as shown in Figure 9-22.

In order to answer technical needs generated by these developing markets, polishing powders producers are challenged to tune and develop high performance products.

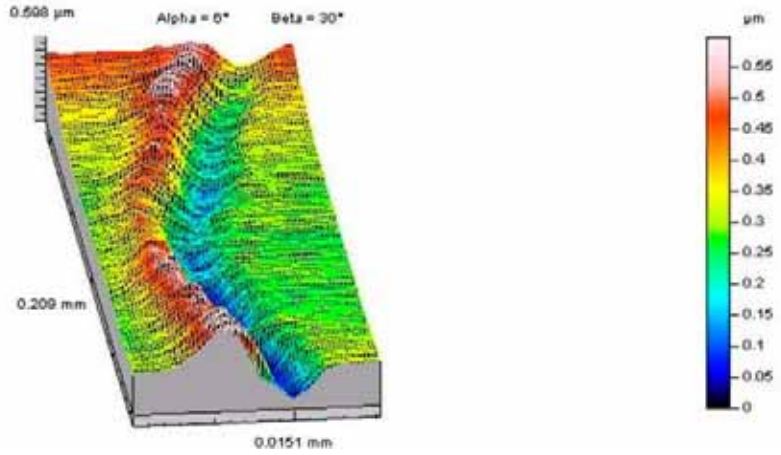

Figure 9-22. Surface quality after polishing, an example of a scratch.

9.4. FUEL CELLS

9.4.1. *Introduction to fuel cells*

Fuel Cells (FCs) convert the primary energy released by an electrochemical reaction directly into electric power and heat.The inherent efficiency and design flexibility of fuel cells, offers the solution to some of tomorrow's power generating needs. For example, since FCs operate as standalone units, electric power generation can be decentralized, simplifying the task of powering isolated facilities. FCs are also likely to be used in transportation, as they produce clean power, without excessive CO_2 emissions and with minimal atmospheric pollution, helping to limit greenhouse gases.

Fuel cells can be classified by the kind of electrolyte, there are Alkali fuel cells (AFCs), Polymer electrolyte fuel cells (PEFCs), Phosphoric acid fuel cells (PAFCs), Molten carbonate fuel cells (MCFCs) and Solid oxide fuel cells (SOFCs).

9.4.2. *Principle of SOFCs*

The electrochemical reaction in SOFCs is the reverse reaction of the electrolysis of H_2O. Gibbs free energy for the electrochemical reaction between hydrogen and oxygen is used as electricity.

Figure 9-23 shows the principle of SOFCs using oxide ion conductive electrolyte. Oxygen gas introduced to cathode receives the electron on the electrode and changes oxide ion, as shown in the next formula.

$$O_2 + 2e^- \rightarrow O^{2-}$$

The oxide ion diffuses in electrolyte and the electrochemical reaction between hydrogen and oxygen occurs on anode.

$$O^{2-} + H_2 \rightarrow H_2O + 2e^-$$

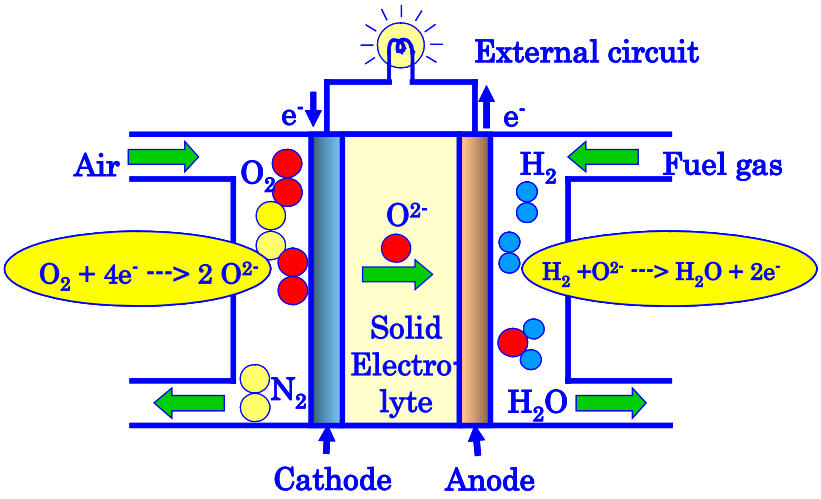

Figure 9-23. Basic principle of SOFC.

System design, performance and cost of such SOFC depend on the properties of innovative materials and advanced ceramics. The careful design and manufacture of these materials is essential to system integration and performance, and may ultimately determine the success or failure of the technology. Important factors include; stability, durability, processibility catalytic, electro-chemical and ionic properties. Figure 9-24 shows SEM image of ceramic layers used in a SOFC cell.

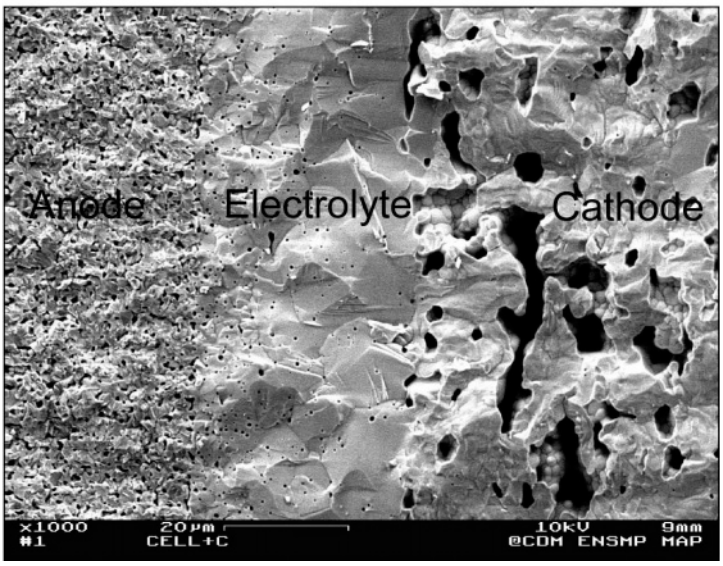

Figure 9-24. SEM image of the structure of ceramic layers used in a SOFC cell.

9.4.3. *Use and Role of Rare Earths in SOFCs materials*

9.4.3.1. Use of Rare Earths

Due to their chemical and physical properties, rare earth compounds, zirconia and other metal elements are key elements for this application and are used in all the different strategic components of the SOFC: solid electrolyte, electrodes and interconnector (Table 9-2).

The development of mass applications now requires large amounts of advanced high performance ceramics powder presenting a higher reactivity and a better phase purity.

For medium and low temperature operating conditions, cerium oxide doped with other rare earth elements (such as Gadolinium, Samarium or Yttrium) are very good candidates as electrolytes or anode materials. Traditional preparation routes such as solid state reactions starting from separated oxides did not allow achieving a good phase purity excepted at very high temperatures. The reactivity of the corresponding ceramics powders was then very low, limiting thus their sinterability (their ability to be transformed into dense thin layers).

As mentioned in Table 9-2, different perovskite compounds are used as cathode or interconnector materials.

TABLE 9-2. Rare earth oxides in SOFCs.

	High Temperature T > 750 ºC	Middle Temperature 750 > T > 600 ºC	Low Temperature 600 > T > 500 ºC
Anode	$Ni\text{-}ZrO_2{:}Y_2O_3$	$Ni\text{-}ZrO_2{:}Y_2O_3$ $Ni\text{-}YSZ{:}CeO_2$	$Ni\text{-}CeO_2{:}Ln_2O_3$ $TM\text{-}CeO_2{:}Ln$
Electrolyte	$Y_2O_3{:}ZrO_2$ $Sc{:}ZrO_2$	$Sc{:}ZrO_2$ $(La, Sr)(Ga, Mg)O_3$	$(La, Sr)(Ga, Mg)O_3$ $Gd{:}CeO_2$
Cathode	$(La, Sr)MnO_3$	$(La, Sr)(Fe, Co)O_3$	$(La, Sr)(Fe, Co)O_3$
Bipolar Plate (interconnect)	$(La, Sr, Ca)CrO_3$	Alloys (Y_2O_3)	Stainless Steel

9.4.3.2. Role of rare earths

Rare Earths are used in SOFCs because they give compounds with stable ionic or electrical conductive materials at high temperature. The crystal structure of typical materials contained Rare Earths for SOFCs are shown in Table 9-3. The classified crystal structures are fluorite structure and perovskite structure. In Table 9-3, Rare Earths except for Ce^{4+} have 3 valences and could be the dopant for the solid solution. For fluorite, a part of Zr^{4+} or Ce^{4+} is substituted by RE^{3+} (Rare Earths with 3 valences) or AE^{2+} (alkali earth metal with 2 valences), which has similar ionic radius and stable valence. The ionic radius of Ce^{4+} is larger than that of Zr^{4+}. CeO_2 shows the cubic fluorite structure at temperature range, from room temperature to melting point, although there is no dopant in CeO_2. RE^{3+} doped ceria has higher oxide ion conductivity than YSZ.

TABLE 9-3. Crystal structure of typical materials contained rare earths for SOFCs.

	Ionic conductor (Electrolyte)	Electronic conductor (Electrodes, Interconnector)
Fluorite structure	RE_2O_3 stabilized ZrO_2 $(CeO_2)_{1-x}(REO_{1.5})_x$	
Perovskite structure	$La_{0.8}Sr_{0.2}Ga_{0.8}Mg_{0.2}O_3$ $A(CeRE)O_{3-\delta}$ (A = Sr, Ba; RE = Y, Gd, Dy)	$(REA)MnO_3$ (RE = Y, La, Pr, Ce; A =Ca, Sr) $(REA)(CoB)O_3$ (RE = La, Gd; A = Sr ; B = Fe) $(LaA)(CrB)O_3$ (A =Ca, Sr ; B = Co, Ni, Fe, Mg)

Pyrochlore structure oxides have also oxide ion conductivity. The crystal structure of pyrochlore is similar to that of fluorite, and the 1/8 of oxygen in fluorite structure is removed regularly. The pyrochlore structures change to fluorite structures through order-disorder transition at high temperature, and then the high oxide ion conductivity similar to yttria stabilized zirconia (YSZ) appears. Although there are many fundamental data for crystallographic properties of $Ln_2Ti_2O_7$ pyrochlores with a stoichiometric composition [26, 27], few papers for non-stoichiometric $Gd_2Ti_2O_{7-\delta}$ have been published on the relationship among crystal structures, sintering characteristics, electrical conductivity and thermal expansions of the pyrochlores.

In the case of perovskite structure, a part of Rare Earths or transition metal is substituted by alkali earth metal. The positive charge for fluorite and perovskite is deficient because of the substitution for the both of fluorite and perovskite. The charge in crystal is kept neutral by the formation of oxygen vacancy for fluorite. And the valence change of transition metal for perovskite keeps the neutral charge in crystal. As a result, the oxide ion conductivity in fluorite structure and the electrical conductivity in perovskite appear.

The characteristics of Rare Earths are the large ionic radius similar to oxide ion, the stable valence and the unpaired electron in 4f-orbital. Especially, the large ionic radius and the stable valence contribute to the oxide ionic or the electrical conduction of materials for SOFCs.

9.4.4. *Requirements and new solutions of materials for SOFCs*

SOFCs consist of cells and electrical interconnectors cells itself consist of electrolyte, anode and cathode. The SOFCs components using Rare Earths are shown in Table 9-2 and Table 9-4.

9.4.4.1. New materials for electrolyte

For electrolyte, the high conductivity and dense ceramics are required. A proprietary new wet chemistry route has been developed [28-30], which allows to reach at lower temperature both good crystallographic phase purity and good sinteribility (Figure 9-25).

9.4.4.2. New materials for anode; Ni CGO composite

Porous ceramics, with high electronic conduction and chemical stability in the fuel gas are required for anode and cathode. The electrode should be porous and have homogeneous microstructures because the electrode reaction occurs on three phase boundary (TPB), which consists of electrolyte, electrode and gas. The reaction site increases with TPB length. Using a new technique of spray dry process, a new

TABLE 9-4. The SOFCs components using Rare Earths.

	Materials	Composition	Characteristics
Electrolyte	ZrO_2	Y_2O_3 stabilized ZrO_2 (YSZ)	Basic material
		Al_2O_3 mixed YSZ	To strengthen
		Yb_2O_3 stabilized ZrO_2	Higher ionic conductivity, higher power density, lowering of operation temperature
		Sc_2O_3 stabilized ZrO_2	
	CeO_2	$(CeO_2)_{1-x}(REO_{1.5})_x$ (RE=Y, Sm, Gd)	
	$LaGaO_3$	$La_{0.8}Sr_{0.2}Ga_{0.8}Mg_{0.2}O_3$	
	$ACeO_3$ (A=Sr, Ba)	$A(CeRE)O_{3-\delta}$ (A=Sr, Ba: RE=Y, Gd, Dy)	Proton cinductor
Anode	Ni	Ni-YSZ	Basic material
		Ni-MgO-YSZ	Long term stability, to prevent the sintering of Ni
		Ni-CeO_2	Low over potential, high reforming activity for fuel
		Ni-$(CeO_2)_{0.8}(SmO_{1.5})_{0.2}$	
		Ni-Pr_6O_{11}	
	Ru	Ru-YSZ	
	TiO_2	TiO_2-YSZ	Chemical stability, high reforming activity for fuel
	$LaCrO_3$	$(La_{0.8}Ca_{0.2})CrO_3$	
Cathode	$REMnO_3$	$(RESr)MnO_3$	Basic material
		$(PrSr)MnO_3$	Low over potential at low temperature
		$(REA)MnO_3$ (RE=Y, La, Pr, Ce: A=Ca, Sr)	Cost reduction
		$\{(La_{0.6}Y_{0.4})_{0.8}Sr_{0.2}\}MnO_3$	Compatibility of TEC for YSZ
		$(GdA)MnO_3$ (A=Ca, Sr)	To prevent the reaction with YSZ
	$RECoO_3$	$(LaSr)CoO_3$	High electronic conductivity
		$(GdSr)CoO_3$	To prevent the reaction with YSZ
		$(LaSr)(CoFe)O_3$	Low over potential at low temperature
Interconnector	$RECrO_3$	$(LaA)(CrB)O_3$ (A=Ca, Sr: B=Co, Ni, Fe, Mg)	Basic material
		$La(CrMg)O_3$	Low lattice expansion under reducible atmosphere
		$(LaCa)(CrCoFeNi)O_3$	Inmprovement of sinterability
	CrFe alloy	$(CrFe)_5(Y_2O_3)_1$	Low TEC alloy

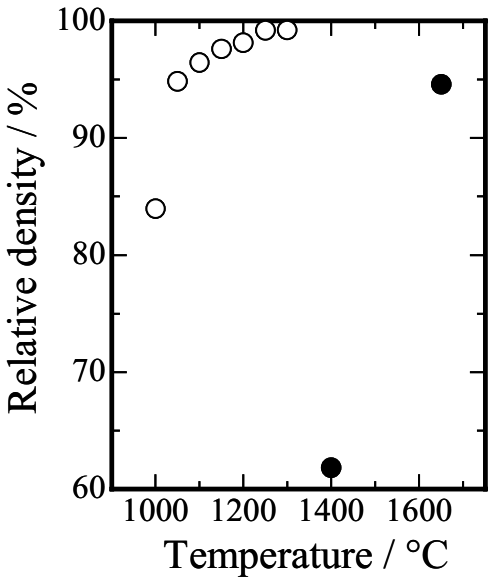

Figure 9-25. Relative density of $Ce_{0.9}Gd_{0.1}O_{1.95}$ powder as a function of temperature. Open circles and closed circles represent co-precipitation method and solid state technique, respectively.

composite of 50 vol % Ni-$Ce_{0.9}Gd_{0.1}O_{1.95}$ (CGO) cermets for anode materials at intermediate and low temperature SOFCs has been developed [31]. Such a composite gave a microstructure of anode ceramic part more homogeneous than the one obtained with conventional ball mill process as shown on Figure 9-26. Such materials proved to have a higher performance; much lower over-potential and ohmic loss (see Figure 9-27).

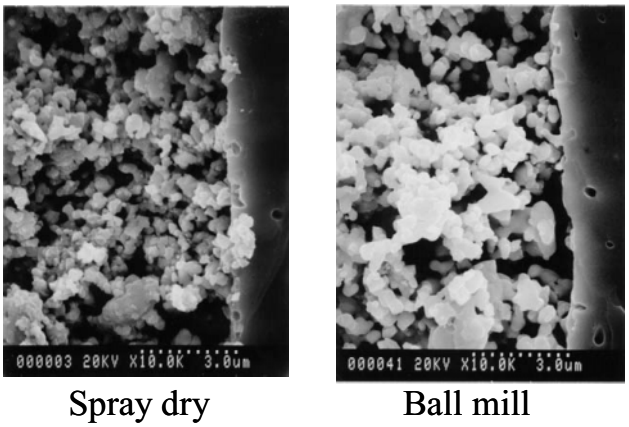

Figure 9-26. SEM micrographs of cross section of anodes produced at 1300°C.

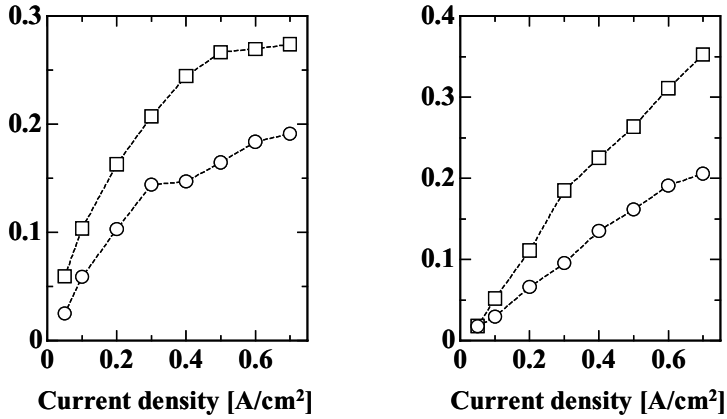

Figure 9-27. Electric performance of NiO-CGO anodes made at 1300ºC. NiO-CGO powders were prepared by various synthesis methods; circles and squares represent spray dry and ball mill, respectively.

9.4.4.3. New perovskites for electrolyte, electrodes, and interconnectors

As mentioned in Table 9-2, different perovskite compounds are used as cathode or bipolar plates materials.

An industrial process to prepare those materials with well controlled composition has been developed, particle size, surface area, and phase purity. The resulting application properties are superior to conventional products obtained by solid state routes. Table 9-5 gathers the typical characteristics of such compounds. An example of a study conducted on lanthanum chromite is given in reference 32. New lanthanum manganite products were also patented [33].

TABLE 9-5. Characteristics of various perovskites commercially available.

	Sample	Specific surface area ($m^2 \cdot g^{-1}$)	D50 (µm)
Electrolyte	$La_{0.9}Sr_{0.1}Ga_{0.8}MgO_{3-\delta}$	23.0	1.6
	$BaCe_{0.8}Gd_{0.2}O_{3-\delta}$	5.5	0.7
Electrode	$La_{0.86}Sr_{0.14}MnO_{3-\delta}$	3.0	2.4
	$La_{0.6}Sr_{0.4}Co_{0.2}Fe_{0.8}O_{3-\delta}$	8.0	1.0
Interconnector Separator	$(La, Sr)CrO_{3-\delta}$	2.7	2.9

9.5. SOLID ELECTROLYTES

9.5.1 *Yttria stabilized zirconia*

Solid electrolytes are one of functional materials which only single ion species can generally migrate in solid and are greatly expected to be applied for the electrical devices such as all solid-state batteries and chemical sensing devices

utilizing their unique characteristics. After discovering the O^{2-} ionic conducting ZrO_2 doped with a small amount of Y_2O_3 as an electric light which called "Nernst glower" in 1897, many kinds of solid electrolytes have been extensively developed. This material is now well known as YSZ (yttria stabilized zirconia) which is commercially applied for oxygen gas sensor.

The O^{2-} ion conduction in YSZ was firstly demonstrated by Nernst in 1899 [34]. The minimum content of Y_2O_3 doped in the host ZrO_2 is 9 mol% for the stabilization of the cubic fluorite phase. The solution of Y_2O_3 in ZrO_2 becomes possible because of the structural similarity between cubic ZrO_2 and cubic C-type rare-earth oxides. In the case of the La^{3+} doping, however, a pyrochlore phase of $La_2Zr_2O_7$ is dominantly produced because of the large ionic size of La^{3+}. Among the rare earth ions, the most interesting dopant cation is Sc^{3+}. Since the ionic radius of Zr^{4+} (0.098 nm; CN = 8 [35]) and Sc^{3+} (0.101 nm; CN = 8 [35]) are similar, it is enough for only 6% Sc^{3+} to fully stabilize the fluorite phase. In the ZrO_2-R_2O_3 series, the fluorite-type solid solutions have a maximum conductivity at 8-10 mol % $RO_{1.5}$ (R = Nd-Lu, Y, Sc) at compositions corresponding to near the lower fluorite phase boundary, and an increase in rare-earth doping decreases the conductivity. Since the ionic radii of rare earth ions are larger than that of Zr^{4+}, the free volume for oxide ion migration decreases with the increase of the rare earth content. The oxide ion conductivity linearly increases with reducing ionic radius of the dopant rare earth in the sequence Nd < Gd < Dy < Ho = Y < Er < Yb < Lu < Sc as expected [36]. Among the rare-earth doped stabilized zirconia series, the highest ion conductivity was obtained for the ZrO_2-Sc_2O_3 system. On the contrary to the highest oxide ion conductivity, the critical disadvantage of low stability of the solid solution exists in this material. Details of each ZrO_2-R_2O_3 series are available in the references.

In the 20^{th} century, many kind of conducting ion species from monovalent to tetravalent ions have been discovered as well as a large number of host crystal lattices. Although some binary rare earth oxides for solid electrolytes have also been investigated, their ion conducting properties were, unfortunately, not enough except the ceria-based materials.

9.5.2. *Solid electrolytes based on ceria*

Cerium oxide, ceria, has a fluorite structure and shows oxide anion conducting behavior differ from other rare earth oxides. However, the O^{2-} ionic conductivity of pure ceria is low because of a lack of oxide anion vacancies. For ion conduction, especially for anion, it is important to have such an enough vacancy in the crystal lattice for ion conduction. Therefore, the substitution of tetravalent Ce^{4+} by a lower valent cation is applied in order to introduce the anion vacancies. For the dopant cation, divalent alkaline earth metal ions and some rare earth ions which stably hold trivalent state are usually selected. Figure 9-28 shows the dopant ionic radius dependencies of the oxide ionic conductivity for the doped ceria at 800°C. In the case of rare earth doped CeO_2, the highest O^{2-} ion conductivity was obtained for

Sm^{3+} doped CeO_2 [36]. The conductivity of $Ce_{1-x}Gd_xO_{2-x/2}$ solid solution even at 700°C, which is the secondly highest O^{2-} ion conductivity among the $Ce_{1-x}R_xO_{2-x/2}$ (R: rare earths) series, shows a comparable conductivity to that of the stabilized zirconia at 1000°C. In the case for doping the divalent alkaline earth metal ions into CeO_2, the maximum conductivity was realized for Ca^{2+} which has almost the same ionic radius as Sm^{3+}, although the conductivity was lower than those of rare earth doped ceria. These phenomena clearly indicate that the oxide ion conduction in the doped ceria depends on the ionic radius of the dopant cation as well as the valence.

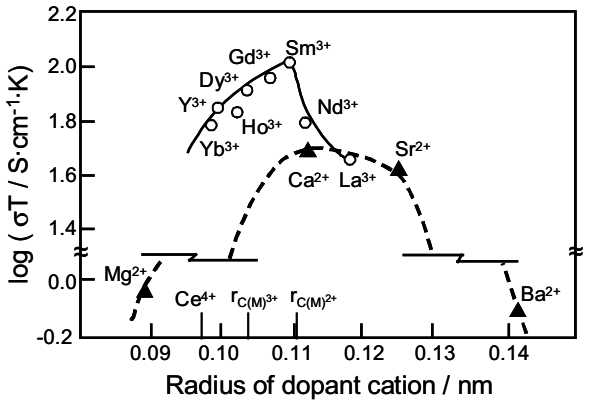

Figure 9-28. The dopant ionic radius dependencies of the oxide ionic conductivity for the doped ceria at 800°C. (Reprinted with permission from ref 36. Copyright 1996 Elsevier Science B.V.)

The range of the oxygen partial pressure where the rare earth doped ceria exhibits oxide anion conduction is limited over 10^{-8} Pa in Po_2 at 800°C (The oxide anion transference number decreased to 0.5 at this condition.), whereas the well-known stabilized zirconia shows the stable ion conduction between 10^{-15} and 10^{15} Pa. This low stability against reducing atmosphere observed in the rare earth doped ceria is a fatal problem for applications.

As described in the previous section, oxide ion conducting solid electrolytes have been focused on a component of solid oxide fuel cells (SOFCs) from 1970's, and YSZ is mainly investigated as a candidate of the solid electrolyte because of the high O^{2-} ion conductivity and high chemical stability under both oxidizing and reducing atmospheres at high temperatures. However, it is necessary for obtaining the applicable O^{2-} ion conductivity to heat up the solid electrolyte to ca. 1000°C. One approach to reduce the inner cell resistance is to reduce the thickness of the YSZ layer, and another way is to employ a new ionic conductor with higher ionic conductivity than YSZ even if its oxide ion conductivity is lower than those for above mentioned doped ceria. This is because ceria is easily reduced in reducing atmosphere of the fuel side, and a consequent appearance of considerable electronic conduction causes the power loss. Furthermore, the oxide lattice is expanded by the

formation of oxygen vacancies and serious problem such as bend is caused at the anodic fuel gas side according to the following equation.

$$2CeO_2 \rightarrow 2Ce_{Ce}' + 3O_O\times + V_O\ddot{} + 1/2O_2$$

Therefore, it is not suitable to use ceria based solid electrolytes in the cell type shown in Figure 9-23. However, in the case for the other types shown Figures 9-29(a) and (b) [37], both the cathode and the anode are in the same atmosphere where air and fuel gas exist at the same time. Therefore, the volume change of the cell becomes negligible and it is greatly expected to apply the Sm-doped ceria which shows higher oxide ion conductivity than that of YSZ at intermediate temperature.

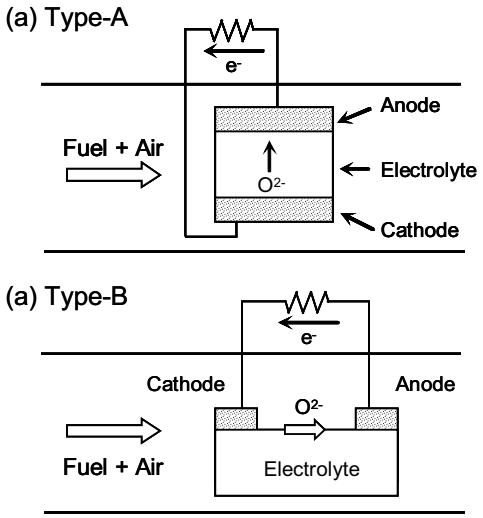

Figure 9-29. The basic structures of the single chamber type SOFC. (Reprinted with permission from ref 37. Copyright 2003 T.I.C)

Figure 9-30 shows the I-V characteristics at 500°C for the SOFC cell using $Ce_{0.8}Sm_{0.2}O_{1.9}$ as a solid electrolyte. In this condition, Ce^{4+} was not reduced at all and considerably large current density was obtained in comparison with the case for YSZ. Therefore, it is possible to operate the cell at low temperatures below 773 K. Considering the power density of the single chamber type of SOFC cells, the further improvements are necessary for the practical use, because the power density of the cell with $Ce_{0.8}Sm_{0.2}O_{1.9}$ (281 $mW \cdot cm^{-1}$ at 500°C) is still lower than that (1 $W \cdot cm^{-1}$) of the high temperature SOFC with YSZ which is composed of the dual chamber cell operating at around 1000°C.

For the practical application of the oxide ion conducting solid electrolytes for the SOFCs, there is another problem that they usually need high operation temperature over 800°C. In fact, the SOFCs based on the YSZ thin film electrolyte cannot provide acceptable power output due to the fundamental limit of YSZ that it is difficult to obtain enough conductivity below 650°C. The ceria-based oxides are,

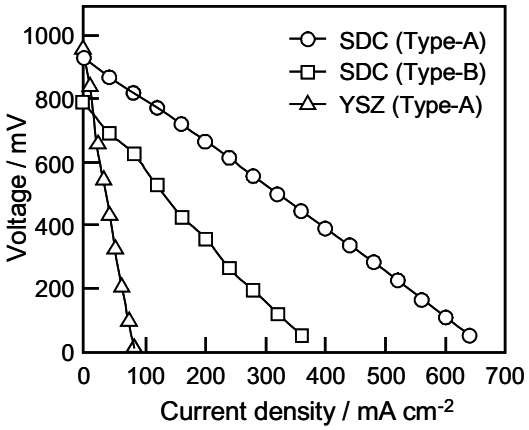

Figure 9-30. I-V characteristics at 500°C for the single chamber types of SOFC cell with $Ce_{0.8}Sm_{0.2}O_{1.9}$ as a solid electrolyte: Ni-$Ce_{0.8}Sm_{0.2}O_{1.9}$ | $Ce_{0.8}Sm_{0.2}O_{1.9}$ | $Sm_{0.5}Sr_{0.5}CoO_3$. The thickness of the SDC was 0.5 mm and the mixture gas of ethane and oxygen (1:1 in a molar ratio) flowed into the chamber. (Reprinted with permission from ref 38. Copyright 2001 The Ceramics Society of Japan)

therefore, commonly attracted as the alternative SOFC materials. However, as mentioned above, the pure ceria cannot be applied because of its critical problems concerning reduction. On the contrary, the doped ceria materials show high conductivity of ca. 0.1 $S \cdot cm^{-1}$ at 800°C which is equal to that of the YSZ at 1000°C. Although the ceria-based materials are strongly expected to be a component of the SOFCs operated at low temperatures around 600°C, the ion conductivity reduces to 5×10^{-3} $S \cdot cm^{-1}$ at 600°C which does not satisfy the required conductivity level of 0.1 $S \cdot cm^{-1}$. In addition, the problem on the reduction of Ce^{4+} to Ce^{3+} is also remained in these materials [39].

9.6. SUNSCREEN COSMETICS

9.6.1. *CeO_2 for sunscreens*

Although exposure of the human body to sunlight to attain a tanned look has been fashionable in recently, the UV-ray included in the sunlight causes damaging effects on human's skin. In order to protect us from such the harmful problems, many kinds of organic and inorganic sunscreen materials have been developed. Among them, organic UV absorbers show effective UV-B (290–320 nm) absorption property, but with modest UV-A (320–400 nm) absorbing ability, and some of the organic filters have caused irritation on the skin of sensitive individuals [40]. Therefore, they may pose a safety problem when used at high concentrations. In addition, some organic UV filters are not photostable.

In the case of the inorganic sunscreens, fine particles of titanium oxide (TiO_2) and zinc oxide (ZnO) are effective and are popularly used in the cosmetics [41]. Although titanium oxide is the most popular inorganic sunscreen agent, it is known

that TiO_2 is an excellent photocatalyst [42], which can oxidize sebum and degrade other ingredients in the sunscreen cosmetics. In addition, titanium oxide may cause the user's skin to look unnaturally white when incorporated into sunscreen products, due to the high refractive index (2.6-2.7). ZnO is another widely utilized sunscreen agent, but it also possesses photo- and thermal catalytic properties [43].

On the other hand, cerium oxide (CeO_2) has characteristics ideal for use as a broad-spectrum inorganic sunscreen for cosmetics, because it is not only transparent to visible light but also has excellent ultraviolet radiation absorption properties, due to the appropriate refractive index (2.1) [44] and the bandgap energy (3.1eV) [45], respectively. In addition, the photocatalytic activity of CeO_2 is much lower than those of TiO_2 and ZnO. However, because of the high thermal catalytic activity for oxidation of organic materials, ceria has not been used commercially as a sunscreen material.

In order to overcome this problem and to develop a safe and stable inorganic sunscreen with superior UV absorption capability, the catalytic activity of CeO_2 has been successfully decreased by coating the surface with amorphous silica (SiO_2) [46, 47] or boron nitride (BN) [48, 49] without decreasing the UV shielding property of CeO_2. Figure 9-31 shows the transmittance spectra of a 0.25 mm thick wax base film containing $0.7CeO_2$-$0.3SiO_2$ composite, compared with those of the micronized TiO_2 and ZnO samples [47]. The concentrations of these particles are 20%, 4%, and 10%, respectively, adjusting to give the same transparent level in the visible region for all the films. Compared with these samples, only the $70\%CeO_2$-$30\%SiO_2$ composite exhibits both high transparency in the visible region and good absorption in the ultraviolet region.

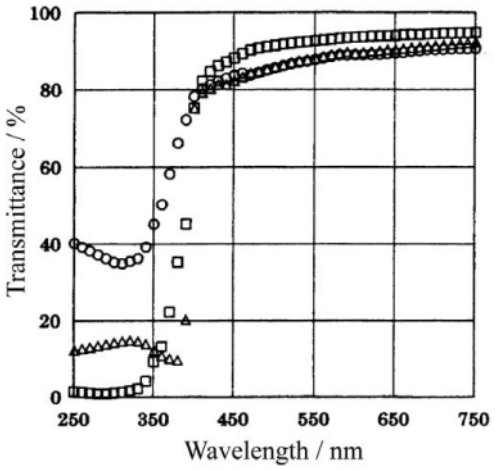

Figure 9-31. Transmittance spectra of thin films containing with 20% $0.7CeO_2$-$0.3SiO_2$ (□), 4% TiO_2 (○), and 10% ZnO (Δ). (Reprinted with permission from ref 47. Copyright 1998 Japanese Cosmetic Science Society)

Figure 9-32 depicts the reflectance spectra of the pressed powders of the BN/CeO_2 and CeO_2 samples [49]. In these spectra, low reflectance means high absorption in the corresponding wavelength region. Although the absorption spectrum of the BN/CeO_2 slightly blue-shifted compared with that of CeO_2, it maintained good absorption behavior in the ultraviolet region. A representative TEM image of the BN/CeO_2 particles is depicted in Fig. 9-33 [48]. The powder consists of CeO_2 nanoparticles of 20–50 nm, and neither aggregation nor agglomeration was observed. The inset picture shows the top surface of a BN/CeO_2 particle and existence of a very thin BN layer is recognized, where the BN layer covering the CeO_2 particles was in a few nanometer's thickness.

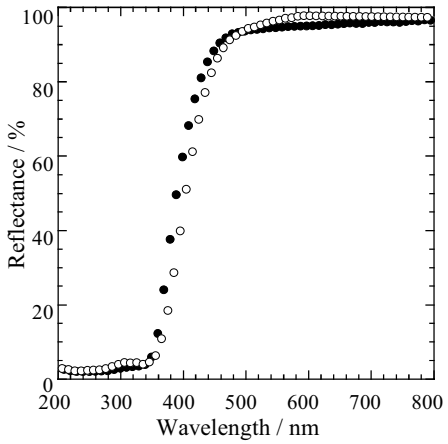

Figure 9-32. Reflectance spectra of the BN/CeO_2 (●) and uncoated CeO_2 (○). (Reprinted with permission from ref 49. Copyright 2003 The Royal Society of Chemistry)

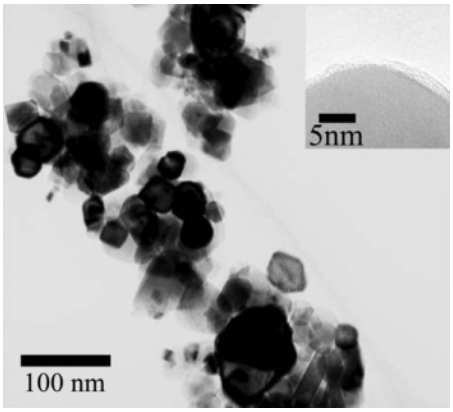

Figure 9-33. Transmission electron microscopic image of CeO_2 nanoparticles coated with boron nitride. The inset high-resolution image shows that the surface of the CeO_2 particles is covered with a very thin layer. (Reprinted with permission from ref 49. Copyright 2003 The Royal Society of Chemistry)

9.6.2. *Modification of CeO_2*

In another way for depressing the catalytic activity of CeO_2, doping a metal ion possessing lower valence and/or larger ionic size than those of Ce^{4+} into CeO_2 lattice has been proposed [50-53]. Figure 9-34 shows the catalytic activity which was evaluated by measuring the increase in the conductivity of distilled water by trapping volatile molecules formed by the oxidation of castor oil on heating. In this figure, low conductivity means low catalytic activity. The catalytic activity for the air oxidation of castor oil at 120ºC decreased substantially by doping with Ca^{2+} and Zn^{2+}. Doping Nd^{3+}, Sm^{3+}, and Eu^{3+} also resulted in a decrease in the catalytic activity, but the decrease was not so significant as in case of doping Ca^{2+}.

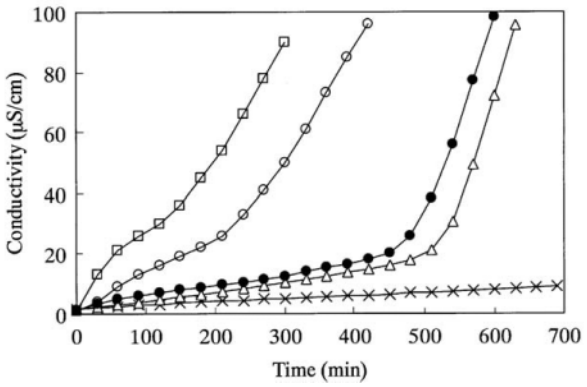

Figure 9-34. Evaluation of the catalytic activity at 120ºC. ×: blank (without catalyst), □: undoped CeO_2, Δ: 20mol% Ca^{2+}-doped CeO_2, ●: 20mol% Zn^{2+}-doped CeO_2, and ○: 30 mol% Eu^{3+}-doped CeO_2. (Reprinted with permission from ref 53. Copyright 2003 Elsevier Science)

The effect of the dopant was considered in relation to the formation of oxide ion vacancies and simultaneous oxygen evolution. The equilibrium reaction of the oxygen evolution and absorption in CeO_2 is expressed by the following equation.

$$CeO_2 = Ce^{4+}_{1-x}Ce^{3+}_{x}O_{2-x/2}\square_{2-x} + x/4O_2 \qquad (9.1)$$

$\square$: Oxygen defect; $0 < x < 1$

The ideal $r(M^{n+})/r(O^{2-})$ ionic size ratio of MO_8 eight coordination oxide is 0.732. However, $r(Ce^{4+})/r(O^{2-})$ is 0.703 in the case of CeO_2, which is smaller than that of the ideal value. This result suggests that Ce^{4+} is not large enough to stabilize the fluorite structure and it is reasonable that some Ce^{4+} have a tendency to be reduced to Ce^{3+} to take a more stable eight coordination of the fluorite structure, because Ce^{3+} (0.1143 nm) [35] has a larger ionic radius than Ce^{4+} (0.097 nm) [35]. By the doping of lower valence cations, oxygen molecules are released in advance to form oxygen vacancies. Therefore, the oxidation activity of CeO_2 can be depressed by doping lower valence cations. In addition, doping larger size cation is also suitable for stabilization of fluorite structure, and therefore, Ca^{2+} was considered to be the most effective dopant because it possesses a lower valence and larger ionic size than Ce^{4+}.

9.6.3. *New materials for sunscreens*

As mentioned above, ultrafine titanium oxide, zinc oxide, and recently cerium oxide have proven to be effective inorganic sunscreens and are widely utilized. However, it is imperative that the surface of these inorganic compounds be coated with an inert substance to minimize the catalytic activities. Recently, a series of amorphous phosphates of $Ce_{1-x}Ti_xP_2O_7$ have been developed as promising new materials for advanced sunscreens [54]. The UV absorption edge of these phosphates can be carefully manipulated to absorb at the desired range by simply adjusting the composition, from UV-B to UV-A (Fig. 9-35).

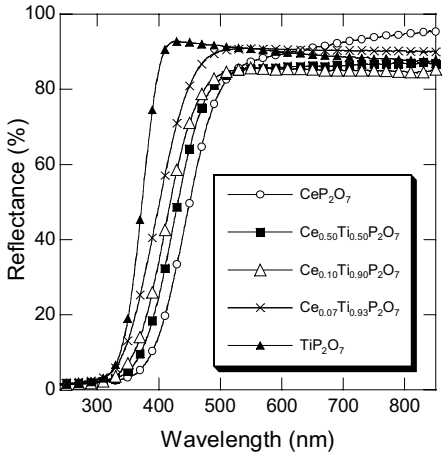

Figure 9-35. Optical reflectance spectra of the $Ce_{1-x}Ti_xP_2O_7$ sunscreens having various Ce/Ti ratios. (Reprinted with permission from ref 54. Copyright 2003 American Chemical Society)

Furthermore, metal phosphate is known as a component of bones and teeth, and therefore it is inert and safe with no known side effects to the human body. Not only are these metal phosphates stable, but they are also very inert and do not possess the ability to catalyze the formation of active oxygen species, as seen in several conventional oxide sunscreens.

9.7. ADDITIVE FOR THE IRON AND STEEL INDUSTRY

9.7.1. *Deoxygenation*

Rare earth metals have been used as additives in steel as deoxigenation and desulfurization agents, because the affinity of them with oxygen and sulfur is extremely strong. Compared with Ca and Mg, the rare earth metals are added more easily because of the higher melting point and lower vapor pressure. When the small amount of rare earth metals is introduced into iron and steel, they act as strong reductants and induce fine dispersion of oxide inclusions because of the high affinity of rare earth metals to oxygen [55].

For example, the addition of rare earths such as La and Ce decreased the strength of Fe and steel and in several cases resulted in the complete elimination of zonal segregation in the ingot [56]. The rare earth oxides formed were distributed in the ingot homogeneously for small amounts of rare earths, but they accumulated in the lower part of the ingot for high rare earth content. Modification of stainless steels by adding Fe-Ce (with 90% Ce) or rare-earth metal oxides reduced the number of surface defects of the steel arising in rolling [57]. The amount of the α-phase was reduced, and not only the corrosion resistance of the steel increased, but also the ductility and other mechanical properties were improved.

9.7.2. *Surface modification*

Deposition effects of rare earth oxides on the surface of iron and stainless steels have also been reported [58]. The corrosion rate constants decreased significantly by the coating in corrosion tests under isothermal conditions. In thermal cyclic conditions, protective scale spallation completely disappeared for coated samples. The rare earth effect is more remarkable with elements located on the left part of the lanthanide series (lighter rare earths). For example, ceria coatings strongly modify the microstructure and texture of the wustite (FeO) scale formed during low pressure oxidation of pure iron [59]. Cerium is located in the wustite matrix as a $CeFeO_3$ phase which dissolves in FeO in time.

Recently, laser cladding is becoming an effective way to produce a surface layer having good wear and corrosion resistant properties without dilution. The application of rare earth elements has been carried out on laser claddings containing CeO_2 [60] and La_2O_3 [61]. The wear and corrosion resistance of coatings can be remarkably increased by the addition of these oxides. The addition of La_2O_3 refines the microstructure, decreases the dendrite arm spacing, purifies the grain boundaries, and improves the coefficients of friction of laser clad coatings [61]. The corrosion rate of different laser coatings versus the corrosion time is depicted in Fig. 9-36.

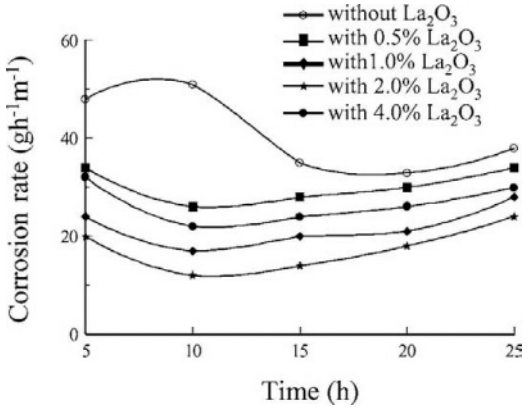

Figure 9-36. Effect of La_2O_3 on the corrosion rate of laser clad coatings. (Reprinted with permission from ref 61. Copyright 2003 Kluwer Academic Publishers)

The addition of the rare earth improves the corrosion resistance of the laser coatings. The microstructure becomes more compact by the refining and purifying effect of La_2O_3, which suppresses the corrosion.

9.8. BIOLOGICAL APPLICATION

9.8.1. *Radiotherapy for cancer*

Radiotherapy is one of the most effective treatments of cancers, but external irradiation often causes damage to healthy tissues. In order to avoid the external irradiation therapy, it has been reported that glass microspheres containing radioactive species are useful for in situ irradiation of cancers. For example, $17Y_2O_3$-$19Al_2O_3$-$64SiO_2$ (mol%) (YAS) glass microspheres are applied [62-64]. The glass whose size is 20 to 30 μm in diameter is insoluble in body fluids and non-toxic. Yttrium-89 in this glass is activated to ß-emitter ^{90}Y with a half-life of 64.1 h by neutron bombardment [65]. As shown in Fig. 9-37, the microspheres of the activated glass can give large local irradiation by short-ranged highly ionizing ß-ray to the tumors when they are injected into liver through the hepatic artery, with only a little radiation to the neighboring healthy organs. This glass has been subjected to clinical trials on the irradiation of diseased kidneys and liver cancer, and radiation synovectomy of arthritic joints [66-74]. In addition, the glass has already been used commercially in USA, Canada, and China [73].

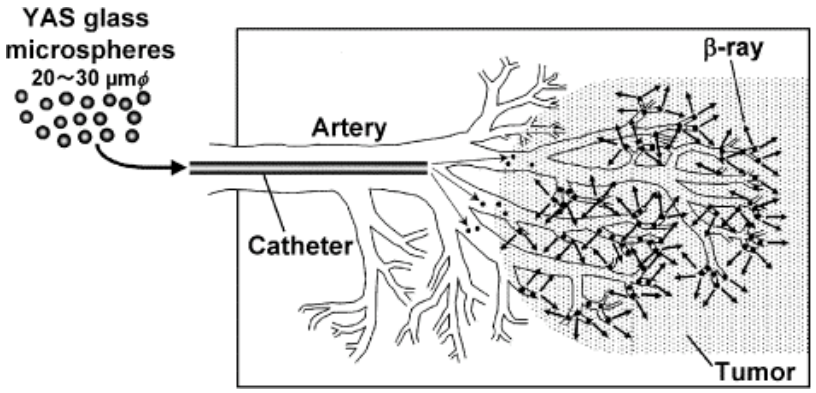

Figure 9-37. Cancer treatment with radioactive YAS glass microspheres. (Reprinted with permission from ref 75. Copyright 2002 Elsevier Science B.V.)

However, the number of yttrium ions present in the YAS glass is not so large, and the half-life of ^{90}Y is not long enough to avoid substantial decay even before the cancer treatment. Therefore, Y_2O_3 and YPO_4 microspheres have been suggested to be more effective for in situ radiotherapy of cancer than the YAS glass microspheres [75], because these materials are chemically durable ceramics containing larger amount of yttrium which are activated to ß-emitter.

Figure 9-38 shows micro X-ray transmission image of rabbit liver implanted with Y_2O_3 microspheres [75]. It is evidenced from this image that a large amount of Y_2O_3 microspheres can be distributed uniformly in hepatic artery, which indicates that the present Y_2O_3 microspheres can show hepatic radioembolization effects to the tumors. In addition, the implanted Y_2O_3 microspheres were successfully entrapped only in the liver uniformly and did not distribute to any other organs such as lung, stomach, and spleen. Therefore, the present microspheres are believed to be useful for in situ radiotherapy of cancer.

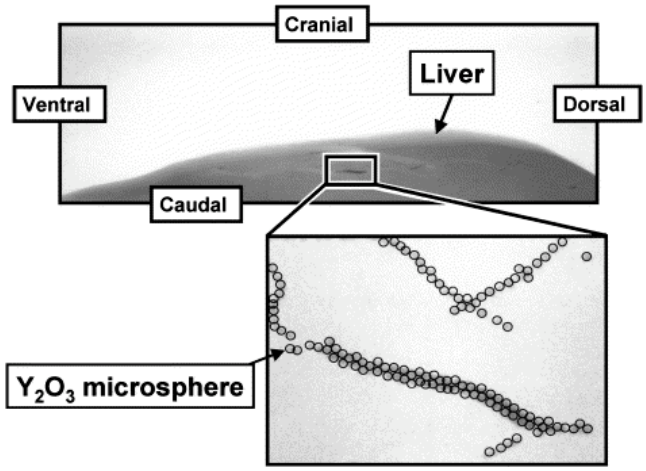

Figure 9-38. Micro X-ray transmission image of rabbit liver implanted with Y_2O_3 microspheres. (Reprinted with permission from ref 75. Copyright 2002 Elsevier Science B.V.)

9.8.2. *Basic studies on markers for brain tumor and digestibility estimation*

The primary malignant brain tumor is also a serious disease because there is no effective therapy. Although surgical resection of the tumor mass is the standard care, the invasive action of the malignant cells inevitably results in relapse of the tumor. Otherwise, effective chemotherapeutic and gene therapy agents are also well-known, but their use is limited by the presence of the blood-brain barrier. Therefore, it has been proposed the post-surgical positive pressure infusion of such agents directly into the bulk brain tissues [76]. The agents are distributed into the interstitial space of the brain and subsequently are delivered to the invading tumor cells.

For the purpose of the basic research on electrophoretic transport phenomenon in brain, some basic researches have been carried out using alternatives such as collagen and agarose gels instead of a living mammalian brain [77]. In order to explore the similarity between the porosity of the brain's extracellular compartment and that of the nanoscale polymeric structure of the gel, slurry of fluorescent nanoparticles has been applied to monitor the distribution of the nanoparticles within the gel [78]. As seen in Figure 9-39, for example, the nanoparticles of Y_2O_3:Eu^{3+}

whose size is 8-12 nm have clearly been spread through the interstitial structure of the gel by the positive pressure infusion process. This indicates that the equivalent inter-cross-link pore size within bulk samples of this polymeric gel mimics that of the extracellular space within in vivo mammalian brain.

Figure 9-39. Infusion mass viewed in visible light (left). Infusion mass viewed during UV excitation at 254 nm (right). (Reprinted with permission from ref 78. Copyright 2002 IOP Publishing Ltd.)

Binary rare earth oxides have also been evaluated as inert markers in apparent digestibility studies. An inert marker for the estimation of digestibility needs the following conditions.

- homogeneously incorporated into the feed and easily and accurately analysed, even at low concentrations
- indigestible and does not affect the metabolism of the animal
- pass through the gastro-intestinal tract at the same rate as the dietary nutrients
- hygienic and harmless to people and the environment

The predominant inert marker in fish studies is chromic oxide. However, chromic oxide does not only satisfy the criteria listed above, but also is not always totally recovered in the faeces [79]. In addition, chromium may be toxic even at low concentrations and, in some cases, allergenic to man, which makes it necessary to take extra care during the manufacture, use, and analysis of feeds and faeces with high concentrations of chromium.

On the contrary, binary rare earth oxides satisfy the criteria and should not affect the metabolism. They are slightly soluble in weak acid, but have a very low solubility under neutral conditions. The feasibility of Y_2O_3 and oxides of lanthanides such as La_2O_3 and Yb_2O_3 as inert markers has been verified in the digestibility studies with salmonids [80], and it was evidenced that Y_2O_3, La_2O_3, and Yb_2O_3 gave accurate estimates of apparent digestibility at much lower dietary concentrations (0.1 $g \cdot kg^{-1}$) than necessary when using Cr_2O_3 (10 $g \cdot kg^{-1}$). Since absorption of rare earth oxides in their soluble form does not occur from the stomach and the markers appear to be precipitated once entering the intestine, they can be used accurately at much lower dietary concentrations. The estimates of the apparent digestibility

obtained when using rare earth oxides were similar to the estimates obtained with Cr_2O_3.

Furthermore, rare earth oxides have an affinity for plant cell walls, and have been used in their soluble form to label indigestible plant fiber, in order to study digestion in ruminants [81]. Samarium, scandium, ytterbium and europium oxides have already been successfully used as inert markers to measure apparent utilization of nutrients in humans [82].

References

1. European patent, EP 05 81621, Japanese patent JP 2858617
2. European patent, EP 05 81622, Japanese patent JP 2914602
3. European patent, EP 08 74879, Japanese patent JP 11-503712
4. French patent, FR 28 03281
5. US patent, US 6,022,471 (2000)
6. M Shelef et al., Ceria and Other Oxygen Storage Components in Automotive Catalysts, in A. Trovarelli (Ed.), *Catalysis by Ceria and Related Materials*, Imperial College Press (2002).
7. H. S. Gandhi, A. G. Piken, M. Shelef, and R.G.Delosh, *SAE Paper*, 760201 (1976).
8. J.P. Cuif, G. Blanchard, O. Touret, A. Seigneurin, M. Marczi, and E. Quemere, *SAE Paper*, 970463 (1997).
9. J.P. Cuif, G. Blanchard, O. Touret, M. Marczi, and E. Quemere, *SAE Paper*, 961906 (1996).
10. R.M. Heck and R.J. Farrauto, *Catalytic Air Pollution Control – Commercial Technology*, *2nd ed.*, Wiley (2002).
11. M. Sugiura, *Catal. Surv. Asia*, **7**, 77 (2003).
12. J. Kaspar, P. Fornasiero, and N. Hichey, *Catal. Today*, **77**, 419 (2003).
13. E. Rohart, O. Larcher, C. Hédouin, F. Fajardie, H. Aimin, S. Deutsch, M. Allain, and P. Macaudière, *Congress on Automotive Pollution Control (CAPoC 6), Poster session (P66)*, Bruxelles (2003).
14. E. Rohart, O. Larcher, C. Hédouin, S. Deutsch, M. Allain, and P. Macaudière, *SAE Paper*, 2004-01-1274 (2004).
15. E. Rohart et al., Publication at Fisita Congress (Barcelona, May 2004), in press.
16. S. Matsumoto, Y. Ikeda, H. Suziki, M. Ogaiu, and N. Miyoshi, *Appl. Catal. B,* **25**, 115 (2000).
17. European patent, EP 1317953 (2002).
18. US patent, US 2003/0039597 (2003).
19. J. Theis et al., *SAE Paper*, 2003-01-1160 (2003).
20. L. Jacques et al, Cerium Based Fuel Additive for Diesel Particulate Emission Control, 27th ISATA, Aachen ,31st Oct-4th Nov 1994.
21. S.Olivier et al, *SAE paper*, 2000-01-0473 (2000).
22. M. Quigley and T. Seguelong, *SAE paper*, 2002-01-0436 (2002).
23. J.C. Gadea, L'industrie Céramique, N°854, 11/90.
24. J.E. Khaladji, Conference of tele-radiotechnic institute of Warsaw - Technical Paper, 1979 November 6th (1979).
25. D.C. Cornish and I.M Watt, The Mechanism of Glass Polishing, SIRA-Research Report, R267 (1961).

26. R. Kannno, Y. Takeda, T. Yamamoto, Y. Kawamoto, and O. Yamamoto, *J. Solid State Chem.*, **102,** 106(1993).
27. T. Yamamoto, R. Kannno, Y. Takeda, O. Yamamoto, Y. Kawamoto, and M Takano, *J. Solid State Chem*., **109,** 372(1994).
28. Japanese Patent, JP 08-169713
29. E. Suda, B. Pacaud, Y. Montardi, M. Mori, M. Ozawa, and Y. Takeda, *Electrochemistry*, **71**, 66 (2003).
30. E. Suda, B. Pacaud, Y. Montardi, M. Mori, and Y. Takeda, in contribution.
31. E. Suda, B. Pacaud, Y. Montardi, M. Itagaki, S. Ohara and Y. Takeda, in contribution.
32. E. Suda, B. Pacaud, and T. Seguelong, International Symposium on soft solution processing, 2000-12.
33. Japanese Patent, JP2000-236809
34. W.Z. Nernst, *Electrochem*., **6**, 41 (1899).
35. R.D. Shannon, *Acta Cryst*., **A 32,** 751 (1976).
36. H. Inaba and H. Tagawa, *Solid State Ionics*, **83**, 1 (1996).
37. T. Omata and S. Matsuo, *Materials Integration*, **16**, 48 (2003).
38. T. Hibino, *Ceramics*, **36**, 486 (2001).
39. B. Zhu, X. Liu, M. Sun, S. Ji, and J. Sun, *Solid State Sience*, **5**, 1127 (2003).
40. M.S. Reisch, *Chem. Eng. News*, **79,** 25 (2001).
41. G.P. Dransfield, *Radiat. Prot. Dosim*., **91**, 271 (2000).
42. A. Fujishima, and K. Honda, *Nature*, **238**, 37 (1972).
43. J.M. Herrmann, C. Guillard, and P. Pichat, *Catal. Today*, **17**, 7 (1993).
44. G. Hass, J. B. Ramsey, and R. Thun, J. Opt. Soc. Am., 48, 324 (1958).
45. C.A. Hogarth and Z.T. Al-Dhhan, *phys. status solidi (b)*, **137**, K157 (1986).
46. S. Yabe and S. Momose, *Proceedings of the 3rd Scientific Conference of the Asian Society of Cosmetic Science*, Taichung, Taiwan, p. 103 (1997).
47. S. Yabe and S. Momose, *J. Soc. Cosmet. Chem. Jpn.*, **32**, 372 (1998).
48. T. Masui, M. Yamamoto, T. Sakata, H. Mori, and G. Adachi, *J. Mater. Chem.*, **10**, 353 (2000).
49. T. Masui, H. Hirai, R. Hamada, N. Imanaka, G. Adachi, T. Sakata and H. Mori, *J. Mater. Chem.,* **13**, 622 (2003).
50. S. Yabe, M. Yamashita, S. Momose, K. Tahira, S. Yoshida, R. Li, S. Yin, and T. Sato, *Int. J. Inorg. Mater.*, **3**, 1003 (2001).
51. R. Li, S. Yabe, M. Yamashita, S. Momose, S. Yoshida, S. Yin, and T. Sato, *Mater. Chem. Phys.*, **75**, 39 (2002).
52. R. Li, S. Yabe, M. Yamashita, S. Momose, S. Yoshida, S. Yin, and T. Sato, *Solid State Ionics*, **151**, 235 (2002).
53. S. Yabe and T. Sato, *J. Solid State Chem.*, **171**, 7 (2003).
54. N. Imanaka, T. Masui, H. Hirai, and G. Adachi, *Chem. Mater.*, **15**, 2289 (2003).
55. E.M. Savitskii, V.F. Terekhova, V.A. Tsikalov, *Trudy Soveshchaniya*, 31 (1959).
56. V.E. Roshchin, D.Y. Povolotskii, A.V. Katkov, A.V. Rechkalova, and L.B. Stanovnova, *Izv. Akad. Nauk SSSR, Metally*, **5**, 17 (1974).
57. E.M. Savitskii, V.F. Popov, N.V. Keis, V.N. Lyubimov, *Akad. Nauk SSSR*, 214 (1964).
58. J.C. Colson, H. Buscail, G. Bonnet, P. Sotto, and J.P. Larpin, *Trans. Mater. Res. Soc. Jpn.*, **14A**, 107 (1994).

59. H. Buscail, C. Courty, and J.P. Larpin, *J. Phys. IV*, **5**, C7/375 (1995).
60. L. Mukin, M. Chen, and S. Dechun, *J. Rare Earths,* **9**, 294 (1991).
61. X.H. Wang, Z.D. Zou, S.L. Song, and S.Y. Qu, *J. Mater. Sci. Lett.*, **22**, 713 (2003).
62. G.J. Ehrhardt and D.E. Day, *Nucl. Med. Biol.*, **14**, 233 (1987).
63. M.J. Hyatt and D.E. Day, *J. Am. Ceram. Soc.*, **70**, C283 (1987)
64. E.M. Erbe and D.E. Day, *J. Biomed. Mater. Res.*, **27**, 1301 (1993).
65. R.C. Weast, D.R. Lide, M.J. Astle, and W.H. Beyer, in *CRC Handbook of Chemistry and Physics*, vol. B-28, p. 231, CRC Press, Florida (1989).
66. R.V.P. Mantravadi, D.G. Spignos, W.S. Tan, and E.L. Felix, *Radiology*, **142** 783 (1982).
67. M.J. Herba, F.F. Illescas, M.P. Thirlwell, L. Rosenthall, M. Atri, and P.M. Bret , *Radiology*, **169**, 311 (1988).
68. I. Wollner, C. Knutsen, P. Smith, D. Prieskorn, C. Chrisp, J. Andrews, J. Juni, S. Warber, J. Klevering, J. Crudup, and W. Ensminger, *Cancer*, **61**, 1336 (1988).
69. S. Houle, T.K. Yip, F.A. Shepherd, L.E. Rotstein, K.W. Sniderman, E. Theis, R.H. Cawthorn, and K. Richmond-Cox, *Radiology*, **172**, 857 (1989).
70. J.H. Anderson, J.A. Goldberg, R.G. Bessent, D.J. Kerr, J.H. McKillop, I. Stewart, T.G. Cooke, and C.S. McArdle, *Radiother. Oncol.*, **25**, 137 (1992).
71. M.A. Burton, B.N. Gray, C. Jones, and A. Coletti, Nucl. Med. Biol., **16**, 495 (1992).
72. F.A. Shepherd, L.E. Lotstein, S. Houle, T.K. Yip, K. Paul, and K.W. Sniderman, *Cancer*, **70**, 2250 (1992).
73. D.E. Day and T.E. Day, in L.L. Hench and J. Wilson (Eds.), *An Introduction to Bioceramics*, World-Science Publishing, Singapore, p. 305 (1993).
74. J.C. Andrews, S.C. Walker, R.J. Ackermann, L.A. Cotton, W.D. Ensminger, and B. Sharpiro, *J. Nucl. Med.*, **35,** 1637 (1994).
75. M. Kawashita, *Mater. Sci. Eng.*, **C22**, 3 (2002).
76. W.C. Broaddus, G.T. Gillies, and J. Kucharczyk, *Neuroimag. Clin. N. Am.*, **11**, 727 (2001).
77. Z.-J. Chen, H.L. Fillmore, G.T. Gillies, E. Bieberich, and W.C. Broaddus, *Neuro-Onc.*, **3**, 321 (2001).
78. G.T. Gillies, S.W. Allison, and B.M. Tissue, *Nanotechnology*, **13**, 484 (2002).
79. E. Lied, K. Julshamn, and O.R. Braekkan, *Can. J. Fish. Aquat. Sci.*, **39**, 854 (1982).
80. E. Austren, T. Storebakken, M.S. Thomasse, S. Refstie, and Y. Thomassen, *Aquaculture*, **188**, 65 (2000).
81. L.W. Smith, *J. Anim. Sci.*, **67**, 2123 (1989).
82. D.P. Hutcheson, B. Venugopal, D.H. Gray, and T. Lucky, *J. Nutr.*, **109**, 702 (1979).

7. THERMOCHEMISTRY OF BINARY RARE EARTH OXIDES

L.R. Morss
Office of Basic Energy Sciences
U.S. Department of Energy
Washington, D.C. 20585 USA

R.J.M. Konings
European Commission, Joint Research Centre
Institute for Transuranium Elements, P.O. Box 2340
D-76125 Karlsruhe, Germany

7.1. INTRODUCTION AND SCOPE

The thermochemical properties of chemical substances have long been realized to be among the most important fundamental properties. Until about the early 20th century it was generally believed that the enthalpy of a reaction was the driving force for the reaction, although it was known that some spontaneous reactions are endothermic. Although scientists have realized since the publishing of seminal thermodynamic works that Gibbs free energies of reactions determine equilibrium properties and directions of reactions, it remains important to determine reaction enthalpies to characterize substances because the Gibbs free energy is the sum of the enthalpy and the product of temperature and entropy of the reaction. With the aid of heat capacities the Gibbs free energy can be described as a function of temperature.

This chapter centers on the determination of enthalpies of formation of pure rare earth binary oxides at 298.15 K. Inasmuch as possible, the other properties and the properties at temperatures other than 298.15 K are also presented. In this chapter the "rare earths" are considered to be yttrium, lanthanum, and the lanthanide elements Ce-Lu. The thermochemistry of scandium oxides is not treated in this chapter.

Because the tripositive ions are the most stable for all the rare earth elements in almost all compounds, the thermochemistry of the solid (crystalline) rare earth sesquioxides dominates this chapter. Some rare earths have divalent or tetravalent states, so the chemistry of solid monoxides and dioxides are included. There are also many nonstoichiometric binary oxides of cerium, praseodymium, and terbium. As much as possible, the thermochemistry of these nonstoichiometric binary oxides is included. The stability, phase diagrams, and structures of ternary and polynary

G. Adachi et al. (eds.), Binary Rare Earth Oxides, 163–188.

oxides are extensive and important, but this chapter does not treat these materials comprehensively.

The thermochemical properties of gaseous rare earth monoxides and related gaseous species encompass their ionization potentials and bond strengths. These properties of gaseous oxides are summarized in this chapter. The changes of bond energies of the gaseous monoxides across the lanthanide series dramatically reflects the changing electronic configuration of the Ln(g) atoms, as we will discuss in the present chapter.

Gschneidner *et al.* [1] published a comprehensive and critical review of the thermochemical properties of all rare earth oxides, including that of yttrium (which is a rare earth) and that of scandium (which is not). Their review included non-trivalent oxides: EuO, Eu_3O_4, CeO_2, and the hypostoichiometric dioxides RO_{2-x} (R = Ce, Pr, and Tb). They included tables of $\Delta_fH°(RO_x, cr)$ and $\Delta_fG°(RO_x, cr)$ from T = 298.15 K to T = 2000 K or higher. Morss [2] conducted a complete review of enthalpies of formation of rare earth sesquioxides. Chandrasekharaiah and Gingerich [3] reviewed the properties of the gaseous rare earth oxides. Haire and Eyring [4] summarized synthesis, structures, phase diagrams, and thermochemical properties of all solid and gaseous rare earth oxides. Cordfunke and Konings [5] carried out a detailed and critical review of enthalpies of formation of lanthanide sesquioxides. The heat capacity studies of rare earth oxides, most of which carried out before 1970 were reviewed by Holley *et al.* [6], Gschneidner *et al.* [1] later by Westrum [7].

7.2. HISTORICAL

The rare earth elements are given the name “earths” because most of them were discovered as minerals that were later analyzed as oxides (earths). Rare earth oxides have been known for over 200 years [8]. Relatively pure lanthanum metal and oxide were available in a few laboratories by 1900; the first thermochemical studies of any rare earth materials were measurements of enthalpies of combustion by Muthmann and Weis [9], whose combustion calorimetry of La metal resulted in publication of the enthalpy of formation of La_2O_3(cr), -444 kcal·mol^{-1}. In 1924, Moose and Parr [10] reported -456 kcal·mol^{-1} for this reaction, and in 1940 Roth *et al.* [11] reported -539 kcal·mol^{-1}. The presently accepted value is –(1791.6 ± 2.0) kJ·mol^{-1} or 428.2 kcal·mol^{-1}.

I In the first of a series of papers on rare earth calorimetry, Bommer and Hohmann [12] noted that the combustion-calorimetry results of these three research teams were unusually exothermic, probably because of the poor purity of the metal samples. Bommer and Hohmann determined enthalpies of formation of rare earth aquo-ions by dissolving rare earth metals in dilute acids. The rare earth oxides from which they prepared metals were well separated from other rare earths. The enthalpies of formation of Bommer and Hohmann are now known to be far too exothermic because the metals were prepared by reduction with potassium, and

unreacted potassium must have been mixed or alloyed with the rare earth metal samples. (On a mass basis, the enthalpy of solution of potassium metal is much more exothermic than that of a rare earth metal.)

In the 1950s and 1960s the rare earth elements became available in chemically pure form due the improvements of chemical separation techniques [13]. This stimulated systematic studies of the thermodynamic properties in several laboratories, especially in the USA. Not all of them can be mentioned here, but some groups deserve special attention:

- The seminal rare-earth scientist F. H. Spedding carried out many calorimetry experiments to determine enthalpies of solution of rare earth elements and chlorides (e.g., [14]), which are indispensable for the determination of the enthalpies of formation of the oxides. In addition he and his team used oxygen combustion calorimetry to determine $\Delta_f H°$ of Nd, Sm, Gd, and Er sesquioxides [15].
- In the 1950s Huber and Holley and their co-workers carried out combustion calorimetry studies with most of rare earth metals. Later the same group re-studied some of the compounds with combustion calorimetry, but also used solution calorimetry to check their earlier combustion calorimetry results.
- Researchers at the U.S. Bureau of Mines carried out combustion and solution calorimetry experiments to determine some $\Delta_f H°(R_2O_3, cr)$ values (e.g. [16]) and also many adiabatic and drop calorimetric measurements to derive heat capacities up to about 1800 K (Pankratz, Kelley and coworkers).
- Soviet researchers (Gvelesiani and coworkers) made systematic studies using solution and enthalpy drop calorimetry on many of the rare-earth sesquioxides in the 1960s and early 1970s.
- Justice and Westrum [7] measured the low-temperature heat capacity of ten lanthanide sesquioxides by adiabatic calorimetry in the 5 K to 350 K range, from which the standard entropy can be derived, though the complex electronic structure of the f-element ions result in significant contributions at very low temperatures.
- Walsh and White and coworkers [17-20] studied the vaporisation of the rare-earth sesquioxides systematically, carrying out mass-spectrometric studies on most of the rare-earth in the gas-phase to derive enthalpies of formation of the monoxide molecules, using vaporisation and isomolecular exchange reactions, and explained the trend observed in the LnO dissociation energies.
- Ackermann *et al.* [21] performed pioneering work to determine the ionization energies of gaseous rare earth monoxide ions using electron impact studies by time-of-flight mass spectrometry, using a comparative method with known standards.

Many of these studies are still the basis of the current recommended values for the lanthanide oxides, as we will discuss in the present chapter. However, several

recent studies have helped to resolve open questions, and to better define trends and systematics.

7.3. THERMOCHEMICAL TECHNIQUES

7.3.1. *Combustion Calorimetry*

The determination of enthalpies of formation by combustion is a classical calorimetric method. Combustion of most of the rare earth metals in oxygen produces their sesquioxides. There are, however, some exceptions. Combustion of cerium metal produces the dioxide. Because also the sesquioxide of cerium burns in oxygen, forming stoichiometric CeO_2, combustion calorimetry has been used to derive $\Delta_f H°(Ce_2O_3,cr)$. Europium monoxide also burns in oxygen, forming stoichiometric Eu_2O_3, so combustion calorimetry has been used to derive $\Delta_f H°(EuO,cr)$.

The principal drawback of combustion calorimetry occurs when the product cannot be well characterized. This especially applies to the oxides of Pr and Tb. When Pr metal is burned in oxygen, Pr_6O_{11} is obtained, and so its sesquioxide, dioxide and all intermediate oxides cannot be studied with this technique. When Tb metal is burned in oxygen, the oxide is nonstoichiometric and heterogeneous. Therefore, solution calorimetry is the method of choice for determination of enthalpies of formation of the sesquioxides of Pr and Tb and, in fact, for their dioxides and nonstoichiometric oxides.

7.3.2. *Solution calorimetry*

Most of the rare earth oxides (monoxides, sequioxides, and higher oxides, with the exception of CeO_2) dissolve readily in dilute mineral acids. All of the rare earth metals also dissolve in dilute acids, in particular HCl(aq). Therefore, the enthalpies of formation of all rare earth oxides with the exception of CeO_2 can be determined by dissolving the metals and their oxides in acids of the same composition. The simplest reaction cycle is thus:

$2\ M(cr) + 6\ HCl(aq) = 2MCl_3(sln) + 3\ H_2(g)$	$\Delta_r H_1$
$M_2O_3(cr) + 6\ HCl(aq) = 2MCl_3(sln) + 3\ H_2O(sln)$	$\Delta_r H_2$
$3\ H_2(g) + 3/2\ O_2(g) = 3\ H_2O(sln)$	$\Delta_r H_3$
$2\ M(cr) + 3/2\ O_2(g) = M_2O_3(cr)$	$\Delta_r H_4$

so that the enthalpy of formation of the sesquioxide is $\Delta_r H_4 = \Delta_r H_1 - \Delta_r H_2 + \Delta_r H_3$.

7.3.3. *Low-temperature adiabatic calorimetry*

Since the entropy is an integral quantity, its absolute value at the standard reference temperature (T = 298.15 K) must be obtained by calorimetry from 0 K to 298.15 K. The most convenient technique is adiabatic calorimetry and this technique has been

used for most of the rare-earth oxides. The problem encountered for the lanthanide elements is, however, that the 4*f* electronic configurations lead to complex effects at very low temperatures, which are often not attained by the traditional calorimeters. Special techniques using ^{3}He are needed for that, and have been used for some of the lanthanide sesquioxides.

7.3.4. *High-temperature drop calorimetry*

The high temperature heat capacity of the rare-earth sesquioxides is derived from measurements of the enthalpy increment $\{H^o(T) - H^o(298.15\ K)\}$ using so-called drop calorimeters, in which the enthalpy difference between a temperature T and the reference temperature of the calorimeter is determined (e.g. 273.15 K for an ice calorimeter). The heat capacity can be derived from the enthalpy data by differentiation of the (polynomial) enthalpy equation, which normally has the form:

$$\{H^o(T) - H^o(298.15\ K)\} = a(T/K) + b(T/K)^2 + c(T/K)^{-1} + d$$

which yields, after differentiation for the heat capacity:

$$C^o_p = a + 2b(T/K) - c(T/K)^{-2}$$

7.3.5. *Mass spectrometry*

The enthalpies of formation of the gaseous species of the rare earth oxides are generally derived from mass spectrometric studies. The enthalpy of formation of a gaseous rare earth monoxide can be derived from the vapor pressure of the MO species and its rate of change as a function of temperature above the condensed phase:

$$M_2O_3(cr,l) = 2\ MO(g) + O(g)$$

which relates it to the enthalpy of formation of the solid, or from isomolecular exchange reactions of the type:

$$MO(g) + A(g) = M(g) + AO(g)$$

which relates it to the enthalpy of formation of another, generally well known, gaseous species (A) such as TiO(g) or AlO(g).

7.4. SOLID RARE EARTH SESQUIOXIDES

7.4.1. *Enthalpies of Formation*

Table 7-1 shows the recommended values for the enthalpies of formation of all rare earth sesquioxides. The enthalpy of formation of yttrium sesquioxide was re-

determined by Morss *et al.* [22] by solution calorimetry. To calculate the enthalpy of formation, they took advantage of a recent determination of the enthalpy of formation of Y^{3+}(aq) using high-purity yttrium metal [23]. Most of the entries for the lanthanide sesquioxides are those of the review of Cordfunke and Konings [5], who made a critical evaluation of the sequioxides of the lanthanides (and trihalides and tripositive aqueous ions) recently. However, their $\Delta_fH°(Ce_2O_3, s)$ requires additional evaluation. Cordfunke and Konings [5] based their selection on the weighed mean of two recent studies. Huntelaar *et al.* [24] studied Ce_2O_3 in detail, as many of the older studies were made on materials with O/Ce > 1.5. They re-determined the enthalpy of formation using solution calorimetry, based on a thermochemical cycle using the enthalpy of solution of the metal from Spedding and Miller [14]. The latter value is not without doubt as the enthalpy of solution of Nd reported in the same paper is significantly different from later values Putnam *et al.* [25] measured the enthalpy of formation of Ce_2O_3 by high temperature oxide melt solution, using the same material.

When the enthalpies of formation of rare earth sesquioxides are combined with enthalpies of formation of rare earth aqueous ions R^{3+}(aq) to calculate enthalpies of solution,

$$RO_{1.5}(cr) + 3H^+(aq) = R^{3+}(aq) + 1.5H_2O(liq)$$
$$\Delta_{soln}H°(RO_{1.5}) = \Delta_fH°(R^{3+},aq) - \Delta_fH°(RO_{1.5}, cr) - 1.5\,\Delta_fH°(H_2O, liq)$$

the $\Delta_{soln}H°(RO_{1.5})$ values should plot on three smooth curves, one curve for each of the three isomorphs of the sesquioxides. (It is known that the structure of the aqueous R^{3+} ions changes in solution [26]). Figure 7-1 shows this plot. If the $\Delta_fH°(CeO_{1.5})$ recommended by Cordfunke and Konings [5] were used for this plot the Ce point would be anomalously high. This review has selected the $\Delta_fH°(CeO_{1.5})$

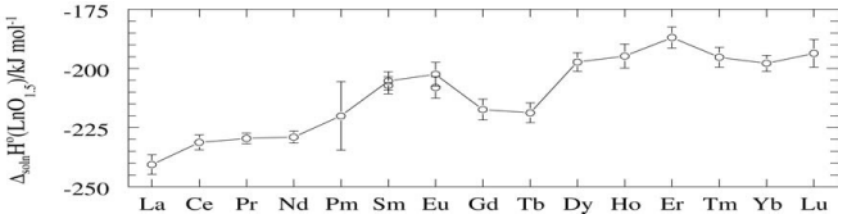

Figure 7-1. Enthalpies of solution of the lanthanide sesquioxides as a function of Z; note that for Sm and Eu data for two crystal modifications are known.

of Baker and Holley [27] because their combustion calorimetry study was performed with $CeO_{1.5+x}$ samples that were thoroughly analyzed and extrapolated to $CeO_{1.500}$

and because the correlation shown by Figure 7-1 reinforces the systematic trend of enthalpies of solution.

Gschneidner [28,29] showed that the enthalpies of formation of several classes of lanthanide compounds can be correlated systematically as a function of atomic number. He pointed out [30] that the correlations for europium and ytterbium are anomalous because they are divalent in their metallic state but trivalent in the compounds. As shown in Figure 1, the enthalpies of formation of the lanthanide sesquioxides (or of any other class of compounds of R^{3+}) do not change in a smooth fashion as a function of Z or of the ionic radius of R^{3+}. These enthalpies of formation correspond to the reactions that appear to be similar throughout the rare earths,

$$Ln(cr) + 3/2\ O_2(g) = LnO_{1.5}(cr)$$

but the electronic configurations of some of the metals are different from those of the sesquioxides, all of which have Ln^{3+} configurations $4f^{n-3}$. The metallic character of europium and ytterbium metals is similar to that of strontium and barium, with a divalent bonding metallic configuration $d^{0.5}sp^{0.5}$ [31]. The other rare earth metals are trivalent, with bonding metallic configuration $d^{1.5}sp^{0.5}$. This property was first shown when the enthalpies of formation of the rare earth aqueous ions were plotted as a function of *Z* [32]. However, the enthalpies of the reactions

$$LnO_{1.5}(cr) + 3\ H^+(aq) = Ln^{3+}(aq) + 3/2\ H_2O(l)$$

do plot smoothly as a function of *Z* because each pair of Ln^{3+} ions, $LnO_{1.5}(s)$ and $Ln^{3+}(aq)$, has the same electron configuration $4f^{n-3}$. Figure 7-1 shows subtle changes

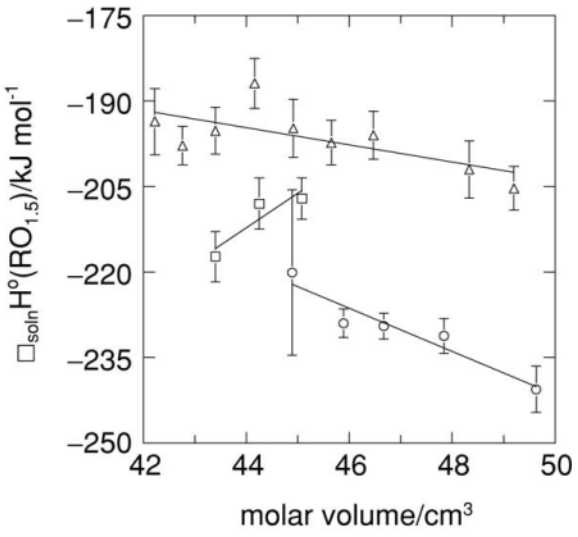

Figure 7-2. Enthalpies of solution of the lanthanide sesquioxides as a function of the molar volume; (○), hexagonal; (□), monoclinic; (Δ) cubic crystal structure (modified after [5]).

in this smooth plot due to the fact that there are three crystal structures of the sesquioxides: hexagonal La_2O_3-Nd_2O_3 monoclinic Sm_2O_3-Gd_2O_3, and bcc Tb_2O_3-Lu_2O_3. These differences become more evident when $\Delta_{soln}H°(RO_{1.5})$ is plotted as a function of the molar volume of the unit cell, as shown in Figure 7-2. In this figure three distinct trendlines are visible for the hexagonal, monoclinic and bcc structures. Figure 7-2 allows estimations to be made of the enthalpies of formation of those compounds and modifications that are unknown (e.g. Pm_2O_3 or bcc Gd_2O_3).

7.4.2. *Standard Entropies and Heat Capacities*

The entropies of most of the lanthanide sesquioxides have been determined by low-temperature heat capacity measurements, principally by Justice and Westrum Jr. [7,33-38]. Recently new measurements for Y_2O_3 [39] and Ce_2O_3 [24] and the first measurements of Pr_2O_3 [40] have been reported. The measurements for the lanthanide sesquioxides reveal the presence of Schottky and Kramer components related to electronic structure of the lanthanide ions. The trend in the lanthanide sesquioxide series, shown in Figure 7-3, is typical for many lanthanide compounds, as discussed by Konings [41]. The heat capacity, as well as the entropy, can be described by a lattice and an excess component, the latter representing the Schottky

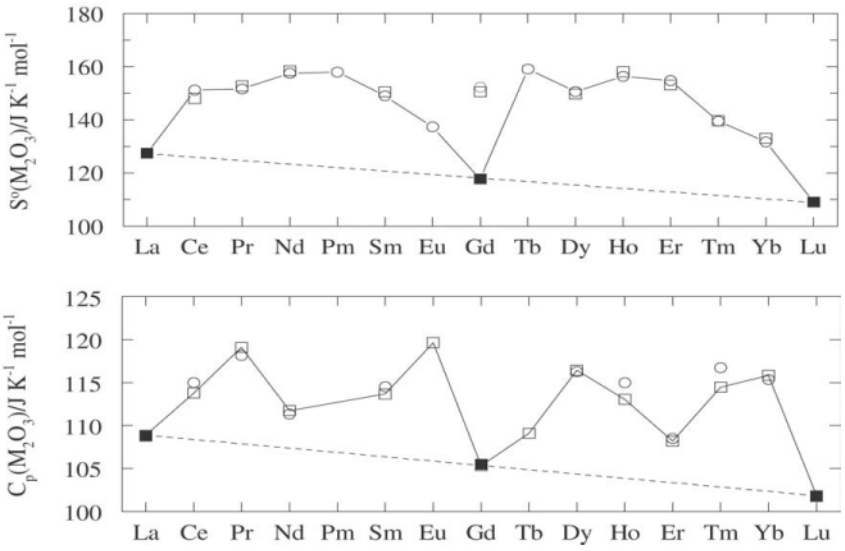

Figure 7-3. The entropy (top) and heat capacity (bottom) of the lanthanide sesquioxides at T = 298.15 K, showing the linear lattice component derived for the f^0, f^7 and f^{14} configuration (■); calculated values (□) and the experimental values (○).

and Kramer contributions:

$$C_p = C_{lat} + C_{exs} \tag{1a}$$

$$S = S_{lat} + S_{exs} \tag{1b}$$

The excess contribution can be calculated from the crystal field energies according to the following equations where Q is the partitioning function described by the Maxwell-Boltzmann distribution law in equation (4), T the temperature, R the universal gas constant, E_i the energy of the level i, and g_i its degeneracy:

$$S_{exs} = R \cdot \ln(g_0) + R \cdot \ln\left\{\sum_{i=1}^{n} g_i \cdot \exp\left(-E_i / R \cdot T\right)\right\} \tag{2}$$

$$C_{exs} = Q^{-2} \cdot R^{-1} \cdot T^{-2} \cdot \left[Q \cdot \sum_{i=1}^{n} g_i \cdot E_i^2 \cdot \exp\left(-E_i / R \cdot T\right) - \left\{\sum_{i=1}^{n} g_i \cdot E_i \cdot \exp\left(-E_i / R \cdot T\right)\right\}^2\right] \tag{3}$$

$$Q = \sum_{i=0}^{n} g_i \cdot \exp\left(-E_i / R \cdot T\right) \tag{4}$$

The lattice component varies regularly within the series (Figure 7-3), decreasing slightly from La to Lu, revealing no significant effect of the crystal structure. The excess component varies irregularly, depending mainly on the ground state multiplets of the lanthanide ions (and in some cases low-lying excited states) and their splitting as a result of the crystal field effect. It must here be mentioned that the cubic lanthanide sesquioxides have two inequivalent lanthanide sites of different symmetry (C_2 and C_{3i}) with different splitting. The crystal field energies of most of the lanthanide ions in the sesquioxide structures are known (see for example Morrison and Leavit [42]). Thus the entropy values could be estimated for those compounds for which no data are available were estimated by Konings [41] and a complete list is given in Table 7-1. Figure 7-3 shows there is an excellent agreement between the experimental values and the calculated values, based on a linear decrease of the lattice components from La to Lu. This procedure might be further refined if low temperature data for monoclinic Gd_2O_3 would become available (the existing data for this compound refer to the cubic modification).

The heat capacity of the sesquioxides above room temperature is principally derived from enthalpy increment measurements. The vast amount of data is however not always concordant. The results from the most reliable studies have been critically reviewed and fitted to polynomial equations that were constrained to the

results from the low-temperature measurements [43], the coefficients of which are given in Table 7-3. For Sm_2O_3, Eu_2O_3 and Gd_2O_3 measurements for the C- and B-phase have been reported from 298.15 K to about 2000 K. The C-phase of these compounds is the thermodynamically stable phase at room temperature, but the energetics of the two phases are close and the transformation kinetics are sluggish. As a result the transformation temperatures are not well defined, and the enthalpies of transition must be derived from the differences of enthalpy of formation at 298.15 K and of the enthalpy increment equation at the accepted transition temperature. These calculations yield for the transition enthalpies (3.5 ± 6.5) $kJ \cdot mol^{-1}$ for Sm_2O_3 at about 900 K and (10.9 ± 7.4) $kJ \cdot mol^{-1}$ for Eu_2O_3 at about 1350 K.

The enthalpy increment studies are all limited to about 2000 K. Above this temperature the rare earth oxides show a complex polymorphism (see Chapter 3 of this book), with the appearance of the hexagonal H-type and cubic X-type structures [44]. No experimental data on the heat capacity of these phases are known, nor on the enthalpies of transition and fusion, which makes the description of the thermodynamic properties for these phases highly uncertain.

The description based on lattice and excess components outlined above can be extended to the high temperature heat capacity, provided the crystal field energies of not only the ground state but also of the excited states are known. As discussed above, the values for La_2O_3, Gd_2O_3 and Lu_2O_3 represent the lattice components. They are shown in Figure 7-4, which indicates a regular trend at the lowest temperatures (T < 600 K) but significant differences above that temperature, even within the cubic C series. It can be that the values for C-Lu_2O_3 very nicely approach the Dulong-Petit value (3R per atomic) whereas the values for C-Gd_2O_3 show a continuous increase, like for A-La_2O_3. Figure 7-5 compares the experimental heat capacity of Eu_2O_3 with that calculated from the lattice component (Gd_2O_3, with a

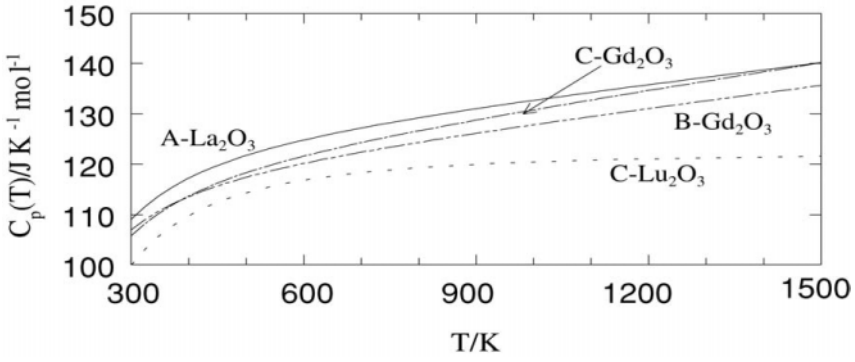

Figure 7-4. The heat capacity of the lanthanide sesquioxides La_2O_3, Gd_2O_3 and Lu_2O_3 as a function of temperature.

small correction for the trend suggested in Figure 7-3) plus the excess component obtained from the energy levels of the $^7F_0$ to $^7F_4$ multiplets of Eu:Gd_2O_3(cubic) [42]. It can be seen that there is an acceptable agreement. With a similar approach Gruber *et al.* [38] calculated the excess contributions in the hexagonal lanthanide sesquioxides up to T = 1000 K, deriving the lattice for the hexagonal series from the values of La_2O_3 and Nd_2O_3, the latter by subtracting the known excess contribution. They also obtained an acceptable agreement between calculated and experimental excess (Schottky) contributions for Ce_2O_3 and Pr_2O_3.

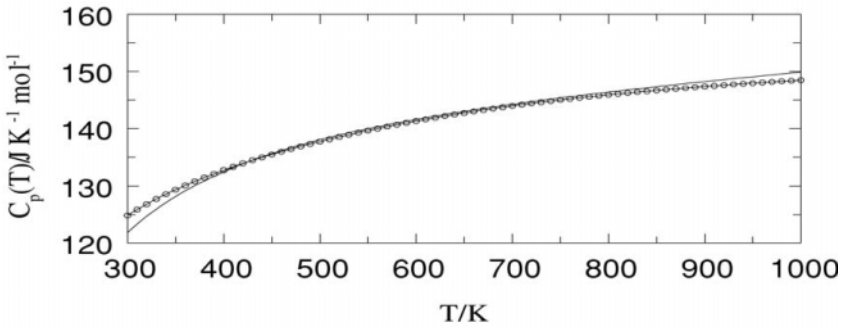

Figure 7-5. The heat capacity of the cubic Eu_2O_3 as a function of temperature; the line shows the experimental values, the symbols show the values calculated from the lattice component and the excess component.

7.5. OTHER SOLID BINARY RARE EARTH OXIDES

7.5.1. *Solid Rare Earth Monoxides*

Ionic Monoxides

Europium monoxide is the only ionic rare earth monoxide. It is a dark red compound with the NaCl structure, slightly nonstoichiometric, and has semiconducting properties that vary as a function of composition [45]. It has been prepared as slightly nonstoichiometric material $EuO_{1.02}$ by reaction of Eu metal with stoichiometric Eu_2O_3 in a sealed tube as a polycrystalline solid [32,46] or (stoichiometry not reported) from a melt as single crystals [45]. When heated it decomposes:

$$4\ EuO(s) = Eu_3O_4(s) + Eu(g)$$

Haschke and Eick [47] derived for the enthalpy of formation –(599.1 ± 17.2) kJ·mol^{-1} from the equilibrium pressures of this reaction. The enthalpy of formation

of $EuO_{1.02}$ was determined by solution calorimetry [46], yielding –(607.5 ± 5.4) $kJ \cdot mol^{-1}$ after recalculation, and by oxygen bomb calorimetry [48,49], yielding –(600.6 ± 3.5) $kJ \cdot mol^{-1}$ after recalculation. The enthalpy of formation of $EuO_{1.00}$ was calculated from the latter study by assuming that $EuO_{1.02}$ is an ideal solution of EuO and $EuO_{1.5}$, giving –(591.3 ± 5.4) $kJ \cdot mol^{-1}$ using the $\Delta_f H°(Eu_2O_3, cr)$ accepted in this chapter.

The standard entropy for this compound was derived from the low-temperature heat capacity measurements by Teany and Moruzzi [50]. The high-temperature heat content of EuO was determined shortly thereafter by McMasters *et al.* [51]. The two measurements are in good agreement, and the derived values are included in Tables 7-1 and 7-2.

Monoxides with Metallic Character

Challenged by the successful syntheses of dihalides of Sm and Yb as well as of Eu, synthetic inorganic chemists sought to make SmO and YbO. Brauer *et al.* [52] summarized earlier efforts but this experienced team of synthetic inorganic chemists was unable to synthesize "lower oxides" of Nd, Sm, or Yb. Soon thereafter a claim was made for synthesis of YbO, also with the NaCl structure [53]. Within months two of these authors admitted that "YbO" was actually Yb_2OC [54]. (Similarly, claimed PuO and AmO appear to be oxycarbides or oxynitrides.) McCarthy and White [55] provided a thermodynamic basis for the successful synthesis of EuO and Eu_3O_4 but not of corresponding oxides of other rare earths.

Several monoxides with metallic properties (LaO, CeO, PrO, NdO, and SmO) have subsequently been synthesized by subjecting stoichiometric mixtures of metallic R and R_2O_3 to high pressures [56]. These oxides have metallic conductivity and can be described as $(R^{3+})(O^{2-})(e^-)$. The trivalent nature of the lanthanide ions in these oxides was confirmed by the Sm^{3+} X-ray absorption edge in SmO and by the magnetic susceptibilities of PrO (Pr^{3+}, $4f^2$), NdO (Nd^{3+}, $4f^3$), and SmO (nearly Sm^{3+}, $4f^5$) [57]. The oxides are stable under high pressure because the volume decrease that accompanies the reaction

$$R(cr) + R_2O_3(cr) = 3\ RO(cr)$$

is responsible for a favorable Gibbs free energy of the reaction. They are metastable at room temperature. It is possible that the high pressure forces the metallic electrons to bond by filling empty low-lying 5d orbitals (but there is no evidence for such bonding of which the authors are aware).

Their thermodynamic properties were calculated in that paper but have not been independently determined. (Both one of the authors and Professor J. Fuger obtained samples of NdO from Professor Leger and carried out solution calorimetry measurements on several samples. However their results were unusually exothermic, indicating that metallic Nd was present, and the non-reproducible measurements

indicated that the samples were not sufficiently homogeneous to warrant further study.)

7.5.2. *Solid Rare Earth Dioxides*

Solid rare-earth dioxides have been reported for Ce, Pr and Tb. They have a fcc structure like the actinide dioxides. In addition, a compound of stoichiometry NdO_2 is known [58]. It is not a true dioxide but a Nd(III) peroxide, $Nd_2O_2(O_2)$. It is reported to be thermally stable, decomposing to $NdO_{1.5}$ at 420 ^oC in argon.

Cerium dioxide is the best-studied rare earth dioxide. The enthalpy of formation of CeO_2(cr) has been determined by combustion calorimetry at LANL by Holley and coworkers two times [59,60] and by Kuznetsov *et al.* [61]. In addition, Kuznetsov *et al.* [62] reported emf measurements for samples of varying O/Ce ratios, from which they derived the enthalpy of formation. The average of these values was accepted by Gschneidner *et al.* [1]. Cordfunke and Konings [5] selected the value of Baker *et al.,* -(1090.4 ± 0.8) kJ mol^{-1} because of the higher purity of the Ce metal used. The low-temperature heat capacity of CeO_2 was measured by Westrum and Beale [63] and the standard entropy can be derived from these results. The high-temperature heat capacity and enthalpy increment has been measured by several authors, in good agreement (Figure 7-6).

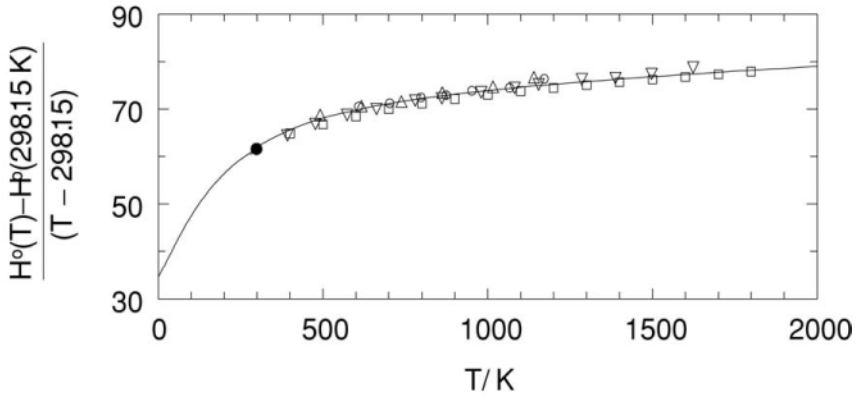

Figure 7-6. Shomate plot of the reduced enthalpy increment of CeO_2; the symbols represent the experimental values; the solid line the recommended equation; the ● symbol the value of the heat capacity at T = 298.15 K from the low-temperature measurements.

The enthalpy of formation of PrO_2(cr) was determined by Gramsch and Morss [64] by solution calorimetry. Hyde *et al.* [65] showed that PrO_2 is stable in oxygen up to 587 K and Ushakov and Navrotsky [66] showed that that PrO_2 is stable in oxygen up to 663 K, above which it decomposes to Pr_6O_{11}. Ushakov and Navrotsky measured the enthalpy of reaction 1/6 Pr_6O_{11}+ 1/12 O_2(g) = PrO_2 by DSC as well as

drop calorimetry as (10 ± 2) kJ·mol^{-1}. This value is in excellent agreement with the selected values for Pr_6O_{11} and PrO_2 given in Table 7-1.

The enthalpy of formation of TbO_2(cr) was derived from the solution calorimetry measurements by Fitzgibbon and Holley [67] and by Stubblefield *et al.* [68] for samples of varying O/Tb ratios. The results have been extrapolated to O/Tb = 2 (see Figure 7-7).

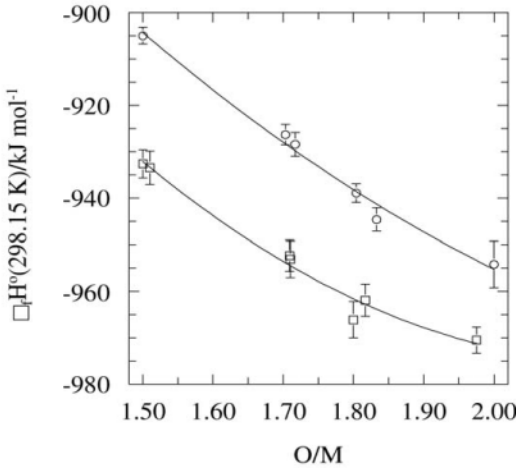

Figure 7-7. The enthalpy of formation of the PrO_x (○) and TbO_x(□) phases at T = 298.15 K plotted as a function of the O/M ratio.

7.5.3. *Nonstoichiometric Solid Rare Earth Oxides*
CeO_{2-x}, PrO_{2-x}, and TbO_{2-x}

The phase diagrams of these oxides have been summarized by Haire and Eyring [4]. Most of the nonstoichiometric oxides have compositions of R_nO_{2n-2} with n = 4, 7, 8, 10, 11, 12, and 16. There is a σ phase related to the *bcc* $RO_{1.5+\delta}$ and an α phase related to the fluorite RO_{2-x}.

Partial molar thermodynamic quantities for oxygen in the CeO_{2-x} system were determined by Bevan and Kordis [69], Kitayama *et al.* [70] and by Sørensen [71] by thermogravimetry. The same quantity was determined for the entire region $CeO_{1.5}$-CeO_2 by high-temperature calorimetry [72]. The CeO_{2-x} system has been modeled in terms of defects [73,74] or two sublattices.

The enthalpy of formation of $PrO_{1.833}$ (Pr_6O_{11}) was determined by Stubblefield *et al.* [68] using solution calorimetry and by Fitzgibbon *et al.* [75] using combustion and solution calorimetry. Enthalpies of formation of other nonstoichiometric Pr oxides were determined by solution calorimetry by Stubblefield. These studies have been recalculated using the selected value for Pr_2O_3 and these numbers are included in Table 7-1. Figure 7-7 shows that the enthalpies of formation vary regularly as a

function of the O/Pr ratio of the various phases. The enthalpy increment of $PrO_{1.833}$ was reported by two groups of authors, the results being differing significantly above about 750 K. This is the peritectic decomposition temperature of $PrO_{1.833}$. Thermodynamic properties of PrO_{2-x} can also be derived from the thermogravimetric studies by Hyde *et al.* [76]. Subsequent isobaric [77] and isoplethic (constant composition [78]) studies of the α-PrO_{2-x} phase region have been made. Inaba *et al.* [79] determined the partial molar enthalpy and entropy change for oxides in the $PrO_{1.714}$ (Pr_7O_{12}) to $PrO_{1.78}$ region. They found $\Delta H_{O2}(PrO_{1.714}) \sim -243$ kJ mol^{-1} and $\Delta H_{O2}(PrO_{1.78}) \sim -356$ kJ mol^{-1}.

Enthalpies of formation of terbium oxides were determined by Fitzgibbon and Holley [67] and by Stubblefield *et al.* [68] by solution calorimetry. These studies have been recalculated using the selected value for Tb_2O_3 and these numbers are included in Table 7-1. Figure 7-7 shows that the enthalpies of formation vary linearly as a function of the O/Tb ratio, as is the case for the PrO_x compounds. Thermodynamic properties of TbO_{2-x} can also be derived from the thermogravimetric study by Hyde and Eyring [80]. Inaba *et al.* [81] determined the partial molar enthalpy and entropy change for oxides in the $TbO_{1.51}$ to $TbO_{1.714}$ (Tb_7O_{12}). They found $\Delta H_{O2}(TbO_{1.51}) \sim -80$ kJ·mol^{-1} and $\Delta H_{O2}(TbO_{1.714}) \sim -222$ kJ·mol^{-1}.

Eyring and co-workers [82] developed a macroscopic van der Waals thermodynamic model of a part of the nonstoichometric rare earth oxide phase diagram. This model accounts for hysteresis in thermogravimetric cycles.

EuO-Eu_3O_4-Eu_2O_3

Eu_3O_4(cr) can be prepared by reacting stoichiometric amounts of EuO and Eu_2O_3 in a sealed tube at 1170 K, which indicates that it is stable with respect to the end-member oxides, or by other methods, e.g. reaction of the sesquioxide, the oxide chloride and lithium hydride [83], or even by high-temperature decomposition of EuO [47]:

$$4\ EuO(cr) = Eu_3O_4(cr) + Eu(g)$$

Eu_3O_4 decomposes at higher temperature:

$$Eu_3O_4(cr) = 4\ Eu_2O_3(cr) + Eu(g)$$

The enthalpy of formation of Eu_3O_4 was calculated by Gschneidner *et al.* [1] from its enthalpy of decomposition at high temperature [54]. Sukhushina *et al.* [84,85] studied the EuO-Eu_3O_4-Eu_2O_3 system by electromotive force measurements. From analysis of the reactions:

$$4Eu_3O_4(cr) + O_2(g) = 6\ B\text{-}Eu_2O_3(cr)$$

$4Eu_3O_4(cr) + O_2(g) = 6\ C\text{-}Eu_2O_3(cr)$
$6EuO + O_2(g) = 2\ Eu_3O_4(cr)$

they derived $\Delta_f H^o(298.15\ K) = -(2255.6 \pm 9.9)\ kJ \cdot mol^{-1}$, which is in good agreement with the result from the dissociation pressure measurements by Haschke and Eick [83], from which Rard [86] derived $-(2270.4 \pm 12.0)\ kJ \cdot mol^{-1}$.

7.6. GASEOUS RARE EARTH OXIDES

Gaseous rare-earth oxide species with the formulas RO, R_2O, and R_2O_2 have been identified [3,87]. This section reviews measurements and calculations of enthalpies of formation and dissociation energies of gaseous rare earth monoxides and the monoxide ions $RO^+(g)$. For the monoxides and the monoxide ion the enthalpies of formation are, respectively

$$R(cr) + ½\ O_2(g) = RO(g)$$

$$R(cr) + ½\ O_2(g) = RO^+(g) + e^-(g)$$

and the dissociation energies are, respectively,

$$RO(g) = R(g) + O(g)$$

$$RO^+(g) = R^+(g) + O(g)$$

The determination of these properties of the gaseous molecule has traditionally been carried out by Knudsen-cell effusion followed by mass spectrometric detection of gaseous species. Contemporary methods [88,89] are laser ablation with prompt reaction and detection (LAPRD). Critical reviews of the bond energies of the rare earth monoxides were made by Pedley and Marshall [90] and Chandrasekharaiah and Gingerich [3]. The bond dissociation energies have been recalculated by Gibson [89] in terms of intrinsic bond energy, the energy needed to break the double bond in the covalently bonded molecule R=O in which the lanthanide has $5d^26s$ configuration. The enthalpies of formation and bond dissociation energies of LnO(g) are shown in Table 7-3. Figure 7-8 shows that the bond dissociation energies for the neutral monoxides follow a smooth trend as a function of *Z*; see detailed discussion below.

The ionization energy of a gaseous compound, e.g. LaO(g), represents the energy U of the gas-phase removal of one electron from the compound, e.g. $LaO(g) \rightarrow LaO^+(g) + e^-(g)$. The ionization energy of RO is given by $\Delta_f H°(RO^+,g) - \Delta_f H°(RO,g)$ but does not vary smoothly as a function of Z because of electronic configuration changes. Ackermann *et al.* [21] pioneered the determination of this property by

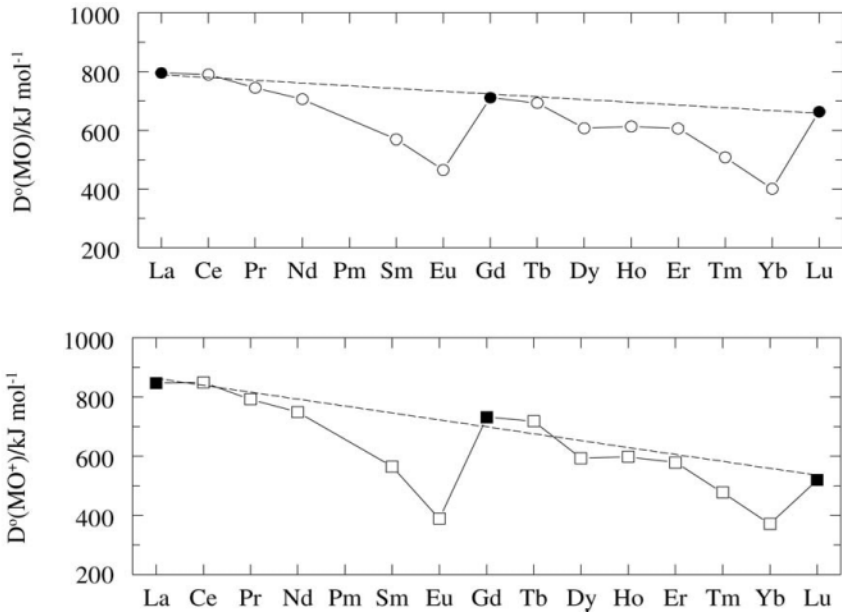

Figure 7-8. Enthalpies of dissociation of gaseous lanthanide monoxides (○) and monoxide ions (□).

vaporizing the oxide, e.g. La_2O_3, ionizing the gaseous molecules by electron impact, and determining the appearance potentials (extrapolating the linear portions of ionization efficiency curves). The resulting appearance potential may be too low because thermal excitation of the oxide molecule may occur during high-temperature volatilization, leading to ionization of the molecule from an excited state rather than the ground state. Contemporary methods are resonantly enhanced multi-photon ionization (REMPI) and mass analyzed threshold ionization (MATI) [91]. These methods avoid the potential error of measuring ionization from a molecular excited state.

For the actinide molecules ThO, UO, UO_2, and PuO_2, contemporary methods [89,91,92] yield ionization energies as much as 2.4 eV smaller than those from the electron impact method [93]. Although one could arbitrarily correct the ionization energies of Chandrasekharaiah and Gingerich [3] by this amount, it is preferable to treat the electron-impact results with suspicion until the LnO ionization energies can be re-measured.

The gaseous rare earth monoxides are best represented as partially ionic diatomic molecules with a double bond created by two valence atomic oxygen 2*p* electrons (configuration $1s^2 2s^2 2p^4$) bonding with rare-earth valence electrons. The ground state configuration of Y(g) is $4d5s^2$, the ground state configurations of gaseous La,

Ce, Gd, and Lu are $4f^{n-3}5d6s^2$, where n is the number of electrons outside the Xe core (La: n=3, Ce: n=4, etc.). The configurations of all other gaseous lanthanide atoms are $4f^{n-2}6s^2$. The 4*f* electrons are considered not to be involved in chemical bonding [89]. The early explanations [20,21,94,95] of the trend in the bond dissociation energies suggested that an excited "bonding" state was obtained by promotion of a *f* electron to a *d* level to create a *ds* state. The trend in Figure 7-8 could thus be explained by a base energy given by the LaO-GdO-LuO line, those elements that already have a *d*-electron, and a ΔE corresponding to the promotion energy $4f^{n-2}6s^2$ to $4f^{n-3}5d6s^2$. Recently it has been suggested that the excited "bonding" state is obtained by promotion of an *s* electron to a *d* level, to create the double bond [96,97]. The lowest-lying excited states to be considered are $4f^{n-3}5d^26s$ and $4f^{n-2}5d6s$. Gibson [89] showed how the energy required to promote gaseous lanthanide atoms to the excited "bonding" state is responsible for the trends in the LnO dissociation energies. He defined the intrinsic Ln=O bond energy as "the bonding interaction between an oxygen atom and a lanthanide atom, Ln*, that has an electron configuration suitable for formation of the covalent formally double bond in the Ln=O molecule." The intrinsic Ln=O bond energy, D^{0*}(LnO), calculated by Gibson is 827 kJ·mol^{-1}. He identified the $4f^{n-3}5d^26s$ configuration as the appropriate one for bonding and the two 5d electrons as the electrons that provide bonding with the oxygen. Thus the trend was explained as:

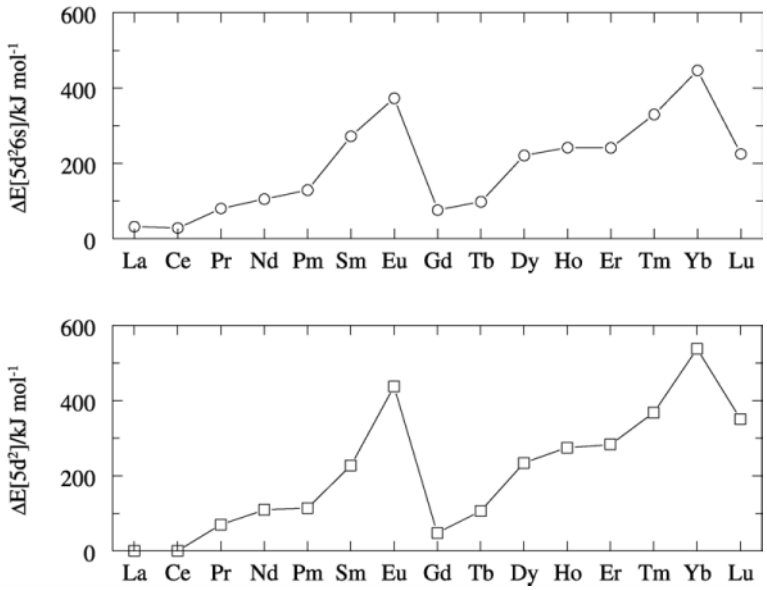

Figure 7-9. The variation of the promotion energies ΔE to the $4f^{n-3}5d^26s$ state for the gaseous lanthanide monoxides (○) and the $4f^{n-3}5d^2$ for the gaseous monoxide ions (□); the values were calculated by Gibson [89] from the atomic energy levels given by Martin *et al.* [114].

$$D^0(LnO) = D^{0*}(LnO) - \Delta E\ [\text{ground} \rightarrow \text{bonding configuration}] \qquad (5)$$

The variation in the promotion energy to the $4f^{n-3}5d^26s$ configuration of the monoxides, $\Delta E[5d^26s]$, is shown in Figure 7-9.

Ackermann *et al.* [21], Chandrasekharaiah and Gingerich [3], and Gibson [89] also discussed the bond dissocation energies of the gaseous monoxide ions LnO^+. Ackermann *et al.* [21] considered these ions to be represented as ionic $(Ln^{3+})(O^{2-})$, in which all Ln^{3+} ions have ground state configuration $4f^{n-3}$ and showed that no promotion of a *f* electron to a *d* level was needed. Gibson [89] assumed that the *f*-electrons are localized in these ions and that two outer valence electrons are needed for the double bonds in the Ln^+=O ions. He showed that the $4f^{n-3}5d^26s$ configuration is too high in energy to be viable for the double bond formation. The lowest excited configurations of the gaseous Ln^+ ions with two non *f*-electrons in the valence orbitals are $4f^{n-2}5d6s^2$ and $4f^{n-2}5d^2$, the latter giving the best agreement with the experimental bond dissociation values. Thus Gibson calculated the intrinsic Ln^+=O bond energy to be 847 $kJ \cdot mol^{-1}$. The enthalpies of formation and bond dissociation energies of the gaseous RO^+ ions and the ionization energies of RO(g) are shown in Table 7-3, the bond dissociation energies are plotted in Figure 7-8 and the promotion energy to the $4f^{n-3}5d^2$ configuration, $\Delta E[5d^2]$, in Figure 7-9.

7.7. CONCLUSIONS

In this chapter we have shown that the thermochemistry of the rare-earth oxides is well established for the majority of the stoichiometric compounds. The thermodynamic properties follow clear trends that can be understood in terms of valence states and electronic configurations of the lanthanide ions and metals. For the sesquioxides, the principal group of rare earth compounds, the data are reliable up to 2000 K, an interval in which the A, B and C phases are stable. However, for the high-temperatures, where the H and X phases are stable, no experimental data exist.

Enthalpies of formation remain to be measured for some of the lanthanide sesquioxides, e.g. La_2O_3(bcc), Nd_2O_3(monoclinic) and Gd_2O_3(monoclinic). The enthalpy of formation of Ce_2O_3 remains in doubt because of the discrepancy between solution and combustion calorimetry values (section 4.1). The thermochemical properties of metallic monoxides should be measured, but only when stoichiometric samples that are free of unreacted metal can be synthesized.

An area that needs further systematic study is the thermochemistry of gaseous oxides. Utilization of REMPI, MATI, and theoretical computations should lead to a systematic understanding of excitation energies and intrinsic bond energies that will enable better predictions to be made of corresponding trends for the actinide monoxides.

TABLE 7-1. Recommended Values for Thermochemical Properties of Crystalline Rare Earth Oxides at 298.15 K; estimated or calculated values in italics.

Oxide	$\Delta_f H°$(kJ mol^{-1})	C_p(J mol^{-1} K^{-1})	S°(J mol^{-1} K^{-1})
Y_2O_3 (bcc)	-1932.8 ± 5.2 [a]	103.4 ± 0.26 [b]	98.96 ± 0.40 [b]
La_2O_3(hex)	-1791.6 ± 1.0 [c]	108.78 ± 0.10 [d]	127.32 ± 0.84 [d]
Ce_2O_3(hex)	-1799.8 ± 1.8 [e]	115.0 ± 0.3 [f]	148.1 ± 0.4 [f]
CeO_2	-1090.4 ± 0.8 [c]	61.63 ± 0.06 [d]	62.29 ± 0.07 [d]
Pr_2O_3 (hex)	-1809.9 ± 3.0 [c]	118.14 ± 0.06 [g]	152.7 ± 0.3 [g]
Pr_2O_3 (bcc)	-1809.9 ± 3.0 [c]		
$PrO_{1.703}$	-926.3 ± 2.2 [h]		
$PrO_{1.717}$	-928.4 ± 2.6 [h]		
$PrO_{1.804}$	-938.9 ± 2.0 [h]		
$PrO_{1.833}$	-944.6 ± 2.5 [h]		*79.9 ± 2.0* [i]
PrO_2	-954.2 ± 5.0 [h]		*80.8 ± 3.0* [i]
Nd_2O_3 (hex)	-1806.9 ± 3.0 [c]	111.34 ± 0.12 [d]	158.7 ± 1.0 [d]
Pm_2O_3(monocl)	*-1811 ± 21*		*158.0 ± 3.0* [i]
Sm_2O_3 (monocl)	-1823.0 ± 4.0 [c]	114.52± 0.12 [d]	150.6 ± 0.3 [d]
Sm_2O_3 (bcc)	-1826.8 ± 4.0 [c]		
EuO	-591.3 ± 5.4 [j]	48.74 ± 0.20 [k]	83.6 ± 0.8 [k]
$EuO_{1.333}$	-756.8 ± 4.0 [k]		69.7 ± 2.9 [l]
Eu_2O_3(monocl)	-1650.4 ± 4.0 [c]	*123.9 ± 2.0* [i]	*138.6 ± 3.0* [i]
Eu_2O_3(bcc)	-1662.5 ± 6.0 [c]		
Gd_2O_3(monocl)	-1819.7 ± 3.6 [c]		
Gd_2O_3(bcc)	*-1854 ± 15*	105.52 ± 0.10 [d]	150.9 ± 0.15 [d]
Tb_2O_3(bcc)	-932.6 ± 3.0 [c]	*109.1 ± 2.0* [i]	*159.2 ± 3.0* [i]
$TbO_{1.510}$	-933.4 ± 3.6 [c]		
$TbO_{1.709}$	-952.3 ± 3.4 [h]		
$TbO_{1.710}$	-953.1 ± 3.9 [h]		
$TbO_{1.800}$	-966.1 ± 3.3 [h]		
$TbO_{1.817}$	-961.9 ± 3.5 [h]		
$TbO_{1.975}$	-970.5 ± 2.8 [h]		
TbO_2	*-972.1 ± 5.0* [h]		*86.9 ± 3.0* [i]
Dy_2O_3(bcc)	-1863.4 ± 5.0 [c]	116.28 ± 0.12 [d]	149.80 ± 0.15 [d]
Ho_2O_3(bcc)	-1883.3 ± 8.2 [c]	114.98 ± 0.12 [d]	156.38 ± 0.15 [d]
Er_2O_3(bcc)	-1900.1 ± 6.5 [c]	108.50 ± 0.12 [d]	153.13 ± 0.15 [d]
Tm_2O_3(bcc)	-1889.3 ± 5.7 [c]	116.74 ± 0.12 [d]	139.7 ± 0.4 [d]
Yb_2O_3(bcc)	-1814.5 ± 6.0 [c]	115.14 ± 0.12 [d]	133.1 ± 0.3 [d]
Lu_2O_3(bcc)	-1877.0 ± 7.7 [c]	101.76 ± 0.10 [d]	126.79 ± 0.13 [d]

[a] Morss *et al.* [22]
[b] Gavrichev *et al*. [39]
[c] Cordfunke and Konings [5], critically evaluated values
[d] Justice and Westrum [33-37]
[e] see text for reason why –(906.5 ± 1) kJ·mol^{-1} (selected by Cordfunke and Konings [5]) was not used
[f] Huntelaar *et al.* [24]
[g] Lutsareva *et al.,* as cited by Gruber et al. [38]
[h] recalculated, as explained in the text
[i] estimated, see also Konings [41,43], review
[j] recalculated, see text
[k] Teany and Moruzzi [50]
[l] Rard [86]

TABLE 7-2. High temperature heat capacity of selected complex actinide oxides; $C_p/J\cdot K^{-1}\cdot mol^{-1}$ = $a(T/K)^{-2} + b + c(T/K)$ (estimated values in italics, maximum temperatures in brackets).

		a 10^{-6}	b	c 10^{3}	T_{max}/K	Refs
Y_2O_3	cub	-1.93130	122.9107	7.43018	2000	a,b
La_2O_3	hex	-1.13668	120.6805	13.42414	2000	c,d,e
Ce_2O_3	hex	-0.641205	113.736	28.4344	1500	f
CeO_2	fcc	-1.29710	74.4814	5.83682	2000	b,g,h,i,
Pr_2O_3	hex	-0.98942	121.6594	25.5611	2000	j
$PrO_{1.833}$	fcc	-0.80968	68.4932	15.9207	750	j
Nd_2O_3	hex	-1.25845	117.1079	28.13655	2000	a,d
Sm_2O_3	mon	-1.86227	129.7953	19.03114	2000	a,k
Sm_2O_3	fcc	-2.40860	132.4358	18.7799	1150	a,k
Eu_2O_3	mon	-0.359472	123.5747	26.5436	2000	a,k
Eu_2O_3	fcc	-1.93169	139.6776	12.1460	1400	a,k
EuO			46.5453	7.3600	1800	l
Gd_2O_3	mon	-1.93587	118.9943	12.1248	2000	a,m
Gd_2O_3	fcc	-1.28397	114.8086	16.9162	1550	a,m
Tb_2O_3	fcc	-1.00261	120.6682	22.17194	2000	j
Dy_2O_3	fcc	-0.84580	121.2302	15.27609	2000	n
Ho_2O_3	fcc	-0.88628	121.9340	19.11623	2000	o,p
Er_2O_3	fcc	-1.54433	123.2921	8.62245	2000	o,q
Tm_2O_3	fcc	-1.17891	128.4322	5.23209	2000	o,r
Yb_2O_3	fcc	-1.44820	130.6438	3.34628	2000	o,r
Lu_2O_3	fcc	-2.03414	122.4593	7.29001	2000	b,n

[a] Pankratz *et al.* [98]
[b] Yashvili *et al.* [99]
[c] King *et al.* [100]
[d] Blomeke *et al.* [101]
[e] Yashvili *et al.* [102]
[f] Huntelaar *et al.* [24]
[g] King and Christensen [103]
[h] Kuznetsov and Rezukhina [104]
[I] Mezaki et al. [105]
[j] Pankratz [106]
[k] Gvelesiani *et al.* [107]
[l] McMasters *et al.* [51]
[m] Tsagareishvili *et al.* [106]
[n] Pankratz and Kelley [109]
[o] Pankratz and King [110]
[p] Tsagareishvili and Gvelesiani [111]
[q] Tsagareishvili and Gvelesiani [112]
[r] Tsagareishvili and Gvelesiani [113]

TABLE 7-3. Recommended Values for Thermochemical Properties of Gaseous Rare Earth Monoxides at 0 K [a]

Oxide	$\Delta_f H°$(kJ mol^{-1})	Bond dissociation energy D_0^o (kJ mol^{-1})	Ionization energy IP(MO,g) (kJ mol^{-1}) [b]
YO	-46 ± 10	715 ± 10	590 [c]
YO^+	+544		
LaO	-121 ± 10	795 ± 11	486
LaO^+	-62 ± 17	847 ± 15	
CeO	-117 ± 21	790 ± 17	475
CeO^+	-75 ± 17	849 ± 15	
PrO	-114 ± 12	745 ± 10	481
PrO^+	-22 ± 17	792 ± 15	
NdO	-126 ± 12	706 ± 12	490
NdO^+	+27 ± 17	749 ± 15	
SmO	-117 ± 12	569 ± 10	549
SmO^+	+225 ± 17	565 ± 15	
EuO	-46 ± 12	465 ± 15	623
EuO^+	+404 ± 17	389 ± 15	
GdO	-67 ± 12	711 ± 12	572
GdO^+	+107 ± 17	732 ± 15	
TbO	-54 ± 21	693 ± 21	541
TbO^+	+93 ± 17	718 ± 15	
DyO	-75 ± 21	607 ± 21	587
DyO^+	+226 ± 17	593 ± 15	
HoO	-54 ± 12	613 ± 10	596
HoO^+	+230 ± 17	598 ± 15	
ErO	-38 ± 12	607 ± 10	617
ErO^+	+256 ± 17	579 ± 15	
TmO	-31 ± 21	508 ± 10	627
TmO^+	+366 ± 17	478 ± 15	
YbO	+2 ± 21	401 ± 21	632
YbO^+	+478 ± 17	372 ± 15	
LuO	+8 ± 12	663 ± 10	667
LuO^+	+250 ± 17	520 ± 15	

[a] Chandrasekharaiah and Gingerich [3]).

[b] IP(MO,g) = D_0^o(MO,g) - D_0^o(MO^+,g) + IP(M,g) except for YO. D_0^o values from column 3 of this table [3]; IP(M,g) from Martin, *et al.* [114] 1974). *J. Phys. Chem. Ref. Data* **3,** 771-9.

[c] Linton et al. [115]

References

1. K.A. Gschneidner Jr., N. Kippenhan, and O.D. McMasters, *Report IS-RIC-6*, Ames Laboratory, Iowa State University, 1973.
2. L.R. Morss, *Chem. Rev.* **76**, 827 (1976).
3. M.S. Chandrasekharaiah, and K.A. Gingerich, in *Handbook of the Chemistry and Physics of the Rare Earths* (K.A. Gschneidner Jr. and L. Eyring, eds.), Vol. 12, Chapter 86, North-Holland, Amsterdam, p. 409, 1989.
4. R.G. Haire, and L. Eyring, in *Handbook of the Physics and Chemistry of the Rare Earths, (*K.A. Gschneidner Jr., L. Eyring, G.R. Choppin, and G.H. Lander, eds.) Vol. 18, Chapter 125, p. 413, North-Holland, Amsterdam, 1994.
5. E.H.P. Cordfunke and R.J.M. Konings, *Thermochim. Acta* **375**, 65-79 (2001).
6. C.E. Holley Jr., E.J. Huber Jr. and F.B Baker, in *Progress in the Science and Technology of the Rare Earths. Vol. 3,* (L. Eyring, ed.), Pergamon Press, New York, p. 343, 1968.
7. E.F. Westrum Jr. *J. Chem. Thermodyn.* **15**, 305-325 (1983).
8. M.E. Weeks and H.M. Leicester, *Discovery of the Elements,* 7th ed., Journal of Chemical Education, Easton, PA, 1968.
9. W. Muthmann and L. Weis, *Annals* **331**, 1 (1904).
10. J.E. Moose and S.W. Parr, *J. Am. Chem. Soc.* **46**, 2656 (1924).
11. W.A. Roth, U. Wolf, and O. Fritz, *Z. Elektrochem.* **46**, 42 (1940).
12. H. Bommer and E. Hohmann, *Z. anorg. Allg. Chem*. **248**, 357 (1941).
13. F.H. Spedding, B.J. Beaudry, J.J. Croat and P.E. Palmer, *Coll. Int. CNRS* **180**, Tome I, p.27 (1970).
14. F.H. Spedding and C.F. Miller, *J. Am. Chem. Soc.* **74**, 4195 (1952).
15. F.H. Spedding, R.E. Eberts, and A.W. Naumann, *Report ISC-934*, Ames Laboratory, 1959.
16. R.L. Montgomery and J. M. Stuve, *U. S. Bureau of Mines, Report RI 5892*, 1961.
17. H.W. Goldstein, P.N. Walsh, and D. White, *J. Phys. Chem.* **65**, 1400 (1960).
18. P.N. Walsh, D.F. Dever, D. White, *J. Phys. Chem.* **65**, 1410 (1960).
19. D. White, P.N. Walsh, H.W. Goldstein, and D.F. Dever, *J. Phys. Chem.* **65**, 1404 (1960).
20. L.L. Ames, P.N. Walsh, and D. White, *J. Phys. Chem.* **71**, 2707 (1967).
21. R.J. Ackermann, , E.G. Rauh, and R.J. Thorn, *J. Chem. Phys.* **65**, 1027 (1976).
22. L. R Morss, P.P. Day, C. Felinto, and H. Brito, *J. Chem. Thermodyn.,* **25**, 415 (1993).
23. X.-Y. Wang, J.T. Zhu, J. Goudiakas, and J. Fuger, *J. Chem. Thermodyn.,* **20**, 1195 (1988).
24. M. E. Huntelaar, A.S. Booij, E.H.P.Cordfunke, R.R. van der Laan, A.C.G. vamn Genderen, and J.C. van Miltenburg, *J. Chem. Thermodyn.* **32**, 465 (2000).
25. R.L. Putnam, A. Navrotsky, E.H.P. Cordfunke, M.E. Huntelaar, *J. Chem. Thermodyn.* **32**, 911 (2000).
26. F. David, *J. Less-Comon Met.* **121**, 27 (1986).
27. F.B. Baker and E.J. Holley Jr., *J. Chem. Eng. Data* **13**, 405 (1968).
28. K.A. Gschneidner Jr., *J. Less-Common Metals,* **17**, 1, 1969).
29. K.A. Gschneidner Jr., *J. Less-Common Metals,* **17**, 13 1969).
30. K.A. Gschneidner Jr., *Metals Materials and Processes,* **1**, 241 (1990).
31. L. Brewer, in *Systematics and the Properties of the Lanthanides,* (S.P. Sinha ed.), D. Reidel, 17-69 (1983).

32. J.L. Burnett and B.B. Cunningham, in *Proc. 4th Conf. on Rare Earth Research,* (L. Eyring, ed.) Gordon and Breach, New York, pp. 585, USAEC Report UCRL-11126, 1964.
33. B.H. Justice and E.F. Westrum Jr., *J. Phys. Chem.* **67**, 339 (1963).
34. B.H. Justice and E.F. Westrum Jr., *J. Phys. Chem.* **67**, 345 (1963).
35. B.H. Justice and E.F. Westrum Jr., *J. Phys. Chem.* **67**, 659 (1963).
36. B.H. Justice and E.F. Westrum Jr., E. Chang, and R. Radebaugh, *J. Phys. Chem.* **73**, 333 (1969).
37. B.H. Justice and E.F. Westrum Jr., *J. Phys. Chem.* **73**, 1959 (1969).
38. J. B. Gruber, B.H. Justice and E.F. Westrum Jr., and B. Zandi, *J. Chem. Thermodyn.*, 34, 457-473 (2002).
39. K.S. Gavrichev, V.E. Gorbunov, L.N. Golushina, G.E. Nikiforova, G.A. Totrova, and I.S Shaplygin, *Russ. J. Phys. Chem.* **67**, 1554 (1993).
40. N.S. Lutsareva, V.N. Naumov, and I.E. Paukov, cited in Gruber et al. [38].
41. R.J.M. Konings, *J. Nucl. Mater.* **295**, 57 (2001).
42. C.A. Morrison and R.P. Leavitt, in *Handbook on the Physics and Chemistry of Rare Earths (K.A. Gschneidner Jr., and L. Eyring, eds.)*, Vol. 5, Chapter 46, p. 461-692, 1982.
43. R.J.M. Konings, in preparation (2004).
44. M. Foex and J.-P. Traverse, *Rev. Int. Hautes Tempér. et Réfract.* **3**, 49 (1966).
45. M.R. Oliver, J.D. Dimmock, A.L. McWhorter, and T.B. Reed, *Phys. Rev. B,* **5**, 1078 (1972).
46. J.L. Burnett Ph.D. Thesis, University of California, Berkeley; Report UCRL-11850 (1964).
47. J.M. Haschke and H.A. Eick, *J. Phys. Chem.* **73**, 374 (1969).
48. E.J. Huber Jr. and C.E. Holley Jr., *J. Chem. Thermodyn.* **1**, 301 (1969).
49. E.J. Huber Jr. and C.E. Holley Jr., *J. Chem. Thermodyn.* **2**, 896 (1970).
50. D.T. Teany and V.L. Moruzzi, *Coll. Int. CNRS* **180**, Vol II, p 131 (1970).
51. O.D. McMasters, K.A. Gschneidner Jr., E. Kaldis, and G. Sampietro, *J. Chem. Thermodyn.* **6**, 845 (1974).
52. G. Brauer, H. Bärnighausen, and N. Schultz, *Z. anorg. allg. Chem.* **356**, 46 (1967).
53. N.A. Fishel, J.M. Haschke, and H.A. Eick, *Inorg. Chem.* **9**, 413 (1970).
54. J.M. Haschke and H.A. Eick, *Inorg. Chem.* **9**, 851 (1970).
55. G.J. McCarthy and W.B. White, *J. Less-Common Metals* **22**, 409 (1970).
56. J.M. Leger, N. Yacoubi, and C. Loriers, *J. Solid State Chem.* **36**, 261 (1981).
57. G. Krill, M.F. Ravet, J.P. Kappewr, L. Abadli, J.M. Leger, N. Yacoubi, and C. Loriers, *Solid State Commun.* **33**, 351 (1980).
58. K-J. Range, M. Stadler, F. Rau, and U. Klement, *Angew. Chem. Int. Ed. Engl.* **26**, 1174 (1987).
59. E.J. Huber Jr. and C.E. Holley Jr., *J. Am. Chem. Soc.,* **75**, 5645 (1953).
60. F.B. Baker, E.J. Huber Jr. and C.E. Holley Jr., and N.H. Krikorian, *J. Chem. Thermodyn.* **3**, 77 (1971).
61. F.A. Kuznetsov, T.N. Rezukhina, and A.N. Gobulenko, *Russ. J. Phys. Chem.* **34**, 1010 (1960).
62. F.A. Kuznetsov, V.I. Belyi, T.N. Rezykhina, and Ya.I.. Gerasimov, *Dokl. Akad. Nauk SSSR* **139**, 1405 (1961).
63. E. F. Westrum Jr. and A.F. Baele Jr., *J. Chem. Phys.* **65**, 353 (1961).
64. S.A. Gramsch, and L.R. Morss, *J. Chem. Thermodyn.* **27**, 551 (1995).
65. B.G. Hyde, E.E. Garver, U.E. Kuntz, and L. Eyring, *J. Phys. Chem.* **69**, 1667 (1965).

66. S.V. Ushakov and A. Navrotsky, 23rd Rare Earth Research Conference, Davis, 2002.
67. G.C. Fitzgibbon and C. E. Holley Jr., *J. Chem. Eng. Data* **13**, 63 (1968).
68. C.T. Stubblefield, H. Eick, and L. Eyring, *J. Am. Chem. Soc.* **78**, 3877 (1956).
69. D.J.M. Bevan and J. Kordis, *J. Inorg. Nucl. Chem.* **26**, 1509 (1964).
70. K. Kitayama, K. Nojiri, T. Sugihara, and T. Katsura, *J. Solid State Chem*. **56**, 1 (1985).
71. O.T. Sørensen, *J. Solid State Chem.* **18**, 217 (1976).
72. J. Campserveux and P. Gerdanian, *J. Chem. Thermodyn.* **6**, 795 (1974).
73. J. Campserveux and P. Gerdanian, *J. Solid State Chem.* **23**, 73 (1978)**.**
74. T.B. Lindemer, *CALPHAD*, **10**, 129 (1986).
75. G.C. Fitzgibbon, E.J. Huber Jr., C.E. Holley Jr., *Rev. Chim. Minerale* **10**, 29 (1973).
76. B.G. Hyde, D.J.M. Bevan, and L. Eyring, *Phil. Trans. Royal Soc. A* **259**, 583 (1966).
77. M.S. Jenkins, R.P. Turcotte, and L. Eyring, in *The Chemistry of Extended Defects in Non-Metallic Crystals* (L. Eyring and M. O'Keeffe, eds.) pp. 36-53, North-Holland, Amsterdam, 1970.
78. F.J. Lincoln, J.R. Sellar, and B.G. Hyde, *J. Solid State Chem*. **74**, 268 (1988).
79. H. Inaba, A. Navrotsky, and L. Eyring, *J. Solid State Chem.,* **37**, 67 (1981).
80. B.G. Hyde and L. Eyring, in *Rare Earth Research III,* (L. Eyring, ed) Gordon & Breach, New York, pp 623, 1965.
81. H. Inaba, A. Navrotsky, and L. Eyring, *J. Solid State Chem.,* **37**, 77 (1981).
82. D.R. Knittel, S.P. Pack, S.H. Lin, and L. Eyring, *J. Chem. Phys.* **67**, 134 (1977).
83. J.M. Haschke and H.A. Eick, *J. Phys. Chem.* **72**, 4235 (1968).
84. I.S. Sukhushina, and I.A. Vasil'eva, *Russ. J. Phys. Chem.* **64**, 1734 (1990).
85. I.S. Sukhushina, and I.A. Vasil'eva and R.F. Balabaeva, *Russ. J. Phys. Chem.* **70**, 49 (1996).
86. J.A. Rard, *Chem. Rev.* **85**, 555 (1985).
87. K.A. Gingerich, in *Current Topics in Materials Science,* (E. Kaldis ed.), North-Holland, Amsterdam, Ch. 5, 1980.
88. J.K. Gibson, *J. Phys. Chem.* **100**, 15688 (1996).
89. J.K. Gibson, *J. Phys. Chem. A* **107**, 7891 (2003).
90. J.B. Pedley and E.M. Mashall, *J. Phys. Chem. Ref. Data* **12**, 967 (1983).
91. J. Han, L.A. Kaledin, V. Goncharov, A.V. Komissarov, and M.C. Heaven, *J. Am. Chem. Soc.* **125**, 7176 (2003).
92. J. Han, V. Goncharov, L.A. Kaledin, A.V. Komissarov, and M.C. Heaven, *J. Chem. Phys.* in press, 2004.
93. E.G. Rauh, and R.J. Ackermann, *J. Chem. Phys.* **60**, 1396 (1974).
94. E. Murad, and D.L. Hildenbrand, *J. Chem. Phys*. **73**, 4005 (1980).
95. R.G. Haire, *J. Alloys Comp.* **213/214**, 185 (1994).
96. M. Santos, J. Marçalo, A. Pires de Matos, J.K. Gibson, and R.G. Haire, *J. Phys. Chem.* A, 2002, 7190 (2002).
97. M. Santos, J. Marçalo, P. Leal, A. Pires de Matos, J.K. Gibson, and R.G. Haire, *Int. J. Mass Spectrom.* **228**, 457 (2002).
98. L.B. Pankratz, E.G. King, and K.K. Kelley, *U. S. Bureau of Mines, Report RI-6033,* 1962.
99. T.S. Yashvili, D.Sh.Tsagareishvili, and G.G. Gvelesiani, *Bull. Acad. Sci. Georgian SSR* **46**, 410 (1967).

100. E.G. King, W.W. Weller, and L.B. Pankratz, *U. S. Bureau of Mines, Report RI –5857*, 196.
101. J.O. Blomeke and W.T. Ziegler, *J. Am. Chem. Soc.* **73**, 5099 (1951).
102. T.S. Yashvili, D.Sh. Tsagareishvili, and G.G. Gvelesiani, *Teplofiz. Vys. Temp.* (transl) **6**, 781 (1968).
103. E.G. King and A.U. Christensen, *U. S. Bureau of Mines, Report RI-5789* (1960).
104. F.A. Kuznetsov and T.N. Rezukhina, *Russ. J. Phys. Chem.* **34**, 1164 (1960).
105. R. Mezaki, E.W. Tilleux, T.F. Jambois, and J.L. Margrave, in *Adv. Thermophys. Prop. Extreme Temp. Press. 3rd ASME Symp. Lafayette Indiana (Gratch S., Ed.), p.138, 1*965.
106. L.B. Pankratz, *U. S. Bureau of Mines, Report RI-6781*(1966).
107. G.G. Gvelesiani, D.Sh. Tsagareishvili, and T.S. Yashvili, *Inorg. Mat.* **4**, 476 (1968).
108. D.Sh.Tsagareishvili G.G. Gvelesiani, and T.S. Yashvili, *Russ. J. Phys. Chem.* **43**, 487 (1969).
109. L.B. Pankratz, and K.K. Kelley, *U. S. Bureau of Mines, Report RI-6248,* 1962.
110. L.B. Pankratz, and E.G. King, *U. S. Bureau of Mines, Report RI-6175*, 1962.
111. D.Sh. Tsagareishvili and G. G. Gvelesiani, *Teplofiz. Vys. Temp.* (transl) **9**, 1679 (1971).
112. D.Sh. Tsagareishvili and G. G. Gvelesiani, *Teplofiz. Vys. Temp.* (transl) **9**, 588 (1971).
113. D.Sh. Tsagareishvili and G. G. Gvelesiani, *Russ. J. Phys. Chem.* **10**, 171 (1968).
114. W.C. Martin, R. Zalubas, and L. Hagan, *Atomic Energy Levels – The Rare Earth Elements.* Report US-NBS NSRDS-60. U.S. Department of Commerce; Washington DC, 1978.
115. C. Linton, B. Simard, H.P. Loock, S. Willin, G.K. Rothschopf, R.F. Gunion, M.D. Morse, and P.B. Armentrout, *J. Chem. Phys.* **111**, 5017 (1999).

8. TRACE AND ULTRATRACE DETERMINATION OF LANTHANIDES IN MATERIAL AND ENVIRONMENTAL SAMPLES

T.P. Rao
Regional Research Laboratory (CSIR)
Trivandrum - 695 019
India

8.1. INTRODUCTION

The determination of trace and ultra trace amounts of individual Rare earth elements (REE) in complex matrices is one of the most challenging areas of analytical chemistry. Rapid studies made in analytical methodology have brought forth many powerful analytical tools for the determination of trace and ultra trace amounts of lanthanides. These are based on spectral, nuclear, X-ray, electrochemical and other chemical properties of lanthanides. Each technique provides a different and unique approach for the determination of lanthanides and offers certain advantages over others for a given analysis of complex materials. Hence it is desirable to compare the performance of various techniques available in terms of **i)** primary criteria like sensitivity, selectivity and precision and accuracy and **ii)** auxiliary criteria like speed, cost of equipment, availability etc. while choosing analytical technique.

The chemical elements with atomic numbers 57-71 along with lanthanum are known as lanthanides. Yttrium has similar ionic radius as that of lanthanides. Further, Yttrium exists along with lanthanides in nature and is usually grouped with lanthanides. With increasing demand for lanthanides and their compounds individually and collectively based on their newer and proven applications in modern technology, the analysis of these elements in variety of real samples assumes increasing importance [1,2]. Further the electrical and magnetic properties of various Rare earth based materials are influenced by the levels of trace and Ultratrace impurities. It is therefore important to determine these trace impurities in high purity Rare earth oxides. The non rare earth analyses in Rare earth oxides can be determined by any of the analytical techniques either directly or by using prior separation techniques like ion exchange, Liquid-Liquid extraction, solid phase extraction, co-precipitation, flotation, electrodeposition and sorption or immobilization. [3-6]. On the other hand, the determination of trace lanthanides in natural & sea water (as they are at ng/l) and high purity materials of different

G. Adachi et al. (eds.), Binary Rare Earth Oxides, 189–214.

purities are more important and arduous tasks. Hence a judicious selection of analytical technique based on primary and auxiliary criteria mentioned above is essential during the trace and ultratrace determination of individual lanthanides in real complex samples. The salient features of analytical procedures developed for this purpose since 1980 are summarized in Tables 1-3.

8.2. ANALYTICAL TECHNIQUES

8.2.1. *Molecular absorption spectrometry (MAS)*

Mas is concerned with the determination of the concentration of analyte by measurement of the relative absorption of light with respect to a known concentration of the substance. The fundamental equation of MAS is $\log I_o/I_t$ or $A = \in ct$ where I_o and I_t are intensity of incident and transmitted lights, A is absorbance, c is concentration in moles/liter, t is thickness of the cell and $\in$ is molar absorption coefficient or molar absorptivity. REE have characteristic absorption peaks in UV and visible regions due to f electron transitions and can be used for their monitoring but are less sensitive i.e. characterized by low $\in$ values. However, as incase of other inorganics, REE can be determined by forming coloured complexes (binary or ternary) with various chromogenic reagents. In this case the $\in$ values vary in the range 10^4-10^5 and can be used for determination of REE in electronic, metallurgical and environmental samples which has been reviewed elsewhere [174]. However, these determinations are limited by the fact that all REE - chromogenic reagent complexes will have similar molecular absorption spectra with almost identical wavelength maxima. Hence, REE as a group or any one REE present in complex matrices could only be determined.

8.2.2. *Higher order derivative MAS (HDMAS)*

Derivative techniques were employed in instrumental methods of analysis for many decades. The technique of second and higher order derivative spectroscopy was patented as early as 1940. The rapid evolution of microcomputers and advent of low noise operational amplifiers led to renaissance of interest in derivative techniques. HDMAS was used in inorganic analysis only in 1985. The first few reports pertains to resolution of closely related molecular absorption spectra of Rare earths during the determination of individual REE in their mixtures [175]. These include **(i)** second and fourth order derivative spectrophotometric determination of Nd, Ho & Er after reaction with 4-benzoyl 3-methyl-1-phenyl pyrazolin - 5 one [176] **(ii)** third order derivative MAS determination of Nd, Ho, Er & Tm by using thenoyl trifluroacetone as chromogenic reagent [177] and **(iii)** simultaneous determination of lanthanum and europium by using higher order derivative MAS techniques [178].

8.2.3. *Molecular fluorescence spectrometry (MFS)*

Fluorescence is caused by the absorption of radiant energy and the re-emission in the form of light. The light emitted is almost always of higher wavelength than that absorbed (stroke's law). In true fluorescence the absorption and emission take place in a short but measurable time - of the order of 10^{-12} - 10^{-9} second.

The total fluorescence intensity, F is given by the equation

$$F = I_a \phi_f,$$

Where I_a is the intensity of light absorption and ϕ_f the quantum efficiency of fluorescence. Since, $I_o = I_a + I_t$, where I_o = intensity of incident light and I_t = intensity of transmitted light, then

$$F = (I_o - I_t)\, \phi_f$$

And since $I_t = I_o e^{-\epsilon ct}$ (Bear lambert Law)

$$F = I_o (1 - e^{-\epsilon ct})\, \phi_f$$

For weakly absorbing solutions, when ϵct is small, the equation becomes

$$F = I_o . 2.3\, \epsilon ct \phi_f$$

so that for very dilute solutions (a few ppm, or less) the total fluorescence intensity F is proportional to both the concentration of the sample and the intensity of the incident light.

Fluorescence spectroscopy has several analytical advantages over other spectroscopic methods such as absorption spectrometry. The most significant are selectivity and sensitivity, which are inherent to the technique. The selectivity arises from the fact that both the absorption and emission occur at specific wavelength ranges for a given flurophore. The detection limits are typically 100 to 1000 times better in MFS than MAS. These attributes make MFS a powerful tool for analytical measurements.

Factors such as dissociation, association or solvation, which results in deviation from the Beer-Lambert law, can be expected to have a similar effect in MFS. Fluorescence is affected by the pH of the solution, by the nature of the solvent, the concentration of the reagent which is added in the determination of inorganic ions, and, in some cases, by temperature. The time taken to reach the maximum intensity of fluorescence varies considerably with the reaction. Another limitation of this technique for Rare earth analysis is that only few REE exhibit fluorescence and other REE cannot be used for their quantification [179]. Attempts to the use of fluorimetric regents such as dyes results in non - selectivity and thus does not distinguish individual REE when present in mixtures.

8.2.4. *Atomic absorption spectrometry (AAS)*

Flame AAS (FAAS)

FAAS involves aspiration of the sample solution into a flame whose high temperature convert the analyte metal ions into atoms in the vapour state. Most of this atomic vapour exists in the ground electronic state and can therefore absorb resonant radiation of an appropriate wavelength. A hollow cathode lamp consisting of a cathode of element of interest and tungsten anode enclosed under reduced pressure and filled with an inert gas. When a voltage is applied across the electrodes, the filler gas is positively ionized at the anode and accelerated towards the cathode, which under this bombardment sputters to form an atomic vapour in an excited electronic state. While returning to ground state, lines characteristic of the element are emitted. These lines pass through the flame, which are absorbed by atoms of their own and not other atoms. Sample has to be brought into solution before measurement. Use of aqueous as well as some organic solvents allow determination of around 70 elements by FAAS. As atomic lines are sharp unlike molecular spectral lines, FAAS was initially thought to be free of all interferences. However, experience gained over last few decades showed that there are large number of problems such as molecular / spectral interferences, ionization interferences, mutual chemical interferences and matrix interferences because of differing viscosity and surface tension between samples and standard solutions. The main draw back of this technique is only one element is determined at a time although few manufactures supply the instruments capable of determining more than one element simultaneously. Nitrous oxide - Acetylene flame was used for quantification of Rare earth elements. In spite of this, except europium the sensitivities obtainable for other REE were very poor and are not enough to determine REE in natural water samples and some electronic materials even after preconcentration. However, FAAS is ideal for the determination of REE in metallurgical samples.

Electrothermal atomization - AAS (ETA-AAS)

Electrically heated graphite tubes or rods reaching temperatures upto 3000K replace the regular flame of FAAS. Except for flameless environment, the principles of ETA-AAS are the same as in case of FAAS. The electrical power to the furnace is applied in 3 steps - drying to remove the water and acid vapour, ashing to remove organic and volatile compounds in the sample, and finally atomization of the analyte metal species. Though attempts have been made to analyse solid samples directly by ETA-AAS, there are difficulties encountered in this approach. These include **i)** difficulty in obtaining a representative sample as only mg amounts are analysed and **ii)** problems in finding a calibration procedure that accounts for a solid matrix.

Like FAAS, ETA-AAS is a single element technique and is specific for the element being determined. Two major advantages of ETA-Aas over FAAS are small sample volume and high sensitivity. Usually, 5 to 10µl of sample is needed for

ETA-AAS Vs several ml needed for aspiration in FAAS. The sensitivities obtained by ETA-AAS are 100 fold or more compared to FAAS. On the other hand, measurement time is more than FAAS, since the sample has to go through the stages of in situ drying, ashing and atomization, and then cooling of the carbon furnace. When first introduced, the ETA-AAS technique was hailed as extremely sensitive and completely free of interferences. The sensitivity claim is certainly true, but it has now been recommended even by the manufacturers to use ETA-Aas only when FAAS cannot meet the demands of sensitivity. Accordingly, ETA-Aas was widely used for determination of REE in metallurgical and environmental samples. (after preconcentrative separation of matrix in case of seawater) and electronic materials.

8.2.5. *X- ray fluorescence (XRF)*

If an X-ray photon removes an electron from the K or L shell of an atom, characteristic K or L X-rays of that atom are emitted as an electron falls from another higher energy level to fill the vacancy. Typically the K X-rays of adjacent elements in the periodical table with atomic numbers ≥15 are separated by energies of a few 100 ev. With the recent advent of high resolution solid state Si(Li) detectors, which have resolutions down to 150 ev, it is possible to determine many elements simultaneously by recognizing their characteristic x-rays emitted from a sample. X-Ray tubes usually with Mo or Cu tubes provide X-ray emission of the order 10^{12}-10^{13} photons s^{-1} $sterdian^{-1}$ are often preferred over Radioactive or electron excitation sources. Radioisotopes are commonly used because of their stability and small size when continuous & monochromatic sources are needed. However, safety regulations require that X-ray emission from these sources is limited to about 10^{7} photons s^{-1} $sterdian^{-1}$. This difference is only partly compensated for by the small size of the source, which allows very compact source – specimen – detector to be constructed that are very convenient due to their portability. If heavy charged particles like protons are used for excitation, the technique is called proton induced X-ray excitation (PIXE) and the sensitivity is several orders higher.

Wavelength dispersive X-ray fluorescence (WDXRF) spectrometers employ diffraction by a single crystal to separate characteristic wavelengths emitted by a sample. Energy dispersive X-ray fluorescence (EDXRF) spectrometers use the proportional characteristics of a photon detector, typically lithium drifted silicon, to separate the characteristic photons in terms of their energies. Since there is a simple relationship between wavelength and energy, these techniques provide the same basic types of information and the characteristics of the two methods differ mainly in their relative sensitivities and the way in which data are collected and presented. WDXRF is generally one or two orders more sensitive than EDXRF. Total reflection XRF(TXRF) is similar to EDXRF in the sense that energy at which intensity is maximum is the characteristic of that element. The only difference between these two techniques is that the X-rays produced by X-ray tube are reflected over a double reflector before passing through the sample.

Unless a comparison is made with a standard, which is identical in composition to the sample, systematic errors in XRF may be large. Particle size and shape are important and determine the degree to which incident beam is absorbed or scattered. Hence, standards and samples must be powdered to the same mesh size, preferably finer than 200 mesh. Simultaneous determination of several elements is possible by XRF with automated equipment.

8.2.6. *Luminescence spectrometry (LS)*

The terms Luminescence refers to all other forms of light emission and involves a radiative transition where by a molecule lowers its energy by emission of a photon. In order for the luminescence process to exist for any period of time, energy must be supplied to the system to maintain an excited state population. Different forms of luminescence have been classified based on the source of this energy. While several interesting forms of luminescence exist (eg. Electroluminescence, bioluminescence, radioluminescence, triboluminescence, and sonoluminescence) the type of luminescence, which is of analytical importance is photoluminescence. In photoluminescence the excited state is produced by the absorption of light.

Luminescence processes can further be categorized as fluorescence or phosphorescence. This distinction is based on the multiplicity of the two energy levels involved in radiative deactivation from the excited state. If the electron spin state of the two energy levels are the same, the process is referred to as fluorescence. In contrast, if the spin states are not the same, the process is appropriately called as phosphorescence.

8.2.7. *Neutron activation analysis (NAA)*

One of the most sensitive trace element technique is NAA where in the danger of contamination and loss of elements is eliminated. NAA started as a single element technique when only Geiger – Muller counters and NaI(TI) detectors were available. However, with the availability of multichannel analysers and high resolution Ge(Li) & Si (Li) detectors, it has become a truly multielement technique. In NAA, the samples and the standards containing the elements of interest are irradiated in a nuclear reactor with a beam of thermal neutrons. The resultant daughter isotopes are measured in a X-ray spectrometer or in a β –counter after suitable decay periods. Instrumental NAA (INAA) does not involve any chemistry and the irradiated samples are simply counted over a period of time which gives the elemental concentration in the sample directly. The NAA technique is on par with ETA-AAS or Inductively coupled plasma atomic emissionspectroscopy (ICP-AES) in terms of sensitivity and is ideally suited for multi element analysis. Depending upon the half life of the isotope produced, an analysis can take from a few minutes (eg ^{28} Al-2.3 min) to several weeks (eg ^{60} Co-5.23 years), The main virtue of NAA is its nondestructive nature and the same sample can be used for determination by other analytical techniques for comparison. Hence, NAA is most suited for the

determination of individual REE in metallurgical and environmental samples and electronic materials.

8.2.8. *Atomic emission spectrometry (AES)*

ES is based on light emission at characteristic wavelengths by the elements. When heated to a high enough temperature, every element emits discreet and characteristic spectral lines. The number of lines of an element varies inversely with its sensitivity. Thus, Na with a simple spectrum of dozen or so lines widely dispersed from the UV to IR regions is highly sensitive in ES. Uranium on the other hand, with thousands of lines is very less sensitive. However by taking advantage of characteristic wavelengths and specific identification, the quantification of elements is possible.

Direct current plasma (dcp) AES

In DCP-AES, the powdered samples were homogeneously mixed with high purity graphite and packed onto graphite electrodes and are subjected to a DC ark or spark for a few seconds. The resultant light emission is dispersed by a prism or a grating spectrograph and can be either recorded on a photo plate or electronically detected. Upto 70 elements at levels down to 10ng can be analysed by DCPAES without excessive pretreatment of samples. Sensitivity varies widely from ppm levels for simpler low atomic number elements to 0.1% for some of the transition or semi metal elements.

Inductively coupled plasma - AES (ICP-AES)

The development of plasma sources for ES led to the development of more powerful technique known as ICP-AES. ICP derives its sustaining power by induction from high frequency magnetic fields. The plasma is formed and maintained at the open end of a quartz tube assembly. The open end is surrounded by the induction coil connected to the high frequency generator. The plasma is stabilized by a pattern of two or three argon flows. When these flows are properly adjusted, the plasma is readily initiated by tickling the quartz tubes inside the induction coil with a Tesla discharge. Gas temperatures in the range 9,000 to 10,000°K are achieved in the plasma. The sample (usually solutions but sometimes finely powdered solids) is injected into the plasma, where the metals undergo atomization and excitation. The emission spectrum of metal ions is then analyzed as in case of ES. However, since it is essentially a solution technique where sample solution is nebulized, takes few minutes as compared with several hours in DCP - AES [180].

ICPAES is well suited for real time simultaneous multielement analysis. The high temperatures used result in greater freedom from chemical interferences and increase the range of elements that can be determined. This technique has extremely high sensitivity and calibration curve is linear over six orders of magnitude.

8.2.9. *Mass spectrometric techniques (MS)*

Inductively coupled plasma MS (ICP-MS)

The combination of ICP torch and mass spectrometric resolution resulted in a much more powerful technique than ICP-AES in terms of sensitivity, selectivity and precision. Further, the coupling of MS to ICP results in the analysis of isotopes of various elements. In ICP-MS, the plasma torch is in a horizontal position and it works under normal pressure. An interface cone is placed between a plasma source and mass spectrometer. Ions produced in ICP are transferred to the mass spectrometer through a small hole (about 1 mm in diameter) in the cone. The mass spectrometer is usually a quadrapole analyser.

ICPMS can be used for both qualitative and quantitative trace and ultra trace elemental analysis of inorganics and in isotope ratio determinations. Both cations and anions can be determined. Normally, the sample is introduced in the form of a solution into the plasma, but direct analysis of gaseous or solid sample is also possible. Hence, ICP-MS has grown into a referral technique for the ultra trace analysis of REE in electronic materials, and metallurgical samples. The individual REE concentrations in natural and sea waters are so low and require preconcentration techniques prior to determination by ICP-MS. Separation in addition to preconcentration is also needed as high salt matrix of sea waters results in irreproducible results in ICP-MS analysis of individual REE.

Spark Source Mass Spectrometry (SSMS)

SSMS is one of the most sensitive and comprehensive techniques of trace analysis of inorganic systems. It employs a vacuum spark in which a high voltage radio frequency discharge (20 to 100 KV) is produced between two closely spaced electrodes of the material to be analyzed. The repetition rate and duration of the radio frequency spark source is variable in order to meet the various analytical requirements. The design of the instrument employs double-focusing Mattuch-Herzog geometry, which allows simultaneous focusing of all masses. This permits simultaneous photographic recording of nearly all elemental masses and integration over a period of time to provide high sensitivity. In the source of region of the SSMS spectrometer, two electrodes made from the material being analyzed are sparked resulting in vaporization and ionization of sample constituents. After acceleration of ions into the slit system, the electrostatic analyser selects for transmission ions of a certain energy range with no mass separation. The magnetic field then separates the ion beam according to mass to charge ratio, providing the mass analysis at the same time. The ions may be recorded either electrically or photographically. For SSMS, the sample has to be electrically conductive. This is achieved for non conducting materials by blending them with high purity graphite followed by briquetting to form electrodes that sustain the vacuum spark.

The technique is capable of providing information simultaneously on about 50 or more elements in the concentration range from 100 ppm to a few ppb with reproducibilities in the order of 10 to 25% and with comparable accuracy when

standards are employed. Quantitative analysis can be carried out by comparing the intensity of element of interest to that of an internal matrix element line.

8.2.10. *Ion Chromatography (IC)*

Ion chromatography (IC) is widely used for separation of inorganics viz. alkali, alkaline earth, transition, heavy metals and lanthanides. Conductivity or refractive index detectors are widely used for the determination of alkali & alkaline earths. On the other hand, transition, heavy metals and REE were usually determined by chelation ion chromatography with post column UV - visible detection. The choice of chelating agent helps in separating the alkali and alkaline earth matrix present in complex samples like seawater, alloys etc. Chelation ion chromatography with α-hydroxyisobutyric acid as chelating agent [181] allows the determination of transition metals & individual REE in single injection with 4-(2-pyridylazo) resorcinol as the post column reagent. Isocratic separation of 14 lanthanides and yttrium was described using a chromatographic column packed with iminodiacetic acid bonded to silica and Dil. HNO_3 solutions in the presence of KNO_3 as eluent [182]. Arsenazo III was used as a post column reagent in this case. IC separation followed by UV - visible spectrophotometric detection is not sensitive enough to determine individual REE in natural or sea waters as their concentration are at ng/l level. The limitation is with the detection technique and not in IC separation as was proved later by coupling IC with ICP MS detector.

8.2.11. *Coupled techniques*

Coupled techniques are widely used in organic chemistry for identification and analysis, which include GC-MS, GC-FTIR and GC-MS-FTIR. On the other hand, coupled techniques are introduced in inorganic analysis only recently. Coupled techniques offer the advantages of better resolution, better selectivity and high sensitivity over the singular techniques. Coupled techniques like FIA-AAS, FIA-ICPAES, FIA-ICPMS, IC-ICPMS,HPLC-ETA AAS, HPLC-ICPAES and HPLC-ICPMS are employed for trace and ultra trace analysis of inorganics. A few of these coupled techniques are also employed for the determination of individual REE in a variety of real samples of metallurgical and environmental origin and high purity electronic materials as seen form Tables 1-3.

8.3. CONCLUSIONS

As projected in our chapter in Handbook on the physics and chemistry of Rare earths in 1990, ICP-AES and ICP-MS were widely used in last 10 years [183]. These techniques almost replaced spectrography and XRF techniques employed in 1970's and 1980's as the detection limits of individual REE are much lower (See Table 4) and also latter techniques require elaborate and cumber some sample preparation. ICP-AES and ICP-MS procedures developed were frequently tested by

analysing real complex samples of environmental, metallurgical and biological origin and electronic materials during last 10 years. As in earlier period, these techniques are being used widely for analysis of individual REE in geological samples even now. Recently we have highlighted the need for the preparation of certified reference materials (CRM's) for REE in samples of waters, sediments, soils and high purity materials [184]. Further, the preparation of CRM's involves the use of various analytical techniques based on different principles viz. X-ray (WDXRF or TXRF) spectral (ICPAES or icpms) and nuclear (NAA) and through inter laboratory exercises. Another aspect which will be paid maximum attention in coming years is to develop coupled techniques for offline or online preconcentrative separation followed by multielement determination techniques like ICPAES or ICP-MS.

ACKNOWLEDGEMENT

The author thanks Mr. Biju V.M. for his unstinted co-operation during the preparation of this manuscript.

TABLE 8-1. Trace and ultra trace determination of REE in electronic materials

Sl..No (1)	Analytical technique (2)	REE[R] (3)	Matrix (4)	Special features of analytical procedure (5)	Sensitivity/ Detection limit (6)
1	MAS	Ce [7]	Mixed RE	Oxidation of methyl orange	0-1µg/ml
2.	MAS	Nd [8]	YAG	------	------
3.	MAS	Nd [9]	Laser glasses	λ_{max} = 795.5nm	
4.	MAS	Sm [10]	ZrO_2	$_P$H 7.0 - 7.9, Arsenazo I	10-35% Sm_2O_3
5.	MAS	Eu [11]	RE oxides	Reduction of molybdo-phosphoric acid	------
6.	MAS	Eu [12]	RE oxides	Extraction of Mo/blue into isopentanol	2-50 µg/ml
7.	MAS	Eu [13]	Red phosphor	Dibromocarboxy arsenazo	0.04 - 1.0 µg/ml
8.	MAS	Er [14]	Silicate glasses	λ_{max} = 377.5 nm	------
9.	MAS	Y [15]	Y-Ba-Cu oxide	Arsenazo III, $_P$H 4.7	
10.	MAS	Y [16]	------	Arsenazo III, λ_{max} - 650nm	------
11.	HDMAS	Dy, Ho & Er [17]	RE_2O_3	Second Order derivative	0.001 - 0.2%
12.	HDMAS	Dy & Y [18]	RE_2O_3	Fourth Order derivative	------
13.	FIA-MAS	REE [19]	RE_2O_3	Arsenazo III	0.7mg/l
14.	MAS	REE [20]	Synthetic Mixtures	DBC - CPA	------
15.	MES	Lu [21]	RE_2O_3	TTA-salicylic acid	------
16.	MFS	Er [22]	Sea water	5,7-dichloroquinoline--8-ol, Rhodamine 6G	------
17	AAS	Nd [23]	YAG	------	------
18	AAS	Y [24]	Y-Ba-Cu oxide	597.2 mm	5.50µg/ml
19	AAS	Y [25]	------	------	35-200 g/ml
20	XRF	Nd [26]	YAG	------	10 µg/ml
21	XRF	Sm [27]	Co-Sm thin film	------	38%Sm
22	XRF	Sm [28]	Co-Sm magnetic powders	------	------
23	XRF	Gd [29]	Co-Gd thin films	------	------
24	XRF	Y [30]	Y-Ba-Cu oxide film	------	------

25	EDXRF	Dy [31]	Tb-Dy-Fe films	------	------
26	EDXRF	Y [32]	Y-Ba-Cu oxide	------	------
27	EDXRF & PIXE	Y [33]	Y-Ba-Cu oxide	------	70 ng
28	EDXRF	Y [34]	Ceramics	------	------
29	WDXRF	Ha [35]	Pb-Zr-Titanate	$L_{\alpha 1}$ line	------
30	XRF	La, Nd, Ce, Sm, Eu & Gd [36]	RE_2O_3	------	------
31	XRF	La, Gd, Sm, Pr, Dy & Nd [37]	Nd-Fe-B magnet	------	------
32	XRF	La & Y [38]	Y-Ba-Cu oxide or Ba Sr - La-Cu oxide	------	------
33	XRF	Ce & Y [39]	Ceria & Yttria mixtures	------	15-88 % & 12-85 %
34	XRF	REE [40]	High purity europia	------	<1µg
35	LS	Eu [41]	La, Pr & Dy oxides	TTA, Dibenzo-18-Crown-6,	10^{-11}-10^{-6} M
36	LS	Eu [42]	Ge semiconductor	PH5-6, Benzoyl - trifluoroacetone TOPO	0.5 ng/ml
37	NAA	La [43]	Semiconductor grade Si	------	6.5 ng/ml
38	NAA	Y [44]	Y-Ba-Cu oxide	------	------
39	NAA	REE [45]	High purity U	After extraction with 4-(l-butyl pentyl) pyridine	------
40	AES	La [46]	RE concentrate	441.8 nm	0.8µg/ml
41	ICPAES	La [47]	La doped Ba titanate	------	------
42	ICPAES	Ce [48]	Zirconia based ceramic materials	318.286 & 328.471 nm	93 & 84µg/l
43	ICPAES	Nd [49]	La tungstate crystals	------	------

44	ICPAES	Y [50]	Y-Ba-Cu oxide	371.030 nm	1-50µg/ml
45	ICPAES	Y [51]	Bi(Pb,Y) SrCa CuO	371.04 nm	
46	ICPAES	Y [52]	Y-Ba-Cu oxide film		1500µg/ml
47	ICPAES	Y [53]	Y-Ba-Cu oxide	321.609 & 324.228 nm	------
48	ICPAES	La, Nd, Sm, Ce & Y [54]	Pr	------	7.1, 13, 17.5, 10.1 & 0.73 µg/g
49	ICPAES	La, Ce, Pr, Nd, Sm & Gd [55]	Permanent magnet	------	------
50	ICPAES	Ce, Nd, Lu, Er & Ho [56]	YAG Crystals	------	------
51	ICPAES	Ce, Sm, Eu, Gd & Dy [57]	U	------	------
52	ICPAES	Y & REE [58]	Lu & Y Oxide	------	
53	ETV-ICPAES	REE [59]	La_2O_3	------	>0.8 & <48µg/l
54	ETV-ICPAES	REE [60]	Y_2O_3	------	------
55	GD-AES	REE [61]	RE_2O_3	------	------
56	ICP-MS (Laser ablation)	REE [62]	Garnets	------	0.1 - 1.0 µg/g
57	HPLC or ETV - ICP-MS	REE [63]	Gd_2O_3	------	------
58	IC	La [64]	Super conductor materials	Anion ion exchange separation	Upto 100 µg/ml
59	Spectrography	Ce [65]	$ZrWO_4$ monocrystal	------	------
60	Spectrography	Nd [66]	Titanate ceramics	------	------
61	Dc arc spectrography	Eu [67]	Phosphor	268.Oµm	------
62	Amperometry	La & Y [68]	Y-Ba-Cu oxide	pH 3.5 - 6.0	64% La & 13% Y

TABLE 8-2. Trace and ultra trace determination of REE in metallurgical samples.

Sl.No (1)	Analytical technique (2)	REE [R] (3)	Matrix (4)	Special features of analytical procedure (5)	Sensitivity/Detection limit (6)
1	MAS	Ce [69]	Ni alloy	pH 11.5, tetra bromo pyrocatechin, λ_{max} = 540mm.	------
2	MAS	Ce [70]	Ag alloy	λ_{max} = 380 nm	$\varepsilon = 1.2 \times 10^3 l mole^{-1} cm^{-1}$
3	MAS	Ce [71]	Steel and cast iron	λ_{max} = 330 nm	0.001-0.2% Ce
4	MAS	Ce [72]	Brasses	λ_{max} = 350 nm	0.01-0.1% Ce
5	MAS	Ce [73]	Fe & Steels	O-Tolidine, λ_{max} = 440nm	0.01-0.05% Ce
6	MAS	Ce [74]	Ni-Cr alloys	Dibromo-p-nitro chlorophosphanazo, λ_{max} = 640 nm.	------
7	MAS	Ce [75]	Al alloys	Tribromoarsenazo	$\varepsilon = 1.27 \times 10^5$ $l\ mole^{-1} cm^{-1}$
8	MAS	Pr [76]	Al metal, steels & alloys	Bromopyrogallol Red	1-20µg/25ml
9	MAS	Pr [77]	Al metal	5,7- dicholorquinoline 8-ol, Rhodamine 6G	$\varepsilon = 1.83 \times 105$ $l\ mole^{-1} cm^{-1}$
10	MAS	Nd [78]	Al metal	5,7-dichloroquinoline-8-ol, rhodamine 6G	$\varepsilon = 1.36 \times 10^5$ $l mole^{-1} cm^{-1}$
11	MAS	Nd [79]	Ti alloys	λ_{max} = 645 nm	0.01-0.16%Nd, $\varepsilon = 8.1 \times 10^4$ l mole cm^{-1}
12	MAS	Y [80]	Al alloys	Arsenazo III, λ_{max} = 670nm	2 - 5%Y
13	MAS	Y [81]	Mg alloys	Bromophosphanazo,	5-40µg/25ml
14	MAS	Y [82]	Mg-Y alloys	Chromotropic acid	$\varepsilon = 8.33 \times 10^4$ $l\ mole^{-1} cm^{-1}$
15	MAS	Y [83]	Zr alloys	Arsenazo I, pH 7.7 - 7.8	0.2 - 3µg/ml
16	MAS	Y [84]	Ni base alloys	p-nitrochloro -phosphanazo	13 - 20 µg of Y

17	MAS	Ce & Ce group RE [85]	Cu based alloys	p-nitrochlorophs - phanazo, λ_{max} =680nm	------
18	MAS	REE [86]	Cast iron	Solid liquid extraction with diethylodithio carbamate	------
19	MAS	REE [87]	Steels	Liquid chromatographic separation	------
20	HDMAS	Sm, Gd, Dy & Nd [88]	RE alloys	------	------
21	AAS	Y [89]	Ni or Co alloys	------	0.2 - 2% Y, 20 - 130µg/ml
22	GFAAS	Y [90]	Steels	------	------
23	XRF	Ce, La, Pr, Nd & Sm [91]	RE-Al alloys	------	------
24	XRF	REE [92]	Steels	Co-precipitation as fluorides	1µg/ml
25	WDXRF	Nd [93]	Nd-Fe-B alloys	W target, Nd L_{α} lines	
26	WDXRF	Y [94]	Cr-Ni alloys & Steel	------	0.001 - 0.1 % Y
27	WDXRF	Ce & La [95]	Cast iron	------	3-60 & 3-30 µg/ml of Ce & La
28	EDXRF	Ce, La & Y [96]	Cast iron	------	10&9µg/ml for La & Ce.
29	NAA	Lu [97]	Alloyed wires & foils	------	------
30	NAA	Ce, La, Pr, Nd, Sm, Y & Lu [98]	Ce based alloys	------	1000, 100, 1500, 2000, 1700, 750 & 4000 µg
31	NAA	Sm, La, Eu, Ho & Yb [99]	Steels	Fe matrix was removed by extraction into isopropylketone	------
32	NAA	REE [100]	Steels	------	1ng/ml-10µg/ml
33	NAA	REE [101]	Steels	Ion exchange separation	------
34	AES	REE [102]	Ferrous alloys	------	0.5 - 20%
35	ICPAES	Dy [103]	RE-Fe alloys	------	------
36	ICPAES	Y [104]	Ni base alloys	360.07 nm	10-2000µg/ml.

37	ICPAES	Ce, La, Pr, Sm & Nd [105]	Mg-Nd alloys	------	------
38	ICPAES	Ce, Pr, Sm & La [106]	Nd-Fe-B alloys	Gradient elution with α-hydroxy-isobutyric acid	0.05, 0.09, 0.05 & 0.01%
39	ICPAES	Ce, La, Pr & Nd [107]	Al alloy	413-7, 398.8, 414.3 & 401.2 nm	0.05 & 0.01%
40	ICPAES	Ce, Sm, & Y [108]	RE-Co magnets	------	------
41	ICPAES	Ce, La, Pr & Nd [109]	Nd-Fe-B alloy	------	------
42	ICPAES	Ce, La & Y [110]	Steels & Ni alloys	413.76, 408.07 & 360.07 nm	
43	ICPAES	Ce & Sm [111]	Permanent magnet alloys	413.& & 359.2 nm	5-30% Ce or Sm
44	ICPAES	Ce, La, Pr, Nd & Y [112]	Si-Al alloys	------	------
45	ICPAES	Ce, La, Pr & Nd [113]	Steels	------	Upto 40 µg/l
46	ICPAES	Ce & La [114]	Steels	413.7 & 433.3	------
47	ICPAES	Ce, La & Y [115]	Steels	-----	------
48	ICPAES	REE [116]	Steels	Extracted with benzyl Phenylhydroxylamine	------
49	ICPAES	REE [117]	Steels	------	0.0003 - 0.0009% of REE
50	ICPAES	REE [118]	Al	------	1-75µg/l
51	ICPAES	REE [119]	Cu alloys	------	------
52	ICPAES	REE [120]	Al alloy	------	<84 ng/g
53	ICPAES	Ce, La, Nd & Pr [121]	Ni & Fe based alloys	------	------
54	ICPAES	Ce, La, Pr, Nd, Sm & Eu [122]	Carbon steel	------	------
55	ICPMS	REE [123]	Pure iron & low alloyed steels	Extraction chroma -tographic separation	------

56	FIA-ICPMS	REE [124]	High purity iron & steels	------	------
57	SIMS	La [125]	Fe-20 Cr - 5 Al alloys	------	------
58	IC	REE [126]	Mg alloy	PAR as post Column reagent	0.01µg/ml.

TABLE 8-3. Trace and ultra trace determination of REE in environmental samples.

Sl. No (1)	Analytical technique (2)	REE [R] (3)	Matrix (4)	Special features of analytical procedure (5)	Sensitivity/Detection limit (6)
1	MAS [127]	La [127]	Waste water	-------	-------
2	MAS	Ce [128]	Seawater	2-(3,5-dichloro-2-pyridylazo) 5 - dimethyalamino phenol, λ_{max} =592 nm.	-------
3	MFS	Ce [129]	Natural Water	2MHCl, λex=256nm, λem-358 nm	0.5µg/ml to 0.7 µg/l
4	MFS	Tb [130]	Faeces	pH 11.9, Sulphosalicylic acid, λex=320nm, λem=545nm	-------
5.	GFAAS	La [131]	Food & Water		7.8 ng
6.	GFAAS	Yb [132]	Sea water	Preconcentration on $Fe(OH)_3$	-------
7.	GFAAS	Yb [133]	Sea water	PH 8, Coprecipitation on $Fe(OH)_3$ followed by extraction into 2,6-dimethyl - 4- heptanone	-------
8.	ETAAS	Er [134]	Natural Waters	-------	-------
9.	XRF	Y [135]	River Sand		0.005-1%
10.	XRF	Y [136]	River Sand		0.01-0.02%
11.	LS	Eu & Tb [137]	Waters	Polymethylmeth-acrylate as solvent	-------
12.	NAA	La [138]	Sea water	-------	-------
13.	NAA	La [139]	Coal dust particles	-------	-------

14.	NAA	Ce [140]	Sea water	-------	-------
15	NAA	Ce & Yb [141]	Airborne particles	-------	-------
16.	NAA	Pr, Nd, & Er [142]	Lake water	-------	<10µg/l
17.	NAA	REE[143]	Natural waters	Separation with hydrated Sb_2O_5 & precipitation using CaF_2 & $CaCl_2$	-------
18	NAA	REE [144]	Ground water	Coprecipitation on $Fe(OH)_3$ followed by separation on Dowex Ag1-X 8 resin.	-------
19.	NAA	REE [145]	Hot spring & Lake waters	$Al(OH)_3$ as collector	µg /l level
20.	NAA	REE [146]	Hot spring water	$Al(OH)_3$ as collector	µg/l level
21.	NAA	REE [147]	Volcanic water	-------	-------
22	NAA	REE [148]	Catalysts & Airborne particles	-------	-------
23.	NAA	REE [149]	Spring water	Preconcentration on hydrated MgO	-------
24.	NAA	REE [150]	Certified reference materials	-------	-------
25	FIA-ICP AES	La [151]	Natural waters	-------	0.7µg/ml
26.	ICPAES	Ce [152]	Reprocessing solutions	-------	Upto 5 µg/l
27.	ICPAES	Y [153]	Natural Waters	-------	0.1-3µg/l
28.	ICPAES	Ce & Y [154]	Sea & Pore water	Double coprecipitation with $Mg(OH)_2$ & CaC_2O_4 sor	-------
29	ICPAES	Dy, Ho, Er & Yb [155]	Waste water	Sorption on resin	-------
30.	ICPAES	REE [156]	Mineral waters	Ion-exchange separation	-------
31.	ICPAES	La, Y, Yb, Eu & Dy [157]	Environmental samples	nm sized TiO_2 as sorbent	-------
32.	ICPAES	REE [158]	Fly ash	HPLC Separation	
33.	ICP MS	REE [159]	Natural waters	-------	<0.5 pg/ml
34.	ICP MS	REE [160]	Sea water	-------	-------

35.	ICP MS	REE [161]	Duch drinking water	-------	-------
36.	ICP MS	REE [162]	Sea water	Preconcentration on Chelex 100	-------
37.	ICP MS	REE [163]	Apple leaves & pine needles	Extraction with bis (2-ethyl hexyl) phosphoric acid	
38.	ICP MS	REE [164]	Water		0.03-0.4pg/l
39.	ICPMS	REE [165]	Sea water	Preconcentration of quinoline-8-ol complexes on Amberlite XAD-7 resin	0.0015 - 0.016 µg/ml
40.	IC-ICPMS	REE [166]	Sea water		1-10 ng/l
41.	FIA-ICPMS	REE [167]	Geothermal waters		0.05-0.5µg/l
42.	ICP MS	REE [168]	Sea water	Preconcentration of CETAC DSX-100	
43.	FIA-ICPMS	REE [169]	Natural waters		
44.	FIA-ICPMS	REE [170]	Pore water	pH 8.3-9.0	0.06-0.27ng/l
45.	ICP- Time of flight MS	REE [171]	Natural waters	pH 3.7 - 4.6	3-40 µg/l
46.	ICP - Time of flight MS	REE [172]	Sea water	Iminodiacetate based resin column	20-50 pg/l
47.	IC	REE [173]	Sea water	PAR as post column reagent	Upto 16µg/l

TABLE 8-4 Comparison of Detection limits of REE in aqueous solution by different analytical Techniques

Elements	AAS µ g / l	AFS µ g / l	XRF µ g / g	XEOL µ g / g	ICP-AES µ g / l	ICP-MS µ g / l
Ce	NA	7	500	200	NA	0.01
Pr	4000	60	1000	100	0.1	0.01
Nd	2000	50	2000	100	0.1	0.02
Sm	600	20	150	200	0.01	0.04
Eu	40	1	20	10	0.01	0.02
Gd	NA	7	800	30	0.03	0.04
Tb	2000	200	500	200	0.001	0.01
Dy	200	4	300	100	0.0001	0.04
Ho	100	10	150	60	0.01	0.01
Er	100	1	500	50	0.01	0.02
Tm	80	7	100	10	0.01	0.01
Yb	20	0.9	10	10	0.1	0.03
Lu	3000	8	3000	20	NA	0.01
La	2000	3	NA	20	NA	0.01
Y	300	0.2	NA	NA	NA	0.02

NA : Not Available

Abbreviations

REE	-	Rare earth elements
MAS	-	Molecular absorption spectrophotometry
HDMAS	-	Higher order derivative molecular absorption spectrophotometry
MFS	-	Molecular fluorescence spectrometry
FAAS	-	Flame atomic absorption spectrometry
ETAAS	-	Electrothermal atomic absorption spectrometry
AFS	-	Atomic fluorescence spectrometry
EDXRF	-	Energy dispersive X-ray fluorescence spectrometry
WDXRF	-	Wavelength dispersive X-ray fluorescence spectrometry
TXRF	-	Total reflection X-ray fluorescence spectrometry
PIXE	-	Proton induced X-ray emission
LS	-	Luminescence spectrometry
NAA	-	Neutron activation analysis
DCP – AES	-	Direct current plasma atomic emission spectrometry
ICP-AES	-	Inductively coupled plasma atomic Emission spectrometry
ICP-MS	-	Inductively coupled plasma mass spectrometry
SIMS	-	Secondary Ion Mass Spectrometry
IDMS	-	Isotope dilution mass spectrometry.
IC	-	Ion chromatography
FIA	-	Flow injection analysis
ETV-ICP-MS	-	Electrothermal vaporization ICP-MS
XEOL	-	X-ray exicited optical luminescence.
HPLC	-	High performance liquid chromatography

References

1. T. Prasada Rao and V.M. Biju, *CRC Critical Reviews in Anal. Chem.*, **30**, 179 (2000).
2. T. Prasada Rao and V.M. Biju, *Reviews in Anal. Chem.*, **21**, 233 (2002).
3. T. Prasada Rao and J. Mary Gladis, *Reviews in Anal. Chem.*, **20,** 145 (2001).
4. T. Prasada Rao and J. Mary Gladis, *Anal. Sci.*, **18**, 517 (2002).
5. T. Prasada Rao, N.M. Sita, and C.S.P. Iyer, *Reviews in Anal. Chem.*, **18**, 157 (1999).
6. T. Prasada Rao and C.R. Preetha, *Separation & Purification methods*, (communicated).
7. D. Huang and W. Huang, *Yejin Fenxi*, **11**, 51 (1991).
8. M.A. Acharekar, *Laser Focus Fibrcopt. Technol*., **18**, 63 (1982).
9. L.P. Rigdon and W.F Sunderland, *Lawrence Livermore Lab*, **UCRL – 53070**, 9 (1981).
10. G.I. Dmitrenko, A.S. Babenko, and Z. Nazarenko, *Proizvod. Spets. Ogneuporov*, **8,** 61 (1981).
11. S. Lyle and N.A. Zatar, *Anal. Chim. Acta*, **135**, 327 (1982).

12. S. Lyle and N.A. Zatar, *Fresenius J. Anal. Chem,* **314**, 463 (1983).
13. S.L. Zhao, Z.J. Xu, and J.M. Pan, *Lihua Jianyan, Huaxue Fence*, **31**, 213 (1995).
14. R.E. Gago Garcia and S. Arribas Jimeno, *An. Quim.*, **80**, 516 (1984).
15. O. Grossmann and A.N. Turanob, *Anal. Chim. Acta*, **257**, 195 (1992).
16. V.P. Shaburova and I.G. Yudelevich, *Zh. Anal. Khim.*, **44**, 1319 (1989).
17. M. Anbu, T. Prasada Rao, C.S.P. Iyer, and A.D. Damodaran, *Chem. Anal.*, **41**, 781 (1996).
18. Y. Yan and Y. Ren, *Fenxi Huaxue*, **18**, 897 (1990).
19. J.M. Sanchez, M. Hidalgo, M. Valiente, and V. Salvado, *Anal. Lett.*, **33**, 553 (2000).
20. D.L. Liu, *Spectroscopy and spectral Analysis,* **20**, 744 (2000).
21. V.M. Biju, N.M. Sita, and T. Prasada Rao, *Anal. Lett.*, **34**, 211 (2001).
22. V.M. Biju and T. Prasada Rao, *Anal. Sci.***, 17**, 1343 (2001).
23. E.S. Zolotovitskaya and V.G. Potapova, *Zh. Anal. khim.*, **37**, 416 (1982).
24. I.M. Kotelyanski, V.B. Kravchenko, Z.M. Lebedeva, V.A. Luzanov, A.T. Sobolev, and V.V. Shemev, *Zavod Lab*., **56**, 32 (1990).
25. V.P. Shaburova and I.G. Yudelevich, *Zh. Anal. Khim.*, **43**, 603 (1988).
26. M.I. Shevtsov, A.B. Blank, and I.I. Miranskaya, *Zh. Anal. Khim.***, 38**, 2259 (1983).
27. J. Cheng, C. Li, and R. Xie, *Ghangpuxue Yu Guangpu Fenxi*, **7**, 63 (1987).
28. S.B. Bu, *Fenxi Huaxue*, **24**, 841 (1996).
29. J. Cheng and S. Zheng, *Wuli*, **11**, 47 (1982).
30. V.A. Trunova, V.S. Danilovich, V.B. Baryshev, and K.V. Zolatarev, *Nucl. Instrum.Methods Phys. Res. Sect A.*, **A308**, 321 (1991).
31. A.G. Karydas, C. Zarkadas, V. Katselis, T. Paradellis, and A. Speliotis, *X-ray spectrom***, 26**, 174 (1997).
32. V. Kliment, *J. Radioanal. Nucl. Chem.***, 187**, 215 (1994).
33. M. Lal, H.N. Bajpai, D. Joseph, and R.K. Choudary, *Pramana*, **34**, L 377 (1990).
34. J. Cheng, Y. Zhao, and B. Zhao, *Appl. Spectrosc.B***, 44**, 826 (1990).
35. G. Tao and M.S. Yi, *Huaxue Xuebao*, **40**, 41 (1982).
36. L.V. Agopova, A.V. Zavod Antonov, N.V. Troreva, and M.V. Bagaev, *Zavod Lab*, **47**, 45 (1981).
37. Y. Liang, *Lihua Jianyan, Huaxue Fence*, **26**, 157 (1990).
38. K. Kaneko, H. Kaneko, H. Ihara, T. Hoshino, K. Okai, M. Hirabayashi, N. Terada, M. Jyo, and H. Unoki, *Mol cryst. Liq. Cryst.*, **184**, 297 (1990).
39. P.A. Pella, G. Tao, A.L. Drago, and J.M. Epp, *Anal. Chem.***, 57**, 1752 (1985).
40. S. Lu, Z. Wang, S. Li, J. Li, and X. Wu, *Zhongguo xitu Xuebao*, **7**, 68 (1989).
41. N.M. Sita, T. Prasada Rao, C.S.P. Iyer, and A.D. Damodaran, *Talanta*, **44**, 423 (1997).
42. E.T. Karaseva and V.E. Karosev, *Zh. Anal. Khim.*, **37**, 1330 (1982).
43. Chou Chi-Chiang, Pung Tong Chuin, Tsai Hui-Tuh, and Wu Shaw Chii, *J. Chin. chem. Soc.***, 28**, 141 (1981).
44. I. Salma and E. Zemplen - Papp, *J. Radioanal. Nucl. Chem.*, **146**, 407 (1990).
45. S. Ahmad, M.S. Choudary, and I.H.Quershi, *J. Radioanal. Nucl. Chem.*, **83**, 201 (1984).
46. M. Kumar and P.K. Srivastava, *Analyst*, **118**, 193 (1993).
47. D. Guenther, M. Gaeckle, L. Moenke-Blankenburg, and H.P. Abicht, *Silikatechnik*, **41**, 10 (1990).
48. S.R. Marian, S.G. Cornejo, and L. Arriagada, *J. Anal. At. Spectrom.*, **9**, 93 (1994).

49. Y. Zhuang, *Guangpu shiyanshi*, **10**, 1 (1993).
50. L. Paama, P. Peramaki, and L.H. Lajumen, *Anal.Chim.Acta*, **330**, 259 (1996).
51. Y.Z Zhao, *Fenxi Shiyanshi*, **12**, 67 (1993).
52. G.N. Mazo, G.G. Glavin, and A.A. Zheleznavo, *Zh. Anal. Khim.*, **47**, 1901 (1992).
53. M.P. Balogh and N.M. Potter, *Anal. Chim. Acta*, **221**, 167 (1989).
54. F. Yuan, W.D. Qi, and Z.P. Hao, *Guangpu Shiyanshi*, **10**, 1 (1993).
55. C. Zhang and L. Wang, *Fenxi Shiyanshi*, **6**, 63 (1987).
56. C.M. Wu and Y.S. Lin, *Guangpuxue, Yu Guangpu Fenxi*, **13**, 101 (1993).
57. P.S. Murthy and R.M. Barnes, *J. Anal. At. Spectrom.*, **1**, 145 (1986).
58. S. Velichkov, E. Kostadinava, and N. Daskalova, *Spectrochim. Acta*, **53 B**, 1863 (1998).
59. Q. Shuai, Y.C. Qin, B. Hu, H.C. Xiong, and Z.C. Jiang, *Anal. Sci.*, **16,** 957 (2000).
60. B. Cai, B. Hu, and Z.C. Jiang, *Fresenius J. Anal. Chem.*, **367**, 259 (2000).
61. W.H. Huang, B. Hu, and Z.C. Jiang, *Fresenius J. Anal. chem.*, **366**, 36 (2000).
62. F. Bea, P. Montero., G. Garuti, and F. Zacharini, *Geostand. Newst.*, **21**, 253 (1997).
63. H.Z. Wu, N. Watanabe, R. Tsukahara, T. Itoh, Y. Goshi, and M. Owari, *Bunseki Kagaku*, **49**, 91 (2000).
64. E.A. Gautier, R.T. Gettar, and R.E. Servant, *Anal. Chim. Acta*, **283**, 350 (1993).
65. S. Wu and W. Zhang, *Fenxi Shiyanshi*, **10**, 65 (1991).
66. H. Schroth, *Fresenius Z Anal. chem.*, **296**, 286 (1979).
67. K. Horkay, *Tungseram Tech. Mitt.*, **48**, 1897 (1982).
68. N.A. Ezerskaya, I.N. Kiseleva, N. Belsku, L.J. Okertyanava, and N.A. Kulysov, *Zavod Lab*, **57**, 11 (1991).
69. V.I. Simonenko, V.V. Soloshnok, T.L. Vinogradova, and V.V. Sukhan, *Ukr. Khim. Zh.*, **58**, 175 (1992).
70. R. Wu and L. Zhu, *Yejin Fenxi*, **10**, 17 (1990).
71. I. Janousek, *Hutn. Listy*, **39**, 200 (1984).
72. Z. Holzbecher, L. Kabrt, and M. Haffmanova, *Chem. Listy*, **75**, 543 (1981).
73. H. Konno and S. Takeyama, *Bunseki Kagaku*, **32**, T41 (1983).
74. Y. He, J.Q. Cai, and J.M. Pan, *Lihua Jianyan, Huaxue Fence*, **29**, 306 (1993).
75. H.Y. Yang and S. Li, *Yejin Fenxi*, **13**, 57 (1993).
76. R. Sukumar, T. Prasada Rao, and A.D. Damodaran, *Analyst*, **113**, 1061 (1988).
77. V. Bhagavathy, T. Prasada Rao, and A.D. Damodaran, *Anal. Chim. Acta*, **280**, 169 (1993).
78. V. Bhagavathy, M.L.P. Reddy, T. Prasada Rao, and A.D. Damodaran, *Indian J. of chemistry,* **32A**, 463 (1993).
79. L. Li and T. Pan, *Yejin Fenxi*, **10**, 7 (1990).
80. E.T. Udod, A.Kh. Klibus, V.V. Sukhan, and T.A. Sivyakova, *Zavod Lab*, **57**, 12 (1991).
81. J. Xu, *Yejin Fenxi*, **10**, 19 (1990).
82. X. Song and B. Wu, *Lihua Jianyan, Huaxue Fence*, **24**, 206 (1988).
83. T.M. Barbina, Polezhaev, and M. Yu, *Zavod Lab*, **50**, 12 (1984).
84. W. Wang, J. Wu, and J. Pan, *Fenxi Huaxue*, **11**, 913 (1983).
85. W. Jin and R. Yang, *Fenxi Shiyanshi*, **11**, 40 (1992).
86. X.Z. Du, J.G. Hou, S. Zhao, J.W. Kang, and J.Z. Gao, *Analyst*, **119**, 1891 (1994).

87. R. Saraswathi, N.R. Desikan, S.Y. Athavale, and T.H. Rao, *Anal. chim. Acta*, **237**, 325 (1990).
88. G.Q. Lao and L.R.Chem, *Lihu Jianyan, Huaxue Fence*, **28**, 353 (1992).
89. O.V. Roman, V.A. Chekan, L.M. Kirilyuk, M.A. Dvoretskaya, and G.S. Makarerich, *Zavod Lab.*, **56**, 45 (1990).
90. B.V. Lvov and L.A. Pelieva, *Zavod Lab.*, **45**, 1010 (1979).
91. Q. Yan,X. Du, Z, Xin, P. Den, and D. Liu, *Fenxi Shiyanshi*, **6**, 15 (1987).
92. Y. Inokuma and J. Endo, *Bunseki Kagaku*, **37**, 503 (1988).
93. D. Ning, *Xiyou Jinshu*, **7**, 305 (1988)
94. J. Ciba and J. Jurczyk, *Fresenius J. Anal. Chem.*, **313**, 542 (1982).
95. F. Alluyn, J. Billiet, R. Dams, and J. Hoste, *Anal. Chim. Acta*, **155**, 209 (1983).
96. N.L. Akmaeva, A.A. Anipin, Yu.V. Krivopalov, V.Yu. Kuznetsov, and V.A. Semenov, *Izb. Vyssh. Uchebn Zaved. chern. Mettal.*, **5**, 145 (1979)
97. F. Decorte, K. Masumoto, A. Devispelaera, and F. Bellemans, *J. Radioanal. Nucl. Chem.*, **192**, 91 (1995).
98. M.G. Davidov, I.B. Rakhamanov, S.A. Mareskin, and N.A. Agrinskaya, *Zh. Anal. Khim*, **48**, 703 (1993).
99. I. Huber, F. Ludewing, L. Poecze, L. Riedelmayer, and H. Zeder, *BHM*, **126**, 12 (1981).
100. E.A. Kapralov, N.N. Dogadkin, and O.I. Kuchinskaya, *Zavod Lab.*, **55**, 38 (1989).
101. K.S. Park, N.B. Kim, H.J. Woo, K.Y. Lee, W. Hong, and S.K. Chun, *J. Radioanal. Nucl. Chem.*, **160**, 529 (1992).
102. Z.I. Otmakhova, O.V. Chatschina, L.A. Bobkova, and S.V. Dozmorov, *Zavod Lab.*, **56**, 47 (1990).
103. T. Yamashita, *Bunseki Kagaku*, **42**, 111 (1993).
104. P.A. Vozella and D.A. Condit, *Anal. Chem.*, **60**, 2497 (1988).
105. S.Y. Wang, L.H. Pan, Z.Y. Qin, and J.G. Jin, *Fenxi Huaxue*, **21**, 1452 (1993).
106. M. Renko, A. Osojnik, and V. Hudnick, *Fresenius J. Anal. Chem.*, **351**, 610 (1995).
107. D. Ni, *Guangpuxue Yu Guangpu Fenxi*, **7**, 53 (1987).
108. K. Iwasaki and H. Uchida, *Anal. Sci.*, **2**, 261 (1986).
109. Y. Zhao, *Guangpuxue Yu Guangpu Fenxi*, **6**, 38 (1986).
110. L.A. Ramashko, I.P. Kharamov, N.N. Bazargin, Yu.G. Rozorskii, Yu.F. Ziborova, N.P. Krivenkova, and V.M. Zharova, *Zavod Lab.*, **53**, 21 (1987).
111. D. Ni, *Lihua Jianyan, Huaxue fence*, **23**, 227 (1987).
112. Y. Liu and P. He, *Fenxi Shiyanshi*, **8**, 56 (1989).
113. A.M. Grossman, J. Ciba, J. Jurczyk, and W. Spiewok, *Talanta*, **37**, 815 (1990).
114. O.I. Nikitana, T.A. Nicolaichuk, O.A. Romashkira, and L.A. Slinko, *Zavod Lab.*, **56**, 38 (1990).
115. V. Rett and I. Hlavacek, *Hutn. Listy*, **34**, 428 (1979).
116. Z.H. Yin and Y.J. Zhang, *Fenxi Huaxue*, **23**, 1292 (1995).
117. X.J. Li, *Lihua Jianyan, Huaxue Fence*, **32**, 366 (1996).
118. H.S. Mahanti and R.M. Barnes, *Appl. Spectrosc.*, **37**, 261 (1983).
119. S. Wang and J. Liu, *Fenxi Huaxue*, **19**, 80 (1991).
120. H.Y. Zhu, Y.L. Yu, S.D. Chai, and C.L. Zhao, *Guangpuyu Guangpu Fenxi*, **12**, 47 (1992).
121. P.T. Fischer, and A.J. Ellgreen, *Spectrochim.Acta Part B*, **38**, 309 (1983).
122. S. Rubi, T. Ito, H. Kawaguchi, and A. Mizuike, *Nippon Kagaku Kaishi*, **1**, 172 (1981).

123. V.K. Karandashev, A.N. Turanov, H.M. Kuss, I. Kumpmann, L.V. Zadnepreuk, and V.E. Baulin, *Mikrochim. Acta B*, **130**, 47 (1998).
124. A.G. Coedo, I. Padilla, T. Dorado, and F.J. Alguacil, *Anal.Chim.Acta*, **389**, 247 (1999).
125. Y. Usui, A. Yamamoto, J. Shimonura, M. Kouna, K. Ishii, and K. Yoshioka, *Bunseki Kagaku*, **45**, 625 (1996).
126. A.W. Al-Shawi and R. Dahal, *Anal. Chim. Acta*, **333**, 23 (1996).
127. W.Zhou, J. Pan, and J. Wang, *Gaodeng Xuexiao Huaxue Xuebao*, **14**, 784 (1993).
128. M.F. Silva, L.P. Fernandez, and R.A. Olsina, *Analyst*, **123**, 1803 (1998).
129. B. Xiao, *Fenxi HuaxueB*, **15**, 45 (1987).
130. A.R. Karimi, S.P. Haat, and F.N. Owens, *Can. J. Anim. Sci.*, **68**, 1305 (1988).
131. M. Shen and Y. Shi, *Analyst*, **117**, 137 (1992).
132. O. Fujino, Y. Nishimura, Y. Koga, Y. Nakagudi, T. Aono, and K. Hiraki, *Kidorui*, **14**, 38 (1989).
133. O. Fujino, S. Nishida, H. Togawa, and K. Hiraki, *Anal. Sci.*, **7**, 889 (1991).
134. A. Mazzucotelli, R. Frache, and F. Depaz, *Appl. Spectrosc.*, **45**, 501 (1991).
135. L.C. Chandola, I.J. Machado, and S.K. Kapoor, *BARC* **1047,** 11 (1980).
136. L.C. Chandola, I.J. Machado, and S.K. Kapoor, *Fresenius J. Anal. Chem.*, **319**, 432 (1984).
137. S.B. Meshkova, Z.M. Topilova, and G. Gerasimenko, *Zh. Anal Khim.*, **48**, 65 (1993).
138. K. Ammann and K. Knoechel, *Fresenius J. Anal.Chem.*, **306**, 161 (1981).
139. H.K. Wankhade and A.N. Garg, *Indian J. Environ. Health*, **31**, 125 (1989).
140. E. Heuse and K.H. Liesee, *J. Radioanal. Nucl. Chem.*, **50**, 289 (1979).
141. M.A. Qadir, M.Z. Iqbal, and J.H. Zaidi, *J. Radioanal. Nucl. Chem.*, **201**, 347 (1995).
142. T. Honda, T. Oi, T. Osaka, T. Nozaki, and H. Kakihana, *J. Radioanal. Nucl. Chem.*, **134**, 13 (1989).
143. S. Bigot and M. Trenil, *J. Radioanal. Nucl. Chem.,* **59**, 341 (1980).
144. J.C. Laul, A.E. Lepel, and M.R. Smith, *J. Radioanal. Nucl. Chem.,* **123**, 349 (1988).
145. T. Honda, T. Oi, T. Ossaka, T. Nozaki, and H. Kakishana, *J. Radioanal. Nucl. Chem.,* **130**, 81 (1989).
146. T. Oi, T. Kikawada, T. Honda, T. Ossaka, and H. Kakihana, *J. Radional. Nucl. Chem.*, **140**, 365 (1990).
147. T. Oi, K. Kakegawa, T. Ossaka, and T. Honda, *Nippon Kagaku Kaishi*, **5**, 543 (1993).
148. M.E. Kitto, D.L. Anderson, G.E. Gordon, and I. Olmez, *Environ. Sci. Technol.*, **26**, 1368 (1992).
149. S.J. Yeh, C.S. Tsai, and A.T. Yang, *J. Radioanal. Nucl.Chem.*, **192**, 163 (1995).
150. E. Orvini, M. Speziali, A. Salivini, and C. Herborg, *Microchem. J.*, **67**, 97 (2000).
151. S.H. Fan and Z.L. Fang, *Guangpu Yu Guangpu Fenxi,* **12**, 63 (1992).
152. R.W. Stone and V.R. Olsen, *US Dep. Energy Rep. ENICO – 1056*, p 16 (1981).
153. G.P. Panteleev, G.I. Isizin, A.A. Formanovskill, N.P. Starshinova, E.M. Sedykh, N.M. Kuzmin, and Yu.A. Zolotov, *Zh. Anal.khim.,* **46**, 355 (1991).
154. M. Achilli, G. Ciceri, R. Ferrodroli, D. Hetai, and W. Martinotti, *Analyst,* **114,** 319 (1989).
155. G. Zhan, Z. Su, X. Lou, and X. Chang, *Anal. Lett.,* **25**, 561 (1992).
156. J. Kubova, V. Nevoral, and V. Stresko, *J. Anal At. Spectrom.,* **9**, 241 (1994).
157. P. Liang, B. Hu, Z.C. Jiang, Y.C. Qin, and T.Y. Peng, *J. Anal. At. Spectrom.,* **16**, 863 (2001).
158. D.S. Braveman, *J. Anal. At. Spectrom.,* **7**, 43 (1992).
159. A. Stroh, *At. Spectrosc.,* **13**, 89 (1992).

160. P. Moeller, P. Dulskii, and J. Luck, *Spectrochim.Acta,* **47B**, 1379 (1992).
161. J.L.M. De Boer, W. Verweij, T. Vander Veldekoerts, and W. Mennes, *Water Research,* **30**, 190 (1996).
162. H. Sawatari, T. Toda, T. Saizuka, C. Kimata, A. Itoh, and H. Haraguchi, *Bull. Chem. Soc. Japan,* **68**, 3065 (1995).
163. V.K. Panday, K. Hoppstock, J.S. Becker, and H.J. Dietze, *At. Spectrosc.,* **17,** 98 (1996).
164. W. Zhu, E.W.B. de Leer, M. Kennedy, and G.J.F.R. Aaerbs, *Fresenius' J. Anal. Cehm.,* **360,** 74 (1998).
165. O. Vicente, A. Padro, L. Martinez, R. Olsina, and E. Marchevsky, *Spectrochim.Acta,* **53B**, 1281 (1998).
166. M. Bettinelli and S. Spezia, *At. Spectrosc.,* **16**, 133 (1995).
167. J.K. Aggarwal, M.B. Shabani, M.R. Palmer, and K.V. Ragnassdottir, *Anal.Chem,* **68**, 4418 (1996).
168. M. Kuehn and M. Kriews, *Fresenius J. Anal. chem,* **367**, 440 (2000).
169. M. Oshimi, K.H. Lee, Y.H. Gao, and S. Motomizu, *Chem. Lett.,* 1338 (2000).
170. X.P. Yan, R. Kerrich, and M.J. Hendry, *J. Anal. At. Spectrom.,* **14**, 215 (1999).
171. K. Bemkhedda, H.G. Infante, E. Ivanova, and F.C. Adams, *J. Anal. At. Spectrom.,* **16**, 995 (2001).
172. S.N. Willie and R.E. Sturgeon, *Spectrochim. Acta,* **56B**, 1707 (2001).
173. C.Y. Liu and T.H. Wang, *Anal. Chim. Acta,* **337**, 173 (1997).
174. T. Prasada Rao, M.L.P. Reddy, and A.R. Pillai, *Talanta,* **46**, 765 (1998).
175. V. Bhagavathy, R. Sukumar, T. Prasada Rao, and A.D. Damodaran, *Adv. in Rare earth Research,* p122 (1993).
176. J. Kang, R. Chen, and G. Bai, *Huaxue Xuebao,* **42**, 921 (1984).
177. Y. Ren and H. Zhou, *Fenxi Huaxue,* **13**, 6 (1985).
178. T. Prasada Rao and R. Sukumar, *Anal.Lett.,* **19**, 1731 (1986).
179. T. Prasada Rao, B. Vijayalakshmy, and C.S.P. Iyer, *Reviews in Anal.Chem.,* **20**, 27 (2001).
180. T. Prasada Rao and C.S.P. Iyer, *Standards India,* **11**, 149 (1997).
181. Dionex corporation, CA, USA Technical Note TN 23 (1987).
182. P.N. Nesterenko and P. Jones, *Anal. Commun.,* **34**, 7 (1997).
183. V. Bhagavathy, T. Prasada Rao, and A.D. Damodaran, *Handbook on physics and chemistry of Rare earths*, Ed.K.A.Gschneidner and L. Eyring Vol.21, chapter 146, p. 367 (1995).
184. B. Vijayalakshmy and T. Prasada Rao, *Fresenius J. Anal. Chem.,* **370,** 251 (2001).

9. APPLICATIONS

J.-P. CUIF (9.1), E. ROHART (9.2.1),
P. MACAUDIERE (9.2.2), and C. BAUREGARD (9.3)
Rhodia Electronics & Catalysis
Z.I. 26 rue chef de baie, 17041 La Rochelle Cedex 1 - France

E. SUDA and B. PACAUD (9.4)
Anan Kasei Co., Ltd.
210-51 Ohgata-cho, Anan, Tokushima 774-0022, Japan

N. IMANAKA, T. MASUI, and S. TAMURA (9.5 – 9.8)
Department of Applied Chemistry, Faculty of Engineering,
Osaka University
2-1 Yamadaoka, Suita, Osaka 565-0871, Japan

9.1. PHOSPHORS

9.1.1. *A wide range of applications, thanks to a great variety of emissions*

Luminescent materials have been under development since the 1960's, in conjunction with the industrial availability of rare-earths of sufficient purity: television color, fluorescent lighting, and medical X-ray photography. The intense emissions and almost monochromatic tones obtained by diluting the rare-earths based activators in the appropriate host networks (very often simple rare-earth compounds at 0, 7, or 14 *f* electrons: yttrium, lanthanum, gadolinium and lutetium)

Figure 9-1. A great variety of emissions from rare earths phosphors.

G. Adachi et al. (eds.), Binary Rare Earth Oxides, 215–255.

are the primary reason for this development. They made it possible to meet the very specific criteria for use that traditional band emission phosphors could not satisfy. A great variety of emissions can be obtained, depending on the type of activator brought into play and on the respective positions of the excited or fundamental energy levels as shown in Figure 9-1.

9.1.1.1. Color television with cathode ray tube (CRT)

In color television, where the image is reproduced by selective cathode excitation of three phosphors (blue, green and red) deposited on the internal face of the screen, yttrium oxysulfides activated with trivalent europium ($Y_2O_2S:Eu^{3+}$) facilitate such a gain in the brilliance of red over ZnS:Ag (more than double it) that they have totally replaced it at a cost about five times less. The exceptional performance of the rare-earth phosphors has also been used gainfully in a vast number of cathode tubes for professional applications: color computer monitors, tubes for aviation use, projection television, etc.

9.1.1.2. Fluorescent lighting

In the fluorescent lighting domain, rare-earth phosphors have made it possible in theory that daylight can be reconstituted by adding three primary emissions in defined proportions at 450, 550 and 610 mm. In a low pressure fluorescent tube, conversion ultraviolet rays emitted by excited mercury into visible light is traditionally done using an off-white band emitter, the calcium halophosphate activated by antimony and manganese. The perfection of phosphors using blue emissions from divalent europium (specific case of a narrow band emission from transitions bringing the 5d levels into play) and green emissions from trivalent terbium co-activated by cerium, respectively, and red from trivalent europium has made it possible to make tri-chromatic fluorescent tubes recently miniaturized in the form of compact lights for use in the home. Giving off a color very close to

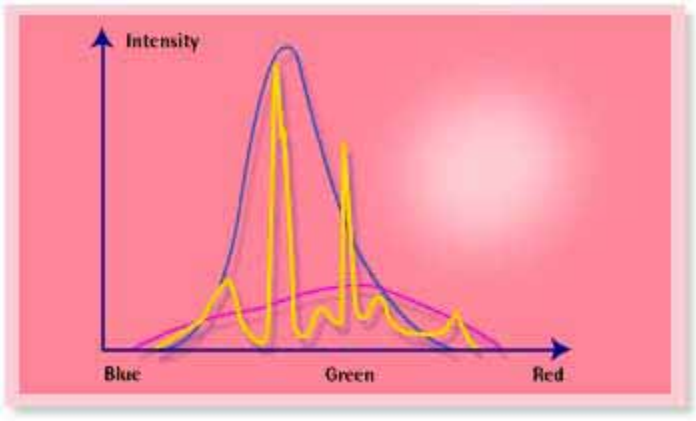

Figure 9-2. Production of daylight in the tri-chromatic lighting system.

incandescent lights, the tri-chromatic system of fluorescent light bulbs has a 5 to 8 times greater light output and a life span that is more than a thousand hours longer, resulting in significant savings to the user. In the tri-chromatic lighting system, daylight is reproduced by adding 3 fundamental emissions around 450, 550, and 610 nm as shown in Figure 9-2.

9.1.1.3. Flat screen technology

There is a strong demand for replacing the cumbersome cathode ray tubes on TVs and computers with large dimension flat screens. Different technologies using rare earths are emerging:

- Field emission screens operating at low tension (< 8000 V) use rare-earth based phosphors:
  Red (Y_2O_3:Eu^{3+}; $SrTiO_3$:Pr^{3+})
  Green ($Y_3(Al,Ga)_5O_{12}$:Tb^{3+}; Y_2SiO_5:Tb^{3+})
  Blue (Y_2SiO_5:Ce^{3+})
- Plasma technology screens
  In this case, the phosphors are excited by the discharge of the plasma placed between two electrodes. The screen is broken down into small cells or pixels, the size of which is small enough to obtain high definition screens. There is a clear improvement in the life span of these screens. Rare earths are present in the blue $BaMgAl_{10}O_{17}$:Eu^{2+} and red $(Y,Gd)BO_3$:Eu^{3+} phosphors. The latter is preferable to Y_2O_3:Eu^{3+} due to its stronger VUV absorption. Comparable technologies are now used in lamps.

9.1.1.4. Signs and Signals

There has also been a marked increase in the use of phosphors in signs and signals. Numerous safety signs (exit lights, reflective safety bands and highway markings, etc.) require the use of phosphorescent. Rare earths are part of the mineral phosphorescent product with the longest known phosphorescence duration, namely $SrAl_2O_4$:Eu^{2+}, Dy^{3+}.

9.1.1.5. Medical Radiography

A third domain using rare-earth luminescence is medical radiography. The radiological image is transformed into an optical image by a screen intensifier using the ability of a phosphor to transform the X-ray into visible blue or green light, to which photographic emulsions are far more sensitive than X-rays.

The use of rare-earth phosphors for this application was developed and thus replaced the calcium tungstate used in traditional systems.

This results in :

- the intrinsic absorption of X-rays on the range of energies brought into play
- the more effective conversion into visible light (10 to 20% output rather than 6% for $CaWO_4$)

- the spectral separation of the emission (from trivalent terbium or thulium) adapted to the maximum sensitivity of the emulsions used,

which are three essential criteria in defining the efficiency factor of screen intensifiers.

There are three major types of rare-earth phosphors used: $Gd_2O_2S:Tb^{3+}$ (green), $LaOBr:Tm^{3+}$ in $YTaO_4:Nb^{5+}$ or Tm^{3+} (blues), which make it possible to appreciably improve the quality of the images obtained and at the same time decrease patient exposure time by a factor of 2 to 4.

TABLE 9-1. Use of rare-earth phosphors in electronic applications

Excitation	Phosphor	Application	
γ-Rays	$CaSO_4:Dy^{3+}$	Detection of ionizing radiation	
	$Gd_2O_2S:Pr^{3+}$	Ceramic scintillators	
X-rays	$Gd_2O_2S:Tb^{3+}$		
	$LaOBr:Tm^{3+}$		
	$YTaO_4:Nb^{5+}$ or Tm^{3+}	X-ray screen intensifiers	
	$BaFBr:Eu^{2+}$		
Electrons	$ZnS:Tb^{3+}$	Electroluminescent Panels	
Cathode Rays	$Y_2O_2S:Eu^{3+}$	Red for television	
	$Gd_2O_2S:Tb^{3+}$	Green for professional tubes	
	$Y_3Al_5O_{12}:Ce^{3+}$		
UV (High pressure)	$YVO_4:Eu^{3+}$	Red corrector for high pressure mercury vapor lamps	
	$Y_3Al_5O_{12}:Ce^{3+}$		
UV (Low pressure)	$BaMgAl_{16}O_{17}:Eu^{2+}$	Blue Component	
	$Sr_5(PO_4)_3Cl:Eu^{2+}$		
	$LaPO_4:Ce^{3+},Tb^{3+}$	Green Component	Tri-chromatic fluorescent tubes
	$(Ce,Tb)MgAl_{11}O_{19}$		
	$(Gd,Ce,Tb)MgB_5O_{10}$		
	$Y_2O_3:Eu^{3+}$	Red Component	
Laser Pumping	$Y_3Al_5O_{12}:Nd^{3+}$	Lasers	

9.1.2. *New demands and recent developments in applications: a step forward for phosphors*

There are plenty of advanced products for phosphors used in tri-chromatic fluorescent lighting, phosphor converted light emission diodes (pcLED), X-ray imaging, specialty lamps, back lighting for liquid crystal displays (LCD), cathode ray tubes (CRT) for televisions and monitors, plasma display panels (PDP), projection televisions (PRT), and field emission displays (FED).

During the past several years, the lighting industry has witnessed a significant growth in high energy saving lamps such as tri-chromatic lamps and a need for higher quality standards. At the same time, the display industry has seen new technologies emerging such as flat CRT, high resolution CRT and flat panel displays. These changes have created the challenging demand for “New phosphors”:

- More efficient phosphors with improved brightness and performance
- Lower cost products allowing technology expansion

These new applications show some significant benefits:

- High rare-earth purity as well as very low luminescence killer content
- Controlled reactivity facilitating phosphor manufacture

Customized products combining controlled composition of a high number of elements included in various matrices.

9.1.2.1. Tri-chromatic lamps and colored phosphors

Tri-chromatic fluorescent lamps generate white light using three primary emissions at around 450 nm (blue), 550 nm (green) and 610 nm (red). Some advanced rare-earth based raw materials used for the three phosphors are being manufactured. For red, yttrium and europium based co-precipitates only are used by the industry. The new range of Y-Eu oxide co-precipitates include highly controlled products with improved purity. Only the highest purity and carefully controlled products deserve the new applications quality standard. A range of $LaPO_4:Ce^{3+},Tb^{3+}$ products [1, 2] is facilitating the manufacture of lanthanum phosphate (LAP) green phosphor. The LAP phosphor is now the standard for green phosphors in tri-chromatic lamps. Composition, purity as well as special morphology are carefully controlled in these proprietary products.

Recently, new proprietary advanced products for blue phosphors based on a $BaMgAl_{10}O_{19}:Eu^{2+}$ are also launched. A single thermal treatment is sufficient to make highly efficient blue BAM phosphor with controlled morphology and particle size distribution.

9.1.2.2. Tri-chromatic lamps and colored phosphors

Although CRT monitors are partially being replaced by LCD, there is still a significant demand for large screen CRT, high resolution CRT and flat CRT. The typical red phosphor used for CRT is $Y_2O_2S:Eu^{3+}$. This phosphor is manufactured from separate or mixed oxides based on yttrium and europium. Some additives such as terbium or samarium are used as doping agents in these phosphors, to enhance brightness for instance. The new range of products for red CRT phosphor includes high purity $Y_2O_3:Eu^{3+}$ with some doping agents. Products with various Eu^{3+} contents from 4.0 to 10% are manufactured for this application depending on the specific requirements of customers.

9.1.2.3. New phosphors for PDP

The new flat screen PDP uses ultra-violet as a source of excitation. This still new technology has required the development of new phosphors in the 90's. The most common phosphors are for red $(Y,Gd)BO_3:Eu^{3+}$, for green $(Y,Gd)BO_3:Tb^{3+}$ as well as $Zn_2SiO_4:Mn^{2+}$ and for blue $BaMgAl_{10}O_{17}:Eu^{2+}$ called BAM. For all three color PDP phosphors, three ranges of advanced, proprietary rare-earth based new products have been developed [3, 4]:

Red: $(Y, Gd)BO_3:Eu^{3+}$

Green: $(Y, Gd)BO_3:Tb^{3+}$

Blue: $BaMgAl_{10}O_{17}:Eu^{3+}$

Examples of morphology of precursors are shown in Figures 9-3 and 9-4. All products can be easily transformed into PDP phosphor by adding a flux and applying a thermal treatment. The composition of each product can be customized upon request.

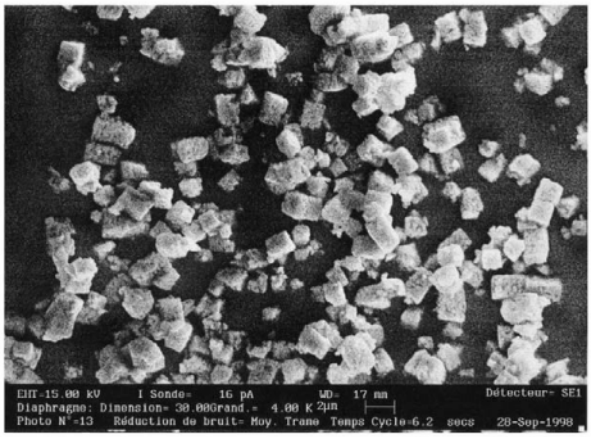

Figure 9-3. SEM image of cubic shape europium doped yttrium orthoborate particles.

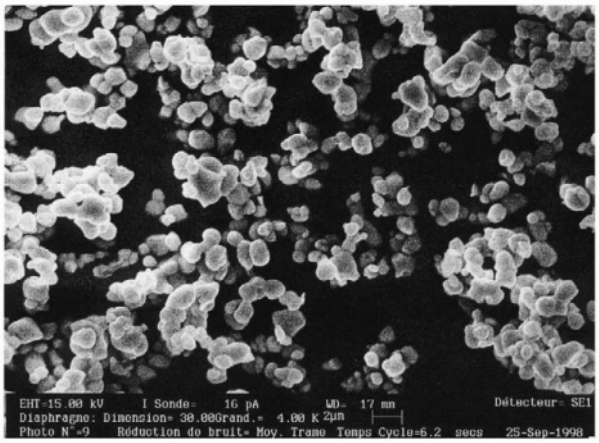

Figure 9-4. SEM image of spherical shape europium doped yttrium orthoborate particles.

9.1.2.4. Other applications

Some other applications of these brand-new products include field emission displays (FED), CRT projection TV (PTV), various lighting and medical imaging applications.

9.2. CATALYSTS

9.2.1. *Three Way Catalysis (TWC) and NO_x trap catalyst*

Among the different applications of rare earths, intensively investigated, catalysis is undoubtedly one of the most important.

Large amounts of catalysts, including lanthanides (i.e. cerium oxide; ceria [5]) are used for refinery operations to convert crude oil into lower molecular-weight fractions. However, today a major technological application of steadily growing importance for cerium and its '*derivatives*' (i.e. other rare earth oxides such as Nd_2O_3, Pr_6O_{11}, La_2O_3, and Y_2O_3) is the vehicle emission control to remove pollutants from vehicle (auto-exhaust) emissions. Since the early 70's, there has been a large number of scientific communications relating to this topic.

9.2.1.1. Use of rare earths in Three-Way Catalysis (TWC) for gasoline engines

There are three main types of pollutants at the outlet of the exhaust pipe :

- Carbon monoxide (CO)
- Unburned hydrocarbons (HC)
- Nitrogen oxides (NOx)

The quantity of pollutants varies with the operating conditions of the engine, but is influenced predominantly by the Air/Fuel ratio in the combustion cylinder. Generally speaking, when the engine is operated in *rich* of stoichiometric, CO and HC emissions are high, while NO_x emissions are low (in lean of stoichiometric, trends are reversed). Thus the very first and important challenge for catalysis was to convert CO and HC when engine operates under lean conditions according to the reactions from eq.1 to 3 and to convert NO_x when engine operates under rich conditions as summarized from eq.4 to 6.

$$C_xH_n + (1+n/4)\ O_2 = x\ CO_2 + (n/2)\ H_2O \quad (1)$$

$$CO + ½\ O_2 = CO_2 \quad (2)$$

$$CO + H_2O = CO_2 + H_2 \quad (3)$$

$$NO + CO = ½\ N_2 + CO_2 \quad (4)$$

$$NO + H_2 = ½\ N_2 + H_2O \quad (5)$$

$$(2 + n/2)\ NO + C_xH_n = x\ CO_2 + (n/2)\ H_2O + (1+n/4)\ N_2 \quad (6)$$

These reactions take place in a very short period of time (1 sec or less) and in many cases are performed in a honeycomb monolith made of cordierite or metal. The monolith is coated with some freely-available components such as:

- noble metals, mainly Rh, Pt and Pd
- alumina
- promoters and/or stabilizers such as La, Nd, Ba
- **oxygen storage promoters such as ceria**

Among all the components, the 'oxygen storage material' is certainly the one which has been the most studied [6] and is definitely considered as a key component

of the washcoat. The beneficial effects of ceria-based materials were already discussed about 30 years ago by Gandhi et al. [7]. Ceria promotes:

- the precious metal dispersion and boost their 'intrinsic' activity
- the thermal stability of alumina
- the water gas shift reaction (eq.3) and steam reforming reaction
- CO and HC oxidation under lean conditions
- NO_x reduction under rich conditions
- store and release oxygen when richness varies from lean to rich

Generally speaking, the most important role of ceria is the oxygen storage capacity (OSC). Among the rare earths, cerium oxide (and in a small proportion of Pr and Tb oxides) shows different valences (Ce^{4+}/Ce^{3+}) in respect of the temperature and the nature of the atmosphere. The OSC is the result of this very particular property.

In the 80's pure ceria was used as an OSC component in the catalytic converter. But as the legislation got more and more severe to reduce exhaust emissions, car manufacturers developed new sophisticated technologies. Among them, the Close-Coupled Catalyst (CCC), located closer to the manifold, showed improved performance and especially very good light-off activity. Nevertheless, this type of catalyst is submitted to harsh ageing conditions (>1000°C) and the OSC components had to be more thermally stable. The 1st generation CeO_2/ZrO_2 mixed oxides have thus gradually replaced pure ceria. These materials show not only higher surface area at 900°C than pure ceria [8, 9] but also improved OSC behavior. Reference [6] highlights the main reasons for this improvement.

To meet the future legislation requirements (such as SULEV in California), modern TWC technologies have recently taken the lead with different washcoat architectures to enhance the activity including inorganic carriers able to resist temperatures as high as 1100°C. Highly thermally-stable ternary (Ce/Zr/X) and even quaternary (Ce/Zr/X/Y) mixed oxides are emerging [10-12].

Recently, a new generation of CeZr based mixed oxide for severe demanding temperature applications and low loading precious metal (PM) catalysts have been developed [13, 14]. The sinterability of such new OSC materials (referred as 2nd generation CeZr materials) is less than 1st generation OSC materials (Figure 9-5). The open-pore texture of the oxide (Figure 9-6 and 9-7) as well as the fine tuning of the homogeneous solid solution at the wet part of the process leads to significantly improved materials with no phase segregation up to 1100°C (Figure 9-8).

To conclude, continued improvements in ceria and its derivatives will be needed within the next years to increase thermal durability in order to meet the more stringent legislation. In parallel new materials with very high and fast OSC (much more than the current one) and/or completely stable OSC materials within the range from 900 to 1200°C will be needed for the development of low-cost, reduced-load, noble metal catalysts [15].

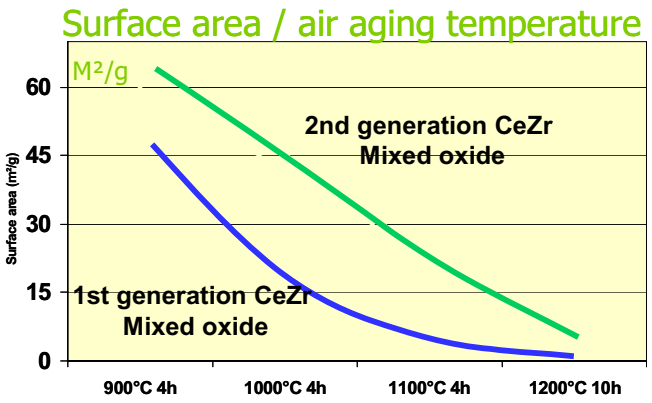

Figure 9-5. BET surface area (m^2/g) versus temperature of calcinations in air for two CeZr mixed oxides [13].

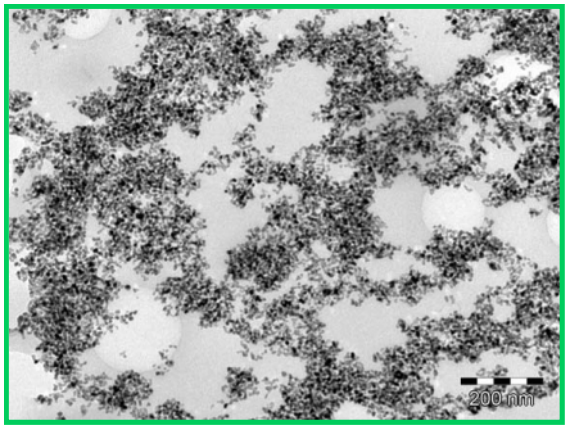

Figure 9-6. TEM analysis of the 2nd generation CeZr mixed oxide after air calcination at 900°C [13]

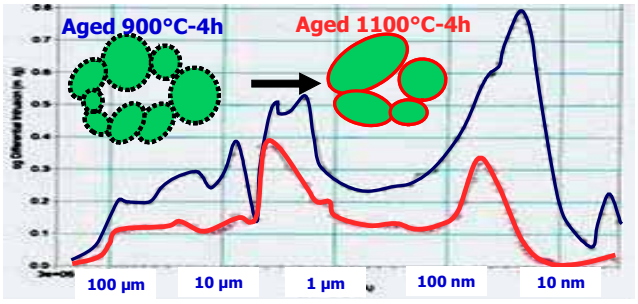

Figure 9-7. Mercury porosimetry profile of 2nd generation CeZr mixed oxide after air calcination respectively at 900°C and 1100°C [13].

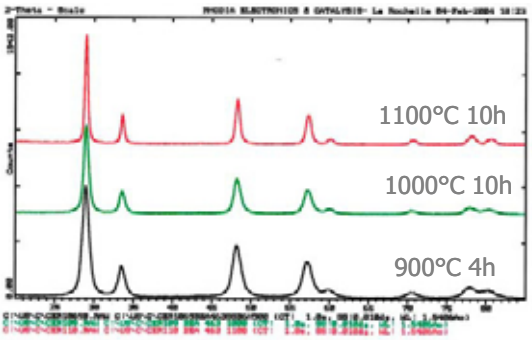

Figure 9-8. XRD analysis of 2nd generation CeZr mixed oxide (composition : $CeO_2/ZrO_2/La_2O_3/Pr_6O_{11}$ – 60/30/3/7 wt oxide %) after air calcination at 900°C / 1000°C / 1100°C [13] – Pure cubic solution up to 1100°C.

Finally, as suggested by M. Shelef and co-authors [6], ceria's dual role as an oxygen storage component in the TWC and as the basis for on-board catalyst monitoring, suggests that there may be future opportunities to 'tune' these characteristics separately (some OSC material designed for oxygen storage and PM carrier, some for on-board diagnoses).

9.2.1.2. Use of rare earths in NO_x-trap Catalysts for diesel and lean-burn engines

The demand for better fuel economy and lower CO_2 emissions from automotive engines leads to the development of lean-combustion technology. Under these conditions, conversion of NO_x is much more critical than for TWC. Recently, Toyota [16] proposed to store NO_x on a trap during extended periods of engine operation under lean conditions, and periodically to regenerate the trap by having engine operation shifted briefly to rich conditions.

Barium carbonate is the most commonly proposed material to trap NO_x. Nevertheless, due to its high sulfur sensitivity, catalyst makers are looking at alternative solutions including rare earth oxides such as La, Pr or Ce [17, 18].

On the other hand, incorporation of an oxygen storage component (such as ceria and/or ceria/zirconia mixed oxide) into the NO_x-trap leads to the generation of exothermic heat during NO_x trap regeneration, which helps for NO_x and SO_x desorption [6, 17, 19].

9.2.2. *A new catalytic solution for diesel engine exhausts cleaning*

The reduction of pollutant emission from passenger and utility vehicles is one of the major challenges of the new century due to the impact of such emissions on public health and environment (acid rains, destruction of ozone shelter…). One of the major challenges concerns diesel engines: compared to it gasoline counterparts, diesel engine displays improved long-term reliability and greater fuel efficiency (up

to 20% lower fuel consumption). This engine is the choice for the foreseeable future if its NO_x and particulate matter emission can be sufficiently reduced.

One elegant solution to get rid of particulate matter (PM) is to use a diesel particulate filter (DPF). The DPF system consists of a filter positioned in the exhaust stream designed to physically collect the particulate emissions, preventing thus their release to the atmosphere, while allowing the exhaust gases to pass through the system. DPF technology is the most effective means for reducing particulate emissions, with efficiencies exceeding 99.5% based on particulate number.

The most common design of DPF is the wall-flow monolith, which consists of many small parallel ceramic channels running axially through the part (Figure 9-9).

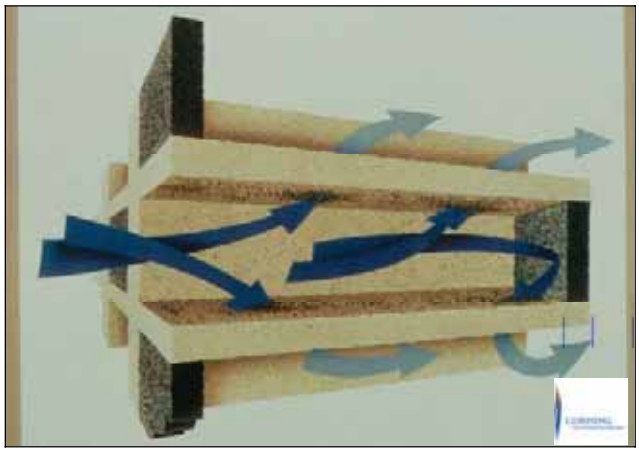

Figure 9-9. Ceramic wall-flow filtration design.

Adjacent channels are alternatively plugged at each end in order to force the diesel exhaust gases through the porous substrate walls which act as a mechanical filter. The filtration mechanism is a combination of surface and cake filtration. As the soot load increases, a particulate layer develops at the inlet channel walls and the cake filtration becomes the prevailing mechanism.

Since the volume of PM generated by a diesel engine is sufficient to fill up and plug a reasonably sized filter in a matter of few hundred kilometers, combustion of the accumulated soot in the DPF must occur frequently in order to regenerate the trap for the next accumulation step.

In fact, contrary to what one might expect, it is the regeneration of the DPF that poses the major technological challenge and not the filtration of the particulates.

One attractive method to meet the regeneration challenge is to dose diesel fuel with a Ceria-based fuel-borne catalyst at low concentration. Combustion of the resulting fuel leads to in-cylinder generation of ceria particles (a highly effective catalyst for soot combustion) intimately mixed with the diesel particulates which are

simultaneously formed from incomplete combustion of the diesel fuel. These mixed ceria-soot particles are trapped in the downstream DPF giving a soot bed containing a homogeneous dispersion of Ceria (Figure 9-10).

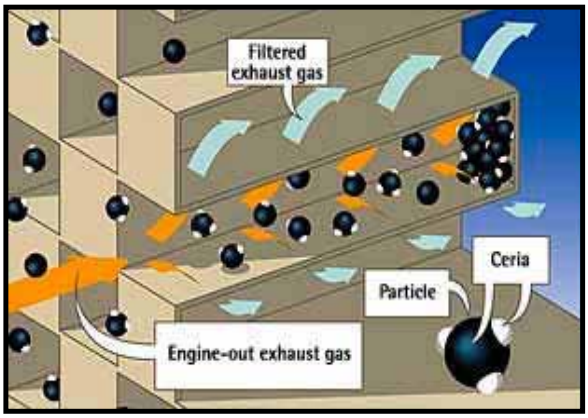

Figure 9-10. Principle of Operation of the Ceria-based fuel-borne catalyst.

The primary function of the ceria-based fuel-borne catalyst (FBC) [20] is to lower the combustion temperature of the soot accumulated in the DPF (currently around 450°C) compared to that of non-catalytically assisted combustion (usually around 600°C), thus allowing the DPF to regenerate more readily (Figure 9-11, combustion temperature of model soot decreases by the addition of a ceria-based catalyst).

As shown in Figure 9-12, the interest of the FBC technology is to ensure homogeneous and large number of contact points between the nano-crystals of ceria-based catalyst, the carbonaceous particulate forming the large soot aggregates and oxygen from the gas phase.

In addition, FBC [21] technology provides constant and continuously fresh ceria-based catalyst to the soot layer. This explains why, unlike many other catalyst-based DPF-regeneration technologies, the ceria-based fuel-borne catalyst is relatively insensitive to fuel-sulfur levels and is able to function with fuel containing over 2,500ppm of sulfur, as demonstrated in marine and stationary applications. However, in the presently described automotive application, the permissible level of sulfur is limited by the sulfur-sensitivity of other components of the complete DPF system.

The secondary function of the ceria-based fuel-borne catalyst [22] is to ensure, once the soot combustion is initiated, a complete and smooth regeneration avoiding exothermic peaks responsible for DPF aging, potentially leading to DPF breakage (Figure 9-13). This is achieved either by the good dispersion of the catalyst in the

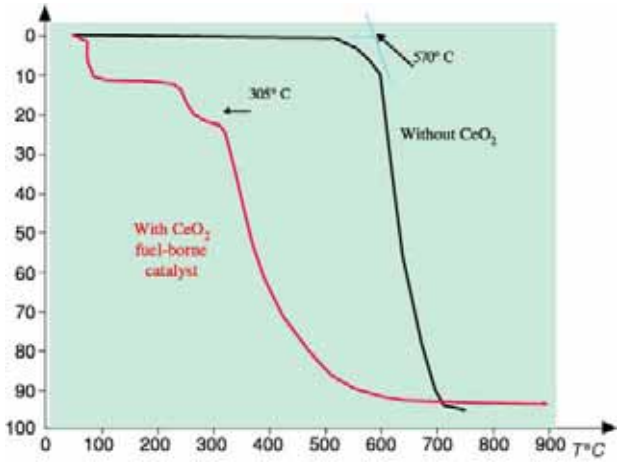

Figure 9-11. Comparison of combustion efficiency between a virgin (black) and cerium containing (red) carbon black. The ignition temperature of the cerium containing carbon black is more than 200ºC lower.

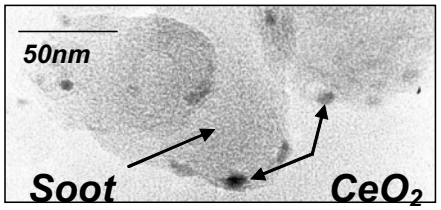

Figure 9-12. Ceria repartition within the soot particles

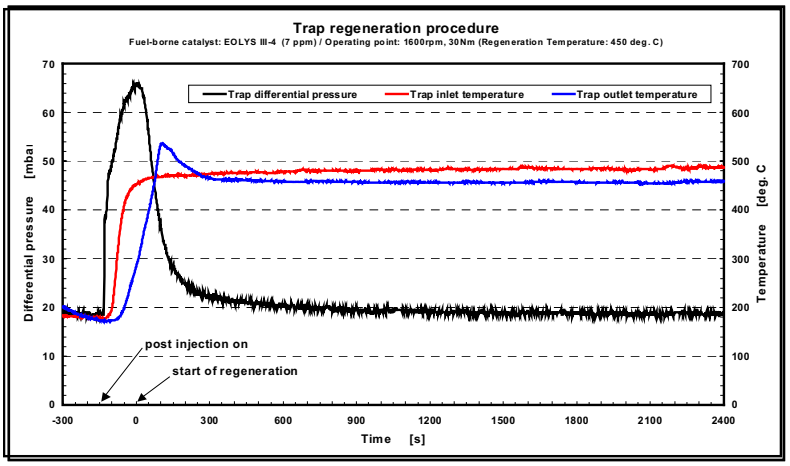

Figure 9-13. Exothermic peak observed during regeneration in specific conditions

soot bead or by the specific catalytic oxidation process of ceria, that could be the consequence of the well known oxygen-storage-capacity (OSC) properties of ceria nanocrystals that can provide locally native and reactive oxidizing species to burn soot and adsorbed hydrocarbons.

In order to introduce the catalyst inside the soot particles, it has been proposed that a fuel-borne catalyst made of cerium nanoparticles (Figure 9-14**)** perfectly dispersed in a solvent compatible with the Diesel fuel.

This first catalyst generation was used in 2000 by PSA-PEUGEOUT-CITROËN (hereafter PSA) on the Peugeot 607. One drawback of the solution was the necessity to clean the filter after 80,000 km due to ash accumulation in the DPF (Figure 9-15).

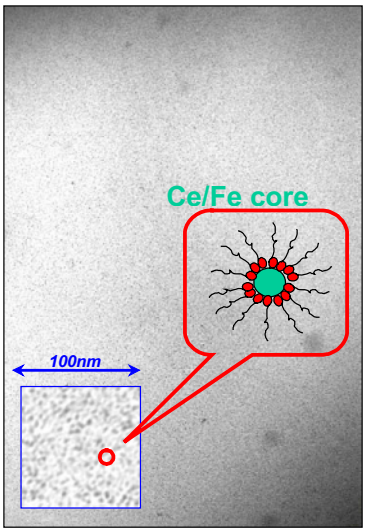

Figure 9-14. Fuel-borne catalyst made of cerium nanoparticles dispersed in an organic solvent.

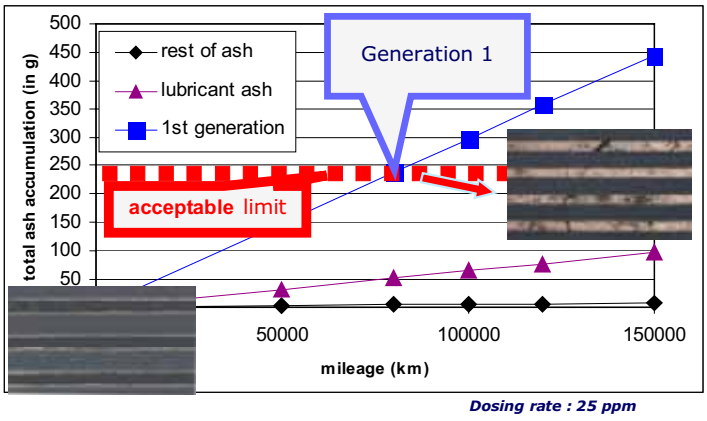

Figure 9-15. Ash accumulation observed for the first generation of ceria based catalyst

During the last two years, numerous research programs were launched in order to improve the catalytic activity of the cerium-based catalyst. The introduction of iron into ceria nanoparticles, multiplying by 2.5 the activity of the catalyst, allowed us to decrease the amount of catalyst from 25 ppm to 10 ppm while keeping constant the ignition temperature and the exothermic peak observed on the filter during regeneration. With the same filter size, the interval between servicing (ie. the cleaning of the filter) increase from 80000 to 120-150 000 km depending on vehicle engines (Figure 9-16).

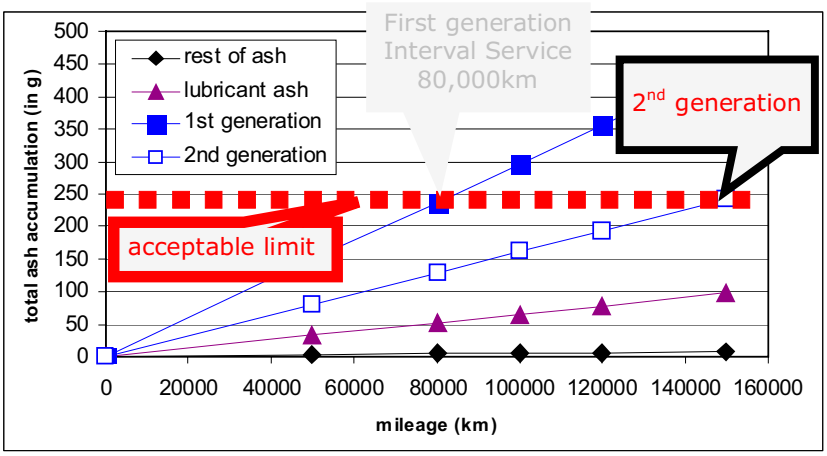

Figure 9-16. Ash accumulation observed for the second generation of ceria based catalyst.

The second generation catalyst was introduced by PSA on the European market End of 2002. Up to date, more than 600,000 passenger cars have been equipped without noticeable problem. Ford is also introducing the technology for its European diesel passenger cars.

However, achieving reliable and durable filter regeneration in automotive applications under all operating conditions is a major challenge, since driving cycle conditions are unpredictable and can range from prolonged periods of idling and low speed driving, to high speed cruising under laden conditions. Even using our Ceria-based fuel-borne catalyst, it is strongly recommended to use a completely active system approach for passenger car, light-duty, and heavy-duty vehicle applications, as it is done on all reliable commercial developments.

With a high level of activity whatever the quality of the fuel (sulfur content), the fuel-borne catalyst allows emission levels lower than the ones requested by the most severe regulations that will be effective in 2007 in the US and 2008 in Europe.

9.3. GLASS INDUSTRY

The glass industry is a traditional big user of Rare Earths, which are used both for the manufacturing of the glass material itself, and also for the surface treatment of glass pieces.

9.3.1. *Glass composition*

9.3.1.1. Glass coloration

The use of Rare Earths oxides in the glass composition allows the manufacturing of bright and stable colored glass pieces with good thermal and chemical resistance. Choice of Rare Earth element and concentration of addition, usually ranging from 2 to 6%, is driven by final desired shade [23].

Glass colored with neodymium shows pink to purple colors. The corresponding transmission curve (Figure 9-17) shows absorption peaks at 570-600nm (yellow) and 530nm (green).

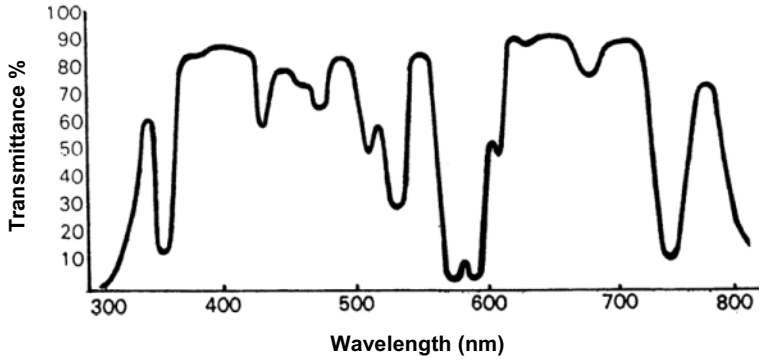

Figure 9-17. Transmission spectrum of a glass colored with 2.5% Nd_2O_3.

With an absorption zone at 450nm (Figure 9-18), praseodymium gives light and bright green tones.

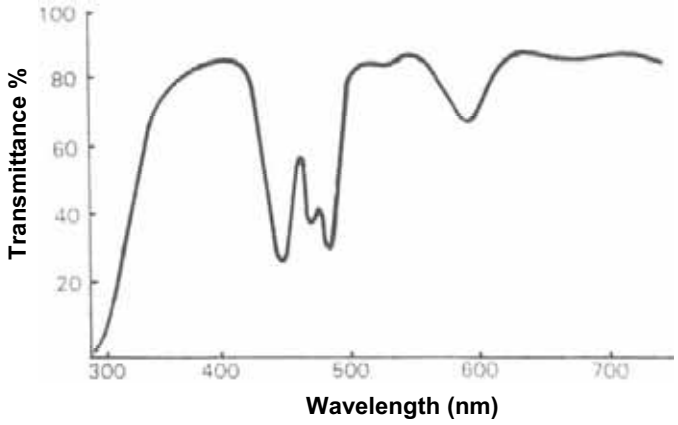

Figure 9-18. Transmission spectrum of a glass colored with Pr_6O_{11}.

Thanks to Erbium a specific light pink shade can be obtained, characterized by an absorption peak at 525nm (Figure 9-19).

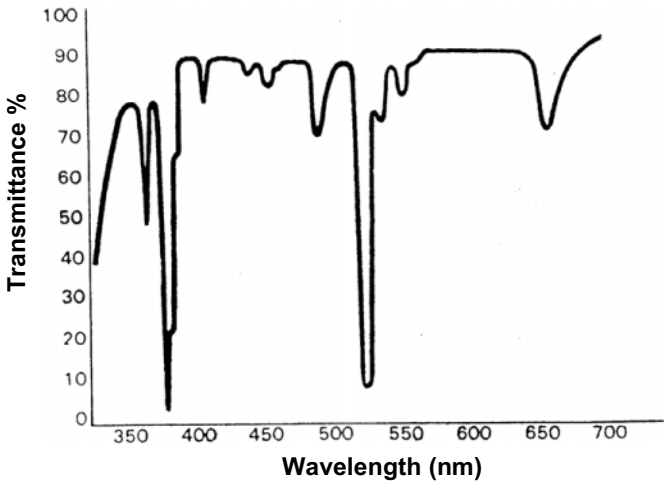

Figure 9-19. Transmission spectrum of a glass colored with Er_2O_3.

9.3.1.2. Glass discoloration

As some impurities may remain in the glass, namely iron oxides FeO or Fe_2O_3, an undesirable coloration can be observed, which can be eliminated in two steps:

- first chemical action followed by
- secondly physical discoloration

The tetravalent cerium ion in CeO_2 acts as an oxidizing agent relative to Fe^{2+}:

$$Fe^{2+} + Ce^{4+} \rightarrow Fe^{3+} + Ce^{3+}$$

The deep blue color of FeO disappears and turns into the light yellowish shade of Fe_2O_3. The resulting yellowish tone is eliminated with an element absorbing light in the yellow range of the visible light. Neodymium, possibly completed by Erbium in the case of greenish tone, provides the adequate spectrum and preserves the transparency of the glass.

9.3.1.3. Special Glasses

Rare Earths are also used to tune properties of glass for a series of applications like optical glass, irradiation stabilized glass, Laser glass, optical fibers [23].

Lanthanum oxide (La_2O_3) is thus widely added to increase refraction index and decrease light scattering in optical pieces like lenses and prisms. Cerium oxide (CeO_2) stabilises glass towards strong irradiation and avoids consequent darkening effect on CRT screens for example. Cerium is also recognized as an UV filter. Used at ca. 1%, neodymium enhances contrast and allows better image quality without changing colors. High purity neodymium also used, is certain types of laser glass.

9.3.2. *Glass polishing*

Cerium oxide is of major importance in the glass industry because of its ability to polish glass, thanks to its natural hardness and to the chemical reaction [24, 25] that takes place at the interface between the glass silica substrate and the cerium oxide particles. This reaction occurs in water and involves the creation of a silicate stratum which makes the glass surface more fragile and less resistant to mechanical erosion and physical modifications.

Cerium oxide powders can be incorporated into synthetic polishing pads or wheels or more frequently they are used in aqueous slurry fed onto the polishing tool. Cerium oxide polishing powders are thus traditionally used in numerous applications like spectacles, precision optics lenses for camera, CRT displays. Their role is to remove damaged layers of glass resulting from previous operations (moulding, grinding) and provide a smooth and glossy surface. Performance criteria are removal rate (ability to remove a certain amount of glass in a given time) and surface quality.

9.3.2.1. Removal rate

Removal rate is resulting from:

- first polishing powder characteristics
- second polishing conditions

Based on long experience of Rare Earths technology, it becomes possible to design ceria powders with proper physical properties for polishing applications, namely hardness, morphology and particle size distribution as shown in Figure 9-20.

Polishing conditions are driven by productivity and quality targets defined by the glass polisher and the equipment (machine, pad) used. They may also be adjusted depending on glass type. Speed, pressure, and slurry concentration are obvious key parameters, but water hardness and slurry temperature also influence polishing efficiency as shown in Figure 9-21.

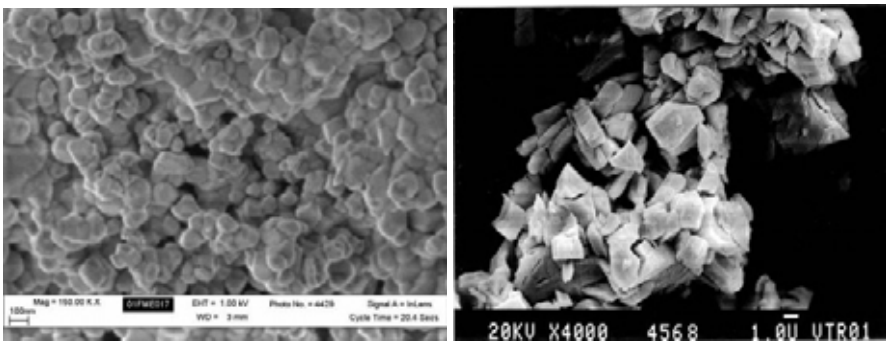

Figure 9-20. Morphology of cerium oxide powders tuned for polishing; cerium oxide powder composed of aggregates of fine and round particles (left) and cerium oxide powder composed of large and sharp edges particles (right).

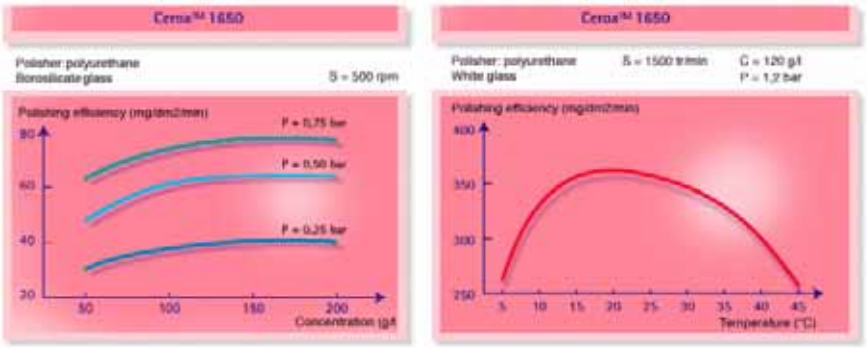

Figure 9-21. Influence of operating conditions on polishing efficiency.

9.3.2.2. Surface quality

A glossy and defectless surface is expected after polishing. Scratches, spots and any other marks coming either from previous operating steps or from polishing can cause rejection of glass piece. Glass should also be perfectly clean. Surface quality is often judged visually, usually under specific illumination conditions.

Surface quality is the consequence of:

a) processing steps prior to polishing
b) proper polishing and handling conditions
c) absence of contamination
d) quality of polishing powder.

Finer particles tend to give better surface quality. Hard particles and contamination should also be eliminated from the product are they can scratch the surface.

With evolution of technologies and markets, cerium oxide polishing powders, are now used for demanding applications like photomasks, LCD displays and glass hard disks. In these markets control of the surface quality, roughness and flatness is critical for the end application. LCD industry for example requires surface polishing prior to ITO (Indium Tin Oxide) sputtering. Not only the glass substrate must be free of any scratch and residue, but it must also comply with precise specifications of roughness. Surfaces are first examined visually, and evaluated more accurately with surface analysers, which can detect microscratches and measure roughness properties of the surface as shown in Figure 9-22.

In order to answer technical needs generated by these developing markets, polishing powders producers are challenged to tune and develop high performance products.

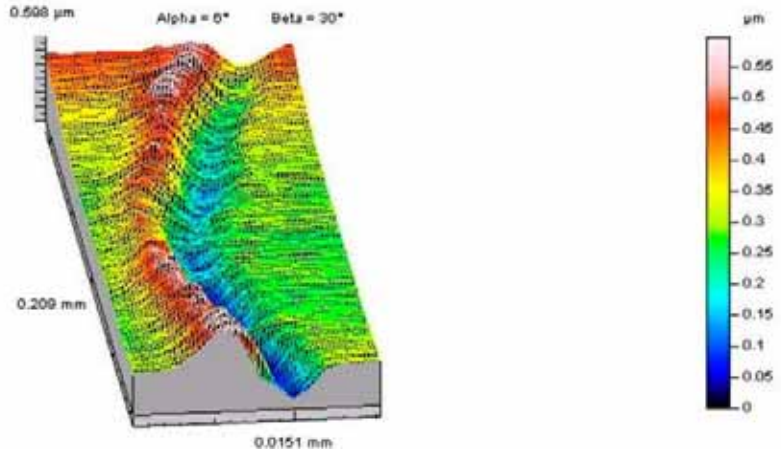

Figure 9-22. Surface quality after polishing, an example of a scratch.

9.4. FUEL CELLS

9.4.1. *Introduction to fuel cells*

Fuel Cells (FCs) convert the primary energy released by an electrochemical reaction directly into electric power and heat.The inherent efficiency and design flexibility of fuel cells, offers the solution to some of tomorrow's power generating needs. For example, since FCs operate as standalone units, electric power generation can be decentralized, simplifying the task of powering isolated facilities. FCs are also likely to be used in transportation, as they produce clean power, without excessive CO_2 emissions and with minimal atmospheric pollution, helping to limit greenhouse gases.

Fuel cells can be classified by the kind of electrolyte, there are Alkali fuel cells (AFCs), Polymer electrolyte fuel cells (PEFCs), Phosphoric acid fuel cells (PAFCs), Molten carbonate fuel cells (MCFCs) and Solid oxide fuel cells (SOFCs).

9.4.2. *Principle of SOFCs*

The electrochemical reaction in SOFCs is the reverse reaction of the electrolysis of H_2O. Gibbs free energy for the electrochemical reaction between hydrogen and oxygen is used as electricity.

Figure 9-23 shows the principle of SOFCs using oxide ion conductive electrolyte. Oxygen gas introduced to cathode receives the electron on the electrode and changes oxide ion, as shown in the next formula.

$$O_2 + 2e^- \rightarrow O^{2-}$$

The oxide ion diffuses in electrolyte and the electrochemical reaction between hydrogen and oxygen occurs on anode.

$$O^{2-} + H_2 \rightarrow H_2O + 2e^-$$

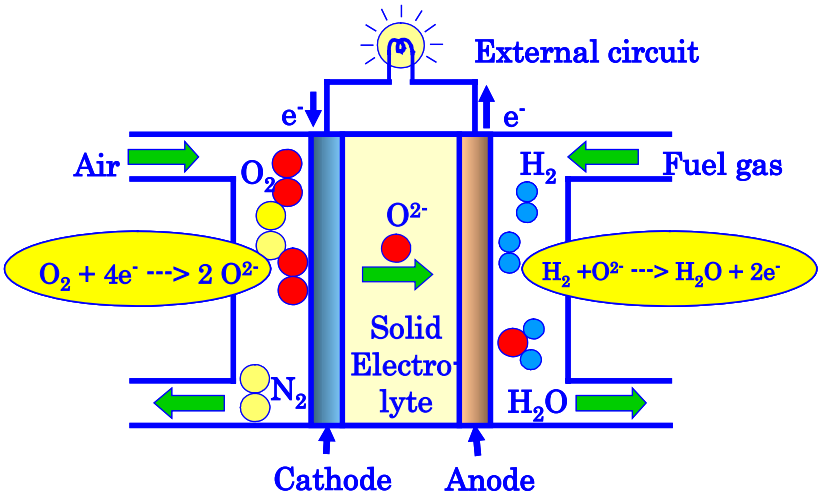

Figure 9-23. Basic principle of SOFC.

System design, performance and cost of such SOFC depend on the properties of innovative materials and advanced ceramics. The careful design and manufacture of these materials is essential to system integration and performance, and may ultimately determine the success or failure of the technology. Important factors include; stability, durability, processibility catalytic, electro-chemical and ionic properties. Figure 9-24 shows SEM image of ceramic layers used in a SOFC cell.

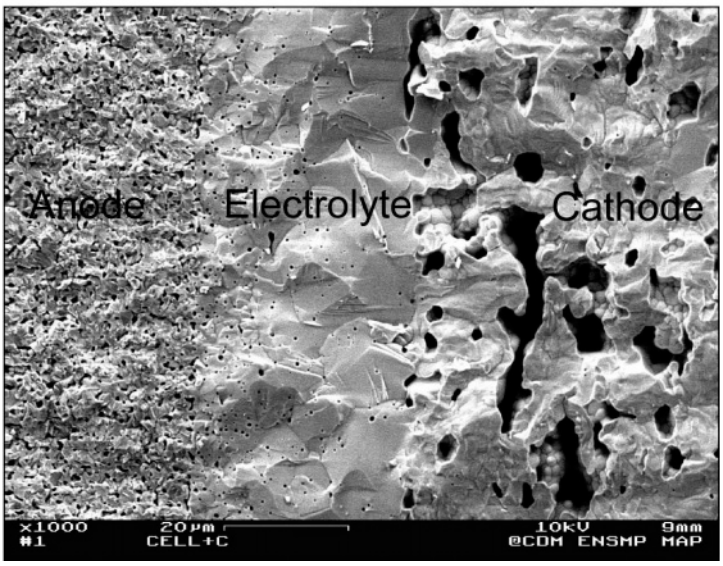

Figure 9-24. SEM image of the structure of ceramic layers used in a SOFC cell.

9.4.3. *Use and Role of Rare Earths in SOFCs materials*

9.4.3.1. Use of Rare Earths

Due to their chemical and physical properties, rare earth compounds, zirconia and other metal elements are key elements for this application and are used in all the different strategic components of the SOFC: solid electrolyte, electrodes and interconnector (Table 9-2).

The development of mass applications now requires large amounts of advanced high performance ceramics powder presenting a higher reactivity and a better phase purity.

For medium and low temperature operating conditions, cerium oxide doped with other rare earth elements (such as Gadolinium, Samarium or Yttrium) are very good candidates as electrolytes or anode materials. Traditional preparation routes such as solid state reactions starting from separated oxides did not allow achieving a good phase purity excepted at very high temperatures. The reactivity of the corresponding ceramics powders was then very low, limiting thus their sinterability (their ability to be transformed into dense thin layers).

As mentioned in Table 9-2, different perovskite compounds are used as cathode or interconnector materials.

TABLE 9-2. Rare earth oxides in SOFCs.

	High Temperature T > 750 ºC	Middle Temperature 750 > T > 600 ºC	Low Temperature 600 > T > 500 ºC
Anode	$Ni\text{-}ZrO_2{:}Y_2O_3$	$Ni\text{-}ZrO_2{:}Y_2O_3$ $Ni\text{-}YSZ{:}CeO_2$	$Ni\text{-}CeO_2{:}Ln_2O_3$ $TM\text{-}CeO_2{:}Ln$
Electrolyte	$Y_2O_3{:}ZrO_2$ $Sc{:}ZrO_2$	$Sc{:}ZrO_2$ $(La, Sr)(Ga, Mg)O_3$	$(La, Sr)(Ga, Mg)O_3$ $Gd{:}CeO_2$
Cathode	$(La, Sr)MnO_3$	$(La, Sr)(Fe, Co)O_3$	$(La, Sr)(Fe, Co)O_3$
Bipolar Plate (interconnect)	$(La, Sr, Ca)CrO_3$	Alloys (Y_2O_3)	Stainless Steel

9.4.3.2. Role of rare earths

Rare Earths are used in SOFCs because they give compounds with stable ionic or electrical conductive materials at high temperature. The crystal structure of typical materials contained Rare Earths for SOFCs are shown in Table 9-3. The classified crystal structures are fluorite structure and perovskite structure. In Table 9-3, Rare Earths except for Ce^{4+} have 3 valences and could be the dopant for the solid solution. For fluorite, a part of Zr^{4+} or Ce^{4+} is substituted by RE^{3+} (Rare Earths with 3 valences) or AE^{2+} (alkali earth metal with 2 valences), which has similar ionic radius and stable valence. The ionic radius of Ce^{4+} is larger than that of Zr^{4+}. CeO_2 shows the cubic fluorite structure at temperature range, from room temperature to melting point, although there is no dopant in CeO_2. RE^{3+} doped ceria has higher oxide ion conductivity than YSZ.

TABLE 9-3. Crystal structure of typical materials contained rare earths for SOFCs.

	Ionic conductor (Electrolyte)	Electronic conductor (Electrodes, Interconnector)
Fluorite structure	RE_2O_3 stabilized ZrO_2 $(CeO_2)_{1-x}(REO_{1.5})_x$	
Perovskite structure	$La_{0.8}Sr_{0.2}Ga_{0.8}Mg_{0.2}O_3$ $A(CeRE)O_{3-\delta}$ (A = Sr, Ba; RE = Y, Gd, Dy)	$(REA)MnO_3$ (RE = Y, La, Pr, Ce; A =Ca, Sr) $(REA)(CoB)O_3$ (RE = La, Gd; A = Sr ; B = Fe) $(LaA)(CrB)O_3$ (A =Ca, Sr ; B = Co, Ni, Fe, Mg)

Pyrochlore structure oxides have also oxide ion conductivity. The crystal structure of pyrochlore is similar to that of fluorite, and the 1/8 of oxygen in fluorite structure is removed regularly. The pyrochlore structures change to fluorite structures through order-disorder transition at high temperature, and then the high oxide ion conductivity similar to yttria stabilized zirconia (YSZ) appears. Although there are many fundamental data for crystallographic properties of $Ln_2Ti_2O_7$ pyrochlores with a stoichiometric composition [26, 27], few papers for non-stoichiometric $Gd_2Ti_2O_{7-\delta}$ have been published on the relationship among crystal structures, sintering characteristics, electrical conductivity and thermal expansions of the pyrochlores.

In the case of perovskite structure, a part of Rare Earths or transition metal is substituted by alkali earth metal. The positive charge for fluorite and perovskite is deficient because of the substitution for the both of fluorite and perovskite. The charge in crystal is kept neutral by the formation of oxygen vacancy for fluorite. And the valence change of transition metal for perovskite keeps the neutral charge in crystal. As a result, the oxide ion conductivity in fluorite structure and the electrical conductivity in perovskite appear.

The characteristics of Rare Earths are the large ionic radius similar to oxide ion, the stable valence and the unpaired electron in 4f-orbital. Especially, the large ionic radius and the stable valence contribute to the oxide ionic or the electrical conduction of materials for SOFCs.

9.4.4. *Requirements and new solutions of materials for SOFCs*

SOFCs consist of cells and electrical interconnectors cells itself consist of electrolyte, anode and cathode. The SOFCs components using Rare Earths are shown in Table 9-2 and Table 9-4.

9.4.4.1. New materials for electrolyte

For electrolyte, the high conductivity and dense ceramics are required. A proprietary new wet chemistry route has been developed [28-30], which allows to reach at lower temperature both good crystallographic phase purity and good sinteribility (Figure 9-25).

9.4.4.2. New materials for anode; Ni CGO composite

Porous ceramics, with high electronic conduction and chemical stability in the fuel gas are required for anode and cathode. The electrode should be porous and have homogeneous microstructures because the electrode reaction occurs on three phase boundary (TPB), which consists of electrolyte, electrode and gas. The reaction site increases with TPB length. Using a new technique of spray dry process, a new

TABLE 9-4. The SOFCs components using Rare Earths.

	Materials	Composition	Characteristics
Electrolyte	ZrO_2	Y_2O_3 stabilized ZrO_2 (YSZ)	Basic material
		Al_2O_3 mixed YSZ	To strengthen
		Yb_2O_3 stabilized ZrO_2	Higher ionic conductivity, higher power density, lowering of operation temperature
		Sc_2O_3 stabilized ZrO_2	
	CeO_2	$(CeO_2)_{1-x}(REO_{1.5})_x$ (RE=Y, Sm, Gd)	
	$LaGaO_3$	$La_{0.8}Sr_{0.2}Ga_{0.8}Mg_{0.2}O_3$	
	$ACeO_3$ (A=Sr, Ba)	$A(CeRE)O_{3-\delta}$ (A=Sr, Ba: RE=Y, Gd, Dy)	Proton cinductor
Anode	Ni	Ni-YSZ	Basic material
		Ni-MgO-YSZ	Long term stability, to prevent the sintering of Ni
		Ni-CeO_2	Low over potential, high reforming activity for fuel
		Ni-$(CeO_2)_{0.8}(SmO_{1.5})_{0.2}$	
		Ni-Pr_6O_{11}	
	Ru	Ru-YSZ	
	TiO_2	TiO_2-YSZ	Chemical stability, high reforming activity for fuel
	$LaCrO_3$	$(La_{0.8}Ca_{0.2})CrO_3$	
Cathode	$REMnO_3$	$(RESr)MnO_3$	Basic material
		$(PrSr)MnO_3$	Low over potential at low temperature
		$(REA)MnO_3$ (RE=Y, La, Pr, Ce: A=Ca, Sr)	Cost reduction
		$\{(La_{0.6}Y_{0.4})_{0.8}Sr_{0.2}\}MnO_3$	Compatibility of TEC for YSZ
		$(GdA)MnO_3$ (A=Ca, Sr)	To prevent the reaction with YSZ
	$RECoO_3$	$(LaSr)CoO_3$	High electronic conductivity
		$(GdSr)CoO_3$	To prevent the reaction with YSZ
		$(LaSr)(CoFe)O_3$	Low over potential at low temperature
Interconnector	$RECrO_3$	$(LaA)(CrB)O_3$ (A=Ca, Sr: B=Co, Ni, Fe, Mg)	Basic material
		$La(CrMg)O_3$	Low lattice expansion under reducible atmosphere
		$(LaCa)(CrCoFeNi)O_3$	Inmprovement of sinterability
	CrFe alloy	$(CrFe)_5(Y_2O_3)_1$	Low TEC alloy

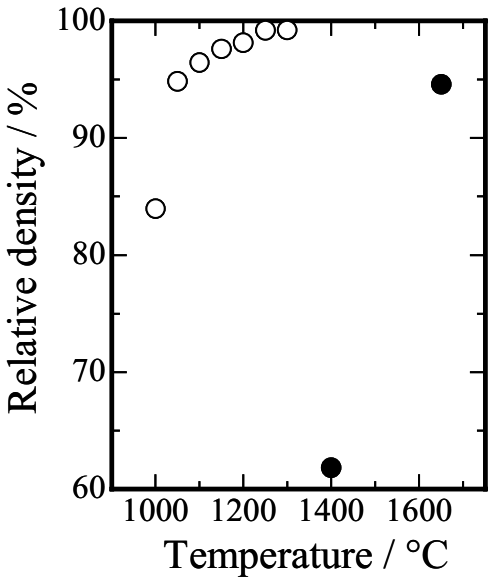

Figure 9-25. Relative density of $Ce_{0.9}Gd_{0.1}O_{1.95}$ powder as a function of temperature. Open circles and closed circles represent co-precipitation method and solid state technique, respectively.

composite of 50 vol % Ni-$Ce_{0.9}Gd_{0.1}O_{1.95}$ (CGO) cermets for anode materials at intermediate and low temperature SOFCs has been developed [31]. Such a composite gave a microstructure of anode ceramic part more homogeneous than the one obtained with conventional ball mill process as shown on Figure 9-26. Such materials proved to have a higher performance; much lower over-potential and ohmic loss (see Figure 9-27).

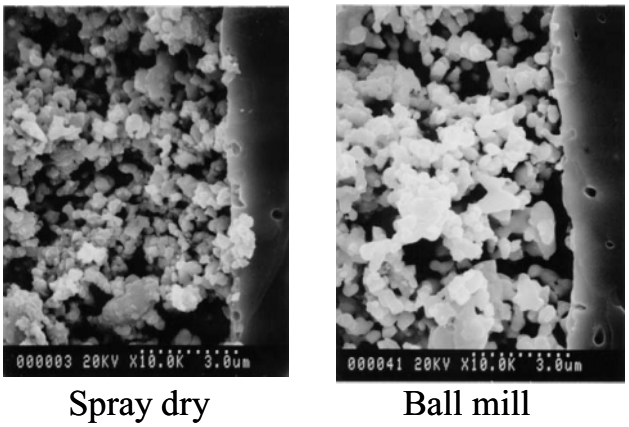

Figure 9-26. SEM micrographs of cross section of anodes produced at 1300°C.

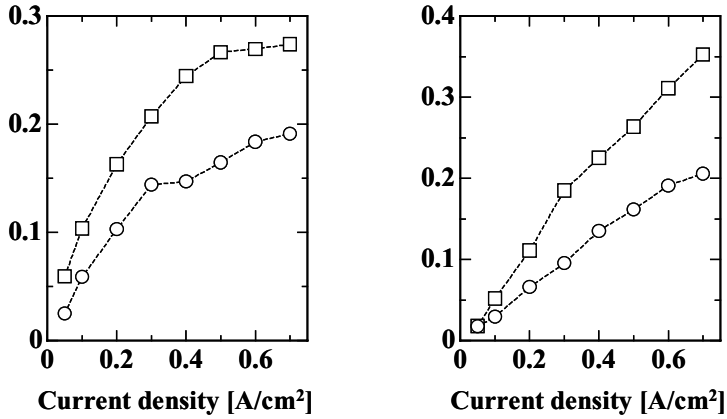

Figure 9-27. Electric performance of NiO-CGO anodes made at 1300ºC. NiO-CGO powders were prepared by various synthesis methods; circles and squares represent spray dry and ball mill, respectively.

9.4.4.3. New perovskites for electrolyte, electrodes, and interconnectors

As mentioned in Table 9-2, different perovskite compounds are used as cathode or bipolar plates materials.

An industrial process to prepare those materials with well controlled composition has been developed, particle size, surface area, and phase purity. The resulting application properties are superior to conventional products obtained by solid state routes. Table 9-5 gathers the typical characteristics of such compounds. An example of a study conducted on lanthanum chromite is given in reference 32. New lanthanum manganite products were also patented [33].

TABLE 9-5. Characteristics of various perovskites commercially available.

	Sample	Specific surface area ($m^2 \cdot g^{-1}$)	D50 (µm)
Electrolyte	$La_{0.9}Sr_{0.1}Ga_{0.8}MgO_{3-\delta}$	23.0	1.6
	$BaCe_{0.8}Gd_{0.2}O_{3-\delta}$	5.5	0.7
Electrode	$La_{0.86}Sr_{0.14}MnO_{3-\delta}$	3.0	2.4
	$La_{0.6}Sr_{0.4}Co_{0.2}Fe_{0.8}O_{3-\delta}$	8.0	1.0
Interconnector Separator	$(La, Sr)CrO_{3-\delta}$	2.7	2.9

9.5. SOLID ELECTROLYTES

9.5.1 *Yttria stabilized zirconia*

Solid electrolytes are one of functional materials which only single ion species can generally migrate in solid and are greatly expected to be applied for the electrical devices such as all solid-state batteries and chemical sensing devices

utilizing their unique characteristics. After discovering the O^{2-} ionic conducting ZrO_2 doped with a small amount of Y_2O_3 as an electric light which called "Nernst glower" in 1897, many kinds of solid electrolytes have been extensively developed. This material is now well known as YSZ (yttria stabilized zirconia) which is commercially applied for oxygen gas sensor.

The O^{2-} ion conduction in YSZ was firstly demonstrated by Nernst in 1899 [34]. The minimum content of Y_2O_3 doped in the host ZrO_2 is 9 mol% for the stabilization of the cubic fluorite phase. The solution of Y_2O_3 in ZrO_2 becomes possible because of the structural similarity between cubic ZrO_2 and cubic C-type rare-earth oxides. In the case of the La^{3+} doping, however, a pyrochlore phase of $La_2Zr_2O_7$ is dominantly produced because of the large ionic size of La^{3+}. Among the rare earth ions, the most interesting dopant cation is Sc^{3+}. Since the ionic radius of Zr^{4+} (0.098 nm; CN = 8 [35]) and Sc^{3+} (0.101 nm; CN = 8 [35]) are similar, it is enough for only 6% Sc^{3+} to fully stabilize the fluorite phase. In the ZrO_2-R_2O_3 series, the fluorite-type solid solutions have a maximum conductivity at 8-10 mol % $RO_{1.5}$ (R = Nd-Lu, Y, Sc) at compositions corresponding to near the lower fluorite phase boundary, and an increase in rare-earth doping decreases the conductivity. Since the ionic radii of rare earth ions are larger than that of Zr^{4+}, the free volume for oxide ion migration decreases with the increase of the rare earth content. The oxide ion conductivity linearly increases with reducing ionic radius of the dopant rare earth in the sequence Nd < Gd < Dy < Ho = Y < Er < Yb < Lu < Sc as expected [36]. Among the rare-earth doped stabilized zirconia series, the highest ion conductivity was obtained for the ZrO_2-Sc_2O_3 system. On the contrary to the highest oxide ion conductivity, the critical disadvantage of low stability of the solid solution exists in this material. Details of each ZrO_2-R_2O_3 series are available in the references.

In the 20^{th} century, many kind of conducting ion species from monovalent to tetravalent ions have been discovered as well as a large number of host crystal lattices. Although some binary rare earth oxides for solid electrolytes have also been investigated, their ion conducting properties were, unfortunately, not enough except the ceria-based materials.

9.5.2. *Solid electrolytes based on ceria*

Cerium oxide, ceria, has a fluorite structure and shows oxide anion conducting behavior differ from other rare earth oxides. However, the O^{2-} ionic conductivity of pure ceria is low because of a lack of oxide anion vacancies. For ion conduction, especially for anion, it is important to have such an enough vacancy in the crystal lattice for ion conduction. Therefore, the substitution of tetravalent Ce^{4+} by a lower valent cation is applied in order to introduce the anion vacancies. For the dopant cation, divalent alkaline earth metal ions and some rare earth ions which stably hold trivalent state are usually selected. Figure 9-28 shows the dopant ionic radius dependencies of the oxide ionic conductivity for the doped ceria at 800°C. In the case of rare earth doped CeO_2, the highest O^{2-} ion conductivity was obtained for

Sm^{3+} doped CeO_2 [36]. The conductivity of $Ce_{1-x}Gd_xO_{2-x/2}$ solid solution even at 700°C, which is the secondly highest O^{2-} ion conductivity among the $Ce_{1-x}R_xO_{2-x/2}$ (R: rare earths) series, shows a comparable conductivity to that of the stabilized zirconia at 1000°C. In the case for doping the divalent alkaline earth metal ions into CeO_2, the maximum conductivity was realized for Ca^{2+} which has almost the same ionic radius as Sm^{3+}, although the conductivity was lower than those of rare earth doped ceria. These phenomena clearly indicate that the oxide ion conduction in the doped ceria depends on the ionic radius of the dopant cation as well as the valence.

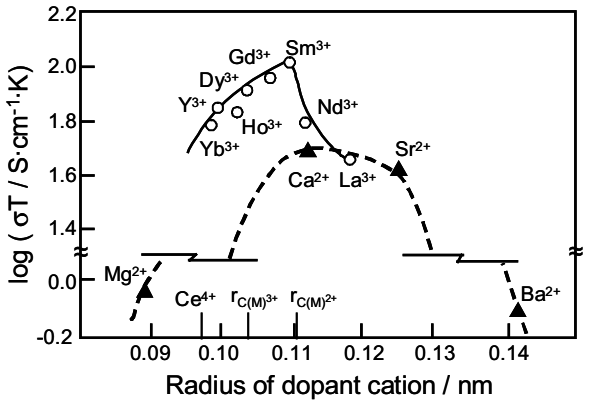

Figure 9-28. The dopant ionic radius dependencies of the oxide ionic conductivity for the doped ceria at 800°C. (Reprinted with permission from ref 36. Copyright 1996 Elsevier Science B.V.)

The range of the oxygen partial pressure where the rare earth doped ceria exhibits oxide anion conduction is limited over 10^{-8} Pa in Po_2 at 800°C (The oxide anion transference number decreased to 0.5 at this condition.), whereas the well-known stabilized zirconia shows the stable ion conduction between 10^{-15} and 10^{15} Pa. This low stability against reducing atmosphere observed in the rare earth doped ceria is a fatal problem for applications.

As described in the previous section, oxide ion conducting solid electrolytes have been focused on a component of solid oxide fuel cells (SOFCs) from 1970's, and YSZ is mainly investigated as a candidate of the solid electrolyte because of the high O^{2-} ion conductivity and high chemical stability under both oxidizing and reducing atmospheres at high temperatures. However, it is necessary for obtaining the applicable O^{2-} ion conductivity to heat up the solid electrolyte to ca. 1000°C. One approach to reduce the inner cell resistance is to reduce the thickness of the YSZ layer, and another way is to employ a new ionic conductor with higher ionic conductivity than YSZ even if its oxide ion conductivity is lower than those for above mentioned doped ceria. This is because ceria is easily reduced in reducing atmosphere of the fuel side, and a consequent appearance of considerable electronic conduction causes the power loss. Furthermore, the oxide lattice is expanded by the

formation of oxygen vacancies and serious problem such as bend is caused at the anodic fuel gas side according to the following equation.

$$2CeO_2 \rightarrow 2Ce_{Ce}' + 3O_O\times + V_O\ddot{} + 1/2O_2$$

Therefore, it is not suitable to use ceria based solid electrolytes in the cell type shown in Figure 9-23. However, in the case for the other types shown Figures 9-29(a) and (b) [37], both the cathode and the anode are in the same atmosphere where air and fuel gas exist at the same time. Therefore, the volume change of the cell becomes negligible and it is greatly expected to apply the Sm-doped ceria which shows higher oxide ion conductivity than that of YSZ at intermediate temperature.

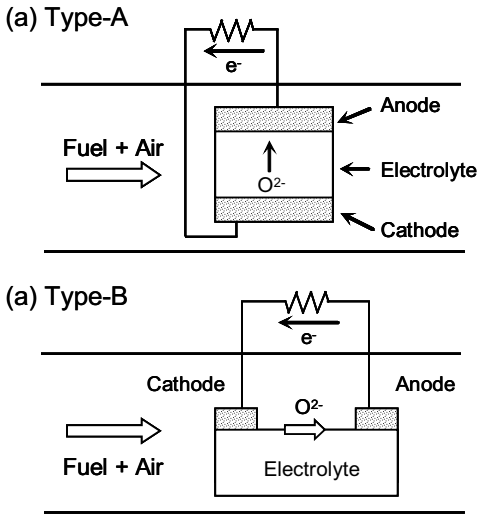

Figure 9-29. The basic structures of the single chamber type SOFC. (Reprinted with permission from ref 37. Copyright 2003 T.I.C)

Figure 9-30 shows the I-V characteristics at 500°C for the SOFC cell using $Ce_{0.8}Sm_{0.2}O_{1.9}$ as a solid electrolyte. In this condition, Ce^{4+} was not reduced at all and considerably large current density was obtained in comparison with the case for YSZ. Therefore, it is possible to operate the cell at low temperatures below 773 K. Considering the power density of the single chamber type of SOFC cells, the further improvements are necessary for the practical use, because the power density of the cell with $Ce_{0.8}Sm_{0.2}O_{1.9}$ (281 $mW \cdot cm^{-1}$ at 500°C) is still lower than that (1 $W \cdot cm^{-1}$) of the high temperature SOFC with YSZ which is composed of the dual chamber cell operating at around 1000°C.

For the practical application of the oxide ion conducting solid electrolytes for the SOFCs, there is another problem that they usually need high operation temperature over 800°C. In fact, the SOFCs based on the YSZ thin film electrolyte cannot provide acceptable power output due to the fundamental limit of YSZ that it is difficult to obtain enough conductivity below 650°C. The ceria-based oxides are,

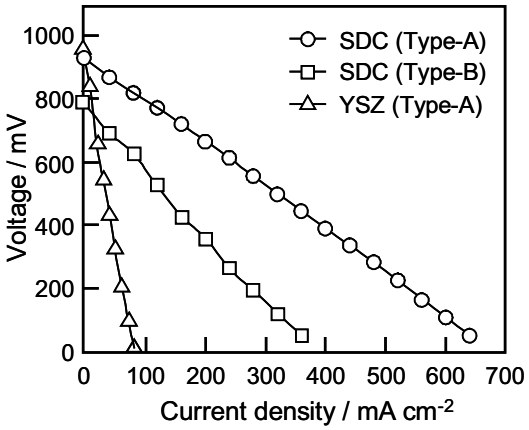

Figure 9-30. I-V characteristics at 500°C for the single chamber types of SOFC cell with $Ce_{0.8}Sm_{0.2}O_{1.9}$ as a solid electrolyte: Ni-$Ce_{0.8}Sm_{0.2}O_{1.9}$ | $Ce_{0.8}Sm_{0.2}O_{1.9}$ | $Sm_{0.5}Sr_{0.5}CoO_3$. The thickness of the SDC was 0.5 mm and the mixture gas of ethane and oxygen (1:1 in a molar ratio) flowed into the chamber. (Reprinted with permission from ref 38. Copyright 2001 The Ceramics Society of Japan)

therefore, commonly attracted as the alternative SOFC materials. However, as mentioned above, the pure ceria cannot be applied because of its critical problems concerning reduction. On the contrary, the doped ceria materials show high conductivity of ca. 0.1 $S \cdot cm^{-1}$ at 800°C which is equal to that of the YSZ at 1000°C. Although the ceria-based materials are strongly expected to be a component of the SOFCs operated at low temperatures around 600°C, the ion conductivity reduces to 5×10^{-3} $S \cdot cm^{-1}$ at 600°C which does not satisfy the required conductivity level of 0.1 $S \cdot cm^{-1}$. In addition, the problem on the reduction of Ce^{4+} to Ce^{3+} is also remained in these materials [39].

9.6. SUNSCREEN COSMETICS

9.6.1. *CeO_2 for sunscreens*

Although exposure of the human body to sunlight to attain a tanned look has been fashionable in recently, the UV-ray included in the sunlight causes damaging effects on human's skin. In order to protect us from such the harmful problems, many kinds of organic and inorganic sunscreen materials have been developed. Among them, organic UV absorbers show effective UV-B (290–320 nm) absorption property, but with modest UV-A (320–400 nm) absorbing ability, and some of the organic filters have caused irritation on the skin of sensitive individuals [40]. Therefore, they may pose a safety problem when used at high concentrations. In addition, some organic UV filters are not photostable.

In the case of the inorganic sunscreens, fine particles of titanium oxide (TiO_2) and zinc oxide (ZnO) are effective and are popularly used in the cosmetics [41]. Although titanium oxide is the most popular inorganic sunscreen agent, it is known

that TiO_2 is an excellent photocatalyst [42], which can oxidize sebum and degrade other ingredients in the sunscreen cosmetics. In addition, titanium oxide may cause the user's skin to look unnaturally white when incorporated into sunscreen products, due to the high refractive index (2.6-2.7). ZnO is another widely utilized sunscreen agent, but it also possesses photo- and thermal catalytic properties [43].

On the other hand, cerium oxide (CeO_2) has characteristics ideal for use as a broad-spectrum inorganic sunscreen for cosmetics, because it is not only transparent to visible light but also has excellent ultraviolet radiation absorption properties, due to the appropriate refractive index (2.1) [44] and the bandgap energy (3.1eV) [45], respectively. In addition, the photocatalytic activity of CeO_2 is much lower than those of TiO_2 and ZnO. However, because of the high thermal catalytic activity for oxidation of organic materials, ceria has not been used commercially as a sunscreen material.

In order to overcome this problem and to develop a safe and stable inorganic sunscreen with superior UV absorption capability, the catalytic activity of CeO_2 has been successfully decreased by coating the surface with amorphous silica (SiO_2) [46, 47] or boron nitride (BN) [48, 49] without decreasing the UV shielding property of CeO_2. Figure 9-31 shows the transmittance spectra of a 0.25 mm thick wax base film containing $0.7CeO_2$-$0.3SiO_2$ composite, compared with those of the micronized TiO_2 and ZnO samples [47]. The concentrations of these particles are 20%, 4%, and 10%, respectively, adjusting to give the same transparent level in the visible region for all the films. Compared with these samples, only the $70\%CeO_2$-$30\%SiO_2$ composite exhibits both high transparency in the visible region and good absorption in the ultraviolet region.

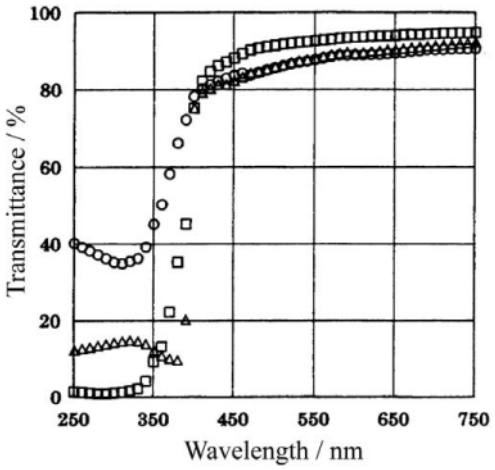

Figure 9-31. Transmittance spectra of thin films containing with 20% $0.7CeO_2$-$0.3SiO_2$ (□), 4% TiO_2 (○), and 10% ZnO (Δ). (Reprinted with permission from ref 47. Copyright 1998 Japanese Cosmetic Science Society)

Figure 9-32 depicts the reflectance spectra of the pressed powders of the BN/CeO_2 and CeO_2 samples [49]. In these spectra, low reflectance means high absorption in the corresponding wavelength region. Although the absorption spectrum of the BN/CeO_2 slightly blue-shifted compared with that of CeO_2, it maintained good absorption behavior in the ultraviolet region. A representative TEM image of the BN/CeO_2 particles is depicted in Fig. 9-33 [48]. The powder consists of CeO_2 nanoparticles of 20–50 nm, and neither aggregation nor agglomeration was observed. The inset picture shows the top surface of a BN/CeO_2 particle and existence of a very thin BN layer is recognized, where the BN layer covering the CeO_2 particles was in a few nanometer's thickness.

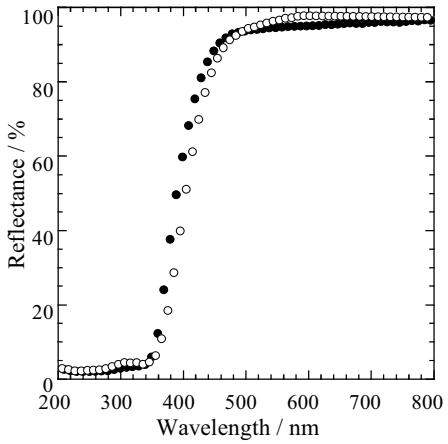

Figure 9-32. Reflectance spectra of the BN/CeO_2 (●) and uncoated CeO_2 (○). (Reprinted with permission from ref 49. Copyright 2003 The Royal Society of Chemistry)

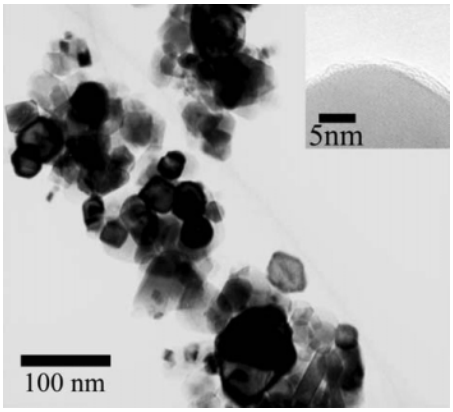

Figure 9-33. Transmission electron microscopic image of CeO_2 nanoparticles coated with boron nitride. The inset high-resolution image shows that the surface of the CeO_2 particles is covered with a very thin layer. (Reprinted with permission from ref 49. Copyright 2003 The Royal Society of Chemistry)

9.6.2. *Modification of CeO_2*

In another way for depressing the catalytic activity of CeO_2, doping a metal ion possessing lower valence and/or larger ionic size than those of Ce^{4+} into CeO_2 lattice has been proposed [50-53]. Figure 9-34 shows the catalytic activity which was evaluated by measuring the increase in the conductivity of distilled water by trapping volatile molecules formed by the oxidation of castor oil on heating. In this figure, low conductivity means low catalytic activity. The catalytic activity for the air oxidation of castor oil at 120ºC decreased substantially by doping with Ca^{2+} and Zn^{2+}. Doping Nd^{3+}, Sm^{3+}, and Eu^{3+} also resulted in a decrease in the catalytic activity, but the decrease was not so significant as in case of doping Ca^{2+}.

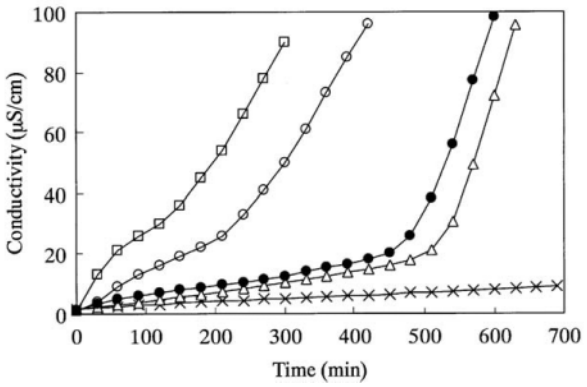

Figure 9-34. Evaluation of the catalytic activity at 120ºC. ×: blank (without catalyst), □: undoped CeO_2, Δ: 20mol% Ca^{2+}-doped CeO_2, ●: 20mol% Zn^{2+}-doped CeO_2, and ○: 30 mol% Eu^{3+}-doped CeO_2. (Reprinted with permission from ref 53. Copyright 2003 Elsevier Science)

The effect of the dopant was considered in relation to the formation of oxide ion vacancies and simultaneous oxygen evolution. The equilibrium reaction of the oxygen evolution and absorption in CeO_2 is expressed by the following equation.

$$CeO_2 = Ce^{4+}_{1-x}Ce^{3+}_{x}O_{2-x/2}\square_{2-x} + x/4O_2 \qquad (9.1)$$

$\square$: Oxygen defect; $0 < x < 1$

The ideal $r(M^{n+})/r(O^{2-})$ ionic size ratio of MO_8 eight coordination oxide is 0.732. However, $r(Ce^{4+})/r(O^{2-})$ is 0.703 in the case of CeO_2, which is smaller than that of the ideal value. This result suggests that Ce^{4+} is not large enough to stabilize the fluorite structure and it is reasonable that some Ce^{4+} have a tendency to be reduced to Ce^{3+} to take a more stable eight coordination of the fluorite structure, because Ce^{3+} (0.1143 nm) [35] has a larger ionic radius than Ce^{4+} (0.097 nm) [35]. By the doping of lower valence cations, oxygen molecules are released in advance to form oxygen vacancies. Therefore, the oxidation activity of CeO_2 can be depressed by doping lower valence cations. In addition, doping larger size cation is also suitable for stabilization of fluorite structure, and therefore, Ca^{2+} was considered to be the most effective dopant because it possesses a lower valence and larger ionic size than Ce^{4+}.

9.6.3. *New materials for sunscreens*

As mentioned above, ultrafine titanium oxide, zinc oxide, and recently cerium oxide have proven to be effective inorganic sunscreens and are widely utilized. However, it is imperative that the surface of these inorganic compounds be coated with an inert substance to minimize the catalytic activities. Recently, a series of amorphous phosphates of $Ce_{1-x}Ti_xP_2O_7$ have been developed as promising new materials for advanced sunscreens [54]. The UV absorption edge of these phosphates can be carefully manipulated to absorb at the desired range by simply adjusting the composition, from UV-B to UV-A (Fig. 9-35).

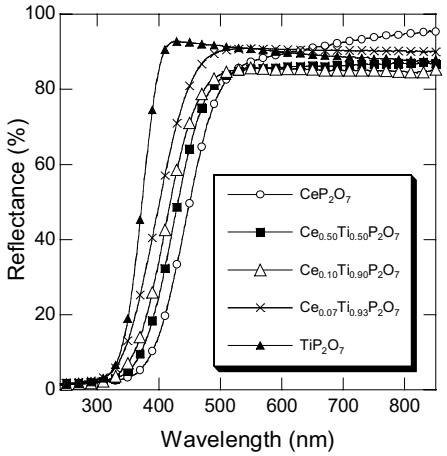

Figure 9-35. Optical reflectance spectra of the $Ce_{1-x}Ti_xP_2O_7$ sunscreens having various Ce/Ti ratios. (Reprinted with permission from ref 54. Copyright 2003 American Chemical Society)

Furthermore, metal phosphate is known as a component of bones and teeth, and therefore it is inert and safe with no known side effects to the human body. Not only are these metal phosphates stable, but they are also very inert and do not possess the ability to catalyze the formation of active oxygen species, as seen in several conventional oxide sunscreens.

9.7. ADDITIVE FOR THE IRON AND STEEL INDUSTRY

9.7.1. *Deoxygenation*

Rare earth metals have been used as additives in steel as deoxigenation and desulfurization agents, because the affinity of them with oxygen and sulfur is extremely strong. Compared with Ca and Mg, the rare earth metals are added more easily because of the higher melting point and lower vapor pressure. When the small amount of rare earth metals is introduced into iron and steel, they act as strong reductants and induce fine dispersion of oxide inclusions because of the high affinity of rare earth metals to oxygen [55].

For example, the addition of rare earths such as La and Ce decreased the strength of Fe and steel and in several cases resulted in the complete elimination of zonal segregation in the ingot [56]. The rare earth oxides formed were distributed in the ingot homogeneously for small amounts of rare earths, but they accumulated in the lower part of the ingot for high rare earth content. Modification of stainless steels by adding Fe-Ce (with 90% Ce) or rare-earth metal oxides reduced the number of surface defects of the steel arising in rolling [57]. The amount of the α-phase was reduced, and not only the corrosion resistance of the steel increased, but also the ductility and other mechanical properties were improved.

9.7.2. *Surface modification*

Deposition effects of rare earth oxides on the surface of iron and stainless steels have also been reported [58]. The corrosion rate constants decreased significantly by the coating in corrosion tests under isothermal conditions. In thermal cyclic conditions, protective scale spallation completely disappeared for coated samples. The rare earth effect is more remarkable with elements located on the left part of the lanthanide series (lighter rare earths). For example, ceria coatings strongly modify the microstructure and texture of the wustite (FeO) scale formed during low pressure oxidation of pure iron [59]. Cerium is located in the wustite matrix as a $CeFeO_3$ phase which dissolves in FeO in time.

Recently, laser cladding is becoming an effective way to produce a surface layer having good wear and corrosion resistant properties without dilution. The application of rare earth elements has been carried out on laser claddings containing CeO_2 [60] and La_2O_3 [61]. The wear and corrosion resistance of coatings can be remarkably increased by the addition of these oxides. The addition of La_2O_3 refines the microstructure, decreases the dendrite arm spacing, purifies the grain boundaries, and improves the coefficients of friction of laser clad coatings [61]. The corrosion rate of different laser coatings versus the corrosion time is depicted in Fig. 9-36.

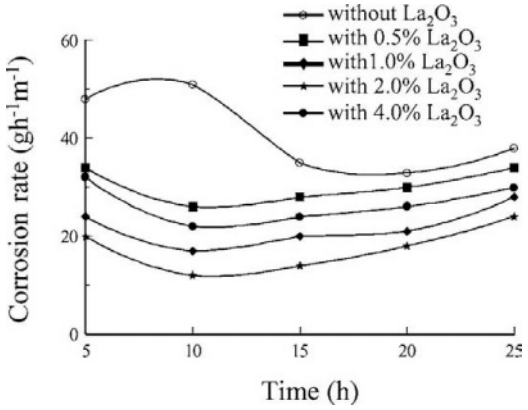

Figure 9-36. Effect of La_2O_3 on the corrosion rate of laser clad coatings. (Reprinted with permission from ref 61. Copyright 2003 Kluwer Academic Publishers)

The addition of the rare earth improves the corrosion resistance of the laser coatings. The microstructure becomes more compact by the refining and purifying effect of La_2O_3, which suppresses the corrosion.

9.8. BIOLOGICAL APPLICATION

9.8.1. *Radiotherapy for cancer*

Radiotherapy is one of the most effective treatments of cancers, but external irradiation often causes damage to healthy tissues. In order to avoid the external irradiation therapy, it has been reported that glass microspheres containing radioactive species are useful for in situ irradiation of cancers. For example, $17Y_2O_3$-$19Al_2O_3$-$64SiO_2$ (mol%) (YAS) glass microspheres are applied [62-64]. The glass whose size is 20 to 30 μm in diameter is insoluble in body fluids and non-toxic. Yttrium-89 in this glass is activated to ß-emitter ^{90}Y with a half-life of 64.1 h by neutron bombardment [65]. As shown in Fig. 9-37, the microspheres of the activated glass can give large local irradiation by short-ranged highly ionizing ß-ray to the tumors when they are injected into liver through the hepatic artery, with only a little radiation to the neighboring healthy organs. This glass has been subjected to clinical trials on the irradiation of diseased kidneys and liver cancer, and radiation synovectomy of arthritic joints [66-74]. In addition, the glass has already been used commercially in USA, Canada, and China [73].

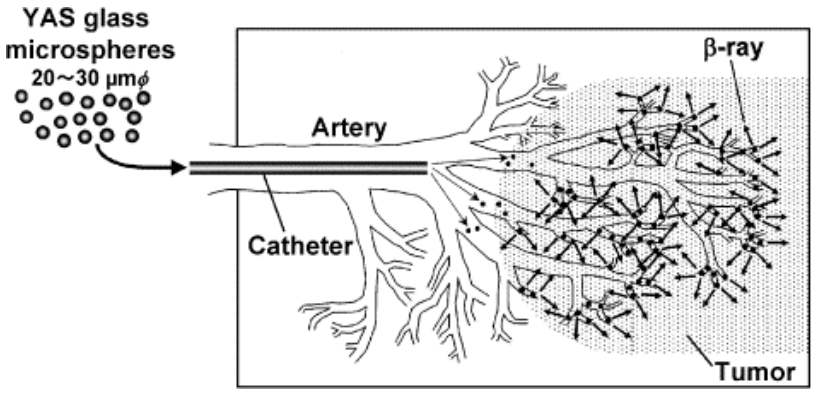

Figure 9-37. Cancer treatment with radioactive YAS glass microspheres. (Reprinted with permission from ref 75. Copyright 2002 Elsevier Science B.V.)

However, the number of yttrium ions present in the YAS glass is not so large, and the half-life of ^{90}Y is not long enough to avoid substantial decay even before the cancer treatment. Therefore, Y_2O_3 and YPO_4 microspheres have been suggested to be more effective for in situ radiotherapy of cancer than the YAS glass microspheres [75], because these materials are chemically durable ceramics containing larger amount of yttrium which are activated to ß-emitter.

Figure 9-38 shows micro X-ray transmission image of rabbit liver implanted with Y_2O_3 microspheres [75]. It is evidenced from this image that a large amount of Y_2O_3 microspheres can be distributed uniformly in hepatic artery, which indicates that the present Y_2O_3 microspheres can show hepatic radioembolization effects to the tumors. In addition, the implanted Y_2O_3 microspheres were successfully entrapped only in the liver uniformly and did not distribute to any other organs such as lung, stomach, and spleen. Therefore, the present microspheres are believed to be useful for in situ radiotherapy of cancer.

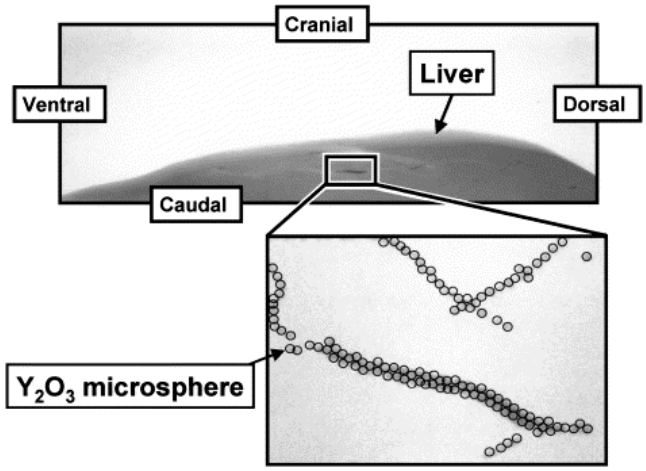

Figure 9-38. Micro X-ray transmission image of rabbit liver implanted with Y_2O_3 microspheres. (Reprinted with permission from ref 75. Copyright 2002 Elsevier Science B.V.)

9.8.2. *Basic studies on markers for brain tumor and digestibility estimation*

The primary malignant brain tumor is also a serious disease because there is no effective therapy. Although surgical resection of the tumor mass is the standard care, the invasive action of the malignant cells inevitably results in relapse of the tumor. Otherwise, effective chemotherapeutic and gene therapy agents are also well-known, but their use is limited by the presence of the blood-brain barrier. Therefore, it has been proposed the post-surgical positive pressure infusion of such agents directly into the bulk brain tissues [76]. The agents are distributed into the interstitial space of the brain and subsequently are delivered to the invading tumor cells.

For the purpose of the basic research on electrophoretic transport phenomenon in brain, some basic researches have been carried out using alternatives such as collagen and agarose gels instead of a living mammalian brain [77]. In order to explore the similarity between the porosity of the brain's extracellular compartment and that of the nanoscale polymeric structure of the gel, slurry of fluorescent nanoparticles has been applied to monitor the distribution of the nanoparticles within the gel [78]. As seen in Figure 9-39, for example, the nanoparticles of Y_2O_3:Eu^{3+}

whose size is 8-12 nm have clearly been spread through the interstitial structure of the gel by the positive pressure infusion process. This indicates that the equivalent inter-cross-link pore size within bulk samples of this polymeric gel mimics that of the extracellular space within in vivo mammalian brain.

Figure 9-39. Infusion mass viewed in visible light (left). Infusion mass viewed during UV excitation at 254 nm (right). (Reprinted with permission from ref 78. Copyright 2002 IOP Publishing Ltd.)

Binary rare earth oxides have also been evaluated as inert markers in apparent digestibility studies. An inert marker for the estimation of digestibility needs the following conditions.

- homogeneously incorporated into the feed and easily and accurately analysed, even at low concentrations
- indigestible and does not affect the metabolism of the animal
- pass through the gastro-intestinal tract at the same rate as the dietary nutrients
- hygienic and harmless to people and the environment

The predominant inert marker in fish studies is chromic oxide. However, chromic oxide does not only satisfy the criteria listed above, but also is not always totally recovered in the faeces [79]. In addition, chromium may be toxic even at low concentrations and, in some cases, allergenic to man, which makes it necessary to take extra care during the manufacture, use, and analysis of feeds and faeces with high concentrations of chromium.

On the contrary, binary rare earth oxides satisfy the criteria and should not affect the metabolism. They are slightly soluble in weak acid, but have a very low solubility under neutral conditions. The feasibility of Y_2O_3 and oxides of lanthanides such as La_2O_3 and Yb_2O_3 as inert markers has been verified in the digestibility studies with salmonids [80], and it was evidenced that Y_2O_3, La_2O_3, and Yb_2O_3 gave accurate estimates of apparent digestibility at much lower dietary concentrations (0.1 $g \cdot kg^{-1}$) than necessary when using Cr_2O_3 (10 $g \cdot kg^{-1}$). Since absorption of rare earth oxides in their soluble form does not occur from the stomach and the markers appear to be precipitated once entering the intestine, they can be used accurately at much lower dietary concentrations. The estimates of the apparent digestibility

obtained when using rare earth oxides were similar to the estimates obtained with Cr_2O_3.

Furthermore, rare earth oxides have an affinity for plant cell walls, and have been used in their soluble form to label indigestible plant fiber, in order to study digestion in ruminants [81]. Samarium, scandium, ytterbium and europium oxides have already been successfully used as inert markers to measure apparent utilization of nutrients in humans [82].

References

1. European patent, EP 05 81621, Japanese patent JP 2858617
2. European patent, EP 05 81622, Japanese patent JP 2914602
3. European patent, EP 08 74879, Japanese patent JP 11-503712
4. French patent, FR 28 03281
5. US patent, US 6,022,471 (2000)
6. M Shelef et al., Ceria and Other Oxygen Storage Components in Automotive Catalysts, in A. Trovarelli (Ed.), *Catalysis by Ceria and Related Materials*, Imperial College Press (2002).
7. H. S. Gandhi, A. G. Piken, M. Shelef, and R.G.Delosh, *SAE Paper*, 760201 (1976).
8. J.P. Cuif, G. Blanchard, O. Touret, A. Seigneurin, M. Marczi, and E. Quemere, *SAE Paper*, 970463 (1997).
9. J.P. Cuif, G. Blanchard, O. Touret, M. Marczi, and E. Quemere, *SAE Paper*, 961906 (1996).
10. R.M. Heck and R.J. Farrauto, *Catalytic Air Pollution Control – Commercial Technology*, *2nd ed.*, Wiley (2002).
11. M. Sugiura, *Catal. Surv. Asia*, **7**, 77 (2003).
12. J. Kaspar, P. Fornasiero, and N. Hichey, *Catal. Today*, **77**, 419 (2003).
13. E. Rohart, O. Larcher, C. Hédouin, F. Fajardie, H. Aimin, S. Deutsch, M. Allain, and P. Macaudière, *Congress on Automotive Pollution Control (CAPoC 6), Poster session (P66)*, Bruxelles (2003).
14. E. Rohart, O. Larcher, C. Hédouin, S. Deutsch, M. Allain, and P. Macaudière, *SAE Paper*, 2004-01-1274 (2004).
15. E. Rohart et al., Publication at Fisita Congress (Barcelona, May 2004), in press.
16. S. Matsumoto, Y. Ikeda, H. Suziki, M. Ogaiu, and N. Miyoshi, *Appl. Catal. B,* **25**, 115 (2000).
17. European patent, EP 1317953 (2002).
18. US patent, US 2003/0039597 (2003).
19. J. Theis et al., *SAE Paper*, 2003-01-1160 (2003).
20. L. Jacques et al, Cerium Based Fuel Additive for Diesel Particulate Emission Control, 27th ISATA, Aachen ,31st Oct-4th Nov 1994.
21. S.Olivier et al, *SAE paper*, 2000-01-0473 (2000).
22. M. Quigley and T. Seguelong, *SAE paper*, 2002-01-0436 (2002).
23. J.C. Gadea, L'industrie Céramique, N°854, 11/90.
24. J.E. Khaladji, Conference of tele-radiotechnic institute of Warsaw - Technical Paper, 1979 November 6th (1979).
25. D.C. Cornish and I.M Watt, The Mechanism of Glass Polishing, SIRA-Research Report, R267 (1961).

26. R. Kannno, Y. Takeda, T. Yamamoto, Y. Kawamoto, and O. Yamamoto, *J. Solid State Chem.*, **102,** 106(1993).
27. T. Yamamoto, R. Kannno, Y. Takeda, O. Yamamoto, Y. Kawamoto, and M Takano, *J. Solid State Chem*., **109,** 372(1994).
28. Japanese Patent, JP 08-169713
29. E. Suda, B. Pacaud, Y. Montardi, M. Mori, M. Ozawa, and Y. Takeda, *Electrochemistry*, **71**, 66 (2003).
30. E. Suda, B. Pacaud, Y. Montardi, M. Mori, and Y. Takeda, in contribution.
31. E. Suda, B. Pacaud, Y. Montardi, M. Itagaki, S. Ohara and Y. Takeda, in contribution.
32. E. Suda, B. Pacaud, and T. Seguelong, International Symposium on soft solution processing, 2000-12.
33. Japanese Patent, JP2000-236809
34. W.Z. Nernst, *Electrochem*., **6**, 41 (1899).
35. R.D. Shannon, *Acta Cryst*., **A 32,** 751 (1976).
36. H. Inaba and H. Tagawa, *Solid State Ionics*, **83**, 1 (1996).
37. T. Omata and S. Matsuo, *Materials Integration*, **16**, 48 (2003).
38. T. Hibino, *Ceramics*, **36**, 486 (2001).
39. B. Zhu, X. Liu, M. Sun, S. Ji, and J. Sun, *Solid State Sience*, **5**, 1127 (2003).
40. M.S. Reisch, *Chem. Eng. News*, **79,** 25 (2001).
41. G.P. Dransfield, *Radiat. Prot. Dosim*., **91**, 271 (2000).
42. A. Fujishima, and K. Honda, *Nature*, **238**, 37 (1972).
43. J.M. Herrmann, C. Guillard, and P. Pichat, *Catal. Today*, **17**, 7 (1993).
44. G. Hass, J. B. Ramsey, and R. Thun, J. Opt. Soc. Am., 48, 324 (1958).
45. C.A. Hogarth and Z.T. Al-Dhhan, *phys. status solidi (b)*, **137**, K157 (1986).
46. S. Yabe and S. Momose, *Proceedings of the 3rd Scientific Conference of the Asian Society of Cosmetic Science*, Taichung, Taiwan, p. 103 (1997).
47. S. Yabe and S. Momose, *J. Soc. Cosmet. Chem. Jpn.*, **32**, 372 (1998).
48. T. Masui, M. Yamamoto, T. Sakata, H. Mori, and G. Adachi, *J. Mater. Chem.*, **10**, 353 (2000).
49. T. Masui, H. Hirai, R. Hamada, N. Imanaka, G. Adachi, T. Sakata and H. Mori, *J. Mater. Chem.,* **13**, 622 (2003).
50. S. Yabe, M. Yamashita, S. Momose, K. Tahira, S. Yoshida, R. Li, S. Yin, and T. Sato, *Int. J. Inorg. Mater.*, **3**, 1003 (2001).
51. R. Li, S. Yabe, M. Yamashita, S. Momose, S. Yoshida, S. Yin, and T. Sato, *Mater. Chem. Phys.*, **75**, 39 (2002).
52. R. Li, S. Yabe, M. Yamashita, S. Momose, S. Yoshida, S. Yin, and T. Sato, *Solid State Ionics*, **151**, 235 (2002).
53. S. Yabe and T. Sato, *J. Solid State Chem.*, **171**, 7 (2003).
54. N. Imanaka, T. Masui, H. Hirai, and G. Adachi, *Chem. Mater.*, **15**, 2289 (2003).
55. E.M. Savitskii, V.F. Terekhova, V.A. Tsikalov, *Trudy Soveshchaniya*, 31 (1959).
56. V.E. Roshchin, D.Y. Povolotskii, A.V. Katkov, A.V. Rechkalova, and L.B. Stanovnova, *Izv. Akad. Nauk SSSR, Metally*, **5**, 17 (1974).
57. E.M. Savitskii, V.F. Popov, N.V. Keis, V.N. Lyubimov, *Akad. Nauk SSSR*, 214 (1964).
58. J.C. Colson, H. Buscail, G. Bonnet, P. Sotto, and J.P. Larpin, *Trans. Mater. Res. Soc. Jpn.*, **14A**, 107 (1994).

59. H. Buscail, C. Courty, and J.P. Larpin, *J. Phys. IV*, **5**, C7/375 (1995).
60. L. Mukin, M. Chen, and S. Dechun, *J. Rare Earths,* **9**, 294 (1991).
61. X.H. Wang, Z.D. Zou, S.L. Song, and S.Y. Qu, *J. Mater. Sci. Lett.*, **22**, 713 (2003).
62. G.J. Ehrhardt and D.E. Day, *Nucl. Med. Biol.*, **14**, 233 (1987).
63. M.J. Hyatt and D.E. Day, *J. Am. Ceram. Soc.*, **70**, C283 (1987)
64. E.M. Erbe and D.E. Day, *J. Biomed. Mater. Res.*, **27**, 1301 (1993).
65. R.C. Weast, D.R. Lide, M.J. Astle, and W.H. Beyer, in *CRC Handbook of Chemistry and Physics*, vol. B-28, p. 231, CRC Press, Florida (1989).
66. R.V.P. Mantravadi, D.G. Spignos, W.S. Tan, and E.L. Felix, *Radiology*, **142** 783 (1982).
67. M.J. Herba, F.F. Illescas, M.P. Thirlwell, L. Rosenthall, M. Atri, and P.M. Bret , *Radiology*, **169**, 311 (1988).
68. I. Wollner, C. Knutsen, P. Smith, D. Prieskorn, C. Chrisp, J. Andrews, J. Juni, S. Warber, J. Klevering, J. Crudup, and W. Ensminger, *Cancer*, **61**, 1336 (1988).
69. S. Houle, T.K. Yip, F.A. Shepherd, L.E. Rotstein, K.W. Sniderman, E. Theis, R.H. Cawthorn, and K. Richmond-Cox, *Radiology*, **172**, 857 (1989).
70. J.H. Anderson, J.A. Goldberg, R.G. Bessent, D.J. Kerr, J.H. McKillop, I. Stewart, T.G. Cooke, and C.S. McArdle, *Radiother. Oncol.*, **25**, 137 (1992).
71. M.A. Burton, B.N. Gray, C. Jones, and A. Coletti, Nucl. Med. Biol., **16**, 495 (1992).
72. F.A. Shepherd, L.E. Lotstein, S. Houle, T.K. Yip, K. Paul, and K.W. Sniderman, *Cancer*, **70**, 2250 (1992).
73. D.E. Day and T.E. Day, in L.L. Hench and J. Wilson (Eds.), *An Introduction to Bioceramics*, World-Science Publishing, Singapore, p. 305 (1993).
74. J.C. Andrews, S.C. Walker, R.J. Ackermann, L.A. Cotton, W.D. Ensminger, and B. Sharpiro, *J. Nucl. Med.*, **35,** 1637 (1994).
75. M. Kawashita, *Mater. Sci. Eng.*, **C22**, 3 (2002).
76. W.C. Broaddus, G.T. Gillies, and J. Kucharczyk, *Neuroimag. Clin. N. Am.*, **11**, 727 (2001).
77. Z.-J. Chen, H.L. Fillmore, G.T. Gillies, E. Bieberich, and W.C. Broaddus, *Neuro-Onc.*, **3**, 321 (2001).
78. G.T. Gillies, S.W. Allison, and B.M. Tissue, *Nanotechnology*, **13**, 484 (2002).
79. E. Lied, K. Julshamn, and O.R. Braekkan, *Can. J. Fish. Aquat. Sci.*, **39**, 854 (1982).
80. E. Austren, T. Storebakken, M.S. Thomasse, S. Refstie, and Y. Thomassen, *Aquaculture*, **188**, 65 (2000).
81. L.W. Smith, *J. Anim. Sci.*, **67**, 2123 (1989).
82. D.P. Hutcheson, B. Venugopal, D.H. Gray, and T. Lucky, *J. Nutr.*, **109**, 702 (1979).

CONCLUDING REMARKS

The binary rare earth oxides bring us a variety of interesting characteristics and understanding of their fundamental mechanisms builds a bridge between solid state chemistry and materials science. This book is the first monograph to cover the whole aspects of the binary rare earth oxides, which provides a comprehensive introduction to the unique characteristics of the binary rare earth oxides with their chemistry, physics and applications.

The purity of rare earth oxides is an important factor for the reliability on the characterization of their basic properties. In some earlier works, the presence of impurities in the oxides led to erroneous determinations of structure and polymorphism. However, due to development of effective separation technologies such as liquid/liquid extraction and precipitation/crystallization purification processes, high purity rare earth oxides can now be easily supplied for higher reliability studies as well as industrial manufacturing.

In the first half of this book, chemical stability, reactivity, structural features, and chemical bonding including band calculation of the rare earth oxides, have been examined from the viewpoints of the fundamental characterization and appearance mechanism of the properties. Particularly, further development of high resolution electron microscopy (HREM) and quantum band calculation will be of great aid for us to understand the unique characteristics of binary rare earth oxides from both the experimental and theoretical approaches. In addition, physical and chemical properties of the rare earth oxides such as electrical, magnetic, optical, and diffusion properties are also analyzed in details, leading to find relationships between basic science and applications in several functional materials.

The last half of the book has given a space to thermochemistry, trace determination, and applications of the rare earth oxides, as well as single crystal growth and fine particle preparation. From a practical aspect, synthesis and application of the nanoparticles is going to exploit new application areas in a broad range from traditional ceramics to some biological processes, which could not be addressed previously with the use of conventional large particles.

The book presented here will become a “bible” not only for understanding the basis to the comprehensive chemistry of the binary rare earth oxides but also for providing the recent advance in feature characteristics of them.

Finally, again, it is a great pleasure for us to publish this book in honor of a great scientist, Prof. Dr. Leroy Eyring, who has dedicated his life for studying the physics and chemistry of rare earth oxides.

Gin-ya Adachi
Nobuhito Imanaka
Zhenchuan Kang

G. Adachi et al. (eds.), Binary Rare Earth Oxides, 257.

5. PHYSICAL AND CHEMICAL PROPERTIES OF RARE EARTH OXIDES

N. IMANAKA
Department of Applied Chemistry, Faculty of Engineering,
Osaka University
2-1 Yamadaoka, Suita, Osaka 565-0871, Japan

5.1. ELECTRICAL PROPERTIES

The conductivities (σ) of the rare earth sesquioxides decrease with the atomic number (Z) increase as tabulated in Table 5-1 [1] (Oxygen pressure (Po_2): 0.2 atm) with showing a p-type conduction. A break appears at 550-600˚C (T_B) in the relationship of log σ vs. 1/T for most of the rare earth oxides. In contrast, the increase in the activation energy with an increase in Z was observed simultaneously accompanying a decrease in conductivity. A considerable increase in ionic conductivity was observed for rare earth oxides at higher temperatures above the inflection point (T_B) mentioned. For example, the ionic transference number (t_i) is estimated to be 0.5 for Gd_2O_3 at 1100˚C and Po_2 of 10^{-3} atm, and the value of 0.5 for Dy_2O_3 at 1100˚C and 6.3 x 10^{-5} atm. The t_i value increases up to 0.9 at 1200˚C and 10^{-7} atm. For Nd_2O_3, the electronic and ionic contributions to electrical conductivity were investigated and from the dependency upon oxygen pressure, it was concluded that the ionic conduction is mainly due to oxygen vacancies.

TABLE 5-1. Electrical Conductivity Data of Rare Earth Sesquioxides (R_2O_3). (Reprinted with permission from ref. 1. Copyright 1970 Academic Press)

R	T_B[a] (˚C)	E_1 (eV) ($T < T_B$)	E_2 (eV) ($T < T_B$)	$\sigma_{400°C}$($\times 10^9$ $\Omega^{-1}cm^{-1}$)	$\sigma_{650°C}$($\times 10^9$ $\Omega^{-1}cm^{-1}$)
La	270	0.7	1.05	230	1700
Pr	320	0.4	0.95	300	3450
Nd	-	-	1.15	25	1450
Sm	560	0.6	1.28	20	880
Eu	570	0.6	1.35	5	150
Gd	560	0.5	1.57	5	130
Tb	280	0.4	0.95	3	200
Ho	575	0.7	1.61	5	160
Yb	605	0.5	7.5:11.61	3	50
Y	-	-	1.10	-	55

[a] T_B is the break temperature in log σ - 1/T plots.

G. Adachi et al. (eds.), Binary Rare Earth Oxides, 111–133.

The electrical conductivity of some rare earth oxides (Sm_2O_3, Eu_2O_3, and Yb_2O_3) is also shown in Fig. 5-1 (Oxygen pressure: 0.2 atm) [1]. In general, the conductivity of rare earth oxides is low and especially low for the heavier rare earth oxides. The conductivity reduces with the increase of atomic number of rare earths for Sm, Eu, and Yb and the activation energy above the break temparature (T_B) increases. The onset of ionic conductivity results in the abrupt change in the slope of the conductivity vs. temperature plot at T_B. Rare earth sesquioxides belong to mixed conductors where main conducting species is electron with some contribution by ion. The conductivities of the rare earth oxides are reported to be in the region between 10^{-9} and 10^{-1} ohm^{-1} cm^{-1}.[1] Rare earth oxides with the composition of LnOx ($1.50<x<1.75$) are p-type semiconductors. By measuring Seebeck coefficient in the temperature range from 400-800˚C, rare earth oxides are found to be p-type semiconductors except for praseodymium. In contrast, the conduction becomes n-type characteristics above that composition and up to LnO_2. For LnOx ($x>1.5$), the extra oxygen occupies a lattice site in the oxides and as a result of it, holes (p-type conduction) appear. On the contrary, for the composition close to LnO_2, most of the cations are Ln^{4+} accompanying small amount of Ln^{3+}, the charge carriers are electron with showing a n-type conduction. A change from p- to n-type conducting characteristics is also observed at a composition of $PrO_{1.72}$ (Pr_7O_{12}) as the oxygen content increases in Pr-O system. In addition, this behavior of the positive to negative change was observed in the sign of Seebeck coefficient at $PrO_{1.72}$ [2].

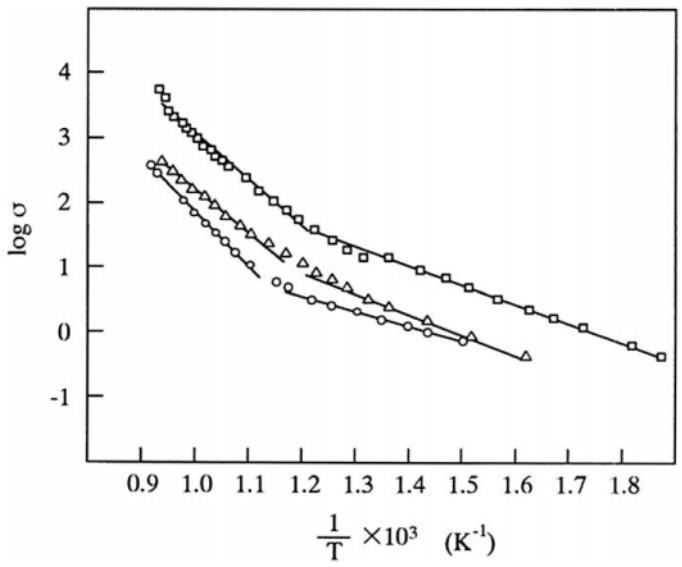

Figure 5-1. Plots of electrical conductivity ($m\Omega^{-1}\cdot cm^{-1}$) against the reciprocal of absolute temperature (pO_2 = 0.2 atm) squares, Sm_2O_3 (□); triangles, Eu_2O_3 (△); and circles, Yb_2O_3 (○). (Reproduced with permission from ref. 1. Copyright 1970 Academic Press.)

The electrical conductivity of Pr and Tb oxides is the highest and the activation energy for conduction is the lowest at x=1.75, whether phase is ordered of narrow homogeneity or disordered. The main reason for the maximum conductivity at x=1.75 is attributed to the stoichiometry (Ln^{3+} and Ln^{4+} concentrations) and not to the defect structure. From a consideration of the nonstoichiometric rare earth oxides to be electron hopping, the behavior that the conductivity in LnOx becomes the highest at around x=1.75 can be calculated as is observed experimentally [1]. Among the various LnOx systems, the composition of $LnO_{1.75}$ seems to hold a random distribution of both Ln^{3+} and Ln^{4+} ions in such a way to show a maximum electronic disorder. The conduction mechanism has been interpreted in terms of both the hopping process [3] and intermediate polaron theory [4]. In the rare earth sesquioxide series, the predominant defects are expected to be fully ionized cation vacancies.

The compounds of higher rare earth oxides are complex and very sensitive to ambient conditions. Hopping-type electron conduction is predominantly occurred for the mixed valence higher oxides. The minimum resistivity is observed for R_7O_{12} (τ phase, $PrO_{1.72}$) which phase is well known to appear over a narrow composition region. The conductivity of the Pr_7O_{12} phase is less dependent on oxygen pressure, since the oxide is compositionally stable in a much wider temperature range.

As EuO has both intrinsic scientific interest and potential commercial value, this lower oxide has been most extensively investigated among rare earth compounds. Electrical conductivity of EuO (I, II, III shown in Fig. 5-2 [5]) shows similar insulating behavior. The most spectacular effect of the oxygen vacancies is the phenomenon appears between 69 and 49 K where the conductivity increases by 13 orders of magnitude. This insulator-metal transition is the characteristics of samples obtained from Region IV (Fig. 5-2). In Region V, the EuO conductivity becomes metallic at high temperatures as well as at low temperatures.

In contrast, the electrical conductivity of Ce_2O_3 shows a clear break at approximately 950˚C in the relationship of logarithmn of conductivity vs. 1/T. The conduction mechanism seems to be similar to that for mixed valence oxides by a kind of hopping-type conduction in the lower temperature region. On the contrary, the conduction in Ce_2O_3 resembles to other stable rare earth oxides in the higher temperature range.

Electrical transport properties of non-stoichiometric oxides of yttrium, praseodymium, and gadolinium oxides have been also reported. In this paper [6], the temperature dependence of the resistivity is shown as depicted in Fig. 5-3. From the figure, it becomes clear that they can be divided into two regions. One is below 200°C, where the resistivity remains almost unchanged and showing an insulating behavior. The other is higher than 200°C, where the resistivity decreases with the increase in temperature, showing a semi-conducting behavior. They suggest that the conductivity enhancement at temperatures higher than 200°C is attributed to the non-stoichiometry and the creation of quasi-free electrons. From their measurements

above 727°C, the conductivity of yttrium oxide is higher than that of praseodymium and gadolinium oxides, suggesting that the concentration of quasi-free electron in yttrium oxide is greater than that of praseodymium and gadolinium oxides and the concentration enhances with the high temperature above 727°C.

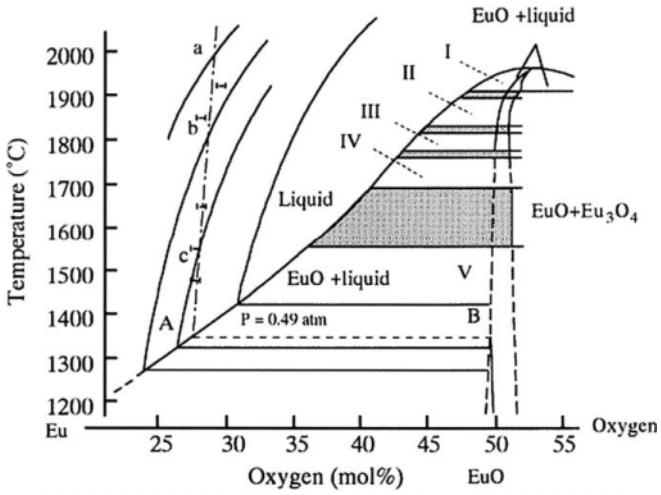

Figure 5-2. The EuO region of the Eu-O phase diagram. (Reproduced with permission from ref. 5. Copyright 1972 Pergamon Press.)

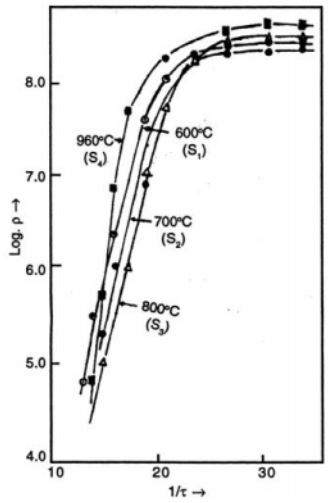

Figure 5-3. Temperature dependence of the electrical resistivity of yttrium oxide. (Reproduced with permission from ref. 6. Copyright 2000 Indian Association for the Cultivation of Science.)

By studying the oxidation of Gd and Dy at oxygen pressure between $10^{-0.3}$ and $10^{-14.5}$ atm and temperatures from 727 to 1327°C, both semiconducting and ion-conducting domains are recognized in the sesquixides fromed. Especially, at low oxygen pressure, the oxides are mainly ionic conductors and the electronic conductivity is estimated from the metal oxidation rates to the order of 10^{-6} to 10^{-7} $S \cdot cm^{-1}$. The dependence of the oxygen diffusion coefficients in the oxides calculated on temperature is plotted in Fig. 5-4 [7]. The conducting characteristics of rare earth oxides (Gd_2O_3, Dy_2O_3, Sm_2O_3, and Y_2O_3) between electronic and ionic has also been studied by Tare and Schmalzried [8].

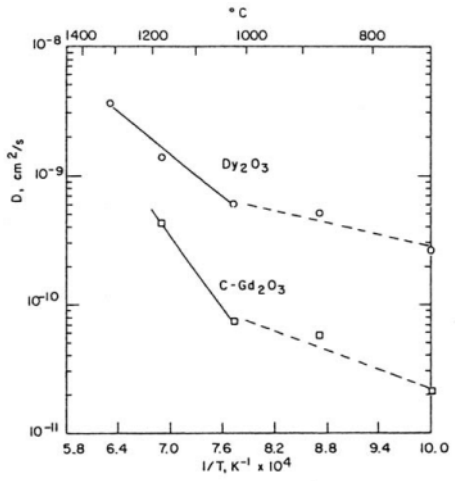

Figure 5-4. Temperature dependence of oxygen diffusion coefficients ($PO_2 > 10^{-10}$ atm) in Dy_2O_3 and cubic (*C*-type) Gd_2O_3. (Reproduced with permission from ref. 7. Copyright 1974 American Ceramic Society.)

Electrical properties of thin rare earth oxide film have also been studied. The conductivity of praseodymium thin film oxide was measured as a function of temperature and oxygen pressure [9]. The oxide film was found to act as a p-type conduction at temperatures high than 630°C and was a n-type semiconductor at the temperatures of 400-630°C. Thermally evaporated Eu_2O_3 thin film on a glass substrate is also obtained in an amorphous state. From the measurement of frequency dependence of the ac conductance, the predominant mechanism could be ascribed to the result of a hopping type. The ac conductivity measurements were also carried out for thin film of Sc_2O_3 at temperatures between 4 and 295 K [10]. The conductivity was found to obey the relationship of $\sigma_1(\omega)=A\omega^s$ which depends on frequency and s is dependent on temperature and is a little lower than unity. By using a classical hop mechanism between randomly distributed localized states, a model was proposed and applied to scandium oxide with the assumption that the localized states are caused by lattice vacancies. The model is expected to be

applicable for situations where site potentials are similarly distributed. The characteristics of thin films of various rare earth sesquioxides were investigated by Gasgnier [11].

Generally, the density of vacant site is high in the deposited films. This facilitates the atom migration through vacancies, and results in a low activation energy. In the case for Eu_2O_3, the conduction is reported to occur both oxide anion and electron hopping from Eu^{2+} to Eu^{3+} ions [12]. The rare earth oxide films of scandium, yttrium, and lanthanum to lutetium were obtained by evaporating of the rare earth metal as a film under vacuum and followed by oxidation. The oxide films show insulating characreristics. The electrical resistivity was higher than 10^{12} Ω·cm [13]. A similar deposition technique was also applied for Er_2O_3 and the resistivity was about 10^{10} Ω·cm, estimated from the ohmic character region [14].

Praseodymium and terbium oxides were found to show semiconducting characteristics and Ce, Nd, Eu, Gd, Dy, Ho, Er, Tm, Yb and Lu oxides were dielectrics [15]. Oxide ion conductivity is also appreciably observed in these oxides. Dielectric properties of Dy_2O_3 [16-18], Yb_2O_3 [19], Dy_2O_3 and Yb_2O_3 [20], Er_2O_3 [21], and Nd_2O_3 [22] have also been studied and reported. Details are described in the papers.

As described above, for the rare earth oxides, the dielectric constants are available from some experimental data and plotted as a function of the atomic number of the rare earth ions in Fig. 5-5 [23]. From the deduced linear correlation, the missing data can be obtained and the results are tabulated in Table 5-2. This method is effective for the determination of the properties of crystals not yet obtained. However, it should be mentioned here that the present method is applicable only to the crystals showing a uniform crystal symmetry.

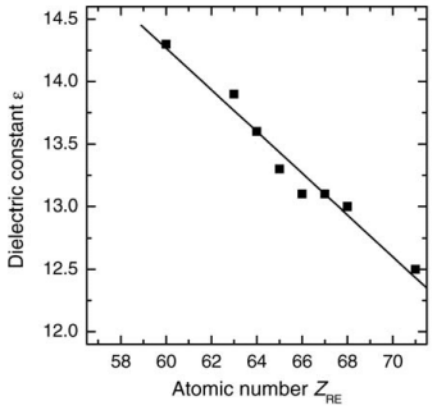

Figure 5-5. Dielectric constants of rare-earth oxides RE_2O_3 (RE = Lu, Er, Ho, Dy, Tb, Gd, Eu, and Nd) as a function of the rare-earth atomic number. (Reproduced with permission from ref. 23. Copyright 2000 Institute of Physics and IOP Publishing Ltd.)

TABLE 5-2. Dielectric constants ε of rare-earth oxides RE_2O_3; comparison between experimental values and data derived on the basis of the linear model discussed here. (Reprinted with permission from ref. 23. Copyright 2000 IOP Publishing Ltd.)

Oxide	Z_{RE}	ε_{exp}	ε_{calc}
La_2O_3	57	-	14.77
Ce_2O_3	58	-	14.60
Pr_2O_3	59	-	14.43
Nd_2O_3	60	14.3	14.27
Pm_2O_3	61	-	14.10
Sm_2O_3	62	-	13.93
Eu_2O_3	63	13.9	13.77
Gd_2O_3	64	13.6	13.60
Tb_2O_3	65	13.3	13.43
Dy_2O_3	66	13.1	13.27
Ho_2O_3	67	13.1	13.10
Er_2O_3	68	13.0	12.93
Tm_2O_3	69	-	12.77
Yb_2O_3	70	-	12.60
Lu_2O_3	71	12.5	12.43

Very thin dielectric layers are increasingly requested on semiconductors in the nano-scale device technology. One of the solutions is to identify a new insulating material with a dielectric constant of high dielectrics to replace SiO_2 gate oxides. However, in many cases, there appears an interfacial SiO_2 layer at least 1 nm in thickness is inevitable. Among various metal oxide candidates for dielectric materials, rare earth oxides are attractive from the view point of thermodynamic energy and a high conduction band offset (higher than 2 eV). As the rare earth oxides, Gd_2O_3 and Y_2O_3 were prepared in both crystalline and amorphous phases and their properties as the new gate dielectrics for Si was investigated [24]. Since Y_2O_3 seems to be better than Gd_2O_3, due to its higher dielectric constant in comparison with that of Gd_2O_3 and also the absence of magnetic ion in the oxide. As one of their critical tests for the dielectrics, the thermal stability to the high temperature as high as 950^{o}C was investigated. Whether the heat treatment was processed or not, very little difference in leakage was observed, indicating that the stability of the Y_2O_3 film is demonstrated. Amorphous Gd_2O_3 also shows the similar result. This high thermal stability of these dielectrics offers another attractive properties to be considered for application.

New dielectric materials should show a satisfactory performance in high breakdown strength, low leakage-current and also thermodynamically high stability on Si surface at temperature over 1000^{o}C so as not to form silicides and silicates. Among various high relative dielectric (κ) gate materials, rare earth oxides are focussed, especially, high thermodynamic properties and high conduction band

offset higher than 2 eV. Among rare earths oxide series, Pr_2O_3 film in hexagonal form shows an advanced merit in its point of leakage-current densities compared with other high-κ films [25]. The hexagonal Pr_2O_3 film also shows a high thermal stability after a post-annealing process and no degradation occurs in its morphologies. Since this high-κ Pr_2O_3 thin film can be fabricated by inexpensive and simple way and proposes a new potential fabrication.

The thin film of high-κ praseodymium and lanthanide oxides (with starting target of Sm_2O_3, Tb_4O_7, Er_2O_3, and Yb_2O_3) was prepared by Pulsed Laser Deposition method on p-Si(100) [26]. By heating above 400°C, crystallinity and roughness of the deposited film were improved. Lanthanoid oxides have been attracted recently, since very thin thickness of amorphous oxides with reasonably thin SiO_2-equivalent oxide thickness (EOT) can be obtained. The relationship between leakage current at 1V and EOT is presented in Fig. 5-6. The difference in the leakage current in those lanthanide oxides is not significant. However, among them, it becomes clear that the PrOx and YbOx films show a low leakage current, suitable for the high-κ oxide.

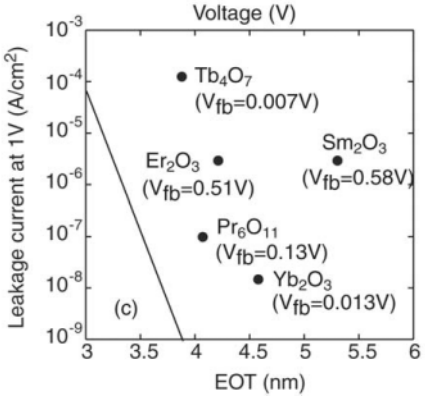

Figure 5-6. The relationships of leakage current and EOT. Solid line in (c) is the calculated direct tunneling current of p-Si/SiO_2/metal structure. (Reproduced with permission from ref. 26. Copyright 2003 The Japan Society of Applied Physics)

Lanthanum oxide thin film was grown on Si substrates by the metall-organic chemical vapor deposition (MOCVD) method (400-650°C) [27]. Thin silicon oxynitride layer on the Si substrate functions well to suppress the interfacial reaction between lanthanum oxide and Si and results in the increase in the dielectric constant of deposited lanthanum oxide. The formed oxynitride layer is also effective in decreasing the leakage current .

During the exploring suitable gate dielectrics, various up to date analyses such as STEM, XPS etc. have been carried out. One example is the report on Y_2O_3 and Gd_2O_3 [28].

Also, dielectric materials, especially, during the exposure to the atmosphere, absorb water and OH leads to detrimental interface reactions and water absorption and interface reactivity of yttrium oxide gate dielectrics on silicon was investigated. From the infrared absorption analysis, water vapor was significantly absorbed in the atmosphere. Similar oxidation are expected other high-κ materials while the rate of OH absorption is expected to depend on the deposition process and their thermal history [29].

Structure factor for small single crystals of C-type rare earth oxides of Y_2O_3, Dy_2O_3, and Ho_2O_3 was investigated from the synchrotron X-radiation point of view [30]. Approximate symmetry in the deformation electron density ($\Delta\rho$) around a rare earth atom with pseudo-octahedral oxygen coordination is similar to the cation geometry. Interactions appeared between heavy rare earth atoms show a pronounced effect on the $\Delta\rho$ map. The electron-density symmetry around second rare earth atom is also influenced appreciably by cation-anion interactions and the oxides magnetic properties also reflect this complexity.

New calculation was suggested to include the possibility of subshell contributions and effective electron numbers are derived for all the ions including rare earths whose polarizabilities are experimentally published [31]. They suggest that, in the case for rare earth ions, probably more than one contributing electron subshell appears. From Table 3, it becomes clear that as the number of 4f electrons increases from zero (La^{3+}) to 14(Lu^{3+}), both the polarizability and the effective number of electrons decrease monotoneously (See Table 5-3 and Fig. 5-7)).

TABLE 5-3. Ion polarizability data—effective number of electrons. (Reprinted with permission from ref. 31. Copyright 1998 IOP Publishing Ltd.)

Ion	Modified crystal radius r (Å)	r^2 (Å^2)	Pol. α_D (Å^3)	Effective number of electrons	Electronic configuration
La^{3+}	1.232	1.518	6.07	17	$4d^{10}5s^25p^6$
Ce^{4+}	1.07	1.145	3.94	14.63	$4d^{10}5s^25p^6$
Ce^{3+}	1.21	1.464	6.15	17.86	$4f^15s^25p^6$
Pr^{3+}	1.19	1.416	5.32	15.97	$4f^25s^25p^6$
Nd^{3+}	1.183	1.399	5.01	15.23	$4f^35s^25p^6$
Sm^{3+}	1.158	1.341	4.74	15.03	$4f^55s^25p^6$
Eu^{3+}	1.147	1.316	4.53	14.64	$4f^65s^25p^6$
Eu^{2+}	1.37	1.877	4.83	10.94	$4f^75s^25p^6$
Gd^{3+}	1.138	1.295	4.37	14.35	$4f^75s^25p^6$
Tb^{3+}	1.123	1.261	4.25	14.33	$4f^85s^25p^6$
Dy^{3+}	1.112	1.237	4.07	13.99	$4f^95s^25p^6$
Ho^{3+}	1.101	1.212	3.97	13.93	$4f^{10}5s^25p^6$
Er^{3+}	1.09	1.188	3.81	13.64	$4f^{11}5s^25p^6$
Tm^{3+}	1.08	1.166	3.82	13.93	$4f^{12}5s^25p^6$
Yb^{3+}	1.068	1.141	3.58	13.34	$4f^{13}5s^25p^6$
Lu^{3+}	1.061	1.126	3.64	13.74	$4f^{14}5s^25p^6$

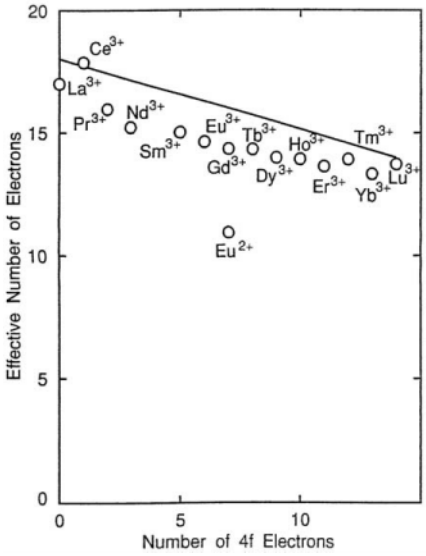

Figure 5-7. Effective number of electrons—rare earth ions—for the significance of the linear interpolation. (Reproduced with permission from ref. 31. Copyright 1998 IOP Publishing Ltd.)

The ionicity of binary oxides is shown as a function of the inverse of cation radius [32]. Table 5-4 presents the ionicity of binary oxides calculated from Eq. (1).

$$\text{Ionicity} = \exp(-0.1131/r_{\text{cation}}^{2}) \qquad (1)$$

TABLE 5-4. The ionicity of binary rare earth oxides calculated via Eq. (1). (Reprinted with permission from ref. 32. Copyright 1999 Elsevier Science B.V.)

Oxide	Ionisity
Sc_2O_3	0.842
Y_2O_3	0.875
La_2O_3	0.917
Pr_2O_3	0.904
Nd_2O_3	0.901
Sm_2O_3	0.893
Eu_2O_3	0.889
Gd_2O_3	0.887
Tb_2O_3	0.877
Dy_2O_3	0.875
Ho_2O_3	0.872
Er_2O_3	0.867
Yb_2O_3	0.858
Lu_2O_3	0.855

Hygroscopic nature of rare earth oxides such as Pr_2O_3, Sm_2O_3, Gd_2O_3 and Dy_2O_3 which are deposited by electron-beam evaporation method, were measured [33]. By investigating the hygroscopicity of rare earth oxides and its effect on electrical characteristics are discussed. Among prepared four oxides, Pr_2O_3 in which Pr has a larger ionic radius and lower electro-negativity shows the highest reactivity with water and easily forms a hydroxide among the oxides. The hygroscopicity gradually decreases from Pr_2O_3 to Dy_2O_3 with the increase of electro-negativity as shown in Fig. 5-8.

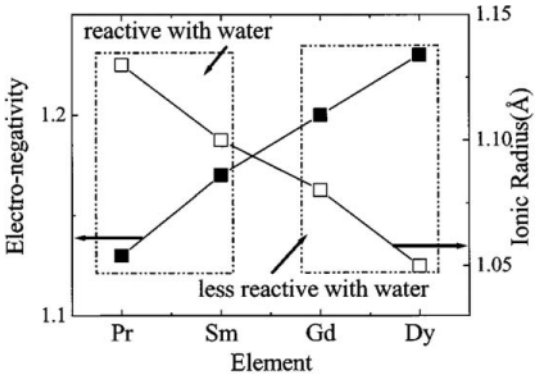

Figure 5-8. Ionic radii and electronegativity of lanthanide metal elements such as Pr, Sm, Gd, and Dy. It is well known that ionic radius decreases and electronegativity increases with atomic number such as from Pr to Dy. (Reproduced with permission from ref. 33. Copyright 2003 American Institute of Physics)

5.2. MAGNETIC PROPERTIES

Magnetic susceptibility (χ) measurements have been extensively carried out on the lanthanide oxides, mainly for the sesquioxides such as Eu_2O_3, Gd_2O_3 and Dy_2O_3 over temperature range from 300 to 1300 K and found to accord satisfactorily with Van Vleck's theory. In the case for Eu_2O_3, a good agreement was assured with Judds' energy levels for free Eu^{3+}. From the magnetic susceptibility measurements of single crystals of Dy_2O_3, Er_2O_3 and Yb_2O_3, the Néel temperatures where antiferromagnetic onset appears, are found to be 1.2, 3.4, and 2.3 K, respectively. In the C-type rare earth sesquioxide, there are two sets of metal atom positions [34] as presented in Fig. 5-9 [35]. Each metal atom is coordinated by six oxygens instead of the eight for the corner cube in fluorite. Two of them are missing across the face diagonal and results in a C_2 site. For the other set of eight, the two oxygen vacancies appear at opposite ends of the body-diagonal to form a S_6 site. The magnetic structure of Er_2O_3 and Yb_2O_3 was investigated. For Er_2O_3, the moments on the C_2 and S_6 sites are determined to be 5.36±0.08 and 6.06±0.23 μ_B, respectively. For Yb_2O_3, the moments corresponding to the same C_2 and S_6 sites are 1.86±0.06

and 1.05±0.06 μ_B, respectively. The magnetic susceptibility of Ce_2O_3 was also studied and clarified that the relationship between $1/\chi$ and T followed the Curie-Weiss law. The results (θ_p=-90 K, μ_{eff}=2.44 B.M.) are close to both theoretical and experimental data in literatures [36].

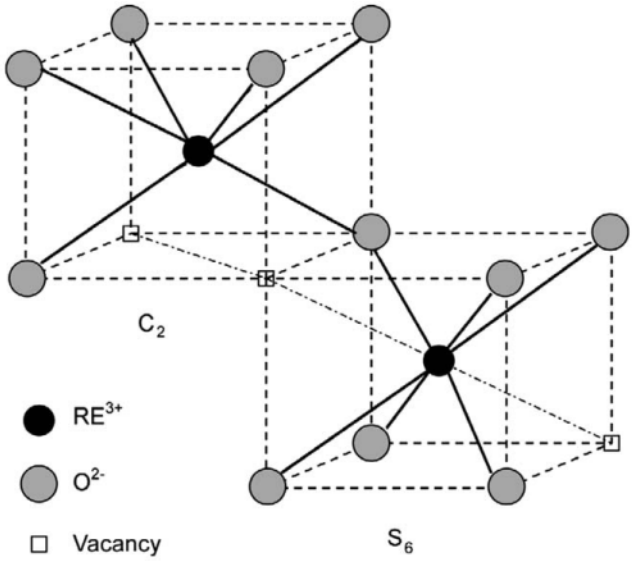

Figure 5-9. Schematic presentation of the two six-coordinated RE sites in cubic C-type rare earth oxides, RE_2O_3. (Reproduced with permission from ref 35. Copyright 2002 Elsevier Science B.V.)

Some magnetic properties of the Sm, Nd, and Pr monoxides obtained at high pressures and temperatures, have been also reported [37]. From the thermal change of the magnetic susceptibilities and the lattice constants for both NdO and PrO, a trivalency of their metal atom state is identified. On the other hand, Sm ion in SmO seems to hold a nearly trivalent state from the crystallographic and X-ray absorption data.

EuO has such unusual characteristics to become ferromagnetic, with a Curie temperature of 77±1 K [38]. Europium in EuO posesses a divalent state contrary to other rare earth monoxides. Eu_3O_4, prepared by the solid state reaction of Eu and Eu_2O_3, is also ferrimagnetic, with a Curie point of 77 K [39]. Each mole of Eu_3O_4 contains one Eu^{2+} and two Eu^{3+} ions. The praseodymium oxides such as $PrO_{1.50}$, $PrO_{1.72}$, $PrO_{1.83}$, and PrO_2 [40], have been reported to show a paramagnetic behavior at higher temperatures and obey the Curie-Weiss law. The magnetic moment obtained was in good agreement with the predicted theoretical value for the free ion. In the case for PrO_2, which is prepared under 200 atm of oxygen pressure, it was reported that an antiferromagnetic ordering is observed with a Néel temperature of 14 K[41], which is contradictory to the report by Kern [40].

Terbium oxides with the composition of Tb_2O_3(the B and the C forms [42]), $TbO_{1.715}$, $TbO_{1.809}$, $TbO_{1.823}$, and TbO_2 have been investigated at the temperatures between 1.4 K and 330 K [43]. Representative characteristics observed are their antiferromagnetic ordering, with Néel temperature of 2 and 7 K, respectively, for the B and C-type sesquioxides and 7, 6, and 3 K for $TbO_{1.715}$, $TbO_{1.823}$, and TbO_2. On the other hand, $TbO_{1.809}$ did not order over 1.4 K. At temperatures appreciably higher than the ordering temperatures, the paramagnetic moment of the terbium is almost equivalent to the expected value from the free ion for above described six kind of terbium oxides. While terbium in TbO_2 has a magnetic moment of 6.25±0.10 μB at 1.5 K, the total moment of Tb in Tb_2O_3 is 4.2 μB at 1.5 K, appreciably below in comparison to the case for the free ion. Neutron diffraction analysis has also been applied to determine the magnetic structures in the rare earth sesqioxides [44, 45].

The ^{17}O NMR chemical shifts of a series of lanthanoid oxides are presented in Table 5-5 [46].While Nd_2O_3 and La_2O_3 are the hexagonal phase with two oxygen sites, which are assigned on the basis of their integrated intensities, all other oxides are cubic and have a single oxygen site. There is a linear relationship between the averaged spin momoents and the ^{17}O NMR chemical shifts of those of the oxides as shown in Fig. 5-10, and the hyperfine interaction constant (a) can be calculated by using the slope of the averaged spin moments vs. the ^{17}O NMR chemical shifts.

TABLE 5-5. Solid State Oxygen-17 NMR Chemical Shifts of Some Lanthanide Oxides.[a] (Reprinted with permission from ref. 46. Copyright 1992 Elsevier Inc.)

Oxide	Shift (ppm)	Uncertainty (ppm)
La_2O_3	584,[b] 467 [c]	±5
Ce_2O_3	877	±5
Pr_6O_{11}	2190	±100
Nd_2O_3	3040,[b] 1140 [c]	±400
Sm_2O_3	10	±5
Eu_2O_3	-3290	±100
Gd_2O_3	-11400 [d]	±1000
Dy_2O_3	-8800 [d]	±1500
Er_2O_3	-6600 [d]	±1000
Tm_2O_3	-4450	±200
Yb_2O_3	-1670	±100
Lu_2O_3	305	±5

[a] In parts per million from an external standard of tap water (IUPAC scale).
[b] Tetrahedrally coordinated site.
[c] Octahedrally coordinated site.
[d] Estimated from static spsctra.

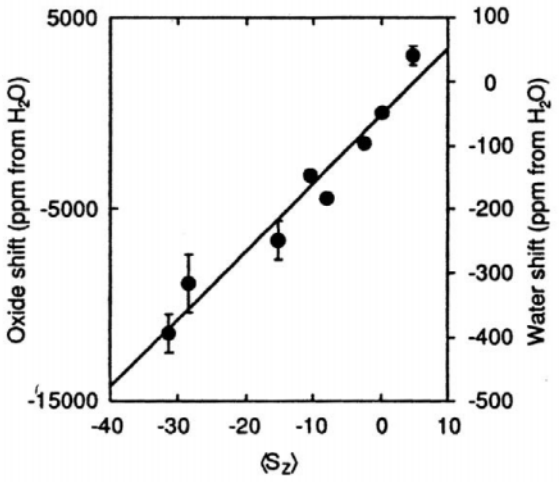

Figure 5-10. Plots of the ^{17}O NMR chemical shifts for solid lanthanide oxides as a function of $<S_z>$, the calculated spin moment. (Reproduced with permission from ref. 46. Copyright 1992 Elsevier Inc.)

5.3. SPECTROSCOPIC PROPERTIES

All the stoichiometric oxides appear white or light pastel color except for PrO_2 and TbO_2 which are in black or reddish-brown color. The nonstoichiometric oxides such as CeO_x, PrO_x, and TbO_x are dark bluish, black, and dark brown, respectively. The color of the oxides varies distinctly with the deviation from stoichiometric ratio except for PrO_2 and TbO_2. The colors of the substoichiometric sesquioxides exist all dark. Some optical characteristics have been reviewed by Eyring [34] and Röhler [47]. Absorption spectrum from the UV down to the near IR has been investigated for some praseodymium oxides (Pr_2O_3-PrO_2) [48]. The spectra of the oxides changed in a regular manner with an increase of the oxygen content which is in good accordance with the proposed phase relationship. The oxygen-rich EuO samples were also studied from infrared spectra and it is clear that it contains Eu_3O_4 as a secondary phase and Eu^{3+} appears in the solid solution [5]. The IR absorption decreased and then enhanced by increasing the Eu-metal in the starting composition. The minimum point in the IR absorption is expected to appear from the stoichiometric EuO. However, due to the excess Eu, oxygen-vacancies were formed and a new absorption peak recognized.

The diffuse reflectance spectra of eleven rare earth sesquioxides have also been applied for identification purpose [49]. Nondestructive qualitative analysis of trivalent rare earth ions can be performed with the spectra in the near infrared region. Because there is no partially filled f shells in La_2O_3 (f_0 electronic configuration) and Lu_2O_3(f_{14} configuration), no absorption is expected in the region investigated.

For EuO single crystal, a remarkable change was observed in the position and sharpness of the transmission edge in the transmission of 0.9-2.7 mm in wavelength as each condition was changed in the temperature region between 30 and 293 K and magnetic fields up to 2.7 kOe. Optical absorption was measured for cerium oxide, praseodymium oxide by Haensel et al. [50] in the extreme ultraviolet region by using synchrotron radiation (light source: the 7.5 GeV electron synchrotron DESY). The predominant part of the absorption is attributed to the transitions from the 4d level of the rare earths. The absorption spectra of Ce and Ce-oxide indicate a distinctly different in its character, while the absorption spectra of Pr and Nd are very similar to those metals and their oxides.

The films of Pr oxides exhibit transparent characteristics irrespective of the temperature deposited whether it is at room or higher temperatures. The transmittance of the Pr-O films was high about 90 % and sometimes it is as high as 97 % in the red region. The transparent nature indicates that the absorption edge appears in the UV region. The optical energy band gap (E_{opt}) was identified to be 3.4 eV from the relationship between absorption coefficient and incident energy. The value was in good accordance with the approximate value obtained by the resistance variation with temperature [51].

For the investigation of the kinetics and thermodynamics of intermediate phases of rare earth oxides and photochemical reactions of the surface of rare earth oxides [52], it is reported that photoacoustic spectroscopy (PAS) technique is effective enough. Some information on the lattice structure of powder grains can be attained from the spectra. Raman and resonance Raman spectroscopy were also investigated on rare earth oxides of Eu_2O_3, Dy_2O_3, and Tm_2O_3 [53].

Rare earth oxides are also useful for various optical and electronic applications. Cerium oxide has been used as a gate insulator. In addition, since CeO_2 has a high dielectric constant of ca. 26, it can be applicable stable capacitors with small dimension such as the storage capacitor in the dynamic random access memory devices. Some spectroscopic characterization was done for the film form of CeO_2 prepared by using rf magnetron sputtering method in various oxygen-argon gas flow ratios. Details are described in Ref. 54.

A new method for the synthesis of luminescent nano-sized particles was reported [55]. Ultrafine, equiaxed and monodisperse particles of rare earth oxides was obtained with the grain size of 2-5 nm by applying a direct precipitation from high-boiling polyalcohol solutions. The prepared oxides are europium, terbium, and neodymium activated Y_2O_3 and Gd_2O_3. By applying this method, Eu_2O_3, Gd_2O_3 and Nd_2O_3 nanoparticles were also obtainable. Since luminescent nanoparticles are attractive for increasing technological and industrial interest, new technological break through is expected.

The attempt to determine the content of rare earth oxides in the mixtures of La_2O_3, Pr_6O_{11}, and Y_2O_3 was performed [56]. The method applied was conducted using Auger electron spectrometry by utilizing the working curve method. The

experimental determination of the composition was almost equivalent to the results of SIMS and XPS and the Auger electron spectrometry seems to be another determination tool.

High purity rare earth oxides have been extensively applied as the starting materials of various functional materials. The determination of individual rare earths in high purity rare earth oxides is becoming an important but difficult task. Higher order derivative spectrophotometry has been utilized for the simultaneous determination of Dy, Ho, and Er in high purity rare earth oxides [57]. This method is simple and also reliable and it can detect rare earths of 0.001 to 0.2 %. Details are also described in Chapter 8 by Rao.

The Raman spectra of Sc_2O_3, Y_2O_3, Ho_2O_3, and Yb_2O_3 single crystals with C-type cubic strcture was also investigated and refer to Ref. 58.

Because of its potential for laser emission around 1 μm, Yb^{3+} ion spectroscopy has been paid a considerable attention. The main interest of Yb^{3+} ion arises from its simple energy level diagram. There appears no additional manyfold, which is contrary to other trivalent rare earth ions. Absorption and emission spectra for Yb^{3+}-doped Y_2O_3, Lu_2O_3 and Gd_2O_3 single crystals at room temperature are studied. Since Y_2O_3 and Lu_2O_3 hold the same C-type cubic structure, Yb^{3+} similar spectra were observed, in the case for Yb^{3+} in Gd_2O_3, the different spectra were obtained due to its monoclinic structure. The Raman spectrum of single crystal of Lu_2O_3 was firstly assigned [59].

The cubic C-type oxides of R_2O_3 (R=Eu-Lu, as well as Y, In and Sc) are suitable candidates for high efficient luminescence materials due to the extended structural isomorphism of C-type cubic phase. The strength of the crystal field effect calculated, was related to the structural stresses occurred by doping of the host lattice with the Eu^{3+} ion. In the C-type cubic structure, rare earth ions enter into crystallographically non-equivalent sites of six-fold coordination as presented in Fig. 5-9 [35]. One site is the C_2 point symmetry where rare earth ion exists in the center of a distorted cubic lattice with two oxygen vacancies on one face diagonal. The other is S_6 site which possesses inversion symmetry and two oxygen vacancies appears on one body diagonal (See Fig. 5-9). Under broad band UV excitation, an intense red luminescence between 575 and 715 nm was observed for the C-type R_2O_3:Eu^{3+} power samples (R=Gd, Lu, Sc) as shown in Fig. 5-11. The spectra were assigned to be composed of the groups of sharp lines ascribed to transitions from the singlet $^5D_0$ to the crystal field components of the $^7F_{0\text{-}4}$ levels of Eu^{3+} (See Fig. 5-12). The emission can be assigned to originate from a Eu^{3+} ion in a C_2 site, while the exception is the magnetic dipole induced $^5D_0 \rightarrow {}^7F_1$ transition arises from the emission of Eu^{3+} ions in the high symmetry S_6 sites. The crystal field strength parameter Nv increases monotoneously with decreasing ionic radius of the rare earth host cation(R=Gd-Lu, Y, Sc) and In cation (Fig. 5-13 [35]). This result comes from the increased electrostatic effect of the host lattice on the Eu^{3+} ion. Similar study for

the case of the crystal field energy level of Yb^{3+} in the C_2 and S_6 sites of the cubic C-type R_2O_3 was reported in Ref. 60.

In order to detect small deviations from stoichiometric composition, physical properties such as electrical, magnetic, or optical characteristics provide us a valuable information. The measurements of physical properties described above are commonly used with many other systems where variations in stoichiometry appear in compounds as well as with rare earth oxides.

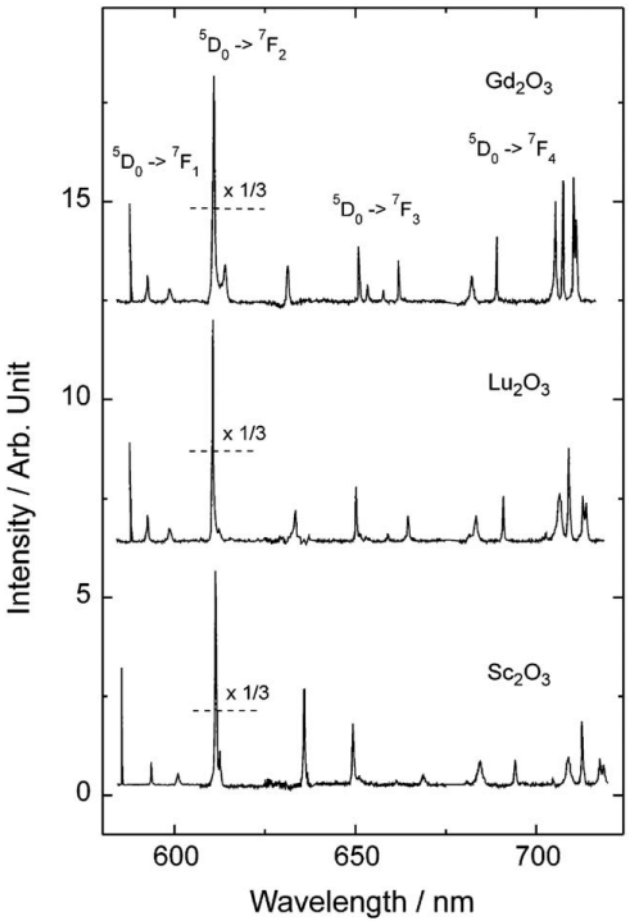

Figure 5-11. Characteristic $^5D_0 \rightarrow {}^7F_{0-4}$ transitions of the Eu^{3+} ion in the RE_2O_3:Eu^{3+} (RE = Gd, Lu, Sc; $X_{Eu} = 0.02$) series. (Reproduced with permission from ref. 35. Copyright 2002 Elsevier Science B.V.)

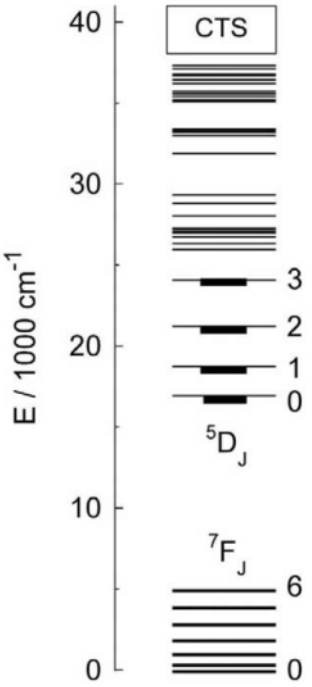

Figure 5-12. Schematic energy level structure of the Eu^{3+} ion in the C_2 site of Gd_2O_3. (Reproduced with permission from ref. 35. Copyright 2002 Elsevier Science B.V.)

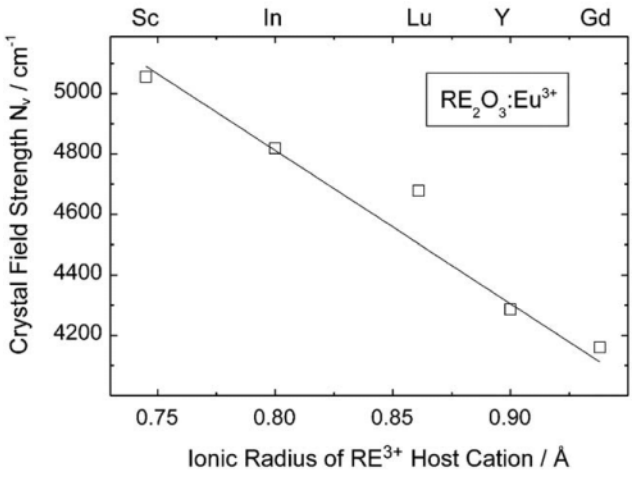

Figure 5-13. Evolution of the crystal field strength parameter N_v in the $RE_2O_3:Eu^{3+}$ series. (Reproduced with permission from ref. 35. Copyright 2002 Elsevier Science B.V.)

5.4. ATOMIC TRANSPORT PROPERTIES

The fluorite-related lanthanide oxides show very unusual diffusion characteristics. Until the temperature of one-half of the melting point (called the Tammann temperature), atomic mobility in the oxide solid does not become significant. In these lanthanide oxides, this value is around 1200˚C [61]. Around the Tammann temperature is achieved, the metal atoms in lanthanide oxides just start to migrate in the oxides as is generally evident by the temperatures required for solid-state reactions. In the lanthanide oxides, the metal substructure is rigid up to the melting temperatures, and temperatures of 1200-1400˚C, which is approximately half of the melting point, are necessary to obtain a reasonable metal atom migration in the oxide lattice. However, in the case for the counter anion of oxide, the oxygen substructure becomes mobile far below the Tammann temperature and in some cases even at the temperatures lower than 300˚C.

In the fluorite-related oxide systems, relatively high mobility of oxygen has been reported and data have suggest that the oxide ionic transference number is almost unity at 971˚C [62]. The oxygen migration is even higher than that in the fluorite structure such as calcia-stabilized zirconia (CSZ). In spite of the high oxide mobility in rare earth oxides at the temperatures as low as 300˚C, the oxides are mostly thermodynamically stable compounds, with melting temperatures in the range around 2500˚C (See Fig. 5-14 [63]). Oxide anion transport rapidly decreases as the atomic number of the lanthanide in the oxide increases. For example, the

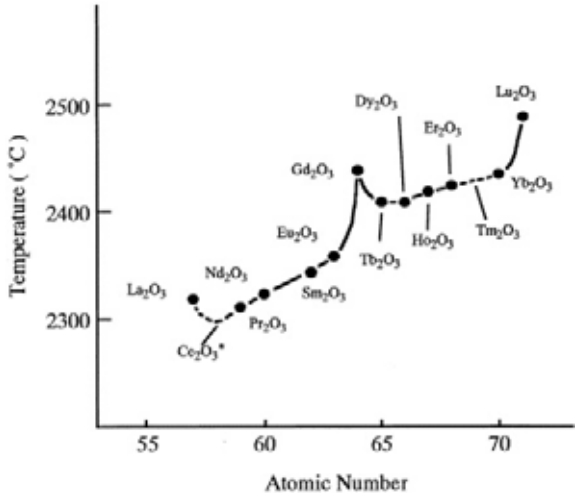

Figure 5-14. The relation between the solidification point and the atomic number of lanthanoid sesquioxides. Ce_2O_3 which is a nonstoichiometric oxide such as $CeO_{1.53\text{-}1.50}$, is designated as Ce_2O_3*. (Reproduced with permission from ref. 63. Copyright 1975 Revue Internationale des Hautes Temperatures et des Refractaires.)

mobility drop between lanthanum and erbium is by a factor of 10^2. Oxygen transport characteristics of rare earth oxides such as Nd_2O_3, Sm_2O_3 and Er_2O_3 were also extensively investigated by Eyring [64]. Relatively high oxygen mobility is reported for the fluorite-related oxides with anion-deficiency. Isomorphs of rare earth oxide of the iota(ι) phase (R_7O_{12}) are belong to this category.

The diffusion of oxygen in monocrystal (nearly single or twinned crystals) of Sc_2O_3, Y_2O_3, Dy_2O_3, Ho_2O_3, Er_2O_3, Tm_2O_3, and Lu_2O_3 was investigated by a thermobalance technique and tabulated in Table 5-6 [65]. The D_o data are the value on the assumption that all unoccupied anion sites are filled with dissolved oxygen ions. In another word, this means that the 16 oxygen ions are dissolved in each unit cell. The values of the activation energy for oxygen diffusion in sesquioxides are also listed in the table.

TPS (Transient Plane Source) technique has been shown to be effective method to measure the thermal conductivity, diffusivity of rare earth oxide powder such as gadolinium oxide, samarium oxide, and yttrium oxide. The details of the measutrement are described in Ref. 66. The experimental results of effective thermal conductivity as well as thermal diffusivity of the above described three rare earth oxides are tabulated in Table 5-7.

TABLE 5-6. Diffusion parameters and activation energy for oxygen diffusion in rare earth sesquioxides. (Reprinted with permission from ref. 65. Copyright 1968 American Ceramic Society.)

Oxide	D_0 ($cm^2 \cdot sec^{-1}$)	E_a ($cal \cdot mol^{-1}$)
Sc_2O_3	7.72×10^{-4}	38300
Y_2O_3	6.06×10^{-6}	19580
Dy_2O_3	1.63×10^{-5}	26240
Ho_2O_3	7.18×10^{-3}	40530
Er_2O_3	1.31×10^{-4}	30120
Tm_2O_3	1.14×10^{-2}	45560
Lu_2O_3	1.88×10^{-4}	29760

TABLE 5-7. Experimental and theoretical values of effective thermal conductivity and thermal diffusivity of different rare earth oxides. (Reprinted with permission from ref. 55. Copyright 1997 Royal Swedish Academy of Sciences.)

			Thermal conductivity $W \, m^{-1} \cdot K^{-1}$			Thermal diffu.
Oxide	Mesh No.	Porosity	λ_{meas}	$(\lambda_{TD})_{meas}$	λ_{theor}	$10^{-6} \cdot m^2 \cdot s^{-1}$
Gd_2O_3	200 – 240	0.58	0.068	0.1937	0.0610	0.130
	240 – 300	0.54	0.069		0.0687	0.132
	above 300	0.51	0.071		0.0750	0.135
Sm_2O_3	200 – 240	0.65	0.064	0.2270	0.0560	0.125
	240 – 300	0.61	0.064		0.0646	0.133
	above 300	0.57	0.072		0.0736	0.139
Y_2O_3	200 – 240	0.53	0.088	0.2262	0.0820	0.130
	240 – 300	0.50	0.088		0.0899	0.139
	above 300	0.46	0.098		0.0996	0.135

In addition, by thermal decomposition of homo-dinuclear complexes of the type of $Ln_2(L)(NO_3)_4\,xH_2O$ (L=Ligand), the rare earth oxides of Ln_2O_3 such as Dy_2O_3 and Eu_2O_3 are obtained. This decomposition method is effective especially in the case of obtaining hetero-dinuclear oxides of the type $Ln'Ln''O_3$ [67].

References

1. G.V.S. Rao, S. Ramdas, P.N. Mehrotra, and C.N.R. Rao, *J. Solid State Chem*., **2**, 377 (1970).
2. K.H. Lau, D.L. Fox, S.H. Lin, and L. Eyring, *High Temperature Science*, **8**, 129 (1976).
3. J.M. Honig, A.A. Cella, and J.C. Cornwell, *Rare Earth Research*, Gordon and Breach, New York, p. 555 (1964).
4. G.V. Chandrashekhar, P.N. Mehrotra, G.V.S. Rao, E.C. Subbarao, and C.N.R. Rao, *Trans. Faraday Soc*., **63**, 1295 (1967).
5. M.W. Shafer, J.B. Torrance, and T. Penney, *J. Phys. Chem. Solids,* **33**, 2251 (1972).
6. M. Saha, R. Kumar, and S. Bhagat, *Indian J. Phys.*, **74A**, 383 (2000).
7. D.B. Basler and M.F. Berard, *J. Am. Ceram. Soc.*, **57**, 447 (1974).
8. V.B. Tare and H. Schmalzried, *Z. Phys. Chem. (NF)*, **43**, 30 (1964).
9. T. Arakawa, A. Kabumoto, and J. Shiokawa, *J. Less-Common Met.*, **115**, 281 (1986).
10. G.E. Pike, *Phys. Rev. B*, **6**, 1572 (1972).
11. M. Gasgnier, *phys. stat. sol. (a)*, **57**, 11 (1980).
12. A.A. Dakhel, *phys. stat. sol. (a)*, **147**, K79 (1995).
13. V.M. Koleshko and N.V. Babushkina, *Thin Solid Films*, **62**, 1 (1979).
14. C.R. Dutta and K. Barua, *Thin Solid Films*, **104**, L69 (1983).
15. L. Eyring, *High Temperature Oxides*, **2**, 41 (1970).
16. A. Goswami and R.R. Varma, *Thin Solid Films*, **28**, 157 (1975).
17. N.C. Mitra and A.L. Bhattacharyya, *phys. stat. sol. (a)*, **90**, 301 (1985).
18. N.C. Mitra and A.L. Bhattacharyya, *phys. stat. sol. (a)*, **88**, 175 (1985).
19. T. Wiktorczyk and C. Wesolowska, *Thin Solid Films*, **71**, 15 (1980).
20. T. Wiktorczyk and C. Wesolowska, *Vacuum*, **37**, 107 (1987).
21. C.R. Dutta and K. Barua, *Thin Solid Films*, **100**, 149 (1983).
22. V.S. Dharmadhikari and A. Goswami, *Thin Solid Films*, **87**, 119 (1982).
23. D. Xue, K. Betzler, and H. Hesse, *J. Phys. Condens. Matter*, **12**, 3113 (2000).
24. J. Kwo, M. Hong, A.R. Kortan, K.L. Queeney, Y.J. Chabal, R.L. Opila, Jr., D.A. Muller, S.N. G. Chu, B.J. Sapjeta, T.S. Lay, J.P. Mannaerts, T. Boone, H.W. Krautter, J.J. Krajewski, A.M. Sergnt, and J.M. Rosamilia, *J. Appl. Phys.*, **89**, 3920 (2001).
25. R.L. Nigro and R.G. Toro, *Adv. Mater.*, **15**, 1071 (2003).
26. S. Kitai, O. Maida, T. Kanashima, and M. Okuyama, *Jpn. J. Appl. Phys.*, **42**, 247 (2003).
27. H. Yamada, T. Shimizu, A. Kurokawa, K. Ishii, and E. Suzuki, *J. Electrochem. Soc.*, **150**, G429 (2003).

28. B.W. Busch, O. Pluchery, Y.J. Chabal, D.A. Muller, R.L. Opila, J.R. Kwo, and E. Garfunkel, *MRS Bull.*, 206 (2002).

29. D. Niu, R.W. Ashcraft, and G.N. Parsons, *Appl. Phys. Lett.*, **80**, 3575 (2002).

30. E.N. Maslen, V.A. Streltsov, and N. Ishizawa, *Acta Cryst.*, **B52**, 414 (1996).

31. N.W. Grimes and R.W. Grimes, *J. Phys. Condens. Matter*, **10**, 3029 (1998).

32. Y.Y. Guo, C.K. Kuo, and P.S. Nicholson, *Solid State Ionics*, **123**, 225 (1999).

33. S. Jeon and H. Hwang, *J. Appl. Phys.*, **93**, 6393 (2003).

34. L. Eyring, *Handbook on the Physics and Chemistry of Rare Earths*, North-Holland, Amsterdam, Vol.3, p 337 (1979).

35. E.Antic-Fidancev, J. Hölsä, and M. Lastusaari, *J. Alloys Comp.*, **341**, 82 (2002).

36. T. Sata and M. Yoshimura, *J. Ceram. Assoc. Jpn*., **76**, 116 (1968).

37. G. Krill, M.F. Ravet, J.P. Kappler, L. Abadli, J.M. Leger, N. Yacoubi, and C. Loriers, *Solid State Commun*., **33**, 351 (1980).

38. B.T. Matthias and R.M. Bozorth, *Phys. Rev. Lett*., **7**, 160 (1961).

39. F.F.Y. Wang, *phys. stat. sol*., **14**, 189 (1966).

40. S. Kern, *J. Chem. Phys.*, **40**, 208 (1964).

41. J.B. MacChesney, H.J. Williams, R.C. Sherwood, and J.F. Potter, *J. Chem. Phys.*, **41**, 3177 (1964).

42. G. Adachi and N. Imanaka, *Chem. Rev.*, **98**, 1479 (1998).

43. J.B. MacChesney, H.J. Williams, R.C. Sherwood, and J.F. Potter, *J. Chem. Phys.*, **44**, 596 (1966).

44. E.F. Bertaut and R. Chevalier, *C. R. Acad. Sci., Paris, Ser. B*, **262**, 1707 (1966).

45. R.M. Moon, W.C. Köhler, H.R. Child, and L.J. Raubenheimer, *Phys. Rev.*, **176**, 722 (1968).

46. S. Yang, J. Shore, and F. Oldfield, *J. Magn. Reson.*, **99**, 408 (1992).

47. J. Röhler, *Handbook on the Physics and Chemistry of Rare Earths*, North-Holland, Amsterdam, Vol.10, p 453 (1987).

48. J.M. Warmkessel, S.H. Lin, and L. Eyring. *Inorg. Chem*., **8**, 875 (1969).

49. W.B. White, *Appl. Spectro*., **21**, 167 (1967).

50. R. Haensel, P. Rabe, and B. Sonntag, *Solid State Commun*., **8**, 1845 (1970).

51. A. Goswami and A.P. Goswami, *Thin Solid Films*, **27**, 123 (1975).

52. J.R. Schoonover, Y-L. Lee, S.N. Su, S.H. Lin, and L. Eyring, *Appl. Spectrosc.*, **38**, 154 (1984).

53. L.A. Tucker, F.J. Carney, Jr., P.McMillan, S.H. Lin, and L. Eyring, *Appl. Spectrosc.*, **38**, 857 (1984).

54. K.B. Sundaram, P.F. Wahid, and O. Melendez, *J. Vac. Sci. Technol.*, **A15**, 52 (1997).

55. R. Bazzi, M. A. Flores-Gonzalez, C. Louis, K. Lebbou, C. Dujardin, A. Brenier, W. Zhang, O. Tillement, E. Bernstein, and P. Perriat, *J. Lumin.*, **102-103**, 445 (2003).

56. K. Nakane, Y. Uwamino, H. Morikawa, A. Tsuge, K. Naganuma, and T. Ishizuka, *J. Elec. Spec. Related Phenom.*, **85**, 193 (1997).

57. M. Anbu, T.P. Rao, C.S.P. Iyer, and A.D. Damodaran, *Chem. Anal.*, **41**, 781 (1996).

58. J. Gouteron, J. Zarembowitch, and A-M. Lejus, *C. R. Acad. Sci. Paris, Ser. C*, **289**, 243 (1979).

59. L. Laversenne, Y. Guyot, C. Goutaudier, M.Th. Cohen-Adas, and G. Boulon, *Opt. Mater.*, **16**, 475 (2001).

60. E. Antic-Fidancev, J. Hölsä, and M. Lastusaari, *J. Phys. Condens. Matter*, **15**, 863 (2003).

61. R.G. Haire and L. Eyring, *Handbook on the Physics and Chemistry of Rare Earths*, North-Holland, Amsterdam, Vol.18, p 413 (1994).

62. F. Millot and P. de Mierry, *J. Phys. Chem. Solids*, **46**, 797 (1985).

63. J.-P. Coutures, R.Verges, and M. Foëx, *Rev. Int. Hautes Temp. Réfract*., **12**, 181 (1975).

64. L. Eyring, *Heterogeneous Kinetics at Elevated Temperatures*, Plenum Press, p. 343 (1970).

65. M.F. Berard, C.D. Wirkus, and D.R. Wilder, *J. Am. Ceram. Soc.*, **51**, 643 (1968).

66. P. Predeep and N.S. Saxena, *Phys. Scripta*, **55**, 634 (1997).

67. P. Guerriero, S. Sitran, and P.A. Vigato, *Inorg. Chim. Acta*, **171**, 103 (1990).